Western Australian School of Mines

Department of Mining Engineering and Surveying

Near-Field Blast Vibration Monitoring and Analysis for Prediction of Blast Damage in Sublevel Open Stoping

Kelly Gene Fleetwood

This thesis is presented for the Degree of
Doctor of Philosophy
of
Curtin University of Technology

December 2010

Declaration

To the best of my knowledge and belief this thesis contains no material previously published by any other person except where due acknowledgment has been made.

This thesis contains no material which has been accepted for the award of any other degree or diploma in any university.

Signed: 

Date: 23 November, 2010

ABSTRACT

The work presented in this thesis investigates near-field blast vibration monitoring, analysis, interpretation and blast damage prediction in sublevel open stoping geometries. As part of the investigation, seven stopes at two Australian sublevel open stoping mines were used as case studies. The seven stopes represented significant ranges in stope shapes, sizes, geotechnical concerns, extraction sequences, stress conditions, blasting geometries and rock mass properties.

The blast damage investigations at the two mine sites had three main components. The first component was rock mass characterisation, which was performed using static intact rock testing results, discontinuity mapping, mining-induced static stress modelling and geophysical wave propagation approaches. The rock mass characterisation techniques identified localised and large-scale variations in rock mass properties and wave propagation behaviours in relation to specified monitoring orientations and mining areas. The other components of the blast damage investigations were blast vibration monitoring and analysis of production blasting in the seven stopes and stope performance assessments.

The mine-based data collection period for the case studies lasted from January, 2006 to February, 2008. A key element of the data collection program was near-field blast vibration monitoring of production blasts within the seven study stopes. The instrumentation program consisted of 41 tri-axial accelerometers and geophone sondes, installed at distances from 4m to 16m from the stope perimeters. A total of 59 production firings were monitored over the course of the blast vibration monitoring program. The monitoring program resulted in a data set of over 5000 single-hole blast vibration waveforms, representing two different blasthole diameters (89mm and 102mm), six different explosive formulations and a wide range in charge weights, source to sensor distances, blasthole orientations and blasting geometries.

The data collected in the blast vibration monitoring program were used to compare various near-field charge weight scaling relationships such as Scaled Distance and Holmberg-Persson prediction models. The results of these analyses identified that no single charge weight scaling model could dependably predict the measured near-field

peak amplitudes for complex blasting geometries. Therefore, the general form of the charge weight scaling relationship was adopted in conjunction with nonlinear multi-variable estimation techniques to analyse the data collected in the study stopes and to perform forward vibration predictions for the case studies.

Observed variations in the recorded near-field waveforms identified that instantaneous peak amplitude such as peak particle velocity (PPV) did not accurately describe the characteristics of a large portion of the data. This was due to significant variations in frequency spectra, variable distributions of energy throughout the wave durations and coupling of wave types (e.g. P- and S-wave coupling). The wave properties that have been proposed to more accurately characterise complex near-field vibrations are the total wave energy density ($ED_{W\text{-}tot}$), stored strain energy density ($ED_{W\text{-}SS}$) and the wave-induced mean normal dynamic strain ($\varepsilon_{W\text{-}MN}$). These wave properties consider the activity of the blast-induce wave at a point in the rock mass over the entire duration instead of the instantaneous amplitude.

A new analytical approach has been proposed to predict blast-induced rock mass damage using rock mass characterisation data, blast vibration monitoring results and rock fracture criteria. The two-component approach separately predicts the extent of blast-induced damage through fresh fracturing of intact rock and the extent from discontinuity extension. Two separate damage criteria are proposed for the intact rock portion of the rock mass based on tensile and compressive fracture strain energy densities and compressive and tensile fracture strains. The single criterion for extension of existing discontinuities is based on the required fracture energy density to activate all macro-fractures in a unit volume of the rock mass.

The proposed energy-based criteria for intact rock fracture and extension of discontinuities integrate strain rate effects in relation to material strength. The strain-based criterion for intact rock fracture integrates the existing mining-induced static strain magnitudes. These factors have not been explicitly considered in existing empirical or analytical blast damage prediction models. The proposed blast damage prediction approach has been applied to two stopes during the two mine site case studies.

ACKNOWLEDGEMENTS

Many people have contributed to the completion of this thesis. I would like to acknowledge those who provided support financially, intellectually, morally, spiritually and most importantly, genetically.

I would like to thank members of the Western Australian School of Mines (WASM) Rock Mechanics Research Group, without whom this thesis would not have been possible. Firstly, I would like to recognise the supervisory and financial contributions of Professor Ernesto Villaescusa, who served as the project supervisor. The confidence that Professor Villaescusa showed in my ability to manage the many facets of this intensive project granted me the unrestricted freedom to pursue my ideas and interact freely with the sponsoring mine sites. I would hope that I have satisfied and surpassed his expectations. Hearty appreciation goes to Dr. Alan Thompson, associate supervisor, for the many hours of discussion on wave dynamics, stress and strain and any subject I seemed to be struggling with at the time. Dr. Thompson's infinite patience, meticulous proofreading ability and willingness to offer support in times of intellectual crisis were always appreciated. I would like to recognise Mr. Chris Windsor, who provided a constant source of moral support and the willingness to discuss all matters which would ultimately be well over my head. Mr. Peter Cepuritis provided invaluable support in software applications and data management, and made the process of struggling through the PhD program more bearable as a peer combatant in the field of rock mechanics research. I would also like to give my thanks to all of the WASM academics, staff, IT department and fellow post-graduate students with whom I have had the privilege of being associated.

Appreciation is expressed to those providing financial and operational support for this project, including the CRCMining, the Barrick Kanowna Belle Gold Mine and the BHP Billiton Cannington Mine. Without the financial support and site access offered by Kanowna Belle and Cannington, this project would have never materialised. Special appreciation goes to the following mine site personnel for their support during and after data collection at the mine sites:

- Dean O’Brien, Ronald Lachenicht, Richard Varden and the charge-up crews at Kanowna Belle
- Jody Todd, Jianping Li, Shay Carroll, the Geotechnical and Mining Engineering departments and mine site charge-up at the Cannington Mine

The contributions of Dr. John Heilig and Mr. Ian Focks are recognised for their initial and continued support in the supply and manufacture of blast vibration monitoring transducers and equipment. Their vast experience and willingness to exchange ideas were greatly appreciated.

Last but not least, I would like to thank my parents, Thomas D. and Brenda Fleetwood, for instilling in me the genetic gifts of patience, providence, steadfast stubbornness, curiosity and the work ethic of a Himalayan Sherpa. I hope I have made them proud and I thank them for their many sacrifices over the years.

AUTHOR'S STATEMENT OF PREVIOUS PUBLICATION

Some results of data analyses and approaches discussed in this thesis have been previously published by the author during the time of thesis preparation. No references to these publications have been made in the body of the thesis, as the ideas and analysis techniques were developed as part of the thesis background work by the author prior to publication. The following list details the previous publications by the author at the time of submission of this thesis.

Fleetwood, KG and Villaescusa, E (2010), 'Blast Vibration Monitoring and Elastic Wave Reflection Models to Assess Blast-Induced Damage to Mine Infrastructure – An Underground Case Study', Proceedings of the International Symposium on Mine Planning and Equipment Selection, Fremantle, Western Australia (in print).

Fleetwood, KG and Villaescusa, E (2010), 'Void and Initiation-Corrected Distance (VICD) for Use in Blast Vibration Scaling', Proceedings of the 36th Annual Conference on Explosives and Blasting Technique (CD-ROM), International Society of Explosives Engineers, Cleveland, OH, USA.

Fleetwood, KG, Villaescusa, E, Li, J and Varden, R (2009), 'Comparison of Traditional Near-field Vibration Prediction Models with Three-dimensional Vibration Scaling and Blast Wave Energy', Proceedings of the 9th International Symposium on Rock Fragmentation by Blasting, Fragblast 9, Granada, Spain, pp. 579-588.

Fleetwood, K, Villaescusa, E and Li, J (2009), 'Limitations of Using PPV Damage Models to Predict Rock Mass Damage', Proceedings of the 35th Annual Conference on Explosives and Blasting Technique (CD-ROM), International Society of Explosives Engineers, Cleveland, OH, USA.

Fleetwood, K, Villaescusa, E, Lachenicht, R and Todd, J (2008), 'Underground Blast Monitoring and Rock Mass Anisotropy', Proceedings of the 34th Annual Conference on Explosives and Blasting Technique, New Orleans, Louisiana, USA, pp.341-353.

Fleetwood, K, Villaescusa, E, Lachenicht, R and Todd, J (2008) 'Using Results of Underground Blast Monitoring to Indicate Rock Mass Anisotropy at Two Australian Underground Mines', Australasian Mine Safety, Vol.2, No.3, Australasian Publishing Resource Service, Adelaide, SA, Australia, pp. 76-79.

Fleetwood, KG, Villaescusa, E, Lachenicht, R and Todd, J (2008), 'Using Underground Blast Monitoring to Indicate Rock Mass Anisotropy at Two Australian Underground Mines', Proceedings of the 2008 Australian Mining Technology Conference, Twin Waters, Australia, pp.309-322.

TABLE OF CONTENTS

DECLARATION i
ABSTRACT ii
ACKNOWLEDGEMENTS iv
AUTHOR'S STATEMENT OF PREVIOUS PUBLICATION vi
TABLE OF CONTENTS vii
TABLE OF FIGURES xvii
TABLE OF TABLES xxvii
CHAPTER 1: INTRODUCTION 1
1.1 Objectives of the Thesis 3
1.2 Outline of Thesis Contents 5
1.2.1 Chapter 2: The Explosive Breakage Process 5
1.2.2 Chapter 3: Interaction of Blast Waves with Existing Discontinuities 5
1.2.3 Chapter 4: Blast Vibration Monitoring and Data Processing 6
1.2.4 Chapter 5: Blast Vibration Analysis and Interpretation 7
1.2.5 Chapter 6: Proposed Energy and Strain-based Blast Damage Criteria 8
1.2.6 Chapter 7: Case Study - Barrick Gold Corp. Kanowna Belle Gold Mine 9
1.2.7 Chapter 8: Case Study - BHP Billiton Cannington Mine 10
1.2.8 Chapter 9: Conclusions 10
CHAPTER 2: EXPLOSIVELY-DRIVEN ROCK BREAKAGE ... 11
2.1 Introduction 11
2.2 General Description of the Explosive Fracture Process 11
2.3 Definition of Breakage Zones Surrounding an Explosive Charge 13
2.3.1 Prediction of the Extent of Crushing 14
2.3.2 Prediction of the Radial Fracture Zone 16
2.3.2.1 Stress Wave-Driven Tensile Cracking in the Elastic Zone 16
2.3.2.2 Experimental Determination of the Extent of Radial Fracture Zones 17
2.3.3 Fracture Extension Zone 18

2.4 Strain Wave versus Gas Penetration Fracture Models 19
2.4.1 Direct and Reflected Tensile Strain 19
2.4.1.1 Arguments for Strain-Based Fracture Extension Theories 20
2.4.2 Gas Penetration Theory of Fracture Extension 21
2.4.3 Combination of Strain and Gas Penetration Models 23
2.5 Description of Waves Generated by Explosive Detonation 24
2.5.1 Wave Types Generated by an Explosive Source 24
2.5.1.1 Properties of Blast-Generated Body Waves 25
2.5.1.2 Distribution of Wave Types: P-, S-, and Rayleigh Waves 26
2.6 Response of a Rock Mass to Blast-Induced Dynamic Loading 28
2.6.1 Dynamic Intact Rock Properties 29
2.6.1.1 Dynamic Rock Strength 30
2.6.1.2 Dynamic Elastic Constants 33
2.6.2 Calculation of Strain Rate 34
2.7 Discussion and Conclusions 35

CHAPTER 3: INTERACTION OF BLAST WAVES WITH EXISTING DISCONTINUITIES 37

3.1 Introduction 37
3.2 Discontinuity Loading Conditions from Blast Waves 37
3.2.1 Determination of Discontinuity Loading Characteristics by Blast Waves 38
3.2.2 Using Vector Sum Particle Motions to Assess Wave Loading Conditions 39
3.2.3 Observed Loading Orientations from Measured Blasting Vibrations 40
3.3 Effect of Wavelength and Discontinuity Dimension 44
3.4 Models of Wave Attenuation and Discontinuities 45
3.4.1 Laboratory and Field Investigations of Fracture Effects on Wave Attenuation 46
3.5 Numerical Simulation of Attenuation in Jointed Material 49
3.5.1 Simulated Wave Attenuation under Normal Incidence 50
3.5.2 Material Properties Used in the Simulation 51
3.5.3 Modelled Seismic Source Parameters 51

3.5.4 Simulation Results 52
3.5.5 Analysis of Simulation Results 52
3.5.6 Investigation of the Effect of Incidence Angle on Attenuation 53
3.5.7 Simulated Effects of Infill Material Properties on Amplitude Attenuation 55
3.6 Discussion and Conclusions 56
CHAPTER 4: NEAR-FIELD BLAST VIBRATION MONITORING AND DATA PROCESSING 57
4.1 Introduction 57
4.2 Description of Requirements for Near-field Blast Vibration Monitoring 57
4.2.1 Definition of Distance Ranges for Blast Monitoring 57
4.3 Blast Vibration Monitoring System Selected for the Kanowna Belle and Cannington Case Studies 60
4.3.1 Selection of Accelerometers for the Thesis Blast Monitoring Program 60
4.3.2 Selection of Geophones for the Thesis Blast Monitoring Program 61
4.3.3 Control of Transducer Orientation in the Thesis Blast Vibration Monitoring Program 62
4.3.4 Design of the Locations of Near-Field Blast Vibration Transducers in the Thesis Blast Vibration Monitoring Program 64
4.3.5 Thesis Instrumentation Strategy 65
4.4 Waveform Processing of the Thesis Blast Vibration Data 66
4.5 Discussion and Conclusions 68
CHAPTER 5: BLAST VIBRATION ANALYSIS AND INTERPRETATION 69
5.1 Introduction 69
5.2 Three-Dimensional Distances for Blast Vibration Scaling and Prediction in Ring Drilling Applications 69
5.2.1 Ring Drilling in Sublevel Open Stoping and Calculation of Source to Sensor Distances 70
5.2.2 Calculation of Geometric Distance (D_G) 72

5.3 Charge Weight Scaling Relationships for Prediction of Peak Particle Velocity Amplitudes 73
5.3.1 Charge Weight Scaling as Defined by Square Root Scaled Distance and Cube Root Scaled Distance 73
5.3.2 Examples of Published Near-field Scaled Distance Vibration Prediction Equations 75
5.3.3 Alternate Forms of Standard Charge Weight Scaling - Corrections for Charge Length and Use of Linear Charge Density 77
5.3.4 Holmberg- Persson Near-Field Prediction Model 79
5.3.5 Critical Evaluation of the Holmberg-Persson Model 81
5.3.6 Additional Models for Prediction of PPV 83
5.3.7 Comparisons of Vibration Prediction Models using Collected Data 85
5.3.8 Significance of Explosive Type on Blast Vibration Prediction 86
5.4 Multi-Variable and Nonlinear Regression Analysis for Vibration Prediction 88
5.4.1 User-Defined Multi-Variable Regression Using Advanced Statistical Analysis 88
5.4.2 Multi-variable, Nonlinear Estimation of Charge Weight Scaling Vibration Prediction Equations Using Statistica 8.0 89
5.4.3 Comparison of Results of Linear and Nonlinear Regression Approaches 91
5.5 Data Scatter in Vibration Analysis and Prediction due to Variations in Peak Amplitudes 93
5.5.1 Variability in Measured Vibration Amplitudes Due to Confinement or Accumulated Damage 93
5.6 Additional Investigation into the Effect of Underground Voids on Distances Determined for Vibration Analysis 97
5.6.1 Effect of Existing Stope Voids on Wave Travel Paths 98
5.6.2 Modelling of VICD Wave Paths 100
5.6.3 Comparison of D_G and VICD 104
5.6.4 Effect of Initiation Sequence on Wave Path 106
5.6.5 Effect of Wave Travel Path on Charge Weight Scaling of Peak Amplitude 107

5.6.6 Comparison of Statistical Confidence of D_G and VICD Models 108
5.6.7 Theoretical Investigation into the Influence of Underground Stope Voids on Blast Wave Attenuation 110
5.7 Discussion and Conclusions 110
CHAPTER 6: PROPOSED ENERGY AND STRAIN-BASED BLAST DAMAGE CRITERIA 113
6.1 Introduction 113
6.2 Existing Empirical, Semi-Analytical and Numerical Models to Predict Blast-Induced Damage 113
6.2.1 Direct PPV-Related Rock Damage Models 114
6.2.2 Critical Tensile Plane Strain Damage Prediction Models 115
6.2.3 Limitations of the Critical Tensile Plane Strain Model 118
6.2.4 Numerical Modelling of Blast Damage Zones 119
6.2.5 Methods of Indicating Rock Mass Alteration to Validate Blast Damage Predictions 120
6.3 Wave Energy as a Defining Wave Quantity Instead of PPV 121
6.3.1 Comparison of Peak Amplitude and Waveform Energy 121
6.3.2 Calculation of Wave Energy for use in Vibration Analysis 123
6.3.3 Total Wave Energy Density 124
6.3.4 Additional Blasting Assessments using $ED_{W\text{-}tot}$ 129
6.3.4.1 Specific Amplitude or Energy Attenuation 130
6.3.4.2 Interpretation of the Rock Mass Attenuation Rate Curves 134
6.3.5 Limitations of Energy as a Rock Mass Damage Criterion 134
6.4 Ground Strains from Blasting 135
6.4.1 Peak Axial Strain from Complex Waveforms using Plane Strains 136
6.4.2 Limitations of the Assumption of Peak Axial Normal Strain from Concurrent Orthogonal Plane Strains 136
6.4.3 States of Normal Strain Assumed from Recorded Tri-Axial Waveforms 137
6.4.4 Considerations Regarding Shear Strain 140
6.4.5 Determination of Wave-Induced Mean Normal Dynamic Strain from Calculated Total Wave Energy Density 143

6.5 Development of Proposed Strain and Energy-Based Blast-Induced Rock Mass Damage Criteria 146
6.5.1 Compressive and Tensile Fracture Strain Criteria for Damage to Intact Rock under the Influence of Mining-Induced Static Strains 146
6.5.2 Failure Strain Energy Density or Dissipated Energy Density Criteria for Damage to Intact Rock 149
6.5.3 Damage to Discontinuities Based on Fracture Energy 153
6.5.3.1 Fracture Energy of Concrete and Rock 153
6.5.3.2 Required Fracture Energy for Activation of All Fracture Surfaces in a Unit Volume 155
6.6 Implementation of the Proposed Strain and Energy-Based Blast Damage Criteria 156
6.7 Discussion and Conclusions 157
CHAPTER 7: CASE STUDY- BARRICK GOLD CORP. KANOWNA BELLE GOLD MINE 159
7.1 Introduction 159
7.2 Geology of the Deposit at KBGM 159
7.3 Overview of the Mining Operation 160
7.3.1 Mining Sequences for Ore Blocks 161
7.3.2 Selection of Monitored Stopes 161
7.3.3 Stope Naming Convention at KBGM 163
7.3.4 Drilling and Blasting at KGBM 163
7.4 Drillhole Deviations Surveys at KBGM 166
7.5 Rock Mass Characterisation of D block 170
7.5.1 Intact Rock Testing Results 171
7.5.2 Discontinuity Mapping in D block at KBGM 171
7.5.3 Overview of the Blast Monitoring Program 173
7.5.4 Block-Scale Rock Mass Characterisation Using Blast Vibration Data 174
7.5.4.1 Stress Wave Velocity Calculation using Blast Monitoring Results 174
7.5.4.2 Frequency Assessment of Monitored Blasting Vibrations 176
7.5.4.3 Peak Amplitude-Frequency Analysis of D block Data 177

7.6 Blast Vibration Analysis Results of Combined D block Data 181
7.7 dA12-35 Individual Stope Analysis 185
7.7.1 dA12-35 Blast Vibration Monitoring Instrumentation 186
7.7.2 Characterisation of dA12-35 Rock Mass 187
7.7.2.1 Discontinuity Orientation Distributions from Mapping 187
7.7.2.2 Stress Wave Velocities from Blast Vibration Monitoring Results 188
7.7.3 Stope dA12-35 Blast Vibration Monitoring Results 189
7.7.4 Post-Mining Stope Performance Assessment 191
7.8 dB10-38B Individual Stope Analysis 194
7.8.1 dB10-38B Blast Vibration Monitoring Instrumentation 195
7.8.2 dB10-38B Rock Mass Characterisation 195
7.8.3 dB10-38B Blast Vibration Monitoring Results 197
7.8.4 dB10-38B Stope Performance Assessment - Maximum Depth of Overbreak 200
7.9 dB10-38T Individual Stope Analysis 200
7.9.1 dB10-38T Blast Vibration Monitoring Instrumentation 201
7.9.2 dB10-38T Rock Mass Characterisation 202
7.9.2.1 dB10-38T Wave Velocities and Peak Amplitude-Frequency Analyses 202
7.9.2.2 Linear-Elastic Mining-Induced Static Stress Modelling 206
7.9.3 dB10-38T Blast Vibration Monitoring Results 210
7.9.4 Predictions of Blast-Induced Damage: Stope dB10-38T 213
7.9.4.1 Estimation of the Tensile Rock Strength and Static and Dynamic Elastic Constants for the dB10-38T Rock Mass 214
7.9.4.2 State of Mining-Induced Static Strain at the Time of Blasting 215
7.9.4.3 Additional Tensile Strain Required for Tensile Fracture 217
7.9.4.4 Calculation of Induced Dynamic Strains from Blasting 218
7.9.4.5 Prediction of Damage from Fracture Extension 225

7.9.4.6 Comparison of Predicted Damage Extents with Critical Tensile Plane Strain Model Predictions 229
7.9.5 Stope Performance Assessment of dB10-38T 231
7.10 Discussion and Conclusions 234
CHAPTER 8: CASE STUDY- BHP BILLITON CANNINGTON MINE 237
8.1 Introduction 237
8.2 Geology of the Cannington Mine Deposit 238
8.3 Overview of the Mining Operation 239
8.4 Selection of Monitored Stopes 241
8.4.1 North Zone Stopes 22gC6HL and 24jC6HL 242
8.4.2 R4 Stopes 52h09HL and 52h04HL 244
8.5 North Zone Block-Scale Rock Mass Characterisation and Blast Vibration Monitoring Results 245
8.5.1 Rock Mass Characterisation of the North Zone 246
8.5.1.1 Intact Rock Properties 246
8.5.1.2 North Zone Discontinuity Mapping 247
8.5.1.3 Mining-Induced Static Stress Modelling 248
8.5.1.4 Stress Wave Velocities and Peak Amplitude-Frequency Analyses of the North Zone Rock Mass 252
8.5.2 Results of North Zone Block-Scale Blast Vibration Analysis 258
8.6 22gC6HL Blast Monitoring Instrumentation, Vibration Analysis Results and Stope Performance Assessment 260
8.6.1 Dynamic Rock Mass Properties for Stope 22gC6HL 262
8.6.2 22gC6HL Blast Vibration Analysis Results 262
8.6.3 Stope Performance Assessment for 22gC6HL 265
8.6.3.1 Visual Blast Damage Assessments in Stope 22gC6HL 265
8.6.3.2 22gC6HL Post-Extraction Stope Performance Assessment 269
8.7 24jC6HL Blast Monitoring Instrumentation, Vibration Analysis Results and Stope Performance Assessment 270
8.7.1 24jC6HL Stress Wave Velocities and Specific Attenuation Analyses 272
8.7.1.1 Proposed Effects of Mineralisation Type on Stress Wave Velocity 273

8.7.1.2 Specific Amplitude Attenuation Analysis 275
8.7.2 Dynamic Rock Mass Properties for Stope 24jC6HL 276
8.7.3 Blast Vibration Analysis Results for 24jC6HL Data Sets 277
8.7.4 Response of an Unconfined Pillar to Late-Stage Blasting 278
8.7.4.1 Post-Mining Induced Static Stress Modelling 279
8.7.4.2 Comparison of the Confined and Unconfined Southwest Pillar 280
8.7.5 Prediction of Strain-Related Blast Damage around Stope 24jC6HL 282
8.7.5.1 Mining-Induced Static Strain Modelling for Stope 24jC6HL 283
8.7.5.2 24jC6HL Rock Mass Required Tensile Failure Strains 283
8.7.5.3 Modelling of Blasting-Induced Strain Fields for 24jC6HL 286
8.7.5.4 Comparison of Proposed Blast Damage Prediction Results with Results of Critical Tensile Plane Strain Damage Predictions 289
8.7.6 Stope Performance Assessment for Stope 24jC6HL 289
8.7.6.1 24jC6HL Post-Extraction Stope Performance Assessment 292
8.8 R4 Mining Area Rock Mass Characterisation and Blast Vibration Monitoring Results 293
8.8.1 Intact Rock Properties for the R4 Mining Area 293
8.8.2 R4 Discontinuity Mapping 294
8.8.3 R4 Blast Vibration Monitoring Instrumentation 296
8.8.4 Stress Wave Velocities and Peak Amplitude-Frequency Analyses of the R4 Rock Mass 299
8.8.5 Results of R4 Blast Vibration Data Analyses 300
8.8.6 R4 Stope Performance Assessments 304
8.9 Comparison of North Zone and R4 Blast Vibration Monitoring Results 306
8.9.1 Comparison of Blast Vibration Attenuation Behaviours 306
8.9.2 Comparison of Specific Amplitude Attenuations 308
8.10 Discussion and Conclusions 309

CHAPTER 9: CONCLUSIONS 311

9.1 Original Contributions Provided by the Research Program 311

9.2 Limitations of the Research Program 314

9.3 Future Work 316

9.4 Industry Applications and Relevance 317

REFERENCES 319

APPENDIX 1: Example Waveforms and Cannington Stope 52h04hl Footwall Data 339

APPENDIX 2: Mathematical Models of Wave Attenuation 357

APPENDIX 3: Small-Scale to Field-Scale Explosive Breakage Studies 365

APPENDIX 4: Additional Details of Near-Field Blast Monitoring Programs 377

APPENDIX 5: Additional Information on Charge Weight Scaling Approaches ... 401

APPENDIX 6: Numerical Simulation of Wave Propagation Around a Stope Void 411

APPENDIX 7: Use of Wave Frequency for Rock Mass Characterisation 419

APPENDIX 8: Methods of Indicating Rock Mass Damage 427

APPENDIX 9: Nonlinear Multi-Variable Data Regression Results 447

APPENDIX 10: Critical Tensile Plane Strain Damage Predictions for Study Stopes 479

TABLE OF FIGURES

Figure 2.1. Illustration of the detonation process and rock breakage zones behind the detonation front. 12

Figure 2.2. Value of r_c versus r_0 for different models using various borehole diameters in basalt blasted with water-resistant ANFO (after Esen et al., 2003). 15

Figure 2.3. Distribution of elongated radial cracks from 17mm Gurit charges in 38mm holes in a granite block (Olsson et al., 2002)..... 18

Figure 2.4. Pressure profile within a fracture of 65mm length under the action of penetrating detonation gases (after Daehnke et al., 1996)..... 22

Figure 2.5. Distribution of wave energy in wave types from a normal force applied near the surface (Woods, 1968). 28

Figure 2.6. Effect of strain rate on compressive strength in ash-fall tuff (after Olsson, 1991). 31

Figure 2.7. Dynamic tensile spall strength of concrete and rock as presented by several researchers (after Klepaczko and Brara, 2001, Cho et al., 2003, and Wu et al., 2005). 32

Figure 3.1. Vector sum motion and the plane of individual component intersection used to define discontinuity loading conditions. 39

Figure 3.2. Plot of orthogonal components of the peak vector sum particle velocity as calculated from the vibration records in the North Wall of BHP Cannington Stope 24jC6HL 200mLv winze firing #7. 41

Figure 3.3. Horizontal plane rosette plot of discontinuity strike distribution and the trace of the vertical plane containing the peak vibration directional vectors for a wave propagating North from stope 24jC6HL at the Cannington Mine. 42

Figure 3.4. Loading conditions on prominent discontinuity set and directions of wave propagation supplying maximum shear (left) or normal (right) loading. 43

Figure 3.5. Plan view of stope 24jC6HL and the orientations of maximum discontinuity shear loading from blast-induced waves as suggested by the propagation-normal maximum shear loading direction. 44

Figure 3.6. Fracture created by pre-splitting in Lithonia granite (Devine et al., 1965)..... 47

Figure 3.7. Normalised P-wave *Q* values for vertical and horizontal directions based on distance from the excavation face (left) and normalised attenuation values 1/*Q* for vertical and horizontal directions (right) (after King et al., 1986). 48
Figure 3.8. Comparison of amplitude and frequency spectra for intact and fractured samples of varying fracture stiffness under axial loads (Pyrak-Nolte et al., 1990). 49
Figure 3.9. Plan view of *Wave2000 Plus*® simulation geometry for normal P-wave incidence using an array of transducers between equally-spaced discontinuities. 50
Figure 3.10. Plan view of *Wave2000 Plus*® simulation near model completion. 52
Figure 3.11. Comparison of amplitude attenuation curves for unjointed and normal incident jointed models. 53
Figure 3.12. Simulated wave-field generated in the 45 degree incident parallel jointed model. 55
Figure 4.1. OYO 101LT 14Hz high-frequency geophone extended linear frequency response (after Andrieux and Heilig, 1994). 62
Figure 4.2. Prepared transducer orientation control pipes. 63
Figure 4.3. Installation of tri-axial transducers in the hangingwall (left) and footwall (right) of Kanowna Belle Gold Mine stope dB10-38T. 63
Figure 5.1. Effect of blasthole orientation on the defining distances possible for use in blast vibration prediction models. 71
Figure 5.2. PPV prediction curves of various authors based on vibration data. 77
Figure 5.3. Graphs of Square Root Scaled Distance and Holmberg-Persson blast vibration prediction using the same data set (Peterson, 2001). 82
Figure 5.4. Plot of Holmberg Term (a) versus the square root and cube root Scaled Distance for all charges in a stope firing mass blast design. 83
Figure 5.5. Nonlinear multi-variable regression surface of Cannington Mine stope 52h09HL data plotting charge weight, distance and measured PPV. 90
Figure 5.6. Nonlinear quadratic surface regression for BHP Cannington stope 24jC6HL data. 91
Figure 5.7. Histogram of peak vector sum acceleration measured for 11 equally-charged blastholes at approximately equal distances from a monitoring location. 94

Figure 5.8. Plan view of the simulated breakout areas and angles for winze firing 2 in Cannington Stope 24jC6HL 220mLv (numbers are firing order of holes)..... 95
Figure 5.9. Peak amplitude versus firing sequence along 2 orientations in a highly-confined rise blast of 10 equal charges at equal distances. 96
Figure 5.10. Plan view of VICD classifications based on the location of blast vibration monitoring transducers and a blasthole. 99
Figure 5.11. Plan view of the Intact VICD geometry based on the stope void and the blasthole position for a single charge (left) or multiple charges (right)..... 100
Figure 5.12. Conceptual view of different node types used to determine the VICD between a charge and a monitoring point with Parallel Void geometry. 101
Figure 5.13. Conceptual view of the VICD wave path for the first ring charge firing. 102
Figure 5.14. VICD of a firing blasthole after a number of holes have been fired forming the new stope void perimeter. 103
Figure 5.15. Plan view of east wall (blue lines) and south wall (black lines) VICD wave paths for blasthole ring #4 in 220mLv mass blast of stope 24jC6HL. 104
Figure 5.16. D_G and VICD for a ring of blastholes along the Parallel Void orientation (left) and percent difference between D_G and VICD for the ten holes (right). 105
Figure 5.17. D_G and VICD for a ring of blastholes along the Normal Void orientation (left) and percent difference between D_G and VICD for the ten holes (right). 105
Figure 5.18. Plan view of VICD wave paths from three of five detonating holes to a Parallel Void transducer for centre-out initiation (top) and sequential hole initiation (bottom) firing sequences. 106
Figure 5.19. Comparison of void-affected D_G (black squares/black line) and VICD (grey triangles/grey line) cube root Scaled Distance models of VSPPA for the 220mLv mass firing in BHP Cannington Stope 24jC6HL. 108
Figure 6.1. Predicted damage envelopes perpendicular to the axis of a 102mm diameter ANFO at the Kanowna Belle Mine (after Heilig, 2002)..... 117
Figure 6.2. Comparison of two near-field vector sum particle velocity waveforms with equal VSPPV values but largely different durations, peak interval times (t_{peak}) and energy contents. 122

Figure 6.3. Comparison of E_i and $ED_{W\text{-}tot}$ versus measured VSPPV for the BHP Cannington stope 24jC6HL 200mLv Northeast wall data. 125
Figure 6.4. Comparison of $VSPV(t)^2$ waveforms (black lines) and cumulative area under each waveform (red line) as an indication of the wave energy..... 127
Figure 6.5. Relationship between energy attenuation per metre of travel ($ED_{loss/m}$) and input energy density ($ED_{W\text{-}tot1}$) for BHP Cannington stope 24jC6HL 200mLv Northeast wall data. 131
Figure 6.6. Rock mass energy attenuation rate (RMAR) resulting from dividing $ED_{loss/m}$ by $ED_{W\text{-}tot1}$ shown in Figure 6.5. 132
Figure 6.7. Comparison of RMARs for two wave propagation orientations from data measured in two walls of Cannington stope 24jC6HL. 133
Figure 6.8. Rotated unit volume in relation to peak axial strain resulting from the vector direction of VSPPV. 136
Figure 6.9. Comparison of peak component velocity polarities recorded for a series of equally-charged blastholes in KBGM Stope dB10-38T, rise firing #4 footwall transducer. 139
Figure 6.10. RSE_T versus strain rate for granite (after data of Li et al., 2005)..... 151
Figure 6.11. Exponential relationship between $RSE_{T(dynamic)}$ and strain rate ($\dot{\varepsilon}$). 152
Figure 6.12. Proposed exponential relationship for determination of dynamic tensile fracture energy ($FE_{T(dynamic)}$) versus strain rate for granitic rocks..... 155
Figure 7.1. Long section of KBGM showing the mining blocks and the completed open pit (looking north). 160
Figure 7.2. Long section of D block study stopes (in blue) and central fill mass (in yellow) at the time of the blast damage investigation (looking North). 162
Figure 7.3. Plan view of D-block at the 9390RL showing the stope names and mining panels between the Fitzroy Fault and footwall shear. 163
Figure 7.4. Firing stages of stope dB10-38B looking West (1-2) and North (3-5). 165
Figure 7.5. Histogram of toe location errors in surveyed blastholes as a percentage of the hole lengths for stopes dB10-38B and dB10-38T. 167
Figure 7.6. Bullseye graph of the surveyed versus designed hole collar (top) and toe (bottom) positions. 168

Figure 7.7. Section view of blasthole rings 5 and 7 in dB10-38T comparing the designed hole locations (blue strings) with the surveyed blasthole locations at 3m in-hole survey intervals (black strings and points). 170
Figure 7.8. Plan view of digitised discontinuity mapping of 9380RL development. 172
Figure 7.9. Equal-area lower hemisphere stereonet plot of D block discontinuity mapping data. 172
Figure 7.10. Calculated block-scale stress wave velocities for KBGM stopes dA12-35, dB10-38B and dB10-38T plotted against the mean wave travel distance. 176
Figure 7.11. Block-scale blast vibration peak frequency distribution at KBGM. 177
Figure 7.12. Comparison of VSPPV versus VSPPA plots (log-log axes) for the footwall of stopes dA12-35 and dB10-38B and East wall of dB10-38B. 178
Figure 7.13. Comparison of VSPPV versus VSPPA plots (log-log axes) for the East wall, footwall and hangingwall of stope dB10-38T. 179
Figure 7.14. Plot of best-fit lines of VSPPV versus VSPPA for all monitoring orientations in the D block of KBGM. 180
Figure 7.15. Best-fit surface from multi-variable nonlinear estimation of $\varepsilon_{W\text{-}MN}$ versus charge weight and VICD for all KBGM D block data. 184
Figure 7.16. 95% upper confidence prediction surface from multi-variable nonlinear estimation of $\varepsilon_{W\text{-}MN}$ versus charge weight and VICD for all KBGM D block data. 184
Figure 7.17. Cross section of stope dA12-35 showing the Fitzroy Fault, footwall shear and the installed footwall transducer locations (looking west). 186
Figure 7.18. Discontinuity mapping results for levels 9350RL and 9380RL in the vicinity of stope dA12-35. 187
Figure 7.19. Differential stress-wave velocities using blasthole seismic sources for the KBGM stope dA12-35 footwall. 188
Figure 7.20. Overbreak volume (left) and underbreak volume (right) from comparing the CMS survey wireframe and the design stope wireframe for stope dA12-35. 191
Figure 7.21. Plan view of stope dA12-35 CMS and design wireframes at 9360m elevation showing areas of overbreak (blue), underbreak (red) and perimeter blastholes. 192

Figure 7.22. Cross section of stope dA12-35 CMS and design wireframes along blasthole ring 3 showing areas of overbreak (blue), underbreak (red) and blasthole charges (looking west). 193
Figure 7.23. Isometric view of stope dB10-38B and dB10-38T (looking West). 194
Figure 7.24. Plan view of stope design dB10-38B showing sensor locations, adjacent fill masses and faults at 9395RL. 195
Figure 7.25. Plot of VSPPV versus VSPPA for stope dB10-38B East wall and footwall accelerometers and the best-fit equations. 196
Figure 7.26. Log-log plot of the 95% upper confidence prediction curves for the footwall and East wall of stope dB10-38B for a 100kg charge weight. 199
Figure 7.27. Plan view of the installed blast vibration monitoring instrumentation, adjacent pastefill and major geologic features associated with stope dB10-38T. 201
Figure 7.28. Plot of dB10-38T East wall, footwall and hangingwall stress wave velocities versus the mean geometric travel distance. 202
Figure 7.29. Effect of angle of incidence of the blast wave travel path with the Fitzroy Fault and the stress wave velocity. 204
Figure 7.30. Section view of the wave travel paths and incidence angles in relation to the Fitzroy Fault plane normal for the six rise firings in KBGM stope dB10-38T. 204
Figure 7.31. Plots of VSPPV versus VSPPA and best-fit lines for the East wall, footwall and hangingwall accelerometers around stope dB10-38T. 205
Figure 7.32. Comparison of 95% confidence bands for the VSPPV versus VSPPA plots of the East wall, footwall and hangingwall data sets pictured in Figure 7.31. 206
Figure 7.33. Mining-induced σ_1 static stress distribution at the 9417RL horizontal grid for the dB10-38T and dB10-38B pre-mining step. 208
Figure 7.34. Mining-induced σ_2 static stress distribution at the 9417RL horizontal grid for the dB10-38T and dB10-38B pre-mining step. 209
Figure 7.35. Mining-induced σ_3 static stress distribution at the 9417RL horizontal grid for the dB10-38T and dB10-38B pre-mining step. 209
Figure 7.36. Contour plot of the mining-induced mean normal static compressive strain (ε_{MN}) modelling results at the 9417RL for the dB10-38T pre-mining step. 216

Figure 7.37. Contour plot of the required tensile strain for tensile fracture of intact rock at the 9417RL under the influence of the pre-mining static compressive strains. 217
Figure 7.38. Contours of equal strain propagating from a 100kg charge as estimated from the 95% confidence regression constants for the East wall, footwall and hangingwall of dB10-38T (not to scale). 219
Figure 7.39. Contours of $\varepsilon_{W\text{-}MN\text{-}95\%}$ at all 9417RL grid points using Equation 7.8 for a 100kg charge on the perimeter of stope dB10-38T. 220
Figure 7.40. Contours of $\varepsilon_{W\text{-}MN}$ from a 100kg charge superimposed on the required tensile fracture strain contours for dB10-38T at the 9417RL grid. 221
Figure 7.41. Contours of excess strain capacity for a 100kg charge at the East wall perimeter of stope dB10-38T, resulting in prediction of the tensile damage zone. 222
Figure 7.42. Contours of excess strain capacity for a 50kg charge at the East wall perimeter of stope dB10-38T, resulting in prediction of the tensile damage zone. 223
Figure 7.43. Contours of excess strain capacity for a 50kg charge at the hangingwall perimeter of stope dB10-38T, resulting in prediction of the tensile damage zone. 224
Figure 7.44. Estimation of the distance from a 50kg charge where potential fracture extension could occur as a function of the dynamic energy density at 21 m^2/m^3 *FAD*. 227
Figure 7.45. Estimation of the distance from a 50kg charge where fracture extension could occur as a function of the dynamic energy density at 57 m^2/m^3 *FAD*. 228
Figure 7.46. Horizontal section of dB10-38T design and CMS survey wireframes at 9420RL showing overbreak (blue), underbreak (red), pastefill dilution (green) and the locations of perimeter blasstholes. 232
Figure 7.47. Vertical section of dB10-38T design and CMS wireframes at blasthole ring 5 showing overbreak (blue), underbreak (red) and the locations of blastholes. 232
Figure 7.48. Post-mining linear-elastic stress modelling of σ_2 (top) and σ_3 (bottom) showing areas of low confining stresses in the East wall of stope dB10-38T. 233
Figure 8.1. Plan view of the Cannington orebody at the 210mLv mine level showing the zones of mineralisation and the two regional-scale faults. 238

Figure 8.2. Section view of the Cannington orebody at the 1900m Easting showing the zones of mineralisation and the two regional-scale faults. 239
Figure 8.3. Plan view of North Zone stopes 22gC6HL and 24jC6HL in relation to the Trepell Fault and adjacent pastefill masses at the time of monitoring. 242
Figure 8.4. Isometric view of stope 22gC6HL showing the critical mine infrastructure in the vicinity of the stope (looking southeast). 243
Figure 8.5. Isometric view of stope 24jC6HL showing the critical mine infrastructure in the vicinity of the stope (looking southwest). 244
Figure 8.6. Isometric view of R4 stopes 52h09HL and 52h04HL (looking north). 245
Figure 8.7. Plan view of the results of digitised drive backs mapping of the Southern end of North Zone on mine levels 180mLv and 200mLv..... 247
Figure 8.8. Discontinuity distribution from backs mapping of the 180mLv, 200mLv and 220mLv in the North Zone near stopes 22gC6HL and 24jC6HL. 248
Figure 8.9. Plan view of North Zone MAP3D model with position of vertical grids 1, 2 and 4 (top) and isometric view of horizontal grids 3, 5, 6 and 7 (bottom) for stopes 22gC6HL and 24jC6HL. 249
Figure 8.10. Results of MAP3D mining-induced static stress modelling of σ_1 on grid 1 at mining step 2 (looking northeast). 251
Figure 8.11. Results of MAP3D mining-induced static stress modelling of σ_2 on grid 1 at mining step 2 (looking northeast). 251
Figure 8.12. Results of MAP3D mining-induced static stress modelling of σ_3 on grid 1 at mining step 2 (looking northeast). 252
Figure 8.13. Plot of the measured stress wave velocities versus the mean travel distance in different walls of stope 24jC6HL..... 254
Figure 8.14. Plots of VSPPV versus VSPPA for 24jC6HL accelerometer data in the Northeast/Southwest orientations. 256
Figure 8.15. Plots of VSPPV versus VSPPA for 24jC6HL accelerometer data in the Southeast/Northwest orientation. 256
Figure 8.16. Best-fit VSPPV versus VSPPA lines shown in Figures 8.14 and 8.15 for North Zone blast monitoring data showing orientation-specific grouping. 257
Figure 8.17. Plan view of stopes 22gC6HL and 24jC6HL with the discontinuity mapping results and comparisons of peak amplitude-frequency analyses and stress wave velocities (V_p) in the North Zone..... 258

Figure 8.18. 95% upper confidence surface from nonlinear regression of $ED_{W\text{-}SS}$ versus charge weight and VICD for the combined Cannington North Zone data set. 259
Figure 8.19. 95% upper confidence surface from nonlinear regression of $\varepsilon_{W\text{-}MN}$ versus charge weight and VICD for Cannington North Zone data. 260
Figure 8.20. Isometric view of the 22gC6HL blast vibration monitoring transducers (looking southeast). 261
Figure 8.21. Log-log plot of 95% upper confidence $\varepsilon_{W\text{-}MN}$ predicted for the 22gC6HL Northwest and Northeast wall individual transducers at a charge weight of 50kg. 264
Figure 8.22. Pictures of spalled shotcrete in the 240mLv explosives magazine occurring with the mass blast or main rings firing of stope 22gC6HL. 266
Figure 8.23. Plan view of the 180mLv mapped damage occurring with each firing of stope 22gC6HL. 268
Figure 8.24. Photographs of a block fall from 1.2m height after stope firing LHW-COS #5 (left) and spall from floor to grade line after COS #6 firing (right) in drive 180mLv KcDS. 268
Figure 8.25. Isometric view of blast vibration monitoring instrumentation installed for the 220mLv, 200mLv and 180mLv firings in stope 24jC6HL (looking west). 271
Figure 8.26. Plan view of stope 24jC6HL and mineralisation contacts in the Southeast wall of the stope at the 1015m elevation. 274
Figure 8.27. Plot of amplitude loss per metre of travel versus input amplitude for 200mLv firings in stope 24jC6HL. 275
Figure 8.28. Results of σ_2 (left) and σ_3 (right) mining-induced static stress modelling of the 24jC6HL post-mining step at vertical grid 4 (looking northwest). 279
Figure 8.29. Comparison of the VSPPV versus VSPPA plots for the 200mLv accelerometer closed wall and open wall data. 281
Figure 8.30. Specific amplitude attenuation (VSPPA) from 200mLv data for the closed and open wall pillar conditions. 282
Figure 8.31. Plan view of modelled mining-induced mean normal static compressive strains (ε_{MN}) at Grid 5 at the 1038m elevation. 283
Figure 8.32. Plan view of $\varepsilon_{dyn(T)}$ contours at grid 5 around 24jC6HL. 284
Figure 8.33. Contours of the required additional mean normal tensile strain to induce tensile damage ($\varepsilon_{MN(T)}$) at grid 5 around 24jC6HL. 285
Figure 8.34. Contour plot of maximum $\varepsilon_{W\text{-}MN}$ around three modelled explosive charges at the perimeter of 24jC6HL at grid 5. 287

Figure 8.35. Contour plot of the excess strain capacity after superimposing the induced blasting strain onto the required additional tensile strain at grid 5. 288
Figure 8.36. Photograph of 20m^2 of heavy spall damage of thinly shotcreted development on 180mLv drive LaDS after 180mLv mass firing. 290
Figure 8.37. Block failure of 1 tonne from approximately 3.0m height after 220mLv firing #3 (left) and 500kg block fall after 180mLv mass blast (right) in drive 220mLv drive LaDS. 291
Figure 8.38. Picture of a gouge-type fault encountered on the 500mLv development. 295
Figure 8.39. R4 development mapping of the 500mLv (left) and 520mLv (right) in the vicinity of stopes 52h09HL and 52h04HL. 295
Figure 8.40. Discontinuity distribution from mapping of 500mLv and 520mLv in the vicinity of stopes 52h09HL and 52h04HL..... 296
Figure 8.41. Plan view of transducers installed at the 750m elevation (between the 500mLv and 520mLv) in the R4 to monitor blasting vibrations from stopes 52h09HL and 52h04HL. 297
Figure 8.42. Plots of VSPPV versus VSPPA and best-fit relationships for the accelerometer data measured along each monitoring orientation around R4 stopes 52h09HL and 52h04HL..... 300
Figure 8.43. 95% upper confidence surface from nonlinear estimation of $ED_{W\text{-}SS}$ versus charge weight and VICD for Cannington R4 combined data. 302
Figure 8.44. 95% upper confidence surface from nonlinear estimation of $\varepsilon_{W\text{-}MN}$ versus charge weight and VICD for Cannington R4 combined data. 302
Figure 8.45. Predicted 95% upper confidence $\varepsilon_{W\text{-}MN}$ versus distance for the North Zone and R4 combined data sets for a 50kg charge weight. 307
Figure 8.46. Comparison of specific amplitude attenuations for the North Zone and R4 Mining areas. 309

TABLE OF TABLES

Table 2.1. Distribution of energy between wave types from a compression wave source on the ground surface. 27

Table 3.1. Comparison of linear discontinuity dimension and critical frequency of excitation based on similar wavelength to discontinuity dimension. 45

Table 3.2. Material properties used in the *Wave2000*® Plus model in Figure 3.12. 51

Table 3.3. P-wave amplitude attenuation slopes for simulated 30 and 45 degree incidence. 54

Table 4.1. Suggested definitions of blast monitoring regions. 59

Table 4.2. Recommended transducer types, dynamic ranges and sampling rates for monitoring of blasting vibrations in different distance ranges. 59

Table 4.3. Total Installed Instrumentation used in the blast vibration study. 66

Table 5.1. Charge weight scaling *PPV* (mm/s) prediction equations from the published literature based on *W* (kg) and *D* (m) for a variety of blasting conditions. 76

Table 5.2. Holmberg-Persson peak amplitude prediction regression constants published in past literature. 81

Table 5.3. Comparison of VSPPV prediction models for near-field and intermediate-field data from BHP Cannington Stope 52h04HL southeast wall transducers. 85

Table 5.4. Comparison of measured PPV and SD_{SQRT} regression constants and correlations for the three different explosive types in Cannington stope 24jC6HL. 87

Table 5.5. Comparison of measured PPV and SD_{SQRT} regression constants and correlations for the three different explosives types normalised to equivalent ANFO charges in Cannington Stope 24jC6HL. 87

Table 5.6. Comparison of regression constants for blast vibration monitoring data in Cannington Stope 24jC6HL 200mLv Southeast wall. 92

Table 5.7. Comparison of VICDs for firing sequences 1 and 2. 107

Table 5.8. Log-log linear regression results for the void-affected VSPPA versus cube root Scaled Distance calculated using D_G and VICD for the 24jC6HL mass blast. 109

Table 6.1. PPV-based rock fracture criterion as published by past researchers. 114

Table 6.2. $PPV_{fragmentation}$, PPV_{crit} and $PPV_{extension}$ values published in past research. 117
Table 6.3. Numerical modelling parameters and failure criteria used in dynamic breakage investigations. 120
Table 6.4. Published values of stored or dissipated strain energy density resulting from static and dynamic compression testing. 149
Table 6.5. Published values of fracture energy for concrete and rock. 154
Table 7.1. Open stoping dimensions and sequences for each block at KBGM (KBGM, 2008). 161
Table 7.2. Intact rock testing results for KBGM D block (Li, 2002). 171
Table 7.3. Summary of instrumentation utilised in study stopes in KBGM D block. 173
Table 7.4. Best-fit and 95% upper confidence regression constants and correlation coefficients from multi-variable, nonlinear estimation of the KBGM D block combined data set. 182
Table 7.5. Best-fit and 95% upper confidence regression constants for stored strain energy density ($ED_{W\text{-}SS}$) and mean normal strain $\varepsilon_{W\text{-}MN}$ for the combined data set from all three stopes monitored at KBGM. 183
Table 7.6. Rock mass properties for dA12-35 footwall monitoring direction. 188
Table 7.7. Best-fit and 95% upper confidence nonlinear estimation constants of $ED_{W\text{-}SS}$ and $\varepsilon_{W\text{-}MN}$ for the footwall of dA12-35. 189
Table 7.8. Best-fit and 95% upper confidence nonlinear estimation constants of $ED_{W\text{-}SS}$ and $\varepsilon_{W\text{-}MN}$ for the footwall geophone data in stope dA12-35. 190
Table 7.9. Stope overbreak and underbreak calculations resulting from outersection of the post-extraction CMS and the design wireframes for stope dA12-35 192
Table 7.10. Maximum depth of overbreak in each wall of stope dA12-35. 193
Table 7.11. Stress wave velocities for the footwall and East wall of dB10-38B. 196
Table 7.12. In situ dynamic rock mass properties as indicated for stope dB10-38B. 198
Table 7.13. 95% upper confidence regression results for the East wall and footwall data sets. 198
Table 7.14. 95% upper confidence regression results for the dB10-38B individual East wall and footwall transducer data sets. 198
Table 7.15. Maximum depth of overbreak in each wall of stope dB10-38B. 200

Table 7.16. Summary of blast vibration monitoring transducers around dB10-38T. 201
Table 7.17. Input values for the MAP3D pre- and post-mining stress modelling for stope dB10-38T as provided by KBGM. 207
Table 7.18. Stress wave velocities used to calculate $ED_{W\text{-}SS}$ and $\varepsilon_{W\text{-}MN}$ values for dB10-38T blasting. 210
Table 7.19. Static and dynamic rock mass properties used in calculation of $ED_{W\text{-}SS}$ and $\varepsilon_{W\text{-}MN}$ in stope dB10-38T blasting results. 211
Table 7.20. 95% upper confidence multi-variable nonlinear estimation results for each wall of dB10-38T. 211
Table 7.21. 95% upper confidence multi-variable nonlinear estimation results for each transducer around stope dB10-38T. 212
Table 7.22. Predicted tensile rock strengths for D block geologic units. 214
Table 7.23. Static rock properties for the three geologic units around dB10-38T. 214
Table 7.24. Compressive and tensile dynamic failure strains for the three geologic units around stope dB10-38T. 215
Table 7.25. Predicted tensile fracture radii using various forms of the critical tensile plane strain damage model and nonlinear regression of PPV for a 50kg charge. 230
Table 7.26. Overbreak and underbreak calculations resulting from comparison of the post-extraction CMS and the design wireframes for dB10-38B and dB10-38T. 231
Table 7.27. Maximum depth of overbreak in each wall of stope dB10-38T. 231
Table 8.1. Results of intact rock testing for the North Zone of the Cannington Mine (AMC, 1998; WASM, 2009a). 246
Table 8.2. Rock densities supplied by the Cannington reserve model (Li, 2009). 247
Table 8.3. Summary of North Zone Blast Vibration Monitoring Instrumentation. 253
Table 8.4. Best-fit and 95% upper confidence nonlinear estimation results for $ED_{W\text{-}SS}$ and $\varepsilon_{W\text{-}MN}$ for the North Zone combined data set. 259
Table 8.5. In situ dynamic rock mass properties as indicated for stope 22gC6HL. 262
Table 8.6. 95% upper confidence nonlinear estimation results for the 22gC6HL data as combined data sets for each stope wall. 263
Table 8.7. Overbreak and underbreak volumes resulting from comparison of the post-extraction CMS and the design wireframes for North Zone stope 22gC6HL. 269
Table 8.8. Maximum depth of overbreak in each wall of stope 22gC6HL. 269

Table 8.9. Summary of North Zone stope 24jC6HL blast vibration monitoring instrumentation. 272
Table 8.10. Measured (M) and assumed (A) stress wave velocities for the monitoring orientations of stope 24jC6HL. 273
Table 8.11. In situ dynamic rock mass properties as indicated for stope 24jC6HL. 277
Table 8.12. 95% upper confidence nonlinear estimation results from 24jC6HL data as segregated by the individual stope wall orientations. 278
Table 8.13. 95% upper confidence nonlinear estimation results from 24jC6HL data as segregated by each production level. 278
Table 8.14. Estimated rock mass compressive and tensile dynamic fracture strains for the rock mass around 24jC6HL. 284
Table 8.15. Charge weights for blastholes against each wall of stope 24jC6HL as determined by average values from the charge plans of the 200mLv mass blast. 286
Table 8.16. Stope overbreak and underbreak calculations resulting from comparison of the post-extraction CMS and design wireframes for North Zone stope 24jC6HL. 292
Table 8.17. Maximum depth of overbreak in each wall of stope 24jC6HL. 292
Table 8.18. Intact rock testing results for the R4 (WASM, 2009b and AMC, 1998). 293
Table 8.19. Rock density as supplied by the reserve block model (Li, 2009). 294
Table 8.20. Summary of 52h09HL and 52h04HL blast vibration monitoring instrumentation. 298
Table 8.21. Measured (M) or assumed (A) stress wave velocities for the monitored orientations around 52h09HL and 52h04HL. 299
Table 8.22. In situ dynamic rock mass properties for stopes 52h09HL and 52h04HL. 301
Table 8.23. Best-fit and 95% upper confidence nonlinear estimation results for $ED_{W\text{-}SS}$ and $\varepsilon_{W\text{-}MN}$ for the R4 combined data set. 301
Table 8.24. Stope 52h09HL and 52h04HL nonlinear estimation results for 95% upper confidence $ED_{W\text{-}SS}$ and $\varepsilon_{W\text{-}MN}$ as combined data sets for each stope wall. 303
Table 8.25. Stope overbreak and underbreak calculations resulting from comparison of the post-extraction CMS and design wireframes for 52h09HL and 52h04HL. 304
Table 8.26. Maximum depth of overbreak in each wall of stope 52h09HL. 305

CHAPTER 1 : INTRODUCTION

Blasting-related rock mass damage in underground mining or tunnelling can negatively affect the mining process by contributing to small or large-scale rock mass instabilities. Blast damage can manifest as either primary damage such as excavation overbreak and stope dilution or secondary effects related to blasting-induced rock fall or mobilisation of large-scale discontinuities. These types of damage can negatively influence both the localised and regional stability of an underground operation, and lead to increased mining costs from ground support rehabilitation, damage to mine infrastructure, damage to mine equipment and injury of personnel.

In traditional excavation design approaches, blasting-related rock mass damage is not explicitly considered or quantified based on blast design parameters or rock mass characteristics. Approaches to predict or assess blasting damage have therefore been performed independently, using a range of empirical, analytical or mathematical models. Of the models published in the literature over the last 40 years, the most prevalent have been those related to qualitative damage assessment from direct or indirect observations, quantitative prediction based on measured or predicted vibration amplitudes, analytical prediction using strain or energy-based damage criteria and numerical modelling of the damage process. The most notable limitations of these models for blast damage prediction or assessment include a lack of consideration for the rock mass properties, a lack of standardised near-field blast vibration monitoring techniques, insufficient blast vibration analysis techniques for near-field vibration data and no treatment for the influence of underground voids or induced static stresses on blasting vibrations or damage. Investigation of these limitations has formed the basis of the blast vibration monitoring and blast damage assessment techniques developed throughout this thesis.

It is important to note that in the published literature, no standard definition exists for the term “blast-induced damage” as applied to mining or geotechnical engineering. Researchers in the past have proposed definitions for or identified blast damage by degradation of the material elastic modulus (e.g. Grady and Kipp, 1980; Yang et al., 1996; Liu and Katsabanis, 1997), observable fresh fracturing, overbreak or rock fall

(e.g. LeBlanc et al., 1995; Villaescusa et al., 1997; Liu et al., 2000; Keller and Kramer, 2000), or changes in the rock mechanical, seismic or hydraulic properties (e.g. Holmberg and Persson, 1978; Spathis et al., 1985; Pusch, 1989; Brinkmann, 1990; Pusch and Stanfors, 1992; Ouchterlony et al., 1993; Cardarelli et al., 2003; Kilebrant et al., 2009; Ouchterlony et al., 2009). The definition of blast-induced damage adopted in this thesis is degradation of the load-bearing capabilities of a rock mass as a result of an increase in the intensity of fracturing. The increased fracture intensity can be associated with fresh fracturing, or dilation or extension of existing fractures or discontinuities. The degree of strength degradation in the damage-affected zone does not necessarily indicate a loss of immediate rock mass integrity, but would be expected to influence the long-term stability of the rock mass over time or with additional loading.

The terms "near-field" and "far-field" vibrations are used prevalently in published research in reference to distance ranges from a blasting event, but no standard definition exists. Various published definitions are based on multiples of the charge length or blast dimensions (e.g. Andrieux and Heilig, 1994; Yang and Scovira, 2007), absolute distance from a single hole or multiple-hole blast (e.g. Yang et al., 1993), a combination of the charge weight and distance (e.g. Ambraseys and Hendron, 1968), or frequency-related properties (e.g. Spathis, 2006). The amplitude and frequency characteristics of blast-induced waves are dependent on both the intensity of the wave source (charge weight) and the distance over which the wave has propagated. For this reason, four different source and distance-related monitoring ranges have been proposed in this thesis. The four monitoring ranges, discussed in detail in Chapter 4, are "extreme near-field", "near-field", "intermediate-field" and "far-field". The proposed ranges are based on specific values of square root Scaled Distance (SD_{SQRT}), which combines charge weight and distance into a single scaling term. The proposed near-field zone for monitoring is defined by the SD_{SQRT} value between 0.5 and 2.0 m/kg$^{0.5}$. Far-field conditions would be expected for SD_{SQRT} values in excess of 10 m/kg$^{0.5}$.

The recommended procedures for the design and implementation of near-field blast vibration monitoring systems and data collection, processing, analysis, and interpretation presented in this thesis are based on an extensive blast vibration

monitoring program performed by the author. This program took place from January, 2006 to February, 2008 and involved near-field and intermediate-field blast vibration monitoring of production blasts in seven sublevel open stopes at two underground mines in Australia. The data set generated in the program represents one of the most extensive near-field underground vibration monitoring data sets in the world in terms of data quality, quantity and represented blasting conditions. In excess of 5000 single blasthole wave traces were identified out of over 10000 monitored production blastholes.

The extensive data set generated during the blast vibration monitoring program is not provided in its entirety in this thesis due to the great expense and effort of both the author and the project sponsors to collect it over the course of the program. Portions of the data that have been used for blast vibration analysis in the mine site case studies have been included in graphical form and a sample data set is included in Appendix 1. Additional data analysis results are in Appendix 9 and Appendix 10, including 180 individual regressions of the collected data. Access to the data by external researchers for further analysis can be negotiated with the sponsoring mine sites or the author based on collaborative research agreements.

1.1 Objectives of the Thesis

One of the objectives of this thesis is to critically review the practices of near-field blast vibration monitoring used in published studies and attempt to provide suggestions to more accurately measure near-field blasting vibrations. The elements of consideration to ensure accurate near-field blast vibration monitoring include:

- Proper selection of transducer types, dynamic ranges and configurations
- Adequate volumetric coverage of transducers to represent orientation-specific blast vibration attenuation characteristics
- Data acquisition system specifications (e.g. sampling rate, resolution, input sensitivity)
- Waveform post-processing

Once blast vibration data have been collected with high accuracy and processed to represent the transducer-appropriate amplitude and frequency ranges, analysis of the data must be performed to link the measured vibration characteristics with blasting parameters. These analyses allow prediction of the vibration values that may be expected at other locations within the mine or resulting from distance or charge variations. Another objective of this thesis is to review the existing models of blast vibration analysis and prediction and apply them to the near-field data sets collected at the Kanowna Belle Gold Mine and the BHP Billiton Cannington Mine. The accuracies of prediction of measured wave amplitudes, calculated energies and strains using existing charge weight scaling models have been assessed. A modified analysis approach has been discussed using multi-variable nonlinear estimation techniques applied to the general charge weight scaling formula to improve prediction accuracies as indicated by the coefficients of correlation.

The rock mass characteristics, mining geometries, blasting conditions and stress regimes at each mine site included in the author's blast vibration monitoring program were notably different from one another. This allowed assessment of the effects of many different conditions on blasting vibrations. The localised and large-scale differences indicated in the blast vibration analyses and rock mass characterisations provided a great deal of information on the influence of blasting on stope performance under highly variable geologic and geotechnical rock mass conditions.

The final objective of the research project was to develop a more accurate approach for predicting blast-induced damage to confined rock masses under the influence of mining-induced static stresses. No previous model for prediction of blast-induced damage has considered realistic damage mechanisms under the influence of static stresses common in underground mines. The influence of the stress magnitudes and orientations would be expected to affect the behaviour of blasting vibrations and the combined static and dynamic loading conditions experienced in a rock mass in the vicinity of blasting events.

1.2 Outline of Thesis Contents

The chapters of this thesis have attempted to discuss the blasting process and the influence of blast waves on a rock mass by reviewing published literature on the subjects of wave propagation, blast vibration monitoring and analysis, explosive-induced breakage and blast-induced damage. Along with published works, data collected during the near-field blast vibration monitoring program have been applied to various models of blast vibration analysis and damage prediction to evaluate the relevance and efficacy of the prediction of vibration behaviour.

The structure adopted in this thesis attempts to aid future researchers in conducting near-field blast vibration monitoring, analysis and interpretation programs. The ideas discussed in the earlier chapters form the basis by which the proposed blast damage prediction approaches are developed in Chapter 6 and applied to the site investigations in Chapters 7 and 8. The proposed approaches aim to improve the accuracy of prediction and mechanistic representations of blast-induced damage in the underground environment. Limitations of existing blast vibration analysis approaches and blast damage prediction models have also been discussed.

1.2.1 Chapter 2: Explosively-Driven Rock Breakage

Chapter 2 provides an overview of the published concepts of explosive breakage of rock and brittle materials. The concepts related to strain-wave breakage mechanisms versus gas penetration breakage processes are discussed (e.g. Duvall and Petkof, 1958; Field and Ladegaard-Pederson, 1971; Kutter and Fairhurst, 1971; Langefors and Kihlström, 1978; McHugh, 1983; Yu and Vongpaisal, 1996). Due to the dynamic nature of blasting vibrations when loading a rock mass, the dynamic properties of the intact rock portions of the rock mass are also discussed.

1.2.2 Chapter 3: Interaction of Blast Waves with Existing Discontinuities

Chapter 3 is dedicated to investigating the interaction of blast-induced vibrations with existing discontinuity networks within a rock mass. The influence of rock mass fracturing on the attenuation of stress waves represents a critical field of study when

interpreting the results of blast vibration analysis. Therefore, published works pertaining to numerical, laboratory and field investigations of wave attenuation related to discontinuities have been reviewed (e.g. Devine et al., 1965; Morland, 1974; Kjartansson, 1979; Hudson, 1981; Crampin, 1984; King et al., 1986; Pyrak-Nolte et al., 1990; Singh and Narendrula, 2004).

The orientations of particle motions measured during the author's blast vibration monitoring program are discussed along with the introduction of a method of predicting discontinuity loading conditions from blasting vibrations. This method of assessment has not been previously found in published literature. To further investigate the influence of discontinuity orientation on wave attenuation, two-dimensional elastic wave propagation simulations using the software *Wave2000 Plus* have been carried out. The results of the simulations further support the previously reviewed research, and helped to form strategies for interpreting the results of blast vibration analyses.

1.2.3 Chapter 4: Near-Field Blast Vibration Monitoring and Data Processing

Very few recommendations have been made in past investigations for the design and implementation of near-field blast vibration monitoring programs. The differences between transducer types and responses have been characterised in the past (e.g. Andrieux and Heilig, 1994 and Andrieux, 1996), as well as some assessments of the required monitoring specifications of specific charge and distance configurations (e.g. Yang et al., 1993). Transducer types, monitoring configurations and coupling conditions in the published literature are highly variable, and in most cases are not adequately described. This lack of standardised monitoring greatly limits the ability to compare the results of different monitoring programs.

The selection of near-field transducer types, configurations, coupling systems and installation procedures can influence the quality of recorded near-field blast vibration data. Chapter 4 provides unambiguous definitions for four proposed monitoring ranges from far-field to extreme near-field and recommendations for the design and implementation of near-field blast vibration monitoring systems.

1.2.4 Chapter 5: Blast Vibration Analysis and Interpretation

After blast vibration data have been recorded and processed, analysis and interpretation of the data in relation to blasting parameters and rock mass characteristics should be performed. Through five decades of blast vibration investigations, two charge weight scaling relationships have dominated the process of near-field vibration analysis and interpretation. These two relationships are the Scaled Distance approach and the Holmberg-Persson prediction model, both of which attempt to predict peak vibration amplitudes based on the inputs charge weight and distance. Numerous researchers have utilised these two models to investigate near-field vibration modelling and prediction (e.g. Ambraseys and Hendron, 1968; Olson et al., 1972; Holmberg and Persson, 1979; Yu and Vongpaisal, 1996; Villaescusa et al., 1997; Heilig, 2002). The input variables for either of the dominant prediction models differ based on the suggested factors contributing to the peak vibration amplitude. Chapter 5 reviews and compares the various charge weight scaling models as well as other alternate models of peak vibration prediction and applies these models to data collected as part of the blast vibration monitoring program.

Determination of accurate source to sensor distances is critical to the accuracy of vibration analysis and prediction equations. The effect of distance selection on the accuracy of near-field blast vibration prediction has not been adequately represented in the published literature. This effect is investigated in Chapter 5, along with a proposed model for calculating void-affected distances where the wave field is influenced by underground voids. The method of distance calculation proposed by the author is referred to as Void and Initiation Corrected Distance (VICD). An additional investigation into the effects of mining voids on propagating wave fields was performed using two-dimensional elastic wave simulations. These results aided in interpreting the effects of wave diffraction and void-interrupted wave fields on recorded seismograms.

Blast vibration analysis and prediction models have typically used two-dimensional, log-log, linear regression techniques to determine the curve fits describing amplitude attenuation equations. An alternate regression approach has been proposed using

three-dimensional multi-variable nonlinear estimation to improve the accuracy of data fitting of measured vibration data. This approach uses the advanced statistical software package Statistica 8.0 and the general form of the charge weight scaling equation.

1.2.5 Chapter 6: Proposed Energy and Strain-Based Blast Damage Criteria

Chapter 6 and associated Appendix 8 briefly discuss methods of measuring, indicating or predicting rock mass damage from static or dynamic loading. These methods include direct and indirect observation methods (e.g. Li, 1993; LeBlanc et al., 1995; Paventi et al., 1996; Germain and Hadjigeorgiou, 1997; Singh, 2001), geophysical methods (e.g. Spathis et al., 1985; Friedel et al., 1995; Malmgren et al., 2007), deformation measurements (e.g. Li, 1993; Villaescusa et al., 1997), testing of extracted rock samples (e.g. Holmberg and Persson, 1978; Brinkmann, 1990; Ouchterlony et al., 1993) and amplitude or strain-based empirical and analytical damage prediction models (e.g. Holmberg and Persson, 1978; LeBlanc et al., 1995; Zhang and Chang, 1999; Keller and Kramer, 2000).

Chapter 6 also discusses the use of blast wave energy values such as the total wave energy density and stored strain energy density as defining wave quantities instead of single instantaneous peak amplitudes. Calculations of wave energies require rock mass properties such as the P-wave velocity and rock density. Therefore, variations in rock mass properties can be better represented in the modelled wave quantity. In addition, a method is proposed to calculate the cumulative mean normal dynamic strain within a blast wave from the stored strain energy density. The strain calculation approach requires additional dynamic rock mass properties, thus allowing for more rock mass-specific vibration relationships to be identified.

Both the stored strain energy density and mean normal dynamic strain are used to define several proposed rock mass damage criteria. These criteria treat a rock mass as two individual components; intact rock and discontinuities. Separate criteria are proposed to predict damage to each of the two components based on energy or strain-related fracture conditions. The strain-based criteria for compressive and tensile damage to intact rock include a treatment for inclusion of the mining-induced static

stresses and strains. This type of treatment of underground blast damage prediction under the influence of static stresses does not exist in past empirical or semi-analytical models.

1.2.6 Chapter 7: Case Study - Barrick Gold Corp. Kanowna Belle Gold Mine

Using the methods of blast vibration analysis and rock mass assessment discussed and developed in the previous chapters, Chapter 7 presents the case study results from three stopes at the Kanowna Belle Gold Mine (KBGM) in Western Australia. The three stopes studied at KBGM were mined in the deepest active part of the mine at the time of the study, at approximately 950m below the surface. At this depth, the virgin and mining-induced static stresses were significant, as indicated by the seismically-active nature of the rock mass. The work performed at KBGM was designed to investigate the effects of high static stresses and large-scale faults on the performance of the rock mass near stope boundaries.

During the blast vibration monitoring and stope assessment program in the D block of KBGM, a total of 12 tri-axial transducers were installed. Between the three monitored stopes, 27 production firings were recorded resulting in a data set of 1333 vibration data points. Each data point represented a discrete, identifiable waveform generated by a single blasthole and recorded on an individual transducer. The number of identifiable, single charge contributions represented approximately half of the total number of detonating charges in the 27 firings due to apparent charge interactions, misfires or excessive waveform shielding by voids. The combined data set was analysed using the nonlinear estimation tools discussed in Chapter 5; data subsets based on individual stopes and orientations were also analysed.

Traditional geotechnical investigation tools such as intact rock testing, discontinuity mapping and static stress modelling were used to characterise the rock mass surrounding the three monitored stopes. Additional characterisations were performed using geophysical approaches based on the properties of the recorded blast waves. These approaches included stress wave velocity measurements and peak amplitude-frequency analyses. The relationships between blast vibration attenuation equations were also used to assess the rock mass conditions. Stope performance assessments

were also performed by comparing the post-extraction void surveys with the stope design wireframes.

The data collected for stope dB10-38T were used to perform blast damage predictions using both existing prediction models and the proposed rock mass damage criteria discussed in Chapter 6. The results of the prediction using the proposed approach clearly indicated the influence of the existing static compressive strains on the predicted tensile damage envelope from a single blasthole located at the perimeter of the stope.

1.2.7 Chapter 8: Case Study - BHP Billiton Cannington Mine

The characterisation and assessment techniques described in Chapter 7 were also applied to four stopes at the BHP Billiton Cannington Mine in Queensland, Australia. The four stopes were located in two different mining areas, representing different rock mass conditions, stope sizes and blasting geometries. The two mining areas are referred to as the North Zone and R4. In the rock mass surrounding the four stopes, a total of 28 tri-axial accelerometer and geophone sondes were installed to monitor 32 production blasts. A total of 3750 data points were identified out of a possible 8180 fired charges during blast monitoring at the Cannington Mine over the course of the 18 month program. The results of blast-induced damage prediction for North Zone stope 24jC6HL are detailed and discussed.

1.2.8 Chapter 9: Conclusions

The observed characteristics of over 5000 single-hole, near-field and intermediate-field blast vibration waveforms have led to proposed approaches for collection, analysis and interpretation of near-field blast vibration data. Chapter 9 details the original contributions by the author related to the collection, processing and analysis of vibration data and integration of rock mass characterisation and stope assessment approaches. Limitations of the research project are discussed, as well as proposed future work and applications of the research findings in the mining industry.

CHAPTER 2 : EXPLOSIVELY-DRIVEN ROCK BREAKAGE

2.1 Introduction

The first step in characterising blast-induced rock mass damage is to investigate the explosion process and attempt to understand the mechanisms that contribute to explosively-driven rock breakage. Many physical mechanisms and theories have been proposed to explain the complex process of dynamic damage of brittle materials from explosive loading. Of the available models, those related to breakage from strain wave loading and penetration of high-pressure detonation products dominates the literature. Chapter 2 is dedicated to reviewing the process of explosive energy release resulting in breakage of rock and the dynamic properties of a rock mass that influence the extent and degree of fracturing.

2.2 General Description of the Explosive Fracture Process

The processes involved in explosive detonation and propagation have been studied for over six decades. The types of explosive applications discussed in the body of literature include rock breakage for mining and tunnelling, geophysical exploration, in situ perforation for gas and oil extraction and solution mining, chamber blasting for oil or radioactive waste storage and nuclear testing. Although the exact mechanisms that control explosive rock breakage are not completely understood, the general processes and physical phenomena can be separated into several identifiable phases. The generally accepted phases of rock breakage from explosive loading include (after Kutter and Fairhurst, 1971 and others):

1) Initiation of explosive detonation and propagation of the detonation front along the explosive charge.

2) Rapid production of extremely high temperature and high pressure gases immediately behind the detonation front.

3) Rapid expansion of the explosive cavity from shock wave loading and confined initial detonation gases that crush and pulverise the rock adjacent to the borehole or cavity wall.

4) Permanent plastic deformation of material outside the crushed zone

5) Radial crack generation and extension of cracks from the crushed zone boundary due to high tangential stresses and the tensile tail of the initial compression wave.

6) Rapid pressure drop within the explosion cavity leading to circumferential fractures from rapid unloading.

7) Confined residual gas pressure penetrating fractures leading to dilation and further fracture extension.

8) Additional fracturing or fracture extension from tensile reflected P-waves and direct or reflected shear waves.

To graphically represent stages 1-8 of the breakage process, Figure 2.1 shows the zones of induced damage and the characteristic damage mechanism(s).

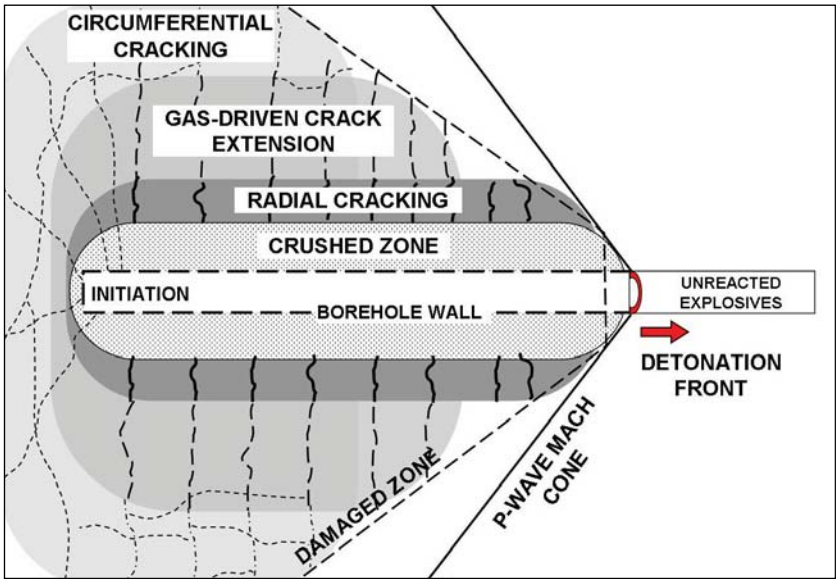

Figure 2.1. Illustration of the detonation process and rock breakage zones behind the detonation front.

2.3 Definition of Breakage Zones Surrounding an Explosive Charge

The rock mass surrounding an explosive detonation can be categorised into four zones of response based on the severity of damage and the assumed material loading mechanism. The four zones are traditionally referred to as the crushed zone, the plastic zone, the elasto-plastic zone and the elastic zone. The degree of material strength degradation in each zone ranges from completely disintegrated (crushed zone) to intact but lightly or moderately fractured (elastic zone). The response of each zone to additional stress loading depends on the degree of fracturing and the interconnectivity of fractures.

Many factors influence the extent and degree of damage from the detonation of an explosive charge. These include explosive properties such as the detonation pressure and velocity of detonation, coupling of the explosive product to the borehole and rock mass properties such as rock strength and elastic deformation constants. Past research has attempted to characterise the zones of damage around simple and complex charging geometries using small-scale to field-scale investigations (e.g. Kutter and Fairhurst, 1971; Siskind and Fumanti, 1974; Wilson and Holloway, 1987; Djordjevic, 1999; Olsson et al., 2002). These investigations have attempted to develop general theories of material breakage or fragment distribution resulting from explosive detonation based on the explosive product or material properties. More information on these studies is provided in Appendix 3.

Detonation of modern commercial explosives can generate borehole pressures up to several gigapascals (Cunningham, 2006). Measurements of strain waves or pressures generated at the borehole wall for fully-coupled explosives do not exist in the literature to confirm this value due to a lack of transducers capable of withstanding the extremely high pressures and temperatures. The inability to measure the material response in the crushed and plastic zones has required the use of mathematical or numerical modelling and scaled blasting tests to estimate the extent of these zones.

2.3.1 Prediction of the Extent of Crushing

Esen et al. (2003) provided a good overview of past empirical-mathematical models for predicting the radius of crushing based on explosive properties, borehole radius, and material properties. This overview included past work performed by Szuladzinski (1993) and Djordjevic (1999), along with a new approximation of the extent of the crushed zone based on an experimental program and numerical modelling of the detonation process. For first approximations of the radius of the crushed zone (r_c), Equations 2.1 to 2.3 were published by Esen et al. (2003).

$$r_c = \sqrt{\frac{2r_0^{\,2}\rho_0 Q_{ef}}{F_c^{'}}} \qquad \text{(Szuladzinski, 1993)} \qquad (2.1)$$

$$r_c = \frac{r_0}{\sqrt{24T/P_b}} \qquad \text{(Djordjevic, 1999)} \qquad (2.2)$$

$$r_c = 0.812 r_0 \left(\frac{(P_b)^3}{K\sigma_c^2} \right)^{0.219} \qquad \text{(Esen et al., 2003)} \qquad (2.3)$$

Where r_0 = blasthole radius (mm)

ρ_0 = explosive density (g/mm^3)

Q_{ef} = effective explosive energy (Nmm/g)

F'_c = rock confined dynamic compressive strength (8 times σ_c: MPa)

T = rock tensile strength (Pa)

P_b = borehole pressure (Pa)

σ_c = rock unconfined compressive strength (Pa)

K = rock stiffness (Pa)

Based on the results of Equations 2.1 to 2.3, a large range in crushed zones can be estimated based on the explosive type, borehole radius and rock properties. Figure 2.2 illustrates the variance between the models based on r_c versus r_0 for a single blasting case using water-resistant ANFO in basalt over a range in borehole diameters.

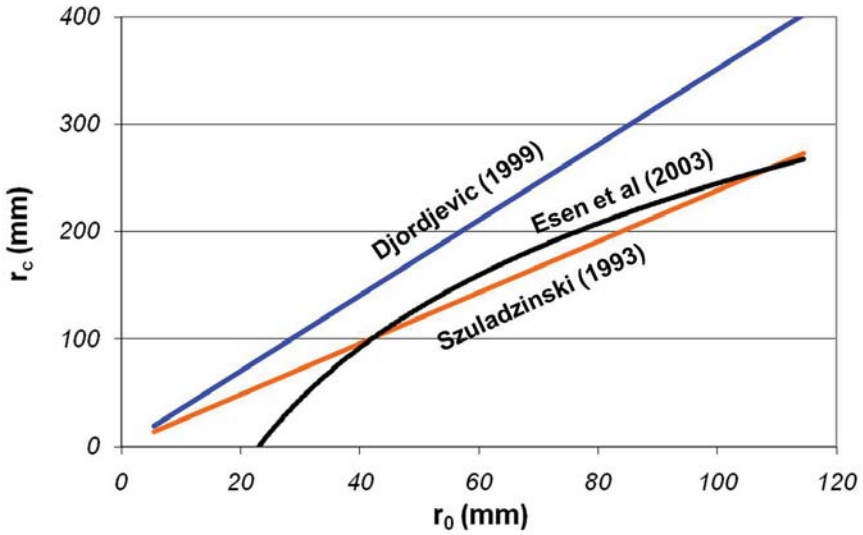

Figure 2.2. Value of r_c versus r_0 for different models using various borehole diameters in basalt blasted with water-resistant ANFO (after Esen et al., 2003).

For the range of common open stoping blasthole diameters of 64 to 102mm (r_0 = 32 to 51mm), the radius of the crushed zone would be estimated to be approximately two to four times the borehole radius according to the models in Figure 2.2. The result would be a radius of approximately 100-200mm of disintegrated material around the fully-coupled borehole. Langefors and Kihlström (1978) proposed a zone of crushing of approximately equal to or slightly less than the radius of the charge for a 40mm diameter blasthole common to tunnel blasting. According to the models of Szuladzinski (1993) and Djordjevic (1999), the ratio of r_c to r_0 does not change significantly with borehole diameter for the same explosive type in the same rock mass. This value ranges between 2 and 3.5.

It would be unlikely that a significant volume of material from the crushed zone would remain self-supporting and therefore would not be expected to influence the overall stability and geotechnical behaviour of an excavation. The crushed volume would be considered to be expected overbreak. The geotechnical performance of a blasted excavation would more likely be controlled by the fractured zone outside the crushed and plastic zones. The residual rock mass strength may be adequate to self-support against immediate gravity-driven rock block failure, but offer little resistance to continued loading. For this reason, the characteristics and extent of the remaining fractured zone is critical to the behaviour of blasted excavations in rock.

2.3.2 Prediction of the Radial Fracture Zone

Energy is expended in disintegration of the crushed zone and permanent deformation of rock in the plastic zone as the initial shock wave travels away from a blasthole wall. The high degree of attenuation in this region reduces the energy in the wave to a point where the wave-induced compressive stresses become less than the compressive failure strength of the rock. The material response to wave loading after this point is assumed to be elasto-plastic in nature. Further attenuation of wave energy leads to elastic behaviour of the material in response to wave loading. For elastic material response, the rock mass no longer permanently deforms under wave-induced displacement and behaves more as a quasi-brittle, elastic material. The distance at which the transition from plastic to elastic behaviour occurs has been identified in past works as the dimension of the equivalent cavity (Sharpe, 1942; Kutter and Fairhurst, 1971), or the transition from compressive to tensile fracture initiation.

2.3.2.1 Stress Wave-Driven Tensile Cracking in the Elastic Zone

Early mathematical wave models suggested that the initial compression wave from an explosive detonation imparts both compressive stresses in the direction of propagation and tangential stresses acting normal to the propagating wave front. The action of the combined compressive and tangential stresses at the wave front load the carrier material in bi-axial tension coupled with uni-axial compression (Favreau, 1969). Additionally, a tensile tail was proposed to exist immediately following the initial compressive front as a result of material unloading. Observations of explosive-induced waves in photo-elastic materials led Rossmanith et al. (1997) to identify the tensile tail developing approximately 3 borehole radii away from an explosive charge. This tensile tail was found to be a maximum at approximately 4-5 borehole radii from the source.

2.3.2.2 Experimental Determination of the Extent of Radial Fracture Zones

Many researchers have carried out experimental investigations in brittle materials to investigate the extent of fracturing around an explosive charge. One of the defining early works on the effect of strain-driven crack formation was that of Kutter and

Fairhurst (1971). Through laboratory testing of small-scale samples of plexiglass and rock, Kutter and Fairhurst (1971) concluded that the approximate zone of cracking around a pressurised blasthole was 6 times the radius of the equivalent cavity or crushed zone. Initial fractures subjected to additional pressurisation such as the quasi-static residual borehole pressure, were extended to approximately 9 times the cavity radius. Through approximation of the equivalent cavity (3 times the borehole radius), the total fracture radius was 12 times the borehole radius.

Additional investigations of the formation of the radial fracture zone both with and without the influence of quasi-static gas pressures were conducted by various researchers on a range of materials including glass, Plexiglas, cement, concrete, and rock. Some of these investigations were published by Field and Ladegaard-Pederson (1971), Bradley and Kobayashi (1971), Bergmann et al. (1973), Siskind and Fumanti (1974), McHugh (1983), Wilson and Holloway (1987), Daehnke et al. (1996), Olsson et al. (2002) and Singh and Narendrula (2004). Additional information on these investigations is provided in Appendix 3. It is important to note that fracture patterns created in scaled models with free surfaces can be influenced by wave reflections and thus may not accurately represent the confined conditions under actual blasting geometries.

The creation of new fractures in the radial cracking zone has been generally accepted as being a product of the shock wave and initial radial and tangential tensile stresses. But, as the level of energy in the initial wave is reduced further and the quasi-static borehole pressures become active, fracture extension in the outer elastic damage zone can occur. This fracture extension process is not well understood and has been the subject of debate for several decades.

2.3.3 Fracture Extension Zone

The outermost damage region surrounding an explosive charge is the zone of radial fracture extension. One characteristic of this region is the propagation of a fewer number of fractures than those contained within the radial cracking zone. Proportionally longer fracture lengths are typically experienced at a regular angular distribution. For the general case of no applied boundary stresses, the angular

distribution of the elongated cracks is approximately 45-120 degrees. Scaled blasting tests have confirmed this distribution of fractures, identifying between three and ten propagating cracks in the outer region of the fractured elastic zone (e.g. Kutter and Fairhurst, 1971; Field and Ladegaard-Pederson, 1971; McHugh, 1983; Olsson et al., 2002). Figure 2.3 shows the fracture pattern resulting from detonation of 17mm decoupled charges in 38mm holes in granite.

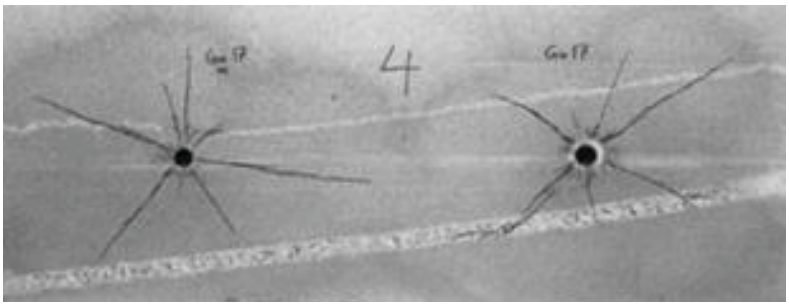

Figure 2.3. Distribution of elongated radial cracks from 17mm Gurit charges in 38mm holes in a granite block (Olsson et al., 2002).

Kutter and Fairhurst (1971) suggested Equation 2.4 for determination of the extension of fractures from direct tangential tensile strain effects.

$$\Delta l = \frac{3t'_{\max}}{2.35\sqrt{\left(\frac{1-v}{1-2v}\right)}-1}\cdot a \qquad (2.4)$$

Where Δl = fracture extension (in)

t'_{max} = rise time for tangential tensile peak strain (s)

a = radius of equivalent cavity (in)

v = material Poisson's ratio

For a material with v = 0.26, Equation 2.4 predicts crack elongation of 2.5 times the cavity radius, or approximately 8-9 times the borehole radius. Siskind and Fumanti (1974) suggested a radius of fracture extension reaching between 8 and 14 times the borehole radius based on the results of measurements of fracturing in granite from blasting of 165mm blastholes.

2.4 Strain Wave versus Gas Penetration Fracture Models

The main mechanism of fracturing in blasting remains a subject of debate, even after several decades of research on the subject. In general, there are two main mechanisms considered plausible for extension of fractures outside the zone of immediate strain-wave tensile fracture. These two mechanisms are gas penetration and reflected tensile wave superposition. In reality, both mechanisms should contribute to fracture extension, but to what degree is highly dependent on the geometry of the blast and the proximity to free surfaces.

2.4.1 Direct and Reflected Tensile Strain

The strain wave theory of fracture formation and extension relies on the dominance of the strain wave in forming the in situ fracture pattern around an explosive charge. Once the fractures are formed, the delayed action of gas penetration only serves to dilate the existing fractures and dislocate the pre-formed fragments. Tests performed by various researchers have illustrated little difference between the fracture patterns and extents of cracking around charges blasted in either unlined or steel tube-lined holes (e.g. Brinkmann, 1990). The steel hole liners isolated the cracks from pressurisation by the detonation gases.

Under a special geometry where a charge is near a free surface, as in most mining-related blasting applications, the extent of fracturing of the burden material can be explained by the reflection of the initial compressive stress wave from the free face. This reflection results in a tensile wave travelling back towards the existing radial fractures, which loads the fracture tips with potentially large tensile stresses. The secondary tensile loading of arrested or propagating fractures can lead to further fracture extension towards the free surface. Researchers such as Duvall and Petkof (1958), Field and Ladegaard-Pederson (1971) and Yu and Vongpaisal (1996) attributed burden breakout and face spalling to these reflected tensile effects.

2.4.1.1 Arguments for Strain-Based Fracture Extension Theories

Strain-dominated breakage theories simplify the physical and mathematical models developed to simulate the explosive process by neglecting the extremely complex

role of gas penetration. Arguments in favour of the strain-based breakage models contend that the effects of confining stresses and compaction of pulverised material from the crushed zone do not allow adequate crack pressurization to occur. These factors would significantly limit the effect of fracture extension through pressure-driven dilation at the propagating crack tip.

In the underground environment, it has been proposed that confining stresses inhibit the dilation of fractures by gas penetration. It is believed that this confinement restricts gas penetration to such a degree that it has no significant influence in underground blast damage outside the zone immediately around the charge (Heilig, 2002). McHugh (1983) noted that gas penetration appeared to cause significant fracture extension compared with stress-wave effects under zero confining stresses. A moderate confining stress was found to decrease gas-driven fracture extension.

To justify the theory that fractures could propagate under the effect of stress waves in the absence of gas penetration, Wilson and Holloway (1987) observed that the fracture dilation front trailed the propagating fracture front by a significant distance. This finding could lead to the conclusion that fractures can form and propagate without the dilation required for gas penetration. In addition, it has been proposed that the pulverised material immediately around the borehole wall in the crushed zone will invade the fracture mouths and inhibit gas penetration. This was supported by the work of Kutter and Fairhurst (1971). In light of these arguments, it is recognised from the work of other researchers that a purely strain-driven fracture propagation model would lead to gross simplification of explosive breakage. These results are reflected in the gas penetration theory of fracture propagation.

2.4.2 Gas Penetration Theory of Fracture Extension

The second main theory of fracture propagation from blasting is the theory of high-pressure gas penetration. The fundamental theory is that the high-pressure and high-temperature detonation products enter the mouths of existing fractures, causing internal pressurisation. The dilatory response of the pressurised crack mouth increases the stress concentrations at the fracture tip, leading to crack propagation. Some of the proponents of gas-driven fracture propagation as the dominant breakage

mechanism include Langefors and Kihlström (1978), McHugh (1983), Forsyth (1993), Daehnke et al. (1996) and Cho et al. (2004).

One of the most highly referenced works on gas penetration fracture extension is that of McHugh (1983), who investigated the role of dynamic gas loading on fracture propagation using computer models and two small-scale experiments with Plexiglas cylinders. McHugh (1983) was the first to suggest the use of a dynamic pressure function in a numerical model instead of quasi-static cavity pressures reported in earlier works (Kutter and Fairhurst, 1971 and Porter and Fairhurst, 1971). McHugh suggested that gas-driven fracture extension increased fracture lengths by 10-100 times over extension from tensile stresses alone. This was determined from mathematical modelling under a condition of zero confining stresses. McHugh (1983) also proposed that fracture extension resulting from gas penetration with an external hydrostatic stress of 6.9MPa was between three and 25 times longer than that for tensile stress alone. McHugh (1983) proposed Equation 2.5 to calculate the final crack length in metres (C) under zero confining pressure.

$$C \approx \left(\frac{2V_i}{n\pi w}\right)^{\frac{2\gamma}{(4\gamma-1)}} \left[\frac{2P_i}{\sqrt{\pi}K_{Ia}}\right]^{\frac{1}{(2\gamma-0.5)}} \tag{2.5}$$

Where P_i, V_i = initial pressure and volume (MPa, m^3)

n = number of cracks

w = crack width (m)

γ = ratio of the specific heats of the gas

K_{Ia} = fracture arrest toughness (MPa$\sqrt{m}$, assumed to be equal to K_{Ic})

For an applied confining stress (σ), the stress intensity at the fracture tips can be adjusted according to Equation 2.6.

$$K_I = \frac{2}{\sqrt{\pi}}(P_c - \sigma)\sqrt{C} \qquad (2.\ 6)$$

Where P_c = internal crack pressure (MPa)

K_I = modified fracture toughness (MPa√m)

Daehnke et al. (1996) developed a model using a complex hydro- and thermo-dynamic code to numerically investigate the gas pressure profile acting along the length of a fracture. The results indicated that a pressure gradient existed within the fracture and the pressure approached zero at the crack tip (Figure 2.4). This model overcame the assumption of a constant pressure along the crack adopted in the model by McHugh (1983).

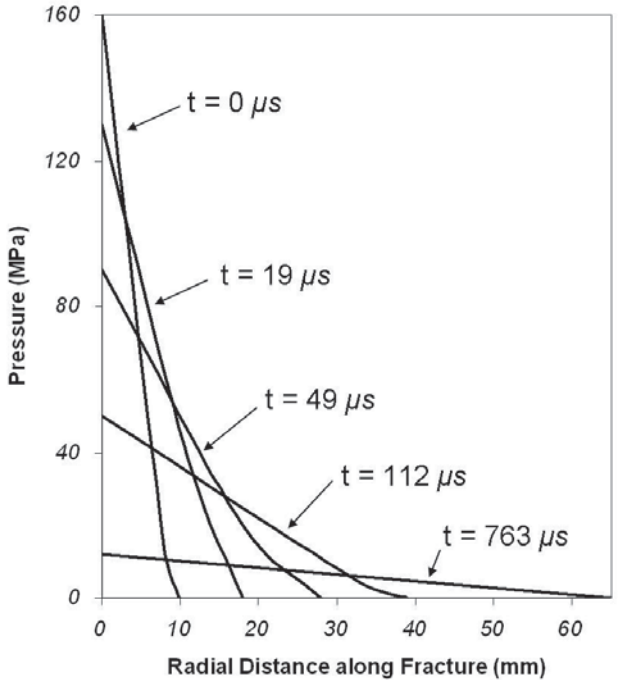

Figure 2.4. Pressure profile within a fracture of 65mm length under the action of penetrating detonation gases (after Daehnke et al., 1996).

Cho et al. (2004) reached the same conclusion as Daehnke et al. (1996) regarding the significance of the gas loading phase through numerical analysis of dynamic fracture formation. According to the principles of fracture mechanics, as crack lengths are increased the stress required to reinitiate and propagate the crack is greatly reduced.

If the initial pressure and crack dilation at the fracture mouth are adequate, the pressure distribution along the crack will be high enough to extend the fracture.

One fact that seems to support the role of gas pressure in fracture creation or extension is the distribution of energy released from an explosive product in the shock and gas phases. According to theoretical models of energy partitioning and analysis of blast vibrations, the amount of explosive energy contained within stress waves propagating from an explosive charge used for rock breakage or excess seismic energy is between 2 and 25% of the total energy (Kutter and Fairhurst, 1971; Field and Ladegaard-Pederson, 1971; Brinkmann, 1990; Hamdi et al., 2001; Sanchidrián et al., 2007). The percentage is a function of the explosive type, coupling and material properties.

Based on the low percentage of total explosive energy contributing to the formation of seismic waves, it could be theorised that a large portion of the energy is expended in formation of gaseous products as well as heat, sound, and other forms of energy. The work of Forsyth (1993) discussed a blasting condition where an explosive charging pattern of higher shock energy reduced rock mass damage through reduction in gas penetration, highlighting the effect of gas penetration of fracture extension and breakage in a poor quality rock mass.

2.4.3 Combination of Strain and Gas Penetration Models

In reality, both tensile strain and gas penetration will contribute to fracture extension from an explosive charge (Singh, 1999). The combined effect will be most pronounced in the immediate proximity of the blasthole. At larger distances where extension of existing discontinuities would be expected to dominate rock mass damage and stability, strain effects have been considered to be the most critical fracturing mechanism. Due to the activity of confining stresses and the geometries considered in the presented blast damage studies, the effect of gas-dominated fracture extension is not explicitly considered in the development of blast damage models discussed in Chapter 6.

To date, no damage prediction approach has been developed with the capacity to accurately model the effects of gas penetration coupled with strain–driven fracturing due to the complex nature of thermodynamic fluid flow under dynamic and quasi-static pressures. Numerical modelling has attempted to obtain a solution for the pressurisation of blasting fractures (e.g. Minchinton and Lynch, 1996; Potyondy et al., 1996; Rossmanith et al., 1997; Furtney et al., 2009) and empirical relationships have been developed from scaled model and field blasting studies (for example, Kutter and Fairhurst, 1971 and McHugh, 1983). In spite of the research focus, the level of understanding of the role of explosion gases in addition to strain wave-driven fracture is still limited. One of the major gaps in the research is an investigation into the effects of realistic confining stresses encountered in the underground environment on gas penetration into fractures.

2.5 Description of Waves Generated by Explosive Detonation

The ability to predict the types of waves emitted during explosive detonation and the behaviour of those waves once propagating have been areas of extensive research for almost two centuries. The initial work by Navier and Poisson in the 1820's identified the transmission of transverse waves through elastic materials and in the 1880's surface waves were identified by Rayleigh (Kolsky, 1953).

2.5.1 Wave Types Generated by an Explosive Source

Since the discovery of body waves and surface waves in the 19th century, many models attempting to predict the response of a material to wave loading have been developed based on the engineering principles of pressure, force, displacement, stress and strain. For several decades, focus has been placed on the waves generated by buried explosives charges due to their use in geophysical exploration and rock breakage.

It is generally accepted that the types of waves generated by an explosive source are highly dependent on the charge geometry and proximity to free surfaces. Under most circumstances in mining, charges of confined cylindrical geometry are detonated near free faces as determined by the rock breakage capacity of the charge size and

explosive type. The types of body waves generated by confined explosive charges are of two fundamental types. These are Primary (longitudinal, P-) body waves and Secondary (distortional, S-) body waves. After body waves interact with free surfaces, a third type of wave is created referred to as a surface wave. Several types of surface waves can result; namely, Rayleigh waves and Love waves.

The transmission of energy within different wave types is a function of the particle motion in relation to the direction of wave propagation. By definition, longitudinal waves induce compression and dilation in the direction of wave propagation and shear waves induce displacements normal to the direction of propagation. Surface waves exhibit displacements similar to body waves, but displacements occur in both the direction of wave propagation and normal to the free surface.

2.5.1.1 Properties of Blast-Generated Body Waves

Waves propagating through a rock mass from an explosive source can be described by general wave parameters such as the wave frequency, period and wavelength. Several properties of the transmission material are also important to the propagation of a wave. For example, the elastic properties and density of the carrier medium influence the wave propagation velocities and the development of energies and strains within the wave.

Both the properties of the wave and the material are important in characterising the displacements and strains applied to a material by a wave. Some general elastic wave properties that will be utilised in defining and analysing wave behaviours can be calculated using Equations 2.7 to 2.10 (Kolsky, 1953 and Graff, 1975).

$$f = \frac{1}{T} \tag{2.7}$$

$$\lambda = \frac{V_{(p,s)}}{f} \tag{2.8}$$

And

$$V_p = \sqrt{\frac{\left(k + \frac{4}{3}\mu\right)}{\rho}} \tag{2.9}$$

$$V_s = \sqrt{\frac{\mu}{\rho}} \tag{2.10}$$

Where f = wave frequency (Hz)

T = wave period of oscillation (s)

λ = wavelength (m)

V_p = longitudinal wave velocity (m/s)

V_s = distortional wave velocity (m/s)

k = material bulk modulus (Pa)

μ = material rigidity modulus (Pa)

ρ = material density (kg/m^3)

2.5.1.2 Distribution of Wave Types: P-, S-, and Rayleigh Waves

Wave fields observed near blasting events can often be complex in nature and represent a combination of P-waves, S-waves and surface waves. Therefore, estimation of the energy content within each wave type can aid in predicting the damage-potential and relative amplitudes of the waves within a recorded waveform.

Miller and Pursey (1955) investigated the distribution of source energy in wave types generated by a non-explosive oscillating compression seismic source in half space. Equations 2.11 to 2.14 summarise the breakdown of theoretical wave energy or work performed by each wave type as a result of the source. In the original work, no units were specified for the equations, but it has been assumed that consistent units would be required to reach accepted units of work or energy.

$$W = W_C + W_{Sh} + W_{Su} = 4.836\left(\frac{\pi^3 v^2 a^4 P_0^2}{\rho V_C^3}\right) \tag{2.11}$$

And

$$W_C = 0.333\left(\frac{\pi^3 \nu^2 a^4 P_0^2}{\rho V_C^3}\right) \tag{2.12}$$

$$W_{Sh} = 1.246\left(\frac{\pi^3 \nu^2 a^4 P_0^2}{\rho V_C^3}\right) \tag{2.13}$$

$$W_{Su} = 3.257\left(\frac{\pi^3 \nu^2 a^4 P_0^2}{\rho V_C^3}\right) \tag{2.14}$$

Where W_C = Power (energy) radiated in the compression wave

W_{Sh} = Power radiated in the shear wave

W_{Su} = Power radiated in the surface (Rayleigh) wave

ν = frequency of vibration

a = area of the circular plate source

P_0 = initial stress factor related to the input source

ρ = density of the medium

V_C = compression wave velocity of the material

The results of the calculation yields a wave energy distribution listed in Table 2.1.

Table 2.1. Distribution of energy between wave types from a compression wave source on the ground surface.

Wave Type	**Percent of total Energy (%)**
Compression (P-Wave)	7
Distortional (Shear)	26
Surface Wave (Rayleigh)	67

Woods (1968) graphically illustrated this distribution of energy using Figure 2.5.

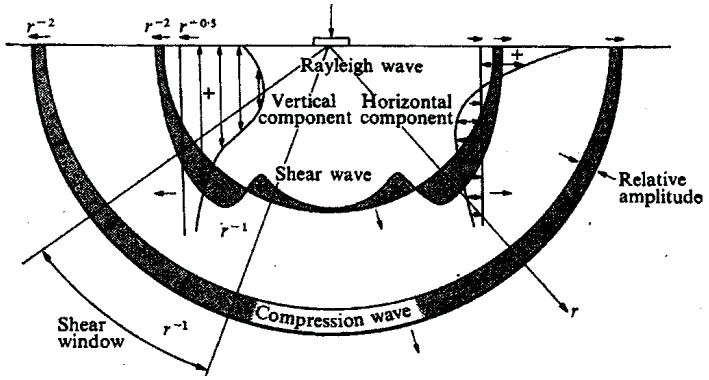

Figure 2.5. Distribution of wave energy in wave types from a normal force applied near the surface (Woods, 1968).

The work of Miller and Pursey (1955) and Woods (1968) can be adapted to a fully confined explosive charge in an underground geometry by assuming that the Rayleigh wave component has not developed and only consider the body P and S-waves generated by the source acting normal to a borehole wall. The distribution between P- and S-waves for the remaining energy would be 21% and 79%, respectively. Heelan (1953) discussed the energy distribution between P-waves and S-waves, proposing a split of approximately 40% within the P-wave and 60% within the SV-wave (vertically-oriented shear wave). White and Sengbush (1963) and Geyer and Martner (1969) also observed large amplitude shear waves at various angles to the borehole axis up to 10 times the amplitude of the P-wave.

2.6 Response of a Rock Mass to Blast-Induced Dynamic Loading

One of the greatest challenges in rock mechanics is accurately and adequately defining the response of a rock mass to mining-induced loads. It is well understood that most rock masses encountered in mining behave characteristically as an anisotropic, non-homogeneous, non-linear material due to variations in strength, deformation modulus and discontinuities of various scales and conditions. A rock mass must be viewed as a constituent material composed of discrete components, where the characteristic behaviours of each component influence the overall response to static and dynamic loading.

For mining-scale problems, the two main components of a rock mass are intact rock and existing or freshly formed discontinuities (Jaeger and Cook, 1979). The intact rock component can be further subdivided to consider the influence of micro-crack density and distribution or mineralogical structure on the behaviour of the pre-existing rock blocks. Discontinuities within the rock mass can be characterised based on scale (persistence), orientation, repeatability (spacing) and condition. The properties of a discontinuity which contribute to the condition or the behaviour under mining loads include the aperture, roughness, infill and degree of saturation.

Sections 2.6.1 and 2.6.2 attempt to identify some of the intact rock properties that are important when assessing or predicting rock mass behaviour under dynamic loading conditions. Chapter 3 further outlines the affects of in situ discontinuities on wave propagation and vibration amplitudes. These two components, when considered both explicitly and as a combined system, provide a better understanding of the behaviour of an integrated rock mass under blast wave loading.

2.6.1 Dynamic Intact Rock Properties

As a wave propagates through a rock mass, dynamic displacements are experienced at points along the wave front at a rate proportional to the wave frequency and the intensity of the wave. The works of past researchers (e.g. Kumar, 1968; Perkins et al., 1970; Grady and Lipkin, 1980; Olsson, 1991; Zhao et al., 1999) have identified distinct differences between rock properties measured through static, quasi-static and dynamic methods. In general, the strength and elastic modulus (Young's Modulus) of a material increases as the stress or strain rate of loading increases.

2.6.1.1 Dynamic Rock Strength

A vast majority of rock testing for mining and tunnelling applications is performed under quasi-static loading conditions. The standard loading rate during quasi-static testing is generally on the order of 10^{-5} strain per second. To investigate the dynamic behaviour of a brittle material, dynamic material testing from low to high dynamic strain rates (10^{0} strain/s to 10^{5} strain/s) can be achieved by high velocity hydraulic or pneumatic machines or impact loading methods such as flyer plates, gas guns or Split

Hopkinson Pressure Bar apparatus (Meyers, 1994). Dynamic material strength testing typically suffers several limitations when attempting to represent large-scale in situ dynamic material properties. These limitations are not exclusive to dynamic testing, as similar effects have been observed for quasi-static testing (Jaegar and Cook, 1969). Due to the methods available for dynamic strength testing, a higher degree of sample size bias may be introduced. Common methods of dynamic material testing such as the Split Hopkinson Pressure Bar apparatus requires the use of small samples approximately 25% of the standard size of samples used in quasi-static testing.

Numerous laboratory studies have been conducted to investigate the effect of loading rate on the compressive strength of rock materials at different temperatures and confining stresses (e.g. Kumar, 1968; Perkins et al., 1970; Lindholm et al., 1974; Grady and Lipkin, 1980; Olsson, 1991; Li et al., 1999; Zhao et al., 1999; Ray et al., 1999; Mohanty and Prasad, 2001; Xia et al., 2008). These dynamic compressive strength testing programs have illustrated the influence of strain rate on the compressive yield strength of rock specimens. Loading rates ranging from quasi-static (10^{-5} strain/s) to high-order dynamic (10^{3} strain/s) applied to various rock types have yielded values of dynamic strength increase factors. These values, expressed as the ratio of dynamic compressive strength to static compressive strength can range from 1.8 (Perkins et al., 1970) to 5 (Olsson, 1991), depending on the rock type. The general relationship between rock compressive strength and strain rate is a gradual increase in strength up to a critical point corresponding with a strain rate of 10^{0} to 10^{2} strain/s, after which the strength increases dramatically with increased strain rate (Figure 2.6).

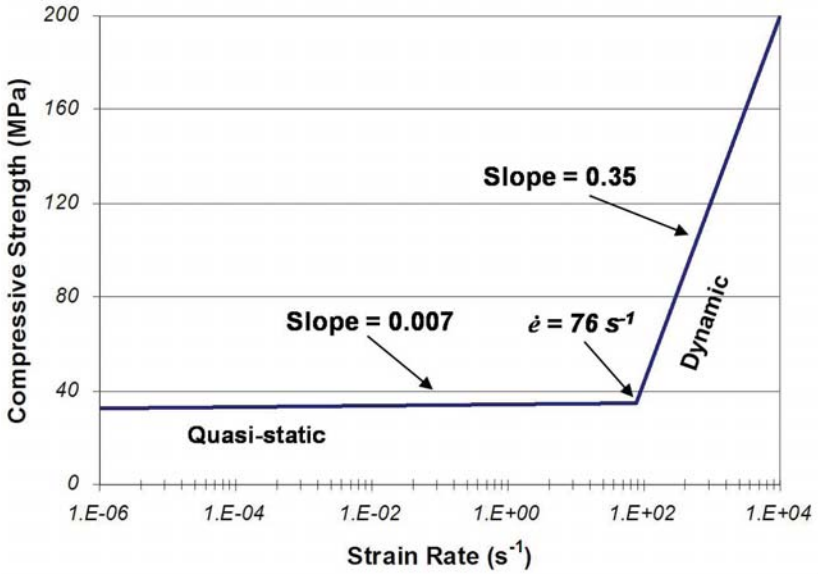

Figure 2.6. Effect of strain rate on compressive strength in ash-fall tuff (after Olsson, 1991).

Other investigations of dynamic strength have yielded additional general relationships between material compressive strength and strain rate. The results have indicated that the material compressive failure stress (σ_C) was proportional to the cube root of the strain rate (Grady and Lipkin, 1980 and Olsson, 1991), an exponential relationship (Perkins et al., 1970) or a cubic exponential (Grote et al., 2001), amongst others. An exponential relationship between material strength and strain rate will be discussed further in Chapter 6.

In the zone of tensile fracture extension, strain wave-induced loading can reach strain rates of 10^3-10^4 strain/s (Chitombo et al., 1999 and Lindholm et al., 1974). At these strain rates, the dynamic tensile rock strength would be expected to increase well above the static tensile strength. Testing results have confirmed increases in dynamic tensile strengths with increased loading rates for concrete and rock specimens. These investigations have identified dramatic increases in dynamic tensile strength occurring at a characteristic point of strain rate sensitivity, similar to the dynamic compressive strength results (e.g. Birkimer, 1970; Bažant et al., 1993; Zhang et al., 2000; Klepaczko and Brara, 2001; Cho et al., 2003; Wu et al., 2005; Zhu, 2007).

Klepaczko and Brara (2001) and Cho et al. (2003) published comprehensive curves of the dynamic tensile behaviour of rock and concrete under various strain rates from quasi-static to dynamic. Wu et al. (2005) reported findings similar to Klepaczko and Brara (2001) at strain rates between 1.0 and 2.0 strain/s. The results of the three testing programs are illustrated in Figure 2.7.

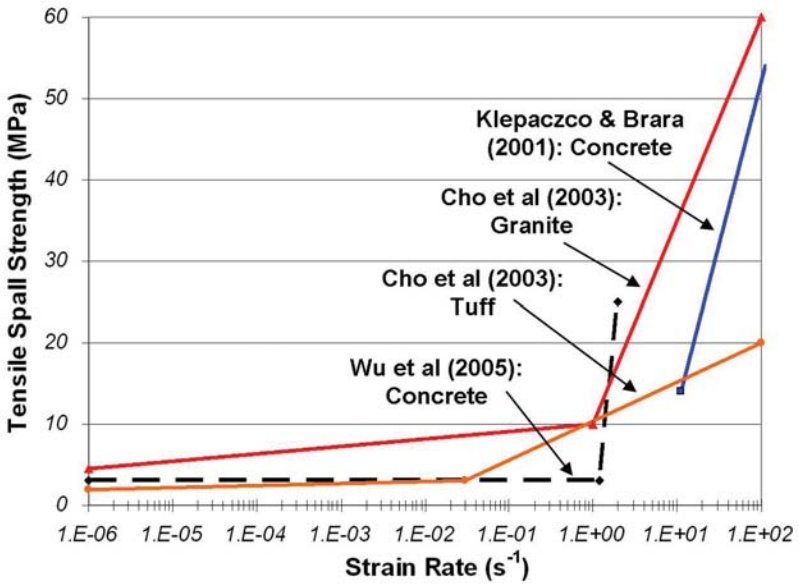

Figure 2.7. Dynamic tensile spall strength of concrete and rock as presented by several researchers (after Klepaczko and Brara, 2001, Cho et al., 2003, and Wu et al., 2005).

Based on the results in Figure 2.7, the intersection point between the highly strain rate-dependent zone and the largely independent zone is between 10^{-2} and 10^{1} strain/s depending on the rock type. Few studies have been performed for tensile behaviour in the region of transition due to a lack of intermediate loading-rate apparatus. As such, the quasi-dynamic behaviour of materials at intermediate loading rates is not well documented. Laboratory tests performed by Lambert and Ross (2000) on notched-cavity concrete specimens studied the effect of intermediate strain rates from approximately 10^{0} to 10^{1} strain/s. Over the tested strain rates, the increase in tensile fracture strength was approximately a factor of 3 over the quasi-static tensile strength.

2.6.1.2 Dynamic Elastic Constants

The dynamic elastic Young's Modulus (E_{dyn}) of a rock sample or rock mass measured through ultrasonic wave propagation methods can be on the order of 80% higher than the static Young's Modulus (E_{st}) determined through quasi-static testing (Hendron, 1968). Eissa and Kazi (1988) found an increase in E_{dyn} of 40% to 100% over E_{st} for a range in rock types. Van Heerden (1987) observed a general decrease in dynamic Poisson's Ratio (v_{dyn}) versus the static value (v_{st}) from quasi-static testing, although the relationship was not as consistent as that for E_{dyn} versus E_{st}. Additional factors contribute to the difference between the elastic constants determined from laboratory testing of intact rock samples and an in situ rock mass. These factors are related to the degree of fracturing, saturation and the magnitudes and orientations of confining stresses.

It is arguable that just as dynamic rock strength influences blast vibration-induced damage, dynamic elastic constants will also influence the degree and extent of explosive damage through influence of the stress-strain relationship. In the blast damage investigations discussed in this thesis, values for in situ E_{dyn} have been calculated from the stress-wave velocity data obtained as part of the blast vibration monitoring program (Chapters 7 and 8). E_{dyn} was then used in subsequent calculations of energy and strain to assess the potential for blast-induced damage.

Values of Poisson's Ratio (v) and rock density (ρ) in the two case studies conducted as part of this thesis were provided from static intact rock testing. Values for v_{dyn} were not available due to the inability to identify shear wave velocities from the recorded waveforms. Using the static values for v and ρ and the measured V_p, E_{dyn} was calculated using Equation 2.15 (Ambraseys and Hendron, 1968).

$$E_{dyn} = V_p^2 \rho \frac{(1+\nu)(1-2\nu)}{(1-\nu)} \qquad (2.15)$$

Where v = Poisson's Ratio (static)

V_p = P-wave velocity (m/s)

ρ = material density (kg/m^3)

2.6.2 Calculation of Strain Rate

In the literature, there does not appear to be a standardised approach to calculate values of strain rate from blasting measurements. This is due to the fact that most blast damage investigations do not explicitly consider the effect of strain rate on rock mass damage potential. The single published approach that has been proposed for use in calculating the strain rate from blasting seismograms was published by Yang et al. (1994) and again by Yang and Scovira (2007). According to this work, the strain rate ($\dot{\varepsilon}$) from dynamic wave loading is a function of the measured particle acceleration and the material P-wave velocity. This approach is based on elastic strain theory and plane wave assumptions such that the strain rate in the direction of wave travel can be calculated using Equation 2.16.

$$\dot{\varepsilon} = \frac{\partial \varepsilon}{\partial t} = \frac{\left(\frac{\partial u}{\partial x}\right)}{\partial t} = \frac{\partial^2 u}{\partial x \partial t} = \frac{\partial^2 u}{\partial t^2}\frac{\partial t}{\partial x} = a(t)\frac{1}{C} \tag{2.16}$$

Such that the maximum strain rate ($\dot{\varepsilon}_{\max}$) is given by:

$$\dot{\varepsilon}_{\max} = \frac{PPA_{\max}}{V_p} \tag{2.17}$$

Where PPA_{max} = measured maximum particle acceleration (m/s2)

V_p = measured or assumed P-wave velocity of the seismic wave (m/s)

Although the plane wave assumption greatly simplifies the interpretation of the complex wave fields in the near-field of a blast, Equation 2.17 has been used in forward estimations of strain rate due to the explicit numeric solution. Approaches for estimating the strain rate using other wave properties such as the wave number or frequency generally lack an explicit solution due to the complex frequency spectra of blast waves.

2.7 Discussion and Conclusions

The process of explosive breakage of rock is very complex. Three main theories are well represented in the literature: strain wave-driven breakage, gas-penetration-driven breakage, and a combination of both. The models used to describe each type of breakage have been developed from observation of explosive fracturing in scaled testing and numerical modelling.

The dynamic response of a material to high strain-rate loading typically results in increases in strength and elastic response. Therefore, blast damage models should consider the dynamic properties of a rock mass. The dynamic material properties described in this chapter have been discussed further in Chapter 6, and integrated into the rock mass characterisations and blast damage predictions performed in Chapters 7 and 8. The models developed and applied in Chapters 6, 7 and 8 consider only the effects of strain-wave loading as applied to the elastic zone, where fracture extension or rock mass damage may be largely attributed to tensile and shear mechanisms.

This page left intentionally blank – KG Fleetwood

CHAPTER 3 : INTERACTION OF BLAST WAVES WITH EXISTING DISCONTINUITIES

3.1 Introduction

Chapter 2 was dedicated to investigating the blasting process and gaining a level of understanding of the influence of stress waves on the intact rock portion of a rock mass. Chapter 3 approaches the subject of interaction of blasting waves with existing discontinuities through examination of both the direction of maximum particle motion in relation to discontinuity planes and wave attenuation. Numerical wave propagation simulations have also been performed to investigate the attenuation of elastic waves under the influence of discontinuities of varying orientations.

3.2 Discontinuity Loading Conditions from Blast Waves

In general, fractures or discontinuities can be extended through three modes of loading. These modes are Mode I (tensile dilatational loading), Mode II (shear loading) and mixed mode loading (Modes I and II together). In the present study, only pure Mode I and pure Mode II loading have been considered. It is beyond the scope of this thesis to conduct an in-depth fracture mechanics investigation, although some consideration has been given to the likely loading mechanisms and potential damage to existing discontinuities from stress wave loading.

Discontinuities can be preferentially loaded by strain waves in normal dilation or shear based on the characteristics of the wave and the orientation of the discontinuity in relation to the wave propagation direction. The direction of maximum particle displacement associated with a strain wave can therefore influence different discontinuity sets in different ways with regards to loading and damage mechanisms. Attenuation of propagating blast waves is also influenced by existing discontinuities.

The first step in determining the effects of measured vibrations on existing discontinuities is to record the in situ discontinuity orientations and distributions through mapping. Different methods of discontinuity mapping include spot mapping, line mapping, window mapping and logging of extracted core samples (Brady and

Brown, 2004). The results of a mapping program can then be used to statistically model the discontinuity networks contained within the rock mass or be represented graphically (e.g. Terzaghi, 1965; Stagg and Zienkiewicz, 1968; Priest and Hudson, 1976; Jaeger and Cook, 1979; Villaescusa, 1991; Villaescusa and Brown, 1992, Hadjigeorgiou et al., 1995).

3.2.1 Determination of Discontinuity Loading Characteristics by Blast Waves

As a blast wave propagates through a rock mass, the oscillatory nature of the particle displacements induced by the wave will create differential loading at a point of interest over time. The displacement field at a single moment in time will be multi-dimensional in nature due to the different wave components, and can be reliably measured using dynamic motion transducers. The equipment and methods of blast wave measurement will be discussed further in Chapter 4.

The vector sum particle motion of wave activity can be determined through simple vector mathematics using the multiple components of measured vibration at a point in time. The resulting measured particle motion can therefore be defined by a vector length (amplitude) and direction based on the measured amplitudes and orientations of the transducer axes. It is important to highlight that the value of three-dimensional motion is a vector quantity. In a majority of blast vibration studies, the results of single or multi-axial measurements are treated as simple scalar quantities (i.e. generic value of peak particle velocity).

The components of the vector sum particle motion at any time t are supplied from the individual axial measurements. Basic vector mathematics can then be used to calculate the magnitude of the resultant vector, referred to as the vector sum particle motion. In addition to the vector magnitude, the angles between the measurement axes and the vector sum direction can be determined from the direction cosines. The time domain vector sum particle motion ($VS(t)$) is calculated using Equation 3.1.

$$VS(t) = \sqrt{R(t)^2 + T(t)^2 + V(t)^2} \qquad (3.1)$$

Where $R(t)$ = radial component of the recorded time domain waveform

$T(t)$ = transverse component of the recorded time domain waveform

$V(t)$ = vertical component of the recorded time domain waveform

3.2.2 Using Vector Sum Particle Motions to Assess Wave Loading Conditions

The vector sum direction represents a vector normal to the plane containing all three components for nonzero values on all three axes (Figure 3.1). For the case of one or more of the instantaneous component measurements being equal to zero, the vector sum lies in the plane containing the individual components.

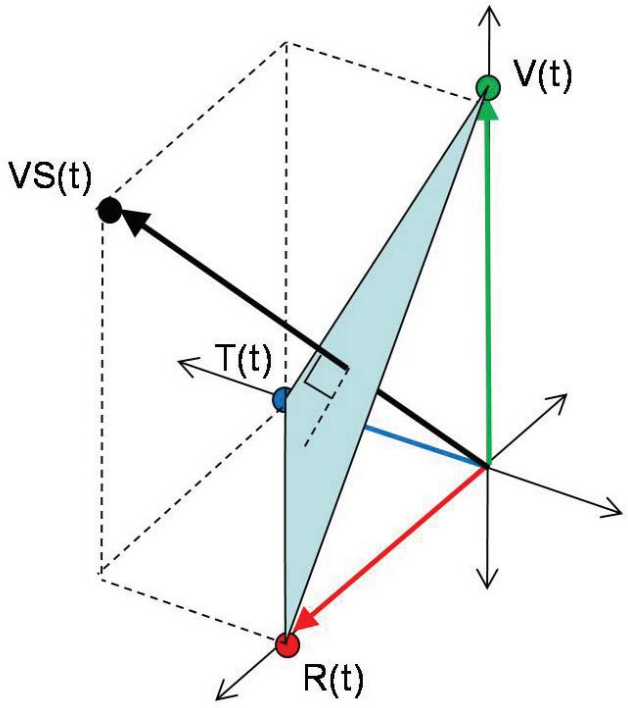

Figure 3.1. Vector sum motion and the plane of individual component intersection used to define discontinuity loading conditions.

The normal vector VS(t) shown in Figure 3.1 defines the direction of the instantaneous aggregate particle motion, and therefore can be viewed as a direction of maximum loading of the rock mass in relation to a point at the axis of the recording transducer. Where the actual orientations of the transducer components are known due to controlled installation practices, the vector direction of maximum particle motion can be transferred to mine-grid coordinates or translated into a direction relative to the propagation direction of the wave. This practice allows comparisons to be made between directions of maximum loading and the orientations of existing discontinuities indicated through mapping.

3.2.3 Observed Loading Orientations from Measured Blasting Vibrations

Analysis of waveforms collected as part of the author's blast vibration monitoring program has indicated dominant shear wave activity in the near field of blasting events. Analyses of individual components identified peak vector motion directions roughly perpendicular to the wave propagation direction in many cases. This orientation of particle motion would be expected to produce dominant shear-type loading normal to the axis of wave propagation. For propagation directions approximately normal to existing discontinuity planes, significant shear loading would be expected. Discontinuity planes parallel with the direction of propagation would be loaded preferentially in either normal compression or dilation depending on the rotation of the peak motion direction in relation to the discontinuities. Figure 3.2 illustrates the vector directions of the peak vector sum particle velocities for a set of blastholes monitored in Stope 24jC6HL at the BHP Cannington Mine. The resulting measured vector sum directions have been oriented in relation to the wave propagation direction.

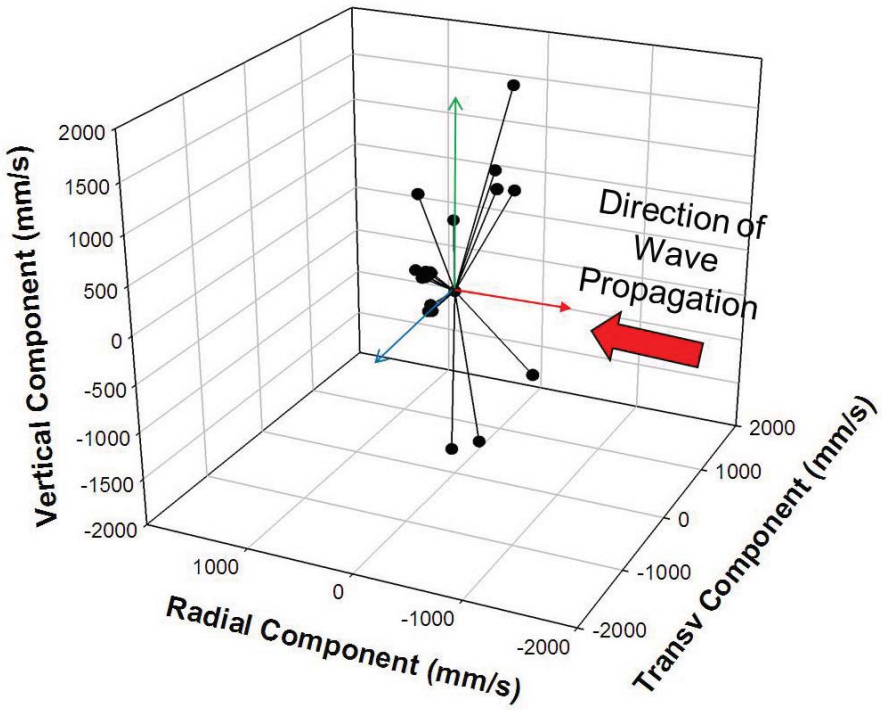

Figure 3.2. Plot of orthogonal components of the peak vector sum particle velocity as calculated from the vibration records in the North Wall of BHP Cannington Stope 24jC6HL 200mLv winze firing #7.

In Figure 3.2, the lines from the central point to each vibration vector sum represent the vector sum particle velocity direction. The information in Figure 3.2 is similar to polarisation analysis used in seismic analysis of earthquakes.

To assess the loading conditions on pre-existing discontinuity sets as a function of the observed peak amplitude orientations, the peak vector motion directions can be plotted on discontinuity distribution plots. Figure 3.3 illustrates a horizontal plane rosette plot of existing discontinuity strike directions compared with the direction of wave propagation and the plane normal to the wave propagation direction. The plane normal to the wave propagation direction would be expected to contain a majority of the peak vector directions as illustrated in Figure 3.2.

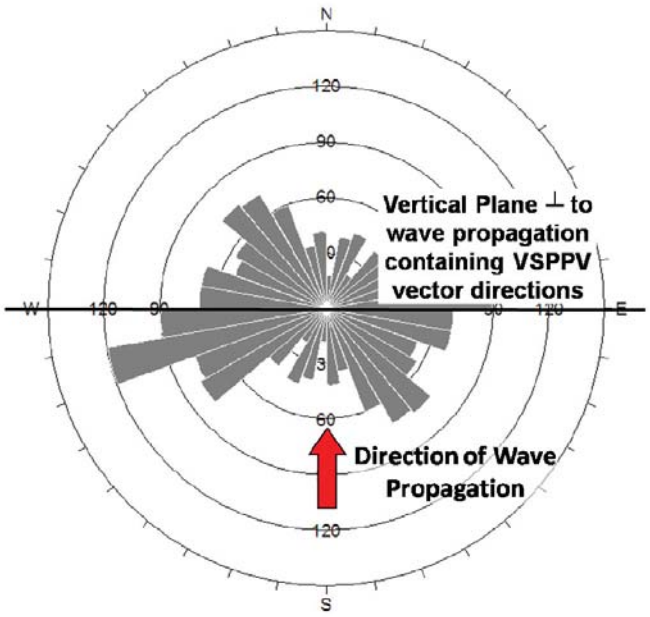

Figure 3.3. Horizontal plane rosette plot of discontinuity strike distribution and the trace of the vertical plane containing the peak vibration directional vectors for a wave propagating north from stope 24jC6HL at the Cannington Mine.

According to the model in Figure 3.3, any discontinuity sets of strike direction East/West at steep dip angles would be expected to experience peak shear-type loading from the indicated wave propagation direction. A joint plane parallel with the direction of propagation (striking North/South) would be expected to experience maximum loading in a combination of joint-normal dilation and shear based on the angle of the peak vector direction in relation to the joint plane.

The analysis method shown in Figure 3.3 can be extended to all orientations of wave propagation around a blasting event to identify the zones and mechanisms of discontinuity loading that may be experienced within a rock mass. The resulting model could therefore predict the existing discontinuity sets likely to experience the maximum normal or shear-type loading based on the direction of wave propagation. Figure 3.4 illustrates the directions of wave propagation resulting in peak dilatational and shear loading on a major discontinuity set at approximate strike of 15 degrees North of East and dipping steeply (yellow plane rosette). The blue arrows represent the directions of peak motion expected within the plane normal to the wave propagation direction, resulting in shear loading (left) and normal loading (right).

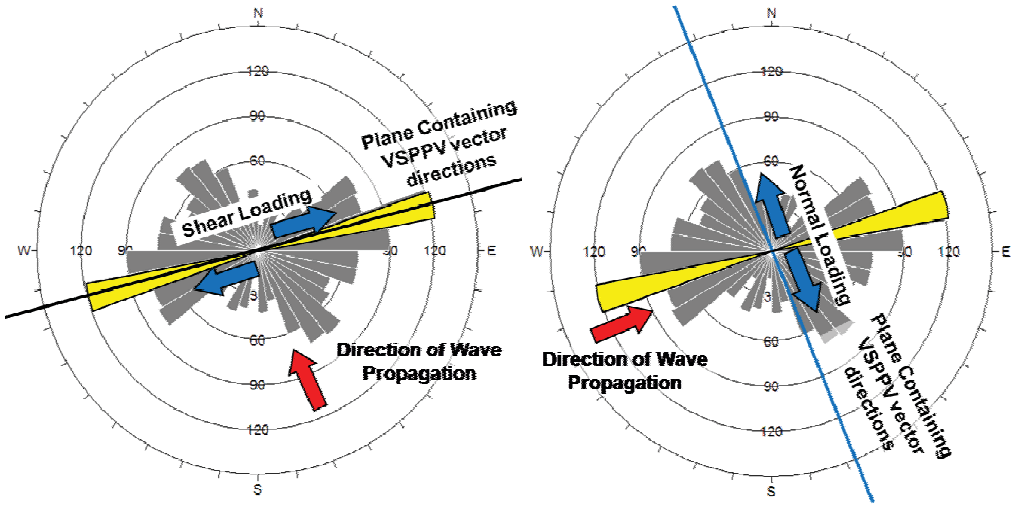

Figure 3.4. Loading conditions on prominent discontinuity set and directions of wave propagation supplying maximum shear (left) or normal (right) loading.

The interpretation of the concept in Figure 3.4 would be that waves propagating in a direction normal to the plane of the identified major discontinuity set would produce maximum motions in a direction of relative shear displacement (Mode II), whereas the same wave propagating along a direction parallel with the joint plane may produce motions of either dilation (Mode I) or shear (Mode II). Likely, the loading conditions for the parallel propagation orientation would be mixed mode. The variation in loading mechanisms based on the direction of wave propagation represents a very complex condition when considering the likely damage to existing discontinuities through either Mode I or Mode II loading.

The zones of peak shear loading around stope 24jC6HL at the BHP Cannington Mine have been identified for two mapped discontinuity sets using the analysis method shown in Figures 3.3 and 3.4. Figure 3.5 illustrates a plan view of stope 24jC6HL and the wave propagation orientations where maximum blast-induced shear loading would be expected for two identified discontinuity sets (shown in the rosette plot).

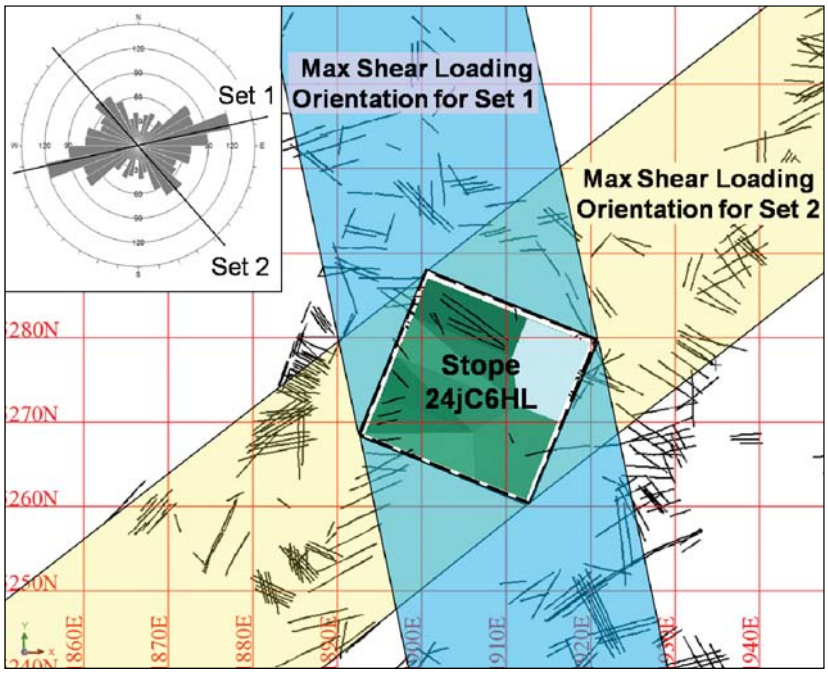

Figure 3.5. Plan view of stope 24jC6HL and the orientations of maximum discontinuity shear loading from blast-induced waves as suggested by the propagation-normal maximum shear loading direction.

3.3 Effect of Wavelength and Discontinuity Dimension

Blast-induced wave loading of discontinuities does not necessarily result in damage under unfavourable loading directions. The wavelength of the displacement wave can influence the degree of interaction with individual discontinuities or existing rock blocks. Wavelengths much greater in scale than the in situ discontinuity length or rock block dimensions would be expected to induce minimal fracture surface excitation due to the relatively low rate of differential deformation.

Micro fractures of average dimension of 1-5 millimetres (typical "Griffith" cracks) would require wavelengths of a comparable dimension to excite the entire fracture surface at an adequate rate to cause damage with the passage of each wave cycle. The required frequency of the displacement wave would therefore be of the order 0.5 – 1.0 MHz. The displacement waves recorded in the elastic zone (5-50m from the explosive charge) at both study sites were typically between 50 and 1000Hz. Velocity waveforms were between 250 and 2500Hz and acceleration waves were

between 1000 and 10,000Hz. Based on the frequency values of the recorded displacement waves, discontinuities of less than 5m length in the elastic wave propagation zone would have been unlikely to be fully activated over the fracture face. Table 3.1 lists the characteristic displacement wave frequencies and discontinuity trace lengths likely to experience activation based on the wavelength of a blast wave of P-wave velocity of 5000 m/s and a shear wave velocity of 2800 m/s.

Table 3.1. Comparison of linear discontinuity dimension and critical frequency of excitation based on similar wavelength to discontinuity dimension.

Discontinuity Trace Length	**Critical P-Wave Frequency (kHz)**	**Critical S-Wave Frequency (kHz)**
100mm-500mm (discrete macro-fracture)	> 10.0 - 50.0	> 6.0 - 30.0
500mm-1m	> 5.0 - 10.0	> 3.0 - 6.0
1m-5m (persistent discontinuity set)	> 1.0 - 5.0	> 0.60 – 3.0
5m-50m (large discontinuity/ local fault)	> 0.10- 1.0	> 0.06 - 0.60
>50m (large-scale fault)	> 0.10	> 0.06

As implied by Table 3.1, large-scale discontinuities and faults are expected to be excited by a wider range of blast-induced vibration frequencies, whereas smaller discontinuities require higher frequencies generally experienced very close to blastholes. Some fracture response would be expected to occur from loading by longer wavelengths, but the degree of excitation has not been well documented in available research.

3.4 Models of Wave Attenuation and Discontinuities

Several processes can occur which modify the amplitudes, frequency spectra and wave types of propagating waves during interaction with in situ discontinuities. These processes are reflection, refraction and diffraction. Reflection, refraction and diffraction depend on the angle of incidence of the wave front relative to the fracture plane, the frequency spectra of the wave and the size and condition of the discontinuity (Achenbach, 1973). Of these processes, reflection and refraction are

closely related to the material and discontinuity properties. Diffraction is largely related to the scale and geometry of the interaction.

The degree to which a wave front is altered while propagating through a rock mass is a function of both the rock mass and the wave properties. The critical parameters of the rock mass include the intact rock properties as well as the discontinuity size, orientation, spacing, and condition (e.g. aperture, roughness and infill). The wave properties of interest include the wave type, energy content, frequency and direction of propagation in respect to discontinuity planes. Geophysical wave propagation research has studied the interaction of waves and discontinuities for many years (e.g. Morland, 1974; Kjartansson, 1979; Hudson, 1981; Crampin, 1984; Schoenberg and Douma, 1988; Peacock and Hudson, 1990). A number of these models are discussed further in Appendix 2.

3.4.1 Laboratory and Field Investigations of Fracture Effects on Wave Attenuation

The effects of fractures on wave velocity and attenuation in laboratory-scale and field-scale studies are generally well documented in the geophysics literature (e.g. Hudson, 1981; Pyrak-Nolte et al., 1990; Hayles et al., 1999; Butt, 2001). Investigations were also performed in mining research to examine the effects of pre-splits, natural discontinuities, jointed rock masses or blasting damage on wave characteristics. Some studies of mining-related applications of wave attenuation includes the works of Devine et al. (1965), King et al. (1986), LeBlanc et al. (1995), Martino and Chandler (2004) and Singh and Narendrula (2004).

The influence of a single large-scale fracture on wave propagation in Lithonia granite was investigated by Devine et al. (1965). The aim was to assess changes in peak vibration amplitudes measured at common points prior to and after formation of a continuous pre-split (Figure 3.6).

Figure 3.6. Fracture created by pre-splitting in Lithonia granite (Devine et al., 1965)

Devine et al. (1965) concluded that no significant changes in wave velocity or amplitude were indicated from the data. The absence of change in the wave velocity would suggest that the presplit was either discontinuous or not of sufficient dilation to noticeably influence the wave behaviour. The results of the study illustrated the importance of the fracture condition and orientation of the wave front relative to the fracture surface to the propagation or reflection of the wave.

High-frequency cross-hole seismic surveys and laboratory pulse tests were conducted by King et al. (1986) to measure the P- and S-wave velocities and seismic quality factors for a strongly jointed, columnar basaltic rock mass. The rock mass in the field trial was composed of regular vertical columnar formations ranging in width of 150-360mm, dipping at 70 to 90 degrees dissected by frequent, low angle discontinuous cross jointing. A cross-hole borehole pattern was drilled in a diamond formation of 3m cross dimensions such that horizontal, vertical and diagonal surveys could be performed. Acoustic measurements were made every 150mm in the first 1.5m of the borehole to indicate the extent of blasting damage, and at 1m intervals for the remaining 9.5m of borehole. The results of the field tests identified strong P- and SH-wave velocity anisotropy between the vertical and horizontal directions due to the interaction with the in situ jointing. Calculated Q (seismic quality) values using the spectral-ratios technique identified significant attenuation differences between the vertical and horizontal directions (Figure 3.7).

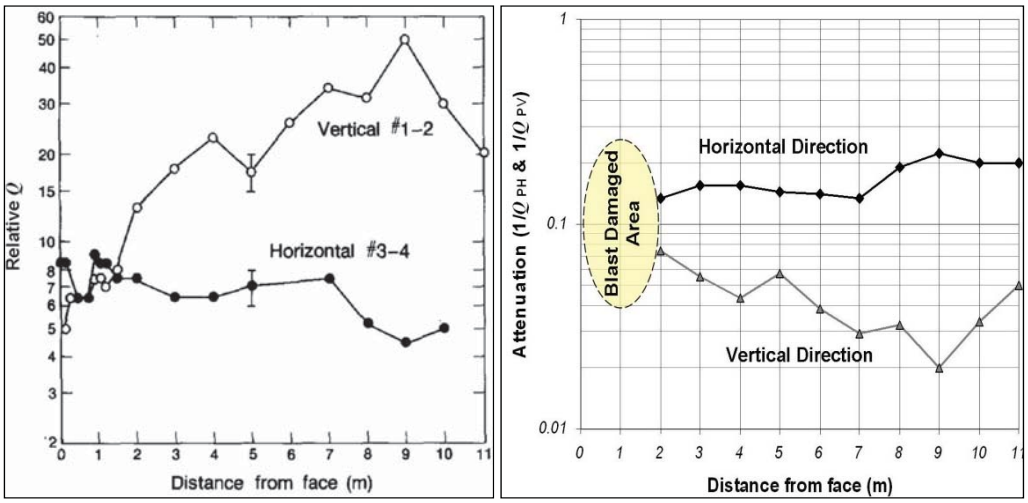

Figure 3.7. Normalised P-wave Q values for vertical and horizontal directions based on distance from the excavation face (left) and normalised attenuation values $1/Q$ for vertical and horizontal directions (right) (after King et al., 1986).

Figure 3.7 illustrates the difference between the amplitude attenuation rates based on the in situ jointing. In the horizontal direction, the 3m spacing between the holes would suggest interaction of the waves with between 8 and 20 fractures based on the columnar thickness. The linear decrease in the vertical attenuation has been attributed to the induced vertical stress around the face of the excavation. Therefore, the attenuation values outside this area of influence (approximately 1 excavation diameter) could be considered to be the virgin rock mass attenuation. The attenuation factor for horizontal direction P-waves was assumed to be approximately 0.2.

Pyrak-Nolte et al. (1990) conducted a series of laboratory experiments to investigate the effects of saturation, fracture stiffness and confining stress on the wave transmission properties across a single natural fracture. The results of the laboratory step-loading tests revealed a change in attenuation, wave velocity and frequency spectra for the three different fracture properties and loading conditions. The models with the highest fracture stiffness and axial loading displayed almost no loss of energy, emulating the properties of the intact rock tests. The least stiff fracture condition experienced significant amplitude loss and shift of the transmitted frequency spectra as observed in Figure 3.8.

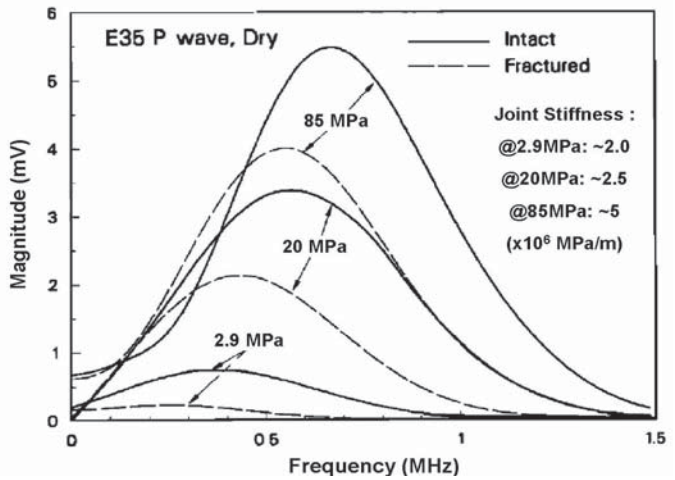

Figure 3.8. Comparison of amplitude and frequency spectra for intact and fractured samples of varying fracture stiffness under axial loads (Pyrak-Nolte et al., 1990).

The measurements performed by Pyrak-Nolte et al. (1990) are very valuable due to the ratio of the wavelength of the input P- and S-waves to the discontinuity dimension (i.e. 0.13-0.19mm:1mm). Through similarity of wave behaviour on different scales, the ratio of interaction of 0.19:1 would represent a P-wave frequency of approximately 5200Hz interacting with a 5m discontinuity. These conditions are realistic for near-field interaction of blasting waves with large discontinuities.

Small-scale concrete blasting models with simulated joints were used by Singh and Narendrula (2004) to study the effect of joint orientation on transmitted vibrations. Similar to the results predicted by mathematical models, the highest attenuation was experienced for wave incidence of 45 degrees. The peak amplitude was approximately 40% of that measured over the same distance in unjointed material.

3.5 Numerical Simulation of Attenuation in Jointed Material

Numerical simulation was performed by the author to investigate the effect of joint properties and orientation on the transmission of stress waves through an infinite, heterogeneous and elastic material. The 2-D wave propagation program *Wave2000 Plus*® developed by CyberLogic was used to model the effects of parallel discontinuities on vibration amplitudes measured on an array of transducers.

Wave2000 Plus® was developed to simulate small-scale ultrasonic testing of engineering designs. The program operates by solving the full-field 2-D elastic wave equations using a finite difference numerical modelling platform. The basic inputs of the program include material properties, material and void shapes and dimensions, boundary conditions, source characteristics and receiver locations and types. The program is capable of modelling multiple linear displacement or pressure function source configurations including longitudinal and shear components of specified input frequencies and durations. As the main functionality of the program is a simulation tool for assessment of small objects, scaling of physical dimensions of the model was required to represent true mining geometries. The model parameters were adjusted to 1/1000 (1m = 1mm) scale to capture realistic mining-scale geometries.

3.5.1 Simulated Wave Attenuation under Normal Incidence

The initial model to investigate the effect of parallel fractures on amplitude attenuation included a set of four discrete parallel discontinuities added to a host linear-elastic homogeneous rock-like material. Five receivers were located on a specified orientation to record the bi-axial in-plane particle velocity fields. Receivers 1-4 were positioned at the midpoint between each discrete discontinuity of 2.5m spacing. One control receiver (5) was positioned in an unaffected direction, 2.5m behind the source. The model is shown in Figure 3.9.

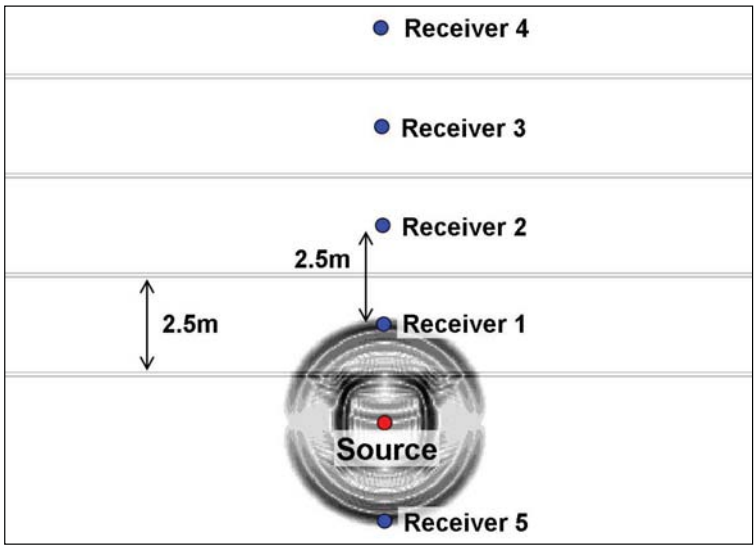

Figure 3.9. Plan view of *Wave2000 Plus*® simulation geometry for normal P-wave incidence using an array of transducers between equally-spaced discontinuities.

3.5.2 Material Properties Used in the Simulation

The material properties for both the host rock and any inclusion required by the software were the material density and Lame's constants λ and μ. These properties along with elastic material equations were used by the program to calculate the P- and S-wave velocities and wave-field particle displacements. The material properties of both the intact host material and the discontinuities used in the first simulation are listed in Table 3.2.

Table 3.2. Material properties used in the *Wave2000*® Plus model in Figure 3.12.

Property	Host Rock	Discontinuity
Material density	2700 kg/m^3	1500 kg/m^3
λ	61 GPa	50 GPa
μ	25 GPa	10 GPa

The material properties of the intact rock have been assumed to be representative of a competent granite or quartzite material common to some underground mining rock masses. The fill material properties within the 100mm thick discontinuities were assumed to be similar to that of a chlorite-type infill with high normal stiffness (λ) and moderate shear stiffness (μ).

3.5.3 Modelled Seismic Source Parameters

The wave source chosen for the initial model was an exponentially-decaying sine wave from a finite linear source of relative length of 1m. The first simulation used only a normal compression source without a direct shear component. This type of source would simulate normal incident P-wave activity only. After performing a trial simulation with a shear source component, the generated wave-field became too complex to perform the required analyses. Additionally, the behaviour of the shear waves would be expected to be similar to the P-waves close to the source due to a lack of uncoupling over short distances (maximum 10m).

3.5.4 Simulation Results

The wave simulation time (10μs equivalent) was selected to allow the propagating waves to reach the extents of the model. The in-plane particle velocity values were recorded at each transducer over the course of the simulation to compare the resulting 2-D waveforms. Figure 3.10 shows the results of the simulated wave field near model completion along with labels of the different direct and reflected waves.

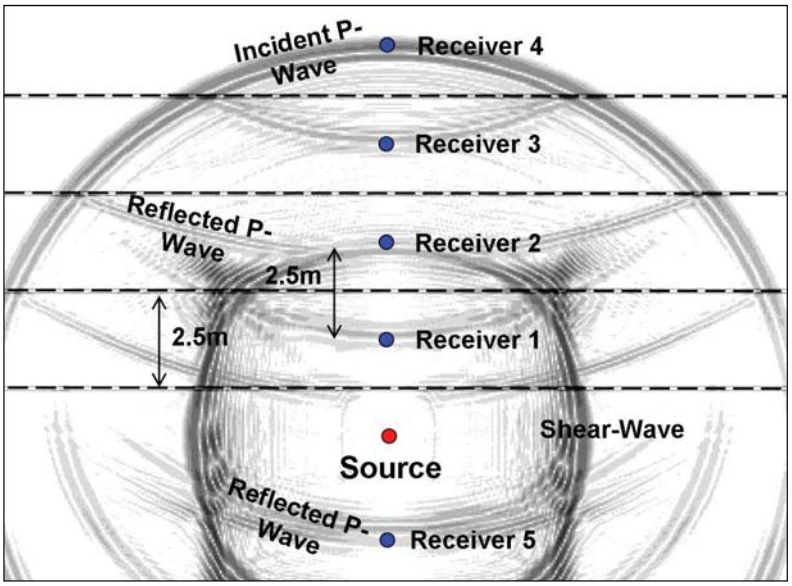

Figure 3.10. Plan view of *Wave2000 Plus*® simulation near model completion.

The incident shear waves observed in Figure 3.10 were a result of angular effects of the linear longitudinal wave source. Although no direct shear waves were specified for the source, shear-type particle motions were observed in the in-plane waveforms due to tangential stresses at the wave front and conversion of P-waves into S-waves at the discontinuity interfaces at acute incident angles.

3.5.5 Analysis of Simulation Results

The effect of the discontinuity set on wave attenuation was determined by comparing the waveforms at each receiver. The compared values were the vector sum peak particle velocity and the wave propagation velocity. The resulting peak particle velocity amplitudes were plotted against the distance between each transducer and the source such that an attenuation curve could be fitted to the data. The attenuation

curve for the discontinuity-affected peak amplitude was compared with the results of an unjointed control model. Comparison of the jointed and unjointed attenuation curves is illustrated in Figure 3.11.

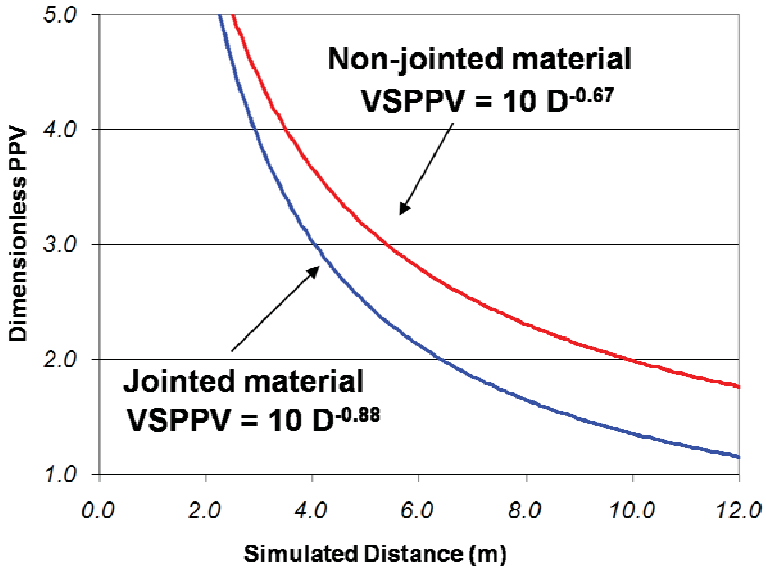

Figure 3.11. Comparison of amplitude attenuation curves for unjointed and normal incident jointed models.

Figure 3.11 clearly demonstrates that the amplitude attenuation over distance was higher for the normal-incident jointed model than for the unjointed control model. In addition to amplitude attenuation, the wave velocity from the source to each receiver progressively decreased due to the delay in stress transfer across the lower-stiffness discontinuities. The attenuation slope of the unjointed model was approximately -0.67, which was close to that expected for a spherical charge, whereas the slope of the jointed normal incident model was -0.88. This result would indicate increased attenuation due to the parallel jointing.

3.5.6 Investigation of the Effect of Incidence Angle on Attenuation

Waves of normal incidence should exhibit the lowest attenuation based on the expected elastic reflection and transmission coefficients. This excludes the case of 90 degree incidence, which is equivalent to the unjointed geometry. To investigate the effect of incident angle on amplitude attenuation, alternate simulations were

performed for 30 degree incidence and 45 degree incidence. The initial 2.5m joint spacing was retained, but the receiver spacing was changed to maintain the mid-joint locations along the array direction. The attenuation slopes for 30 and 45 degree incidence with the same material and joint fill properties as the normal incidence model are listed in Table 3.3.

Table 3.3. P-wave amplitude attenuation slopes for simulated 30 and 45 degree incidence.

Angle of Incidence	Attenuation Slope
30 degrees	-0.88
45 degrees	-0.91

The results of the analysis indicated that little difference was observed between the attenuation slope for normal and 30 degree incidence. A significant increase in the attenuation was observed for 45 degree incidence. The model of wave transmission and reflection published by Rossmanith (2006) suggests that the attenuation rate would increase until a critical incident angle was reached at approximately 70 degrees (Appendix 2). Due to the time required to set up, run and analyse the output data of each simulation, no further models were completed to determine the critical incident angle.

Acute and obtuse angles of incidence resulted in wave fields which were more complex than those for normal incidence. As predicted by elastic wave theories, any angle other than normal incidence would result in both transmitted and reflected P- and S-waves from an incident P-wave. These types of wave conversions were observed in the simulated waveforms at each transducer location. The complex waveforms observed for the simple case of two-dimensional elastic waves in simply jointed media highlighted the extreme difficulty in interpreting the three-dimensional waveforms recorded in actual complex jointing conditions. Figure 3.12 illustrates the two-dimensional elastic wave-field generated for 45 degree incidence.

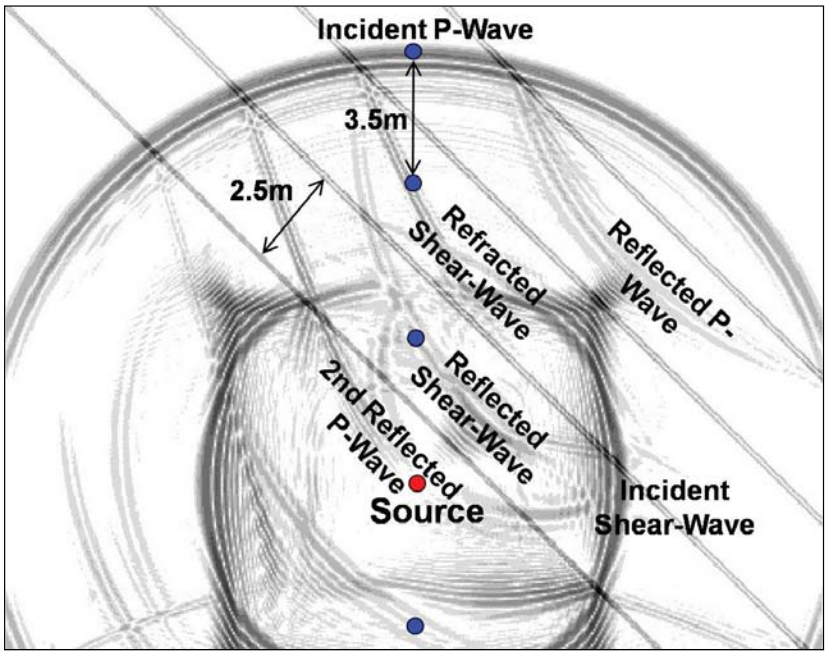

Figure 3.12. Simulated wave-field generated in the 45 degree incident parallel jointed model.

3.5.7 Simulated Effects of Infill Material Properties on Amplitude Attenuation

The effect of discontinuity thickness and infill material properties on attenuation were investigated further using simulations with reduced discontinuity aperture and increased infill material density and stiffness. The new infill density and normal and shear moduli were 90% of the intact rock to simulate a closed or healed fracture under the influence of a high confining stress. The joint thickness was reduced to 10mm. The results of the simulation indicated that the amplitude attenuation for the healed fracture, normal incidence case was similar to the unjointed control attenuation. Similar results were observed in laboratory testing of fractured specimens under high confining stresses by Pyrak-Nolte et al. (1990).

Simulations were also performed for a single large-scale discontinuity with degraded density and modulus values (30% of intact rock) to simulate a fault or shear zone. The observed attenuation rates increased significantly due to the considerable degree of wave reflection at the rock-fault interface. Similar results were observed by the author during blast monitoring in a fault-affected area at the Kanowna Bell Gold Mine (Fleetwood, 2010).

3.6 Discussion and Conclusions

The overall effect of in situ discontinuities on wave propagation has been demonstrated by many researchers using mathematical treatments of anisotropic compliance matrices, advanced material models of stress, strain or displacement across discrete discontinuities, laboratory studies of fractured media, numerical modelling and field seismic measurements. Simplistic treatments for rock mass parameters have been adopted in the field of blast engineering and blast vibration management, assuming ideally-elastic wave propagation and uniform attenuations.

Chapter 3 has been dedicated to the analysis of dynamic loading of discontinuities resulting from blasting waves and the attenuation of waves in fractured media. Near-field waveforms collected during the author's blast monitoring program have identified that maximum particle motions typically occur normal to the direction of wave propagation due to the activity of shear waves. Careful consideration of transducer orientations during installation, and determination of the direction of maximum particle motion resulting from multi-axial blast vibration monitoring allowed vector analyses to be performed. The vector direction of maximum particle motion determined at the peak particle displacement or velocity aided in identifying discontinuity loading conditions. This approach was based on the relationship between the joint plane orientation and the probable peak vector motion directions. A novel technique to determine discontinuity loading has been proposed. This technique has not been previously observed in the published literature.

Existing models of wave attenuation were reviewed and elastic wave propagation modelling was performed. The wave propagation simulations were completed with varying discontinuity characteristics to observe the effect of orientation and infill properties on two-dimensional amplitude attenuation. The results of the simulations led to better understanding of the influence of discrete discontinuities and discontinuity sets on the attenuation behaviour of modelled near-field blasting vibrations.

CHAPTER 4 : NEAR-FIELD BLAST VIBRATION MONITORING AND DATA PROCESSING

4.1 Introduction

Blast-induced wave fields can be measured using transducers that react to the applied particle motions. Selection of the transducer type, dynamic range and frequency response greatly influences the accuracy with which blast-generated vibrations can be measured. In addition, the specifications of the data acquisition system can affect the quality and accuracy of blast vibration measurements.

Blast monitoring requirements change dramatically according to rock mass characteristics, blasting parameters and distance from a blasting event. Definitions for different monitoring ranges have been proposed in this chapter, along with recommendations for the selection of transducers and data acquisition equipment. Digital signal processing is also briefly discussed. Additional information on transducer and data acquisition system specifications, transducer configurations and the thesis blast monitoring program is provided in Appendix 4.

4.2 Description of Requirements for Near-field Blast Vibration Monitoring

Prior to selection of the components of a blast vibration monitoring system, definition of the distance range over which the blasting will be monitored is required. Blast parameters and the distance from a blast will influence the amplitude and frequency characteristics of the generated wave-field, thus contributing to the required monitoring equipment specifications. Distance ranges from blasting events have generally been defined in the literature by two general categories; near-field and far-field vibration behaviour.

4.2.1 Definition of Distance Ranges for Blast Monitoring

The first step in any blast vibration monitoring program should be to estimate the likely amplitude and frequency characteristics of the measured blast-induced waves

based on the distance range over which vibration data are required to be collected. For regulatory vibration monitoring (far-field compliance monitoring), placement of transducers at or near neighbouring structures at large distances from blasting events is common. Compliance monitoring typically requires lower sampling rates and amplitude measurement capacities when compared with near-field blast monitoring, where the amplitudes and frequencies could be several orders of magnitude higher than far-field vibrations.

The transition from near-field to far-field monitoring is not well defined in the published literature. The near-field range has been defined in the past by multiples of the length of explosive charge (e.g. Andrieux and Heilig, 1994 and Andrieux, 1996), distance from the blast (e.g. Yang et al., 1993; Brady and Brown, 2004), relative size of the blast dimensions with respect to distance (e.g. Yang and Scovira, 2007), Scaled Distance value (e.g. Ambaseys and Hendron, 1968) or frequency domain characteristics (Spathis, 2006). The properties of the expected blast-induced waves provide a good indication of the required instrumentation specifications, and should be considered as an integral part of the definition of distance monitoring regions.

Four distinct monitoring regions have been proposed by the author based on observations of the waveforms collected during the thesis blast vibration monitoring program and the dependence of amplitude and frequency on both distance and source energy. The proposed regions are defined by multiples of an integrated value of charge weight and distance, known as the square root Scaled Distance (SD_{SQRT}). SD_{SQRT} is calculated by dividing distance from a source by the square root of the maximum single charge weight. The suggested instrumentation requirements and expected peak amplitude and frequency characteristics in the four defined ranges are listed in Table 4.1. The definitions are based on monitoring of confined body waves by fully-encapsulated transducers in a competent rock mass. The range in blasthole diameters and charge weights considered in the proposed monitoring ranges are typical of sublevel open stoping (76 – 102mm and 10-150kg of explosives respectively).

Table 4.1. Suggested definitions of blast monitoring regions.

Distance Region	Maximum Expected PPV (mm/s)	Expected Frequency (Hz)	Scaled Distance ($m/kg^{0.5}$)
Extreme near-field	2500-10,000	4000-20,000 Hz	$SD_{SQRT} \leq 0.5$
Near-field	1000-2500	1000 – 4000 Hz	$0.5 < SD_{SQRT} < 2.0$
Intermediate-field	200-1000	250 - 1000 Hz	$2.1 < SD_{SQRT} < 10.0$
Far-field	< 200	< 250 Hz	$SD_{SQRT} > 10.1$

As observed in Table 4.1, the instrumentation requirements would be significantly different for each monitoring zone based on the expected vibration characteristics. Therefore, the selection of transducers, data acquisition equipment and sampling rates would significantly impact on the quality and interpretation of blast monitoring results as a function of the monitoring region. Table 4.2 outlines the recommended transducer types and sampling rates for each monitoring range based on the results of the blast vibration monitoring study conducted as part of this thesis. The recommended sampling rates are based on the premise that the sampling required to accurately represent the waveform should be at least two times the expected frequency.

Table 4.2. Recommended transducer types, dynamic ranges and sampling rates for monitoring of blasting vibrations in different distance ranges.

Region	Recommended Transducer Type	Recommended Amplitude Range	Recommended Sampling Rate (kHz)
Extreme Near-field	Accelerometer	1,000g - 10,000g	10 – 50
Near-field	Accelerometer	500g – 1,000g	4 -10
Intermediate-field	Geophone	1,000 mm/s	2 – 4
Far-field	Geophone	500 mm/s	1 – 2

Despite extensive research, few publications have been found that outline monitoring requirements for expected vibration amplitude, frequency and data sampling in the near-field of an explosive charge. Yang et al. (1993) derived expected acceleration

waveform characteristics for monitoring the near-field vibrations from a single 18kg charge of Magnafrac 100. This work proposed a particle acceleration range of 9000 to 500,000 m/s^2 (917 - 51,000g), particle velocity of 200 to 3000 mm/s and frequency of 1 to 50 kHz at distances of 2m to 15m from the charge. In comparison to the recommendations in Tables 4.1 and 4.2, the distances and charge weight represented by Yang et al. (1993) correspond to square root scaled distances of 0.5-3.5 $m/kg^{0.5}$, with fair agreement between the two predictions of acceleration and frequency.

4.3 Blast Vibration Monitoring System Selected for the Kanowna Belle and Cannington Case Studies

The transducers and data acquisition systems selected for the blast vibration monitoring program conducted as part of the PhD research were based on the characteristics discussed in Tables 4.1 and 4.2 and further discussed in Appendix 4. In addition to the required technical specifications, transducer cost was of significant concern in the author's blast monitoring program due to the non-recoverable method of coupling and the short stope turnover times. On only one occasion were transducers able to be reused to monitor two adjacent stopes in the same mining block. These transducers were located in a pillar between two adjacent stopes in the R4 block at the BHP Cannington Mine. In all other study stopes, a single production period was monitored and then the transducers were decommissioned and consequently mined out later in the stoping sequence.

4.3.1 Selection of Accelerometers for the Thesis Blast Monitoring Program

The accelerometers selected for the initial monitoring program conducted at the Barrick Kanowna Belle Gold Mine were PCB 356A02, 500g, pre-fabricated tri-axial accelerometer units. The expected amplitudes at the distances of transducer installation were not expected to exceed 500g according to previous blast monitoring at KBGM (Heilig, 2002). During field data collection period, failure of transducer attenuation circuitry within the junction box resulted in regular saturation of the 500g units at high vibration amplitudes. Initially, nine 500g units were purchased for near-

field vibration monitoring. After the saturations experienced in the first monitored stope, the minimum offset distance for subsequent stopes was increased by 1 to 2 metres (from 5m to 6-7m) to reduce the probability of saturating the accelerometers and compromising the lower amplitude portions of recorded waveforms. The saturations experienced in the stopes at KBGM led to upgrading of the accelerometers selected for the blast monitoring program at the Cannington Mine. The new accelerometer model selected was the PCB 356A01, 1000g accelerometer.

4.3.2 Selection of Geophones for the Thesis Blast Monitoring Program

Due to the large cost of the accelerometer sondes relative to suitable geophone types (approximately 3 times more expensive), a mixture of transducers was selected for the blast vibration monitoring program at the two mine sites. The multiple-transducer array and multiple array configurations within a single stope was intended to characterise the vibration responses of the rock mass along several orientations over near-field and intermediate-field distances. The dual or triple-transducer array layout allowed use of high frequency geophone sondes at some monitoring locations in place of accelerometers due to the expected reduction of frequency and amplitude with distance.

From previous experience and review of past research, the geophone model selected for use in intermediate-field blast monitoring was the OYO Geospace 101LT (long travel) 14Hz, 900Ω high-frequency geophone. This particular geophone was selected due to good signal-to-noise ratio, extended linear frequency response and high dynamic amplitude range. The extended frequency-voltage response graph of the OYO 101LT is illustrated in Figure 4.1.

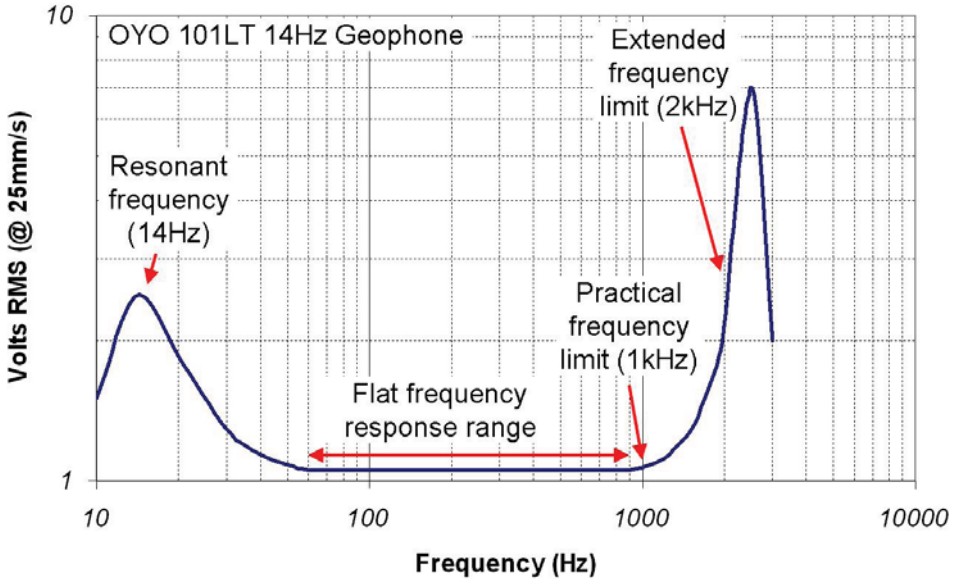

Figure 4.1. OYO 101LT 14Hz high-frequency geophone extended linear frequency response (after Andrieux and Heilig, 1994).

4.3.3 Control of Transducer Orientation in the Thesis Blast Vibration Monitoring Program

Very few detailed descriptions of blast monitoring programs are published in the literature, especially in regards to measures taken to control the orientation of fully-encapsulated tri-axial transducers. In the author's blast vibration monitoring program, significant effort was invested in controlling and maintaining the installed transducer orientations prior to hole grouting. This was achieved using continuously-coupled orientation control pipes attached to each transducer during in-hole deployment.

To allow adequate coupling between sensor strings and the associated borehole over the entire encapsulated length, 25mm diameter grout migration holes were drilled in the orientation pipes every 200-500mm. The migration holes would allow grout to flow freely between the interior and exterior of the pipes and reduce the likelihood of decoupling due to grout shrinkage. Both ends of each 4m orientation pipe were marked with axial lines to transfer the in-hole transducer orientation marks to the collars of the instrumentation holes (Figure 4.2).

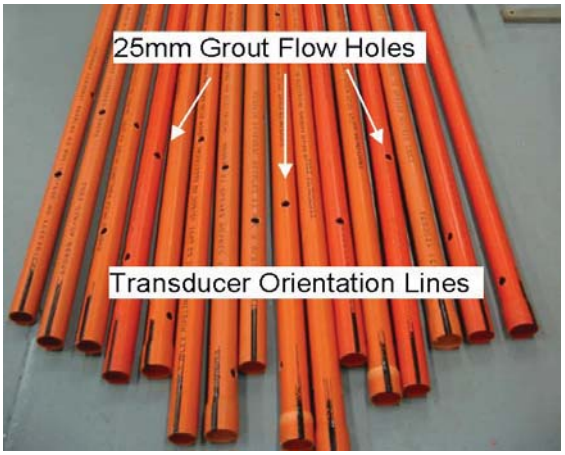

Figure 4.2. Prepared transducer orientation control pipes.

To simplify the installation procedure at the mine site, orientation pipes of the same diameter as the potted transducer were used. This allowed direct coupling of the transducer to the orientation string and provided a stiff coupling between the collar of the hole and the in-hole transducer. The stiff coupling allowed adjustment of the in-hole transducer orientation prior to grout curing, and provided good support of the transducer in up-holes. As part of the pre-installation preparation process, coupling pipes were bundled and cut to match the desired installation depth of each transducer. In all cases, multiple 4m pipes were required to form the orientation string, as the minimum installation depth was approximately 12m. Figure 4.3 shows the continuous coupling of orientation pipes during installation of transducers in the hangingwall and footwall of KBGM stope dB10-38T.

Figure 4.3. Installation of tri-axial transducers in the hangingwall (left) and footwall (right) of Kanowna Belle Gold Mine stope dB10-38T.

4.3.4 Design of the Locations of Near-Field Blast Vibration Transducers in the Thesis Blast Vibration Monitoring Program

The process of determining suitable near-field blast vibration monitoring locations should take into account equipment, operational, geometric and geotechnical factors. The process of instrumentation layout design can take a considerable amount of time prior to blast monitoring and relies heavily on the experience of the designer and familiarity with the drilling equipment and the mining environment.

The design methodology adopted for the blast vibration monitoring program conducted as part of this thesis required a minimum period of 1 month of design and installation time prior to stope production. Back analysis of neighbouring stope overbreak was performed during this month, as well as reviews of stope accesses, mining sequence and scheduling. These factors ultimately influenced the locations of transducers due to constraints on the available positions of drillhole collars and possible drilling orientations of instrumentation holes. Some considerations for the design of transducer locations used during the thesis blast vibration monitoring program are summarised below.

Monitoring Equipment Considerations

- Amplitude and frequency capabilities of transducers
- Maximum cable lengths
- Cable routing from transducers to collection equipment
- Identified monitoring orientations or features of interest (e.g. nearby infrastructure or geologic features)

Operational Considerations

- Drilling capabilities (i.e. accuracy and hole length)
- Rotation and dump capabilities of drilling equipment
- Available grouting equipment
- In-stope and nearby production activities (e.g. drilling, loading, blasting)
- Nearby mine services (i.e. power/air/water)

Geometric Considerations

- Available development from which to drill holes (access)
- Adjacent open voids or fill masses

Geotechnical Considerations

- Expected stope performance
- Areas of "no entry" for stope filling, seismicity or rock fall risk

One of the main objectives of the thesis monitoring program was to characterise the blast-induced vibrations in multiple wave propagation orientations. The multiple-orientation approach was adopted to investigate vibration attenuations and blast-induced damage potential to different walls of instrumented study stopes. Transducers were therefore located in multiple stope walls to allow comparisons of measured vibrations based on geometric or geologic variability. Where transducer stocks were available, dual and triple-transducer arrays were installed in the rock mass perpendicular to each wall of the monitored study stopes. These arrays were cement grouted into boreholes at the horizontal and vertical stope mid-spans between stope production levels. Details of the instrumentation layouts for each study stope are discussed in the Chapter 7 and 8 case studies.

4.3.5 Thesis Instrumentation Strategy

The instrumentation layouts used in the blast vibration monitoring program were comprehensive in relation to orientation-specific measurement, number of transducers and density of coverage. The most densely instrumented stope contained 14 tri-axial transducers and the least contained four, with exception to the first test stope in the monitoring program which had a single array of two transducers. The dense transducer coverage allowed for better understanding of the influences of geometry, geology and stress conditions on blast vibration attenuations. A secondary benefit of the multiple transducer array strategy was the ability to perform geophysical analyses of the rock mass around the study stopes. These analyses will be discussed in depth in Chapters 7 and 8. The instrumentation summary for each of the monitored stopes in the blast monitoring program is listed in Table 4.3.

Table 4.3. Total Installed Instrumentation used in the blast vibration study.

Mine Site	Stope	Mining Levels	Tri-axial Accelerometers	Tri-axial Geophone Sondes
KBGM	dA12-35	1	1	1
KBGM	dB10-38B	1	2	2
KBGM	dB10-38T	1	3	3
Cannington	NZ 22gC6HL	1	1	3
Cannington	NZ 24jC6HL	3	6	8
Cannington	R4 52h09HL	1	3	3
Cannington	R4 52h04HL	1	2	3
Total			**18**	**23**

4.4 Waveform Processing of the Thesis Blast Vibration Data

The waveforms that were recorded during the blast vibration monitoring program were processed using the Instantel Blastware 8.0 software. This software contains functions for performing signal filtering, waveform integration, differentiation and scaling and FFT analysis. A series of steps were utilised to process the recorded waveforms such that the most accurate representation of the actual vibration field could be determined for use in analysis. The steps included in waveform post-processing were:

- Removal of constant DC voltage offsets from the waveform
- Initial high pass or band-pass filtering
- Integration or differentiation to obtain velocity or acceleration waveforms
- Secondary filtering of remnant frequencies
- Scaling into appropriate velocity or acceleration units (mm/s or m/s^2)
- Minimum amplitude filtering to remove background sampling noise
- Calculation of vector sum waveforms
- Selection of wave arrival times using design firing times
- Determination of peak amplitudes and energy calculations

Selection of filtering windows for each individual waveform utilised FFT analyses. FFT modelling of passive and active phases of each waveform was performed to identify artificial (electronics and sampling-related) and actual frequencies contained within the recorded blast waves. These values were then compared with the linear and extended response ranges for the associated transducers to select frequency filtering windows.

For the geophone signals, removal of both low and high frequencies was necessary due to the limited linear response range. Band pass filtering outside window frequencies of 2Hz and 1-2 kHz was performed to remove artificial frequency content or resonance effects. The signals were then differentiated to obtain acceleration waveforms for comparison with accelerometer data. The process of digital signal differentiation is not significantly sensitive to remnant frequencies, and therefore secondary signal conditioning after differentiation was not required.

Integration of recorded accelerometer waveforms to obtain velocity waveforms was considerably sensitive to low-frequency components. High pass filtering of low frequency components was therefore required to maintain the integrity of the waveform integration. No low pass filtering was required as the upper end of the accelerometer response spectrum was above the Nyquist frequency of the data acquisition system. The high pass frequency chosen for accelerometer waveform processing in most cases was between 28Hz and 128Hz. No significant energy content was indicated below 128Hz by FFT analysis in most accelerometer waveforms and therefore no significant loss of true frequency spectra was expected. After signal integration, secondary filtering was required to remove residual low-frequency remnants and restore the waveform to the zero DC offset.

All measured and mathematically-derived waveform files were passed through filtering macros developed by the author to perform threshold amplitude filtering and to calculate time-domain vector sum waveforms. The filtered waveforms were then imported into another custom processing tool to determine the single-hole peak amplitudes and calculate the areas under the squared vector sum particle velocity waveforms. These values were used to calculate the peak instantaneous energy densities and total energy densities based on the wave arrival times. The wave arrival

times were determined through manual selection of points of first break from the original unfiltered waveforms.

4.5 Discussion and Conclusions

The process of near-field blast vibration monitoring includes several key considerations that will ultimately affect the accuracy of, and the appropriate uses for, the collected data. These considerations include transducer and equipment selection, blast monitoring instrumentation design geometries and digital signal processing of the collected waveforms. In the published literature, the only factor that has been adequately outlined and discussed is the general selection of transducer types based on the characteristics of each transducer response. The issues related to near-field blast monitoring that have been largely ignored in previously published works include:

- Required transducer specifications
- Component configuration (uni-axial, bi-axial or tri-axial)
- Number and location of blast monitoring transducers
- Coupling of transducers for near-field blast vibration monitoring
- Specifications of data acquisition systems
- Post-processing of recorded signals

The information presented in Chapter 4 and Appendix 4 has attempted to address all of the previously-mentioned considerations to standardise the process of near-field blast vibration monitoring. Careful consideration of transducer type, location, orientation, density of coverage and installation practices have enabled the author to generate a database of high-quality near-field and intermediate-field blast vibration results to be used in subsequent analyses.

CHAPTER 5 : BLAST VIBRATION ANALYSIS AND INTERPRETATION

5.1 Introduction

Near-field blast vibration monitoring, as discussed in Chapter 4, provides valuable information on the waves produced by the detonation of explosive charges. Blast vibration analysis techniques typically result in characterisation of blast vibration attenuations or development of models to predict peak vibration amplitudes from known charge parameters. Analysis and interpretation of recorded waveforms with respect to charge parameters, blasting geometries and rock mass conditions provide the next step to investigate the potential for blast-induced rock mass damage.

Chapter 5 is dedicated to the review of existing blast vibration analysis and prediction models with particular emphasis on charge-weight scaling relationships such as Scaled Distance and Holmberg-Persson techniques. An alternate nonlinear, multi-variable statistical estimation approach is also discussed for use in near-field vibration analysis to improve predictive capabilities based on collected data. The results of a number of traditional peak amplitude prediction approaches are compared using collected near-field vibration data.

The effects of distance and charge parameters on blast vibration amplitude prediction accuracy are discussed. For the specialty case of underground blast vibration analysis in the presence of existing and developing stope voids, a new method of distance determination has been proposed. This method takes into account the influence of the void on the wave travel path from an explosive charge to a monitoring point. Numerical wave simulation has also been used to investigate the theoretical effects of an existing stope void on the wave-field produced by a confined charge.

5.2 Three-Dimensional Distances for Blast Vibration Scaling and Prediction in Ring Drilling Applications

Arguably the most important variable in any near-field blast vibration prediction model is precise determination of the distance between a charge and a monitoring

location. Of the possible charge geometries used in blasting, those associated with ring drilling for sublevel open stoping represent the highest degree of variability in blasthole geometries due to drilling access limitations. These variations in blasthole orientations and lengths within ring patterns present many challenges to the determination of charge to transducer distances for use in near-field vibration modelling.

Information on source to sensor distance determination in near-field prediction models is scarce in the literature. Within the published charge weight scaling models, no specific distance has been mentioned as the most appropriate for use in near-field vibration prediction. Therefore, no standardised approach exists for determining peak amplitude prediction distances when considering complex blasthole geometries. In simple parallel-blasthole patterns typical of open pit blasting, any standardised distance would be expected to provide similar regression results due to the consistent angles between the charge axis and the monitoring point. For charges varying in orientation by 360 degrees with respect to a fixed monitoring location, changes in propagation angle and detonation direction can lead to large variations in measured amplitudes.

5.2.1 Ring Drilling in Sublevel Open Stoping and Calculation of Source to Sensor Distances

The angles and distances between single explosive column charges and a monitoring point vary significantly in ring blasting applications. With changes in distance and orientation, there is considerable variability in wave characteristics such as travel time, wave type decoupling and changes of wave phase and wave type. Further complications are introduced in the presence of existing and forming stope voids, where the actual wave travel distance through intact rock can be several times greater than the straight-line geometric distance. No existing blast vibration prediction approach considers this effect.

For the most simplistic case of an uninterrupted wave path through intact rock, determination of the most appropriate near-field charge to sensor distance for use in near-field blast vibration analysis and prediction is still not straightforward. In the

case of void-unaffected monitoring geometries, three distances from an explosive charge to a given monitoring point have been considered by the author. These three distances were:

- Toe distance (D_T) - distance from the explosive column point of initiation (charge toe) to the monitoring point
- Midpoint distance (D_M) - distance from the column midpoint to the monitoring point
- Collar distance (D_C) - distance from the column collar to the monitoring point

The three distances for each explosive charge were compared with one another to determine the minimum distance (D_{min}) between the explosive column and the monitoring point. Figure 5.1 illustrates three ring-drilled blastholes and charge configurations common to sublevel open stoping with the distances D_T, D_M, D_C and D_{min} shown between each explosive charge and a monitoring location.

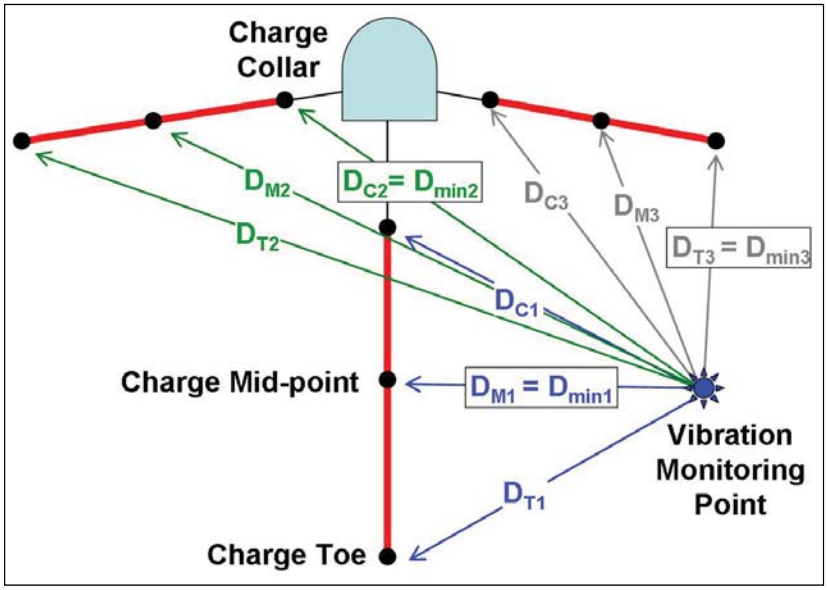

Figure 5.1. Effect of blasthole orientation on the defining distances possible for use in blast vibration prediction models.

For all three explosive charges in Figure 5.1, large variations between the three distances are observed based on the blasthole orientations and positions of the

explosive charges in relation to the monitoring point. The relative differences between these distances would be expected to influence the results of a near-field vibration prediction model.

5.2.2 Calculation of Geometric Distance (D_G)

Drillhole design files and charging plans for all monitored blasts were obtained from the sponsoring mines during the author's blast vibration monitoring program. These files allowed each explosive charge to be modelled using a series of charge collar and toe point coordinates. The midpoint coordinates were then calculated between the collar and toe of each explosive charge. Using the toe, collar and midpoint coordinates for each explosive charge, the geometric distance (D_G) was calculated from each charge point to each transducer location around a monitored stope using Equation 5.1. The geometric distance (D_G) refers to the distance from any charge point to a transducer along an uninterrupted wave path.

$$D_G = \sqrt{(X_S - X_M)^2 + (Y_S - Y_M)^2 + (Z_S - Z_M)^2} \qquad (5.1)$$

Where X_S, Y_S, Z_S = coordinates of toe, collar or midpoint of the charge
X_M, Y_M, Z_M = coordinates of vibration monitoring point

The different charge to sensor distances calculated using Equation 5.1 were applied in various blast vibration prediction models discussed in Section 5.3 to investigate the influence of charge geometry on vibration amplitude prediction accuracy. The most suitable distance for use in analysis of collected data and forward prediction was determined based on the highest model correlations after comparing analyses using D_C, D_M, D_T and D_{min}. The majority of analyses identified that the midpoint distance (D_M) yielded the highest linear regression correlation values. Therefore, D_M was the distance chosen for use in all remaining blast vibration analyses and predictions under void-unaffected geometries.

5.3 Charge Weight Scaling Relationships for Prediction of Peak Particle Velocity Amplitudes

In the fields of mining, tunnelling and blast engineering, models for prediction of peak vibration amplitudes and distance-related attenuations have remained largely unchanged for over 50 years. Based on the early work performed by the United States Bureau of Mines (USBM) in the 1950s and the Swedish Detonics Research Foundation (SveBeFo) in the 1970s, standard far-field and near-field vibration prediction models have been written into blasting regulations in many countries around the world.

Two basic data fitting relationships have been used in a large percentage of blast vibration analyses of near-field monitoring results. These two approaches include various forms of charge weight scaling, in particular the Scaled Distance models, and the Holmberg-Persson (H-P) scaling model. Both the charge weight scaling and H-P approaches identify curve fitting relationships based on measured data and a basic assumption of the wave type (cylindrical or spherical waves). These approaches do not represent the mechanistic properties or propagation characteristics of the blast-induces waves. Sections 5.3.1 to 5.3.8 discuss the development of various charge weight scaling relationships and the H-P approach. Alternate scaling relationships that attempt to represent some of the physical phenomena related to wave formation and propagation are also discussed and compared using data collected in the blast vibration monitoring program conducted by the author.

5.3.1 Charge Weight Scaling as Defined by Square Root Scaled Distance and Cube Root Scaled Distance

The ability to predict vibrations produced by the detonation of explosives became a focus of research from the late 1930s as equipment became available to reliably measure dynamic ground vibrations. Prior to the invention of modern geophones and accelerometers to measure blasting vibrations, mathematical models of wave propagation were relied upon to predict ground motions from explosive charges.

New technologies developed to measure the dynamic response of rock to blast loading allowed data to be collected and analysed to observe actual wave behaviours from explosive sources over varying distances. These observations led to the development of empirical models of wave attenuation and charge weight scaling based on both measured data and theoretical wave propagation models. Investigations performed by the USBM (e.g. Blair and Duvall, 1954; Atchison and Tournay, 1959; Atchison and Roth, 1960; Nicholls and Hooker, 1961; Duvall et al., 1962) formed the basis of modern charge weight scaling relationships; most notably the square root and cube root Scaled Distance models. A general form of charge weight scaling developed for prediction of peak particle velocity (*PPV*) was suggested by Duvall et al (1962) based on the maximum charge weight (*W*) and distance (*D*). The general charge weight scaling form is show in Equation 5.2.

$$PPV = K \times W^{b} \times D^{-n} \qquad (5.2)$$

Where *PPV* = predicted peak particle velocity (mm/s or in/s)
D = distance from explosive source to point of interest (m or ft)
W = instantaneous charge weight (kg or lb)
K, *b*, and *n* = site-specific constants defined by regression

Two popular versions of chare weight scaling that have been applied to the analysis or prediction of PPV based on charge weight and distance are square root Scaled Distance (SD_{SQRT}) and cube root Scaled Distance (SD_{CubRT}). These two models assume specific attenuation characteristics based on cylindrical or spherical waves, respectively. The peak amplitude attenuation factors applied in the two forms of Scaled Distance were assumed to be proportional to either $D^{1/2}$ (cylindrical wave, square root scaling) or $D^{1/3}$ (spherical wave, cube root scaling) based on the assumed source parameters. The equations for predicting PPV as a function of square root or cube root Scaled Distance are listed in Equations 5.3 and 5.4.

$$PPV = K \cdot \left(\frac{D}{\sqrt{W}} \right)^{\beta} \qquad (5.\ 3)$$

Or

$$PPV = K \cdot \left(\frac{D}{\sqrt[3]{W}} \right)^{\beta} \qquad (5.\ 4)$$

Where K, β = dimensionless regression constants

Of the two Scaled Distance charge weight scaling approaches, past researchers have not formed a consensus as to the most applicable for use in near-field vibration prediction. Various researchers have attempted to validate cube root scaling as the most appropriate for use in near-field blast vibration analysis (e.g. Ambraseys and Hendron, 1968 and Olson et al., 1972). Additional researchers have attempted to validate square root scaling behaviour, including Ouchterlony et al. (1993), Yu and Vongpaisal (1996), Peterson (2001) and Singh and Narendrula (2004).

5.3.2 Examples of Published Near-field Scaled Distance Vibration Prediction Equations

Blast vibration analyses published by various authors have yielded site-specific vibration amplitude prediction equations defined by different charge weight scaling relationships (e.g. Olson et al., 1972, Holmberg, 1977; Ouchterlony et al, 1993; Peterson, 2001). The published equations were based on the general charge weight scaling relationship or Scaled Distance approaches listed in Equations 5.2 to 5.4. Table 5.1 lists a number of charge weight scaling-based prediction equations for PPV as published by various authors.

Table 5.1. Charge weight scaling *PPV* (mm/s) prediction equations from the published literature based on *W* (kg) and *D* (m) for a variety of blasting conditions.

Researcher	Prediction Equation	Blast Type and Rock Type
Olson et al., 1972	$PPV = 2150\ (D/W^{1/3})^{-2.04}$	U/G tunnelling-granite
Ambraseys and Hendron, 1968 (reviewed by Yu, 1980)	$PPV = 11455\ (D/W^{1/3})^{-2.8}$	U/G chamber-granite/LS/SS
Lundborg et al., 1978 (reviewed by Holmberg and Persson, 1979)	$PPV = 730\ (W^{0.66}/D^{1.54})$	N/A
Holmberg, 1977 (reviewed by Holmberg and Persson, 1979)	$PPV = 1686\ (W^{0.71}/D^{1.78})$	N/A
Yu, 1980	$PPV = 800\ (D/W^{1/3})^{-1.3}$	U/G chamber-granite/LS/SS
Ouchterlony et al., 1993	$PPV = 698\ (D/W^{1/2})^{-0.74}$	U/G tunnelling-granite
Yu and Vongpaisal, 1996	$PPV = 600\ (D/W^{1/2})^{-1.05}$	U/G stope blasts-rhyolite
Peterson, 2001	$PPV = 229\ (D/W^{1/2})^{-1.02}$	Open Pit- diorite
Singh and Narendrula, 2004	$PPV = 1077\ (D/W^{1/2})^{-1.6}$	U/G drifting-“hard rock”

From the attenuation equations in Table 5.1, it can be observed that the regression constants are largely site specific and based uniquely on specific rock mass and blasting parameters. The wide range in the regression constants demonstrates the variation in vibration behaviours in different rock masses and blasting conditions. To compare the effects of specific blasting conditions on the predicted PPV over a range in Scaled Distances, four of the PPV prediction equations from Table 5.2 have been plotted in a graph of PPV versus square root Scaled Distance (Figure 5.2).

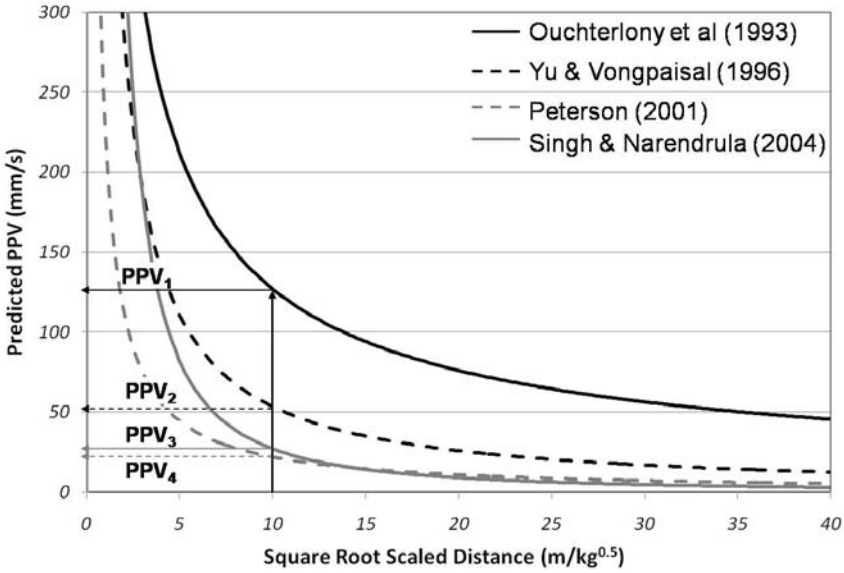

Figure 5.2. PPV prediction curves of various authors based on vibration data.

Site specific effects represented by the *PPV* prediction curves in Figure 5.2 clearly contribute to the large variations in vibration behaviours. For example, at the Scaled Distance of 10 m/kg$^{0.5}$, the variation in the predicted *PPV* between the various models was up to 500%. Therefore, application of one site-specific equation to different blasting conditions or rock mass properties could result in large errors in peak vibration amplitude predictions.

5.3.3 Alternate Forms of Standard Charge Weight Scaling - Corrections for Charge Length and Use of Linear Charge Density

Research conducted in Sweden in the 1970s established that Scaled Distance models generally over-predicted vibration values measured in the near-field of a blast. This over-prediction occurred as a result of the entire charge column being treated as an instantaneous point source, where the entire charge weight was considered in prediction of the peak amplitude. In the far-field of blasting events, instantaneous detonation or point source assumptions are acceptable due to the relatively short length of the charge in relation to the distance from the blast to a monitoring point. In the near-field, charge lengths similar to monitoring distances introduce delay effects related to the velocity of detonation of the explosive and the propagation velocity of the stress waves.

Ouchterlony et al. (1993) attempted to correct for the effects of charge length in the standard Scaled Distance approach for near-field monitoring conditions. This correction used the assumption that the peak vibration value closely corresponded with the minimum distance from a charge column to the monitoring point. Prediction of the maximum expected vibration therefore used a modified form of the Scaled Distance equation integrated over the charge length. The integration approach proposed by Ouchterlony et al. (1993) was similar to the Holmberg-Persson model to be discussed in Section 5.3.4. The new form of the Scaled Distance equation, corrected for charge length as suggested by Ouchterlony et al. (1993) was:

$$SD_{Ouchterlony} = \left(\frac{R}{\sqrt{Qf}} \right) \tag{5. 5}$$

And

$$f = \left[\frac{a\tan\left(\frac{H}{2R}\right)}{\frac{H}{2R}} \right]$$

Where R = distance from charge to monitoring point (m)

Q = charge weight (kg)

H = charge length (m)

Therefore,

$$V_{\max} = A \cdot \left(SD_{Ouchterlony}\right)^{-\beta} \tag{5. 6}$$

Where V_{max} = maximum PPV (mm/s)

A, β = regression constants

Another version of charge weight scaling was proposed by Redpath and Ricketts (1987). This method predicted peak amplitude as a function of distance and the linear charge concentration, *l*, instead of the entire charge weight, *W*. The proposed scaling model was based on vibration data collected at the Logan Wash Mine using a wide range of charge weights and blasthole diameters. The relationship between PPV and charge concentration proposed by Redpath and Ricketts (1987) is listed in Equations 5.7 and 5.8.

$$SD_{\sqrt{l}} = \frac{R}{\sqrt{l}} \tag{5. 7}$$

And

$$PPV = K\left(\frac{R}{\sqrt{l}}\right)^{\alpha} \tag{5. 8}$$

Where R = distance (ft, m)

l = linear charge concentration (lb/ft, kg/m)

K, α = regression constants

The use of linear charge concentration to predict peak ground vibrations as proposed by Redpath and Ricketts (1987) was not a new concept. Holmberg and Persson (1979) were the first to propose an equation for prediction of near-field vibrations based on the linear charge concentration. This approach was developed due to observation of chronic over-prediction of vibration amplitudes in the near-field of blastholes by the standard Scaled Distance equations.

5.3.4 Holmberg- Persson Near-Field Prediction Model

In the 1950s and 1960s, mathematical models were being developed that represented the wave fields generated by long explosive columns using stacked incremental charges (e.g. Jordan, 1962 and Plewman and Starfield, 1965). This approach was adopted in an attempt to investigate the effect of explosive velocity of detonation on the predicted near-field vibrations. The incremental charge methodology was

adopted in a model proposed by Holmberg and Persson (1979) to address the observed over-prediction of near-field vibration values using Scaled Distance.

The fundamental geometry of the Holmberg-Persson (H-P) model represents a long, cylindrical charge as a string of stacked elemental charges of charge weight *l* (linear charge concentration). The peak amplitude at a point in a rock mass could therefore be predicted by integrating the general form of the charge weight scaling equation (Equation 5.2) with respect to the position of an elemental charge (*dx*) along the charge column (Holmberg and Persson, 1979). Details of the geometry represented by the model and other specific characteristics can be found in Appendix 5. Prediction of PPV using the H-P model is listed in Equation 5.9.

$$v = k \cdot l^{\alpha} \left[\int_0^H \frac{dx}{\left[R_0^{\,2} + \left(R_0 \tan\theta - x \right)^2 \right]^{\beta/2\alpha}} \right]^{\alpha} \qquad (5.9)$$

Where l = linear charge concentration (kg/m)

H = charge length (m)

K, α, β = regression constants (K = 700, α = 0.7, β=1.5 suggested)

Just as variations in the regression constants of the charge weight scaling equations in Table 5.1 were identified by various researchers, variations in the regression constants for H-P models also exist based on published literature. The original recommendations by Holmberg and Persson (1979) of K = 700, α = 0.7 and β = 1.5 were for competent Swedish granites and typical Swedish tunnel blasting conditions. Variations in blasting geometries and rock properties would therefore lead to changes in the regression constants from recorded site-specific vibration data. Some examples of published regression constants resulting from the H-P analysis of collected data are listed in Table 5.2.

Table 5.2. Holmberg-Persson peak amplitude prediction regression constants published in past literature.

Researcher	K	α	β
Holmberg and Persson (1979)	700	0.7	1.5
Villaescusa et al. (1997)	456	1.12	2.24
Villaescusa et al. (1997)	515	0.69	1.38
Scott (1998)	329	0.81	1.62
Peterson (2001)	1650	0.79	1.58
Heilig (2002)	790	0.7	1.4

5.3.5 Critical Evaluation of the Holmberg-Persson Model

Researchers in the past have criticised the H-P model due to basic errors in the mathematical derivation of the integral and subsequent summation forms of the equation (for instance, Blair and Minchinton, 1996 and Lu and Hustrulid, 2003). Other limitations that have been identified with the H-P model are the assumption of instantaneous detonation and neglect of directional effects, explosive and rock mass properties and shear wave-affected wave fields. In spite of the limitations, the H-P model has been used by many researchers as an analytical blast vibration prediction tool for near-field geometries (e.g. Holmberg and Persson, 1979; Villaescusa et al., 1997; Scott, 1998; Peterson, 2001; Heilig, 2002).

The H-P model has attempted to provide a more accurate treatment for near-field charge geometries, but in some situations has failed to deliver better correlations from measured data when compared with Scaled Distance approaches. Peterson (2001) noted this relationship during analysis of near-field data in open pit monitoring (Figure 5.3), where no improvement in prediction accuracy was observed using the H-P model. Based on the lack of improved prediction accuracy, Peterson (2001) selected square root Scaled Distance modelling for characterisation of measured near-field blast vibrations.

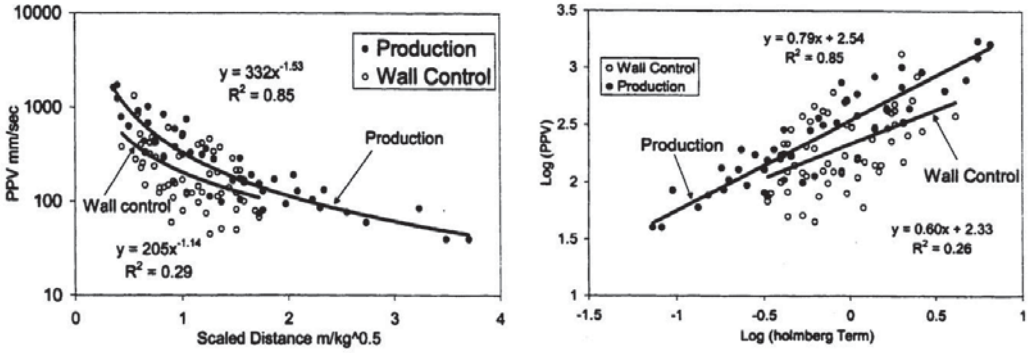

Figure 5.3. Graphs of Square Root Scaled Distance and Holmberg-Persson blast vibration prediction using the same data set (Peterson, 2001).

As observed in Figure 5.3, identical correlation values were observed by Peterson (2001) for production blasting conditions when comparing square root Scaled Distance and the H-P model results. Higher correlation values were observed for the wall control blasts using Scaled Distance when compared with H-P, leading to greater accuracy of vibration prediction.

Data collected as part of the blast vibration monitoring program conducted for this thesis has resulted in similar conditions to those observed by Peterson (2001) where H-P charge weight scaling failed to provide superior data set correlation. In a majority of data sets analysed using traditional charge weight scaling approaches, cube root Scaled Distance provided the most accurate predictions of measured values. When compared with square root Scaled Distance, H-P scaling provided some small improvement in correlation coefficients for some data sets, whereas in other data sets the correlation value was lower.

Under conditions of highly variable blasthole geometries, as experienced in ring blasting in open stoping, a relationship between the calculated Scaled Distance and the Holmberg charge weight scaling term (a) (see Appendix 5) was observed. The relationship between the two scaling factors was a power function. Figure 5.4 shows plots of the Holmberg term (a) versus the square and cube root Scaled Distances calculated at a single monitoring location using all design charges in an actual mass blast design at the BHP Cannington Mine.

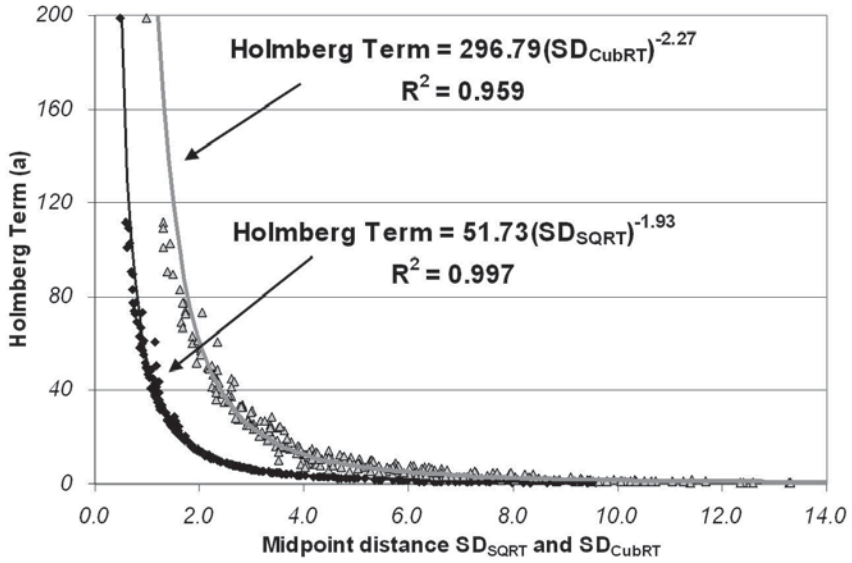

Figure 5.4. Plot of Holmberg Term (a) versus the square root and cube root Scaled Distance for all charges in a stope firing mass blast design.

The data points shown in Figure 5.4 represent actual stope production blasting patterns at the BHP Cannington Mine and cover a range of charge weights, distances and blasthole geometries. The near-perfect power curve relationships between the Holmberg term and both Scaled Distance terms expose the lack of actual complexity considered in the geometric treatment of charges by the H-P model. It is therefore expected that no mechanistic advantage would be gained through use of the H-P approach when compared with other charge-weight scaling relationships for complex ring blasting geometries.

5.3.6 Additional Models for Prediction of PPV

Some of the shortcomings of both Scaled Distance and the Holmberg-Persson models are a lack of explicit treatment of explosive and rock mass properties. These influencing factors along with explosive coupling, orientation effects and others are functionally combined in the regression constants and as such cannot be quantified for each blasting condition. To explicitly consider these variables, some researchers in the last decade have returned to first-order wave propagation principles to derive *PPV* prediction equations. These models combine charge weight scaling with principles of pressure and stress wave transmission. Models proposed by Lu and Hustrulid (2003) and Sambuelli (2009) are listed in Equations 5.10 and 5.11.

$$V = k_w K_n V_0 \left(\frac{a}{R} \right)^{\beta}$$ (Lu and Hustrulid, 2003) (5. 10)

Where k_w, β = regression constants

K_n = influence of total number of blastholes per delay

a = blasthole radius (m)

R = distance from charge (m)

And

$$V_0 = \frac{P_0}{\rho_c C_p}$$

$$P_0 = \frac{\rho_e D^2}{2(\gamma + 1)}$$

Where ρ_c = density of rock (kg/m^3)

C_p = P-wave velocity (m/s)

ρ_e = density of explosive (kg/m^3)

D = velocity of detonation of explosive (m/s)

γ = adiabatic constant of explosive

$$v \cong K \frac{\sqrt{Q}}{\sqrt{r^3}} \left(\frac{2\Phi r_h f}{\delta c} \right)^{1/2}$$ (Sambuelli, 2009) (5. 11)

Where K = site constant

Q = instantaneous charge weight (kg)

r = distance (m)

Φ = Explosive energy per kg (J/kg)

r_h = drillhole diameter (m)

f = wave frequency (Hz)

δ = rock density (kg/m^3)

c = Rayleigh or shear wave velocity (m/s)

Some of the identified limitations of charge weight scaling models are addressed in the Lu and Hustrulid (2003) and Sambuelli (2009) models through explicit consideration of explosive properties and rock mass characteristics. Analysis of surface blast monitoring results published in the studies by Lu and Hustrulid (2003) and Sambuelli (2009) revealed a higher degree of vibration prediction accuracy when compared with traditional charge weight scaling approaches.

5.3.7 Comparisons of Vibration Prediction Models using Collected Data

The reviewed charge weight scaling and prediction models have been compared using a sample data set collected at the BHP Cannington Mine. The objective was to investigate the differences in predicted peak amplitude values and model correlations. The results of the linear regressions for each scaling model versus the measured vector sum peak particle velocity (VSPPV) data are listed in Table 5.3. Additional information is provided in Appendix 5.

Table 5.3. Comparison of VSPPV prediction models for near-field and intermediate-field data from BHP Cannington Stope 52h04HL southeast wall transducers.

Approach	Data Points	K	α	β	Model R^2
SD_{SQRT}	245	126.3		-1.22	0.46
SD_{CubRT}	245	404.5		-1.46	0.44
$SD_{\sqrt{l}}$ (Redpath and Ricketts, 1987)	245	562.2		-1.42	0.23
$SD_{Ouchterlony}$ (Ouchterlony et al., 1993)	245	135.0		-1.26	0.46
Holmberg-Persson (1979)	245	10.6	0.63	1.26	0.46
Lu and Hustrulid (2003)	245	869.7		1.42	0.23
Sambuelli (2009)	245	85.5			0.37

Table 5.3 shows that the models taking into account scaling by incremental charge weight or correction for charge length ($SD_{Ouchterlony}$ and Holmberg-Persson) provided linear-regression correlations approximately equal to the basic Scaled Distance

models. For the examined data set, the poorest correlation of charge weight scaling was observed for the $\sqrt{l}$ model. Of interest are the results of the numerically simplified model of Ouchterlony et al. (1993) compared with the more complicated Holmberg-Persson model. Both models provided an equivalent correlation, but the model proposed by Ouchterlony et al. (1993) reports values in the same form as standard Scaled Distance and therefore in most applications would be easier to use than the H-P approach. Neither of the two models developed from first principles (Lu-Hustrulid or Sambuelli) offered any advantage for prediction of PPV for the analysed data set. Both the Lu-Hustrulid and Sambuelli approaches are highly sensitive to the values selected for the charge properties such as explosive energy and VOD, which can vary significantly and are nearly impossible to determine due to non-ideal detonation conditions.

5.3.8 Significance of Explosive Type on Blast Vibration Prediction

Holmberg and Persson (1979) suggested that different explosive types should be normalised to equivalent ANFO weights to accurately apply charge weight scaling prediction models. To investigate this, an analysis of the effect of explosive type on the measured peak amplitudes has been performed using the square root Scaled Distance model and a single data subset from the author's blast vibration monitoring program.

The data set selected for the analysis included three types of blasting agent used in the BHP Cannington stope 24jC6HL 220mLv firings. The three explosive types were poured ANFO, 1.0 g/cc gassed emulsion and 0.8 g/cc low-density gassed emulsion. The data set collected for the entire stope was subdivided by explosive type and individual linear regressions were performed for each of the three explosive-types. Individual regression results were then compared with the regression performed for the aggregate data set. Table 5.4 lists the linear regression constants resulting from the relationship between measured VSPPV and SD_{SQRT} for the combined data set and the three individual explosive type data sets.

Table 5.4. Comparison of measured PPV and SD_{SQRT} regression constants and correlations for the three different explosive types in Cannington stope 24jC6HL.

Explosive Type	Density (g/cc)	Data points	*K*	*β*	R^2
All		469	1456	-1.65	0.32
Poured ANFO	0.85	104	1239	-1.90	0.60
EP Emulsion	1.0	340	418	-1.70	0.31
Low Density Emulsion	0.80	25	593	-2.08	0.75

The results in Table 5.4 clearly reflect the importance of the explosive type on the predicted peak amplitude, even under conditions of similar distance, total charge weight and charge configurations. The effects of normalising each explosive type to ANFO equivalent charge weight was investigated next in an attempt to remove the variations in attenuation behaviours observed in Table 5.4. Table 5.5 lists the regression constants for each data subset after normalising the individual charge weights to that of ANFO through relative weight strength (Appendix 5).

Table 5.5. Comparison of measured PPV and SD_{SQRT} regression constants and correlations for the three different explosives types normalised to equivalent ANFO charges in Cannington Stope 24jC6HL.

Explosive Type	Linear Charge (kg/m)	ANFO Equivalent Charge (kg/m)	*K*	*β*	R^2
Poured ANFO	5.29	5.29	1239	-1.90	0.60
EP Emulsion	6.22	7.07	375	-1.70	0.31
Low Density Emulsion	4.98	6.63	440	-2.08	0.75

By normalising the charge weights to that of the relative weight strength of ANFO, the slopes (β) and correlation values (R^2) did not change when compared with the results in Table 5.5. The intercept (K) for both emulsion densities decreased, which would lead to reduced values of predicted PPV. None of the regression results

indicated effective normalisation of measured amplitudes to that of the actual ANFO data set. This therefore suggested that explosive properties other than weight strength, such as detonation pressure or velocity of detonation more significantly influences the vibrations produced by explosive charges of different explosive types.

5.4 Multi-Variable and Nonlinear Regression Analysis for Vibration Prediction

Two nonlinear regression techniques have been proposed for use in vibration data analysis based on the limitations of two-dimensional linear regression of measured peak amplitudes and a charge weight scaling terms. The proposed approaches are two-dimensional nonlinear regression and three-dimensional nonlinear estimation.

Nonlinear estimation methods attempt to increase prediction model accuracy in two ways. First, the bias associated with the assumption of a normal data distribution required for linear regression is removed. Second, the forced assumption of cylindrical or spherical wave attenuation characteristics common to charge weight scaling is eliminated. Removing the assumptions related to charge weight scaling by square root or cube root factors would be expected to improve prediction accuracy and model correlations (Yang, 2006).

5.4.1 User-Defined Multi-Variable Regression Using Advanced Statistical Analysis

Simple log-log linear regression approaches used for blast vibration prediction can be performed relatively quickly without the aid of a computer. These methods of data analysis have therefore been preferred in blast vibration prediction for many years. Advances in statistical analysis computer programs and computing speed and power now allow more advanced data analysis techniques to be applied to blasting data.

The advanced statistics software package Statistica 8.0 was selected to perform multi-variable, user-defined, nonlinear estimations of attenuation relationships in the author's blast vibration data analysis. Statistica has been used for many years in advanced process control for manufacturing and scientific statistical analysis. In the

field of blast vibration analysis, Statistica or other advanced statistical packages have not been implemented widely in favour of two-dimensional linear regression in log-log space. The updated capabilities of computer-aided statistical analysis allows for more complicated data sets to be analysed and may provide a greater degree of prediction accuracy when compared with outdated linear regression techniques.

5.4.2 Multi-variable, Nonlinear Estimation of Charge Weight Scaling Vibration Prediction Equations Using Statistica 8.0

The first step in performing nonlinear estimation was identifying the independent and dependent variables to be included in the iterative estimation process. To compare the results of multi-dimensional nonlinear estimation with existing two-dimensional linear regression-based techniques, identical independent and dependent variables were selected. The independent variables selected for use in estimation were charge weight (W) and distance (D) and the dependent variable was the measured or calculated peak particle vibration amplitude (e.g. PPV, PPA, energy or strain).

The relationship specified for the nonlinear estimation between the two independent variables and the measured or calculated vibration amplitudes was the general charge weight scaling form in Equation 5.2. The general charge weight scaling form was selected because of the improved prediction correlations experienced through linear regression when compared with the Holmberg-Persson or other models early in the data analysis program. The general shape of the three-dimensional surface fitting the data was defined by the resulting estimation constants K, b and n.

A number of regression parameters were available in Statistica to govern the iteration process during the nonlinear estimation calculations. These parameters included:

- Case-wise or mean substitution median replacement
- Levenberg-Marquardt or Gauss-Newton estimation methods
- Specified convergence level
- Specified maximum number of iterations
- Full post-processing analysis of variance, distribution and residuals

An additional output of the estimation process was a three-dimensional graph of the regression surface along with the regression constants and the specified regression equation. An example regression surface is displayed in Figure 5.5.

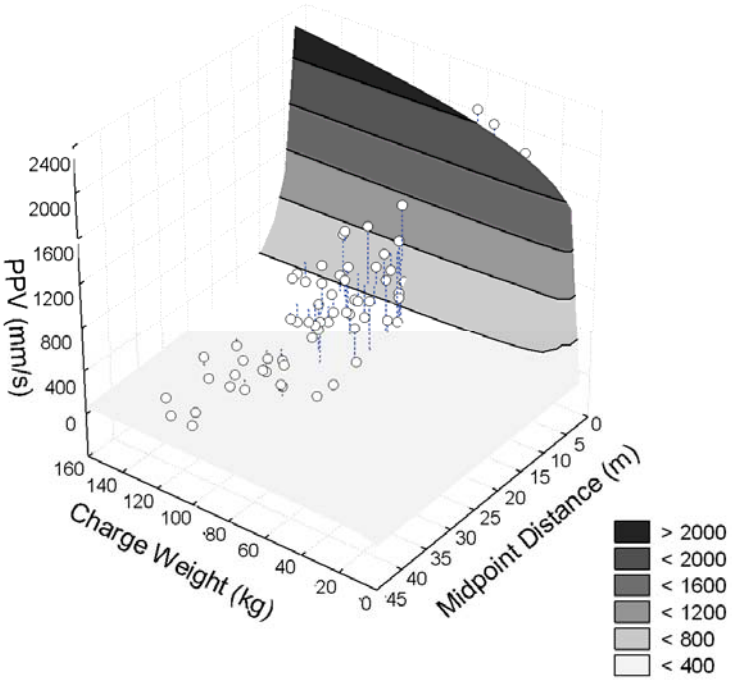

Figure 5.5. Nonlinear multi-variable regression surface of Cannington Mine stope 52h09HL data plotting charge weight, distance and measured PPV.

To further investigate the behaviour of a data set in relation to the charge weight and distance, an additional fitting equation was applied to the multi-variable estimation. The modified scaling relationship was a quadratic surface, using the same input distance, charge weight and PPV data from the first user-defined nonlinear regression. The general form of the quadratic surface is given in Equation 5.12.

$$VSPPV = aW^2 + bD^2 + cWD + dW + eD + f \qquad (5.\ 12)$$

Where W = charge weight (kg)

D = distance (m)

a-f = quadratic regression constants

An example of the output surface for quadratic fitting is illustrated in Figure 5.6.

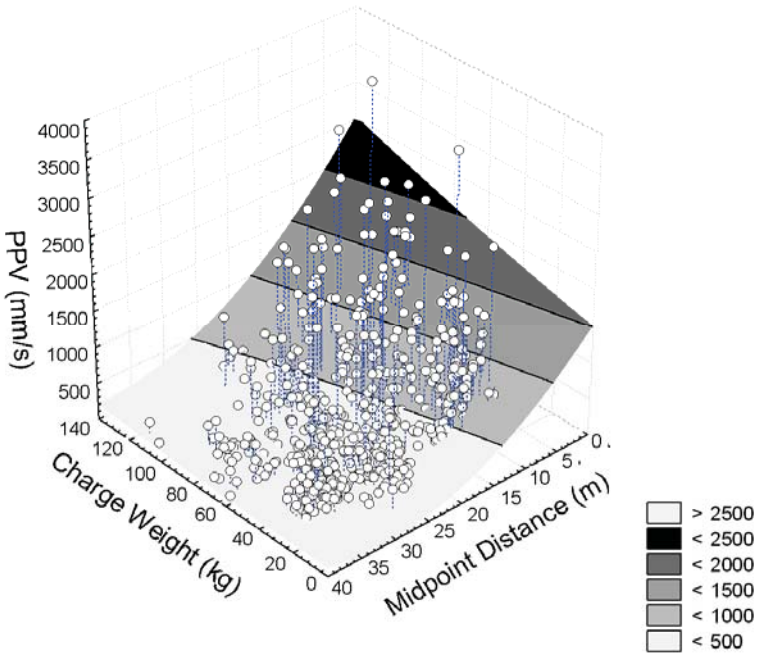

Figure 5.6. Nonlinear quadratic surface regression for BHP Cannington stope 24jC6HL data.

The quadratic surface fit introduced multiple unknown variables (*a* to *f*) and combined relationships between *W* and *D* with respect to the measured vibration amplitudes. To validate this model for use in advanced vibration prediction, these variables and the physical representations require further investigation. This investigation has not been pursued at the current time. The general quadratic form has only been used to gain a better understanding of the defining shape of the surface formed by modelling distance and charge weight independently. The quadratic surface analysis has indicated that the contributions of charge weight and distance to peak amplitude are more complex than single terms with a single scaled behaviour.

5.4.3 Comparison of Results of Linear and Nonlinear Regression Approaches

Nonlinear estimation techniques are highly dependent on the number of data points and the range in values, as there is no initial assumption of data distribution as in linear regression techniques. Through the nonlinear iteration process, each data point

equally influences the shape of the final surface. Therefore, a data set of limited range in either charge weights or distances can result in unrealistic regression constant values, especially *K*. This effect can also be observed in linear regression, as a normal distribution of data points is a background hypothesis.

To validate the use of nonlinear regression techniques to increase peak amplitude prediction accuracy, a number of regression approaches have been applied to a representative data subset from the BHP Cannington 24jC6HL stope. The three charge weight scaling and analysis combinations were: log-log linear regression of PPV versus square root Scaled Distance, log-log linear regression of PPV versus cube root Scaled Distance and nonlinear multi-variable regression of PPV versus distance and charge weight using the general charge weight scaling relationship (Equation 5.2). The results of the regression models as applied to a given data set are listed in Table 5.6.

Table 5.6. Comparison of regression constants for blast vibration monitoring data in Cannington Stope 24jC6HL 200mLv Southeast wall.

Method	***K***	***b***	***n***	**R value**
Linear SD_{SQRT}	299.62	0.61	-1.22	0.71
Linear SD_{CubRT}	803.27	0.44	-1.32	0.70
Nonlinear surface	144.32	0.76	-1.13	0.79

The correlation values listed in Table 5.6 are the R value (coefficient of correlation) instead of an R^2 (coefficient of determination) due to the introduction of a surface regression. R^2 values are typically only applicable to linear regressions; therefore R values have been reported to directly compare the different model types. Based on these reported R values, the nonlinear multi-variable surface regression returned the highest correlation based on the measured vibration data. This trend was observed for nearly all data sets analysed as part of the author's blast vibration monitoring program. For this reason, the nonlinear multi-variable estimation method has been adopted in most forward analysis and predictions of wave amplitudes.

5.5 Data Scatter in Vibration Analysis and Prediction due to Variations in Peak Amplitudes

The confidence in predicting vibration amplitudes using a relationship defined by analysis of measured vibration data relies on the scatter of data points around the best-fit relationship. This scatter represents many different effects related to geological conditions, explosive types, wave types, blast geometries and introduced monitoring errors (Dowding, 1985). It is common in near-field vibration data sets to experience correlation coefficients ranging from very poor to moderate based on standard scientific statistic definitions.

Large blast vibration data sets measured under near-field, variable geometry conditions can report R^2 values of less than 0.5, as observed during the blast vibration monitoring program conducted by the author. In most scientific disciplines, correlation values below 0.95 would be grounds for retesting of the experiment or development of a better regression modelling relationship. The data scatter observed in blast vibration data sets can be related to many factors including geological effects, non-ideal explosive detonation, blast geometry effects and errors in designation of distance, charge weight or amplitude measurement.

5.5.1 Variability in Measured Vibration Amplitudes Due to Confinement or Accumulated Damage

One assumption that has been made in adapting wave propagation models to blast vibration prediction is that the amplitude produced by like charges at similar distances will be equal. In real blasting conditions this is not the case. Variations in non-ideal explosive behaviour, borehole coupling, explosive type, localised geological effects and rock mass damage can significantly influence the stress wave transmitted from an explosive charge into the surrounding rock.

In practice, the peak vibration amplitude measured for identical charges at nearly identical distances can vary significantly (as observed by Yuill and Farnfield, 2001). Vibration data collected during the thesis blast vibration monitoring program confirms this observation. Variability in measured peak amplitudes was investigated

using the data collected from a series of 11 identically-charged blastholes fired in one of the study stopes. The equal charges of approximately 24kg each were fired at near-equal distances from a tri-axial accelerometer. Differences between each single-hole waveform clearly indicated that no consistent or normal distribution in vector sum PPA existed (Figure 5.7).

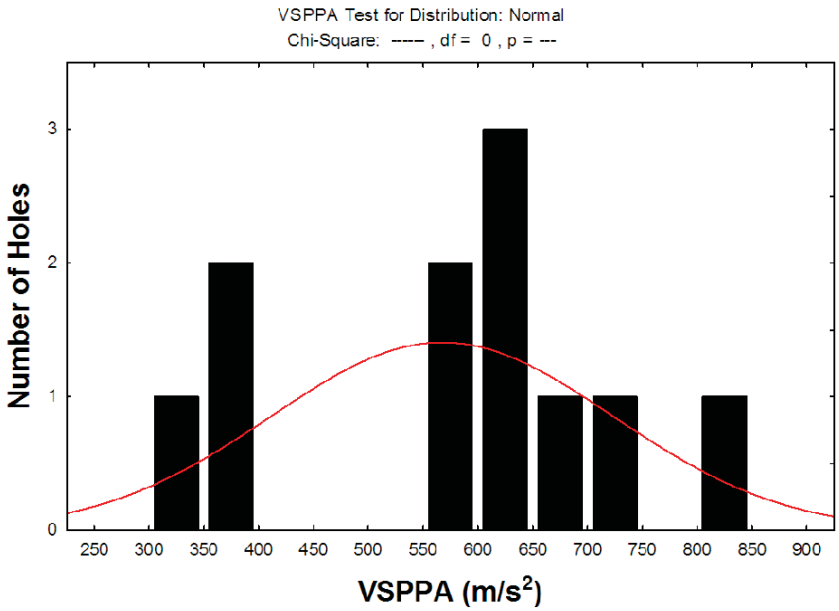

Figure 5.7. Histogram of peak vector sum acceleration measured for 11 equally-charged blastholes at approximately equal distances from a monitoring location.

The observed differences in peak amplitudes in Figure 5.7 may have been linked to differences in the wave frequency, distribution of energy within the wave components, arrival time of the shear wave, differences in blasthole confinement or the accumulation of damage around the blasting area leading to higher near-charge attenuation rates.

Past researchers have argued that increased vibration amplitudes can be expected from charges with higher degrees of confinement or fixation (e.g. Dowding, 1985; Jimeno et al., 1987; Liu and Proulx, 1995; McNally, 1998). These types of confinement conditions can exist where there are excessive burdens leading to narrow breakout angles such as in highly-confined rise blasts (underground) or choke blasts (open pits).

To investigate the relationship between increased charge confinement and peak amplitude, the vector sum peak particle accelerations (VSPPAs) recorded at two equidistant monitoring locations along opposing orientations were compared. Breakout angles were simulated for each charge based on the surveyed hole location and the assumed available void from the previously-fired charges in the sequence. Figure 5.8 shows the assumed breakage areas and associated breakout angles for each blasthole within the longhole winze as a result of the surveyed blasthole locations and the firing sequence.

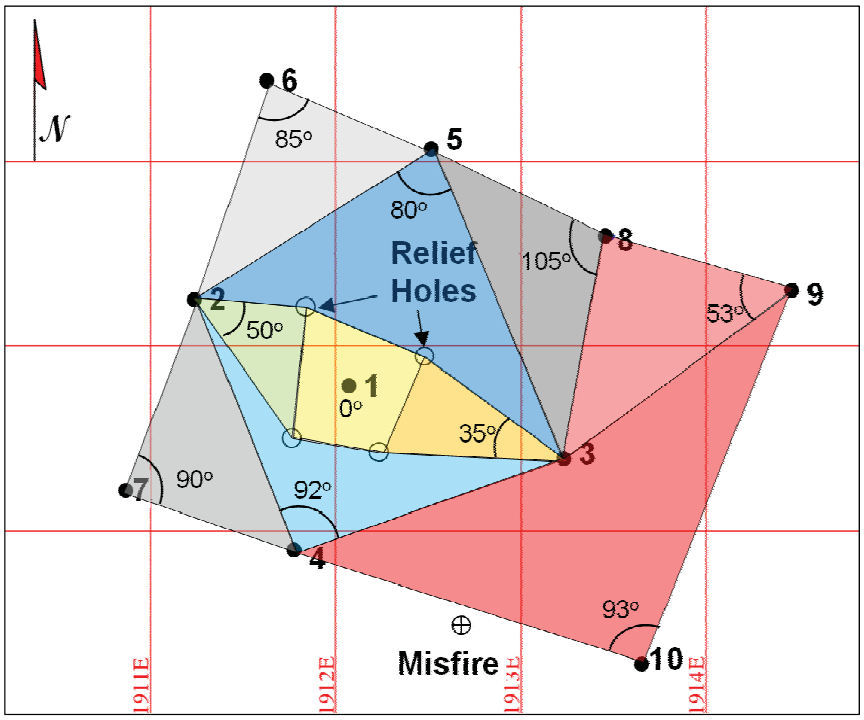

Figure 5.8. Plan view of the simulated breakout areas and angles for winze firing 2 in Cannington Stope 24jC6HL 220mLv (numbers are firing order of holes).

Vibration amplitudes measured at two opposing equidistant monitoring locations from the stope firing (North and South) were compared to observe the change in VSPPA versus the level of charge confinement. Figure 5.9 illustrates the measured VSPPA as a function of the hole firing sequence at the two monitoring locations. Each hole in the blast progressively encountered a higher total void volume and advanced breakout angle due to long delays between blastholes and a centre-out firing sequence.

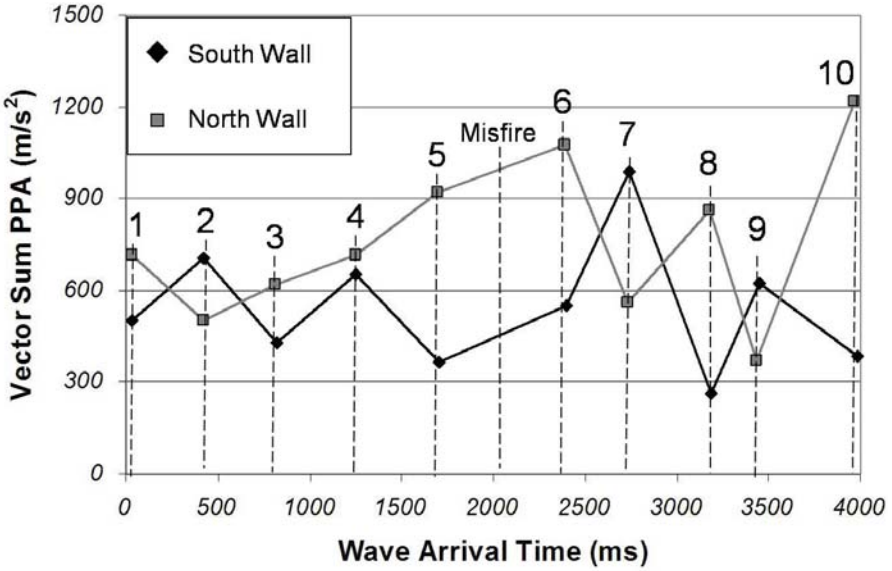

Figure 5.9. Peak amplitude versus firing sequence along 2 orientations in a highly-confined rise blast of 10 equal charges at equal distances.

Under the assumption that the vibration would be greatest where the breakout angle is the smallest due to high confinement, the first 3 blastholes of each data set should have produced peak amplitudes greater than the later firing blastholes. A weak trend of reduction in amplitude based on firing sequence can be observed in Figure 5.9 for the South wall data set (black diamond markers). If the analysis were associated with the burden dimension, hole 10 should have resulted in the highest vibration value at the South Wall monitoring point. As illustrated in Figure 5.9, this was not observed. Additional analyses of the data have been provided in Appendix 5 that examines the influence of breakout angle, broken volume and powder factor on the measured peak amplitude.

For both the North Wall data set (grey squares) and South Wall data set (black diamonds), anomalous measured amplitudes can be observed. These results suggest that both the amplitude and frequency of the measured blast waves were a result of interaction of many factors other than confinement such as rock mass conditions at the time of hole firing, charge coupling, altered explosive properties from loss of confinement or pre-compression, charge geometry and distance from the charge. Blair and Armstrong (2001) observed the no robust statistical relationship existed between peak measured amplitude and charge confinement in a series of open pit

blasts under various conditions of blasthole burden. This result led to the conclusion that confinement did not necessarily increase blast vibrations. Scott (1998) and Ulysal et al. (2007) also observed a counter-intuitive relationship, where increases in burden resulted in a reduction in monitored ground vibrations. Therefore, the direct link between confinement and peak vibration amplitude should be viewed as highly variable due to the additional contributing factors.

It is proposed by the author that some of the variability in measured vibration amplitudes can be related to the degree of existing and developing rock mass damage around the blastholes at the time of firing. Multiple misfired holes have been observed for highly-confined conditions during the blast vibration monitoring program. The locations and sequences of misfired holes indicated heavy rock mass damage up to 1.5m from the confined explosive charges, causing explosive desensitisation or physical damage to adjacent blastholes. Models of rock breakage discussed in Chapter 2 have indicated that a potential radius of fracturing due to strain waves could occur up to 20 times the blasthole radius. For an 89mm blasthole, this zone of heavy damage could therefore extend to 0.89m. With the addition of gas penetration, the damage envelope could extend to several metres.

As successive blastholes detonate in a confined blast pattern, damage would be expected to accumulate in the surrounding rock mass due to the repeated strain wave and gas penetration loading. These effects can introduce strain softening and accumulation of micro- and macro-fractures. The increased fracturing can lead to explosive decoupling effects and a loss of rock mass integrity, which both increasing the rate of wave attenuation near the blasthole.

5.6 Additional Investigation into the Effect of Underground Voids on Distances Determined for Vibration Analysis

An initial and sequentially-expanding void volume is required in open stope blasting to accommodate the swell of blasted material. The wave fields generated by detonating blastholes near the void will interact with the excavation surfaces and corners leading to reflection, refraction and changes of wave types. Any assumption

of isotropic and symmetrical wave propagation under these conditions would therefore be erroneous.

Of the available tools for blast vibration analysis, no software or suggested charge weight scaling approach accounts for the presence of existing or blast-induced voids when determining the source to transducer distances. The common treatment used in past investigations would be to filter out data that appeared to have been collected under void-affected geometries. The effect of existing and forming excavations on blast vibration properties is not a well understood or documented phenomenon.

An approach has been proposed by the author to more accurately represent the wave travel paths between blastholes and blast monitoring locations under the influence of voids. This methodology has been named Void and Initiation-Corrected Distance, or VICD. VICD comprises two different geometric and operational factors; namely, the pre-blast stope void and the dynamically-forming void due to the initiation sequence of the blastholes. Consideration of the blasthole initiation sequence is important, as an additional layer of blast design (initiation sequence) can be introduced to help control blast vibration propagation along specified orientations.

5.6.1 Effect of Existing Stope Voids on Wave Travel Paths

A characteristic geometry of wave-void interaction should be determined to describe the effect of voids on blast-induced wave travel paths and distances. In the stopes encountered in the vibration monitoring program conducted for this thesis, three characteristic geometries have been identified. These are referred to as Intact, Parallel Void and Normal Void geometries. The "Intact" classification refers to geometries where the direct wave path is unaffected by the stope void. "Parallel Void" refers to the geometry where a single wave path disruption occurs. "Normal Void" is the geometry where the point of interest is located on the opposite side of the void from the blasting event. The geometric classifications are determined by the relationship between the monitoring point and the planes of the blasthole rings in relation to pre-existing or forming stope voids. The three geometries and the relationship between the D_G and the VICD for each case are illustrated in Figure 5.10.

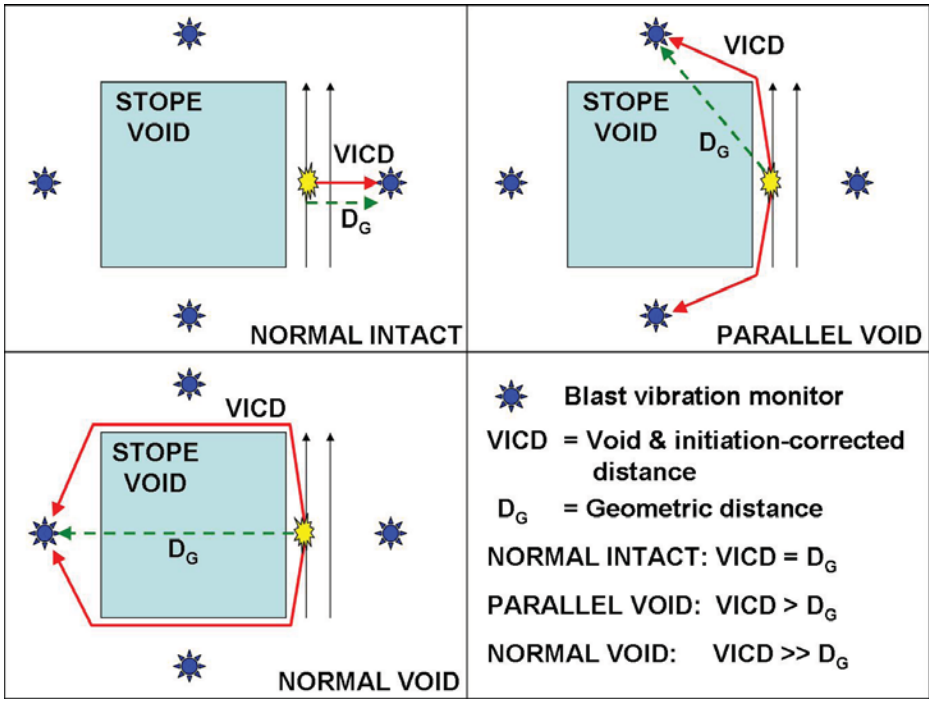

Figure 5.10. Plan view of VICD classifications based on the location of blast vibration monitoring transducers and a blasthole.

The three geometries have been further characterised by the number of "bend points" in the wave path, or the required number of times that a ray path would be required to diffract for a propagating wave to reach the monitoring point. All Intact orientations are those in which the number of bend points is zero, meaning that the direct wave path has not been influenced by a void. In the Intact orientations, the calculated D_G equals the VICD. The Intact geometry generally holds for at least half of the rock mass, based on the location of the vibration monitoring point and the blasthole with respect to the stope void (Figure 5.11). Individual blastholes can experience different geometric classifications with respect to a monitoring location based on the angle formed between the nearest excavation corner and the charge.

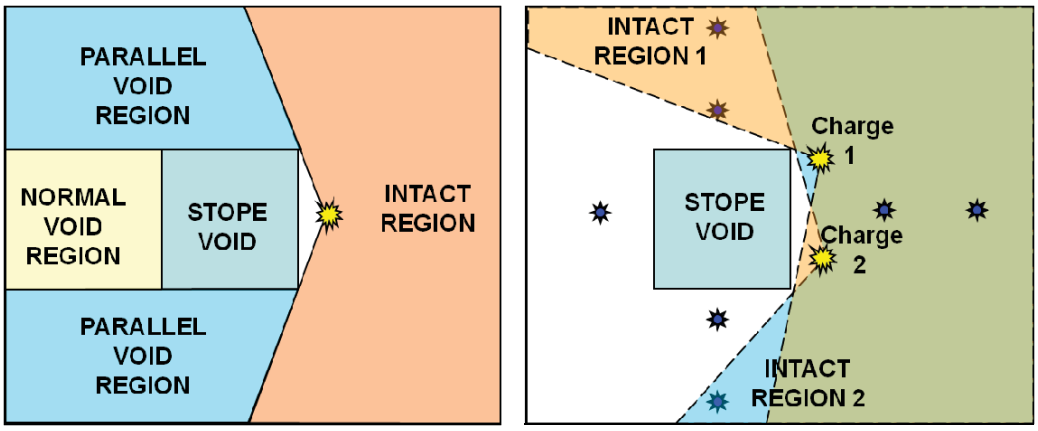

Figure 5.11. Plan view of the Intact VICD geometry based on the stope void and the blasthole position for a single charge (left) or multiple charges (right).

5.6.2 Modelling of VICD Wave Paths

Due to a lack of software to model realistic wave travel paths, VICD wave paths were constructed manually by the author. The process of VICD modelling considered the geometries of each blast and individual charges, blasthole firing sequences and assumptions of the likely paths. To construct the individual wave paths in a realistic way, several assumptions were made. These assumptions included:

- Source points located at the mid-column point of the explosive charge
- The entire burden and spacing became void at the time of charge initiation
- Fired charges were replaced by a node along the line to the nearest bend point
- Only a single minimum-distance ray-path existed (no wave splitting)
- No significant wave transmission existed along void and paste fill interfaces
- No significant loss of energy occurred along the void surface

Realistically, multiple ray-paths resulting from wave splitting will exist around a void. Wave superposition would therefore occur upon convergence of the multiple wave fronts. This effect would be most apparent in the Normal Void orientation. The phase delays and individual travel times of each portion of the split wave-front would be expected to recombine in complex ways and as such cannot be represented

accurately in the VICD model. The current version of the VICD approach only considered a single wave path along the minimum wave travel distance. The complex interactions between combining wavefronts are beyond the scope of this thesis.

The wave travel path represented in VICD distance modelling used a point-to-point (or node-to-node) aggregate distance. Each node within a model was identified by a set of mine-grid three-dimensional coordinates. The wave path was constructed using a series of discrete three-dimensional coordinates from the source (blasthole) to the monitoring point along a line of nodes. The starting point of each VICD wave path string was the midpoint of the explosive column. The intermediate points were nodes on the previously-fired blastholes and the surfaces and corners of the existing stope void, where the void node spacing typically varied from 0.5 to 1m along the corner line of the stope. In the case of a Normal Void monitoring orientation, all surfaces of the existing void were populated with void nodes. The final point along the VICD wave path was the desired transducer location. The VICD was the minimum total distance along the string of nodes from the explosive source to the monitoring location. The types of nodes used to define the aggregate wave path are illustrated in Figure 5.12.

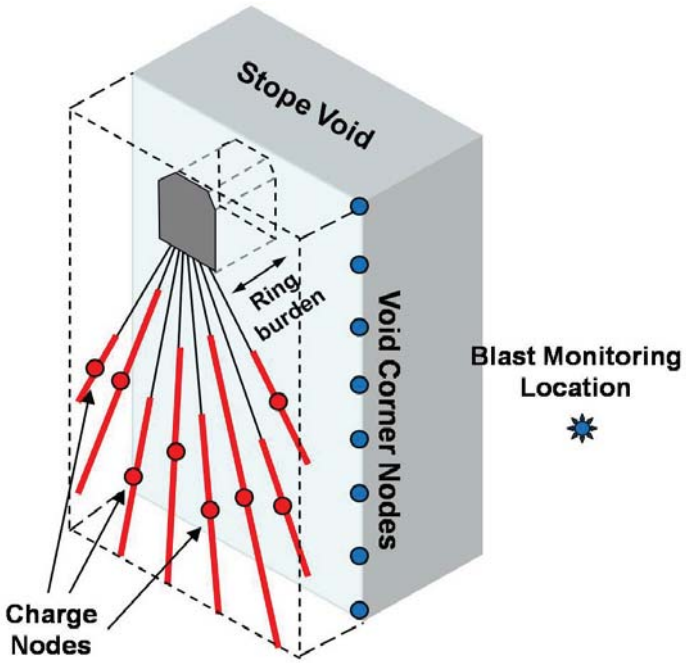

Figure 5.12. Conceptual view of different node types used to determine the VICD between a charge and a monitoring point with Parallel Void geometry.

Each of the charge nodes (as illustrated in Figure 5.12) were assigned a firing sequence based on the mine-issued charge plans. The process for constructing the wave paths for each charge on the ring started with the first firing blasthole. The likely wave path for the initial hole firing on the example ring (figure 5.12) is illustrated in Figure 5.13.

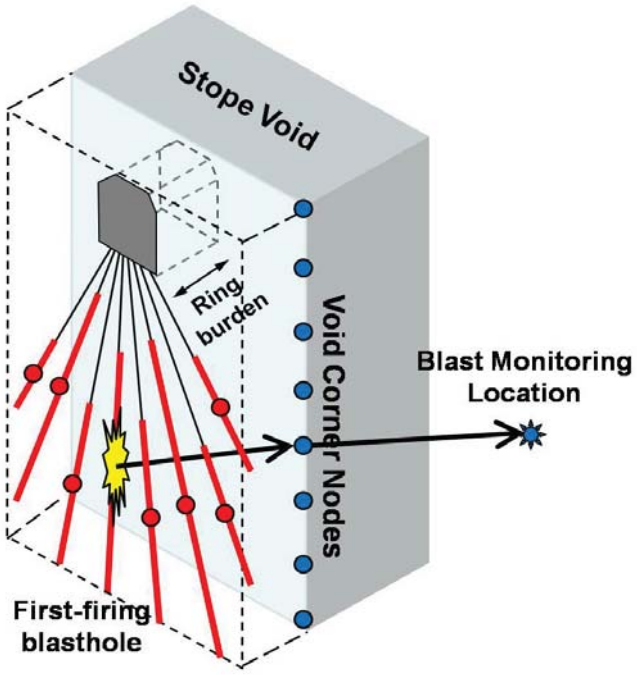

Figure 5.13. Conceptual view of the VICD wave path for the first ring charge firing.

After firing of each charge, the charge node was replaced by a fired node, which aided in representing the forming stope void in relation to the initiation sequence. As the fired charges intersected the design stope boundary, the row of void corner nodes were moved to the ring outline of the firing ring to represent the new post-blasted stope void face. Figure 5.14 demonstrates the wave travel paths after half of the ring intersecting the design stope boundary is detonated and the void nodes are moved to the fired ring void.

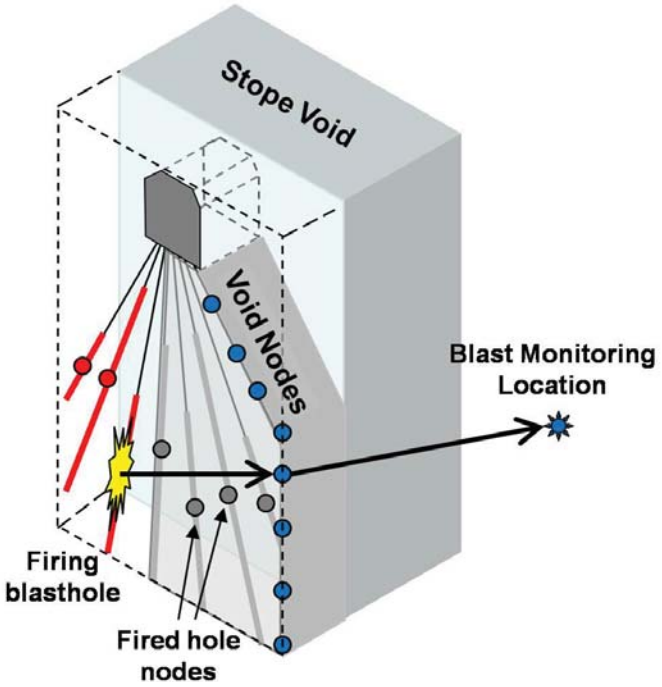

Figure 5.14. VICD of a firing blasthole after a number of holes have been fired forming the new stope void perimeter.

Once the most probable string of nodes between a charge and a blast monitoring location was established for each blasthole, the VICD for each charge was calculated as the sum of the individual node-to-node distances using Equation 5.13:

$$VICD = \sum_{P_S}^{P_M} \sqrt{(X_S - X_i)^2 + (Y_S - Y_i)^2 + (Z_S - Z_i)^2} + \ldots \sqrt{(X_{i+n} - X_M)^2 + (Y_{i+n} - Y_M)^2 + (Z_{i+n} - Z_M)^2} \quad (5.13)$$

Where X_S, Y_S, Z_S = coordinates of a reference point in the explosive charge

X_i, Y_i, Z_i = coordinates of first intermediate void interface point

X_{i+n}, Y_{i+n}, Z_{i+n} = coordinates of sequential void interface points

X_M, Y_M, Z_M = coordinates of vibration monitoring point

The end product of the node-to-node process yielded a series of wave path strings from each blasthole to each transducer location around the seven monitored stopes (Figure 5.15).

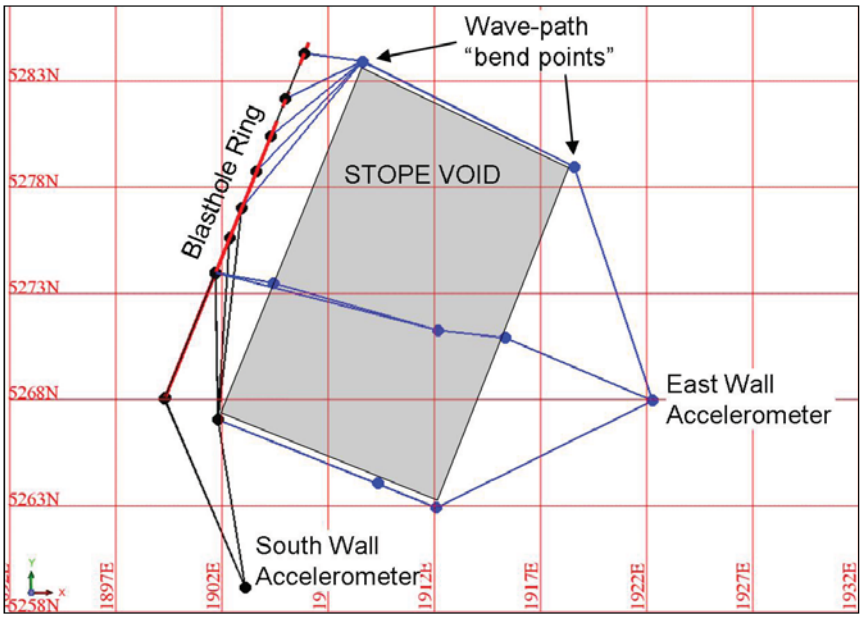

Figure 5.15. Plan view of east wall (blue lines) and south wall (black lines) VICD wave paths for blasthole ring #4 in 220mLv mass blast of stope 24jC6HL.

Due to the three-dimensional geometry of the open void with respect to the charge midpoints, several VICD wave paths in Figure 5.15 appear to pass through the stope void. This result is misleading in appearance, as the wave paths actually travel over the top of the stope and development void.

5.6.3 Comparison of D_G and VICD

The difference between D_G and VICD is small or negligible under certain void geometries such as the intact and shallow-angle parallel void classifications. In other monitoring geometries, the difference between D_G and VICD can be substantial. To compare the effects of void geometry on minimum wave path distances, D_G and VICD have been calculated for a ring of ten, 89mm diameter blastholes fired in stope 24jC6HL at the BHP Cannington Mine. The D_G and VICD source to sensor distances have been compared with one another along with the percent differences for the Parallel Void and Normal Void orientations. These results are illustrated in Figures 5.16 and 5.17.

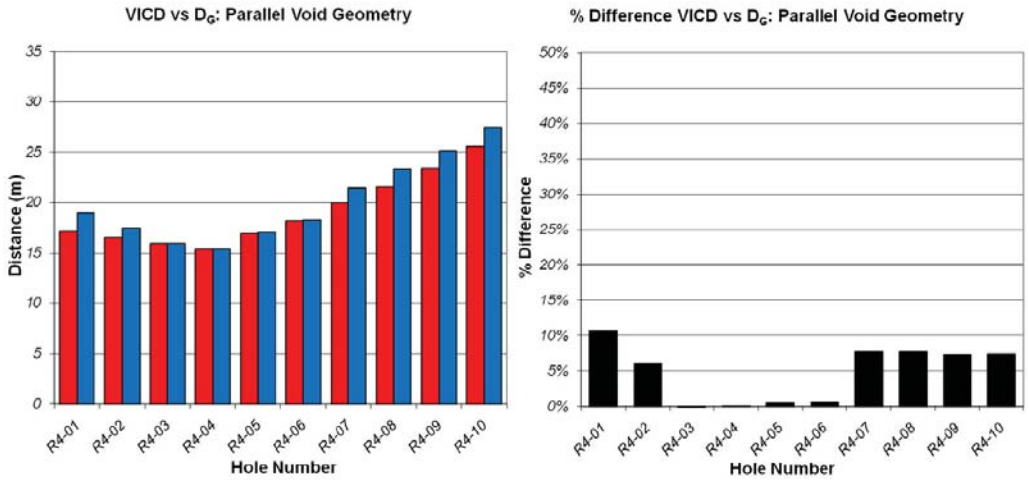

Figure 5.16. D_G and VICD for a ring of blastholes along the Parallel Void orientation (left) and percent difference between D_G and VICD for the ten holes (right).

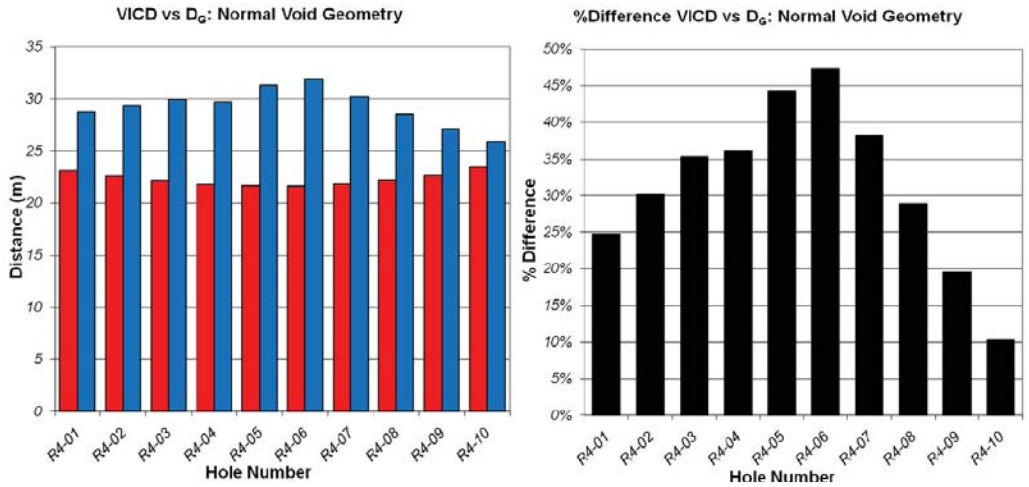

Figure 5.17. D_G and VICD for a ring of blastholes along the Normal Void orientation (left) and percent difference between D_G and VICD for the ten holes (right).

Comparing D_G with VICD, a slight increase in source to sensor distances in the Parallel Void monitoring position can be observed (Figure 5.16). This change would be unlikely to produce significant shifts in distance-based charge weight scaling of vibration values, although the presence of a single diffraction point could affect the wave field. In the Normal Void direction (Figure 5.17), significant differences in distance have been observed which would lead to a substantial shift in the vibration prediction model towards higher charge weight scaling factors.

5.6.4 Effect of Initiation Sequence on Wave Path

The second consideration in modelling of VICD is the effect of blasthole initiation sequence within a blast on the wave path. The effect of blasthole firing sequence can significantly influence the results of distance modelling along affected paths, as the forming void creates both rock mass damage and alters the wave travel path. The proposed influence of initiation sequence on VICD is illustrated in Figure 5.18 for a common stope blasting geometry. The example in Figure 5.18 is a five-hole pattern (holes A-E) with ring burden of 2.5m and toe spacing of 5.0m. The firing sequence is noted by the numbers adjacent to the holes (#1-#5). As each hole is detonated, a void equivalent to one burden and spacing replaces the hole for use in wave path determination. Firing sequence 1 represents a common sequence of centre-opening and alternate firing along the ring towards the stope perimeters. Sequence 2 would be typically applied where there is an attempt to "smooth blast" the final wall of the stope or to fire sequentially away from a geologic feature of interest.

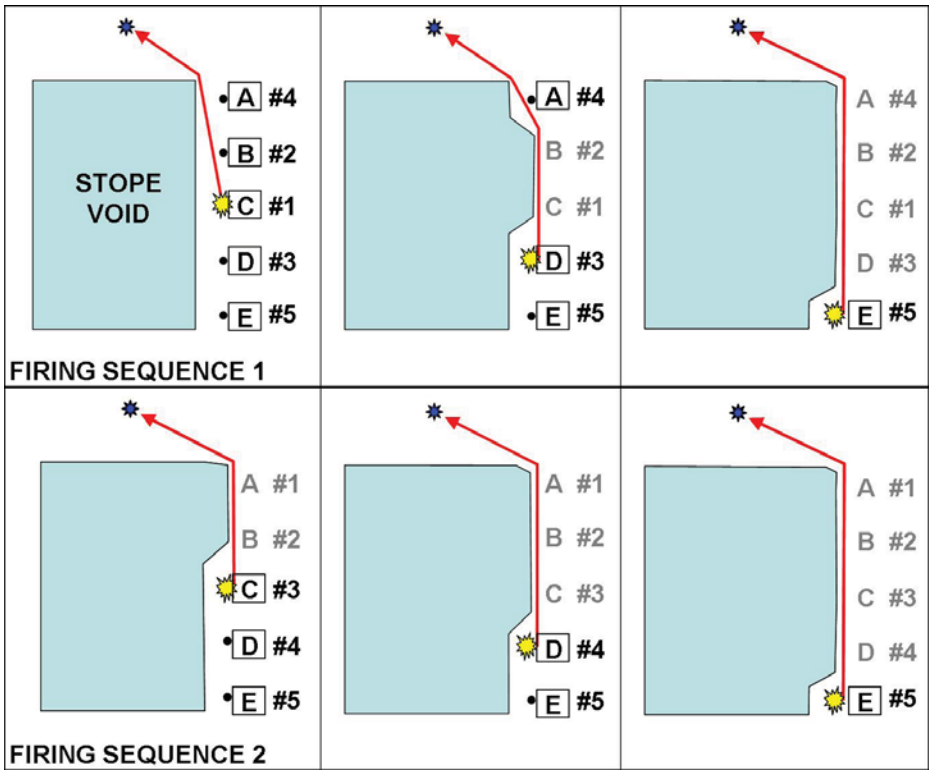

Figure 5.18. Plan view of VICD wave paths from three of five detonating holes to a Parallel Void transducer for centre-out initiation (top) and sequential hole initiation (bottom) firing sequences.

Figure 5.18 illustrates the trend of either decreasing or increasing travel distances based on the firing sequence of the blastholes and the forming void. As the individual blastholes fire, the waves would be required to travel around the forming void prior to being recorded at the Parallel Void vibration transducer location. Table 5.7 demonstrates the differences in wave path distances when comparing the two firing sequences.

Table 5.7. Comparison of VICDs for firing sequences 1 and 2.

VICD for Sequence 1 Firing (m)	Mathematical Relationship	VICD for Sequence 2 Firing (m)
$VICD_{A1} = 9.0$	=	$VICD_{A2} = 9.0$
$VICD_{B1} = 12.6$	<	$VICD_{B2} = 14.0$
$VICD_{C1} = 17.4$	<	$VICD_{C2} = 19.0$
$VICD_{D1} = 22.6$	<	$VICD_{D2} = 24.0$
$VICD_{E1} = 29.0$	=	$VICD_{E2} = 29.0$

5.6.5 Effect of Wave Travel Path on Charge Weight Scaling of Peak Amplitude

The influence of void-affected wave travel distance on the modelling and prediction of vibration amplitudes were investigated using log-scale linear regressions of cube root Scaled Distance and peak amplitude. Two models were compared in which the cube root Scaled Distance values were calculated using either D_G or VICD for the same charges. The comparison used vibration monitoring results at a Normal Void accelerometer in the Southeast wall of stope 24jC6HL at the BHP Cannington Mine. All blast waves from the source holes were therefore required to travel around the stope void to the vibration monitoring locations in the opposite stope wall.

The two variations of the vibration prediction model were compared by plotting the measured vector sum PPAs (VSPPA) against the cube root Scaled Distances calculated using either D_G or VICD. Linear regressions were performed to determine the best-fit curves for each data set. The plot of both data sets is illustrated in Figure 5.19.

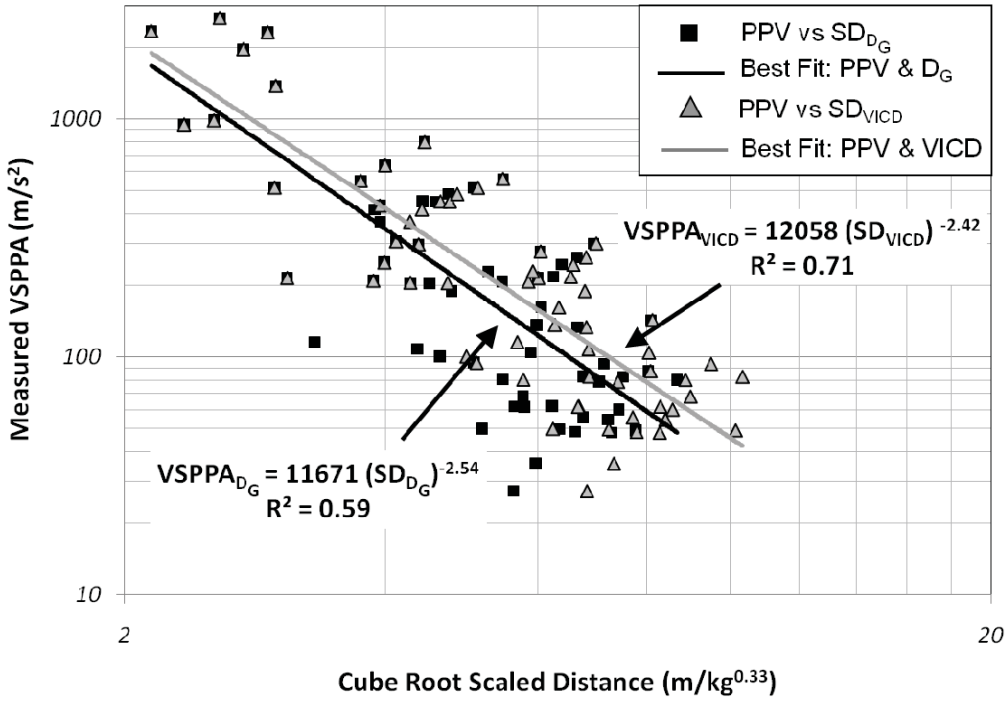

Figure 5.19. Comparison of void-affected D_G (black squares/black line) and VICD (grey triangles/grey line) cube root Scaled Distance models of VSPPA for the 220mLv mass firing in BHP Cannington Stope 24jC6HL.

The best-fit attenuation equations for D_G and VICD-based Scaled Distance in Figure 5.19 differ slightly in slope and significantly in intercepts and correlations. The improvement in the R^2 value for the VICD model (0.71 versus 0.59 for the D_G model) suggests that the use of void-corrected distance more accurately represents the measured vibration amplitudes as a function of cube root charge weight scaling. For the D_G model, the peak amplitude attenuation relationship has been shifted to lower Scaled Distance values due to misrepresentation of the true wave travel distance. Lower values of vibration would therefore be predicted at all distances (void-related or intact) using the D_G-based results.

5.6.6 Comparison of Statistical Confidence of D_G and VICD Models

The two data sets represented in Figure 5.19 appear to be similar, and it is arguable that the scatter experienced in both data sets would negate the differences between the two characteristic best-fit curves. Basic statistical analysis of both data sets was

performed to determine the 95% and 98% upper confidence curves for comparison. The confidence curves were determined by adding multiples of the statistically-derived standard errors to the best-fit intercept *K* value. The 95% upper confidence line intercept was one standard error above *K* and the 98% upper confidence intercept was *K* plus two standard errors. The slopes of the confidence lines were assumed to remain constant as defined by the best-fit lines. Table 5.8 lists the upper confidence log-log linear regression results for each model.

Table 5.8. Log-log linear regression results for the void-affected VSPPA versus cube root Scaled Distance calculated using D_G and VICD for the 24jC6HL mass blast.

Model	**Best-fit Log(*K*)**	**Log Standard Error**	**Best-fit *β***	**95% Confidence Log(*K*)**	**98% Confidence Log(*K*)**
VSPPA-SD_{DG}	4.067	0.312	-2.54	4.379	4.691
VSPPA-SD_{VICD}	4.081	0.262	-2.42	4.343	4.605

The reduced standard error for the VICD model suggests a higher degree of statistical confidence in predicting the measured values when compared with the results from the D_G model. The differences between the best-fit, 95% and 98% confidence *K* values for the D_G regressions when compared with the VICD values are significant. The best-fit regression constants listed in Table 5.8 indicate that the VICD model would predict higher values of VSPPA when compared with the D_G model at higher values of SD_{CubRT} resulting from larger travel distances. At reduced values of SD_{CubRT} (< 0.75 $m/kg^{0.33}$), the D_G model would predict higher values of VSPPA.

The improved correlation of the VICD model resulted in lower values of predicted VSPPA at reduced SD_{CubRT} values using 95% and 98% confidence cases. For example, the D_G model using the 95% confidence prediction of VSPPA at an SD_{CubRT} value of 0.5 $m/kg^{0.33}$ was 18% higher than the VICD model prediction. The 98% confidence prediction using the D_G model was 32% higher than the VICD results for the SD_{CubRT} value of 0.5 $m/kg^{0.33}$. These differences in predicted

maximum amplitudes would be expected to lead to over-prediction of zones of expected damage if peak amplitude blast damage models are used.

5.6.7 Theoretical Investigation into the Influence of Underground Stope Voids on Blast Wave Attenuation

The observed influence of existing stope voids on the measured vibrations in the monitored study stopes prompted a numerical investigation of void-affected wave propagation. The software package *Wave2000 Plus*® discussed in Chapter 3 was used to simulate the interaction of elastic waves with an existing stope void under geometries similar to those experienced during near-field blast monitoring at the two sponsor sites. Details of the modelling program and field validation of the results are discussed in Appendix 6.

5.7 Discussion and Conclusions

Traditional blast vibration analysis and prediction approaches based on charge weight scaling have been discussed and assessed using data collected during the author's near-field blast vibration monitoring program. The results of various models used to predict peak amplitudes have been compared through linear regression to determine those with the highest correlations with measured vibration data. For the data subset investigated in this chapter, traditional charge weight scaling using square root and cube root Scaled Distance yielded correlation values similar to the more complicated scaling models proposed by Holmberg and Persson (1979) and Ouchterlony et al. (1993). Further comparison of values of Scaled Distance and the Holmberg term (a) revealed that for complex blasting geometries, no advantage would be gained by using the more mathematically complicated models. Approaches developed using fundamental wave propagation models such as the Lu-Hustrulid (Lu and Hustrulid, 2003) and the Sambuelli (2009) models also failed to improve predictive capabilities when compared with charge weight scaling approaches.

The limitations of linear regression techniques using set charge weight scaling parameters were addressed by proposing nonlinear multi-variable analysis methods using the advanced statistical software package Statistica 8.0. The proposed analysis

technique determines the regression constants which define a three-dimensional regression surface without assumption set scaling factors based on the assumed source type. This approach was applied to prediction of peak amplitudes, energies and strains in Chapters 7 and 8 using the general charge weight scaling relationship.

Development of a technique for determining the source to transducer distance under void affected geometries has been discussed. The minimum distances between blasthole charges and transducers determined using the VICD approach have been compared to the standard three-dimensional geometric distance (D_G) for several void-affected data sets. Blast vibration analyses using cube root Scaled Distances and measured VSPPAs have been compared using both distance models. This analysis revealed that the VICD distance model improved the correlation of the best fit relationship and reduced the standard error. This improvement in correlation would be expected to lead to an increase in prediction accuracy if used in forward analysis. Numerical simulation of wave propagation around a stope void was also performed and is discussed in detail in Appendix 6.

This page left intentionally blank – KG Fleetwood

CHAPTER 6 : PROPOSED ENERGY AND STRAIN-BASED BLAST DAMAGE CRITERIA

6.1 Introduction

The methods used in the past for prediction of rock mass damage from blasting have included PPV-based empirical models such as the Swedish Tunnelling Damage Tables (Ouchterlony et al., 2002), laboratory or small-scale observations of fracturing (e.g. Kutter and Fairhurst, 1971; Shockey et al., 1974; Olsson et al., 2002), critical tensile plane strain models (e.g. LeBlanc et al.,1995; Heilig, 2002; Singh and Narendrula, 2004), failure stress/strain numerical models (e.g. Butkovich and Hearst, 1976; Donzé et al., 1997; Katsabanis, 2001; Ma et al., 2004; Tawadrous and Katsabanis, 2007; Furtney et al., 2009) and continuum damage models (e.g. Grady and Kipp,1979; Yang et al., 1996). Despite the extensive research on the subject, a complete and accurate approach to predict blast-induced damage in realistic rock mass conditions has not yet been developed.

Due to some of the limitations of existing empirical and semi-analytical blast damage prediction methods, a newly-proposed blast damage prediction approach developed by the author is discussed in this chapter. The damage prediction approach contains multiple components which address both near-field blast wave characterisation and the prediction of rock mass damage using various rock fracture criteria. The proposed criteria are based on energy and strain-related rock fracture principles used in fracture mechanics and rock mechanics.

6.2 Existing Empirical, Semi-Analytical and Numerical Models to Predict Blast-Induced Damage

Past researchers have used empirical, semi-analytical or numerical techniques to predict blast-induced rock mass damage. Results from these investigations have provided valuable information, but those based on empirical or semi-analytical damage criteria such as PPV or tensile plane strain do not accurately describe the complex rock mass loading conditions or blast-induced damage mechanisms for confined explosive charges.

Previously published blast-induced rock mass damage criteria have been established through observation of the results of laboratory, small-scale and field-scale blasting tests and dynamic rock breakage investigations. Some of these investigations have been reviewed and are discussed in Appendix 3. Some of the methods used to validate damage prediction models by indicating rock mass alterations have also been reviewed and are included in Appendix 8.

6.2.1 Direct PPV-Related Rock Damage Models

For four decades, the potential for vibration-related damage to engineered structures near blasting events has been assessed by peak particle velocity (PPV) criteria. Work conducted in Sweden in the 1970s extended this theory to rock mass damage around tunnels blasted in bedrock and quarry production blasts (e.g. Holmberg and Persson, 1978 and 1979). The link between PPV and blast-induced damage was investigated over many blasting experiments, and PPV-related damage envelopes for different tunnel blasting explosive products and geometries were suggested. These standards were eventually included in the Swedish Tunnel Regulations (Ouchterlony et al., 2002). Many researchers have adopted PPV as an indicator of potential rock mass damage, and have established vibration damage thresholds for use in blast design and minimisation of overbreak for tunnelling or mine development. Some suggested PPV-based damage thresholds are listed in Table 6.1.

Table 6.1. PPV-based rock fracture criterion as published by past researchers.

Researcher	Blasting Conditions	PPV Level (mm/s)	Suggested Damage
Holmberg and Persson (1978)	Tunnelling-Swedish granite	700-1000	Fresh fracture
Page (1987)	N/A	2500-3500	Rock breakage
Zhang and Chang (1999)	Crater blast- weathered granite	162-194	Micro-cracking
Rorke and Milev (1999)	Simulated rock burst-unconfined quartzite	650	Fracture of “hard rock”

The PPV values contributing to fresh rock fracture on different scales (micro to macro) in Table 6.1 cover a broad range. These published values were site specific for given blast configurations and did not consider other factors that could influence damage such as time-dependent stress-related effects, degree of ground reinforcement or surface support, existing geological conditions, excavation size, shape or orientation or existing stress-induced or blast-induced damage.

6.2.2 Critical Tensile Plane Strain Damage Prediction Models

A simple peak tensile plane strain rock mass damage criterion has been adopted by past researchers and applied to the prediction of blast damage based on plane wave assumptions (e.g. Holmberg and Persson, 1979; LeBlanc et al., 1995; Keller and Kramer, 2000). The assumption of plane wave conditions allows a tensile plane strain damage criterion to be linked with predicted or measured PPVs. The various published equations using the plane strain criterion have been referred to as critical tensile plane strain models in this thesis due to the derivation of the formula assuming plane strain conditions and a tensile rock fracture criterion. The critical tensile plane strain approach is semi-analytical and considers rock properties and stress-strain relationships to estimate values of PPV likely to cause tensile rock fracture (PPV_{crit}) or extension of existing fractures (PPV_{Min}, $PPV_{extension}$). The general derivation of the approach and published versions of the critical tensile plane strain equations are listed in Equations 6.1 to 6.4.

$$PPV_{crit} = \varepsilon_{T-crit} \times V_p = \frac{\sigma_T \times V_p}{E} \approx \frac{UCS \times V_p}{f_{C/T} E} \qquad (6.\ 1)$$

Where PPV_{crit} = critical PPV at which tensile damage occurs (m/s)

$\varepsilon_{T\text{-}crit}$ = critical tensile failure strain (m/m)

σ_T = rock tensile strength (Pa)

V_p = P-wave velocity of the rock mass (m/s)

E = Young's Modulus of rock (Pa)

UCS = quasi-static unconfined uni-axial compressive strength (MPa)

$f_{C/T}$ = ratio of UCS to σ_T

Alternate forms of Equation 6.1 have been outlined by Keller and Kramer (2000) based on Swedish criterion (Equation 6.2 to 6.4).

$$PPV_{crit} = \frac{\sigma_C \times V_p}{15 \times E} \tag{6. 2}$$

Assuming that the Poisson's Ratio is approximately 0.25 and $f_{C/T}$ equals 10:

$$PPV_{crit} = \frac{0.08 \times \sigma_C}{V_p \times \rho_R} \tag{6. 3}$$

And

$$PPV_{Min} = \frac{0.31 \times \sigma_{DT}}{V_p \times \rho_R} \approx \frac{0.021 \times \sigma_C}{V_p \times \rho_R} \tag{6. 4}$$

Where PPV_{Min} = minimum PPV at which fracture extension can occur (m/s)

σ_{DT} = dynamic tensile strength of rock (15 x σ_C, Pa)

ρ_R = density of rock (kg/m^3)

Some generally-proposed PPV values expected to cause different severities of rock mass damage ranging from rock disintegration ($PPV_{fragmentation}$) to fracture extension ($PPV_{extension}$) have been expressed by Heilig (2002) in relation to PPV_{crit} (Equations 6.5 and 6.6). These values have been roughly based on strain theories of rock breakage.

$$PPV_{fragmentation} = 4 \times PPV_{crit} \tag{6. 5}$$

$$PPV_{extension} = \frac{PPV_{crit}}{4} \tag{6. 6}$$

Using the Equations listed from 6.1 to 6.6, various researchers have suggested values of $PPV_{fragmentation}$, PPV_{crit} and $PPV_{extension}$ for prediction of rock mass damage based on site-specific rock properties. The results are listed in Table 6.2.

Table 6.2. $PPV_{fragmentation}$, PPV_{crit} and $PPV_{extension}$ values published in past research.

Researcher	PPV Level (mm/s)	Suggested Damage
Forsyth (1993)	1275	Fracture of "good" rock mass
LeBlanc et al. (1995)	1450 350	Fresh fracture Fracture extension
Keller and Kramer (2000)	383 1459	Fracture extension Fresh fracture
Heilig (2002)	400 1130 4500	Fracture extension Fresh fracture Fragmentation
Singh and Narendrula (2004)	1500	Fresh fracture

The extent of damage can be predicted by comparing the results of blast vibration monitoring and analysis with the various PPV values to determine the distances from an explosive charge where the critical PPV values are exceeded. This approach defines a series of axis-symmetric damage envelopes of given radius as specified by the severity of damage (fragmentation, fresh fracture or fracture extension). Figure 6.1 illustrates the damage envelopes predicted by Heilig (2002) around 102mm diameter ANFO-charges at the Kanowna Belle Gold Mine.

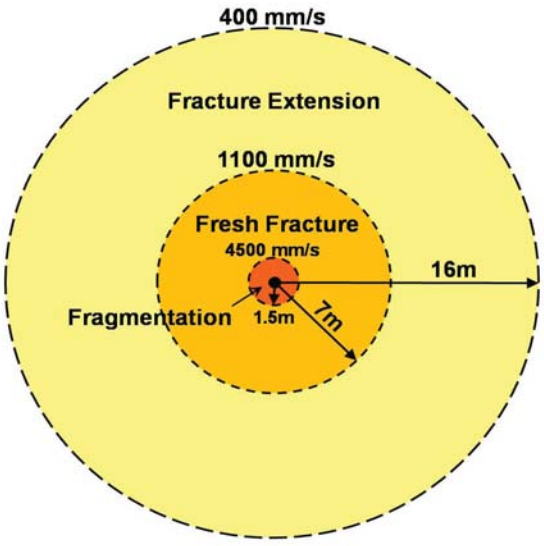

Figure 6.1. Predicted damage envelopes perpendicular to the axis of a 102mm diameter ANFO at the Kanowna Belle Mine (after Heilig, 2002).

6.2.3 Limitations of the Critical Tensile Plane Strain Model

Application of Equations 6.1 to 6.4 to estimate critical vibration amplitudes which are expected to induce tensile mechanism blast damage requires careful consideration of the input variables. These considerations are related to the selection of the intact rock compressive or tensile strength, the ratio of UCS to σ_T, the rock elastic properties and the dynamic loading conditions experienced from blast waves. As discussed in Chapter 2, the behaviour of rock-like materials experiencing dynamic loading conditions differs significantly to that for quasi-static loading. Compressive and tensile strengths can increase by an order of magnitude due to the high strain rates associated with blasting-induced dynamic loading. In addition, the dynamic Young's Modulus can differ significantly from the static Young's Modulus.

The strength of intact rock and discontinuities within a confined rock mass varies with scale effects and confining stresses. Over the scales at which high-frequency blast waves will load a material along the axis of propagation (i.e. the wavelength), scale effects can become important when compared with the characteristic static testing size (NQ core for example). To further complicate the determination of rock mass strength, the in situ strength would be expected to be less than the values determined from laboratory-scale testing of intact rock samples due to the influence of discontinuities. Rock mass tensile strength in the presence of an excavation is assumed to be near zero based on the weak tensile properties of most types of discontinuity (Brady and Brown, 2004).

The original applications of blast vibration-related plane strain were to assess the potential for damage to walls of engineered structures as a result of far-field blast vibrations (Langefors and Kihlström, 1978). This approach was then extended to investigating breakage of burden from the reflection of compression waves at a free face (Holmberg and Persson, 1978). A significant theoretical and mechanistic dislocation has occurred when translating the original model of plane strain-related damage of surface structures to predicting damage around a confined blasthole.

Under conditions of propagating body waves in pre-stressed media, the failure mechanisms proposed in the model (defined by static unconfined tensile strength and

tensile plane strain) are no longer feasible and therefore the terms used in the equation must be viewed critically. Several of the revised forms of the equation have attempted to consider the dynamic loading conditions through use of a dynamic tensile strength (σ_{DT}); but, as illustrated in Chapter 2, dynamic strength varies with strain rate. Additional considerations involve the dynamic elastic properties and wave propagation velocities of an in situ rock mass, which can differ significantly from values determined from laboratory testing of intact rock samples.

Existing semi-analytical rock mass damage prediction models such as the critical tensile plane strain approach grossly simplify rock damage mechanisms and loading conditions. Using the tenets of rock mechanics and fracture mechanics, rock mass damage criteria related to rock failure strains and energies have been proposed by the author in Section 6.5. These approaches more accurately describe the breakage mechanisms under complex stress wave loading when compared with a model using plane strain assumptions and static rock properties. The proposed strain and energy-based damage criteria represent a multi-tier analytical approach to individually predict blast damage to intact rock and existing discontinuities. The influence of mining-induced static stresses, commonly experienced in underground mining, are also considered.

6.2.4 Numerical Modelling of Blast Damage Zones

Many researchers in the past have utilised numerical models to predict blasting behaviour prior to physical testing or to better explain observed behaviours. The levels of complexity in representing the geometry, spatial relationships, materials and damage processes vary significantly in the published literature. Additionally, the applied numerical codes or modelling packages cover a wide range. As computing power has increased exponentially in recent years, complex representations of material properties and dynamic loading conditions have developed such that more complex systems of interaction have been investigated. Table 6.3 outlines some of the numerical modelling parameters used in the published literature to investigate the breakage process.

Table 6.3. Numerical modelling parameters and failure criteria used in dynamic breakage investigations.

Researcher	Model	Modelling Package	Material Model	Damage Criteria
Butkovich and Hearst (1976)	1-D	SOC (Sandia)	Elastic-plastic	Distortional strain
Kleine et al. (1990)	3-D	Custom	Discrete blocks	Comminution energy
Preece and Thorne (1996)	3-D	PRONTO-3D	Fractured continuum	Volumetric strain
Donzé et al. (1997)	2-D	Discrete element	Cohesive elastic-brittle	Normal to shear strength ratio
Keller and Kramer (2000)	3-D	QED	Linear-elastic	Tensile strain
Katsabanis (2001)	2-D	AutoDyn	Mohr-Coloumb	Cumulative damage (AutoDyn)
Ma et al. (2004)	2-D	AutoDyn	Plastic-elastic	PPV and effective tensile strain
Tawadrous and Katsabanis (2007)	2-D	AutoDyn	Elastic-plastic	5 x static strength
Yoon and Jeon (2009)	2-D	PFC2D	Bonded particle	Tensile and shear "bond strength"
Onederra et al. (2009)	3-D	HSBM	Lattice-particle	Tensile "bond strength"

6.2.5 Methods of Indicating Rock Mass Alteration to Validate Blast Damage Predictions

In the published research, many methods of assessment have been used to validate or calibrate blast damage prediction models through indicating changes to rock mass properties. These methods have included direct observation (e.g. Langefors and Kihlström, 1978; Yu, 1980; Holmberg et al., 1984), indirect observation using borehole fracture logging or laser surveying of voids (e.g. LeBlanc et al., 1995; Germain and Hadjigeorgiou, 1997; Villaescusa et al., 1997; Liu et al., 2000; Keller and Kramer, 2000), geophysical characterisation methods (e.g. Spathis et al., 1985; Fletcher et al., 1989; Grandjean and Gourry, 1996; Zou and Wu, 2001; Cardarelli et

al., 2003; Serzu et al., 2004; Malmgren et al., 2007), measurements of physical deformation (e.g. Li, 1993; Liu and Proulx, 1995; Villaescusa et al., 1997; Scott, 1998) rock testing of recovered core (e.g. Holmberg and Persson, 1978; Brinkmann, 1990; Ouchterlony et al., 1993; Kilebrant et al., 2009, Ouchterlony et al., 2009) and measurements of the hydraulic properties of the rock mass (e.g. Pusch, 1989; Pusch and Stanfors, 1992; Souley et al., 2001). Details of these methods of rock mass damage indication or measurement are discussed in Appendix 8.

6.3 Wave Energy as a Defining Wave Quantity Instead of PPV

Semi-analytical models dedicated to the prediction of rock mass damage from blasting are typically related to critical PPV values or plane strains generated as a function of PPV. For surface waves monitored over large distances, assumptions of PPV or plane strain as a damage criterion may be valid due to filtering of frequency spectra, decoupling of wave types and the dominance of surface Rayleigh waves. Within the confined rock mass near blasting events, wide frequency spectra and the coupling of P- and S-waves generally lead to irregular distributions of energy within recorded waves. For complex wave conditions, an instantaneous value at one point in time such as peak amplitude does not appear to accurately characterise near-field waveforms. For this reason, wave energies and strain histories over the duration of wave activity become useful to more accurately represent near-field blast waves.

6.3.1 Comparison of Peak Amplitude and Waveform Energy

Several wave characteristics were observed during the author's analysis of near-field waveforms that contributed to significant data scatter when employing traditional peak amplitude regression approaches. These characteristics were related to variations in wave frequency spectra and arrivals of shear wave components. One observed effect of these two characteristics was inconsistent peak amplitude intervals (the time between the wave arrival time and the vector sum peak amplitude). An additional characteristic of the observed near-field waveforms was the presence of multiple, high-amplitude sub-peak oscillations prior to or immediately following the peak. Instantaneous peak amplitude would likely grossly underestimate the damage-potential of the wave under these circumstances.

The use of instantaneous peak amplitude as a damage criterion would suggest that two waves of equal peak amplitude, but significantly different energy content, frequency spectra and duration would be considered equal. Figure 6.2 compares two peak vector sum vibration waveforms of equal PPV but largely different wave energy content, duration, peak interval and wave shape.

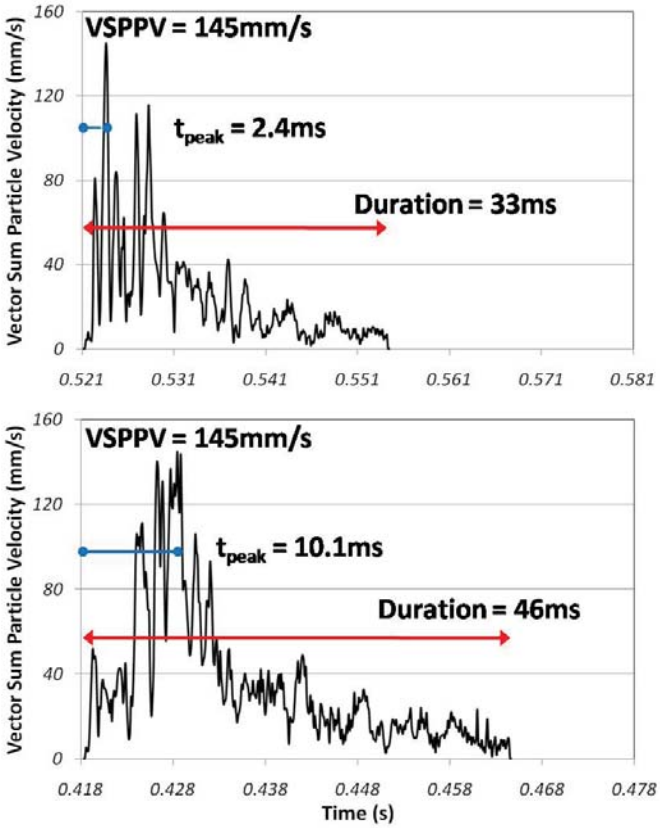

Figure 6.2. Comparison of two near-field vector sum particle velocity waveforms with equal VSPPV values but largely different durations, peak interval times (t_{peak}) and energy contents.

In traditional blast vibration scaling approaches and blast damage prediction models using instantaneous peak amplitude, both waveforms pictured in Figure 6.2 would be weighted equally. This is despite the significant differences in frequency contents, durations and energy contents. These types of variations in waveforms were observed in a majority of the single-hole vibration traces collected during the author's blast vibration monitoring program. Alternate vibration quantities rather than peak instantaneous amplitude were therefore considered to more effectively

characterise wave behaviours. The value deemed appropriate to represent the large range in waveform shapes and characteristics was the energy density contained within the entire active portion of the wave passing a point in the rock mass.

6.3.2 Calculation of Wave Energy for use in Vibration Analysis

Wave kinetic energy has been used by many researchers in the past to characterise seismic waves in geophysics (e.g. Howell and Budenstein, 1955; Nicholls, 1962), investigate the partitioning of energy within a blast (e.g. Lownds, 1991; Persson, 1996; Hamdi et al., 2001; Sanchidrián et al., 2007) or to predict rock mass or structural damage (e.g. Langefors and Kihlström, 1978; Kleine et al., 1990; Li, 1993; Scott, 1998). In the previously mentioned models, the maximum instantaneous kinetic energy flux and energy density or single-period kinetic energy flux and energy density have been the key wave characteristics. Calculation of the peak instantaneous kinetic energy flux (E_{fi}), single-period kinetic energy flux (E_f), instantaneous kinetic energy density (E_i) and single-period kinetic energy density (E_d) utilised Equations 6.7, 6.8, 6.9 and 6.10, respectively (after Li, 1993).

$$E_{fi} = \frac{1}{2}\rho_r \cdot C_p \cdot V(t)^2 \Delta t \qquad (6.7)$$

$$E_f = \frac{1}{2}\rho_r \cdot C_p \cdot \int_{t_0}^{t_0+T} V(t)^2 \, dt \qquad (6.8)$$

$$E_i = \frac{1}{2}\rho_r \cdot V(t)^2 \qquad (6.9)$$

$$E_d = \frac{1}{2}\rho_r \cdot \int_{t_0}^{t_0+T} V(t)^2 \, dt \qquad (6.10)$$

Where ρ_r = density of rock (kg/m^3)

C_p = P-wave velocity (m/s)

t_0 = arrival time of wave (s)

T = single period of wave (s)

$V(t)$ = wave particle velocity at time t (m/s)

Research in dynamic rock fracture due to stress wave loading has identified that dynamic damage potential is highly influenced by both the intensity of loading and the duration over which it is applied, as discussed by Birkimer (1970). Equations 6.7 or 6.9 for calculation of the instantaneous kinetic energy flux or kinetic energy density therefore fail to consider the duration of stress wave loading or the energy history. Such an approach can introduce gross underestimation of potential damage from a complex wave as discussed previously concerning the use of PPV.

Single-period kinetic energy flux or density (Equations 6.8 and 6.10) introduces a loading duration effect over which the wave energy is applied and provides a partial solution for complex wave loading. As proposed by Li (1993), calculation of single-period kinetic energy flux or density requires an estimation of the peak-contained wavelength. This approach has some limitation as the use of a single sine wave approximated wavelength cannot accurately represent the wide frequency spectra within a complex wave.

Another argument against the use of single-period kinetic energy is that high-frequency, near-field waveforms can experience a number of large-amplitude oscillations near the peak amplitude-containing oscillation. Therefore, the single period energy does not necessarily capture the entire damage-inducing energy of the wave. Armstrong (2004) proposed considering the entire wave energy passing through a point within a rock mass to investigate damage occurring as a result of the entire time history of energy. The energy contained within a propagating wave is also used in earthquake analysis and mine seismic analysis. This approach has been adopted in the author's proposed blast vibration analysis technique through calculation of the total wave energy density ($ED_{W\text{-}tot}$) to help predict both wave behaviour and damage potential.

6.3.3 Total Wave Energy Density

The decision to use the total wave energy density ($ED_{W\text{-}tot}$) of single-hole waveforms to characterise near-field blast vibrations instead of PPV or instantaneous energy was based on several observations of monitored near-field waves. These observations included:

- Highly variable peak velocity times after wave arrival
- Wide frequency spectra
- Variable number of near-peak amplitude oscillations
- Variable energy distribution within the peak oscillation half-period
- Decreasing percentage of total energy content within peak oscillation versus peak amplitude

Of the listed considerations, the percentage of energy within the peak-containing half-period compared with the entire wave energy provided the most compelling argument for use of the $ED_{W\text{-}tot}$ as the defining vibration quantity. The variability in distributed energy could have been related to the presence of high-frequency components within the near-field waveforms, where considerable energy was distributed outside of the peak amplitude oscillation. Figure 6.3 illustrates this effect by comparing the instantaneous energy density (E_i), calculated at the VSPPV using Equation 6.9, with total wave energy density ($ED_{W\text{-}tot}$) within the entire waveform. Both values have been plotted against the measured VSPPV.

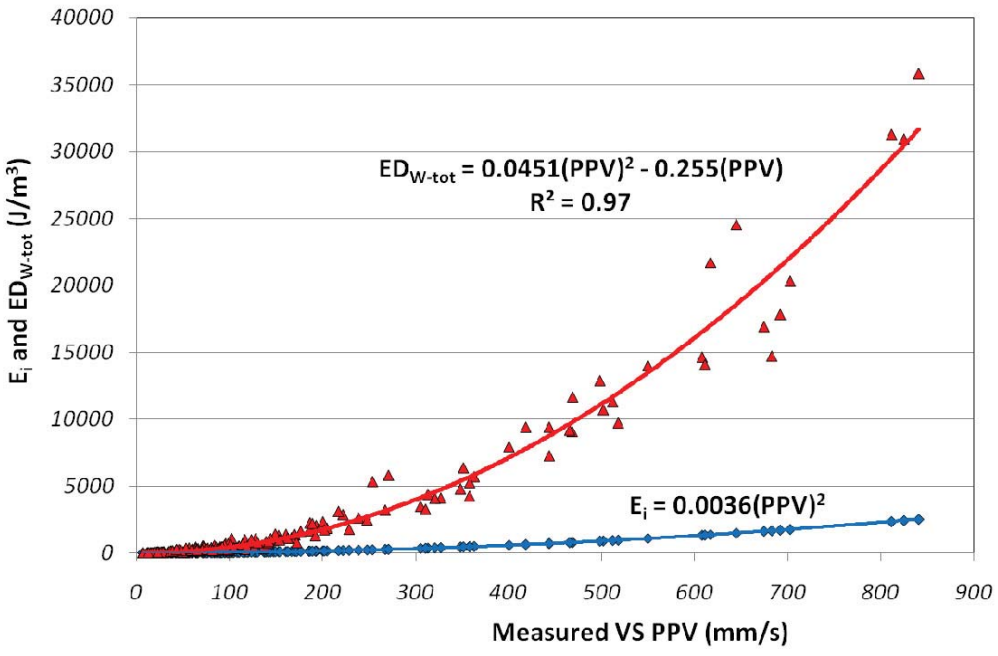

Figure 6.3. Comparison of E_i and $ED_{W\text{-}tot}$ versus measured VSPPV for the BHP Cannington stope 24jC6HL 200mLv Northeast wall data.

As observed in Figure 6.3, the divergence of $ED_{W\text{-}tot}$ from E_i with increasing VSPPV indicates a change in the percentage of energy carried within the peak oscillation as a function of the peak amplitude. Mandal et al. (2007) also observed an irregular distribution of energy within the peak oscillation when compared with the total wave energy related to the distance of monitoring.

Many of the blast monitoring studies used to develop traditional methods of vibration analysis have been concerned with compliance monitoring, where peak vibration levels rarely exceed 50mm/s. For low peak vibration amplitudes, the difference between total wave energy and peak instantaneous energy is negligible, but blast-induced body waves in the near-field and extreme near-field could produce peak amplitudes of up to 10m/s over larger frequency spectra. At a PPV of 10m/s, the extrapolated $ED_{W\text{-}tot}$ would be over 12.5 times higher than the E_i according to the relationships in Figure 6.3. Therefore, divergence between E_i and $ED_{W\text{-}tot}$ extrapolated to higher values becomes more evident and the ability to characterise the damage potential using the instantaneous energy is further reduced.

Calculation of the energy contained within a complex waveform requires several stages of waveform processing and a number of operations. As discussed in Chapters 4 and 5, all waveforms collected during the blast vibration monitoring program required frequency filtering, mathematical derivation of velocity or acceleration waveforms, amplitude filtering and lastly calculation of the vector sum waveforms. The waveforms were then imported into a custom Excel spreadsheet to perform peak amplitude lookups and calculations of the cumulative areas under the squared vector sum velocity waveforms. The peak search and area calculation criteria were based on the specified hole number, dedicated arrival time of the single-hole wave packet determined from the waveform and a maximum wave duration. The results of calculations of the cumulative areas under the time-domain squared vector sum velocity waveforms ($VSPV(t)^2$) are illustrated in Figure 6.4 for the two waveforms in Figure 6.2.

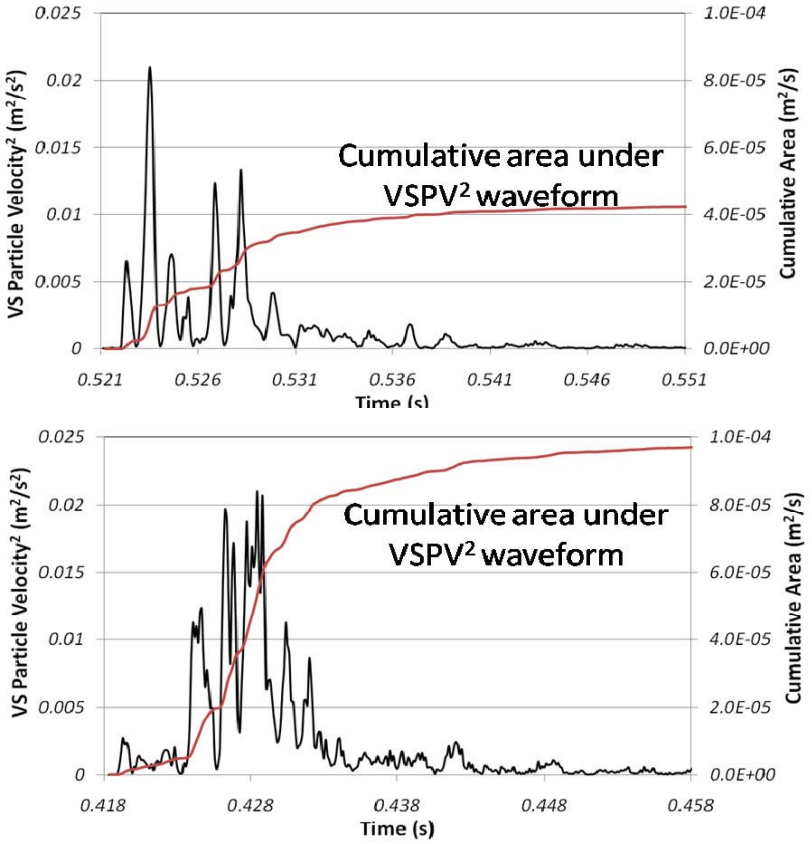

Figure 6.4. Comparison of $VSPV(t)^2$ waveforms (black lines) and cumulative area under each waveform (red line) as an indication of the wave energy.

When comparing the output of the two cumulative area calculations (indications of energy), it becomes clear that the single peak value of instantaneous energy or PPV would severely underestimate the damage potential of each wave packet. For the same VSPPV, the energy content in the lower waveform is almost 2.5 times greater when compared with the upper waveform.

The mathematical function that has been employed to calculate the area under the squared waveform was a point-to-point trapezoidal area estimation technique. Equations 6.11 and 6.12 show the integral and summation forms of the trapezoidal area approximation approach.

$$A_{W-tot} = \int_{t_{arrival}}^{t_{90\%E-loss}} VSPV(t)^2 \, dt \tag{6. 11}$$

$$A_{W-tot} = \sum_{t_{arrival}}^{t_{90\%E-loss}} \left[\frac{1}{2} \left(VSPV(t)^2_{t_{i+1}} + VSPV(t)^2_{t_i} \right) \cdot \left(t_{i+1} - t_i \right) \right] \tag{6. 12}$$

Where $VSPV(t)$ = vector sum particle velocity at time t (mm/s)

$t_{arrival}$ = time of wave arrival (s)

$t_{90\%E\text{-}loss}$ = time of 90% energy attenuation (s)

The results of the integration process yielded a value with units of mm^2/s. This unit does not directly represent an energy density value or match the output units of calculating the instantaneous kinetic energy density (E_i). $ED_{W\text{-}tot}$ was therefore determined from $A_{W\text{-}tot}$ using the calculation process for energy flux and subsequent energy density, applied over $1m^2$ unit areas and $1m^3$ unit volumes. Equation 6.13 is provided to calculate $ED_{W\text{-}tot}$ from $A_{W\text{-}tot}$ and the resulting units are $kgm^2/(s^2m^3)$ or J/m^3.

$$ED_{W-tot} = \frac{\rho_r \cdot V_p \cdot A_{W-tot} \cdot A_u}{V_u} \tag{6. 13}$$

Where ρ_r = rock density (kg/m^3)

V_p = P-wave velocity (m/s)

$A_{W\text{-}tot}$ = cumulative area under $VSPV^2$ waveform (m^2/s)

A_u = unit area ($1m^2$)

V_u = unit volume ($1m^3$)

A difference can be observed in the calculation of the energy content when comparing Equation 6.13 with Equations 6.7 to 6.10. Equations 6.7 to 6.10 have been applied such that only the kinetic energy is calculated. The calculation of $ED_{W\text{-}tot}$ in Equation 6.13 lacks the ½ factor for consideration of only the kinetic energy. The suggested approach allows for both the kinetic and stored potential energy (strain) components to be considered, such that the state of strain within the rock mass over the entire duration is assumed to be continuous.

6.3.4 Additional Blasting Assessments using $ED_{W\text{-}tot}$

Due to large variations in observed wave properties recorded for similarly-charged holes at similar distances, the true nature of energy transmission within a single blast-induced wave is not well understood. When the wave-fields from multiple holes interact, an additional level of complexity is added. Blast vibration prediction models based on peak instantaneous amplitude cannot effectively deal with the interaction of multiple waveforms in the near-field. This is due to unknown contributions of each interacting charge to the measured peak amplitude. Although there is no standard treatment for calculating combined average Scaled Distances for interacting holes, several methods can be used to change the weighting distribution of each charge. These methods include:

- Summation of multiple charge weights and averaging individual distances
- Averaging individual charge weights and distances
- Weighting of single charge weights based on relative distance
- Deconvolution of the multiple-hole waveform into seed waves relative to hole firing times, assumed arrival times and attenuations

Under conditions of multiple blasthole interaction, $ED_{W\text{-}tot}$ may provide a method for assessment of vibration behaviours without considering complex individual charge weighting equations. The calculation of $ED_{W\text{-}tot}$ can be applied over the entire waveform where multiple holes interact. The combined charge weight of the multiple charges could therefore be considered, along with the average distance from each of the charges to the monitoring point.

The multiple-hole energy approach may also provide a method of indirectly assessing the efficiency of a blast design, geometry or initiation timing. This approach would examine the percentage of total input explosive energy reporting as excess elastic seismic energy at vibration monitoring points (Fleetwood, 2010).

6.3.4.1 Specific Amplitude or Energy Attenuation

Energy carried by an elastic wave attenuates through several different mechanisms while propagating in a rock mass. These include dilation or slip of discontinuities and internal losses from inter-grain friction. The transducer configurations used in the author's blast vibration monitoring program have allowed wave energies to be calculated over various wave travel distances and orientations. Data recorded at different transducers locations have allowed specific attenuations to be determined along defined orientations.

Specific amplitude or energy attenuation assessments are performed by comparing the measured amplitude or calculated wave energy at one monitoring point with that at a second or third monitoring point on an array of transducers. Equation 6.14 is used to calculate the loss of energy density (ED_{loss}) between two monitoring locations.

$$ED_{loss} = ED_{W-tot1} - ED_{W-tot2} \tag{6. 14}$$

Where $ED_{W\text{-}tot1}$ = wave energy density at transducer #1 (kJ/m^3)
$ED_{W\text{-}tot2}$ = wave energy density at transducer #2 (kJ/m^3)

The differences in wave travel distances between the two transducers allow the specific amplitude or energy density attenuations per metre ($A_{loss/m}$ or $ED_{loss/m}$, respectively) to be determined. These values can be compared along multiple orientations to give an additional indication of the rock mass conditions along different wave travel pathways. Equation 6.15 is used to calculate the specific energy attenuation per metre ($ED_{loss/m}$).

$$ED_{loss/m} = \frac{ED_{W-tot1} - ED_{W-tot2}}{D_2 - D_1} \tag{6. 15}$$

Where D_1 = distance from a blasthole to transducer #1 in a given array (m)
D_2 = distance from blasthole to transducer #2 in a given array (m)

To investigate the input parameters that most closely affect the energy loss per metre in the elastic propagation zone, different charge and geometric factors were plotted against the specific energy attenuation. The factor that was discovered to be most closely related to the energy attenuation was the input energy density at the first transducer in each array. Figure 6.5 demonstrates the relationship between the energy density loss per metre of travel and the input energy density.

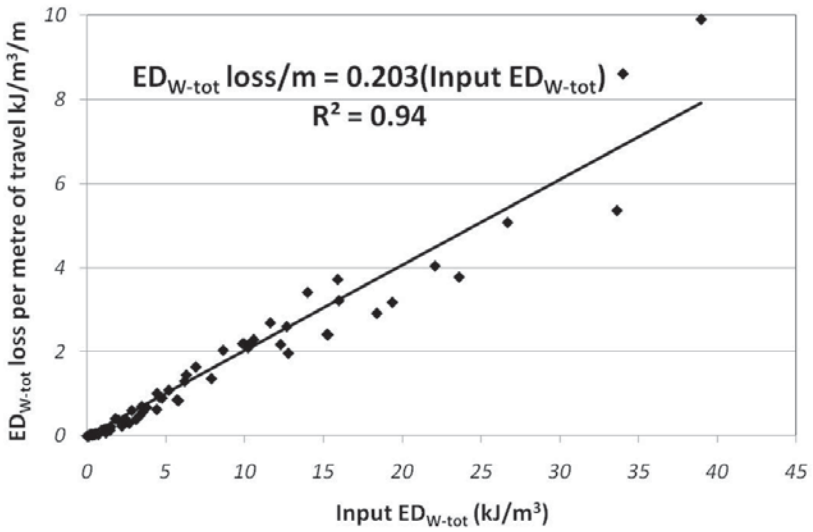

Figure 6.5. Relationship between energy attenuation per metre of travel ($ED_{loss/m}$) and input energy density ($ED_{W\text{-}tot1}$) for BHP Cannington stope 24jC6HL 200mLv Northeast wall data.

The linear relationship between the input energy and $ED_{loss/m}$ observed in Figure 6.5 indicates that higher wave energies resulting from increased charge weights or reduced distances experienced higher attenuation rates than lower-energy waveforms. This would suggest that a higher degree of induced damage or discontinuity activation would result from larger input energies, even after the wave had passed into the supposedly elastic wave propagation zone.

A secondary indication from Figure 6.5 is that the attenuation rate varies with the energy contained within a wave and therefore does not obey set linear elastic attenuation laws as specified in the elastic wave theories. This change in attenuation could be attributed to the interaction between the wave and existing discontinuities. To further investigate the observed behaviour of energy attenuation, specific

amplitude attenuation analyses using measured VSPPVs and VSPPAs have also been performed. The observed attenuation behaviours of peak amplitudes closely matched the attenuation behaviour of energy density, although better model correlations and more consistent results were generally obtained amongst differing data sets using specific energy attenuation.

The linear relationship between the $ED_{W\text{-}tot}$ at the first transducer and the $ED_{loss/m}$ in Figure 6.5 suggests that a further step of data normalisation can be applied to completely isolate the source effects. By dividing $ED_{loss/m}$ by the input energy, the rock mass attenuation rate (RMAR) could be determined independent of the blasthole parameters. This type of analysis can aid in determining a general anelastic wave attenuation relationship for a rock mass or to investigate varying attenuation rates along different orientations within the same rock mass. Figure 6.6 illustrates the results of normalising the data set in Figure 6.5 relative to the input energy (dividing $ED_{loss/m}$ by $ED_{W\text{-}tot1}$) to obtain a source-independent attenuation equation based solely on the distance of wave travel from the source to the transducer array.

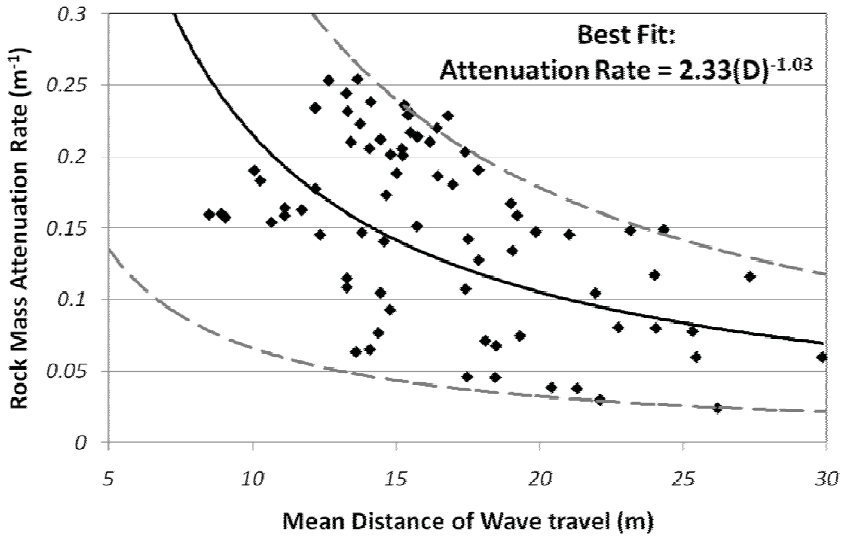

Figure 6.6. Rock mass energy attenuation rate (RMAR) resulting from dividing $ED_{loss/m}$ by $ED_{W\text{-}tot1}$ shown in Figure 6.5.

The best fit attenuation equation for the data set in Figure 6.6 can be defined by two regression constants, K_A and ψ, where K_A is the intercept value (2.33) and ψ is the

power term (attenuation slope, -1.03). For the data sets analysed in the attenuation study, the values of K_A ranged from approximately 0.3 to 3.5 and ψ ranged from -0.7 to -1.2. The differences between the attenuation equations or Rock Mass Attenuation Rates (RMARs) could be used to compare the specific attenuation of energy along multiple orientations in the same rock mass, as illustrated in Figure 6.7.

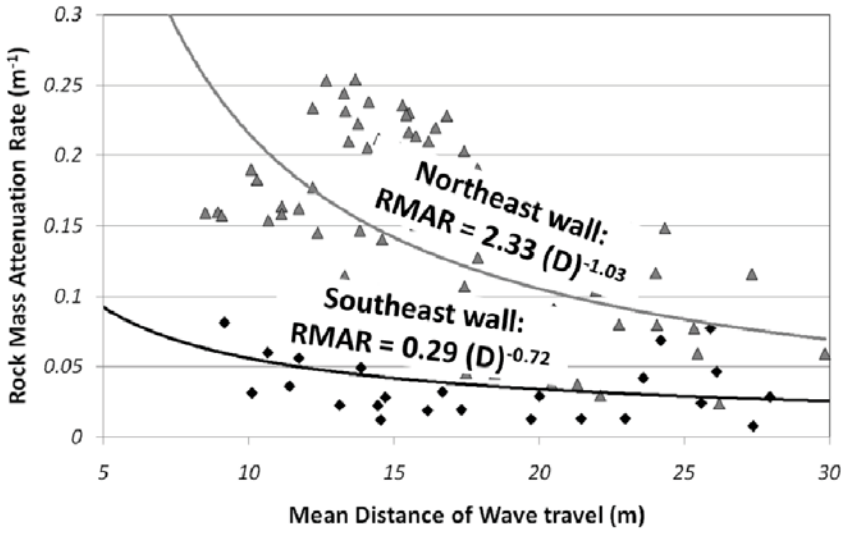

Figure 6.7. Comparison of RMARs for two wave propagation orientations from data measured in two walls of Cannington stope 24jC6HL.

A general behaviour of lower attenuation rate can be observed for the Southeast wall of the stope when compared with the Northeast wall due to the reduced slope. The indicated attenuation rate provides an additional tool that can be used in conjunction with other geotechnical assessment methods such as discontinuity mapping, fracture frequency analysis or wave velocity (discussed in Chapters 7 and 8) to gain a better understanding of rock mass characteristics. The energy attenuation rate can also aid in identifying transducers that have been subject to poor coupling, erroneous output voltages or geological influence. An example of this effect has been observed in several data sets where the transducers were located near large geologic features such as faults or shear zones. Upon plotting of the affected data sets, the slopes of the attenuation curves were positive instead of negative. Using data that has been affected by shielding or poor coupling can adversely influence vibration prediction results.

6.3.4.2 Interpretation of the Rock Mass Attenuation Rate Curves

It is proposed by the author that the value of ψ in the RMAR analysis can be related to the attenuation of the wave in intact rock blocks within a rock mass, otherwise considered the elastic attenuation rate. The observed variations in the values of ψ were small when compared with the variations between K_A values. Over a number of data sets, the average value of ψ was found to be approximately -1 (linear). Approximately linear attenuation of normalised energy over distance has been observed by past researchers, allowing the simplified assumption of near-linear behaviour (Howell and Budenstein, 1955).

Using the linear slope assumption, the energy attenuation over distance became highly dependent on the value of K_A. No attempt has been made in the current work to characterise the rock mass properties defining the value of K_A, but it has been proposed that it is linked to the fracture frequency, the condition of in-situ discontinuities and interaction between the wavefront and the fracture planes.

6.3.5 Limitations of Energy as a Rock Mass Damage Criterion

Some questions arise when considering the total energy of a waveform as a stope-scale rock mass damage criterion. As explained by Langefors and Kihlström (1978) and observed in earthquakes, the energy content of a wave of low frequency can be higher than the energy contained within a wave of equal amplitude and higher frequency. The lower frequency wave can produce significantly higher displacements and consequent strains than a higher frequency wave, but low frequency vibrations were generally not encountered in the near-field of blasting events as indicated by the monitoring program. Therefore, the concept of direct comparisons of total wave energy as a defining wave property to investigate localised blast damage can be justified for the case of high-frequency, confined near-field body waves.

Rock mass failure energy (discussed in Section 6.5) is not a quantity that has been adequately researched and identified as appropriate for application to complex fracture systems. Fracture mechanics investigations of stored strain rupture energy or fracture energy typically utilise small, unconfined samples with an existing crack of

known length and shape. In some cases, the stored rupture strain energy or fracture energy value can be related to the fracture toughness or material strength, which depend on the loading rate, size of the initial crack, sample size and the thickness of the intact material ligament (e.g. Krech, 1974; Oh and Chung, 1989; Wu and Zhang, 1989; Ohlsson et al., 1990). For nearly-isotropic materials such as concrete and some rock types, linear relationships have been observed between the material strength and the fracture energy (e.g. Wu and Zhang, 1989 and Vásárhelyi et al., 2000). Additional research is required to determine fracture energies under different geometries and levels of confinement for application to in situ rock mass damage from dynamic loading.

6.4 Ground Strains from Blasting

A common treatment for blast-induced ground strain is the assumption of plane wave behaviour (as outlined by Langefors and Kihlström, 1978, Holmberg and Persson, 1978, and others). This approach was adopted in development of the critical tensile plane strain blast damage prediction model discussed in Section 6.2.2. The plane wave approach assumes that the wave field produced by an explosive charge is similar to the waves propagating through a slender rod created by controlled dynamic uni-axial impact loading. For elastic plane wave propagation through homogeneous, infinite media, the longitudinal strain (ε_r) can be calculated using the particle velocity (V_r) and the longitudinal wave velocity (c) as given in Equation 6.16 (Ambraseys and Hendron, 1968).

$$\varepsilon_r = \frac{V_r}{c} \tag{6. 16}$$

Extensions of the plane strain assumption have been applied in the past to estimate volumetric or peak axial strains, as observed in the critical tensile plane strain blast damage prediction approach. These extensions are discussed briefly in the following sections along with a method proposed by the author for calculating the wave-induced mean normal dynamic strain from the stored strain energy density.

6.4.1 Peak Axial Strain from Complex Waveforms using Plane Strains

Past applications of the critical tensile plane strain approach have adopted a simplified extension of Equation 6.16 to calculate the maximum axial strain using the vector sum PPV (VSPPV) from bi-axial or tri-axial monitoring and the P-wave velocity. The assumed wave condition is that of three orthogonal plane waves propagating together as a wave front. The assumed peak loading condition using this approach is one of axial tensile strain (ε_{max}) in the peak vector direction. Figure 6.8 illustrates the conceptual process of calculating the maximum axial strain from tri-axial monitoring results and the rotation of the unit volume towards the peak axial (maximum principle) strain.

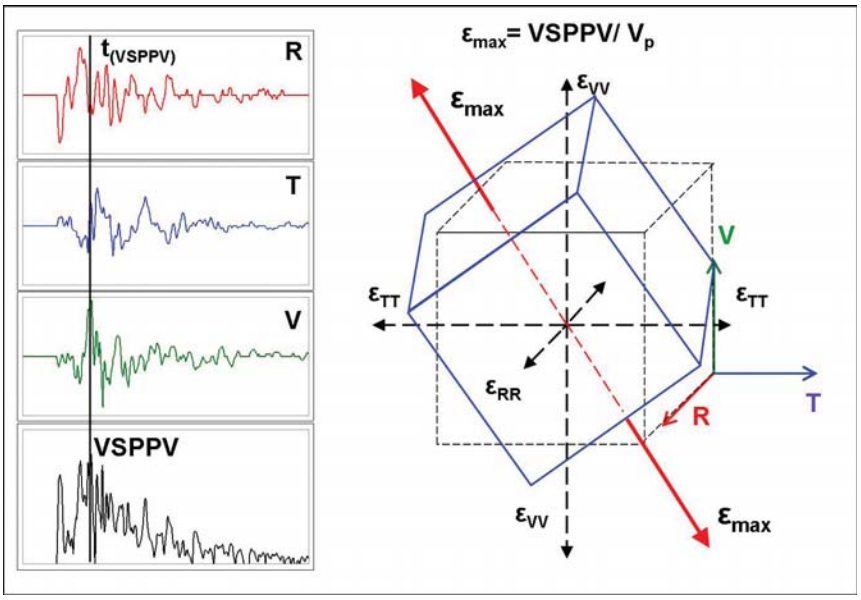

Figure 6.8. Rotated unit volume in relation to peak axial strain resulting from the vector direction of VSPPV.

6.4.2 Limitations of the Assumption of Peak Axial Normal Strain from Concurrent Orthogonal Plane Strains

The assumption that peak axial tensile strain occurs in the resultant PPV vector direction is exceedingly simplistic. This loading assumption does not consider the sense of the three normal dilatational strain components (compressive versus tensile) based on the polarity of the blast wave oscillation. Vector sum calculations effectively remove the polarity of the vibration trace, leading to misrepresentation of

the true normal strain conditions. This factor is likely to be more noticeable for the state of strain induced by body waves within a confined rock mass.

Another factor that must be considered in the calculation of normal strains from measured orthogonal waveforms is the effect of transducer orientation on the individual strain components. Variations in transducer orientations with respect to the charge locations would be expected to result in differences in the vibrations measured on the three orthogonal components. These variations would inevitably result in differences between the calculated axial strain magnitudes and possibly senses (tensile versus compressive).

For unconfined conditions, such as at the surface of an excavation or at the ground surface, the state of poly-axial strain may be considered to be less important with regards to rock surface behaviour. This is due to the zero-stress boundary loading conditions and surface wave activity, where lateral strain components will not significantly affect the behaviour of the material. Within a confined rock mass or at locations near excavations, the state of mining-induced static strains and the sense of the dynamic strain components may significantly affect the material behaviour. At adequate distances from an excavation boundary, typical mining-induced static volumetric strains will be mostly compressive in nature and the magnitude and principal directions can vary. Near excavations or late in a mining sequence, static tensile strains or losses of confinement can be introduced due to stress redistribution, requiring lower induced dynamic tensile strains to cause damage.

6.4.3 States of Normal Strain Assumed from Recorded Tri-Axial Waveforms

Traditional strain-based blast damage prediction approaches typically assume applied tensile strains and tensile material strength criteria, regardless of the actual polarity of the blasting vibrations at the time of the peak amplitude. This simplistic treatment of strain loading conditions can lead to gross overestimation of damage, as the polarity of the wave components (and associated strain) at the peak vector sum motion can be either compressive or tensile. Observation of waveforms recorded during the author's blast vibration monitoring program for a series of blastholes of

identical charging and similar geometries highlights this variability in polarity and consequent normal strain conditions.

Polarity analysis has been made possible in the blast vibration monitoring program presented in this thesis due to close orientation control of the installed transducers. Particular consideration of the polarity of the components with regards to the directions of expected motions was also given during transducer manufacturing and installation. The control of component direction and installation led to the following relationship between particle motion and state of strain:

- Tensile axial strain for negative component velocities
- Compressive axial strain for positive component velocities

At a single point in a rock mass at a given time, several different states of strain can exist based on the polarity of the blast wave components. The radial normal strain component ε_{xx} can be either compressive or tensile based on the wave polarity at that instant in time. The tangential stress and strain components from a purely elastic spherical or cylindrical wave-front is assumed to induce dilatory loading, allowing ε_{yy} and ε_{zz} to only be tensile when ε_{xx} is compressive. The complex wave-fields generated in the near-field of blasts do not necessarily behave as ideal spherical or cylindrical waves due to rotation of wave fronts from diffraction, refraction and reflection, conversion of wave types and dominant shear wave behaviour.

The individual component particle velocity polarities observed in waveforms recorded by the author suggests wave loading conditions similar to that predicted by Favreau (1969), where individual orthogonal strain components exhibit some "pairing" of polarity. Component pairing assumes that when one strain component is compressive, the other two components will be tensile and vice-versa. The potential damage-inducing load on the material would therefore be a state of axial compression or tension with bi-axial lateral tension or compression, respectively. Component polarities of velocity waveforms recorded in the thesis blast vibration monitoring program were analysed for a series of blastholes under conditions of favourable transducer alignment (i.e. transducer components oriented along the assumed principal wave loading directions: radial, transverse and vertical). Figure

6.9 shows the relationship between the measured peak particle velocity component polarities and the associated strain conditions assuming orthogonal plane strains in the footwall of KBGM stope dB10-38T rise firing #4 of 11 holes.

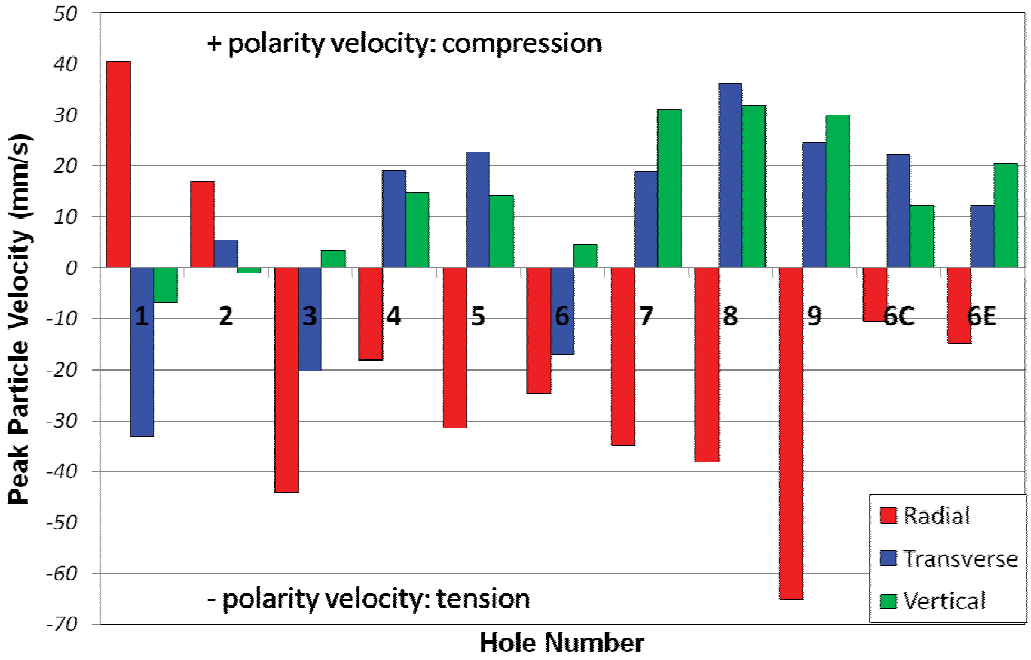

Figure 6.9. Comparison of peak component velocity polarities recorded for a series of equally-charged blastholes in KBGM Stope dB10-38T, rise firing #4 footwall transducer.

All single-hole recorded blast waves shown in Figure 6.9 exhibited the prescribed behaviour of axial tension or compression coupled with bi-axial compression or tension. It is interesting to note that the VSPPV for 9 of the 11 blastholes occurred at a point of tensile radial strain. Additional analysis of the waveforms revealed that the VSPPVs were generally observed several milliseconds after the arrival of the wave and thus may have been more directly related to arrival of the radial tensile tail or shear waves in the tangential directions.

Analysis of a large number of velocity waveforms under conditions of principally-oriented and non-principally oriented transducers revealed a general behaviour of axial/bi-axial wave loading conditions. Combining this information with the theory of strain continuity, a general theory of blasting strain has been proposed by the

author where the state of wave-induced strain at any point in time could be either axial tension with bi-axial compression or axial compression with bi-axial tension. These two states of volumetric strain in the confined rock mass would inevitably result in damage behaviours different from those associated with simple axial peak tensile strain assumed in the critical tensile plane strain models. The impacts of wave-induced dynamic strain loading conditions become even more evident with the introduction of mining-induced static stresses in the rock mass. Although the explicit strain field resulting from interaction of blast-induced dynamic strains and mining-induced static strains is nearly impossible to define, the influence of existing tensile or compressive static strains cannot be overlooked when considering material response to blast-induced strain loading.

6.4.4 Considerations Regarding Shear Strain

Tensor notation of the state of strain in a material under both normal and shear loading is (Windsor, 1987):

$$e_{ij} = \begin{vmatrix} \varepsilon_x & \frac{1}{2}\gamma_{xy} & \frac{1}{2}\gamma_{xz} \\ \frac{1}{2}\gamma_{yx} & \varepsilon_y & \frac{1}{2}\gamma_{yz} \\ \frac{1}{2}\gamma_{zx} & \frac{1}{2}\gamma_{zy} & \varepsilon_z \end{vmatrix} \qquad (6.\ 17)$$

Where ε_x, ε_y, ε_z = normal strain components

γ_{xy}, γ_{xz}, γ_{yx}, γ_{yz}, γ_{zx}, γ_{zy} = shear strain components

In treatment of engineering materials, the tensor is assumed to be symmetric, requiring at least six values to accurately describe the state of strain considering both volumetric and shear strain. These components are the three normal strains and three maximum shear strains.

In traditional plane strain-driven blast damage investigation, only the normal strain components (ε_x, ε_y, ε_z) are considered. Therefore, the true loading conditions in a rock mass are not known due to neglect of the shear strain components. For the assumption of pure volumetric strain, the tensor notation for blasting strain would be:

$$e_{ij} = \begin{vmatrix} \varepsilon_x & 0 & 0 \\ 0 & \varepsilon_y & 0 \\ 0 & 0 & \varepsilon_z \end{vmatrix} \quad (6.\ 18)$$

The above tensor would realistically only occur for two loading conditions. The first condition is where the blasting strains are purely orthogonal and composed only of dilatational strains where the axes of the monitoring instrumentation are oriented in the principal strain directions. The second situation would be where the vibrations are measured on stress-free boundaries along all three orthogonal directions (a free-floating cube of rock) and the blasting strains would be applied only normal to the surfaces. These conditions would be unlikely in the confined rock mass near a blasting event.

To relate the induced strain to particle velocities produced in blasting, the infinitesimal strain matrix in Equation 6.17 can be applied on the basis of differential displacements. The strain matrix takes the form of Equation 6.19 (Windsor, 1987).

$$e_{ij} = \begin{vmatrix} \partial u/\partial x & 1/2\left(\partial v/\partial x + \partial u/\partial y\right) & 1/2\left(\partial w/\partial x + \partial u/\partial z\right) \\ 1/2\left(\partial u/\partial y + \partial v/\partial x\right) & \partial v/\partial y & 1/2\left(\partial w/\partial y + \partial v/\partial z\right) \\ 1/2\left(\partial u/\partial z + \partial w/\partial x\right) & 1/2\left(\partial v/\partial z + \partial w/\partial y\right) & \partial w/\partial z \end{vmatrix} \quad (6.\ 19)$$

Where $\partial u/\partial x, \partial v/\partial y, \partial w/\partial z$ = longitudinal strains in x, y and z

$\partial u/\partial y + \partial v/\partial x, \partial v/\partial z + \partial w/\partial y, \partial w/\partial x + \partial u/\partial z$ = shear strains in x, y and z

If the unit element is subjected to strain loading from a transient source such as a blast wave, displacements over time can be incorporated. From the properties of elastic plane waves, Yang and Scovira (2007) proposed the following conditions:

$$\frac{\partial u_i}{\partial x_j} = \frac{\partial u_i}{\partial t}\frac{\partial t}{\partial x_j} = \begin{cases} v_i(t)\dfrac{1}{C_p}, i = j, u_i \,\&\, x_j - parallel \\ v_i(t)\dfrac{1}{C_s}, i \neq j, u_i \,\&\, x_j - orthogonal \end{cases} \quad (6.\ 20)$$

Combining Equations 6.19 and 6.20, the dynamic infinitesimal strain tensor proposed by Yang and Scovira (2007) could be estimated using Equation 6.21.

$$\varepsilon_{ij}(t) = \begin{vmatrix} \frac{v_R(t)}{C_p} & \frac{v_R(t)+v_T(t)}{C_s} & \frac{v_R(t)+v_V(t)}{C_s} \\ \frac{v_T(t)+v_R(t)}{C_s} & \frac{v_T(t)}{C_p} & \frac{v_T(t)+v_V(t)}{C_s} \\ \frac{v_V(t)+v_R(t)}{C_s} & \frac{v_V(t)+v_T(t)}{C_s} & \frac{v_V(t)}{C_p} \end{vmatrix} \quad (6.21)$$

Where v_R, v_T, v_V = radial, transverse and vertical velocity at the VSPPV (m/s)

C_p, C_s = P-wave and S-wave velocities respectively (m/s)

The matrix in Equation 6.21 would apply for the case of three orthogonally-coupled plane waves. Although this treatment provides some relationship between measured velocity components and the strain tensor, expression of the shear strains as related to the measured volumetric strain components is over simplistic. This simplification may be acceptable for far-field surface wave monitoring, but the waveforms encountered in the near-field confined rock mass are considerably more complex.

The interpretation of individual normal and shear wave components for complex waveforms recorded in the near-field of blasting events have not been adequately described in published works. Through review of mathematical wave models, there appears to be a general lack of understanding of normal and shear strains generated by elongated explosive charges in jointed rock masses. Therefore, individual normal and shear strains have not been explicitly identified in the blast vibration analyses presented in this thesis in favour of the state of volumetric strain. Neglecting the contribution of shear strains could lead to either under or over-estimation of the extent of wave-induced damage, but tensile fracture strain criteria would be expected to reduce the likelihood of under-prediction.

Due to the perceived influence of transducer orientation effects on the represented axial strains and highly variable strain loading conditions and directions, the wave-induced mean normal dynamic strain invariant ($\varepsilon_{W\text{-}MN}$) has been proposed by the author to describe the state of volumetric strain in the near-field. The proposed

calculation of $\varepsilon_{W\text{-}MN}$ from recorded waveforms is based on the concepts of conservation of energy and strain continuity during elastic wave propagation in a non-dispersive medium.

6.4.5 Determination of Wave-Induced Mean Normal Dynamic Strain from Calculated Total Wave Energy Density

In elastic wave propagation, stored strain energy density ($\mathcal{U}$) can be related to kinetic energy density ($\mathcal{K}$) through application of the laws of conservation of energy (Achenbach, 1973). The general relationship between $\mathcal{K}$, $\mathcal{U}$ and the total energy density ($\mathcal{H}$) according to the fundamental of dynamic elasticity is presented in Equation 6.22 (Achenbach, 1973).

$$\mathcal{H} = \mathcal{K} + \mathcal{U} \tag{6. 22}$$

The one-dimensional wave-induced stored strain energy ($\mathcal{U}_{\mathrm{L}}$) in an isotropic, elastic material can be calculated by Equation 6.23 (Achenbach, 1973).

$$\mathcal{U}_{\mathrm{L}} = \frac{1}{2}\lambda_L(\varepsilon_{kk})^2 + \mu\varepsilon_{ij}\varepsilon_{ij} \tag{6. 23}$$

Where λ_L, μ = Lame's constants (Pa)

ε_{kk} = normal strain in the 'k' direction for a 'k' propagating wave

ε_{ij} = shear strain in the 'ij' plane for a 'k' propagating wave

The first term in Equation 6.23 is the normal strain energy density as a function of the axial strain (ε_{kk}) and the second term is shear strain energy density related to the shear strain ε_{ij}. Extension of Equation 6.23 into three dimensions to represent volumetric and distortional strain energy densities is proposed in Equation 6.24.

$$\mathcal{U}_{\mathrm{V}} = \frac{1}{2}\lambda_L(\varepsilon_{ii} + \varepsilon_{jj} + \varepsilon_{kk})^2 + \mu(\varepsilon_{ij} + \varepsilon_{jk} + \varepsilon_{ik})^2 \tag{6. 24}$$

Where ε_{ii}, ε_{jj}, ε_{kk} = orthogonal normal strain components

ε_{ij}, ε_{jk}, ε_{ik} = orthogonal shear strain components

In confined blasting conditions producing complex waves, the true principal stress directions from vibration-induced loading can be highly variable and as such the wave components cannot be successfully decoupled through analysis. The measured waveforms are realistically assumed to be a combination of dilatational and shear vibration components and the seismograms indirectly represent both volumetric and shear strains along the non-principal directions. As discussed previously, separation of normal and shear strain components has not been attempted in this thesis due to the complexity of the measured waveforms. For this reason, only the normal strain components have been considered, reducing Equation 6.24 into 6.25.

$$\mathcal{U}_V = \frac{1}{2}\lambda_L\left(\varepsilon_{ii} + \varepsilon_{jj} + \varepsilon_{kk}\right)^2 \qquad (6.25)$$

To apply Equation 6.25 to calculate volumetric strains from complex blast waves, it is proposed that the strain value most suitable to characterise near-field waves is the wave-induced mean normal strain invariant ($\varepsilon_{W\text{-}MN}$). Mean normal strain has been based on past observations of two near-field wave behaviours identified in the author's blast vibration data. These two observations were: random wave component distributions over time and distance, and loss of individual particle motion polarities and magnitudes during calculation of $ED_{W\text{-}tot}$.

The seemingly random distribution of orthogonal component amplitudes over time, distance and direction of wave propagation removes any predictability of the state of strain or the relationship between the individual strain components over the duration of wave activity. All states of strain, irrespective of distribution between the orthogonal components, are consistent using the mean normal strain invariant. Energy transfer between the three orthogonal wave components or variability in monitoring orientations therefore would not influence the mean normal strain calculated from the waveforms. The definition of elastic mean normal strain (ε_{MN}) for static conditions is given in Equation 6.26.

$$\varepsilon_{MN} = \frac{\varepsilon_{ii} + \varepsilon_{jj} + \varepsilon_{kk}}{3} \qquad (6.26)$$

Translating the static mean normal strain into dynamic conditions ($\varepsilon_{MN} = \varepsilon_{W\text{-}MN}$) and combining Equation 6.25 and Equation 6.26 yields Equation 6.27.

$$\mathcal{U}_V = \frac{1}{2}\lambda_L (3\varepsilon_{W-MN})^2 \qquad (6.27)$$

For the mean normal strain to be represented by Equation 6.27, the form of the three orthogonal strains would have to be of the same sign, such that all strains are either compressive or tensile. In the current work, there has been no attempt to segregate the effects of different strain states along each axis (compressive versus tensile), which would serve to reduce the mean normal stored strain. Future research will attempt to investigate these effects.

The $ED_{W\text{-}tot}$ calculated from recorded waveforms has been assumed to represent the combined values of $\mathcal{K}$ and $\mathcal{U}$. This allows the wave-induced mean normal dynamic strain ($\varepsilon_{W\text{-}MN}$) to be calculated by solving Equation 6.27 for $\varepsilon_{W\text{-}MN}$ and substituting ½ $ED_{W\text{-}tot}$ for $\mathcal{U}_V$ (Equation 6.28).

$$\varepsilon_{W-MN} = \sqrt{\frac{ED_{W-tot}}{9\lambda_L}} \qquad (6.28)$$

Where $ED_{W\text{-}tot}$ = calculated total wave energy density (J/m^3)

λ_L = Lame's constant (Pa)

And

$$\lambda_L = \frac{E \cdot \nu}{(1+\nu)(1-2\nu)} \qquad (6.29)$$

Where E = Young's Modulus (GPa)

ν = Poisson's Ratio

Equation 6.28 has been used for calculation of $\varepsilon_{W\text{-}MN}$ from the waveforms collected in the author's blast vibration monitoring program. The values of $\varepsilon_{W\text{-}MN}$ would be expected to display attenuation behaviours similar to wave energy and to some extent

wave amplitude. Using the strain continuity assumption, the calculated $\varepsilon_{W\text{-}MN}$ could be either compressive or tensile and has been applied in proposed intact rock damage prediction approach.

6.5 Development of Proposed Strain and Energy-Based Blast-Induced Rock Mass Damage Criteria

A rock mass is composed of both intact rock and discontinuities, each of which influence the load-bearing capabilities under static and dynamic conditions. Blast damage prediction models should therefore consider criteria for both the fresh fracturing of intact rock and extension, dilation, or dislocation of existing discontinuities. The blast damage prediction approach proposed in this thesis considers intact rock and discontinuities explicitly and specifies separate damage criteria for each rock mass component. Two individual criteria are suggested for use in prediction of damage to intact rock; fracture strain and strain energy density. The criterion proposed for use in predicting blast damage to existing discontinuities is fracture energy in relation to the density of existing fractures within a unit volume of the rock mass.

6.5.1 Compressive and Tensile Fracture Strain Criteria for Damage to Intact Rock under the Influence of Mining-Induced Static Strains

Hooke's Law of stress-strain transformation, along with the results of tensile and compressive strength and elastic constants laboratory testing, can be used to estimate the elastic compressive and tensile rock rupture strains (Equations 6.30 and 6.31).

$$\varepsilon_C = \frac{\sigma_C}{E} \tag{6. 30}$$

$$\varepsilon_T = \frac{\sigma_T}{E} \tag{6. 31}$$

Where ε_C, ε_T = compressive and tensile failure strains (m/m)

σ_C, σ_T = compressive and tensile failure stresses (Pa)

E = elastic Young's Modulus (Pa)

The results of UCS (σ_C) testing have identified compressive rupture strains on the order of 500-4000 microstrain based on the compressive failure strength and Young's Modulus. The value of tensile failure strain for rocks under uni-axial tensile loading in the general case is approximately 100-200 microstrain (Windsor, 2009), although the number of published tensile strain measurements is extremely limited. Stacey (1981) published values of extensional tensile failure strains for various rock types from 83με to 175με. Okubo and Fukui (1996) measured tensile failure strains between 250με and 750με in direct tensile tests of various rock types, and identified some degree of residual tensile strength. The large range in published compressive and tensile failure strains for different rock types complicates the selection of critical failure strain values.

The value of failure strain is not expected to change significantly under dynamic loading conditions in the elastic wave propagation zone, although the failure strength (stress) changes dramatically with strain rate (up to 1 order of magnitude increase for dynamic loading). The change in the slope of the elastic stress-strain relationship (E) is affected by strain-rate effects along with the failure stress. As the failure stress and Young's Modulus increase with strain rate, it is proposed that the failure strain remains virtually unchanged for the lower strain rates experienced in the elastic wave propagation zone.

Grote et al. (2001) confirmed a degree of independence of failure strain from strain rate by publishing the complete stress-strain curves from dynamic compression testing of mortar over an order of magnitude in strain rates (2.9×10^2 to 1.5×10^3/s). Comparing the stress-strain curves at different loading rates, there was no significant change in peak failure strain values. Shan et al. (2000) published stress-strain curves for dynamic testing of granite and marble rocks using the SHPB apparatus. For the marble rock type, the changes in ultimate strains for various striker bar velocities were minimal. The relative insensitivity of the failure strain to the strain rate has allowed the static rupture strain to be integrated into the intact rock damage prediction model without consideration of dynamic strain increase factors.

The presence of mining-induced and virgin static stresses within the underground rock mass would be expected to influence the degree and extent of blast-induced

damage. To determine the state of aggregate strain in a rock mass at depth as a function of both induced static strains and blast-induced dynamic strains, superposition of the two strain fields is proposed by the author. The aggregate strain conditions at each point in a rock mass could therefore be either tensile or compressive in nature, depending on the existing and applied strain magnitudes.

It has been proposed in this thesis that tensile-related intact rock damage would only occur if the dynamic blast-induced tensile loading were to exceed the sum of the existing static compressive strains and the intact rock tensile rupture strain. For compressive-related intact rock damage, the combined static and dynamic compressive strains would have to exceed the intact rock compressive failure strain. The proposed static and dynamic strain superposition damage criteria for either compressive or tensile blast loading conditions are listed below.

Tensile damage with compressive static strain: $\left|\varepsilon_{W-MN(tension)}\right| > \varepsilon_T + \varepsilon_{M(static)}$

Compressive damage with compressive static strain: $\left|\varepsilon_{W-MN(comp)} + \varepsilon_{M(static)}\right| > \varepsilon_C$

Where $\varepsilon_{W\text{-}MN(tension)}$ = calculated wave mean normal strain (tensile)

$\varepsilon_{W\text{-}MN(comp)}$ = calculated wave mean normal strain (compressive)

$\varepsilon_{M(static)}$ = induced static mean normal strain (generally compressive)

The influence of the mining-induced mean normal static strain magnitudes become apparent when considering the relationships in the suggested damage criteria. For a blast-induced mean normal dynamic compressive strain, compressive damage occurs to the intact rock as a result of the aggregate state of compression in excess of the rock compressive failure strength. This mechanism of damage has been largely ignored in blast damage analysis outside of the immediate crushing zone around the explosive charge. For tensile damage to occur, the wave-induced tensile strain must exceed the sum of the tensile failure strain plus the existing compressive strain to reach a net tension within the intact rock. Therefore, higher static compressive strains in the rock mass may inhibit tensile-related intact rock damage, but enhance the extent of compressive-related damage zones.

Mining-induced static strains in the vicinity of underground excavations can create zones of tension or concentrated compression depending on the directions and magnitudes of the principal stresses. In rock masses having low static compressive or tensile strain distributions, additional tensile loading from blast waves can induce damage at reduced dynamic tensile strain magnitudes. For static compressive strains near the rupture strain of the rock, minimal additional compressive loading would be required to induce compressive damage.

6.5.2 Failure Strain Energy Density or Dissipated Energy Density Criteria for Damage to Intact Rock

The approach for prediction of intact rock damage based on the aggregate mean normal strain assumes that the bulk behaviour of the intact portion of a rock mass will be similar to intact rock samples in the laboratory. Assuming this is valid, an additional intact rock fracture criterion has been proposed related to the critical stored strain energy density or the dissipated energy density (Vásárhelyi et al., 2000). Analysis of stress-strain curves recorded during quasi-static compression testing or dynamic impact tests has allowed researchers to investigate the energy stored or dissipated at failure by different rock types at different loading rates (e.g. Vásárhelyi et al., 2000 and Li et al., 2005). Table 6.4 lists several values of dissipated or stored strain energy density as published by various authors.

Table 6.4. Published values of stored or dissipated strain energy density resulting from static and dynamic compression testing.

Researcher	Rock Type	Test type	Dissipated Strain Energy Density (kJ/m^3)
AMC (1998)	Pb-Ag-Zn ore	UCS	Average 204
Vásárhelyi et al. (2000)	Andesite I Andesite II Granite	Creep and UCS	172 82 210
Li et al. (2005)	Granite	Dynamic: 20-30 strain/s	200-1420

The values in Table 6.4 cover a large range of rock types and a moderate range of strain rates. Due to the limitations of recording stress-strain curves for dynamic loading conditions, failure energies at strain rates above 10^2 strain/s are not well represented. Additionally, stress-strain curves for tensile testing do not appear in the literature. For these reasons, general behaviours with regards to failure energy as related to observed strength must be assumed to propose values of tensile rupture strain energy density under dynamic loading conditions.

The dynamic tensile failure strain energy density proposed in the author's energy-based intact rock damage criterion combines the models published by Vásárhelyi et al. (2000) and Li et al. (2005) along with an estimation of the tensile behaviour based on the ratio of tensile to compressive material strengths. According to the laboratory tests conducted by Vásárhelyi et al. (2000), a relationship between the critical dissipated strain energy for compressive loading (L_c) and the material compressive and tensile strengths was observed (Equations 6.32 and 6.33).

$$L_C = 1.17 \times \sigma_C \tag{6. 32}$$

$$L_C = 11.87 \times \sigma_T \tag{6. 33}$$

Where σ_C = unconfined uni-axial compressive strength (MPa)
σ_T = unconfined tensile strength (Brazilian, MPa)

The critical dissipated energy density criterion for tensile loading has been assumed by the author to be closely linked with the relationship between UCS (σ_C) and σ_T. The ratio of compressive to tensile strength can range from 10 to 20 and a generally accepted value for σ_C/σ_T is approximately one order of magnitude. For σ_C/σ_T equal to 10, Equations 6.32 and 6.33 can be revised to calculate the tensile critical dissipated strain energy density (L_T) as a function of σ_C and σ_T (Equations 6.34 and 6.35).

$$L_T = 0.12 \times \sigma_C \tag{6. 34}$$

$$L_T = 1.19 \times \sigma_T \tag{6. 35}$$

The relationship between stored strain energy (dissipated strain energy density) and loading rate has been assumed to be similar to that of ultimate rock strength and strain rate. This assumption allows the effects of dynamic loading to be introduced into the energy density intact rock damage criterion. Li et al. (2005) published a relationship between the energy absorbed at compressive sample failure and the strain rate of dynamic loading. Figure 6.10 shows this relationship in terms of the tensile criterion of 10% of the stored compressive strain energy, referred to as the Tensile Rupture Strain Energy (RSE_T) versus the strain rate.

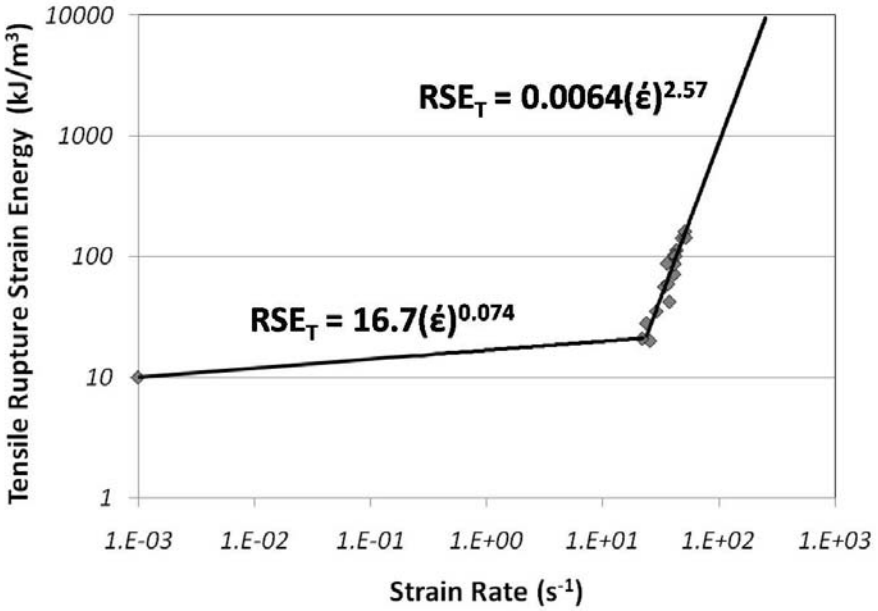

Figure 6.10. RSE_T versus strain rate for granite (after data of Li et al., 2005).

The shape of the piecewise curve of RSE_T versus strain rate is similar to the curves noted for the relationship between tensile or compressive strength versus strain rate as discussed in Chapter 2. Although the slopes and the "take-off point" for the lines would be expected to change for different rock types, similar behaviour would be expected amongst competent rock types encountered in large-scale underground mining. The lack of data in the intermediate strain rate of 10^{-2} to 10^{1} represents a gap in the capabilities of quasi-dynamic testing methods.

An assumption has been made that the general relationship between the rock strength and the dynamic RSE_T ($RSE_{T(dynamic)}$) for different rock types based on the strain rate

would shift the curve in Figure 6.10 upwards or downwards. The amount of curve shift would be based on the relationships given in Equations 6.34 and 6.35 under conditions where $L_T = RSE_{T(static)}$ at a strain rate of 10^{-6} to 10^{-3} strain/s (quasi-static).

To simplify the calculation of $RSE_{T(dynamic)}$ based on strain rate and the static value of RSE_T, an approximate exponential curve has been fitted to the data from Figure 6.10. The continuous exponential function in place of the piece-wise curve allows continuous calculation over the full range of strain rates from static to high-order dynamic. Figure 6.11 displays the data set and the exponential curve that was applied.

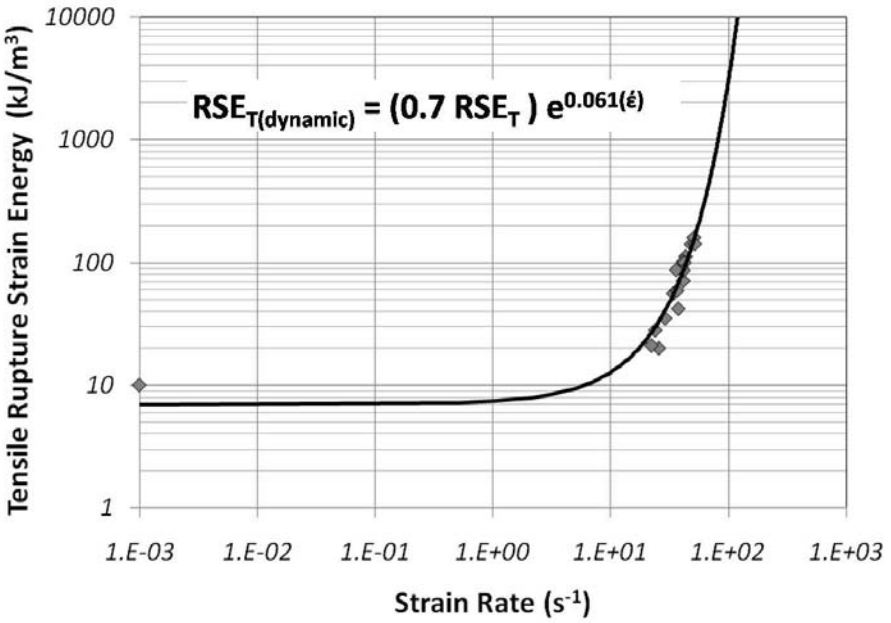

Figure 6.11. Exponential relationship between $RSE_{T(dynamic)}$ and strain rate ($\dot{\varepsilon}$).

The distance from a blasting event where intact rock fracture may occur using this method can be predicted by comparing $RSE_{T(dynamic)}$ at the associated strain rate with the wave-induced stored strain energy density ($ED_{W\text{-}SS}$ = ½ $ED_{W\text{-}tot}$). The critical value of required rupture energy density can be applied to predict either tensile or compressive intact rock fracture over a range of strain rates as determined from blast monitoring results.

6.5.3 Damage to Discontinuities Based on Fracture Energy

It is generally accepted that the weakest component within a rock mass is the network of existing discontinuities. Any stress that is applied in excess of the discontinuity strength will likely induce fracture dilation, sliding or extension prior to damage to the intact rock blocks. The behaviour of discontinuities under the application of static or dynamic loads can therefore control the overall response of a rock mass to mining.

The reduced strength of discontinuities when compared with intact rock blocks has led to a proposed energy-based for prediction of blast damage to existing fractures. This approach assumes that the calculated stored strain energy density ($ED_{W\text{-}SS}$) within a rock mass is distributed evenly over a unit volume of $1m^3$. All macro-fractures contained within that unit volume are therefore assumed to be activated by the wave loading. For the discontinuity fracture energy damage criterion, micro-fractures have not been explicitly considered as the assumption has been made that the micro-fractures are a component of the intact rock portion of the rock mass.

6.5.3.1 Fracture Energy of Concrete and Rock

Values of fracture energy for complex rock masses have not been previously established. Fracture energy testing, as with most material testing for rock mechanics, takes place on small samples in controlled laboratory loading conditions. The results of fracture energy testing are influenced by material properties, sample size, loading rate, initial crack length and the thickness of the remaining intact material ligament (Shah et al., 1995). Therefore, direct application of the laboratory-measured values to large-scale rock mass fracturing conditions should be done with caution. A lack of large-scale fracture energy testing results therefore requires additional research and testing programs to obtain realistic values for in situ rock masses.

Various researchers have performed experiments on concrete and rock samples to obtain values of fracture energy (e.g. Krech, 1974; Wu and Zhang, 1989; Zhang et al., 2000). Investigation of the fracture behaviour of concrete has yielded the majority of studies into fracture energy as a function of loading rate (Oh and Chung,

1989), material composition (Wu and Zhang, 1989) and material temperature and cyclic softening (Ohlsson et al., 1990). Fracture energy tests have also been performed on rock samples using static and dynamic testing (e.g. Krech, 1974; Zhang et al., 2000; Vasconcelos et al., 2008), but published values of fracture energy for rock are scarce in the literature. Table 6.5 lists values of fracture energy published in the aforementioned studies.

Table 6.5. Published values of fracture energy for concrete and rock.

Researcher	**Material Type**	**Test type**	**Fracture Energy**
Krech (1974)	Barre granite	Static tensile	100 J/m^2
	Sioux Quartzite		89 J/m^2
Zhang et al. (2000)	Gabbro	Static wedge	66.1 J/m^2
		Dynamic SHPB	1592 J/m^2
Vasconcelos et al. (2008)	Granite	Direct tensile	145-270 N/m
Wu and Zhang (1989)	Lightweight Concrete	Static 3-point	132.48 N/m
Oh and Chung (1989)	Concrete	Static 3-point	~150 N/m
		Dynamic 3-point	~340 N/m
Ohlsson et al. (1990)	Concrete	Static 3-point	~100 N/m
Wittmann (2002)	High-Strength Concrete	N/A	~300 N/m

The effects of dynamic loading rate on fracture energy have been observed by various researchers including Oh and Chung (1989). As with material strength and dissipated energy at rupture ($RSE_{T(dynamic)}$), increased loading rates result in higher required fracture energies. Testing of a series of concrete beams of various sizes and strain rates between 10^{-6} and 10^{-3} strain/s by Oh and Chung (1989) illustrated an increase in fracture energy of up to approximately 2.5 times. This increase from quasi-static to intermediate loading rates is similar to that observed for increases in material failure strength and rupture strain energy.

An approximate exponential relationship for the dynamic tensile fracture energy ($FE_{T(dynamic)}$) based on strain rate and the static tensile fracture energy (FE_T) is proposed for use in prediction of fracture activation in the newly proposed blast damage criterion. This relationship is theoretical based on the shape of the curve presented in Figure 6.11. Few test results have been published for dynamic fracture energy of rock and the curve in Figure 6.12 has been defined using the limited values in Table 6.5. More data would be required to validate the relationship between dynamic fracture energy and strain rate.

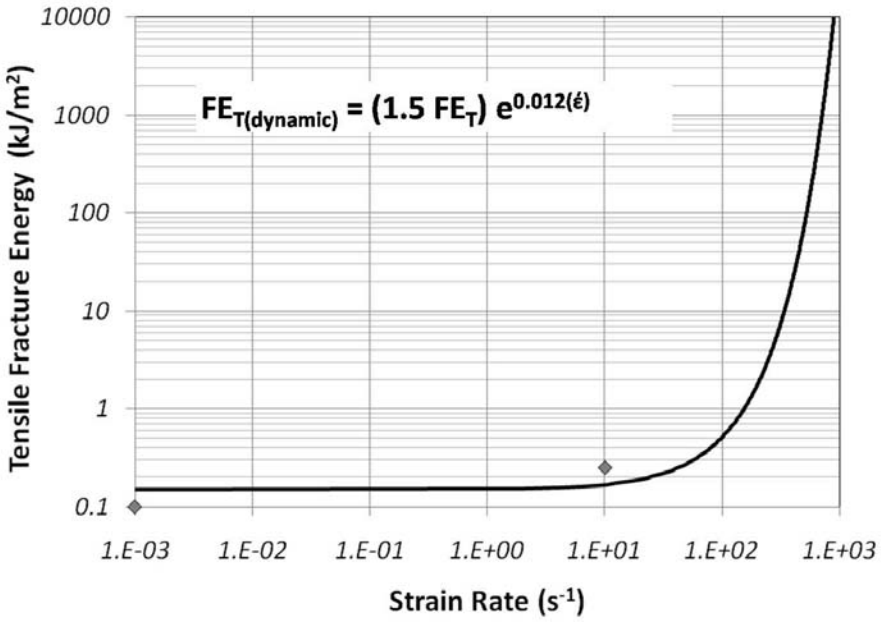

Figure 6.12. Proposed exponential relationship for determination of dynamic tensile fracture energy ($FE_{T(dynamic)}$) versus strain rate for granitic rocks.

6.5.3.2 Required Fracture Energy for Activation of All Fracture Surfaces in a Unit Volume

Calculation of the energy required for activation of all fractures within a unit volume of a jointed rock mass requires values of the critical fracture energy and the fracture area density contained in a $1m^3$ block. The discontinuity model selected for representation of rock mass jointing can be used to determine the total fracture area density within a unit volume based on the number of joint sets, the joint spacing, joint set orientation and the predicted distribution of trace lengths (Weibull, normal,

etc). Based on the joint set information, the final value for the fracture area density (*FAD*) or fracture intensity in m^2/m^3 can be calculated.

The fracture energy density (FED_{crit}) required to activate all fracture faces in a unit volume of $1m^3$ and induce damage through fracture extension is calculated using Equation 6.36.

$$FED_{crit} = FE_{T(dynamic)} \cdot FAD \qquad (6.36)$$

The unit of FED_{crit} is J/m^3, which corresponds with the unit of the wave-induced stored strain energy density ($ED_{W\text{-}SS}$). The predicted damage limit for extension of fractures using Equation 6.36 and the values of $ED_{W\text{-}SS}$ can be determined by comparing the two values. The distance from an explosive charge where the critical fracture energy equals the blasting-induced stored strain energy density (where $FED_{crit} = ED_{W\text{-}SS}$) identifies the limit of predicted fracture extension.

The use of FED_{crit} does not explicitly consider the differences in required fracture energies for different dimensions of existing fracture length. Research has confirmed that the critical fracture energy is reduced with an increase in the initial fracture length (Oh and Chung, 1989). Integration of this effect has not been attempted in the current analytical model due to the complex relationship between the fracture energy and the critical dimensions of the initial crack, the cross-sectional area of the material containing the crack and the thickness of the remaining rock ligament between adjacent cracks.

6.6 Implementation of the Proposed Strain and Energy-Based Blast Damage Criteria

A number of steps are required to apply the concepts developed in Sections 6.3 to 6.5 to predict rock mass damage from blasting in the presence of mining-induced static stresses. The steps listed consider use of the strain-based criteria for intact rock and the fracture energy criteria for existing discontinuities. These steps include:

1) Estimation or testing of intact rock strengths and rock elastic constants.
2) Estimation or testing of the dynamic rock properties.
3) Estimation of the intact rock static failure strain.
4) Stress modelling to determine the mining-induced static stress and strain distribution at the time of blasting.
5) Blast vibration monitoring to characterise $\varepsilon_{W\text{-}MN}$ and $ED_{W\text{-}SS}$ generated by known explosive charges in the rock mass of interest.
6) Selection of a suitable rock failure criterion (compressive versus tensile) based on the superposition of static and dynamic strains.
7) Assessment of the equilibrium position between the required strain to fracture and the aggregate applied static and dynamic strain to indicate the limit of strain-based fracture.
8) Rock mass discontinuity mapping to indicate the fracture area density.
9) Estimation of the dynamic fracture energy for the rock mass required for fracture extension.
10) Assessment of the equilibrium position between the required fracture energy density and the induced dynamic strain energy density to indicate the limit of dynamic fracture extension.

Steps 1-10 have been applied in Chapter 7 and steps 1-7 have been applied in Chapter 8 to predict possible blast-induced damage occurring to the rock masses surrounding two example stopes at the two sponsoring mine sites. Details on the values of failure strains and energies selected in each case study as well as the modelled wave behaviours will be discussed in detail.

6.7 Discussion and Conclusions

The empirical and semi-analytical blast damage prediction models discussed in Section 6.2 clearly lack consideration of the state of rock mass loading from blasting or any explicit consideration of the material response to dynamic loading. In addition, no mechanism exists in these models for addressing the influence of

existing mining-induced static strains on the predicted blast-induced damage. The approaches proposed in Chapter 6 have attempted to improve the prediction of blast-induced damage by more realistically representing the loading mechanisms and conditions contributing to dynamic rock mass damage from blast-induced strains and energies.

The main ideas which are represented in the proposed approaches which differ from existing semi-analytical models include:

- Use of total wave energy density ($ED_{W\text{-}tot}$) as a near-field blast vibration characteristic instead of instantaneous peak amplitude
- Calculation of wave-induced mean normal dynamic strain ($\varepsilon_{W\text{-}MN}$) from stored strain energy density ($ED_{W\text{-}SS}$)
- Secondary consideration of critical rupture strain energy required for damage to intact rock blocks
- Consideration of intact rock damage modes (compressive versus tensile) taking into account induced static strains within the rock mass
- Use of fracture energy density to predict extension of existing discontinuities

The proposed strain-based blast damage criterion for intact rock is based only on the normal strains calculated from the waveforms, without accounting for the direct influence of shear strains. Shear loading is recognised as an additional source of potential blast-induced rock mass damage. The lack of shear strain consideration represents a limitation in the proposed approach, although shear strains are not considered in existing empirical or semi-analytical models either. Future research and improvement of the proposed approach will involve integrations of shear strains into the suggested damage criteria.

Chapters 7 and 8 will apply the concepts developed in this chapter to predict blast damage around two individual stopes based on blast vibration monitoring and rock mass characterisations at the two sponsoring mine sites. These two study sites represented considerably different rock mass conditions, mining geometries and geotechnical concerns.

CHAPTER 7 : CASE STUDY- BARRICK GOLD CORP. KANOWNA BELLE GOLD MINE

7.1 Introduction

The blast damage investigation performed for this thesis was initiated in late 2005 at the Barrick Gold Corp. Kanowna Belle Gold Mine (KBGM). The project was intended to examine the influence of blast-induced damage on stope performance under high stress and geologically variable rock mass conditions. Underground field data collection and blast vibration monitoring took place at KBGM from January to May, 2006. Data provided by mine personnel prior to, during and after the period of field work included geotechnical information, stope and blast designs and post-extraction void surveys. Data collected or analysed by the author included borehole deviation surveys, blast vibration monitoring, discontinuity mapping and mining-induced static stress modelling.

Rock mass characterisations and blast vibration analyses were performed for three study stopes located in the D block at KBGM. An extended analysis was performed for one of the monitored stopes. This included prediction of blast-induced rock mass damage under the influence of mining-induced static stresses using the proposed criteria discussed in Chapter 6. The extent of predicted tensile strain-based damage and discontinuity extension using the proposed approach has also been compared with predictions using the critical tensile plane strain model.

7.2 Geology of the Deposit at KBGM

The Kanowna Belle Gold Mine is owned and operated by Barrick Gold Corporation. The mine was acquired in 2006 from Placer Dome and is located 18km Northeast of Kalgoorlie in Western Australia. The KBGM gold deposit is hosted within a greenstone succession of the Boorara Domain of the Gindalbie Formation. Three mineralisation events formed the deposit through successive metamorphism and porphyry intrusion of the sedimentary conglomerates and volcanoclastic bodies associated with large-scale faulting (KBGM, 2008). The gold mined at KBGM is generally contained within the main feldspar porphyry orebody striking East-

Northeast with a strike length of 500 metres. The orebody dips at approximately 50-60 degrees to the South-Southwest with down-plunge extent of greater than 1250 metres. The Lowes orebody, which contains 80% of the known mineralisation at KBGM varies in thickness from 5 to 50 metres and occurs in conjunction with two mine-scale faults known as the Fitzroy Fault and the Fitzroy Footwall Shear Zone (Villaescusa et al., 2003).

7.3 Overview of the Mining Operation

Gold has been mined from the open pit at Kanowna Belle since 1990, with underground production beginning in 1998. At the time of the field investigation in 2006, the mining rate was 1.2Mt of ore per annum, producing approximately 240k oz of gold (Malatesta, 2006). Figure 7.1 shows a long section of KBGM, divided into the six mining blocks; A to E and the Troy block, classified by depth from surface.

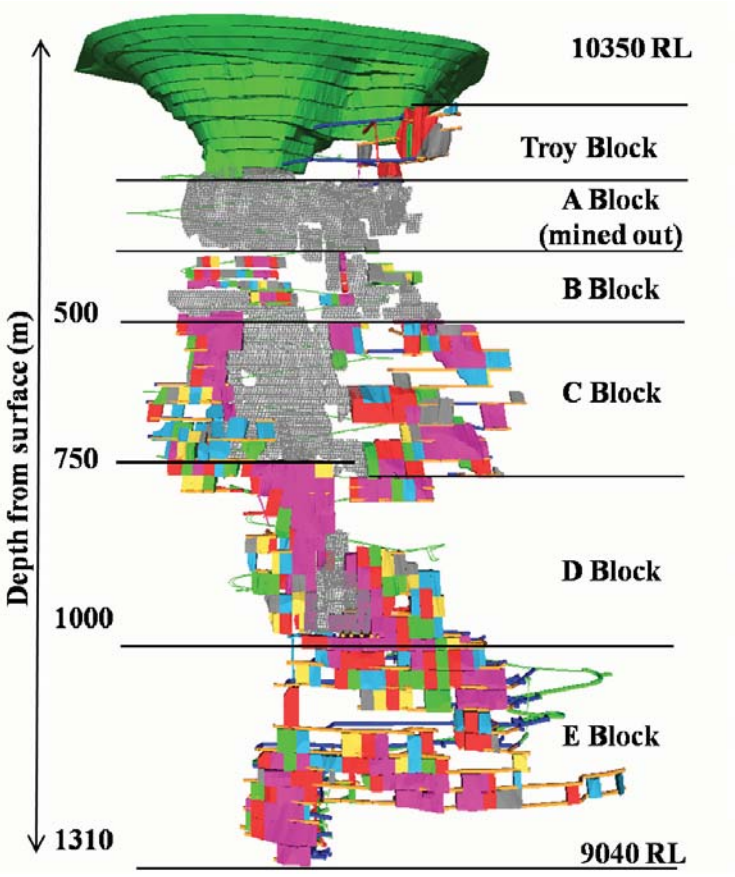

Figure 7.1. Long section of KBGM showing the mining blocks and the completed open pit (looking north).

The mining method utilised at KBGM is sublevel open stoping. A variety of different stoping sequences have been used in the past depending on the mining block. During the field investigation in 2006, a large percentage of the ore extraction was taking place in the C block and D block at depths of 500-1000m below surface. A block and B block were largely mined out; Troy block and E block had not yet been commissioned.

7.3.1 Mining Sequences for Ore Blocks

With the increase in depth from the upper horizons of A and B blocks to the lower C and D blocks, changes in stope dimensions, fill type and mining sequences were adopted to address regional stability concerns. Table 7.1 lists the primary stoping dimensions and sequences used in each mining block.

Table 7.1. Open stoping dimensions and sequences for each block at KBGM (KBGM, 2008).

Mining Block	Stoping Configuration/Sequence	Stope Dimensions	Fill Type
A	Primary/secondary open stoping	Variable	Cemented Aggregate Fill
B	Bench stoping	Variable	Waste Rock/Pastefill
C	Primary/secondary open stoping and pillarless retreat	20m strike x orebody width x 60m high	Pastefill
D	Pillarless retreat	15-20m strike x 20m wide x 30m high	Pastefill
E	Underhand bench stoping	15m strike x 12m wide x 30m high	Pastefill

7.3.2 Selection of Monitored Stopes

The blast damage investigation project was initiated at KBGM because mine personnel were concerned with the impact of blasting on the performance of stopes in the future mining conditions of the E block. For this reason, the deepest operating

mining block at the time (D block) was selected for blast-vibration monitoring and damage assessment and prediction. The mining conditions in the D block also allowed investigation of blasting-induced damage under high stress conditions due to the increase in the mining-induced static stress at depth. E block rock mass conditions were assumed to be more highly-stressed than D block, with a 20MPa increase in the virgin maximum principal stress (KBGM, 2008).

Three D block stopes were selected for rock mass characterisation, blast vibration monitoring and post-extraction stope performance assessment. To remove some of the variables contributing to the performance of individual stopes, all three selected stopes were located along the Eastern mining front at the deepest production levels of D block (9350RL, 9380RL and 9410RL). The stopes selected for the KBGM case study were stope dA12-35 and the top and bottom lifts of the double-lift stope dB10-38. The two lifts of stope dB10-38 were fired independently using different initiation systems and for monitoring purposes they were considered to be two separate stopes. The two lifts were named dB10-38B (bottom lift) and dB10-38T (top lift). Figure 7.2 shows the location of the three stopes in relation to the D block central fill mass.

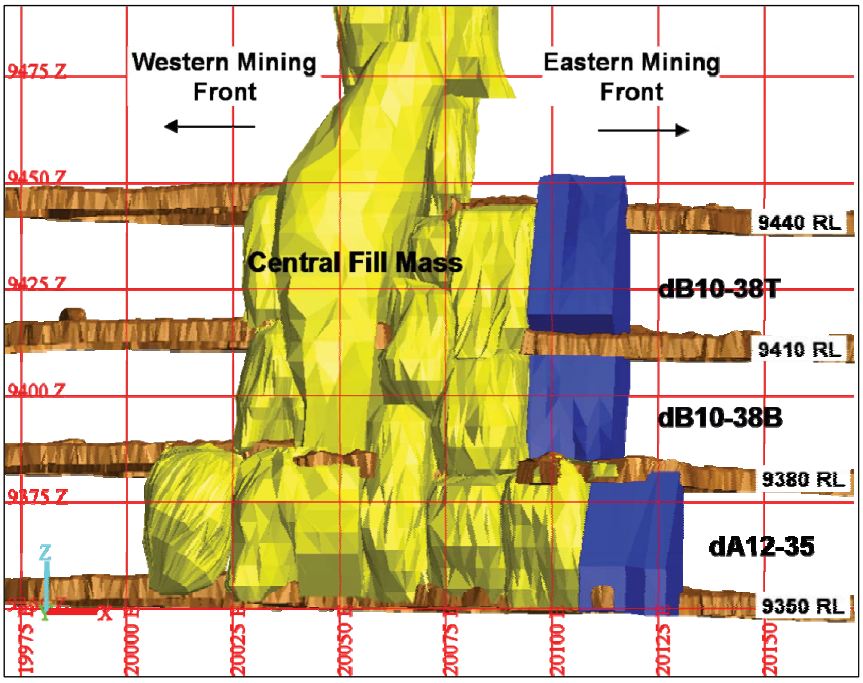

Figure 7.2. Long section of D block study stopes (in blue) and central fill mass (in yellow) at the time of the blast damage investigation (looking north).

7.3.3 Stope Naming Convention at KBGM

The stope naming convention at KBGM was such that the stoping block, panel, Easting stope line and extraction level were included within the name. For example, stope dA12-35 was located in the D block (d), A panel (A), 20120 Easting (12) and drawn from the 9350 RL (35). In the sections of the orebody of sufficient thickness, multiple stoping panels were mined from the hangingwall (A panel) to the footwall shear (B or C panel). Early stope naming conventions in the D block followed a primary (P) and secondary (S) convention. Figure 7.3 shows a plan view of the D block at the 9390RL with the names of some of the stopes in the mining sequence. The yellow shaded stopes represent A-panel stopes and blue shaded stopes are B-panel. The central grey stope was the first primary stope of the block prior to adoption of the new naming convention.

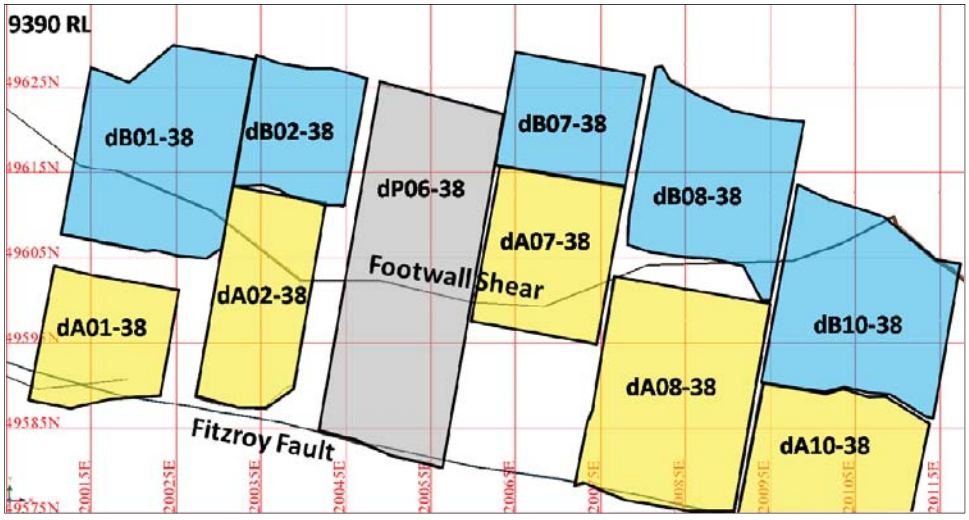

Figure 7.3. Plan view of D-block at the 9390RL showing the stope names and mining panels between the Fitzroy Fault and footwall shear.

7.3.4 Drilling and Blasting at KGBM

The drilling and blasting program in the D block of KBGM was typical of a slot-less single-lift ring-drilling sublevel open stoping configuration. Blastholes of 102mm diameter were drilled from a single access drive along the strike of the stope. The typical pattern for ring drilling was 3.0 to 4.0m ring burden with a toe spacing of 2.5 to 3.5m, resulting in bulk powder factors of approximately 0.25 to 0.3 kg/tonne of

ore. Typical explosive products used in production blasting were pour-loaded ANFO, low-density SANFOLD 50 and 70 (0.55 and 0.7 g/cc density, respectively) and variable-density gassed emulsions. The standard initiation system was the Dyno Nobel long-period pyrotechnic shock-tube system with surface connectors to allow subdivision to millisecond-like timing. The Orica i-kon ™ system was also utilised in complex mass blasting conditions.

The in-stope firing sequence selected for the D block stopes was a non-conventional vertically-retreating sequence with an offset central longhole retreat rise to provide initial void. The vertically-retreating in-stope sequence allowed for minimal vertical exposure of the stope walls and crown prior to paste filling. The flat-bottom stope design required firing of a 5m horizontal sill blast, drilled from the drawpoint development, prior to the initiation of rise firings. The typical firing steps within a single-lift stope of the D block were:

- Slashing of a 5m high horizontal sill at the draw level
- A series of 3m vertical rise firings of 2m x 2m plan area from the sill to a 6m temporary crown
- Slashing of the initial 2m x 2m rise to 6.5m x 6.5m area to a 10m crown
- Firing of two to four rings of toes to a 15m crown
- Firing of remaining ring toes to a 20m crown
- Mass blast of remaining holes to final void

Double-lift stopes required fewer firings within the top lift due to the stope void below from previous extraction of the bottom lift. Some delays were experienced during blasting of the top lift of a double-lift stope to facilitate loading of broken ore to supply adequate void space for the mass firing. Single-lift stopes generally required 9 to 11 firings to reach full extraction, whereas the top lift of double-lift stopes required approximately 8 firings. Figure 7.4 illustrates the stages of firing for the single-lift stope dB10-38B.

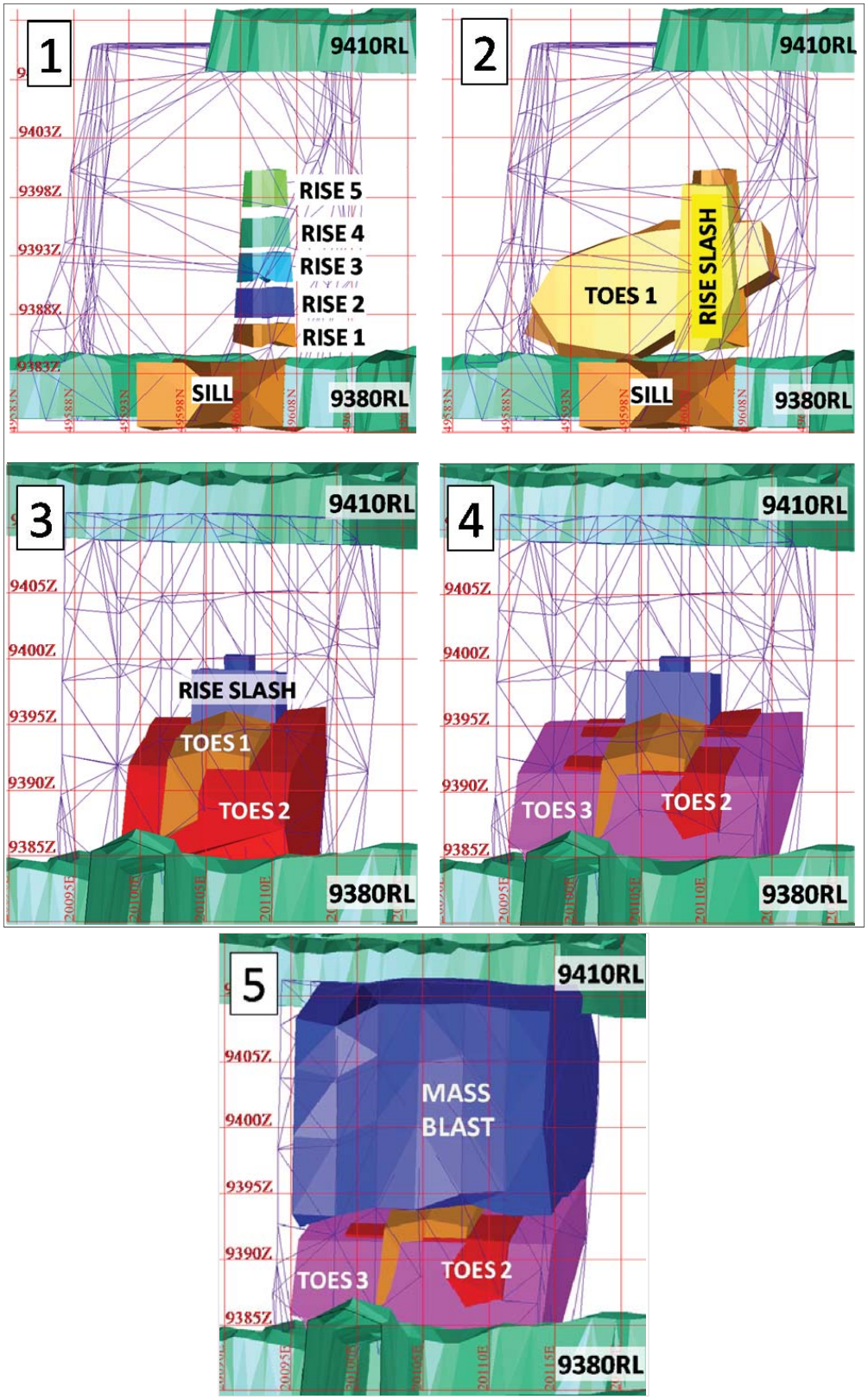

Figure 7.4. Firing stages of stope dB10-38B looking West (1-2) and North (3-5).

7.4 Drillhole Deviations Surveys at KBGM

Blasthole deviation surveys were performed in study stopes dB10-38B and dB10-38T to acquire accurate locations of explosive charges and to investigate possible sources of stope overbreak. Drillhole deviation has been identified as a significant contributor to variability in blasting results and a major contributor to unplanned stope dilution in the mining industry (Hendricks et al., 1991 and Singh, 1996).

The drillhole deviation surveys were performed by the author using the FlexIT Multishot SmartTool magnetic surveying instrument. This equipment was selected for purchase for the project due to ease of use, robust construction, cable-less operation and superior software export capabilities. Over the course of the blasthole surveying program conducted by the author at KBGM, almost 4kms of blasthole lengths were surveyed; 2750m were contained within study stopes dB10-38B and dB10-38T. A recording interval of 3m was selected for the downhole surveys, with irregular intervals near the hole toe or near breakthrough into the existing stope void.

The surveying and analysis procedures adopted in the program allowed the designed hole collar and toe locations to be compared with those measured. These comparisons required that the drilled collar coordinates be surveyed for position in addition to the downhole deviation surveying. The general results identified errors in both the hole collar locations and the toe locations versus design. Collaring location errors were up to 600mm and total toe location errors reached 1.6m from design.

One standard method of presenting drillhole deviation data is expression of the error in location as a percentage of the total hole length. Figure 7.5 shows the results of the blasthole survey program for stopes dB10-38B and dB10-38T in a histogram of the toe location errors as percentages of the blasthole lengths.

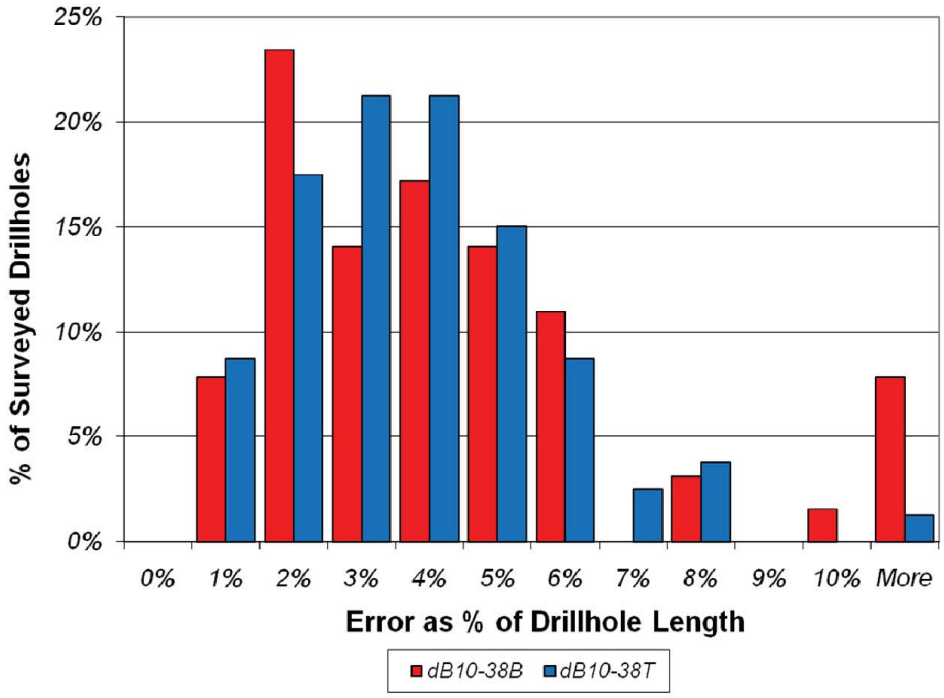

Figure 7.5. Histogram of toe location errors in surveyed blastholes as a percentage of the hole lengths for stopes dB10-38B and dB10-38T.

The histogram results in Figure 7.5 clearly indicate a large variability in the toe location errors, which can be attributed to the in-hole deviation as well as set-up and collaring errors. Results of blasthole deviation surveys performed by the author and other contractors at KBGM resulted in similar deviation percentages for 102mm diameter blastholes (Fleetwood, 2010). Deviation surveys of 76mm diameter blastholes used in stope C9380 at KBGM revealed much higher deviation percentages (over 30%) due to malfunctioning of the drill inclinometer gauge (Fleetwood, 2006).

The general trend of the blasthole location error is an important factor in addition to the magnitude of the error. Figure 7.6 illustrates the collar and toe locations of the surveyed blastholes compared with the design locations using bullseye graphs. Bullseye graphs plot the position of the actual blasthole relative to the designed blasthole axis, which is located in the centre of the plot. General trends in drilling location errors and potential effects on overbreak or fragmentation can be examined using bullseye graphs.

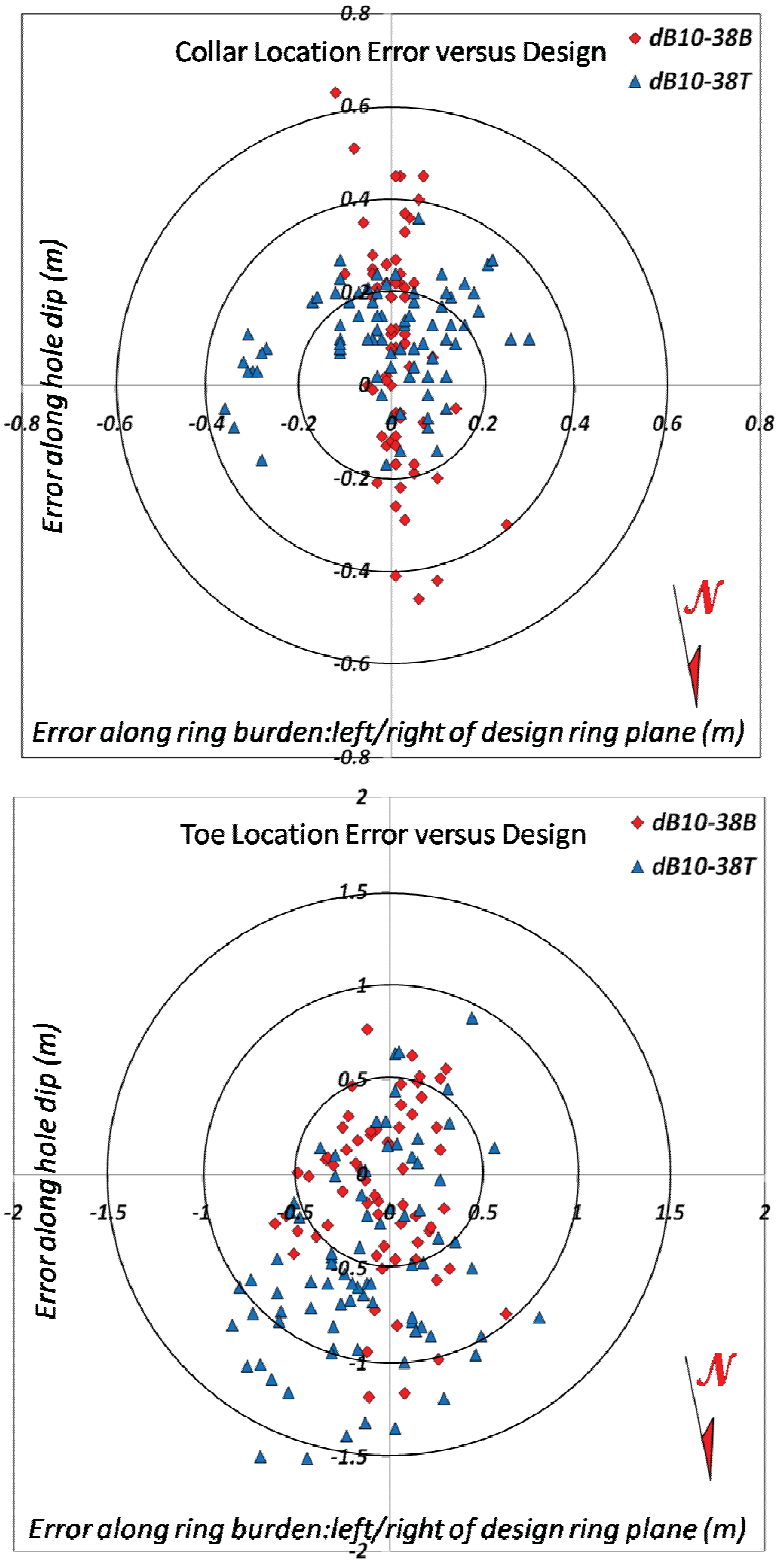

Figure 7.6. Bullseye graph of the surveyed versus designed hole collar (top) and toe (bottom) positions.

Analyses of the bullseye graphs reveal several trends in the orientations of drilling deviations in stopes dB10-38B and dB10-38T. In general, hole collar position errors in stope dB10-38B were concentrated within the plane of the designed rings (approximately North-South). One possible factor for this type of positioning error is related to floor elevation control between the time of drive surveying and drilling.

Prior to stope drilling, the floors of drilling drives were typically cleaned up by a loader to remove loose material. Removal of broken rock from the floor would allow the drill jacks to seat more firmly and make blasthole collaring easier. Floor clean-up typically took place between the times of drive laser profiling (the survey that was used for the drillhole design process) and the actual drilling activities. A change in the actual elevation of the drive floor compared with the floor used in the design could lead to errors in collar position for non-vertical drillholes due to a change in the drill pivot position. Some collar position errors were also observed for stope dB10-38T along the ring burden direction (approximately East-West). These errors could have been associated with ring position laser mark-up errors, drill set-up errors or deliberate movement of collar locations due to collaring difficulties.

The majority of surveyed blasthole toe locations fell to the North of the design locations within the plane of the ring, indicating possible gravity-induced effects on sub-horizontal or moderately-dipping blastholes. In most cases, any lateral blasthole deviation was contained within the stope on internal rings. Significant lateral toe error only occurred in one hole on a perimeter ring, resulting in the blasthole being located outside of the stope boundary (final ring location) by approximately 800mm. Other holes in the perimeter rows did not significantly deviate outside of the designed stope boundaries. The general trend of errors along the dip angle of the blasthole is illustrated in Figure 7.7 for two blasthole rings in stope dB10-38T.

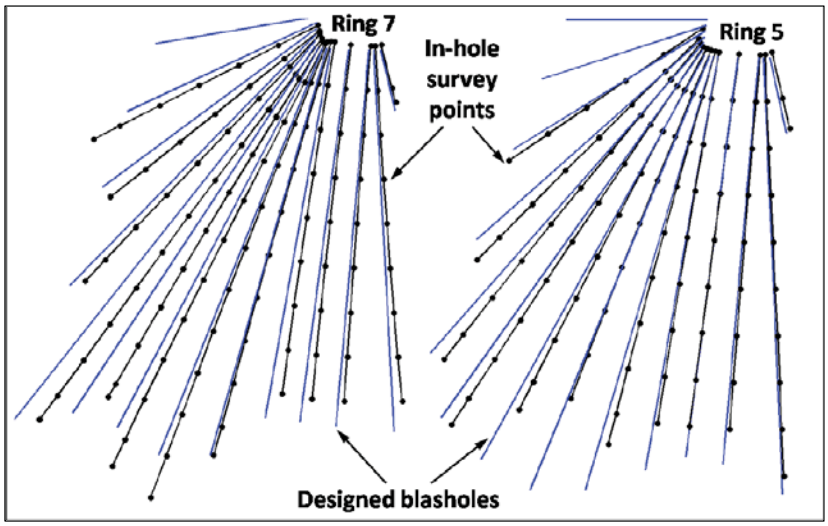

Figure 7.7. Section view of blasthole rings 5 and 7 in dB10-38T comparing the designed hole locations (blue strings) with the surveyed blasthole locations at 3m in-hole survey intervals (black strings and points).

7.5 Rock Mass Characterisation of D block

One of the defining elements of the proposed approach to blast damage investigation is characterisation of the rock mass prior to blasting. This characterisation is an attempt to better understand the geologic and geotechnical elements that contribute to the response of the rock mass to mining. Some of the critical rock mass parameters that have been identified as contributors include the intact rock strength, elastic properties of the intact rock, distribution and orientation of discontinuities, bulk rock mass parameters such as the in situ stress wave velocity and dynamic Young's Modulus and mining-induced static stress redistribution. These parameters are believed to contribute to both the propagation of stress waves and the response of the rock mass to static and dynamic strains.

A number of approaches were applied to characterise the rock mass at KBGM along the Eastern mining front of D block. The techniques included assessment of existing laboratory rock testing results, analysis of underground discontinuity mapping, mining-induced static stress modelling and analysis of geophysically-related stress wave characteristics indicated from the blast vibration monitoring results.

7.5.1 Intact Rock Testing Results

Laboratory testing for UCS and elastic constants (Young's Modulus and Poisson's Ratio) of D block rock samples was performed for three different geologic domains in 2002. The three domains from which rock samples were extracted and tested were the footwall region, the porphyry ore zone and the hangingwall region. The testing results are listed in Table 7.2.

Table 7.2. Intact rock testing results for KBGM D block (Li, 2002).

Geologic Region	Average density (kg/m^3)	Average UCS (MPa)	Average E_{st} (GPa)	Average v_{st}
Ore	2760 (9)	113 (10)	62 (20)	0.28 (20)
Footwall	2770 (9)	136 (11)	65 (18)	0.29 (18)
Hangingwall	2775 (3)	156 (6)	71 (8)	0.30 (8)

(##)- number of samples tested

Table 7.2 clearly indicates significant differences between the intact rock properties for the three geologic domains based on the static uni-axial compressive strength (UCS) and rock stiffness as indicated by the static Young's Modulus (E_{st}). These differences in strength and stiffness would be expected to influence the dynamic response of the rock mass to blast-induced stress wave loading and influence the attenuation behaviour of the propagating blast-induced vibrations. As one part of a complex system of components, the intact rock properties only partially describe the rock mass. The second main component of the rock mass is the in situ discontinuities. Therefore, any characterisation of the rock mass must include some treatment to describe the orientation, persistence and distribution of discontinuities as indicated by core logging or mapping of exposures underground.

7.5.2 Discontinuity Mapping in D block at KBGM

Part of the geologic and geotechnical characterisation of the rock mass for use in stope and ground support design at KBGM is mapping of discontinuities exposed in the backs and walls of development drives. Personnel from KBGM and WASM have performed mapping of drive backs and walls within D block. This information was

digitised into mine design software for use in examination of dominant discontinuity orientations. Figure 7.8 displays the results of digitised mapping for level 9380RL.

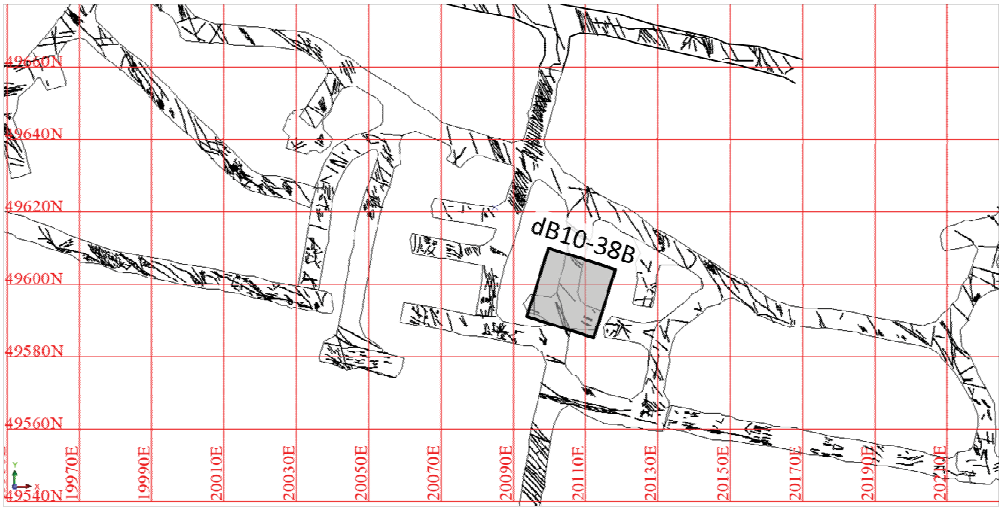

Figure 7.8. Plan view of digitised discontinuity mapping of 9380RL development.

The digitised mapping results were plotted on a polar stereonet projection to examine the orientation and distribution of the mapped discontinuities. The polar distributions were contoured using DIPS 5.1 from Rocscience to represent the most evident discontinuity orientations. Figure 7.9 shows the discontinuity pole distribution contours for all mapped data in D block.

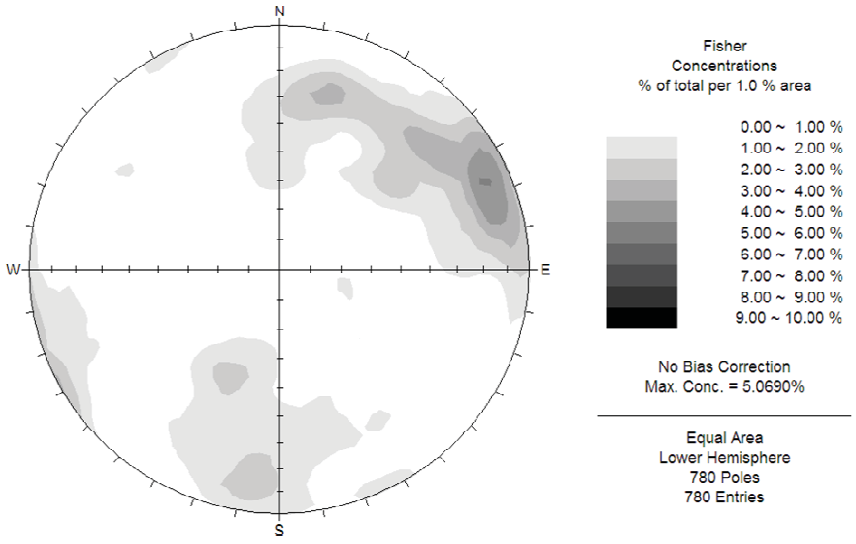

Figure 7.9. Equal-area lower hemisphere stereonet plot of D block discontinuity mapping data.

The results in Figure 7.9 indicate three probable discontinuity sets, with a large distribution representing a steeply-dipping (80 degrees) set with an approximate dip direction of 245 degrees. The lack of a near-horizontal discontinuity set (appearing near the centre of the plot) likely reflects mapping bias due to the majority of data representing mapping of the backs and shoulders of the drives, where intersection of shallow sub-horizontal sets would be unlikely.

7.5.3 Overview of the Blast Monitoring Program

Rock testing and discontinuity mapping largely represent static characteristics of a rock mass. To aid in defining the dynamic characteristics of the rock mass around the three study stopes, geophysical approaches using the blast vibration monitoring results were applied. A brief summary of the transducer locations for all three stopes is presented in Table 7.3 to show the density of transducer coverage. Additional information on the transducers in each stope is provided in Sections 7.7, 7.8 and 7.9.

Table 7.3. Summary of instrumentation utilised in study stopes in KBGM D block.

Stope	Wall of Stope	Transducer Type	Distance from Stope (m)
dA12-35	Footwall (FW)	Tri-axial 500g Accelerometer	7.0
		Tri-axial Geophone	16.7
dB10-38B	Footwall (FW)	Tri-axial 500g Accelerometer	6.5
		Tri-axial Geophone	15.4
	East Wall (EW)	Tri-axial 500g Accelerometer	7.0
		Tri-axial Geophone	12.2
dB10-38T	Footwall (FW)	Tri-axial 500g Accelerometer	6.1
		Tri-axial Geophone	15.1
	East Wall (EW)	Tri-axial 500g Accelerometer	6.0
		Tri-axial Geophone	16.0
	Hangingwall (HW)	Tri-axial 500g Accelerometer	6.0
		Tri-axial Geophone	15.0

7.5.4 Block-Scale Rock Mass Characterisation Using Blast Vibration Data

The blast vibration monitoring program conducted at KBGM enabled a form of differential stress wave velocity tomography to be performed. Wave velocities were calculated using the arrival times of waves generated by production blastholes at each transducer on an array and the differential distance from the source to each transducer. Of the available production blastholes, the short charges utilised in rise firings provided the best seismic sources for use in determining the stress wave velocities within the rock mass. An additional geophysical rock mass characterisation method that was applied at KBGM was peak amplitude-frequency analysis. This type of analysis indicates rock mass conditions through comparisons of inferred wave frequencies at the peak amplitude.

7.5.4.1 Stress Wave Velocity Calculation using Blast Monitoring Results

Successful determination of stress wave velocities using production charges requires that seismic sources be repeatable, largely unaffected by voids along the wave-path and have a low degree of wavefront interaction. These factors enhance the ability to accurately identify the wave arrival times at each transducer as indicated by the first break of the waveform.

A majority of the blastholes used in the stress wave velocity calculations in D block were the relatively short rise firing charges. These charges were similar in length (3m) and location, were fired on long-period delays and were early in the mining sequence such that minimal void interaction was experienced. The calculation of the differential stress wave velocities also required accurate three-dimensional locations of charges and transducers, accurate records of blasthole firing sequences based on design delay timing and adequate waveform sampling rates and resolutions to allow accurate selection of arrival times.

The analysis process used to calculate stress wave velocities in this thesis was referred to as the differential velocity calculation method. This type of approach was adopted due to the unknown absolute times of charge detonations due to detonator scatter. The differential method therefore was based on the differences between wave arrival times at two separate transducers on the same array and the three-dimensional

differences in distances from the source toe locations to each transducer. Where applicable, the distances used in calculation of the stress wave velocity were the VICD discussed in Chapter 5. Equation 7.1 was used to calculate the stress wave velocity (V_w) for each blasthole included in the assessment.

$$V_W = \frac{d_2 - d_1}{t_{arrival-2} - t_{arival-1}} \qquad (7.1)$$

Where d_1, d_2 = distance from the source to transducer 1 and 2 of the array (m)
$t_{arrival-1}$, $t_{arrival-2}$ = arrival time of stress wave at transducer 1 and 2 (s)

The differential velocity calculation method suffered from several limitations for characterisation of the bulk rock mass properties. One of these limitations was that only a relatively small volume of the rock mass was represented by the spacing between the two transducers (typically around 10m). Another limitation was that the use of production charges as seismic sources introduced several potential sources of error, as the frequency of the wave and the coupling characteristics of the source can affect the transmission of the waves. Additionally, the angle of each wave-path with respect to the transducer array varied significantly over the course of successive firings. The change in angle likely influenced the angle of incidence with discontinuities, which would be suspected to contribute to errors in the calculation. The last limitation was that selection of first wave arrival times at each transducer was difficult where waveform masking was observed from poor signal resolution. In spite of these limitations, the wave velocities calculated from production blasthole seismic sources provided valuable information for geophysical characterisation of the D block rock mass. This information was obtained without interruption to the production cycle that would be expected with dedicated seismic surveying.

The individual stress wave velocities calculated from all rise firings of all three D block stopes are shown in Figure 7.10 along with the block-scale average value. The data are plotted as a function of the mean travel distance, which is the average of the two source charge to transducer distances. This type of plot indicates any distance-related effects on stress wave velocity attenuation.

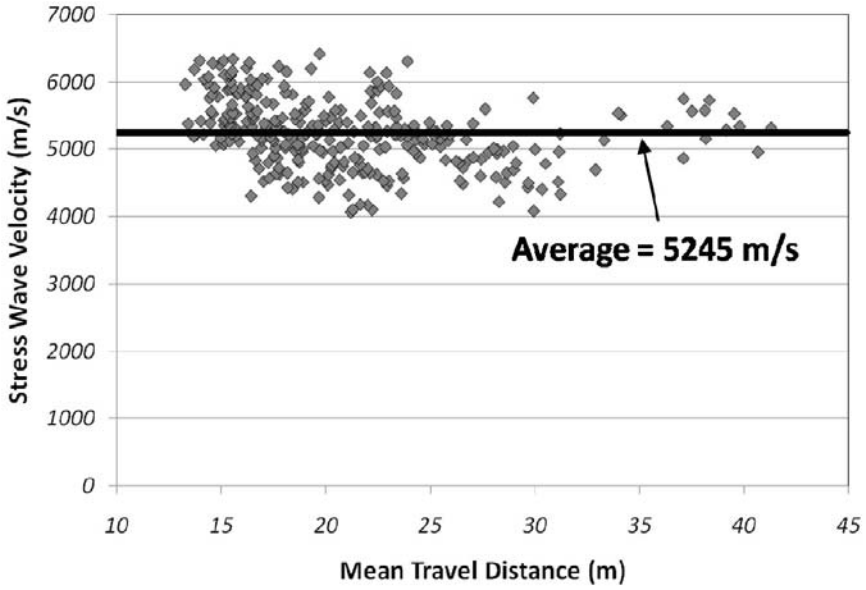

Figure 7.10. Calculated block-scale stress wave velocities for KBGM stopes dA12-35, dB10-38B and dB10-38T plotted against the mean wave travel distance.

The scatter in the in situ wave velocities in Figure 7.10 identifies possible conditions of velocity anisotropy. Although some scatter has been observed within the data subsets for each stope and individual walls of stopes, grouping within the individual subsets has revealed definite differences. These identified anisotropies can indicate variable degrees of fracturing or stress conditions. Differences in stress wave velocities also influence the calculated energy densities and strains developed within a rock mass as a result of the propagation of blast waves.

7.5.4.2 Frequency Assessment of Monitored Blasting Vibrations

Competent rock masses exhibiting a high effective stiffness would be expected to support vibration frequency spectra greater than weak and highly fractured rock masses of low effective elastic constants. Therefore, one method of assessing the relative conditions of a rock mass is by examining the frequency content of propagating seismic waves from blasting. To investigate this effect, vibration frequencies calculated at the peak amplitudes for all blast vibration data collected in D block have been examined. Figure 7.11 shows a histogram of the peak frequencies of all data collected as part of the blast vibration monitoring program in D block.

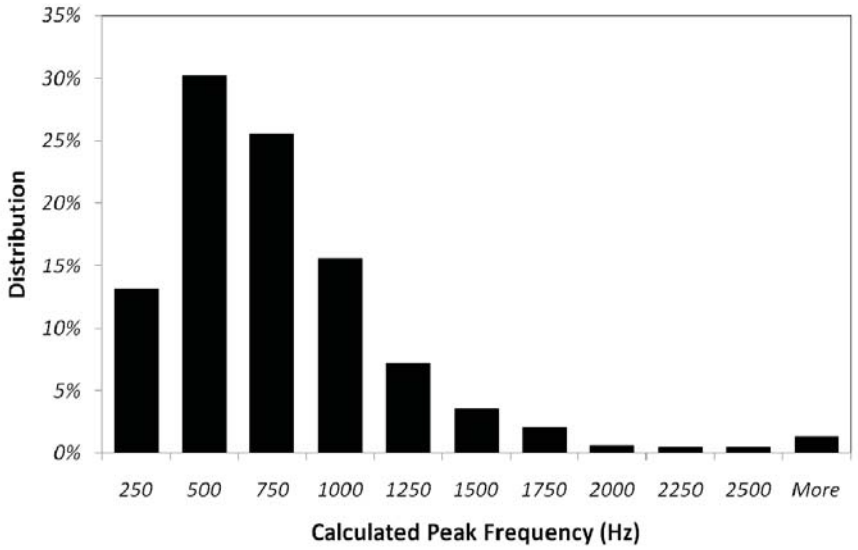

Figure 7.11. Block-scale blast vibration peak frequency distribution at KBGM.

Variability in the rock mass conditions indicated by the scatter in velocity values in Figure 7.10 can also be observed by the lognormal distribution in peak frequency values in Figure 7.11. For consistent rock mass conditions around all three study stopes, the frequency distribution would have been expected to be a normal distribution with a minimal spread around the mean.

7.5.4.3 Peak Amplitude-Frequency Analysis of D block Data

A method of rock mass condition assessment referred to as peak amplitude-frequency analysis has been proposed for use in rock mass characterisations in D block. Peak amplitude-frequency analysis examines the relationship between the peak particle acceleration (PPA) and peak particle velocity (PPV) of recorded blast waves to indicate rock mass conditions based on the wave frequency supporting characteristics. More information on the peak amplitude-frequency analysis method is provided in Appendix 7.

Data collected for each individual monitored stope wall were compared using the peak amplitude-frequency approach. This comparison further investigated the differences in rock mass properties indicated by the stress wave velocities and rock testing results for the three geologic units; namely the D block hangingwall (stope HW), ore (stope EW) and footwall (stope FW) units. Although the peak amplitude-

frequency analysis method cannot determine specific properties of the rock mass, the factors associated with the indicated conditions could be investigated using other geotechnical methods such as stress modelling, deformation measurement and discontinuity modelling. Within the proposed analysis method, the term "indicated stiffness" has been used to refer to the effective elastic bulk modulus of the rock mass.

Figures 7.12 and 7.13 show the plots of vector sum peak particle velocity (VSPPV) versus vector sum peak particle acceleration (VSPPA) from measured D block vibration data. This data includes both the accelerometer and geophone measurements. The results for dA12-35 and dB10-38B are shown in Figure 7.12 and the three monitored orientations in stope dB10-38T are shown in Figure 7.13.

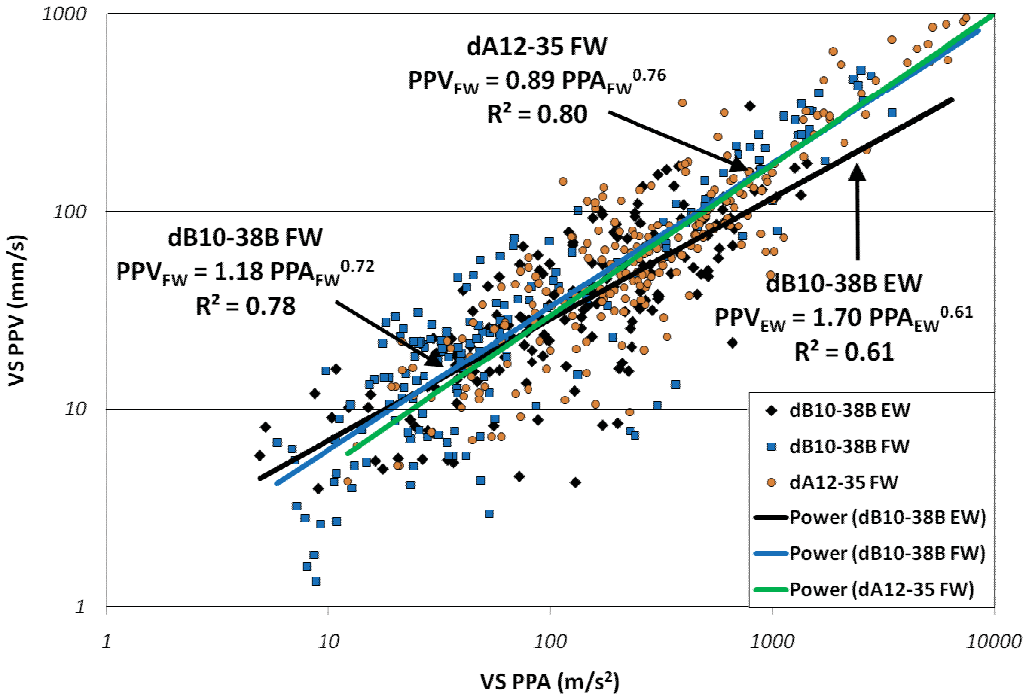

Figure 7.12. Comparison of VSPPV versus VSPPA plots (log-log axes) for the footwall of stopes dA12-35 and dB10-38B and East wall of dB10-38B.

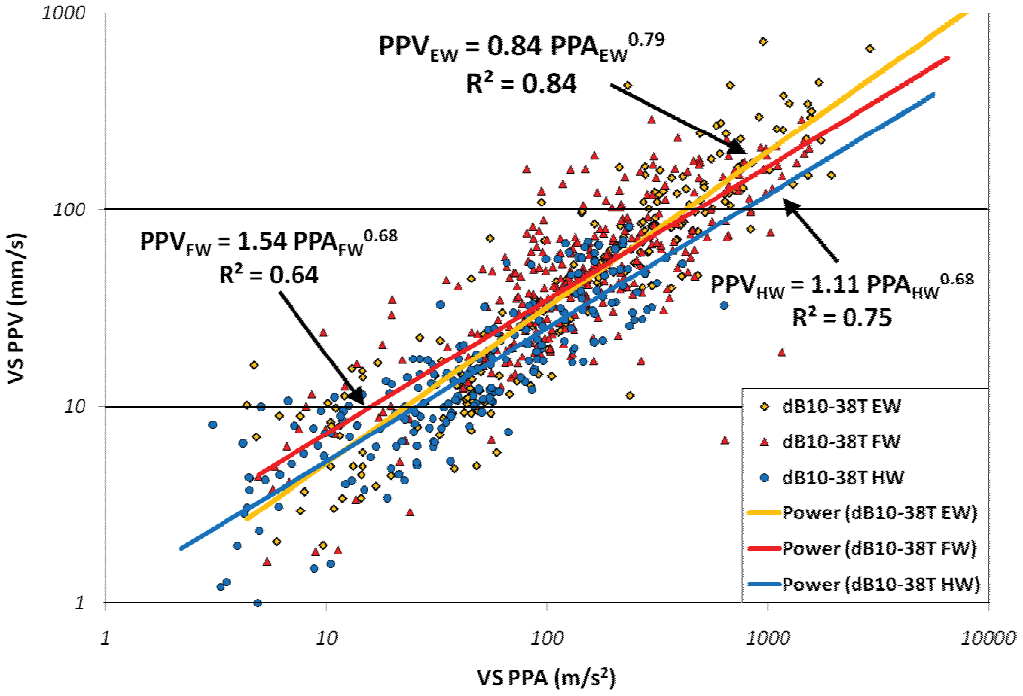

Figure 7.13. Comparison of VSPPV versus VSPPA plots (log-log axes) for the East wall, footwall and hangingwall of stope dB10-38T.

It is proposed by the author that differences between the curves fitting the data for the individual geologic units indicate variations in relative rock mass stiffness as defined by the frequency characteristics of the peak amplitudes. Any indications of rock mass stiffness or condition drawn from these results have been compared with other methods of rock mass assessment throughout this chapter.

Due to considerable scatter of data points around the best fit lines shown in Figures 7.12 and 7.13, it is arguable whether or not the data sets differ statistically. Comparisons of the 95% confidence bands for each data set over the represented ranges do reveal significant overlap. Additional statistical analysis is required to investigate the differences between the individual relationships.

The results in Figures 7.12 and 7.13 have been combined and compared to gain a more comprehensive understanding of the influence of geology on the frequency characteristics of the blast waves in D block. The best fit lines defined in Figures 7.12 and 7.13 have been shown in Figure 7.14 in linear-linear axes as opposed to log

axes to better represent differences in curve shapes. The axes have also been shifted in range to allow better visual separation of the best fit curves.

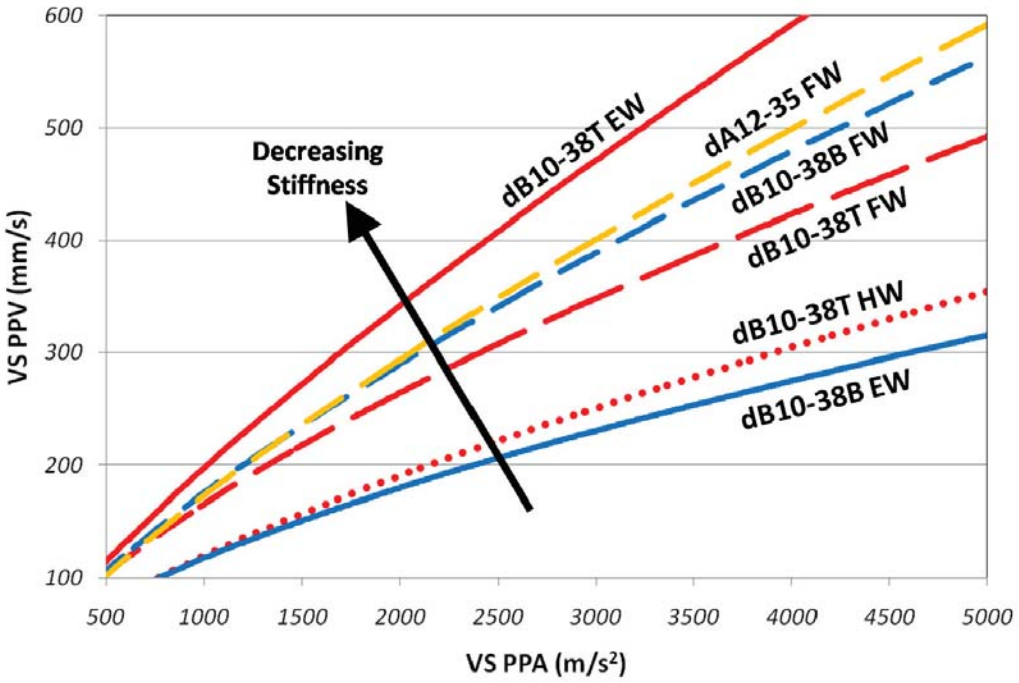

Figure 7.14. Plot of best-fit lines of VSPPV versus VSPPA for all monitoring orientations in the D block of KBGM.

Differences in relative indicated stiffness for different rock units are implied from the peak amplitude-frequency analyses. Particular importance has been placed on the grouping of the footwall data sets for all three stopes (long-dashed lines), which provides some degree of validation to the method of assessment. The footwall unit would have been expected to experience the least amount of rock mass disturbance based on other assessment methods and observations of stope performance.

According to the guidelines presented in Appendix 7 for interpretation of the results of peak amplitude-frequency analysis, an increase in general rock mass stiffness is proposed as the slope of the VSPPV-VSPPA line decreases. This indication is based on the assumption that the same PPV would result in a higher PPA at a lower slope, thus indicating a higher stiffness due to an increase in frequency-supporting characteristics of the rock mass. According to this interpretation, the East wall of stope dB10-38B would have been the stiffest unit, followed by the hangingwall unit

of stope dB10-38T. The occurrence of high stiffness for the hangingwall unit can be partially validated by the results of the static rock testing, where the hangingwall intact rock displayed the highest static Young's Modulus. The reduced stiffness for the East wall of dB10-38T was believed to largely reflect the damage that is regularly observed in the end-walls of the stopes in D block due to stress redistribution and dilation of existing discontinuities (Malatesta, 2006).

Care must be taken when comparing the results of stress wave velocity measurements with peak amplitude-frequency indications of rock mass stiffness in this thesis. The data used to calculate the stress wave velocities were generated during the initial stope rise firings. These firings took place prior to any significant opening of void and localised stress redistribution associated with mining of each study stope. Therefore, the rock mass in which the transducers were installed at the time of the rise firings could be considered to be completely confined. The data collected for the peak amplitude-frequency analyses included all stope firings and therefore represented various stress redistribution and rock mass confinement conditions. Where the results of the two analysis methods appear to disagree in regards to the indicated rock mass conditions, other measurement or modelling methods have been discussed. These include the interpretation of mining-induced static stress modelling and the intact rock testing results. Further research with controlled seismic waves would be required to investigate correlations between the various characterisation approaches.

7.6 Blast Vibration Analysis Results of Combined D block Data

All blast vibration data recorded in the D block has been analysed as a combined data set to investigate the general influence of charge weight and distance on various blast vibration characteristics. These characteristics include the instantaneous amplitudes VSPPV and VSPPA and the values based on the entire wave duration such as the integrated area under the squared velocity waveform ($A_{W\text{-}tot}$), stored strain energy density ($ED_{W\text{-}SS}$) and the mean normal dynamic strain ($\varepsilon_{W\text{-}MN}$). As described previously in Chapter 6, values for $ED_{W\text{-}SS}$ and $\varepsilon_{W\text{-}MN}$ require calculation from the recorded waveforms and various intact rock and rock mass properties.

The first step in analysis of the combined D block blast vibration data set was to perform a traditional peak amplitude analysis using the values of VSPPV and VSPPA. The analysis was then extended to the duration-dependent area under the $VSPV^2$ waveform ($A_{W\text{-}tot}$). VSPPV, VSPPA and $A_{W\text{-}tot}$ do not depend on rock density, stress wave velocity, Young's Modulus or any other rock property. Therefore, these quantities could be viewed as directly-measured blast vibration characteristics.

The general charge weight scaling relationship (Equation 5.2) and the nonlinear, multi-variable estimation approach was used to determine the regression constants, *K*, *b* and *n* for the combined data set. Table 7.4 lists both the best-fit and 95% upper confidence regression constants for VSPPV, VSPPA and $A_{W\text{-}tot}$ along with the coefficient of correlation (R value).

Table 7.4. Best-fit and 95% upper confidence regression constants and correlation coefficients from multi-variable, nonlinear estimation of the KBGM D block combined data set.

Model	**Data Points**	***K***	***B***	***n***	**R Value**
Best-fit VSPPV (mm/s)	1333	4023.4	0.053	-1.407	0.34
95% VSPPV		6600.2	0.151	-1.194	
Best-fit VSPPA (m/s^2)	1333	70195.9	-0.080	-1.170	0.36
95% VSPPA		122742.1	0.035	-1.455	
Best-fit $A_{W\text{-}tot}$ (mm^2/s)	1333	19949.9	0.366	-2.434	0.25
95% $A_{W\text{-}tot}$		49408.2	0.602	-1.920	

Further rock mass data were required to calculate values of blast vibration energy and strain using the methods proposed in Chapter 6. As previously discussed, these material properties included the rock density, dynamic Young's Modulus, Poisson's Ratio and the P-wave velocity. The Young's Modulus measured in the laboratory during quasi-static testing was not used to calculate Lame's constant (Equation 6.29) required for estimation of the mean normal dynamic strain, $\varepsilon_{W\text{-}MN}$ (Equation 6.28). The differences between the static and dynamic Young's Modulus discussed in Chapter 2 and the large variability in observed orientation-dependent stress wave

velocities in D block suggested that the dynamic in situ Young's Modulus would be required. The dynamic Young's Modulus (E_{dyn}) was calculated for each stope wall according to Equation 2.15 using the measured P-wave wave velocities and the quasi-static Poisson's Ratios from laboratory core testing. The quasi-static Poisson's Ratios were used to calculate E_{dyn} due to a lack of information on the differences in P-wave and S-wave velocities. In addition, the actual differences between the static and dynamic values of Poisson's Ratio when comparing laboratory and field measurements have been inconsistent (e.g. Van Heerden, 1987 and Lin and Heuze, 1987). For this reason, the quasi-static value of Poisson's Ratio as determined from laboratory rock testing has been used in all further calculations. Accurate values for V_p and ρ were more critical for the calculation of E_{dyn} than Poisson's Ratio, especially with the large variations in V_p that were observed from field data.

The values of E_{dyn} and λ_L were calculated from the measured rock properties and used in calculation of the stored strain energy density ($ED_{W\text{-}SS}$) and mean normal dynamic strain ($\varepsilon_{W\text{-}MN}$). Nonlinear estimations were performed similar to those for VSPPV, VSPPA and $A_{W\text{-}tot}$. The regression constants are listed in Table 7.5.

Table 7.5. Best-fit and 95% upper confidence regression constants for stored strain energy density ($ED_{W\text{-}SS}$) and mean normal strain $\varepsilon_{W\text{-}MN}$ for the combined data set from all three stopes monitored at KBGM.

Model	**Data Points**	***K***	***b***	***n***	**R Value**
Best-fit $ED_{W\text{-}SS}$ (J/m^3)	1333	107180	-0.40	-2.4	0.25
95% $ED_{W\text{-}SS}$		265449	0.70	-1.90	
Best-fit $\varepsilon_{W\text{-}MN}$ (με)	1333	530.7	0.393	-1.451	0.38
95% $\varepsilon_{W\text{-}MN}$		862.85	0.497	-1.254	

The combined D block $\varepsilon_{W\text{-}MN}$ data set is shown in Figures 7.15 and 7.16 along with the three-dimensional surfaces defined by the best-fit and 95% upper confidence regression constants listed in Table 7.5.

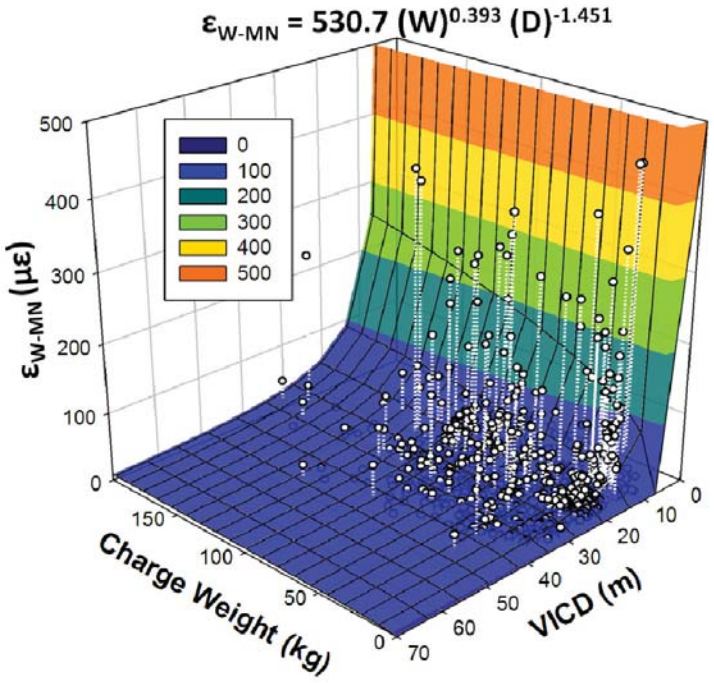

Figure 7.15. Best-fit surface from multi-variable nonlinear estimation of $\varepsilon_{W\text{-}MN}$ versus charge weight and VICD for all KBGM D block data.

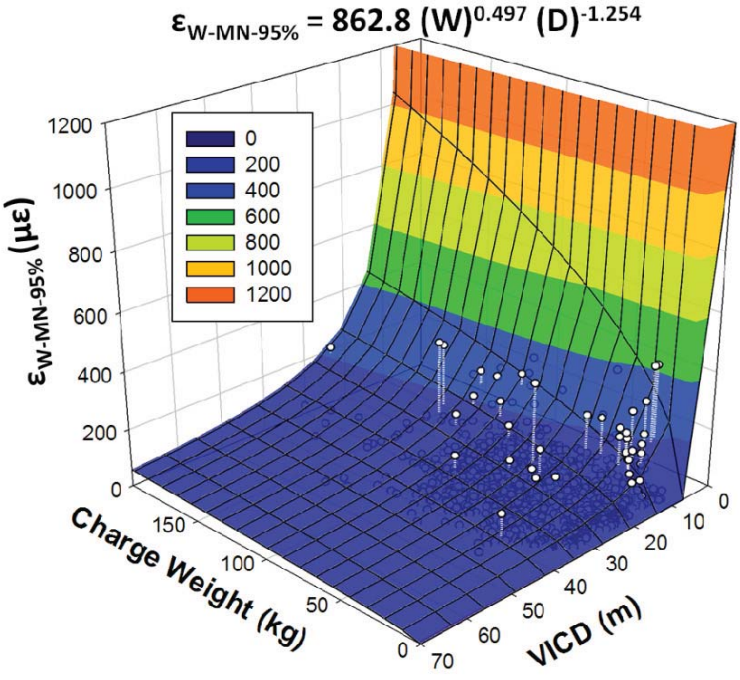

Figure 7.16. 95% upper confidence prediction surface from multi-variable nonlinear estimation of $\varepsilon_{W\text{-}MN}$ versus charge weight and VICD for all KBGM D block data.

The low correlation values observed in Tables 7.4 and 7.5 for all regressions of the combined D block data set identified characteristically different behaviours between data subsets based on individual stopes or orientations. Therefore, segregation of the data according to the individual stope, separate stope wall (monitoring orientation) and distance range (transducer type) was performed. This segregation of data typically resulted in an increase in prediction correlations. Separation of the data into subsets also identified differences in vibration attenuation behaviours at different locations and orientations within the rock mass. These differences in vibration behaviours highlighted the importance of monitoring blasting vibrations along several key orientations within the rock mass. This type of monitoring would be expected to provide a more accurate model for prediction of vibrations based on the direction of wave propagation under the influence of geology and mining-induced stress conditions. Single blast-vibration monitoring points of unspecified geometry do not effectively characterise blasting vibrations for a rock mass along all orientations and locations in the near-field, where discrete geological features and induced static stress distribution can influence vibration attenuation.

All data sets collected in the three study stopes in D block were analysed with respect to PPV, PPA, $ED_{W\text{-}tot}$ and $\varepsilon_{W\text{-}MN}$. For individual stopes, only the results for the regressions of $ED_{W\text{-}SS}$ and $\varepsilon_{W\text{-}MN}$ have been provided due to the damage criteria adopted in the proposed blast damage prediction approach. Results of the other regressions are included in Appendix 9.

7.7 dA12-35 Individual Stope Analysis

Stope dA12-35 was a single-lift stope on the Eastern mining front between the 9380RL and 9350RL and was the first stope monitored at KBGM. The newly-acquired blast vibration monitoring equipment was calibrated in dA12-35 prior to full-scale monitoring of dB10-38B and dB10-38T. As a test stope, limited instrumentation was installed to monitor blasting in dA12-35.

The geotechnical rock mass characterisation performed for stope dA12-35 is discussed in Section 7.7.2. This characterisation included the results of discontinuity mapping, stress-wave velocity measurements and rock mass stiffness assessment

(peak amplitude-frequency analysis). A brief investigation of the blast vibration monitoring results is also briefly discussed along with a review of the post-extraction void analysis. No prediction of the extent of blast damage or stress modelling was performed for dA12-35.

7.7.1 dA12-35 Blast Vibration Monitoring Instrumentation

A single transducer array was installed in the footwall of stope dA12-35 after commissioning of the new blast vibration monitoring equipment. The first transducer in the array was a 500g tri-axial accelerometer, located approximately 7m from the perimeter of the stope at the mid-span elevation (9367RL). Due to the location of the footwall shear in respect to the stope boundary, the accelerometer was technically located within the orebody. The second transducer on the footwall array was a tri-axial geophone sonde, located within the footwall unit 16.7m from the stope perimeter. The different geological units containing each transducer were accounted for in calculations of blasting energies and strains by using different values of rock density and elastic properties. A cross section of stope dA12-35 and the location of the footwall transducers are illustrated in Figure 7.17.

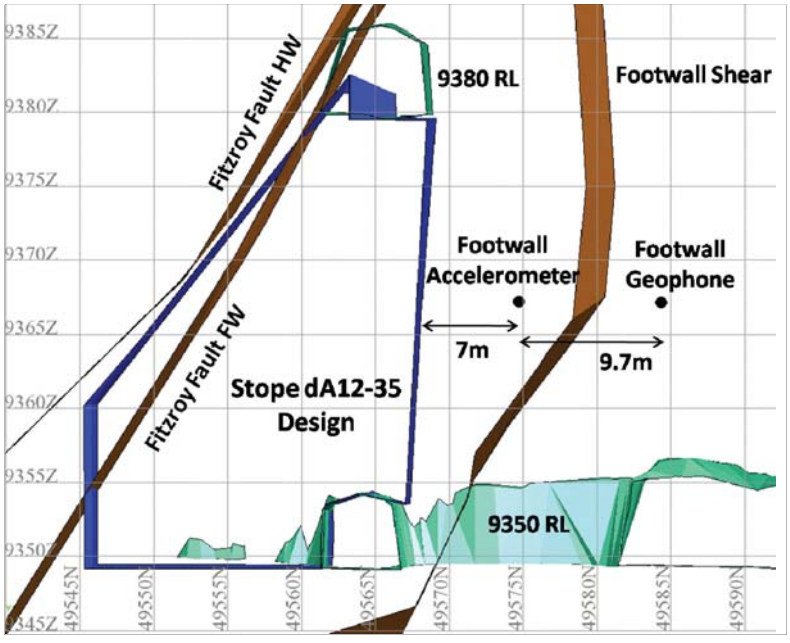

Figure 7.17. Cross section of stope dA12-35 showing the Fitzroy Fault, footwall shear and the installed footwall transducer locations (looking west).

7.7.2 Characterisation of dA12-35 Rock Mass

The static rock strengths and elastic properties for stope dA12-35 were identical to those presented in Table 7.2. The rock testing data for D block were limited in nature. Specific testing of extracted rock blocks or core around each study stope would have been required to obtain more accurate location-specific values. In the absence of additional testing, the results from previous testing have been used.

7.7.2.1 Discontinuity Orientation Distributions from Mapping

The database of mapping results presented in Figure 7.9 for the entirety of D block have been subdivided by level and Easting to obtain only the results for the 9350RL and 9380RL in the vicinity of the Eastern mining front. These results were used to determine the discontinuity distributions for stope dA12-35. The resulting stereonet polar plot is shown in Figure 7.18.

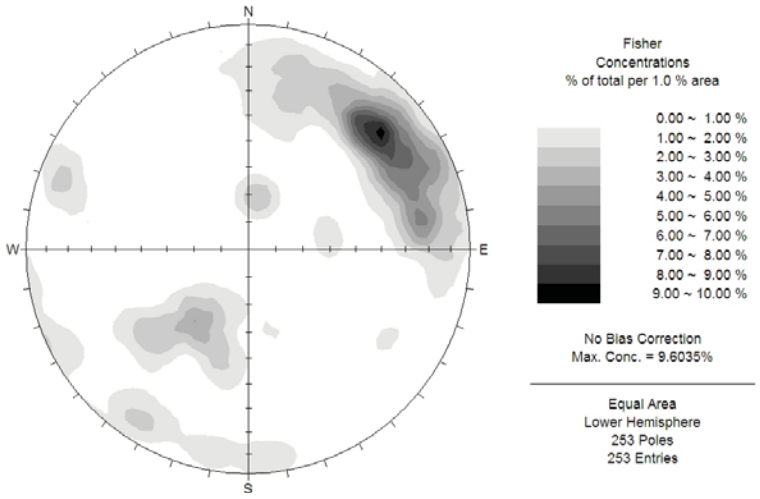

Figure 7.18. Discontinuity mapping results for levels 9350RL and 9380RL in the vicinity of stope dA12-35.

The distribution of discontinuities in Figure 7.18 closely resembles the distribution observed in Figure 7.9 for all D block mapping. The percentage of total mapped structures was higher along the dip/dip direction of 70/230, as characterised by the darker colours within the contours. This predominant orientation was largely accounted for by the splay zones near the footwall shear of close spacing (100-250mm) as opposed to the random spacing of other discontinuity sets.

7.7.2.2 Stress Wave Velocities from Blast Vibration Monitoring Results

The differential stress wave velocities for the footwall of stope dA12-35 were determined using the rise firing holes plus additional holes in the toe firings and sill blast. These charges were selected due to the short charge lengths and the relatively low impact of the rise void on the wave travel path. Figure 7.19 illustrates the results of the stress-wave calculations and the average value used in further calculations of seismic parameters and blast vibration analyses.

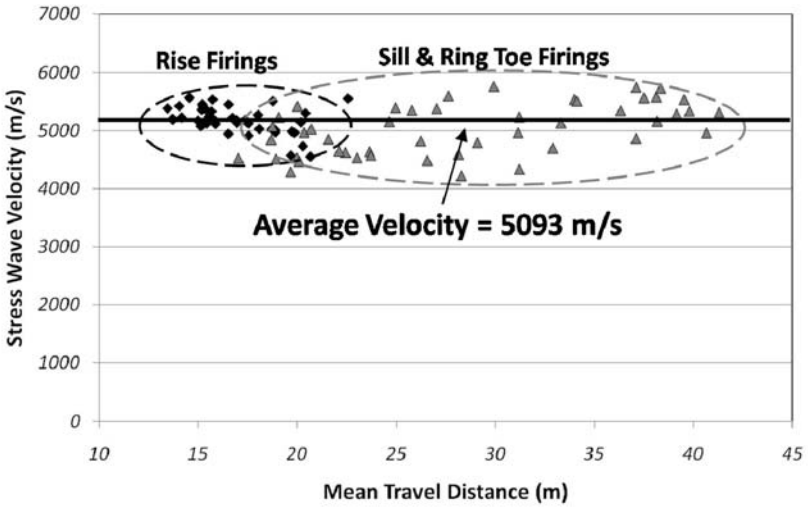

Figure 7.19. Differential stress-wave velocities using blasthole seismic sources for the KBGM stope dA12-35 footwall.

E_{dyn} and λ_L were determined for the dA12-35 footwall rock mass using the value of V_p identified in Figure 7.19 (5093 m/s) and the intact rock properties (ρ and v) listed in Table 7.2. These values are listed in Table 7.6.

Table 7.6. Rock mass properties for dA12-35 footwall monitoring direction.

Wall	Rock Density (kg/m^3)	Calculated E_{dyn} (GPa)	Poisson's Ratio	Wave Velocity (m/s)	λ_L (GPa)
Footwall Ore	2760	56	0.28	5093	28
Footwall Unit	2770	55	0.29	5093	29

The calculated values of E_{dyn} in Table 7.6 appear to contradict what might be expected when compared with the static testing results. As discussed in Chapter 2, E_{dyn} would be expected to be higher than E_{st} for an intact rock sample. The values of E_{dyn} in Table 7.6 for the in situ rock mass are significantly lower than the values determined from quasi-static testing of intact rock samples. Although E_{dyn} is expected to be higher than E_{st} for intact rock, dynamic elasticity of in situ rock masses determined from stress wave testing is dependent on many more factors. These factors include static stress conditions and the degree and characteristics of in situ rock mass jointing. The high degree of rock mass fracturing parallel to the orebody at KBGM could have contributed to the lower in situ value of E_{dyn} for the footwall orientation when compared with E_{st}. A parametric study would be required to assess the influence of different input values on the calculated dynamic rock mass properties.

7.7.3 Stope dA12-35 Blast Vibration Monitoring Results

The combined D block vibration data set was segregated by individual stopes and the dA12-35 data were analysed using the multi-variable nonlinear estimation method. The regression constants for $ED_{W\text{-}SS}$ and $\varepsilon_{W\text{-}MN}$ are listed in Table 7.7. Additional regression results are included in Appendix 9.

Table 7.7. Best-fit and 95% upper confidence nonlinear estimation constants of $ED_{W\text{-}SS}$ and $\varepsilon_{W\text{-}MN}$ for the footwall of dA12-35.

Model	Data Points	*K*	*b*	*n*	R Value
Best-fit $ED_{W\text{-}SS}$	220	430846.4	-0.573	-1.545	0.25
95% $ED_{W\text{-}SS}$	220	1879513	0.100	-0.320	
Best-fit $\varepsilon_{W\text{-}MN}$	220	1018.9	-0.141	-0.939	0.26
95% $\varepsilon_{W\text{-}MN}$	220	2668.0	0.159	-0.356	

The analysis of the combined data set for the dA12-35 footwall accelerometer and geophone resulted in poor coefficients of correlation (R values). Consequently, there would be little confidence in the ability to predict the vibration values for similar

blasting conditions. In addition to the low R values, the negative slopes for the best-fit *b* values clearly indicate an erroneous relationship between charge weight and energy or strain as expected from the assumed charge weight scaling. These model errors could be attributed to a lack in the ability of the general charge weight scaling relationship to describe near-field vibrations, errors in data collection or analysis, or physical effects of the footwall shear on the measured vibrations.

In response to the low correlation values in Table 7.7, separate nonlinear estimations were performed for each footwall transducer data set. These analyses examined the effects of the two distance ranges (near-field and intermediate-field) on the calculated values of $ED_{W\text{-}SS}$ and $\varepsilon_{W\text{-}MN}$. The resulting correlations for each transducer in the array yielded much different results at each monitoring point (as shown in Appendix 9). Regressions of the accelerometer data provided low correlations, similar to the combined data set, whereas the analysis of the geophone data provided much higher correlation values. The results of the nonlinear estimations for the geophone data are listed in Table 7.8.

Table 7.8. Best-fit and 95% upper confidence nonlinear estimation constants of $ED_{W\text{-}SS}$ and $\varepsilon_{W\text{-}MN}$ for the footwall geophone data in stope dA12-35.

Model	**Data Points**	***K***	***b***	***n***	**R Value**
Best-fit $ED_{W\text{-}SS}$	110	63742.7	1.310	-3.570	0.49
95% $ED_{W\text{-}SS}$		486121	1.90	-1.40	
Best-fit $\varepsilon_{W\text{-}MN}$		3042.1	0.605	-2.246	0.61
95% $\varepsilon_{W\text{-}MN}$		11016.6	0.780	-1.380	

The regression constants listed in Table 7.8 more closely follow those expected for the relationship between charge weight, distance and any vibration amplitude or intensity characteristic. The poor correlation values for the combined data set and the initial problems with accelerometer saturation in stope dA12-35 led to the use of only geophone data to represent the $ED_{W\text{-}SS}$ and $\varepsilon_{W\text{-}MN}$ prediction equations for the stope. The 95% upper confidence prediction equations were adopted for future estimation

of vibrations to ensure the predicted values would not exceed an upper threshold. The resulting prediction relationships are shown in Equations 7.2 and 7.3.

$$ED_{W\text{-}SS(95\%)} = 486121\ (W)^{1.90}\ (D)^{-1.40} \quad (7.\ 2)$$

$$\varepsilon_{W\text{-}MN(95\%)} = 11016.6\ (W)^{0.78}\ (D)^{-1.38} \quad (7.\ 3)$$

Due to the inadequate amount of information collected for stope dA12-35, no attempt was made to predict the blast-induced rock mass damage using the criteria developed in Chapter 6.

7.7.4 Post-Mining Stope Performance Assessment

Post-extraction stope performance assessment for each study stope in D block was performed by comparing the post-extraction CMS survey results with the individual stope designs. Solids tools in SURPAC were used to evaluate the post-extraction CMS wireframe against the designed stope wireframe using an "outersection" function. The outersected wireframes represented the stope overbreak and underbreak (Figure 7.20). A wireframe reporting function was used to determine the total volumes of overbreak and underbreak from the two wireframes. Figure 7.20 shows the result of outersection of the design and CMS wireframes.

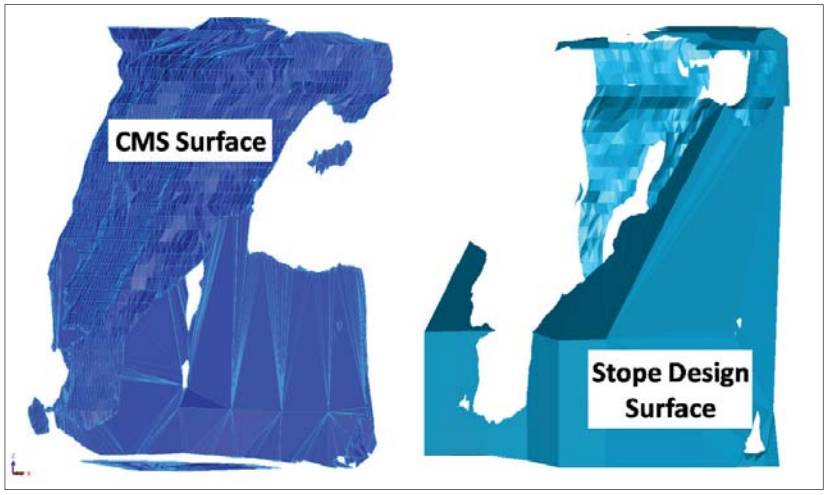

Figure 7.20. Overbreak volume (left) and underbreak volume (right) from comparing the CMS survey wireframe and the design stope wireframe for stope dA12-35.

The results of the volumetric analysis as well as the stope overbreak and underbreak expressed as percentages of the design stope volume are displayed in Table 7.9.

Table 7.9. Stope overbreak and underbreak calculations resulting from outersection of the post-extraction CMS and the design wireframes for stope dA12-35

Stope Performance Criteria	Volume (m^3)	% of Design Volume
Total Overbreak	2231	18.4%
Total Underbreak	1389	11.5%

In addition to volumetric analyses, horizontal and vertical planes passing through the design and CMS wireframes were examined to determine the values of maximum depth of overbreak for each stope wall. An example set of horizontal and vertical sections are illustrated in Figures 7.21 and 7.22 showing locations of perimeter blastholes, charges in a blasthole ring, neighbouring fill masses and the shaded areas of overbreak (blue) and underbreak (red).

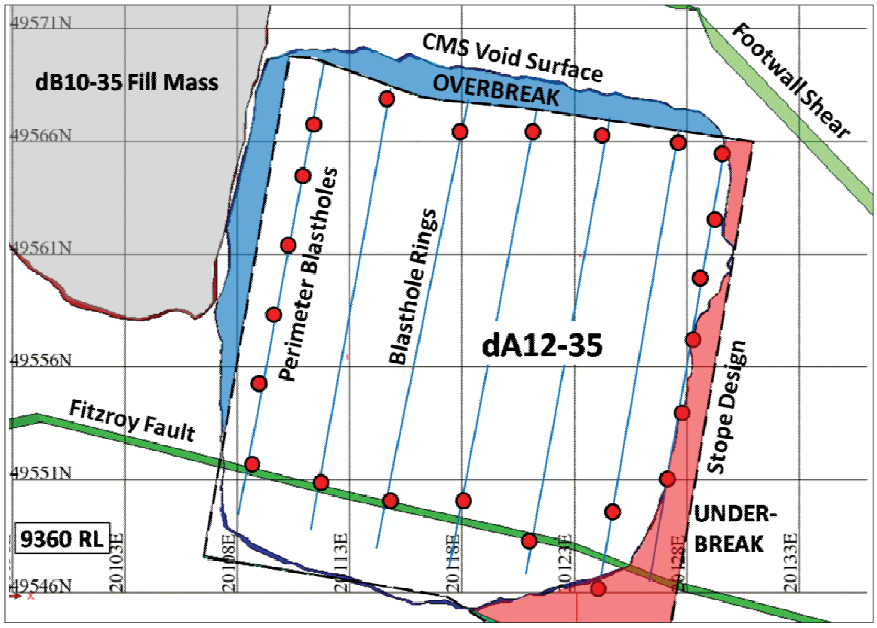

Figure 7.21. Plan view of stope dA12-35 CMS and design wireframes at 9360m elevation showing areas of overbreak (blue), underbreak (red) and perimeter blastholes.

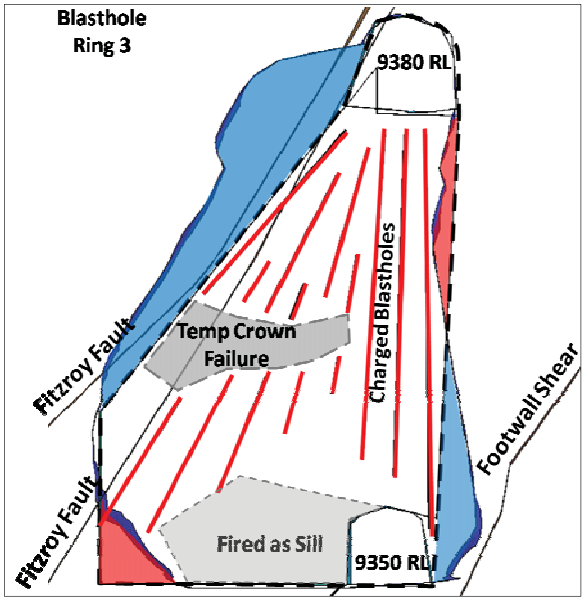

Figure 7.22. Cross section of stope dA12-35 CMS and design wireframes along blasthole ring 3 showing areas of overbreak (blue), underbreak (red) and blasthole charges (looking West).

The maximum depth of overbreak for each stope wall was determined from analysis of all horizontal sections cut through the wireframes. Sections where development drives extended outside of the stope boundary or significantly undercut a stope wall were not used to determine the depth of overbreak due to the influence of the existing void on the rock mass performance. The values for maximum depth of overbreak for dA12-35 are listed in Table 7.10.

Table 7.10. Maximum depth of overbreak in each wall of stope dA12-35.

Stope Wall	**Maximum Depth of Overbreak (m)**
East Wall	0
West Wall (pastefill)	1.8
Footwall	4.4
Hangingwall	7.1

An additional assessment for stope dA12-35 was possible due to close monitoring of blasthole charging logs. This assessment identified possible sources of oversize

reporting to the drawpoint. As observed in Figure 7.22, an area approximately mid-stope (gray shaded) was interpreted from blasthole breakthrough and charging logs. The logs identified blastholes where the depth of recorded breakthrough was significantly offset from the charge collars of the previous firing, thus indicating unblasted material. During stope production, significant oversize was experienced in dA12-35, with oversize blocks being largely tetrahedral in shape (Fleetwood, 2010). The possible source, as indicated by the charging logs, was rock mass failure along existing discontinuities exposed by the unconfined temporary stope crown.

7.8 dB10-38B Individual Stope Analysis

Stope dB10-38B was the second study stope selected on the East mining front of D block. Stope dB10-38B was the first lift (bottom) of a double lift stope located between the 9380RL and 9440RL, with an intermediate sublevel at the 9410RL. Stope dB10-38B was bordered by footwall shear to the North, the central fill mass to the West and the dA10-38 fill mass to the South. The in-stope firing sequence was that of a standard, flat-bottom single-lift stope (Figure 7.4). Figure 7.23 shows both dB10-38B and dB10-38T in relation to the central fill mass and the Fitzroy Fault.

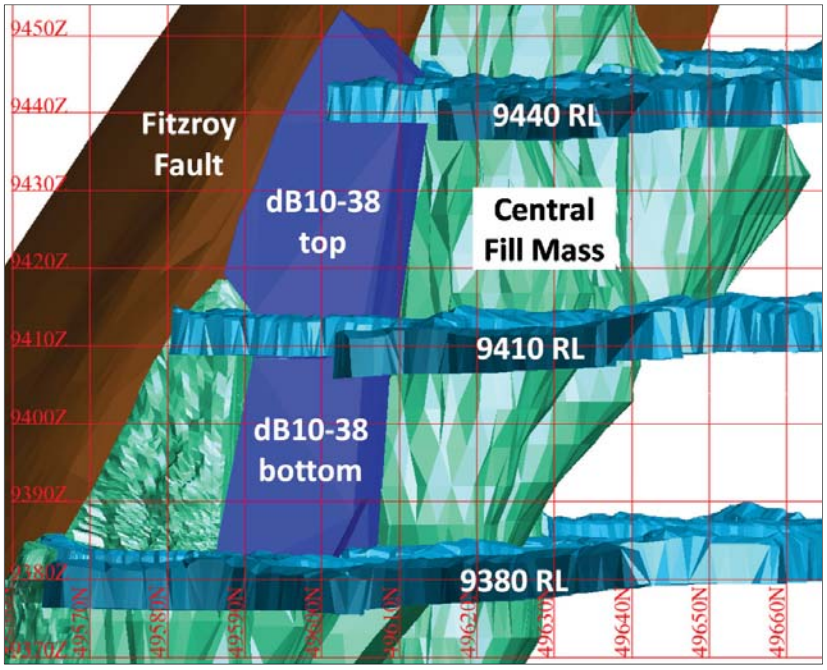

Figure 7.23. Isometric view of stope dB10-38B and dB10-38T (looking west).

7.8.1 dB10-38B Blast Vibration Monitoring Instrumentation

Two arrays of transducers were installed in dB10-38B to measure blasting vibrations in the two intact (non-fill) walls of the stope. The two walls were referred to as the stope East wall (EW) and the stope footwall (FW). A plan view of the installed blast vibration monitoring instrumentation is shown in Figure 7.24.

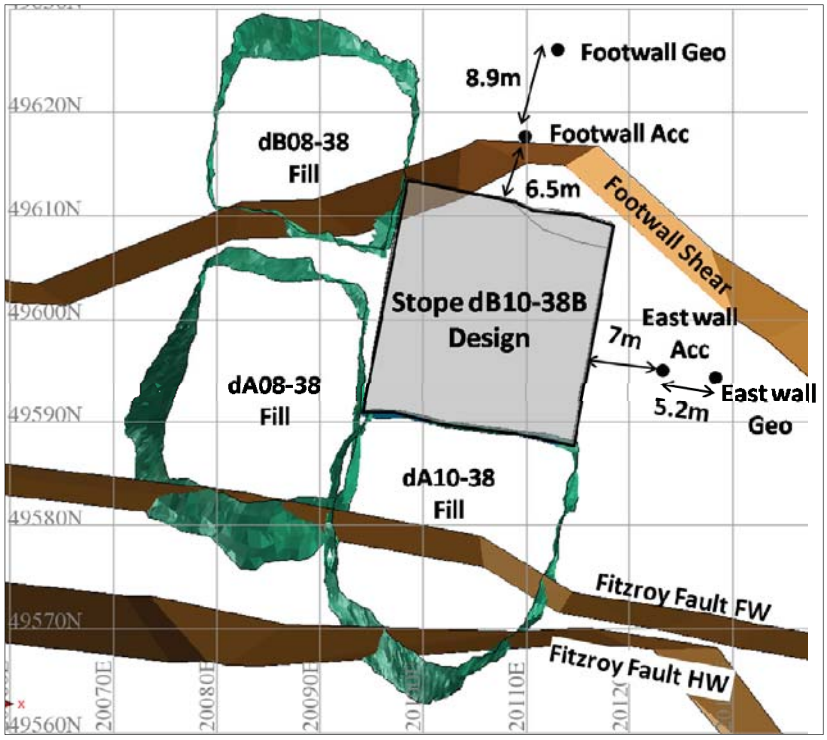

Figure 7.24. Plan view of stope design dB10-38B showing sensor locations, adjacent fill masses and faults at 9395RL.

7.8.2 dB10-38B Rock Mass Characterisation

The same characterisation and analysis techniques used for dA12-35 were carried out for dB10-38B. Similar trends were observed for the data collected for dB10-38B when compared with dA12-35. Significant variations in stress wave velocities, blast vibration attenuations and stope performance were observed for each wall of the stope. Table 7.11 lists the results of stress wave velocity measurements in the two instrumented stope walls.

Table 7.11. Stress wave velocities for the footwall and East wall of dB10-38B.

Stope Wall	Stress Wave Velocity (m/s)
East Wall	4750
Footwall	5000

Observed differences between the wave velocities calculated for each wall of the stope may have been influenced by both the existing discontinuity orientation and the mining-induced static stress distribution around the central fill mass. A high frequency of steeply-dipping discontinuities was mapped striking approximately 20 degrees west of north. This discontinuity set would have been intersected more frequently for the East wall wave-path than for the footwall, possibly contributing to the reduction in the wave velocity. The differences between the observed wave velocities were investigated further using peak amplitude-frequency analysis. The plots of VSPPV versus VSPPA for the East wall and footwall accelerometers are shown in Figure 7.25.

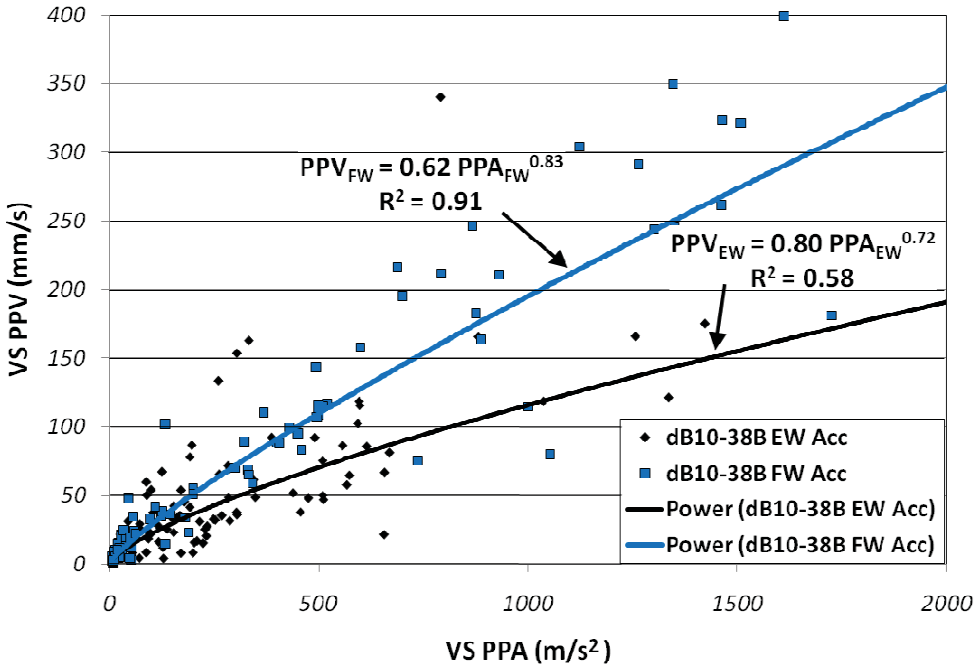

Figure 7.25. Plot of VSPPV versus VSPPA for stope dB10-38B East wall and footwall accelerometers and the best-fit equations.

Comparing the rock mass conditions suggested by the stress wave velocities and the peak amplitude-frequency analyses reveals disagreement between the two approaches for dB10-38B. The higher relative stiffness suggested for the East wall by the peak amplitude-frequency analysis was not reflected in the stress wave velocity. Higher rock mass stiffness would be expected to have a higher relative P-wave velocity, but frequency-supporting characteristics do not necessarily indicate a higher wave velocity, especially in the presence of a major zone of fracturing such as the footwall shear zone.

It must be noted that both the differential stress wave velocity and indication of stiffness using peak amplitude-frequency analysis would be expected to contain inherent flaws. Both approaches require additional research to explicitly characterise the rock mass conditions associated with variations in the values. Both methods of analysis effectively assess conditions within a volume of rock, but can represent different rock mass parameters as a function of fracturing and induced stresses. Additional factors that must be considered when comparing the results of the two methods include the action of the mining-induced static stress distribution and the differences between the peak and maximum wave frequencies.

7.8.3 dB10-38B Blast Vibration Monitoring Results

One issue worth noting is that the East wall accelerometer vibration data were initially held in question due to a water-bearing discontinuity intersecting the instrumentation hole. Extreme difficulties were encountered during installation of the transducer, as dewatering of the hole was ineffective. Coupling conditions of the accelerometer were questionable due to the presence of water and the use of a thickened cement grout mixture to displace the water and achieve coupling. Analysis of the frequency content of recorded signals validated the coupling of the transducer.

Tables 7.12 to 7.14 present the results of the calculated dynamic rock mass properties and the results of nonlinear estimations of the vibration data. The 95% upper confidence regression results (Tables 7.13 and 7.14) have been presented for both the cumulative data sets (accelerometer and geophone data together) and then subdivided into single transducers. Additional results are listed in Appendix 9.

Table 7.12. In situ dynamic rock mass properties as indicated for stope dB10-38B.

Wall	Rock Density (kg/m^3)	Calculated E_{dyn} (GPa)	Poisson's Ratio	Wave Velocity (m/s)	λ_L (GPa)
East Wall	2760	49	0.28	4750	24
Footwall	2770	53	0.29	5000	28

Table 7.13. 95% upper confidence regression results for the East wall and footwall data sets.

Model	Stope Wall	Data Points	*K*	*b*	*n*	Best-Fit R Value
95% $ED_{W\text{-}SS}$	Footwall all	180	8.36×10^9	-0.298	-3.738	0.69
95% $\varepsilon_{W\text{-}MN}$	Footwall all	180	2.73×10^6	-0.355	-2.607	0.79
95% $ED_{W\text{-}SS}$	East Wall all	175	6.54×10^5	1.126	-3.715	0.90
95% $\varepsilon_{W\text{-}MN}$	East Wall all	175	2414.5	0.514	-1.691	0.80

Table 7.14. 95% upper confidence regression results for the dB10-38B individual East wall and footwall transducer data sets.

Model	Transducer	Data Points	*K*	*b*	*n*	Best-Fit R Value
95% $ED_{W\text{-}SS}$	FW Acc	96	6.29×10^9	-0.173	-2.975	0.65
95% $\varepsilon_{W\text{-}MN}$	FW Acc	96	2.25×10^6	-0.363	-2.060	0.79
95% $ED_{W\text{-}SS}$	FW Geo	84	2.82×10^6	3.199	-4.330	0.83
95% $\varepsilon_{W\text{-}MN}$	FW Geo	84	7715.2	1.069	-1.771	0.75
95% $ED_{W\text{-}SS}$	EW Acc	89	8.82×10^5	1.364	-3.846	0.93
95% $\varepsilon_{W\text{-}MN}$	EW Acc	89	5246.9	0.504	-1.831	0.85
95% $ED_{W\text{-}SS}$	EW Geo	86	6259.5	1.567	-1.545	0.66
95% $\varepsilon_{W\text{-}MN}$	EW Geo	86	822.5	0.734	-1.095	0.70

For all data collected in stope dB10-38B, high correlation values were observed in both the combined and transducer-specific nonlinear estimation results. The accuracy

of predicting the observed values would therefore be high. Some distinct differences were noted in the regression constants for each orientation and consequently for individual transducers in each array. A two-dimensional representation of the stope wall regression results at a charge weight of 100kg is shown in Figure 7.26. This graph illustrates the differences between the 95% upper confidence curves for predicted $\varepsilon_{W\text{-}MN}$ between the two walls of the stope as listed in Table 7.13.

Figure 7.26. Log-log plot of the 95% upper confidence prediction curves for the footwall and East wall of stope dB10-38B for a 100kg charge weight.

The slope of the 95% upper confidence prediction curve for the footwall orientation is steeper than that for the East wall. This would suggest that the vibrations measured in the footwall experienced a higher degree of attenuation when compared with the East wall. In addition, a higher intercept value can be observed in Figure 7.26 for the footwall prediction curve. This would suggest that the transfer of explosive energy from the blastholes to the rock mass in the very near-field of the footwall would be greater due to reduced breakage or rock mass displacement effects when compared with the East wall. At approximately 21m from a 100kg charge, the predicted 95% confidence $\varepsilon_{W\text{-}MN}$ values in both the footwall and East wall orientations would be equal. Beyond this distance, the $\varepsilon_{W\text{-}MN}$ would be higher for the East wall direction.

7.8.4 dB10-38B Stope Performance Assessment-Maximum Depth of Overbreak

The results of the overbreak assessment performed for the horizontal stope slices of dB10-38B are listed in Table 7.15. Due to broken stock left in the stope at the time of the intermediate CMS survey of dB10-38B, no assessment of the volume of overbreak and underbreak was performed at this stage of mining. Assessment of the overall stope performance based on volume of overbreak and underbreak was carried out using the final CMS survey (after both lifts were extracted) and presented with the results of dB10-38T.

Table 7.15. Maximum depth of overbreak in each wall of stope dB10-38B.

Stope Wall	Maximum Depth of Overbreak (m)
East Wall	3.0
West Wall (pastefill)	2.6
Footwall	1.0
Hangingwall (pastefill)	1.0

7.9 dB10-38T Individual Stope Analysis

Stope dB10-38T was the top lift of a double-lift sequence, and located directly above stope dB10-38B. The South wall (hangingwall) of stope dB10-38T was located against the Fitzroy Fault and partially undercut by the dA10-38 fill mass. As an A-panel stope, the footwall and East wall were located in ore. The West wall of the stope was against the central fill mass. As the top lift of a double-lift sequence, dB10-38T was fired into the existing void from extraction of dB10-38B.

To aid in reducing ore loss against the Fitzroy Fault, the crown of dB10-38T was inclined to approximately vertical. The inclined crown required the use of upholes and special application of pumped emulsion explosives. The standard Dyno-Nobel LP-MS connector pyrotechnic initiation system was used for all stope firings except for the mass blast, in which electronic detonators were used.

7.9.1 dB10-38T Blast Vibration Monitoring Instrumentation

Transducer arrays were installed in the East wall (EW), footwall (FW) and hangingwall (HW) of stope dB10-38T to measure blasting vibrations. A plan view of the installed instrumentation is shown in Figure 7.27 and Table 7.16 summarises the types of transducers and the offsets from the stope boundaries.

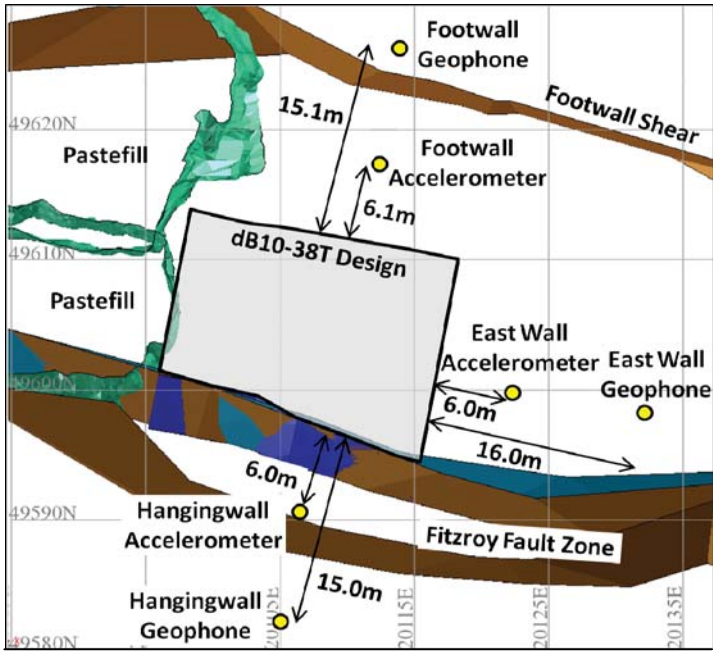

Figure 7.27. Plan view of the installed blast vibration monitoring instrumentation, adjacent pastefill and major geologic features associated with stope dB10-38T.

Table 7.16. Summary of blast vibration monitoring transducers around dB10-38T.

Wall of Stope	Transducer Type	Distance from Stope (m)
Footwall (FW)	Tri-axial 500g Accelerometer	6.1
	Tri-axial Geophone	15.1
East Wall (EW)	Tri-axial 500g Accelerometer	6.0
	Tri-axial Geophone	16.0
Hangingwall (HW)	Tri-axial 500g Accelerometer	6.0
	Tri-axial Geophone	15.0

The dense instrumentation coverage around stope dB10-38T allowed for a rigorous blast-induced vibration assessment to be performed. This assessment investigated the influence of geologic variability on measured wave properties. Transducers installed within the hangingwall rock unit also allowed for an investigation into the effects of the Fitzroy Fault on the propagation of blasting vibrations.

7.9.2 dB10-38T Rock Mass Characterisation

The rock mass characteristics of stope dB10-38T were similar to those observed for stopes dA12-35 and dB10-38B. For this reason, no rock testing or discontinuity mapping data have been discussed for the individual dB10-38T rock mass characterisation. The calculated stress wave velocities and peak amplitude frequency analyses for dB10-38T are discussed, along with an additional assessment of the influence of the Fitzroy Fault on the propagation of blast vibrations. The results of mining-induced static stress modelling around dB10-38T as a result of the mining of nearby stopes are also presented.

7.9.2.1 dB10-38T Wave Velocities and Peak Amplitude-Frequency Analyses

The plot of the stress wave velocities versus mean travel distance for each monitoring orientation is shown in Figure 7.28.

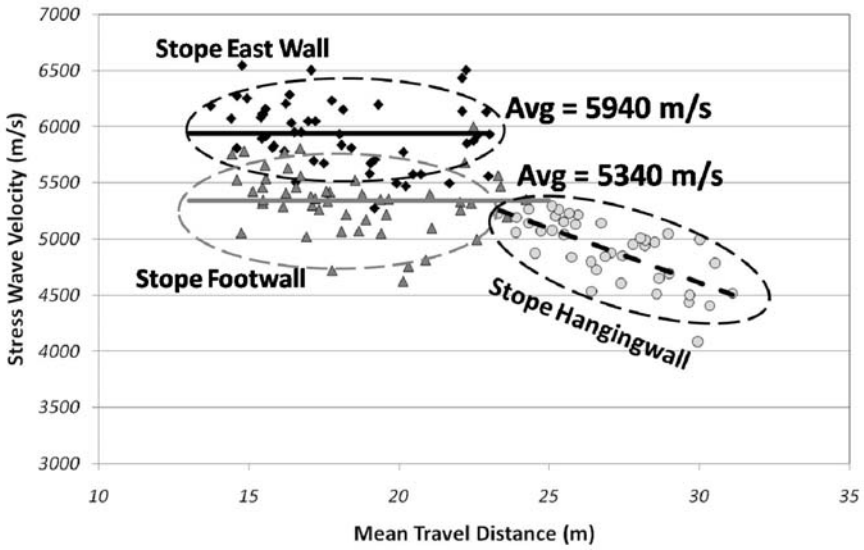

Figure 7.28. Plot of dB10-38T East wall, footwall and hangingwall stress wave velocities versus the mean geometric travel distance.

The stress wave velocities observed in Figure 7.28 for the East wall and footwall of dB10-38T are higher than those observed in dB10-38B and reversed in order of lowest to highest. Although the in situ discontinuity orientations would have been expected to be similar between the two stopes, the stress conditions would have been significantly different due to the presence of the dB10-38B void at the time of firing of dB10-38T. The change in stress conditions may have contributed to the 25% higher wave velocity for the East wall of dB10-38T when compared with the East wall of dB10-38B. The contribution of different factors to the differences in the velocity values is not known at this time and would require additional research to determine.

One factor that complicated the direct comparison of the velocity values for the footwalls of stopes dB10-38B and dB10-38T was the locations of the transducers. The accelerometer of the footwall array in stope dB10-38T was located in ore, on the stope side of the footwall shear, and the geophone was located within the footwall unit. This was similar to the transducers in the footwall of stope dA12-35. In stope dB10-38B, both footwall transducers were located in the footwall unit. According to the range in footwall stress wave velocities from the three stopes, the influence of the footwall shear was not significant. The difference of 340m/s between the lowest (5000m/s for dB10-38B) and the highest (5340m/s for dB10-38T) was only approximately 6% and well within the range of data scatter around the average values.

An interesting output of the plot of wave velocity versus distance for the hangingwall unit can be observed in Figure 7.28. With an increase in mean travel distance, the stress wave velocity is reduced (negative slope). This effect is not apparent in the other data sets. Upon further investigation, the change in travel distances from the rise charges to the hangingwall transducers corresponded with changes in the angle of incidence of the blast waves with the Fitzroy Fault. A secondary analysis of the ray-path incidence angle (θ_i) in relation to the Fitzroy Fault plane normal and the velocity was therefore performed. The analysis results are presented in Figure 7.29 and the graphical representation of the analysis is shown in Figure 7.30.

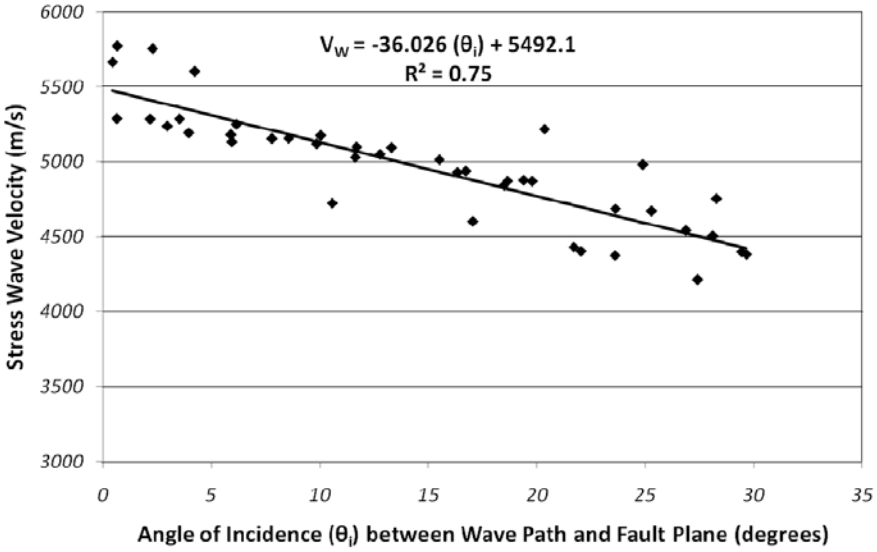

Figure 7.29. Effect of angle of incidence of the blast wave travel path with the Fitzroy Fault and the stress wave velocity.

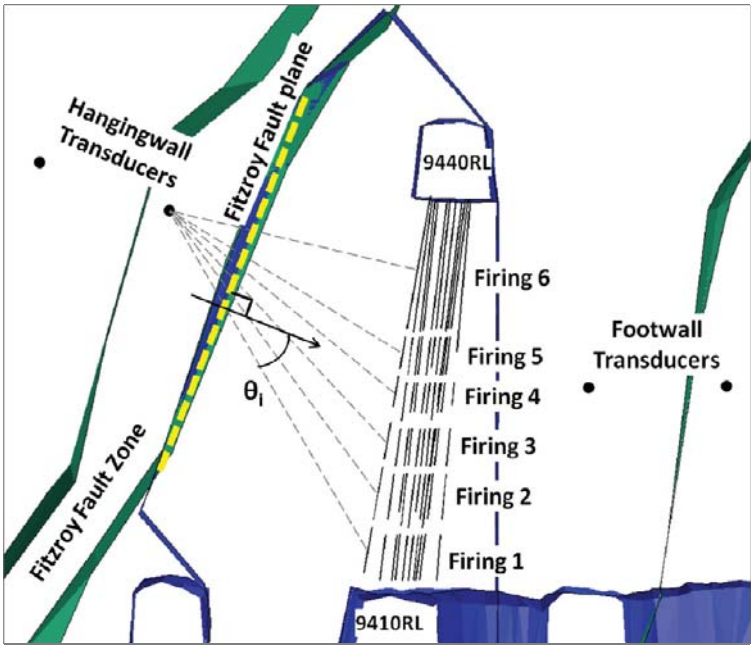

Figure 7.30. Section view of the wave travel paths and incidence angles in relation to the Fitzroy Fault plane normal for the six rise firings in KBGM stope dB10-38T.

Figures 7.29 and 7.30 indicate that higher incident angle intersections between the blast wave and the vector representing the Fitzroy Fault plane normal resulted in larger travel distances and decreased stress wave velocities. Angles of near-normal

incidence for the later rise firings resulted in higher stress wave velocities. These results agree well with the theoretical effect of the angle of incidence on the attenuation of both stress wave velocity and amplitude. The practical application of this information at the mine site is location of seismic events where the travel path between the event and the triggered transducers is interrupted by the Fitzroy Fault. Additional effects of the Fitzroy Fault on measured vibrations have been discussed by the author in a report to the Kanowna Belle Mine (Fleetwood, 2010).

Similar to the other two stopes in the study, a peak amplitude-frequency analysis was performed for the data collected in stope dB10-38T. The specific data shown in Figure 7.31 represents blast vibrations recorded by the East wall, footwall and hangingwall accelerometers.

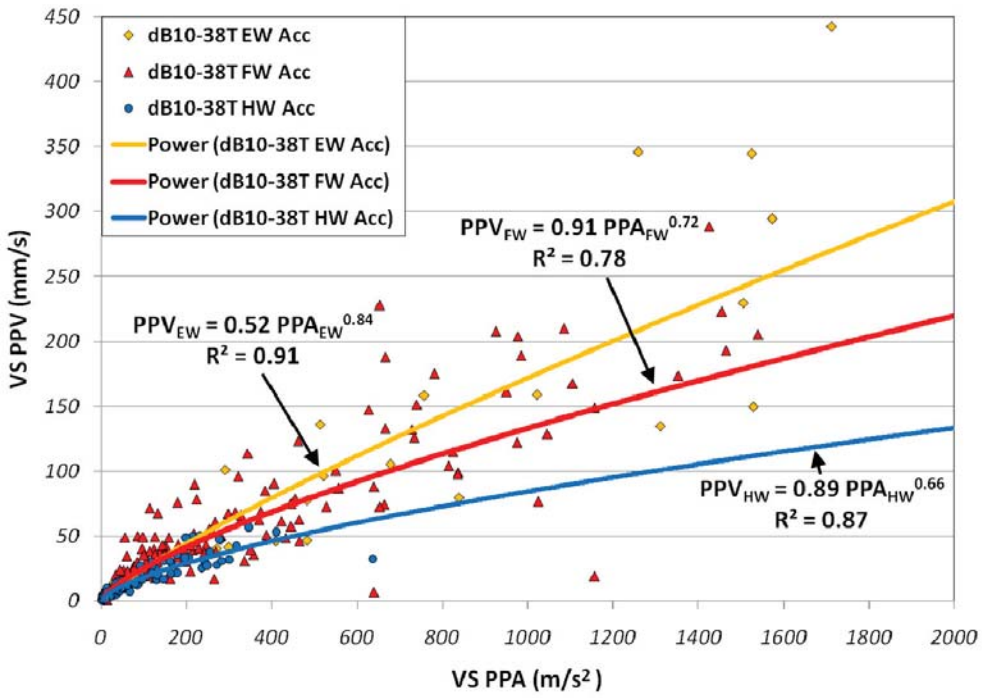

Figure 7.31. Plots of VSPPV versus VSPPA and best-fit lines for the East wall, footwall and hangingwall accelerometers around stope dB10-38T.

Figure 7.31 suggests that each geologic unit around dB10-38T had a different indicated stiffness as implied by the curve shapes, with the hangingwall unit having the highest stiffness and the East wall having the lowest stiffness. The indicated rock mass conditions using peak amplitude-frequency analyses disagreed with the rock

mass conditions implied by the stress wave velocities, but there was agreement between the peak amplitude-frequency analyses and the measured static elastic constants for each unit from rock testing.

Additional statistical analyses comparing the 95% confidence bands for the three data sets in Figure 7.31 revealed a large proportion of overlap between the East wall and footwall data sets and the footwall and hangingwall data sets (Figure 7.32). Minimal overlap between the East wall and hangingwall 95% confidence bands was observed, suggesting that the two data sets were likely statistically different. Additional statistical analysis would be required to further investigate statistical differences between the individual data distributions.

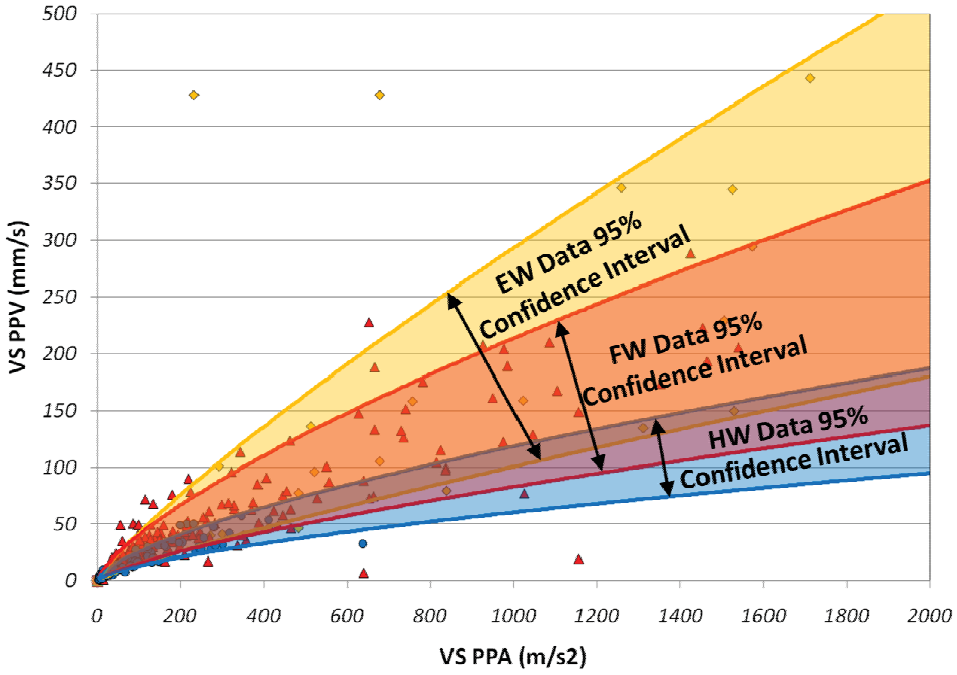

Figure 7.32. Comparison of 95% confidence bands for the VSPPV versus VSPPA plots of the East wall, footwall and hangingwall data sets pictured in Figure 7.31.

7.9.2.2 Linear-Elastic Mining-Induced Static Stress Modelling

Modelling of the magnitudes and distributions of virgin and mining-induced static stresses provides a useful tool for geotechnical engineers performing rock mass characterisations and stope performance assessments. MAP3D linear-elastic stress

modelling is a tool regularly used at KBGM for assessing the effects of stope dimensions and mining sequences on the induced static stresses. MAP3D modelling was performed for stope dB10-38T by the author using model inputs and stope designs provided by KBGM personnel. The output data from the stress models were used in additional interpretations of stope performance and prediction of strain-related blast-induced damage to intact rock around the stope. The material properties and stress field input values provided by KBGM personnel for the MAP3D stress model are listed in Table 7.17.

Table 7.17. Input values for the MAP3D pre- and post-mining stress modelling for stope dB10-38T as provided by KBGM.

Parameter	**Value**
Rock Young's Modulus	62 GPa
Poisson's Ratio	0.270
Elevation Datum	10360 m
σ_a Constant	12
σ_b Constant	5.88
σ_c Constant	0
σ_a Variation	-0.0566
σ_b Variation	-0.0374
σ_c Variation	-0.0299
σ_a Trend	117 degrees
σ_a Plunge	2 degrees
σ_c Trend	13 degrees

The values listed in Table 7.17 can be extracted to evaluate the field stresses applied in the model at the depth of mining (Equations 7.4 to 7.6).

$$\sigma_a = 0.0566 \text{ (depth)} + 12 \text{ (MPa)} \quad (7.4)$$

$$\sigma_b = 0.0374 \text{ (depth)} + 5.88 \text{ (MPa)} \quad (7.5)$$

$$\sigma_c = 0.0299 \text{ (depth)} + 0 \text{ (MPa)} \quad (7.6)$$

Upon completion of the MAP3D model for the pre- and post-mining steps, the output data fields were extracted as a text file. The file contained the three-dimensional coordinates of each point on the specified grid and the values of σ_1, σ_2 and σ_3 as calculated by the software. The number of grid points on the horizontal model plane at the 9417RL above the 9410RL development was 4077. The grid data were imported into the software SigmaPlot 10.0 and contoured to show the distribution of stress magnitudes within the horizontal modelling plane. The resulting stress contours of σ_1, σ_2 and σ_3 at the 9417RL horizontal grid prior to mining of dB10-38B and dB10-38T are shown in Figures 7.33 to 7.35.

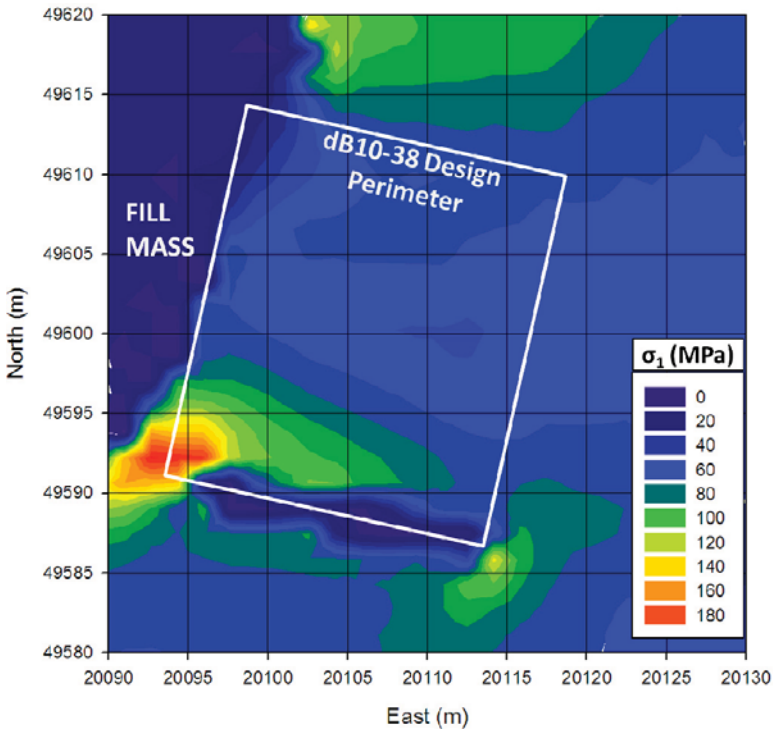

Figure 7.33. Mining-induced σ_1 static stress distribution at the 9417RL horizontal grid for the dB10-38T and dB10-38B pre-mining step.

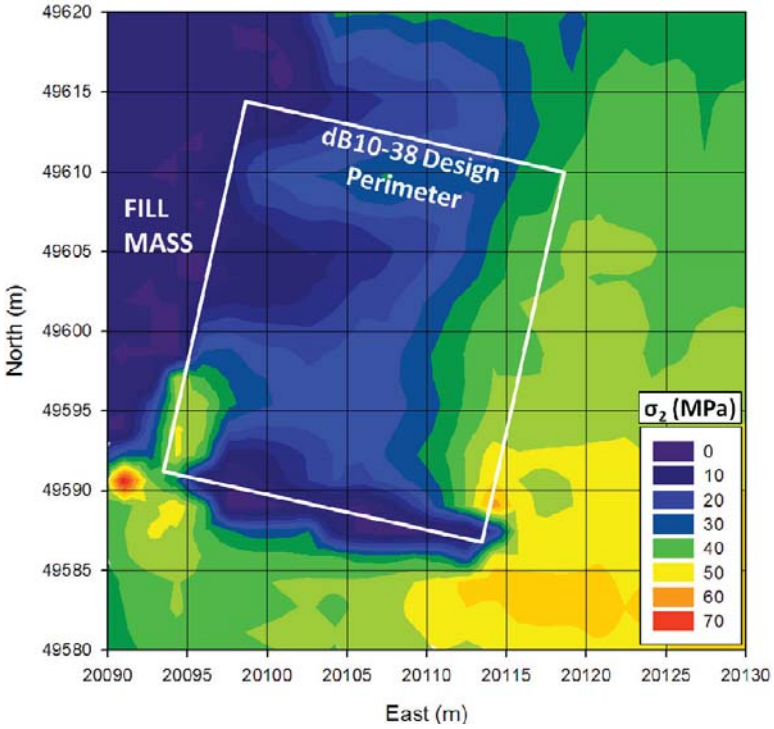

Figure 7.34. Mining-induced σ_2 static stress distribution at the 9417RL horizontal grid for the dB10-38T and dB10-38B pre-mining step.

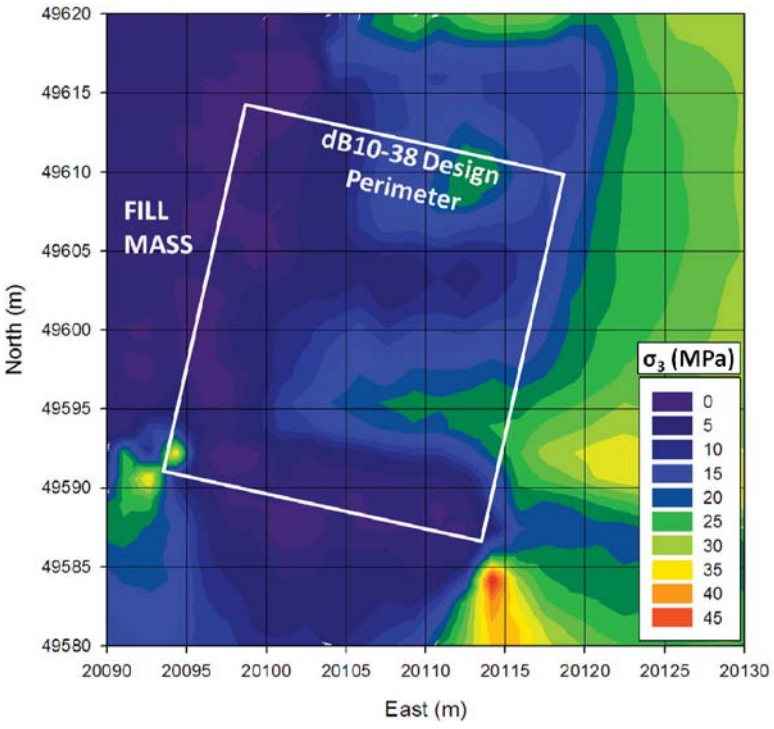

Figure 7.35. Mining-induced σ_3 static stress distribution at the 9417RL horizontal grid for the dB10-38T and dB10-38B pre-mining step.

The stress modelling results for the pre-mining step clearly indicate zones of stress concentration near existing excavation corners and a significant zone of low confinement (σ_2 and σ_3 close to zero) near the central fill mass. The indicated zones of low confinement associated with the central fill mass have been validated by field observations in other stopes, where significant losses of pre-drilled blastholes have occurred. The affected blastholes were typically in the rings against the central fill mass and closure due to movement along detached discontinuities was observed. The stress magnitudes and distributions observed in Figures 7.33 to 7.35 would be expected to influence the shape, extent and severity of rock mass damage with the addition of dynamic strains from blasting as discussed in Chapter 6.

7.9.3 dB10-38T Blast Vibration Monitoring Results

The number of discrete blasthole traces that could be identified in the mass blast waveforms was marginally increased compared with stopes dA12-35 or dB10-38B due to the use of electronic detonators. The more flexible, programmable electronic initiation timing prevented multiple-hole firing. The potential increase in single-hole firings and potential data points for the mass blast was reduced by the necessary cabling paths from the transducers to the data acquisition systems. The hangingwall and East wall transducer cables were all severed early in the mass blast due to rock dislocation and movement along the firing front.

As a result of the D block rock mass characterisation and in-stope measurements, the dynamic rock mass properties used in calculation of the $ED_{W\text{-}SS}$ and $\varepsilon_{W\text{-}MN}$ for stope dB10-38T are listed in Tables 7.18 and 7.19.

Table 7.18. Stress wave velocities used to calculate $ED_{W\text{-}SS}$ and $\varepsilon_{W\text{-}MN}$ values for dB10-38T blasting.

Stope Wall	Stress Wave Velocity (m/s)
East Wall	5940
Footwall	5340
Hangingwall	5200 (average at close to normal angle)

Table 7.19. Static and dynamic rock mass properties used in calculation of $ED_{W\text{-}SS}$ and $\varepsilon_{W\text{-}MN}$ in stope dB10-38T blasting results.

Stope Wall	Rock Density (kg/m^3)	Calculated E_{dyn} (GPa)	Poisson's Ratio	Wave Velocity (m/s)	λ_L (GPa)
East Wall	2760	76	0.28	5940	38
Footwall	2760 - 2770	62 - 60	0.28-0.29	5340	31-32
Hangingwall	2775	56	0.30	5200	32

The two different values listed for the rock density, E_{dyn}, Poisson's Ratio and λ_L for footwall orientation in Table 7.19 is due to the locations of the two transducers in the orebody (accelerometer) and in the footwall unit (geophone). The differences between the rock mass properties of each geologic unit would have been expected to influence the energies and strains developed in the propagating blast waves.

Using the values listed in Table 7.19, the values of $ED_{W\text{-}SS}$ and $\varepsilon_{W\text{-}MN}$ were calculated for each blasthole. Nonlinear multi-variable estimations of the resulting data for the individual stope wall data sets are listed in Table 7.20. As presented previously for stope dB10-38B, only the 95% upper confidence regression results are listed. The additional regression results are provided in Appendix 9.

Table 7.20. 95% upper confidence multi-variable nonlinear estimation results for each wall of dB10-38T.

Model	Stope Wall	Data Points	*K*	*b*	*n*	Best-fit R Value
95% $ED_{W\text{-}SS}$	Footwall all	319	736.1	2.567	-1.415	0.38
95% $\varepsilon_{W\text{-}MN}$	Footwall all	319	36.9	1.489	-0.968	0.51
95% $ED_{W\text{-}SS}$	East Wall all	220	0.185	3.415	-1.295	0.79
95% $\varepsilon_{W\text{-}MN}$	East Wall all	220	19.3	1.312	-0.857	0.59
95% $ED_{W\text{-}SS}$	Hangingwall all	219	0.157	1.574	0.947	0.59
95% $\varepsilon_{W\text{-}MN}$	Hangingwall all	219	0.876	0.765	0.622	0.61

In general, the correlation values for the nonlinear estimations of combined data sets for each stope wall of dB10-38T ranged from poor (0.38) to good (0.79). The high variability in regression results for the combined data sets indicated that the blast vibration attenuation along different orientations around stope dB10-38T were not consistent. The effect of distance range on the regression results for dB10-38T data was investigated by separating the individual transducers. Table 7.21 shows the regression results for each transducer around stope dB10-38T.

Table 7.21. 95% upper confidence multi-variable nonlinear estimation results for each transducer around stope dB10-38T.

Model	Stope Wall	Data Points	*K*	*b*	*n*	Best-fit R Value
95% $ED_{W\text{-}SS}$	FW Acc	167	736.1	2.567	-1.452	0.38
95% $\varepsilon_{W\text{-}MN}$	FW Acc	167	36.9	1.489	-0.968	0.52
95% $ED_{W\text{-}SS}$	FW Geo	152	466.2	2.117	-1.301	0.60
95% $\varepsilon_{W\text{-}MN}$	FW Geo	152	397.2	0.724	-0.900	0.63
95% $ED_{W\text{-}SS}$	EW Acc	45	22228.2	1.560	0.09	0.50
95% $\varepsilon_{W\text{-}MN}$	EW Acc	45	426.4	1.362	-0.310	0.47
95% $ED_{W\text{-}SS}$	EW Geo	175	61865.8	2.320	-3.320	0.90
95% $\varepsilon_{W\text{-}MN}$	EW Geo	175	8935.6	1.015	-2.319	0.83
95% $ED_{W\text{-}SS}$	HW Acc	112	1.854	2.596	-0.121	0.59
95% $\varepsilon_{W\text{-}MN}$	HW Acc	112	80.6	0.708	-0.392	0.58
95% $ED_{W\text{-}SS}$	HW Geo	107	5014.1	1.703	-1.465	0.76
95% $\varepsilon_{W\text{-}MN}$	HW Geo	107	807.5	0.827	-1.015	0.80

In some cases, segregation of the individual transducer data sets as specified by distance (near-field and intermediate-field) resulted in increased correlation values. In all cases, significant changes in the regression constants were observed for the data subsets and significant differences in attenuation behaviours were noted along each monitoring orientation. The variations between the attenuation behaviours based on the distance range (near-field versus intermediate-field) observed in all three monitored stopes suggests that the general charge weight scaling relationship

does a poor job of standardising the prediction of blasting vibrations under complex geologies or geometries. The higher correlation values observed for the intermediate-field geophone transducers on each array would further suggest that charge weight scaling can reliably predict vibrations at larger distances from explosive sources, but is highly limited at distances closer than approximately 10m.

7.9.4 Predictions of Blast-Induced Damage: Stope dB10-38T

The process of rock mass damage prediction required several key steps when incorporating mining-induced static stresses and blast-induced dynamic strains. These steps were discussed in Chapter 6. The approach adopted in the prediction of blast-induced damage in this thesis involved the integration of several different commercially-available software packages and custom models developed by the author. A standardised software package or system does not exist at the current time for integration of stress modelling, blast design, vibration modelling, rock strength modelling and blast damage prediction.

The existing software packages and tools developed by the author used to generate and integrate the information required to perform the blast damage prediction discussed in the following sections included:

- Modelling of blasthole charge strings (SURPAC 6.0)
- Three-dimensional static stress modelling (MAP3D)
- Multi-variable nonlinear regression analysis (Statistica 8.0)
- Blast vibration waveform processing (Instantel Blastware 8.1)
- Blast vibration analysis and calculation of energy/strain (macros in Excel)
- Integration of model grid values of stress/strain and rock strength (Excel)
- Graphical contour outputs (SigmaPlot 10.0)

7.9.4.1 Estimation of the Tensile Rock Strength and Static and Dynamic Elastic Constants for the dB10-38T Rock Mass

Through review of rock testing data in the WASM database from 2004 to present, no tensile strength testing results were available for the D block of KBGM. Other tests such as UCS, tri-axial compressive strength, point load and UCS with elastic constants were discovered. Due to the lack of tensile strength testing results, estimation of tensile strength values was required. The tensile strength (σ_T) was estimated by assuming a general ratio of the measured UCS to σ_T of approximately 12, according to the Griffith theory of rock strength. From the results of earlier rock testing listed in Table 7.2 (Li, 2002), the estimated tensile strengths of the intact rock for the three geologic regions of the D block rock mass are listed in Table 7.22.

Table 7.22. Predicted tensile rock strengths for D block geologic units.

Geologic Region	Measured UCS (MPa)	Predicted σ_T (MPa)
Ore	113	9
Footwall	136	11
Hangingwall	156	13

The static Young's Modulus (E_{st}) provided from laboratory testing (Li, 2002) and the estimated σ_T and measured UCS were used to calculate the static tensile and compressive failure strains ($\varepsilon_{static(T)}$ and $\varepsilon_{static(C)}$, respectively). The resulting values of static compressive and tensile failure strains are listed in Table 7.23.

Table 7.23. Static rock properties for the three geologic units around dB10-38T.

Geologic Region	Average E_{st} (GPa)	Predicted $\varepsilon_{static(C)}$ (με)	Predicted $\varepsilon_{static(T)}$ (με)
Ore	62	1814	151
Footwall	65	2080	173
Hangingwall	71	2213	184

The static tensile failure strains in Table 7.23 fall within the suggested tensile failure range of 100 to 200με as discussed in Chapter 2. The dynamic in situ failure strains in compression ($\varepsilon_{dyn(C)}$) and tension ($\varepsilon_{dyn(T)}$) were then calculated using E_{dyn} values from Table 7.19. The predicted dynamic failure strains are in Table 7.24.

Table 7.24. Compressive and tensile dynamic failure strains for the three geologic units around stope dB10-38T.

Geologic Region	**Calculated E_{dyn} (GPa)**	**Predicted $\varepsilon_{dyn(C)}$ (με)**	**Predicted $\varepsilon_{dyn(T)}$ (με)**
Ore	76	1483	123
Footwall	60	2255	187
Hangingwall	56	2801	233

The values of the dynamic in situ Young's Modulus listed in Tables 7.19 and 7.24 differ considerably from the laboratory-tested value of static Young's Modulus of intact rock samples. For the East wall of the stope, the E_{dyn} was higher than the laboratory obtained quasi-static value. For the footwall and hangingwall, the values of the dynamic in situ Young's Modulus were lower than the static values.

The dynamic failure strains presented in Table 7.24 do not explicitly consider the effects of strain rate based on the information presented in Chapters 2 and 6. The assumption has been made that strain rate significantly influences both the failure stress and the Young's Modulus of a material, but that the changes in strength and elasticity are roughly proportional. This effect would suggest that the failure strain does not change significantly with strain rate. As such, strain-rate effects are assumed not to influence failure strain, but are considered in the energy-based damage criteria for assessment of fracture extension.

7.9.4.2 State of Mining-Induced Static Strain at the Time of Blasting

The stress modelling results have been used to assess the state of mining-induced static strain within the rock mass at the time of blasting of stope dB10-38T. This approach aided in determining the additional dynamic strains required to cause damage to the intact rock blocks within the rock mass around dB10-38T. The

modelling results used in the damage prediction represented the static strain distribution prior to excavation of either dB10-38T or dB10-38B. Modelling results for each discrete in-stope mining step could be applied for better accuracy in representing the stress and strain conditions at the time of each stope firing (e.g. partial stope extraction at the time of mass firing).

One main assumption was required to allow the blast-induced dynamic strains to be superimposed upon the existing mining-induced static strains. This assumption was that the induced static strain at each grid point could be adequately described by the mean normal static strain invariant (ε_{MN}). Based on the assumption that mean normal strain was a legitimate descriptor of the state of mining-induced static loading, the ε_{MN} values at each grid point could be determined from the modelling results. A contour plot of ε_{MN} at the 9417RL modelling grid is shown in Figure 7.36.

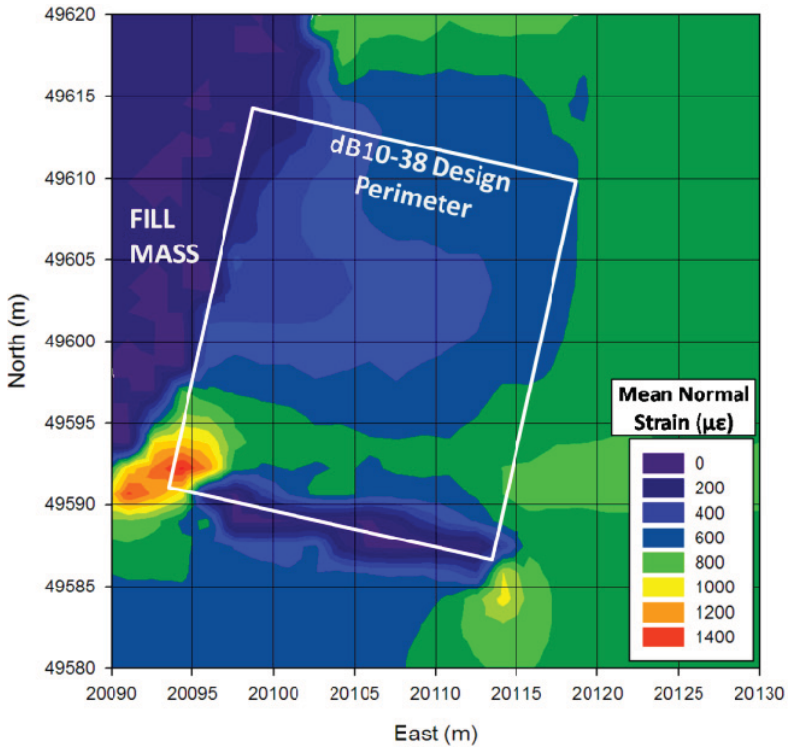

Figure 7.36. Contour plot of the mining-induced mean normal static compressive strain (ε_{MN}) modelling results at the 9417RL for the dB10-38T pre-mining step.

The value of ε_{MN} at each grid point was used to calculate the balance of strain required for either compressive or tensile damage based on the damage criteria

outlined in Chapter 6. Significant mechanistic issues arise when attempting to estimate the confined compressive failure strain of rock under conditions of existing static compressive loading. For this reason, only the tensile failure criterion has been pursued in the prediction of blast-induced intact rock damage for stope dB10-38T. The tensile criterion would be expected to predict a greater extent of damage outside the stope and thus was assumed to be more critical for stope performance.

7.9.4.3 Additional Tensile Strain Required for Tensile Fracture

The tensile fracture criterion and the values of ε_{MN} from the modelling allowed the required tensile strain for tensile fracture to be calculated for the grid at the 9417RL. The required $\varepsilon_{W\text{-}MN}$ to fracture the intact rock under the influence of the existing ε_{MN} at each grid point was the sum of $\varepsilon_{dyn(T)}$ plus ε_{MN}. This value represented the dynamic tensile strain that would be required to overcome the existing static compressive strains and the tensile failure strain of the rock. A contour plot of the required additional tensile strain for each point on the 9417RL grid is shown in Figure 7.37.

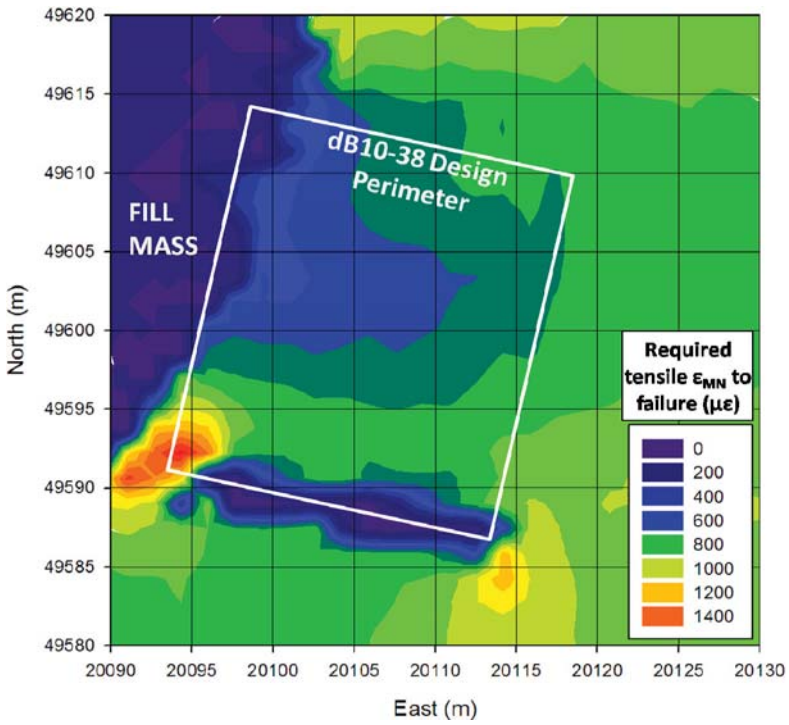

Figure 7.37. Contour plot of the required tensile strain for tensile fracture of intact rock at the 9417RL under the influence of the pre-mining static compressive strains.

The overwhelming influence of the existing static compressive strains on the required tensile strain to cause tensile fracture can be observed in Figure 7.37. In other models used to predict blast damage, such as the critical tensile strain model, no consideration for the influence of existing static stresses or strains is incorporated. With the influence of static compressive strains observed in underground mining conditions, the rock tensile strength alone does a poor job of representing a rock damage criterion.

7.9.4.4 Calculation of Induced Dynamic Strains from Blasting

The blast vibration monitoring and analysis program for stope dB10-38T resulted in equations for predicting the wave-induced mean normal dynamic strains ($\varepsilon_{W\text{-}MN}$) at points in the rock mass. These equations were used to estimate the dynamic blasting strains at various distances from specified charge weights. The values were used to create strain contours around the assumed charge location. The dynamic strain values were then evaluated against the required additional tensile strain values (Figure 7.37) to assess the likelihood of tensile fracture at points on the specified modelling grid.

The prediction equations defined by the regression constants in Table 7.20 were used to estimate values of the blast-induced $ED_{W\text{-}SS}$ and $\varepsilon_{W\text{-}MN}$ at points away from a charge of known explosive weight. Differences in the attenuation behaviours as indicated by the variable regression constants suggested that the transmission field around the charge would be highly irregular. These effects were associated with the influence of the Fitzroy Fault, the footwall shear, the dominant in situ discontinuities and the stress conditions. Contours of equal-strain were roughly elliptical, with the long axis oriented in the directions of the hangingwall and footwall. The ellipsoid axes elongation was approximately 3:1. Figure 7.38 illustrates the shape of the predicted equal-strain contours around a 100kg charge using the equations defined by the regression constants in Table 7.20 for each propagation orientation.

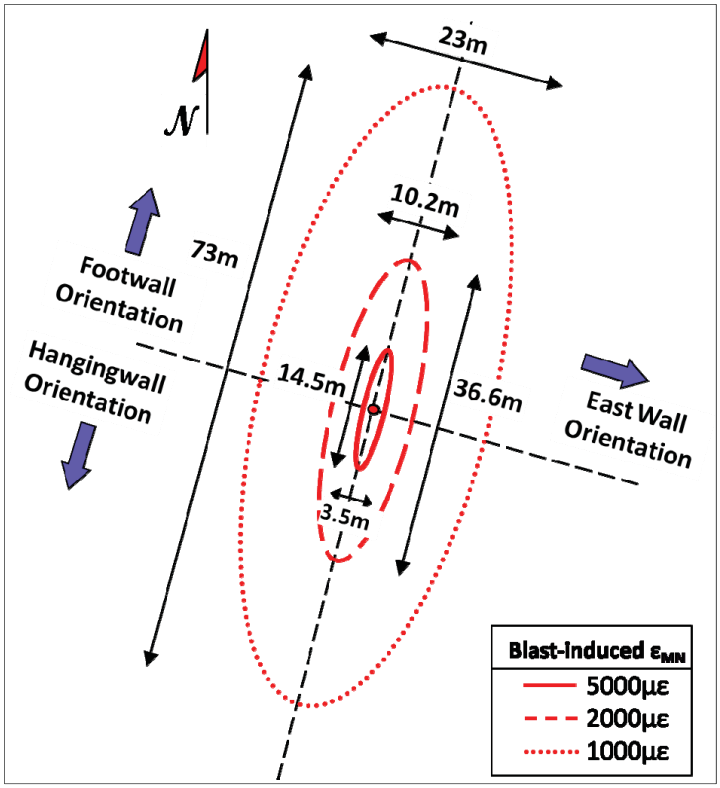

Figure 7.38. Contours of equal strain propagating from a 100kg charge as estimated from the 95% confidence regression constants for the East wall, footwall and hangingwall of dB10-38T (not to scale).

Integration of orientation-specific attenuation equations was not possible in the current version of the damage prediction process due to the configuration of the grid calculations. The method in which strain values were calculated at each grid point required a single attenuation equation based on the charge weight, charge coordinates and distance from the charge to each point in the grid. The $ED_{W\text{-}SS}$ and $\varepsilon_{W\text{-}MN}$ attenuation equations chosen for use in the contour predictions represented the 95% upper confidence equations from nonlinear estimation of the dB10-38T combined stope data set. The resulting equations were:

$$ED_{W\text{-}SS\text{-}95\%\ (dB10\text{-}38T)} = 452.93\ (W)^{2.50}\ (D)^{-2.03}\ (\text{J/m}^3) \qquad (7.\ 7)$$

$$\varepsilon_{W\text{-}MN\text{-}95\%\ (dB10\text{-}38T)} = 32.03\ (W)^{1.49}\ (D)^{-1.33}\ (\mu\varepsilon) \qquad (7.\ 8)$$

Further development of the grid calculation capabilities of the proposed approach would be expected to integrate variable attenuation characteristics as specified by the blast monitoring. This would lead to more accurate representations of irregular attenuation patterns and associated damage predictions.

The dynamic strain field around a 100kg charge using Equation 7.8 was estimated to illustrate the process of superimposing $\varepsilon_{W\text{-}MN}$ on the required strain balance to produce tensile fracture. The prediction equation was analysed against all grid points and contours of the dynamic strains were generated for a single, 100kg charge located at the stope perimeter. Figure 7.39 illustrates the contours of the 95% upper confidence predicted $\varepsilon_{W\text{-}MN}$ at the 9417RL grid.

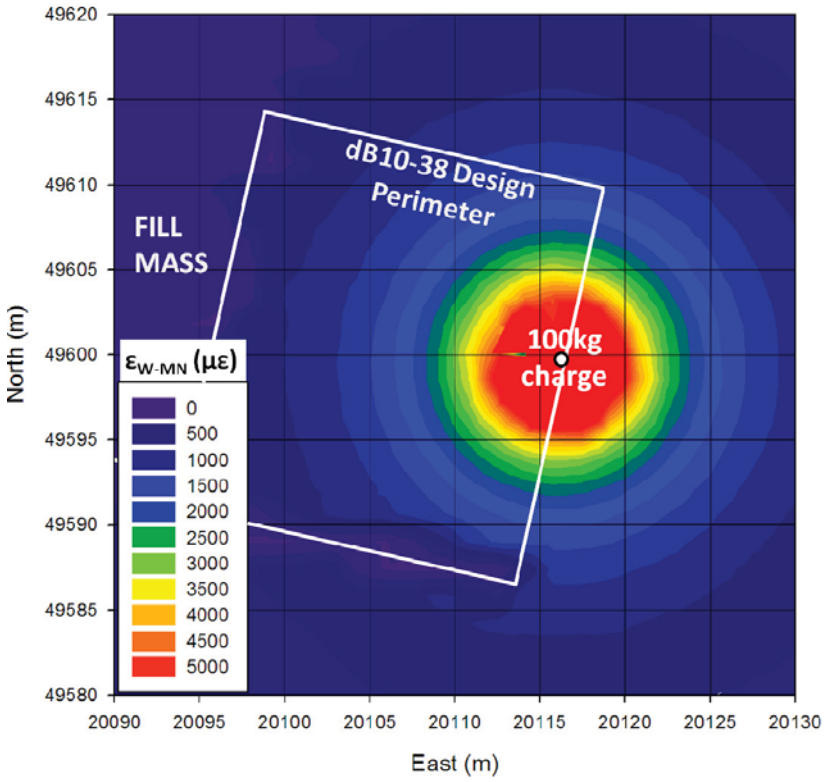

Figure 7.39. Contours of $\varepsilon_{W\text{-}MN\text{-}95\%}$ at all 9417RL grid points using Equation 7.8 for a 100kg charge on the perimeter of stope dB10-38T.

Voids and fill masses in the original stress models were treated as areas incapable of sustaining mining-induced static strains or blast-induced dynamic strains. This

consideration slightly altered the strain field contours observed in Figure 7.39 near the Southern stope boundary.

The next step in the prediction of tensile strain-related blast damage for stope dB10-38T was to superimpose the dynamic strain field from the 100kg explosive charge (Figure 7.39) onto the required tensile strain to tensile fracture (Figure 7.37). Figure 7.40 illustrates the theoretical view of this process, showing the zones of intersection of strain contours with the required tensile strains to fracture.

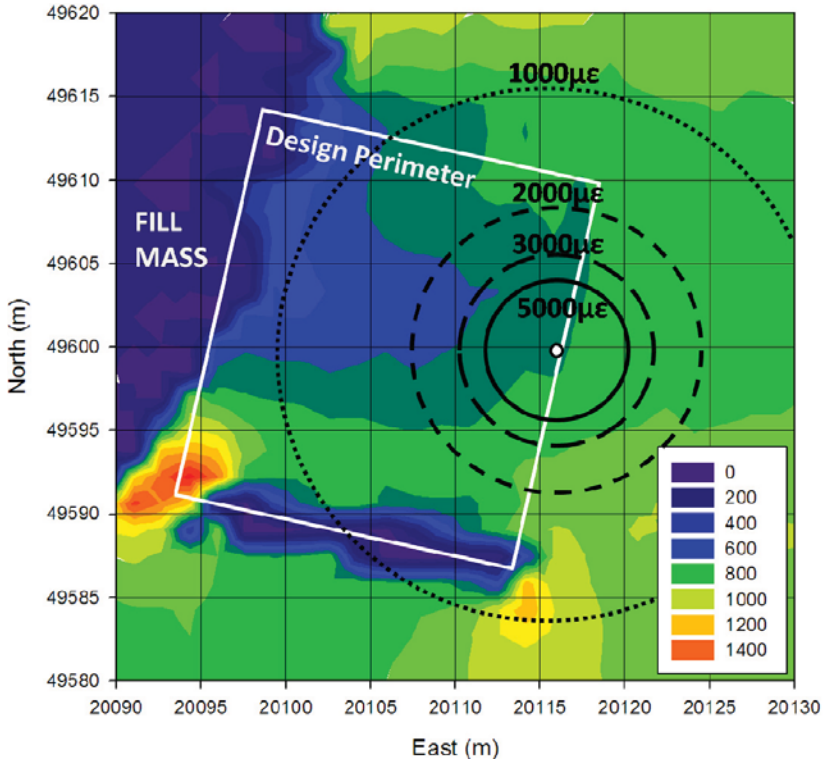

Figure 7.40. Contours of $\varepsilon_{W\text{-}MN}$ from a 100kg charge superimposed on the required tensile fracture strain contours for dB10-38T at the 9417RL grid.

Using the values of $\varepsilon_{W\text{-}MN}$ predicted by the attenuation equation at each grid point, calculations were performed to determine the difference between $\varepsilon_{W\text{-}MN}$ and the required tensile strain to produce tensile fracture. The points in the grid at which the applied dynamic strain exceeded the required strain were assumed to be damaged by tensile mechanisms. Points where $\varepsilon_{W\text{-}MN}$ was less than the required tensile strain to fracture was assumed to be undamaged and considered to have excess strain

capacity. A contour plot of the excess tensile strain capacity for the 9417RL grid is illustrated in Figure 7.41.

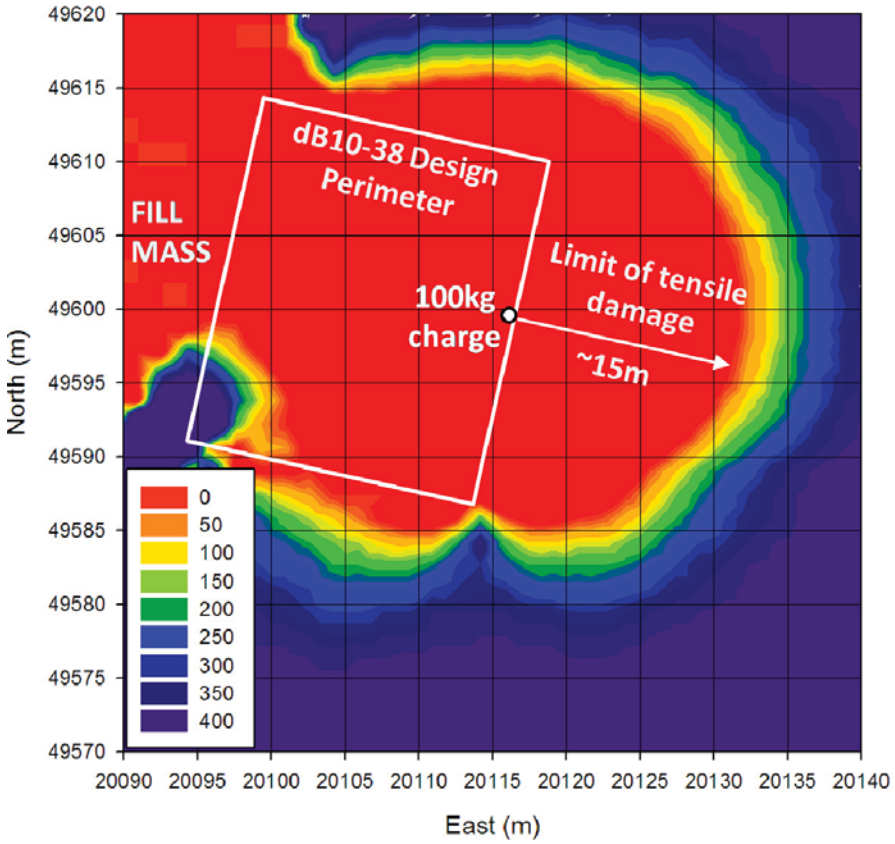

Figure 7.41. Contours of excess strain capacity for a 100kg charge at the East wall perimeter of stope dB10-38T, resulting in prediction of the tensile damage zone.

The red regions in Figure 7.41 represent points in the grid where the excess strain capacity is less than zero, indicating that the blast-induced dynamic tensile strain has exceeded the required tensile strain to fracture. The zones surrounding the tensile damage zone (lower values of excess strain capacity) could be regarded as a transition zone where tensile damage may be likely to occur from the detonation of successive charges in the blast. Outside of this region, the intact portions of the rock mass have been assumed to be largely uninfluenced.

The predicted extent of tensile damage from a single, 100kg charge at the stope perimeter was approximately 15m into the rock mass beyond the East wall of the stope. The influence of the existing static strains can be observed, as well as the

change in material strengths of the separate geologic units. These are indicated by the non-uniform shape of the predicted damage envelope. It is important to note that the severity of damage has not been defined explicitly in the proposed damage prediction approach and that damage does not necessarily indicate a high probability of rock mass failure. Many factors become relevant when assessing the potential for rock mass failure or instability. These include the degree and scale of static and dynamically-induced damage, the geometry of the excavation, installation of deep ground support and the magnitudes and orientations of confining stresses.

The fan drilling geometries and in-stope firing sequences used at KBGM results in a large range in charge weights located at the stope perimeters. In practice, charges of 15 to 150kg have been observed in perimeter holes within the stopes. To investigate the effect of a reduced charge weight at the stope perimeter on the predicted tensile damage zone, the 100kg charge was replaced by a 50kg charge. The predicted limit of tensile fracture for the 50kg charge at the stope perimeter is shown in Figure 7.42.

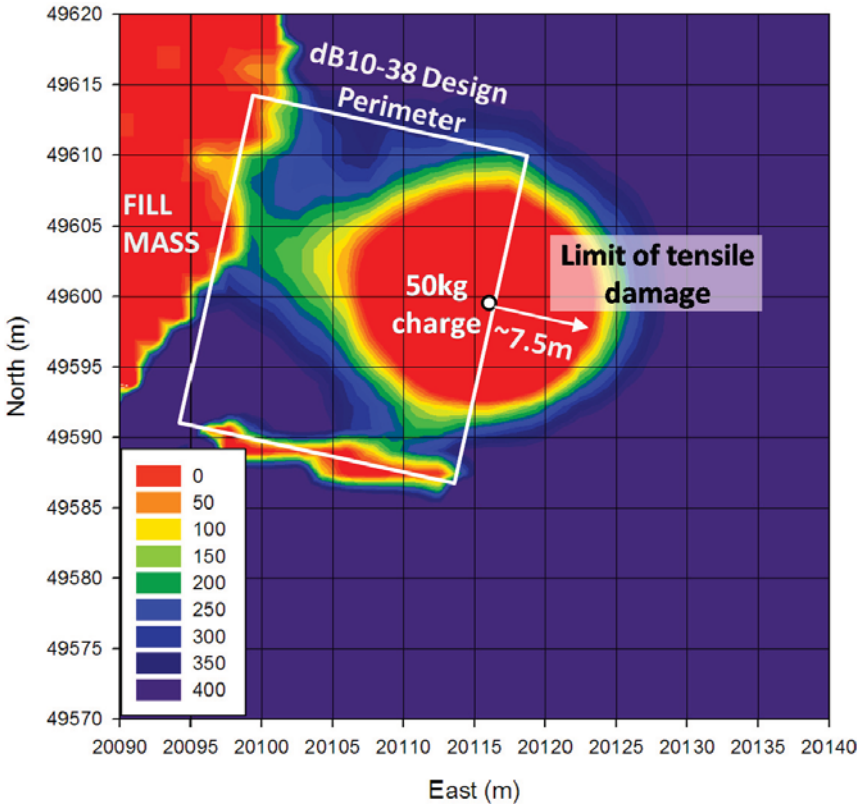

Figure 7.42. Contours of excess strain capacity for a 50kg charge at the East wall perimeter of stope dB10-38T, resulting in prediction of the tensile damage zone.

The potential blast-induced tensile damage was also predicted for a 50kg charge located at the dB10-38T hangingwall boundary. Figure 7.43 shows the contours of the excess strain capacity and predicted tensile damage zone for the 50kg charge at the stope hangingwall.

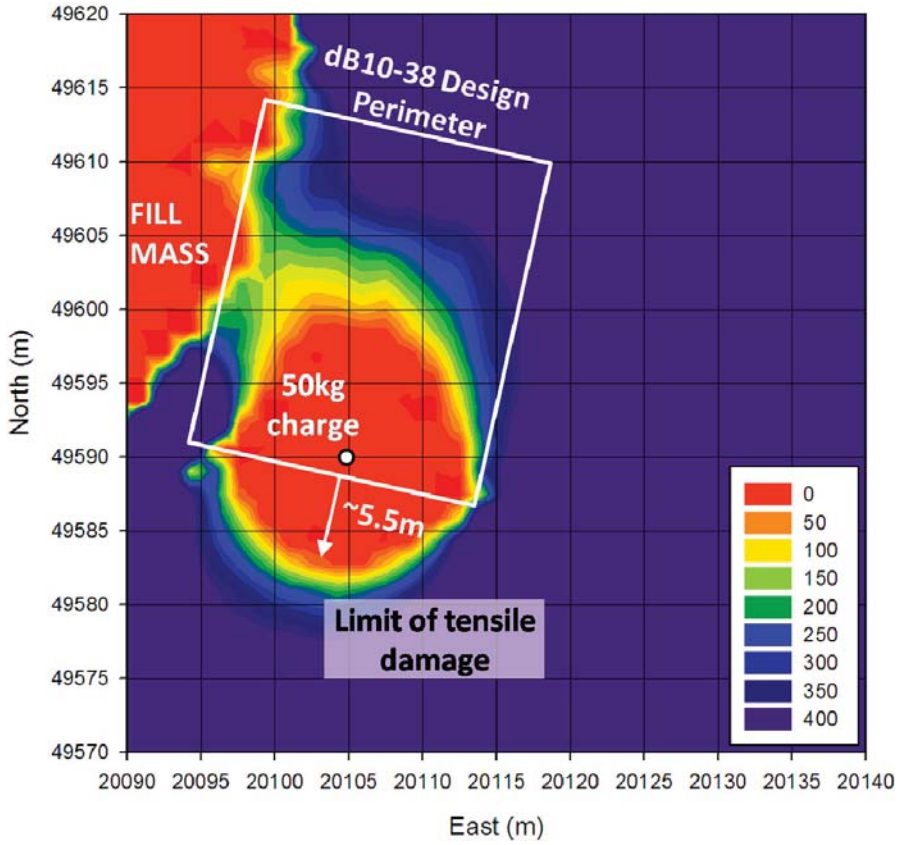

Figure 7.43. Contours of excess strain capacity for a 50kg charge at the hangingwall perimeter of stope dB10-38T, resulting in prediction of the tensile damage zone.

A significant reduction in the damage zone and transition zone can be observed when comparing the results of the 100kg and 50kg charge weight predictions. Additionally, asymmetric damage contours can be observed around each charge due to the influence of the mining-induced static strains as a result of the stress shadowing from the adjacent central fill mass.

The extent of damage predicted for the hangingwall of approximately 5.5m was less than the 7.5m predicted for the East wall for the same charge weight. This difference was due to the shapes of static strain contours and the individual geologic unit

fracture strains. The predicted dynamic tensile fracture strain for the hangingwall unit was almost twice that of the ore in the East wall. The damage prediction in Figure 7.43 from the hole against the stope hangingwall does not explicitly consider the activity of the Fitzroy Fault.

7.9.4.5 Prediction of Damage from Fracture Extension

The fracture energy approach discussed in Chapter 6 was proposed as a method of assessing the potential for extension of existing discontinuities to establish an outer limit of blasting damage. The required fracture energy has been assumed to be influenced by the strain rate, unlike the strain-based criteria for intact rock damage. This consideration required an additional prediction model for strain rate, which was assumed to be related to the peak particle acceleration and the stress wave velocity (Equation 2.17).

The first step in estimating the potential for fracture activation and extension was characterisation of the existing state of fracturing using the fracture area density (*FAD*). Although no specific fracture distribution model was developed for KBGM as part of this thesis, the results of the D block backs mapping program provided some indication of the degree of jointing in the rock mass surrounding dB10-38T. These mapping results identified from two to four joint sets, with an average of three (KBGM, 2008). Therefore, three discontinuity sets have been considered in calculation of the *FAD* for D block.

Within the unit block of $1m^3$, three joint sets of $1m^2$ face area have been assumed to exist with an average joint spacing of 250mm. The digitised backs mapping indicated joint spacing of 100mm to 1m for the three discontinuity sets. Based on the principles of a partially-healed discontinuously-connected fracture plane, each of the two fracture faces of a single discontinuity have been assumed to contribute to the expenditure of energy through fracture activation within the unit block. This assumption essentially doubles the fracture area within the block.

Calculation of the *FAD* for D block using three sets of 250mm average spacing (3.5 fracture planes per meter) resulted in a value of 21 m^2/m^3. The value of 3.5 fracture

planes per unit length was considered to account for the random distribution of the 250mm joint spacing; at 250mm spacing, alternating 1m^3 blocks would contain either three or four fracture planes. The *FAD* of 21 m^2/m^3 did not consider the presence of additional smaller fractures.

The next step in the discontinuity damage prediction was determining the dynamic tensile fracture energy ($FE_{T(dynamic)}$) for the D block rock mass. This process required an assumed value of the static tensile fracture energy (FE_T) and some method of estimating the required dynamic tensile fracture energy based on the strain rate. The relationship proposed in Chapter 6 (Figure 6.12) was used such that:

$$FE_{T(dynamic)} = 1.5(FE_T)e^{0.012\dot{\varepsilon}}$$

Where FE_T = static tensile fracture energy (J/m^2)

$\dot{\varepsilon}$ = strain rate (m/m/s)

The assumed value of static fracture energy (FE_T) for the D block rock mass was 90 J/m^2, based on a quartzite rock type (Krech, 1974). The $FE_{T(dynamic)}$ was then calculated over a range of observed strain rates. A prediction model for strain rate related to charge weight and distance was established by performing nonlinear regression of the strain rate values calculated using Equation 2.17. Equation 7.9 represents the 95% confidence prediction equation for strain rate as related to the charge weight and distance according to the combined data set for all measurements in dB10-38T.

$$\dot{\varepsilon}_{95\%} = 1.264\times10^{-4}(W)^{3.269}(D)^{-2.152} \qquad (7.9)$$

Equation 7.9 allowed the strain rate to be estimated at various distances from a known charge weight to calculate the values of $FE_{T(dynamic)}$. This value was then used to estimate the required dynamic tensile fracture energy density ($FED_{crit\text{-}dyn}$), calculated as the product of the $FE_{T(dynamic)}$ and the *FAD*. $FED_{crit\text{-}dyn}$ was then calculated over a range of distances from a 50kg charge, along with calculation of the $ED_{W\text{-}SS}$ at the same distances.

The current version of the energy-based discontinuity damage prediction approach does not depend on the state of mining-induced stress or strain required for the strain-based prediction for intact rock. For this reason, an alternate plot has been adopted for estimation of the limit of fracture extension. The new method of representation compares the estimated $FED_{crit\text{-}dyn}$ with the estimated $ED_{W\text{-}SS}$ over similar distance ranges to assess the likelihood of fracture extension. Figure 7.44 shows the predicted extent of fracture extension based on the comparison of $FED_{(crit\text{-}dyn)}$ and $ED_{W\text{-}SS}$ at various distances from a 50kg charge.

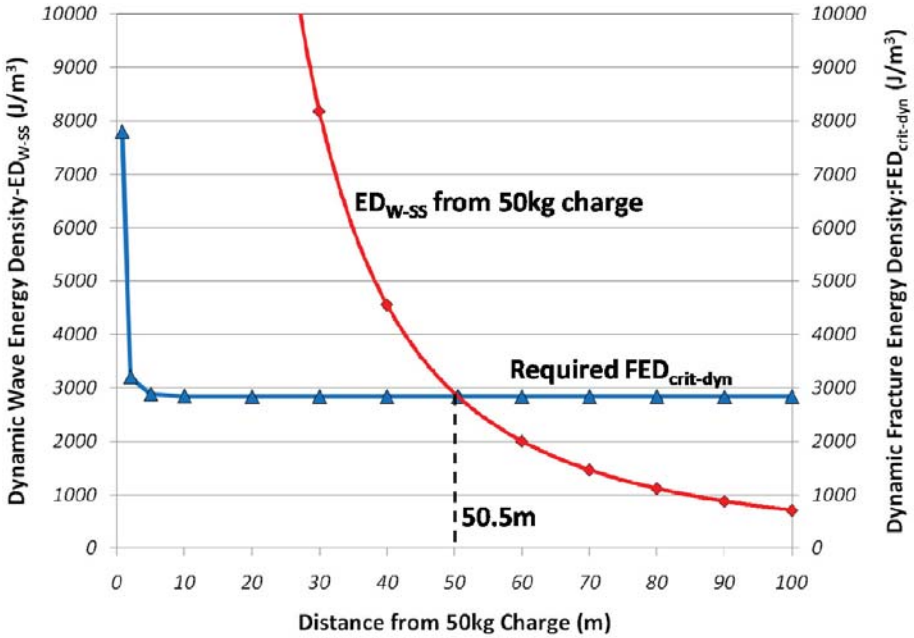

Figure 7.44. Estimation of the distance from a 50kg charge where potential fracture extension could occur as a function of the dynamic energy density at 21 m^2/m^3 *FAD*.

The red lines shown in Figure 7.44 represent the dynamic stored strain energy density predicted for the 50kg charge based on the 95% upper confidence prediction equation for all data collected in dB10-38T. The blue line represents the required dynamic fracture energy density, $FED_{crit\text{-}dyn}$ to activate all fracture faces in the 21 m^2/m^3 *FAD* at the various predicted strain rates. The intersection point of the two lines represents the distance at which adequate energy may be contained within the propagating blast-induced wave to activate the contained fractures. At distances where the $ED_{W\text{-}SS}$ exceeds the $FED_{crit\text{-}dyn}$, fracture extension would be predicted to

occur. In the regions of the graph where the $ED_{W\text{-}SS}$ is less than the $FED_{crit\text{-}dyn}$, there is a low probability that fracture extension would occur for the given value of *FAD*.

The crossing point of the two curves in Figure 7.44 indicates that fracture extension may occur to distance of 50.5m from the 50kg charge. According to the plot, the $FED_{crit\text{-}dyn}$ was largely flat outside of approximately 5m from the explosive charge as the strain rate was rapidly attenuated. Within 5m of the charge, fresh tensile fracture of the intact rock would be expected and therefore damage to discontinuities would not likely represent the most significant damage mechanism.

To investigate the influence of the *FAD* on the predicted fracture extension zone, the original block fracture model was revised for a reduced joint spacing. The more highly fractured jointing condition reduced the spacing to 100mm, which increased the *FAD* to 57 m^2/m^3. The resulting prediction of the fracture extension zone based on the new *FAD* is shown in Figure 7.45.

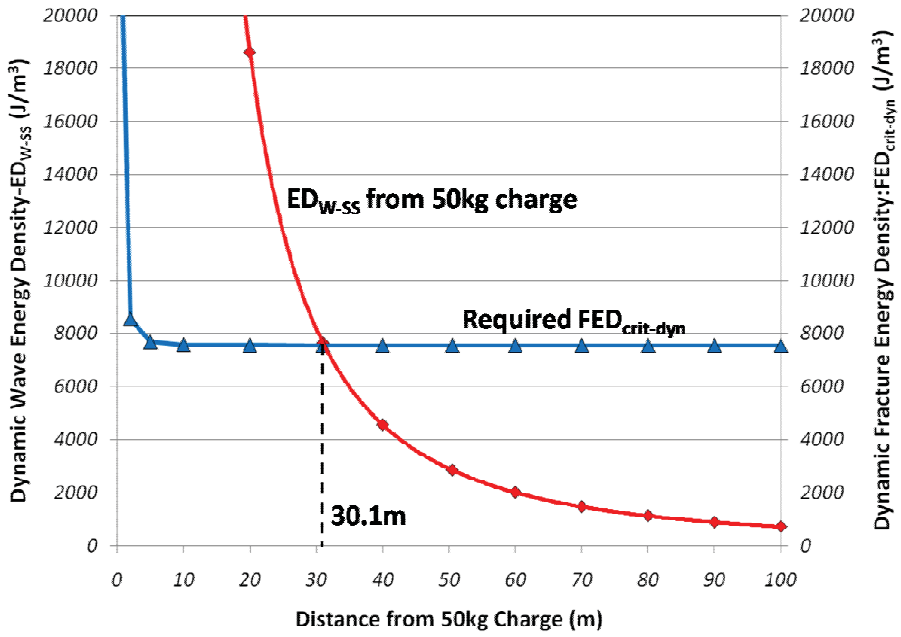

Figure 7.45. Estimation of the distance from a 50kg charge where fracture extension could occur as a function of the dynamic energy density at 57 m^2/m^3 *FAD*.

Due to the sensitivity of the equilibrium point between the $ED_{W\text{-}SS}$ and the $FED_{crit\text{-}dyn}$ to the *FAD*, the new prediction of the extent of fracture extension was 30.1m.

7.9.4.6 Comparison of Predicted Damage Extents with Critical Tensile Plane Strain Model Predictions

The extents of tensile strain-based damage and discontinuity extension predicted using the proposed model were compared with predictions using the critical tensile strain model discussed in Chapter 6 to check for any agreement between the two approaches. The data used to determine the 95% upper confidence PPV prediction equation required for the critical tensile plane strain model was identical to data used to determine the average attenuations of strains and energies in the proposed model.

One factor that was identified during the calculations of PPV_{crit} was the ambiguity related to the selection of input values of rock strength, P-wave velocity and Young's Modulus for the critical tensile plane strain approach. The various forms of the equation provided by different researchers allowed for a range of different rock strengths or ratios of compressive to tensile strengths to be selected. Additionally, the selection of static or dynamic Young's Modulus has not been discussed in association with the various versions of the equation. To represent the different forms of the equation and the range in possible input values, six different calculations of PPV_{crit} were compared. These calculations included different variations of possible static and dynamic input parameters for the dB10-38T orebody based on rock testing results and measured in situ data.

Two different blast vibration prediction methods were used to determine the distances at which the various PPV_{crit} values would be expected for a given charge weight of 100kg and 50kg. These two prediction techniques were traditional log-log linear regression of VSPPV versus cube root Scaled Distance and nonlinear multi-variable estimation of PPV using the general charge weight scaling relationship. A total of 24 damage predictions were performed using the six versions of the critical tensile plane strain equations, the two charge weights (100kg and 50kg) and the two vibration prediction techniques. Table 7.25 shows the predicted extents of tensile fracture using various forms of the critical tensile plane strain equation and nonlinear regression of VSPPV. Additional critical tensile plane strain damage predictions are included in Appendix 10 for the other model inputs, charge weight and regression approach.

Table 7.25. Predicted tensile fracture radii using various forms of the critical tensile plane strain damage model and nonlinear regression of PPV for a 50kg charge.

UCS (MPa)	UCS/σ_T	σ_T (MPa)	V_p (m/s)	E_{st} (GPa)	E_{dyn} (GPa)	PPV_{crit} (mm/s)	PPV_{crit} Radius (m)
113*	10	11	5940**	62*		1083	4.7
113*	12	9	5940**	62*		862	6.1
113*	15	7.5	5940**	62*		719	7.5
113*	10	11	5940**		76**	883	5.9
113*	12	9	5940**		76**	703	7.7
113*	15	7.5	5940**		76**	586	9.5

* data determined from rock testing

** values from field measurement/calculations by the author

The results of the 24 critical tensile plane strain analyses identified values of PPV_{crit} ranging from approximately 580mm/s to 1080mm/s, depending on the combination of input parameters. Based on the various values of PPV_{crit} and the method of PPV prediction, fresh fracture from tensile strain loading was predicted to occur over a radius of between 5m and 18m around a 100kg charge, and a radius of 4m to 9.5m from a 50kg charge. The damage extents predicted using the author's proposed model for 100kg and 50kg charges were 7.5m and 15m, respectively. These values fell within the range of predictions from the critical tensile plane strain models. The ranges over which fracture extension were predicted based on the 25% PPV_{crit} criterion (Heilig, 2002) in the critical tensile plane strain model were between 16m and 90m for the 100kg charge and 13m and 47m for the 50kg charge. The predicted extents of discontinuity extension of 50.5m and 30.1m for the two different *FAD* values using the author's proposed approach again fell within the large prediction ranges using the various forms of the critical tensile strain model.

The most considerable difference between the proposed model results and the critical tensile plane strain results was the shape of the predicted damage envelopes around each charge. The influence of the mining-induced static strain distribution on the predicted strain-based damage predictions was clearly indicated in Figures 7.43 to

7.45. The critical tensile plane strain model in the common forms found in Chapter 6 are not capable of considering the influence of the state of mining-induced static stresses or strains on the predicted blast-induced damage.

7.9.5 Stope Performance Assessment of dB10-38T

CMS surveys of stopes dB10-38B and dB10-38T were performed from the 9410RL and 9440RL once the double-lift stope was completely emptied prior to backfilling. These two surveys were combined to obtain a post-mining void surface wireframe of the entire stope. The combined CMS survey was compared with the double-lift design wireframe and Table 7.26 lists the overbreak and underbreak reporting results.

Table 7.26. Overbreak and underbreak calculations resulting from comparison of the post-extraction CMS and the design wireframes for dB10-38B and dB10-38T.

Stope Performance Criteria	Total Volume (m^3)	% of Design Volume
Total Overbreak	7976	35.1%
Total Underbreak	1342	5.9%

A series of horizontal and vertical stope sections were analysed to determine the maximum depths of overbreak experienced in each wall of dB10-38T. Table 7.27 lists the maximum depth of overbreak for each stope wall and Figures 7.46 and 7.47 illustrate horizontal and vertical sections of the dB10-38T wireframes.

Table 7.27. Maximum depth of overbreak in each wall of stope dB10-38T.

Stope Wall	Maximum Depth of Overbreak (m)
East Wall	5.1
West Wall (pastefill)	3.0
Footwall	2.1
Hangingwall	2.2

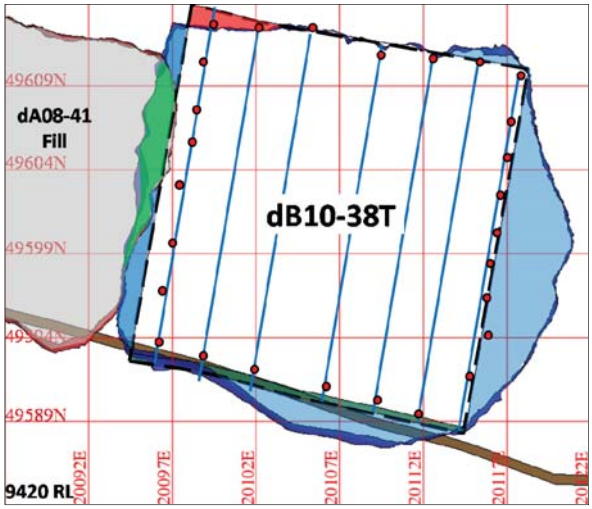

Figure 7.46. Horizontal section of dB10-38T design and CMS survey wireframes at 9420RL showing overbreak (blue), underbreak (red), pastefill dilution (green) and the locations of perimeter blastholes.

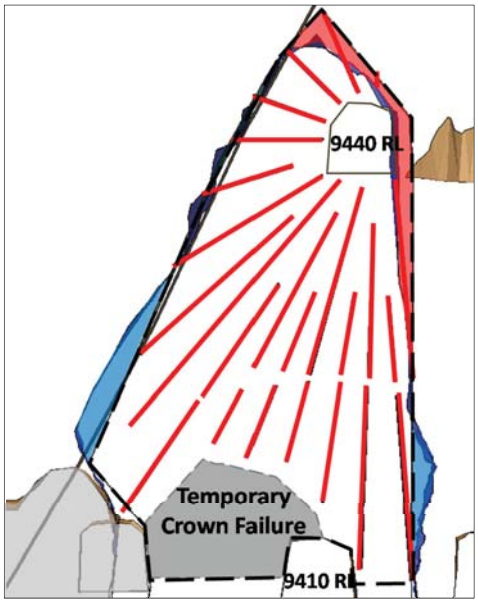

Figure 7.47. Vertical section of dB10-38T design and CMS wireframes at blasthole ring 5 showing overbreak (blue), underbreak (red) and the locations of blastholes.

The East wall of stope dB20-38T was the most severely over broken of the observed walls. Due to the roughly flat shape of some of the failure surfaces represented by the CMS of the East wall, it was proposed that the overbreak was partially associated with geologic features intersecting the stope. Further analysis of the state of post-

mining stress distribution further supported this assumption, as significant zones of low confining stresses were indicated in the East wall. Low confining stresses could have facilitated detachment of large discontinuities and subsequent fall-off into the stope during blasting. Figure 7.48 shows the post-mining distribution of σ_2 and σ_3, which would act as clamping stresses for the major discontinuities.

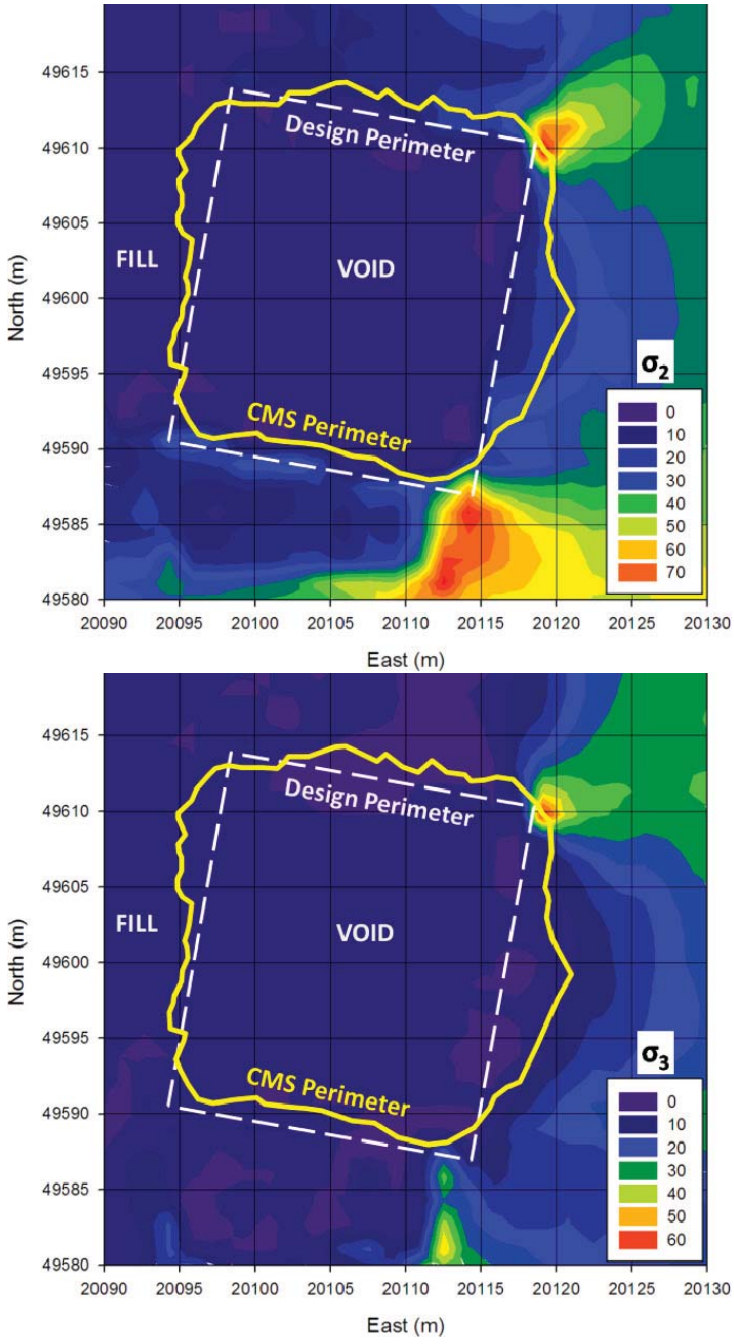

Figure 7.48. Post-mining linear-elastic stress modelling of σ_2 (top) and σ_3 (bottom) showing areas of low confining stresses in the East wall of stope dB10-38T.

The wedge-shaped CMS surface in the East wall of dB10-38T could have indicated interaction of a discrete large-scale discontinuity on strike N-NE with existing dominant discontinuity sets striking N-NW under the presence of low confining stresses. An additional contributing factor could have been the activity of blast-induced fracture propagation causing interconnection of existing discontinuities. Loss of confinement would have been expected to contribute to the wall failure regardless of the fracture mechanism by allowing unravelling of the damaged rock mass. This contribution again illustrated the importance of the induced static stress on assessment of blast damage or stope performance.

7.10 Discussion and Conclusions

The processes of rock mass characterisation, blast vibration monitoring and analysis and post-extraction stope assessment provided valuable tools to investigate the contributions of geology, mining-induced static stresses and dynamic loading from blasting on rock mass behaviour and stope performance at KBGM. A majority of blast damage investigations only focus on blasting aspects defined by blast vibration monitoring and largely ignore the rock mass characteristics. The contribution of other factors such as geology and induced static stresses are rarely included in investigation of blast-induced damage, and therefore existing prediction models do a poor job of representing the complex nature of rock mass behaviour under static and dynamic loading.

The data collected for dB10-38B and dB10-38T clearly indicated differences in blast wave propagation and attenuation along various orientations. These differences were assumed to be associated with the geologically-complex nature of the D block rock mass and the influence of static stresses. The interaction between the numerous factors contributing to stope performance made identification of a single factor such as blasting damage or geologically-influenced behaviours impossible. Therefore, a holistic approach must be adopted to assess or predict stope performance. This approach should include geologic, geometric and geotechnical parameters in addition to rock mass damage or degradation through introduction of blast damage.

The predicted zones of blasting damage for stope dB10-38T specified by the proposed strain and energy-based models were not necessarily reflected in the stope performance as assessed by the post-extraction CMS surveys. Measurements of the actual alterations within the remaining rock mass using detailed geophysical approaches or observation holes were not possible at KBGM due to limitations on equipment and the short stope turnover times. Although the damage predictions could not be validated by measurements of actual rock mass fracture, the predicted damage zones for the 50kg charge could be viewed as realistic according to the observed stope overbreak in the East wall. The predicted extent of tensile strain-based damage in the East wall using the proposed approach was approximately 7.5m, whereas the maximum depth of overbreak was 5.1m. Additional rock mass alteration or strength degradation beyond the limit of overbreak would have been expected.

This page left intentionally blank – KG Fleetwood

CHAPTER 8 : CASE STUDY- BHP BILLITON CANNINGTON MINE

8.1 Introduction

Following the investigation of stope performance at the Kanowna Belle Gold Mine from January to May 2006, a similar project was initiated at the BHP Billiton Cannington Mine starting in August, 2006. The initial blasting concerns at the Cannington Mine were related to potential blast-related damage to mine infrastructure within the North Zone mining area. The second area of concern was the performance of stopes contained within the newly-commissioned R4 mining area.

The rock mass characterisation and blast vibration monitoring program at the Cannington Mine took place from August, 2006 to January, 2008. Two stopes in the massive and competent North Zone mining area and two stopes in the highly-fractured R4 mining area were selected for the case studies. The rock mass conditions, stope dimensions and geotechnical concerns for the two mine areas were significantly different. As part of the case study, rock mass characterisations, blast vibration monitoring and post-extraction void assessments were performed for the four stopes. A total of 29 tri-axial blast vibration monitoring transducers were installed and 32 stope firings were monitored resulting in a database of 3750 individual blasthole vibration wave traces.

Rock mass characterisations and blast vibration monitoring and analysis results have been discussed for the North Zone and R4 as mining block-scale analyses in addition to individual stope assessments. Block-scale analyses refer to characterisations based on all monitored stopes within the two represented mining areas. The extent of tensile strain-related blast damage under the influence of mining-induced static strains has also been predicted for North Zone stope 24jC6HL. This prediction has been compared with predictions using the critical tensile plane strain model.

8.2 Geology of the Cannington Mine Deposit

The orebody at the BHP Billiton Cannington Mine is a high grade, massive, polymetallic deposit containing a range of siliceous and Fe-rich lithologies with associated non-mineralised quartzites, pegmatites, amphibolites and sillimanite-muscovite schists. Lead, silver, and zinc mineralisation is separated into two main zones by the Trepell Fault. The Southern orebody is terminated by the Hamilton Fault. Both faults exhibit signs of large displacements, and are characterised by heavy fracturing and chlorite alteration (Walters and Bailey, 1998). Figure 8.1 shows a plan view of the Cannington orebody at the 210mLv (mine level) and Figure 8.2 shows a longitudinal section of the Cannington orebody at the 1900m Easting.

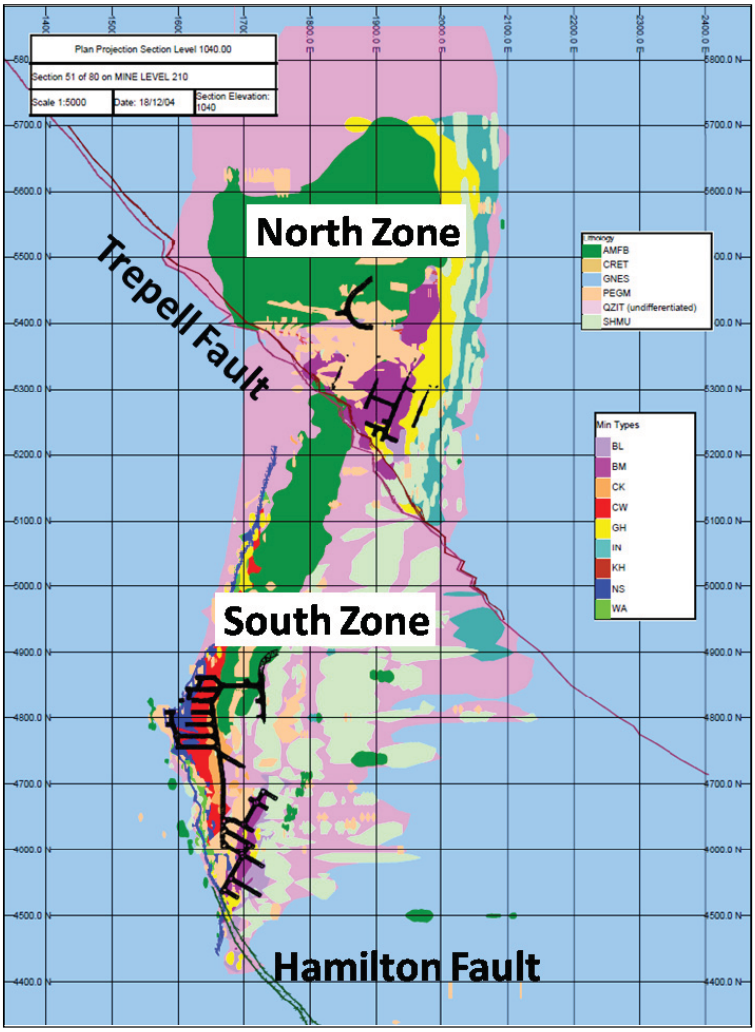

Figure 8.1. Plan view of the Cannington orebody at the 210mLv mine level showing the zones of mineralisation and the two regional-scale faults.

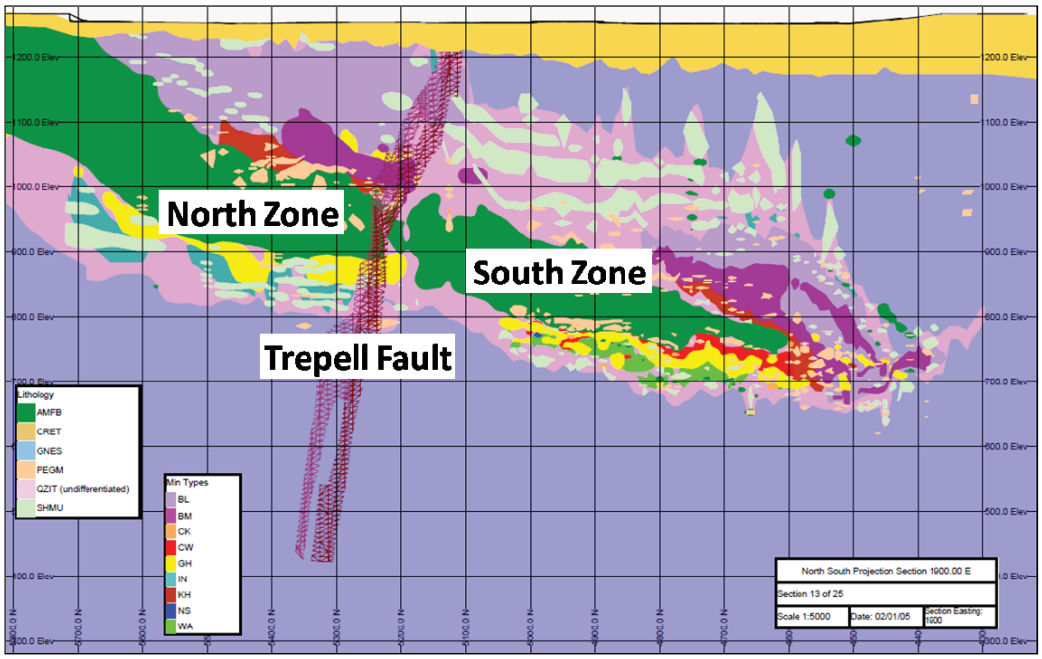

Figure 8.2. Section view of the Cannington orebody at the 1900m Easting showing the zones of mineralisation and the two regional-scale faults.

A number of large parallel faults striking roughly Northeast-Southwest exist in the main Southern orebody between the Hamilton and Trepell Faults. These parallel faults are regionally terminated by the Trepell and Hamilton Faults and are locally referred to as "bird faults". The bird faults negatively influence the behaviour of the stopes in the main Southern Zone as well as the regional mine stability. A barren amphibolite core is an additional geologic factor that influences the shape of the mineable resources at Cannington. This feature is illustrated in green in Figures 8.1 and 8.2. The structural integrity of the amphibolite core is viewed as critical to the long-term stability of the Cannington underground mine (Li, 2007).

8.3 Overview of the Mining Operation

The Cannington Mine, owned and operated by BHP Billiton, is located 280km Southeast of Mt. Isa in Northwest Queensland, Australia. Mining by sublevel open stoping began at the Cannington Mine in late 1996, and at the time of the stope assessment program the mine was producing approximately 2.1Mt per annum of Pb-Ag-Zn ore (Streeton, 2000 and Bloss, 2005). The Cannington Mine is divided into two primary mining areas by the Trepell Fault. The North Zone mining area, located

to the north of the Trepell Fault, contains approximately 20% of the minable reserve. The rock mass of the North Zone is massive and highly competent. The bulk of mining at Cannington takes place in the Southern Zone, which contains the remainder of the mineable reserves. The Southern Zone is subdivided into mining areas based on the locations and characteristics of the individual mineralised lodes. The stope sizes in the North Zone typically range from 60kt to 120kt, mined over 2 to 4 sublevels. The stope sizes in the mining areas of the Southern Zone are highly variable, ranging from approximately 10kt in the R4 to 150kt in the QR5 and Footwall Lead. The moderately shallow depth of mining (less than 600m) at Cannington results in low to moderate measured in situ virgin stresses (Li, 2007).

The drilling and blasting program at the Cannington Mine utilises a traditional sublevel open stoping sequence of slot-and-slash blasting. A central longhole winze is developed between production levels through rise blasting of longholes, followed by opening of a slot the full-length or width of the stope. Rings are then slashed into the void to the final stope perimeter. One modification of this standard sequence has been adopted for mass firing of entire 20m sublevels using electronic detonators. This method has been referred to as vertical retreat open stoping, or VROS (Bloss, 2005). The typical number of firings per sublevel using the VROS approach is two to three instead of the traditional six to ten with a pyrotechnic initiation system. This reduction in the number of firings with the VROS sequence is due to the ability to fire a flexible hole sequence, mixing long-period and millisecond electronic delays. The general firing sequence within a VROS stope at Cannington is:

Bottom sublevel

- Longhole winze (LHW) firings of 4-6m heights to 6-10m crown (2-3 firings)
- Cut-off slot (COS) firing entire stope width to 10m crown
- Ring toes firing to form stope trough
- Mass firing of LHW, COS crowns and remainder of rings

Intermediate sublevels

- LHW firing to 6m crown
- COS firing to 10m crown
- Mass firing of remaining ore on level

One method the Cannington Mine adopted for reducing the expected risk of blasting damage infrastructure in the proximity of an active stope was the use of cleaner rings along the stope wall adjacent to the infrastructure. This approach was expected to both increase the stand-off distance between the main ring toes and the mine infrastructure (to reduce vibrations) and help control the breakage plane of the final stope wall. These outcomes were hoped to be achieved by drilling an extra ring of blastholes parallel to the final stope wall at the stope perimeter. Cleaner ring firings were the final stope firing, blasted after the stope was empty to ensure maximum ring relief. The cleaner ring strategy was similar to the diaphragm ring approach used at other mines (namely Mount Isa Mines).

The blasthole diameter used at Cannington at the time of the study was 89mm and most rings were sub-horizontal (downholes). The typical pattern used in the North Zone of Cannington was a toe spacing of 3.0m with a ring burden of 2.5m to 2.8m, resulting in powder factors of 0.15 to 0.3 kg/tonne. The blasthole ring pattern in the R4 mining area was a 2.4m to 3.1m toe spacing and ring burden of 1.5 to 2.2m, with a powder factor of approximately 0.15 kg/tonne. The explosive types used at Cannington included pour-loaded ANFO, pour-loaded low-density ANFO blends and gassed emulsions with densities of 0.8g/cc to 1.2g/cc. A past study conducted by the Cannington geotechnical department investigated the influence of rock strength and fracture frequency on fragmentation and recommended blast design powder factors for different mine areas (Streeton, 2000). At the time of the author's study from 2006 to 2008, this approach to blast design was not explicitly considered by the engineering department, with preference for standardised patterns.

8.4 Selection of Monitored Stopes

The stopes included in the blast vibration monitoring and stope performance assessment program at Cannington were contained within the North Zone and R4 mining areas. The two stopes in the North Zone were located near the Trepell Fault at a depth of approximately 200m to 250m from surface. The two stopes monitored in the newly-initiated R4 mining area were located in the footwall of the Hamilton Fault, at the southern extent of the Southern Zone, at a depth of approximately 500m. The ore grades in the R4 are on average higher than the main Southern orebody, but

account for less than 3% of the minable deposit (Li, 2007). The R4 was the most recently activated mining area at Cannington, with stoping commencing in late 2007.

Selection of the monitored stopes at the Cannington Mine was influenced by two factors. The first was related to the protection of mine infrastructure and the second was partial shutdown of Southern Zone mining sectors for ground support rehabilitation. Based on these two factors, stopes in the North Zone mining area and the R4 mining area were selected for rock mass characterisation, blast vibration monitoring and assessment of post-extraction performance. The two mining areas were geologically different based on the rock mass alteration, geotechnical performance concerns and the expected stress conditions.

8.4.1 North Zone Stopes 22gC6HL and 24jC6HL

Following a request by Cannington personnel, the blast vibration monitoring program in the North Zone was initiated in August, 2006. Concerns with blast-induced damage to critical mine infrastructure in the vicinity of stopes 22gC6HL and 24jC6HL prompted the near-field vibration monitoring programs. The two stopes monitored in the North Zone were mined sequentially as part of the chequerboard extraction sequence. Figure 8.3 illustrates the locations of stopes 22gC6HL and 24jC6HL along with the adjacent paste fill masses.

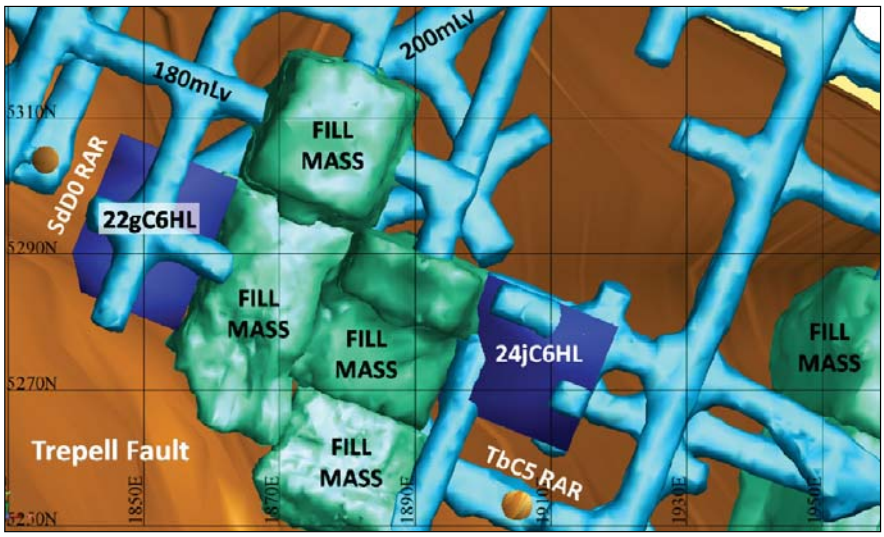

Figure 8.3. Plan view of North Zone stopes 22gC6HL and 24jC6HL in relation to the Trepell Fault and adjacent pastefill masses at the time of monitoring.

Stopes 22gC6HL and 24jC6HL were selected for blast vibration monitoring due to concerns related to blast damage to mine infrastructure and geologic features near the stopes. The main concerns during blasting of stope 22gC6HL were:

- 5m distance between the Southwest stope wall and the Trepell Fault
- 5m distance between the Northwest stope wall and the 4.0m diameter raise-bored SdD0 return air rise (RAR)
- Main access fault crossing at the 240-255mLv
- Main underground explosives storage magazine on the 240mLv

Each of these structures was considered to be susceptible to blasting-related damage. If damaged, these infrastructure features could have compromised the productivity or safety of the mining operations in the North Zone. Figure 8.4 illustrates stope 22gC6HL and the locations of features of concern.

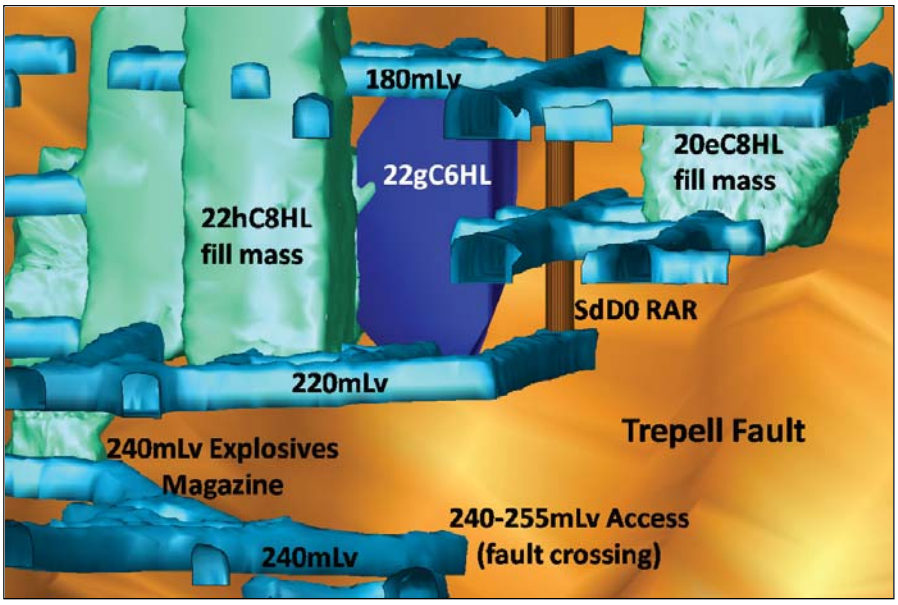

Figure 8.4. Isometric view of stope 22gC6HL showing the critical mine infrastructure in the vicinity of the stope (looking southeast).

Of the structures shown in Figure 8.4, the 240-255mLv Trepell Fault crossing was viewed by Cannington geotechnical personnel as the most critical with regards to the mine production. The Trepell Fault crossing is the main access way between the North Zone and South Zone via the main decline. The importance of the travel way

was highlighted by the addition of sprayed concrete arches through the fault crossing to ensure the long-term stability of the excavation.

Both stopes 22gC6HL and 24jC6HL were both located adjacent to critical ventilation exhaust rises. The 7m separation between the Southwest wall of 24jC6HL and the 4.5m diameter TbC5RAR led to concerns with regards to blasting damage, similar to stope 22gC6HL and SdD0RAR. An additional concern for stope 24jC6HL was the 15m distance from the trough of the stope to the 240mLv main explosives storage magazine. Figure 8.5 shows stope 24jC6HL and the sensitive infrastructure in the proximity of the stope.

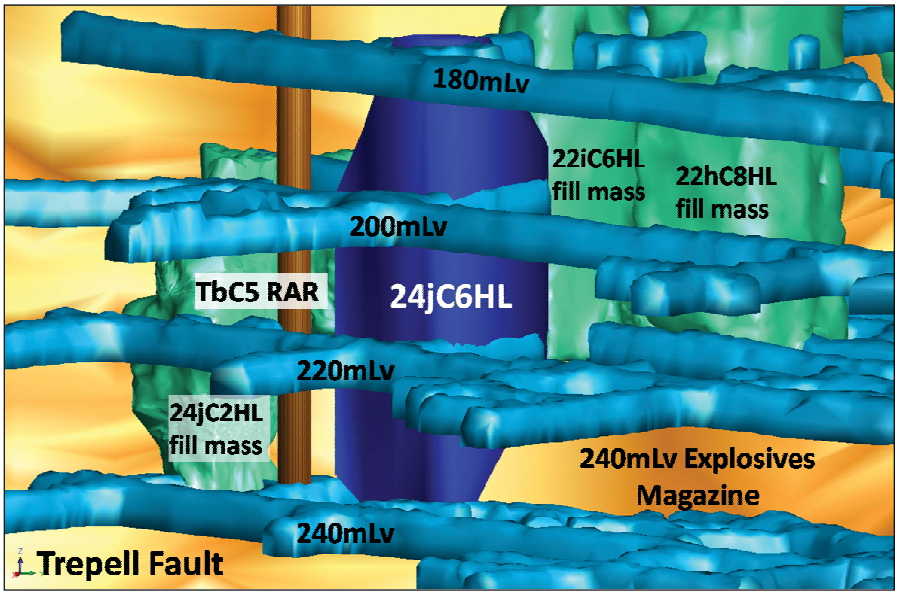

Figure 8.5. Isometric view of stope 24jC6HL showing the critical mine infrastructure in the vicinity of the stope (looking southwest).

8.4.2 R4 Stopes 52h09HL and 52h04HL

The stope designs and mining sequence of the newly-activated R4 mining area in the footwall of the Hamilton Fault was approached with extreme caution by Cannington personnel. Limited tonnage was planned to be mined out of the R4 and the stope size was dramatically reduced to approximately 10kt per stope to limit the exposure of the footwall of the Hamilton Fault. To assess the response of the R4 mining area to mining and stope blasting, two stopes were selected for monitoring and assessment.

The R4 mining area was also selected for assessment due to the suspended production in the main Southern orebody for ground support rehabilitation of the Southern decline and the production levels.

The first two stopes in the R4 stoping sequence were 52h09HL and 52h04HL, located between the 500mLv and 520mLv at the lowest mining level of the R4. The proposed stoping sequence of the R4 was a bottom-up continuous longitudinal retreat with concurrent pastefill (Li, 2007). Due to the complex mineralisation in the R4, a barren pillar was planned between stopes 52h09HL and 52h04HL. Figure 8.6 shows stopes 52h09HL and 52h04HL, along with the Hamilton Fault.

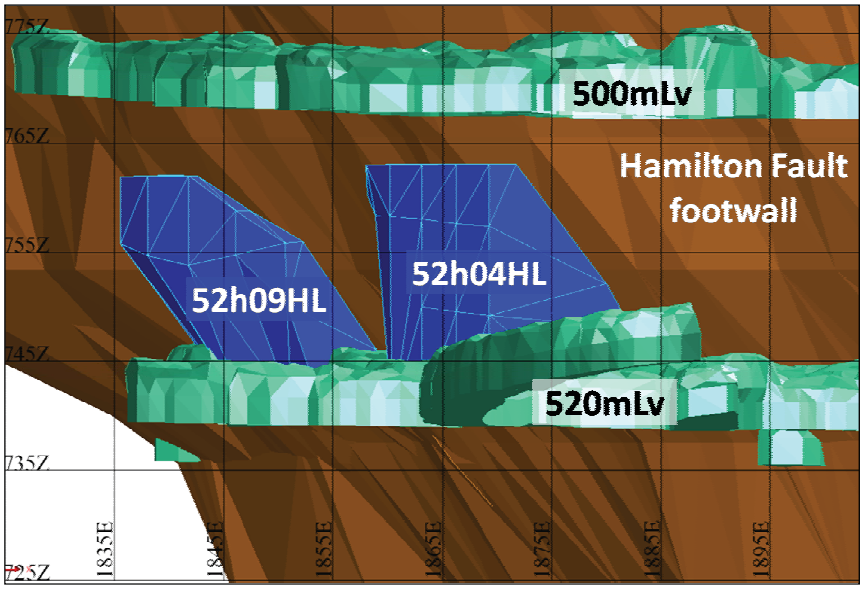

Figure 8.6. Isometric view of R4 stopes 52h09HL and 52h04HL (looking north).

8.5 North Zone Block-Scale Rock Mass Characterisation and Blast Vibration Monitoring Results

All data collected for stopes 22gC6HL and 24jC6HL were combined to perform block-scale analyses to gain a better understanding of the rock mass conditions and blast vibration monitoring results for the North Zone. Part of the decision to investigate block-scale characteristics was based on the observation of large-scale rock mass anisotropies revealed by the stress wave velocity measurements and peak amplitude-frequency analyses.

8.5.1 Rock Mass Characterisation of the North Zone

The North Zone rock mass was characterised using the results of rock testing, geological and geotechnical discontinuity mapping, mining-induced static stress modelling and geophysical approaches. The discontinuity mapping data were collected by Cannington Mine personnel and the blast vibration, geophysical and rock testing data were collected by the author.

8.5.1.1 Intact Rock Properties

Intact rock testing for the upper portion of the North Zone was performed for the Cannington Mine in late 2008 and early 2009 (WASM, 2009a and 2009b). The locations from which samples were extracted for a North Zone rock testing program performed in the 1990s could not be confirmed from the WASM rock testing database. Therefore, only the results of the recent testing program have been considered. The largely massive and homogeneous nature of the North Zone allowed the rock testing results obtained for the upper portions from surface drillholes to be applied to stopes 22gC6HL and 24jC6HL.

In addition to the limited data on rock strengths measured for the North Zone, no testing results were found for the intact rock elastic constants. Values for the quasi-static Young's Modulus (E_{st}) and Poisson's ratio (v_{st}) were therefore obtained from earlier testing of samples from the Southern Zone (AMC, 1998). The rock strengths and elastic constants used for the North Zone rock mass characterisation are listed in Table 8.1.

Table 8.1. Results of intact rock testing for the North Zone of the Cannington Mine (AMC, 1998; WASM, 2009a).

Mine Area	Average UCS (MPa)	Average σ_T (MPa)	Average E_{st} (GPa)	Average v_{st}
North Zone	209[7]	13[6]	80[7]	0.29[7]

The ore grade block model at Cannington correlates closely with the density of the intact rock. Therefore, the average rock density values for each study stope have

been determined from the mine ore grade block model (Li, 2009). Accurate determination of the rock densities for each study stope was important to perform the calculations of blast-induced energies and strains. Table 8.2 lists the values of rock density used for the two North Zone study stopes according to the block model.

Table 8.2. Rock densities supplied by the Cannington reserve model (Li, 2009).

Stope	Average Rock Density (kg/m^3)
22gC6HL	3765
24jC6HL	3585

8.5.1.2 North Zone Discontinuity Mapping

A project was initiated at the Cannington Mine in 2007-2008 to digitise the development backs mapping sheets for the entire mine. The digital files could then be used to examine the mapped discontinuities on each production level to perform rock mass characterisations and designs of ground support and reinforcement schemes. Figure 8.7 shows the digitised mapping for the 180mLv and 200mLv of the North Zone used for the discontinuity orientation distribution shown in Figure 8.8.

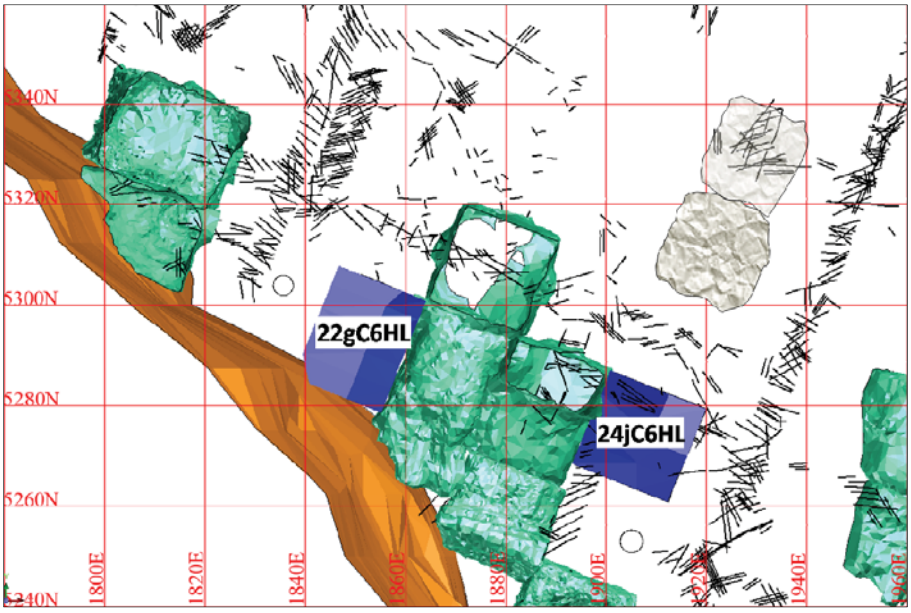

Figure 8.7. Plan view of the results of digitised drive backs mapping of the Southern end of North Zone on mine levels 180mLv and 200mLv.

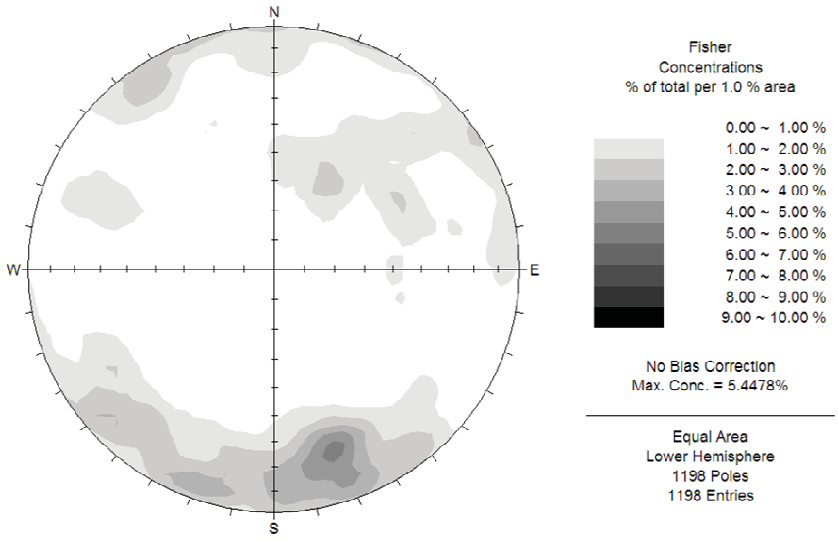

Figure 8.8. Discontinuity distribution from backs mapping of the 180mLv, 200mLv and 220mLv in the North Zone near stopes 22gC6HL and 24jC6HL.

The results in Figures 8.7 and 8.8 indicate possibly three discontinuity sets, although a level of mapping bias could be expected due to the mapping of primarily the backs of the development drives. This practice would be expected to neglect shallow-dipping discontinuities that may have been exposed in the excavation walls, but not in the backs.

Most of the mapped discontinuities shown in Figure 8.8 were steeply dipping, with the exception of one joint set at approximate dip/dip direction of 20º-40º/200º-220º. The mapping program included mostly excavation-scale discontinuities based on the observed trace lengths being greater that 5m. The mapped discontinuity spacing ranged from 500mm to 2m, and most discontinuities observed in the North Zone were tightly-healed.

8.5.1.3 Mining-Induced Static Stress Modelling

The software package MAP3D was used by the author to perform linear-elastic mining-induced static stress modelling for the North Zone over a number of mining steps. Seven modelling grids were included to represent orientations of interest. The grids were either vertical or horizontal and positioned on various orientations and positions with respect to stopes 22gC6HL and 24jC6HL. Figure 8.9 shows the

modelled mining steps as specified by the colour of the block and the position of vertical grids 1, 2 and 4 (top), and horizontal grids 3, 5, 6 and 7 (bottom) used to assess of the state of stress in the vicinity of stopes 22gC6HL and 24jC6HL during the various mining steps.

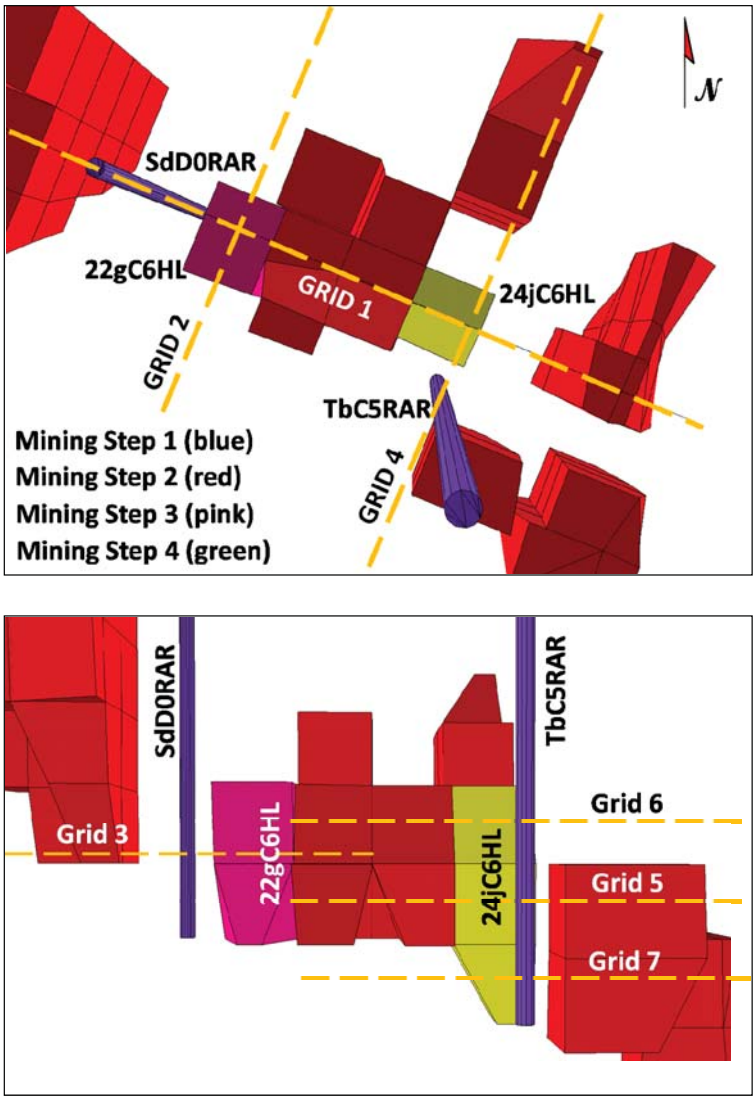

Figure 8.9. Plan view of North Zone MAP3D model with position of vertical grids 1, 2 and 4 (top) and isometric view of horizontal grids 3, 5, 6 and 7 (bottom) for stopes 22gC6HL and 24jC6HL.

The North Zone development and the Trepell Fault were initially included in the MAP3D model, but were removed prior to performing the stress modelling calculations for the two study stopes. These objects were removed due to errors in

the specified fault-slip properties and the excessive number of finite elements required to populate the modelled surfaces. The removal of the development and the fault were not expected to significantly alter the large-scale modelling results due to the low to the linear-elastic nature of the model and the moderate field stresses at the shallow mining depth. Removal of the fault and development would not be expected to reflect reality, as large-scale faults and existing excavations would significantly influence local stress magnitudes and distributions. Therefore, both the characteristic material model (linear-elastic homogeneous) and the inability to include all of the significant features represent limitations to the stress modelling results.

Stress measurements performed by WASM Acoustic Emission (AE) and CSIRO Hollow-Inclusion Cell (HI cell) methods were reviewed as part of a geotechnical audit for the Cannington Mine (Villaescusa, 2004). These measurements were used to determine the virgin field stress magnitudes and orientations for use in numerical modelling at the mine site. The equations for estimation of the principal stress magnitudes and orientations as a result of the review are listed in Equations 8.1, 8.2 and 8.3 (Li, 2007 after Villaescusa, 2004).

$\sigma_1 = 0.0601 \times depth \quad (129^o/14^o : Trend/Plunge)$ (8. 1)

$\sigma_2 = 0.0463 \times depth \quad (223^o/08^o)$ (8. 2)

$\sigma_3 = 0.0265 \times depth \quad (359^o/80^o)$ (8. 3)

The principal stress estimation equations and other material properties provided by Cannington personnel were used to model the mining-induced static stresses for four mining steps on seven specified grids. Vertical grid 1 was the only grid that was designed to pass through both monitored North Zone stopes. The results of the mining-induced static stress modelling for grid 1 is shown in Figures 8.10 to 8.12 for mining step 2. Step 2 was the step prior to extraction of either stope 22gC6HL or 24jC6HL.

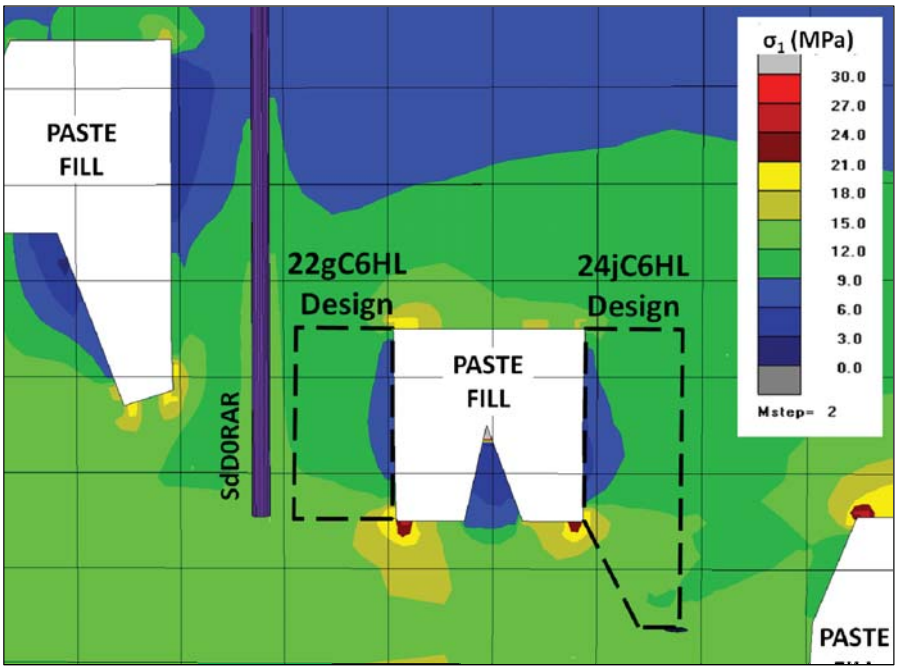

Figure 8.10. Results of MAP3D mining-induced static stress modelling of σ_1 on grid 1 at mining step 2 (looking northeast).

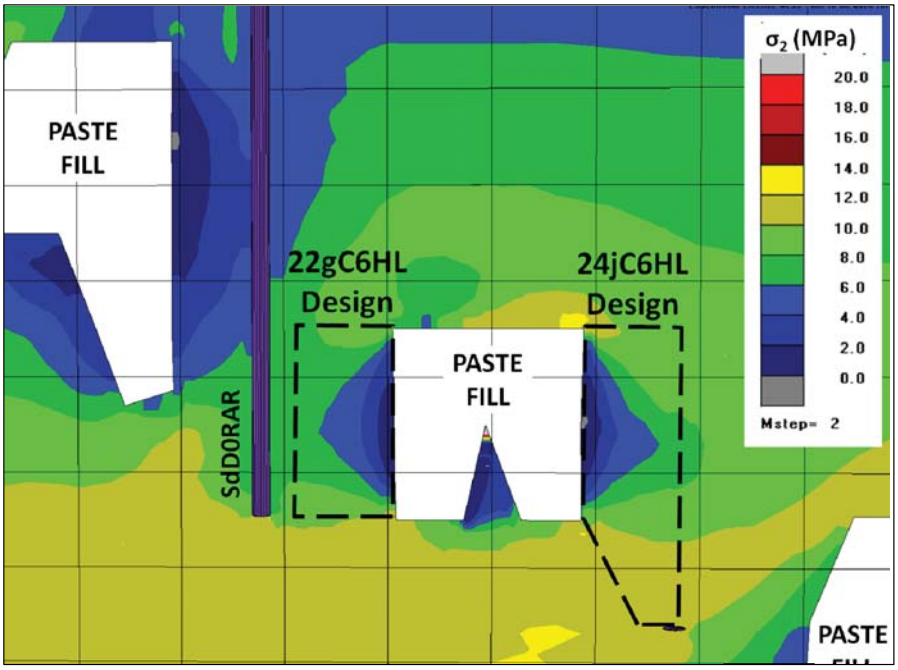

Figure 8.11. Results of MAP3D mining-induced static stress modelling of σ_2 on grid 1 at mining step 2 (looking northeast).

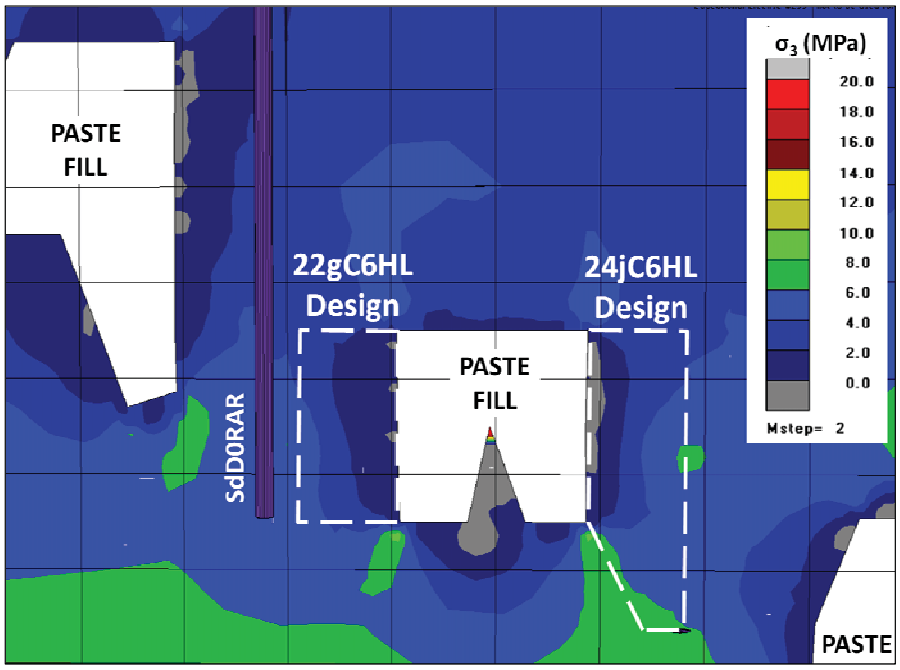

Figure 8.12. Results of MAP3D mining-induced static stress modelling of σ_3 on grid 1 at mining step 2 (looking northeast).

The stress modelling results indicated no regions of significant stress concentration around stopes 22gC6HL or 24jC6HL that would potentially lead to stress-related rock mass damage from compressive crushing. Significant areas of low stress concentrations were observed around the existing fill between stopes 22gC6HL and 24jC6HL. This loss of confining stresses could contribute to rock mass damage through opening of fresh or existing discontinuities prior to paste filling of the mined stopes. The tightly-healed nature of the North Zone discontinuities would be expected to largely resist such relaxation effects, but similar conditions of low confinement in the Southern Zone would likely mobilise bird faults, leading to large-scale rock mass failures.

8.5.1.4 Stress Wave Velocities and Peak Amplitude-Frequency Analyses of the North Zone Rock Mass

Geophysical techniques that were applied to the block-scale rock mass characterisation of the North Zone included stress wave velocity measurements and peak amplitude-frequency analyses of recorded blasting vibrations. These analyses identified several key rock mass behaviours and block-scale rock mass anisotropies.

This evidence conflicted with the previously-held belief that the North Zone was largely homogeneous in nature. The data used for the North Zone geophysical assessments represented a large range of monitoring orientations and blasting geometries. The transducer coverage for the North Zone stopes ranged from four transducers in 22gC6HL to 14 in stope 24jC6HL. The reduced transducer coverage for stope 22gC6HL was due to the location of the stope with respect to fill masses and the Trepell Fault and the limited stock of transducers due to the short period between the two mine monitoring programs. Ample lead time was available for restocking and upgrading of transducers prior to stope 24jC6HL. Table 8.3 lists a summary of the transducers installed in the two monitored stopes of the North Zone.

Table 8.3. Summary of North Zone Blast Vibration Monitoring Instrumentation.

Stope Name	Firing Level (mLv)	Wall of Stope	Tri-axial Transducer Type	Distance from Stope (m)
22gC6HL	180	Northwest (NW)	500g Accelerometer Geophone	5.2 15.0
	180	Northeast (NE)	Geophone	12.1
	240	240-255 Decline	Geophone	16.4
24jC6HL	220	Northeast (220 NE)	Geophone	9.6
	220	Southeast (220 SE)	500g Accelerometer Geophone	6.6 12.5
	220	Southwest (220 SW)	500g Accelerometer Geophone	5.0 15.0
	200	Northeast (200 NE)	1000g Accelerometer Geophone	5.0 10.9
	200	Southeast (200 SE)	1000g Accelerometer Geophone	4.9 12.8
	200	Southwest (200 SW)	1000g Accelerometer Geophone	5.0 15.0
	180	Southeast (180 SE)	Geophone	9.8
	180	Southwest (180 SW)	1000g Accelerometer Geophone	5.1 15.1

The instrumentation strategy for 24jC6HL enabled the differential stress wave velocities to be calculated using the approach described in Chapter 7. No direct measurements of the stress wave velocities were possible for stope 22gC6HL. This was due to a lack of dual-transducer arrays in the Northeast and 240-255mLv orientations and the splitting of the two Northwest wall transducers onto separate, non-synchronised data acquisition systems for cabling purposes. The velocity values measured in stope 24jC6HL along similar orientations were viewed as adequate for application to stope 22gC6HL due to other recorded wave behaviours.

The VROS in-stope firing sequence applied in stope 24jC6HL limited the number of winze blastholes available for calculation of the stress wave velocities along different orientations. Fewer data points were therefore available for determination of the average stress wave velocities, although good grouping was observed. Figure 8.13 shows the measured stress wave velocities for each transducer array paired to common data acquisition systems in stope 24jC6HL.

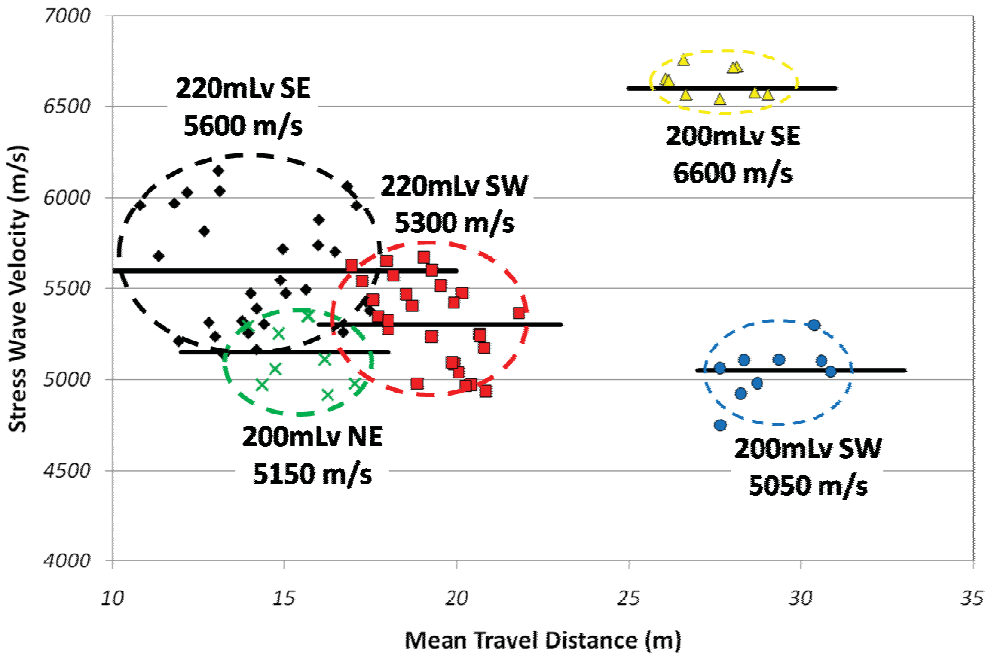

Figure 8.13. Plot of the measured stress wave velocities versus the mean travel distance in different walls of stope 24jC6HL.

Figure 8.13 shows a significant variation in the average stress wave velocities for different propagation orientations around stope 24jC6HL. Additional differences were observed for the different production levels. The apparent data scatter within the 220mLv Southeast (220mLv SE) and 220mLv Southwest (220mLv SW) data sets could have been attributed to the differences in angles of propagation between successive firings and the transducer arrays. The three rise firings of the 220mLv covered a vertical range of approximately 25m. The source holes used for the 200mLv velocity calculations consisted only of a single long-hole winze firing due to the VROS firing sequence. For the 180mLv firings, no velocity measurements were available due to the splitting of common-array transducers onto separate data acquisition systems for cabling purposes.

Of particular interest in Figure 8.13 were the data sets for the 200mLv, where significant differences in stress wave velocities existed between the Southeast (yellow triangles) and the Northeast and Southwest orientations (green exes and blue circles, respectively). The velocities for the Northeast and Southwest orientations were similar at 5150m/s and 5050m/s, whereas the velocity for the Southeast orientation was approximately 30% higher at 6600m/s. The dominant discontinuity orientations observed in Figure 8.8 partially explained the differences between the observations, but another geological condition was also believed to contribute. The lithological model provided by Cannington Mine personnel identified a change in rock and mineralisation types in the Southeast wall of the stope, extending to the Eastern extents of the North Zone. It was believed that the change in rock type and mineralisation type influenced the stress wave velocity. This influence is discussed further in Section 8.7.1.1.

Peak amplitude-frequency analyses were performed to further investigate any orientation-specific differences within the North Zone rock mass near the two study stopes. After the analyses were completed for each data subset, similarities between some of the VSPPV-VSPPA relationships were observed for data measured along similar monitoring orientations in each of the two stopes. Figures 8.14 and 8.15 show some of the individual data subsets of similar orientation and the best-fit equations. The best-fit lines for all data sets in Figures 8.14 and 8.15 were then plotted together in Figure 8.16 to show the proposed block-scale rock mass anisotropy.

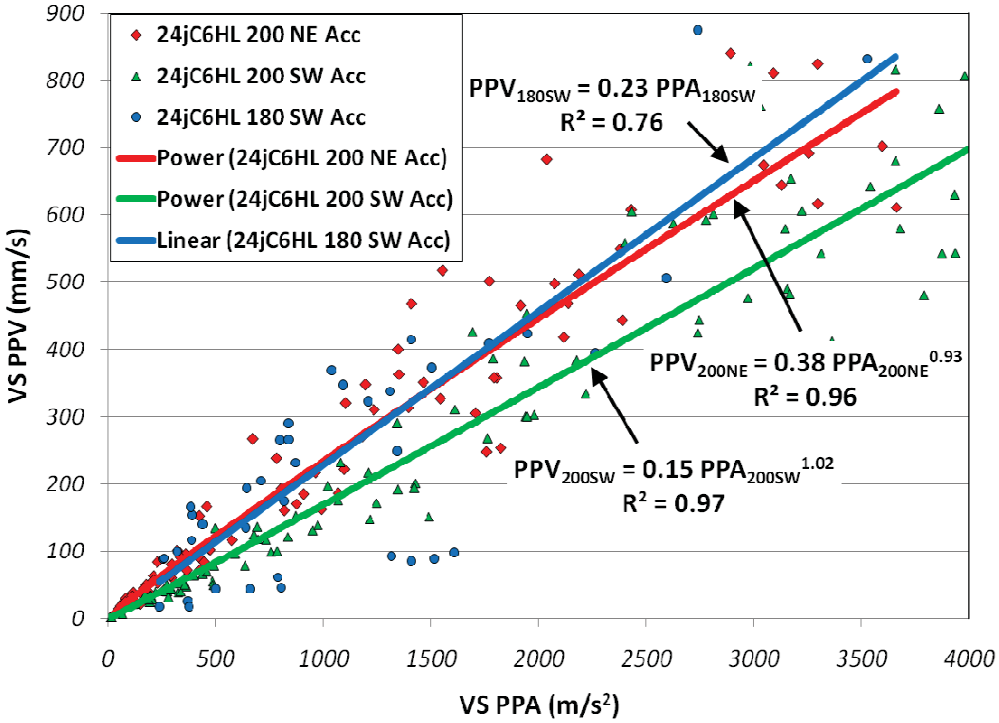

Figure 8.14. Plots of VSPPV versus VSPPA for 24jC6HL accelerometer data in the Northeast/Southwest orientations.

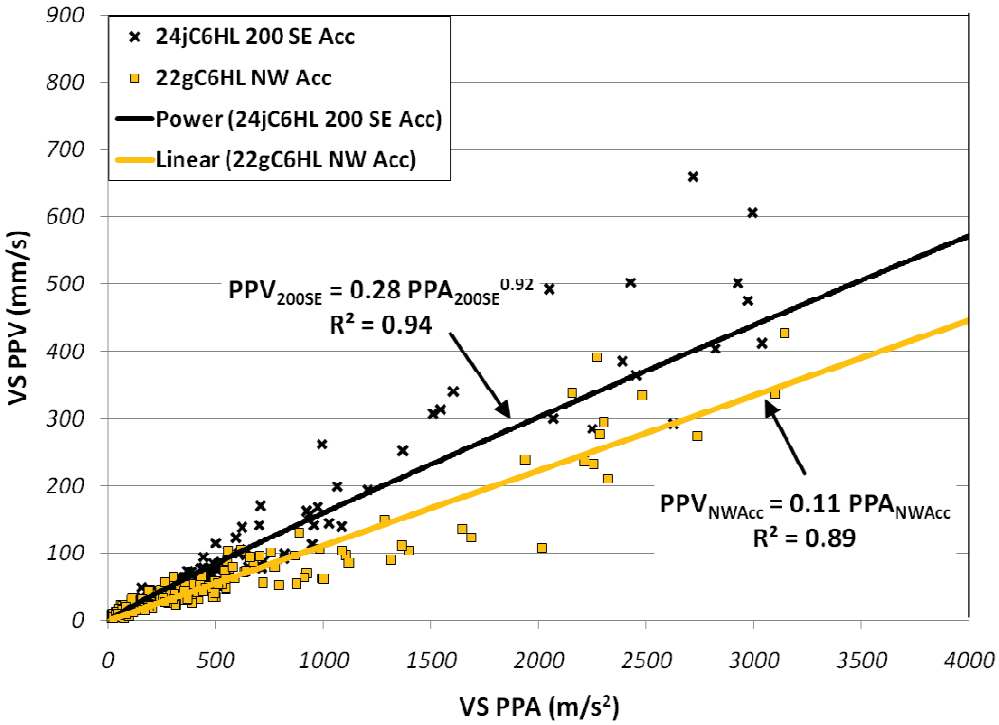

Figure 8.15. Plots of VSPPV versus VSPPA for 24jC6HL accelerometer data in the Southeast/Northwest orientation.

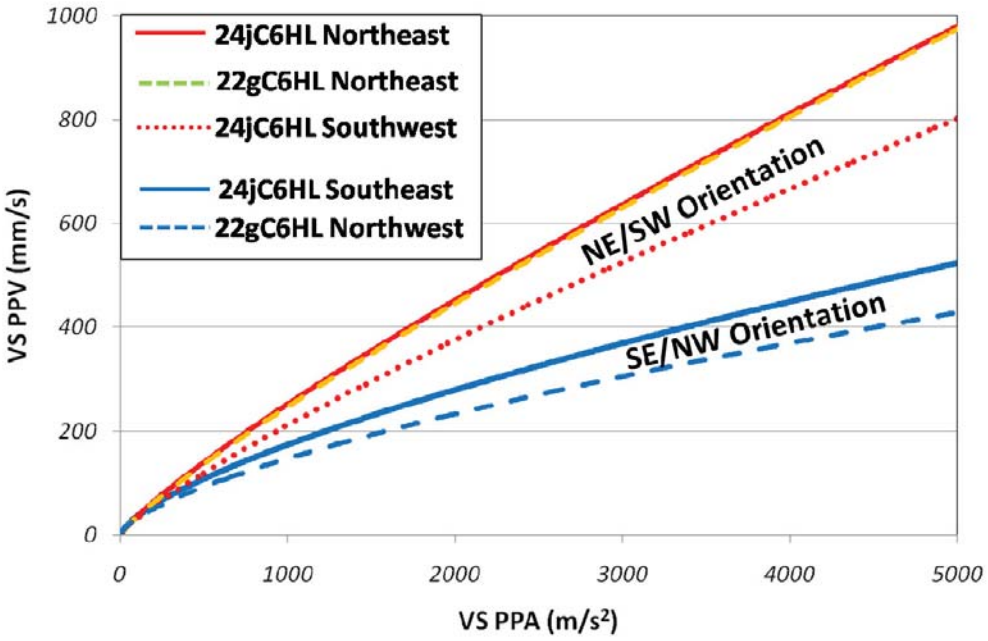

Figure 8.16. Best-fit VSPPV versus VSPPA lines shown in Figures 8.14 and 8.15 for North Zone blast monitoring data showing orientation-specific grouping.

The results of the peak amplitude-frequency analyses for the data collected in the North Zone clearly indicated a level of rock mass anisotropy between the Northeast-Southwest and Southeast-Northwest propagation orientations. This anisotropy was also indicated by the measured stress wave velocities. Therefore, some influence of the in situ discontinuities, induced static stress orientations and geology have been identified. This information has added to the interpretation of the North Zone rock mass characteristics with regard to both blast vibration propagation and the response of the rock mass to induced static stresses. The indicated anisotropy would be expected to influence both the severity and extent of blast-induced rock mass damage as related to the irregularity of propagating blast-induced wave fields.

The stress wave velocity measurements and indicated stiffness results have been combined with the discontinuity mapping in an attempt to characterise the North Zone rock mass anisotropies. Figure 8.17 illustrates the backs mapping from Figure 8.7 with the associated rosette plot of the mapped discontinuity strikes and the indicated directions of rock mass anisotropy as indicated by the stress wave velocities and indicated stiffness.

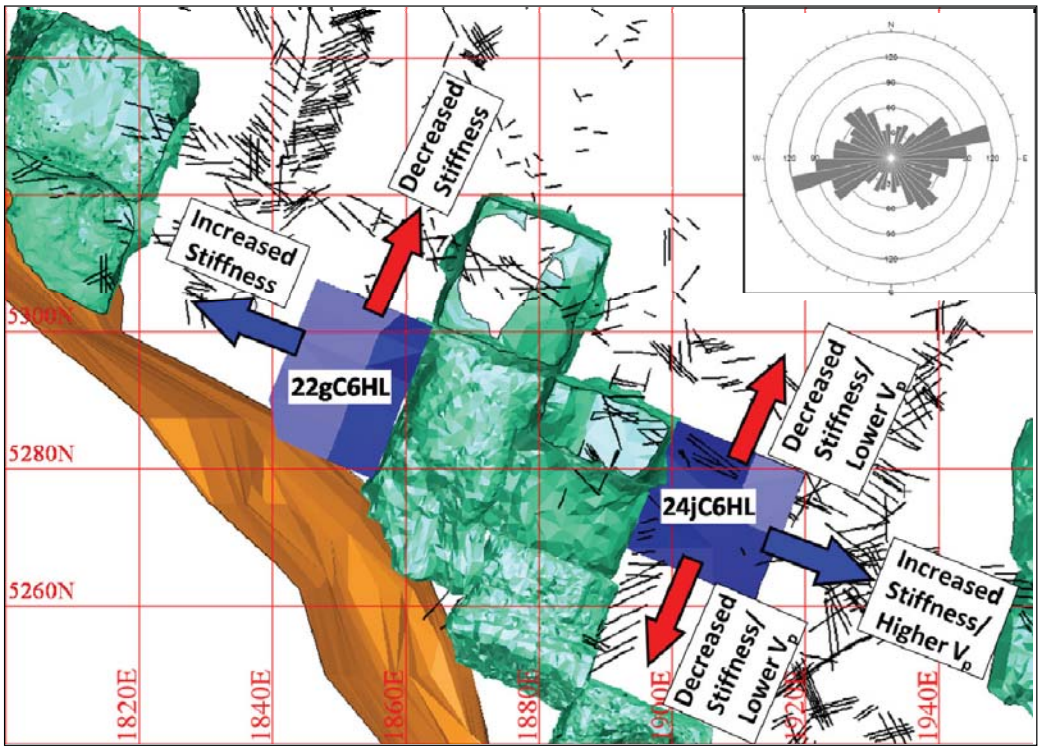

Figure 8.17. Plan view of stopes 22gC6HL and 24jC6HL with the discontinuity mapping results and comparisons of peak amplitude-frequency analyses and stress wave velocities (V_p) in the North Zone.

8.5.2 Results of North Zone Block-Scale Blast Vibration Analysis

The data collected at all monitoring locations from the 23 total firings in stopes 22gC6HL and 24jC6HL were combined as an aggregate data set of 2362 points for the North Zone block-scale characterisation. The nonlinear estimation approach described in Chapter 5 and used in Chapter 7 was then applied to the calculated values of $ED_{W\text{-}SS}$ and $\varepsilon_{W\text{-}MN}$ for the combined data set. The individual dynamic rock mass properties used in calculation of $ED_{W\text{-}SS}$ and $\varepsilon_{W\text{-}MN}$ for each data set will be detailed in the individual stope discussions. The regression constants and correlation values for the best-fit and 95% upper confidence prediction surfaces are listed in Table 8.4.

Table 8.4. Best-fit and 95% upper confidence nonlinear estimation results for $ED_{W\text{-}SS}$ and $\varepsilon_{W\text{-}MN}$ for the North Zone combined data set.

Model	Data Points	*K*	*b*	*n*	Best-fit R Value
Best-fit $ED_{W\text{-}SS}$ (J/m^3)	2362	13,852.56	0.737	-1.913	0.41
95% $ED_{W\text{-}SS}$	2362	28,546.70	0.943	-1.750	
Best-fit $\varepsilon_{W\text{-}MN}$ (με)	2362	423.83	0.435	-1.335	0.58
95% $\varepsilon_{W\text{-}MN}$	2362	593.05	0.510	-1.264	

The three-dimensional surfaces represented by the 95% upper confidence regression results for the $ED_{W\text{-}SS}$ and $\varepsilon_{W\text{-}MN}$ for the combined North Zone data set are shown in Figures 8.18 and 8.19.

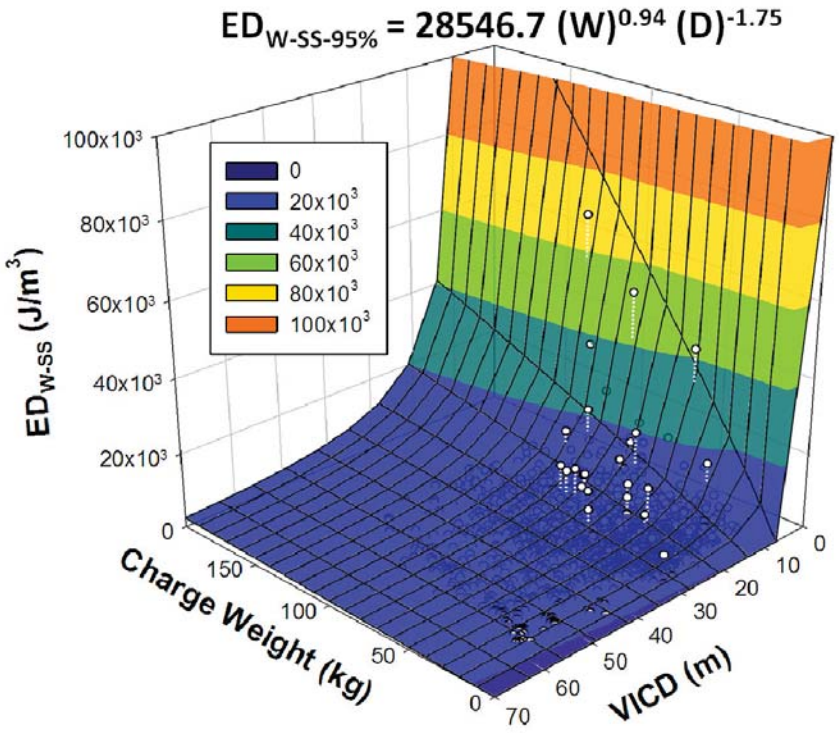

Figure 8.18. 95% upper confidence surface from nonlinear regression of $ED_{W\text{-}SS}$ versus charge weight and VICD for the combined Cannington North Zone data set.

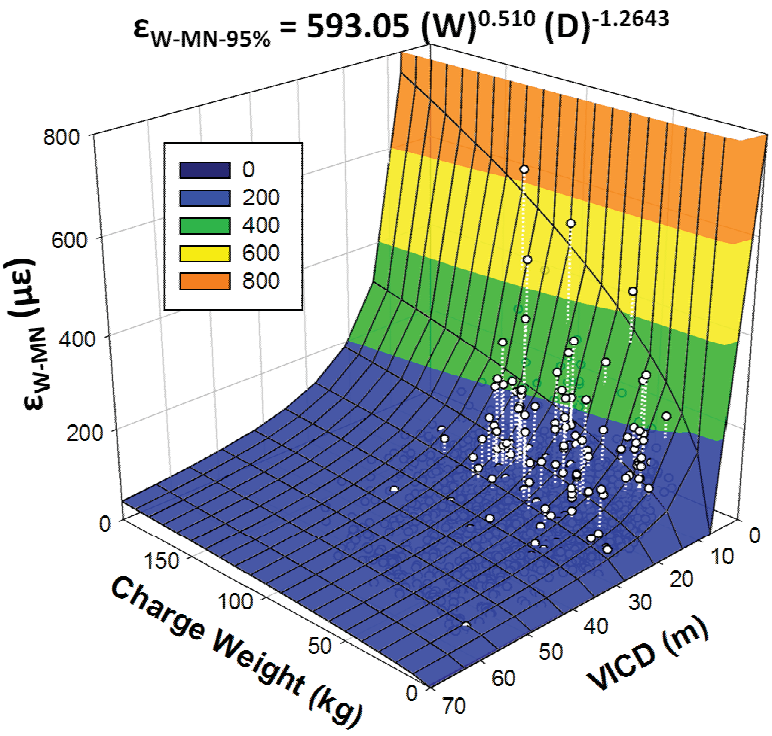

Figure 8.19. 95% upper confidence surface from nonlinear regression of $\varepsilon_{W\text{-}MN}$ versus charge weight and VICD for Cannington North Zone data.

The low correlation coefficients observed for the combined North Zone blast vibration data was similar to that noted in the grouped data set in D block at KBGM. This behaviour could be expected for the stopes of the North Zone based on the newly-proposed block-scale anisotropies observed from the geophysical analysis approaches. Individual nonlinear estimations were therefore performed for each stope and data subset after segregating the data into individual levels or orientations within each of the two North Zone stopes. These results are presented along with rock mass characterisations and stope performance assessments of 22gC6HL and 24jC6HL in Sections 8.6 and 8.7, respectively.

8.6 22gC6HL Blast Monitoring Instrumentation, Vibration Analysis Results and Stope Performance Assessment

At the time of monitoring of stope 22gC6HL, limited blast vibration monitoring transducers were available due to near depletion of stocks from the monitoring program at KBGM. The transducers that were available were therefore installed in

the proximity of the infrastructure with the highest threat of blast-induced damage. A dual-transducer array was installed at the 1053m elevation (roughly mid-span) in the temporary pillar containing the SdD0RAR. A single tri-axial geophone sonde was placed in the Northeast wall of the stope at a similar elevation. These transducers were cement grouted in downholes drilled from the 180mLv. An additional transducer was installed near the 240-255mLv Trepell Fault crossing to monitor the vibrations at the decline-fault intersection. Excessive vibrations were expected at this location from the trough firing, which was drilled and charged from the 220mLv closest to the fault crossing and explosives magazine. No transducers were installed in the pillar against the Trepell Fault due to a lack of drilling access. Figure 8.20 illustrates the locations of transducers for stope 22gC6HL.

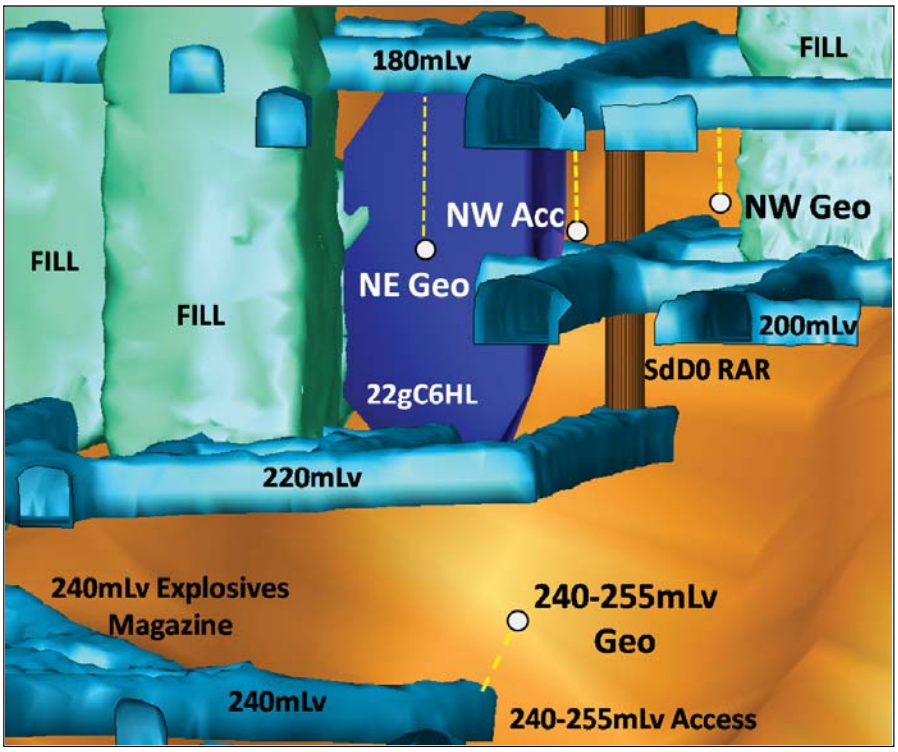

Figure 8.20. Isometric view of the 22gC6HL blast vibration monitoring transducers (looking southeast).

8.6.1 Dynamic Rock Mass Properties for Stope 22gC6HL

Dynamic rock mass properties were required to calculate the values of $ED_{W\text{-}SS}$ and $\varepsilon_{W\text{-}MN}$ for the blast vibration analysis for stope 22gC6HL. These values are listed in Table 8.5.

Table 8.5. In situ dynamic rock mass properties as indicated for stope 22gC6HL.

Wall	Rock density (kg/m^3)	E_{dyn} (GPa)	v_{st}	Wave Velocity (m/s)	λ_L (GPa)
Northwest	3765	90	0.29	5600 (A)	48
Northeast	3765	78	0.29	5200 (A)	42
240-255mLv	3765	84	0.29	5400 (A)	45

The monitoring techniques used in stope 22gC6HL did not allow measurement of the stress wave velocities. The assumed (A) values in Table 8.5 were based on the measurements from similar orientations in stope 24jC6HL. The stress wave velocities for the Northwest and Northeast walls of 22gC6HL were assumed to be similar to those along the same orientations in stope 24jC6HL (5600m/s and 5200m/s, respectively). The value chosen for the 240-255mLv orientation was an average value between the other two walls (5400m/s). Identification of the wave velocity values as measured (M) or assumed (A) has been applied to all other tables.

8.6.2 22gC6HL Blast Vibration Analysis Results

Individual nonlinear estimations were performed for the separate monitoring directions in stope 22gC6HL to investigate the effect of orientation on blast vibration attenuation. The Northeast wall data were combined with the 240-255mLv data due to similarities in the wave propagation orientations. The results of the nonlinear estimations are listed in Table 8.6. Additional regression results are included in Appendix 9.

Table 8.6. 95% upper confidence nonlinear estimation results for the 22gC6HL data as combined data sets for each stope wall.

Model	Stope Wall	Data points	*K*	*b*	*n*	Best-fit R value
95% $ED_{W\text{-}SS}$	Northwest	441	1921.11	1.447	-1.493	0.50
95% $\varepsilon_{W\text{-}MN}$		441	118.09	0.813	-0.980	0.56
95% $ED_{W\text{-}SS}$	Northeast-240-255mLV	563	1034.28	1.625	-1.849	0.67
95% $\varepsilon_{W\text{-}MN}$		563	817.42	0.478	-1.311	0.76

The regression constants and correlation values for individual orientations changed significantly when compared with the combined data set for the entire stope, especially for the models of $\varepsilon_{W\text{-}MN}$. Subdivision of the data into individual transducers further improved the correlation values for $\varepsilon_{W\text{-}MN}$ to 0.77 for the Northwest wall accelerometer and 0.69 for the Northwest wall geophone versus 0.56 for the combined data set. Separation of the Northeast wall geophone and 240-255mLv geophone data was not deemed necessary due to the strong correlations achieved from the combined data set. The 95% confidence $\varepsilon_{W\text{-}MN}$ prediction equations for each individual transducer were:

Northwest Accelerometer: $\varepsilon_{W\text{-}MN\text{-}95\%} = 21488.72\ (W)^{0.59}\ (D)^{-2.35}$ (8. 4)

Northwest Geophone: $\varepsilon_{W\text{-}MN\text{-}95\%} = 819.73\ (W)^{0.74}\ (D)^{-1.27}$ (8. 5)

Northeast/240-255mLv Geophones: $\varepsilon_{W\text{-}MN\text{-}95\%} = 817.42\ (W)^{0.48}\ (D)^{-1.31}$ (8. 6)

Figure 8.21 displays the two-dimensional representation of the regression surfaces for $\varepsilon_{W\text{-}MN\text{-}95\%}$ for the three data sets at a constant charge weight of 50kg to demonstrate the differences in attenuation behaviours based on the monitoring and analysis results.

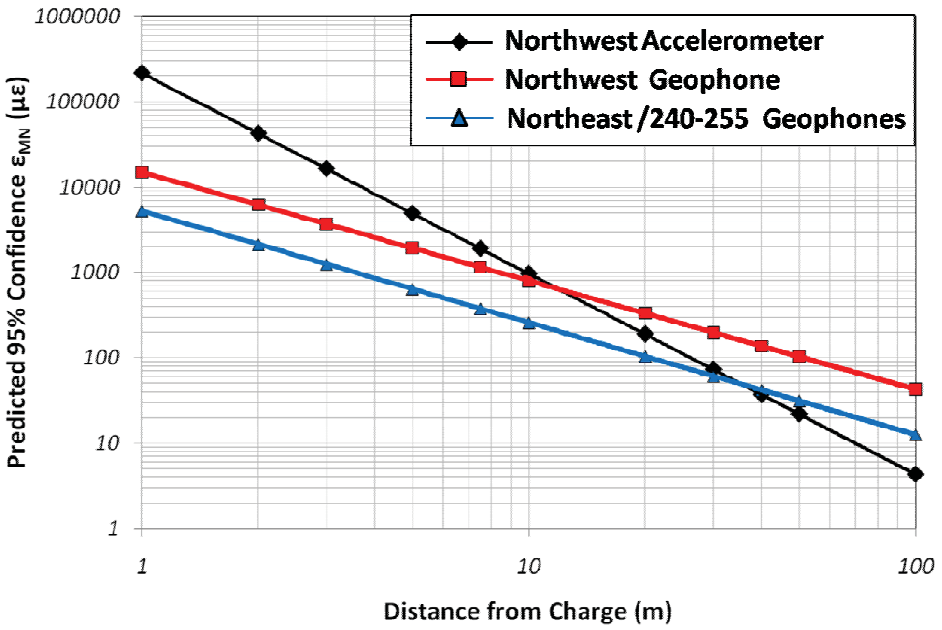

Figure 8.21. Log-log plot of 95% upper confidence $\varepsilon_{W\text{-}MN}$ predicted for the 22gC6HL Northwest and Northeast wall individual transducers at a charge weight of 50kg.

The results from the nonlinear regressions for each individual transducer further identified differences in the vibration behaviours based on distance as well as orientation. The general charge weight scaling relationship did not accurately represent combined near-field and intermediate-field data, but the similarities between the slopes for the Northwest and Northeast geophone data sets suggested that charge weight scaling could be applied confidently in the intermediate-field.

It should be noted that a significant number of accelerometer saturations occurred during monitoring of 22gC6HL due to the 500g amplitude limit. These saturations took place mostly during ring firing against the Northwest stope perimeter. Waveform saturations limited the amount of high-amplitude near-field data that could be collected for the Northwest wall of 22gC6HL, leading to an incomplete characterisation of the blast vibrations.

8.6.3 Stope Performance Assessment for 22gC6HL

Two stope performance assessment techniques were applied to stope 22gC6HL during and after stope production. The two techniques were post-extraction void assessment from the CMS survey and visual inspections of infrastructure and development to record incidences of blast-induced surface damage to excavations.

The inspections conducted in relation to stope 22gC6HL included the 180mLv development, SdD0RAR, shotcrete arches in the 240-255mLv fault crossing and the 240mLv explosives storage magazine. In addition to the visual inspection, photographs were taken within the explosive magazine, SdD0RAR and development drives prior to and during stope production for comparison. The locations and types of development damage observed during stope production were recorded on a damage map.

8.6.3.1 Visual Blast Damage Assessments in Stope 22gC6HL

Visual assessments of excavations near stope 22gC6HL were generally performed one shift after each stope firing upon re-entry. This inspection schedule allowed any freshly-formed large fractures or fall-off from the development or RAR to be detected and mapped prior to disturbance by the mining cycle. Inspection of SdD0RAR was limited to the portions exposed by the ventilation windows located at the 180mLV, 200mLv and 220mLv. Prior to initiation of blasting in 22gC6HL, the 240mLv magazine was inspected and existing cracks in the shotcrete on the walls and back of the magazine were photographed. In general, small cracks were observed in the shotcrete of the magazine prior to blasting, with some larger cracks around the 240mLv level bulkhead.

Due to the concerns of damage to the magazine during blasting, storage of high explosives in the area of the magazine closest to stope 22gC6HL was prohibited. This storage exclusion was extended to the completion of stope 24jC6HL due to similar concerns. Isolated incidents of minor spalling of fibre-reinforced shotcrete from the walls of the magazine occurred during extraction of stope 22gC6HL. These incidents were detected during inspection on August 21, 2006 after the mass and main rings firings. The predicted PPV at the recorded spalling locations was

approximately 40mm/s, which was well below what was expected to cause spalling of competent shotcrete. Figure 8.22 shows two locations of recorded fibrecrete spall within the 240mLv explosive magazine as a result of 22gC6HL stope firings.

Figure 8.22. Pictures of spalled shotcrete in the 240mLv explosives magazine occurring with the mass blast or main rings firing of stope 22gC6HL.

No damage was detected in SdD0RAR during the period of assessment of stope 22gC6HL. Concerns had been originally raised regarding shakedown of mudstones and oxidised material from the upper levels of the raise near the surface. Inspections were performed at the bottom level of the RAR at the 220mLv to look for freshly fallen material after large stope firings. No new material was detected at the 220mLv RAR bottom as a result of fall-off. Additional visual inspections through the ventilation windows at the 180mLv and 200mLv did not indicate any change in fracturing in the leading edge of the RAR nearest 22gC6HL or any change in water flow as a result of increased fracturing of the pillar.

In addition to visual assessment of the permanent infrastructure, the development drives of the 180mLv were also inspected for blast-induced fall-off following stope firing events. The damage areas were mapped and photographed such that the ground

support conditions, locations of damage and types of damage could be recorded. Blast-induced damage to the development in the proximity of stope 22gC6HL generally occurred in areas where there was no surface support or the existing surface support was damaged or poorly installed. Blast vibration monitoring results were used to predict the maximum PPV values at the locations of each mapped damage event. In general, damage occurred at PPV values in excess of 100 mm/s incident PPV values. Surface reflection amplification factors were not considered.

A majority of damage observed in the 180mLv development was either discrete block failures or spall damage. Block failures were typically characterised by fall of pre-formed blocks, which were detached along geologic structure as indicated by oxidised failure surfaces. Spalling damage was indicated by shallow failures and fresh fracture surfaces. On several occasions, existing shotcrete was detached and fell away from the excavation either from behind damaged mesh or from on top of the existing mesh. Fall of shotcrete was characterised as either discrete block fall or spalling depending on the surface area of failure. Discrete block detachments were typically of the order of 20kg up to several tonnes and occurred in the absence of surface support. Spalling failures were generally less than 100mm in thickness and covered areas of $1m^2$ to $10m^2$ below the mesh grade line on the walls of development drives. In one observed instance, spalling occurred behind damage mesh at the drive shoulder.

Most of the discrete block falls or spalling recorded in relation to blasting of 22gC6HL occurred below the 1.5m mesh grade line at PPV values above 100mm/s with the exception of two events. Figure 8.23 shows the results of damage mapping on the 180mLv indicating the locations of observed damage, the indicated type of damage and the firing after which the damage was recorded. Figure 8.24 shows two recorded incidences of blast-related damage below the mesh grade line caused by blasting events in stope 22gC6HL. The two cases of wall damage illustrated in Figure 8.24 occurred at predicted PPV levels of 280mm/s (left) and 150mm/s (right).

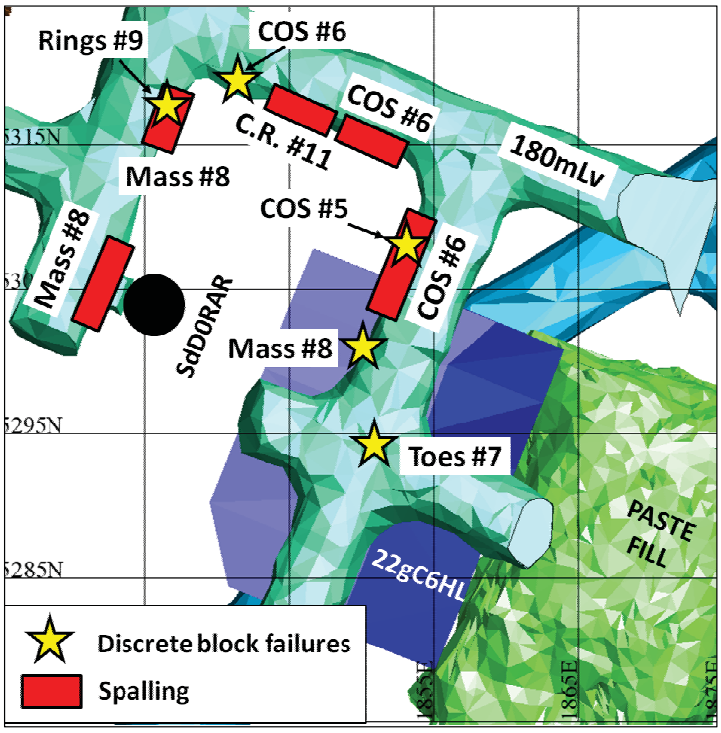

Figure 8.23. Plan view of the 180mLv mapped damage occurring with each firing of stope 22gC6HL.

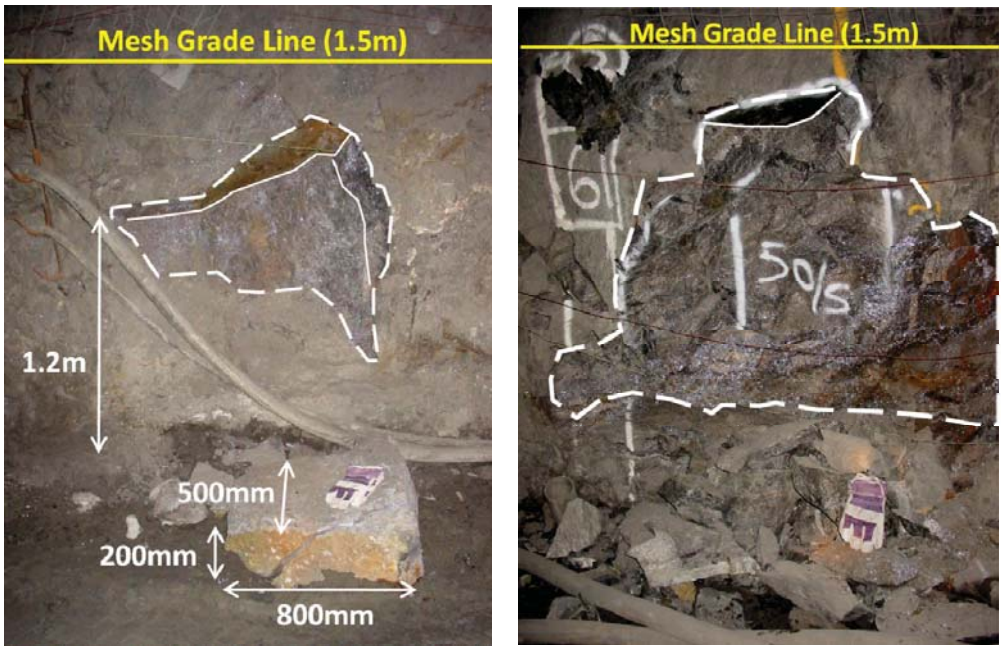

Figure 8.24. Photographs of a block fall from 1.2m height after stope firing LHW-COS #5 (left) and spall from floor to grade line after COS #6 firing (right) in drive 180mLv KcDS.

Although most of the observed blasting-related damage to infrastructure did not pose significant risk to personnel or equipment, additional mine services were required to perform spot scaling where damage was viewed as representing a significant risk to charge-up personnel. The falls of material also caused frequent damage to the blast monitoring instrumentation cables.

8.6.3.2 22gC6HL Post-Extraction Stope Performance Assessment

The 22gC6HL design and CMS wireframes were compared using the approach described in Chapter 7 to assess the post-extraction stope performance. The resulting overbreak and underbreak volumes are listed in Table 8.7 and the maximum depths of overbreak for each stope wall are listed in Table 8.8.

Table 8.7. Overbreak and underbreak volumes resulting from comparison of the post-extraction CMS and the design wireframes for North Zone stope 22gC6HL.

Stope Performance Criteria	Volume (m^3)	% of Design Volume
Total Overbreak	1157	8.9
Total Underbreak	678	5.2

Table 8.8. Maximum depth of overbreak in each wall of stope 22gC6HL.

Stope Wall	Maximum Depth of Overbreak (m)
Northwest	1.0 (ore)
Northeast	1.2 (ore)
Southeast (partial paste)	2.8 (ore)
Southwest	1.4 (ore)

In general, stope 22gC6HL performed well, with a relatively low percentage of overbreak and underbreak. The overbreak observed in the Southeast wall adjacent to a paste fill mass did not appear to breach the rock-paste interface due to the underbreak in the adjacent stope. All overbreak for stope 22gC6HL was therefore in

ore and no dilution was experienced. A single wedge-type failure was observed below the 180mLv development on the Southeast wall near the stope crown in addition to some expected undercutting of the 180mLv. The wedge failure was not considered in the determination of the maximum depth of overbreak due to the influence of the development on the block release. This type of undercutting at the 180mLv was undesirable for the stope crown of 22gC6HL, as the stope was not intended to be tight filled. Paste filling was planned only to the floor elevation of the 180mLv to reduce the preparation work for later mining of stope 18gC6HL directly above 22gC6HL.

8.7 24jC6HL Blast Monitoring Instrumentation, Vibration Analysis Results and Stope Performance Assessment

Stope 24jC6HL was mined as a multiple-lift stope from the 240mLv to the 180mLv. A level-based naming convention for the blast vibration monitoring transducers was adopted to reflect the positions of the transducers related to the level from which the firings were being charged. Production firings of the ore block between the 240mLv and 220mLv (charged from the 220mLv) have been referred to as 220mLv firings. The transducers installed between the 240mLv and 220mLv (at approximately the 230mLv) to monitor these firings have been referred to as 220mLv transducers. Similar conventions have been applied to the transducers installed between the 220mLv and 200mLv (200mLv firings and transducers) and the 200mLv and 180mLv (180mLv firings and transducers). Figure 8.25 shows an isometric view of the transducers installed around stope 24jC6HL.

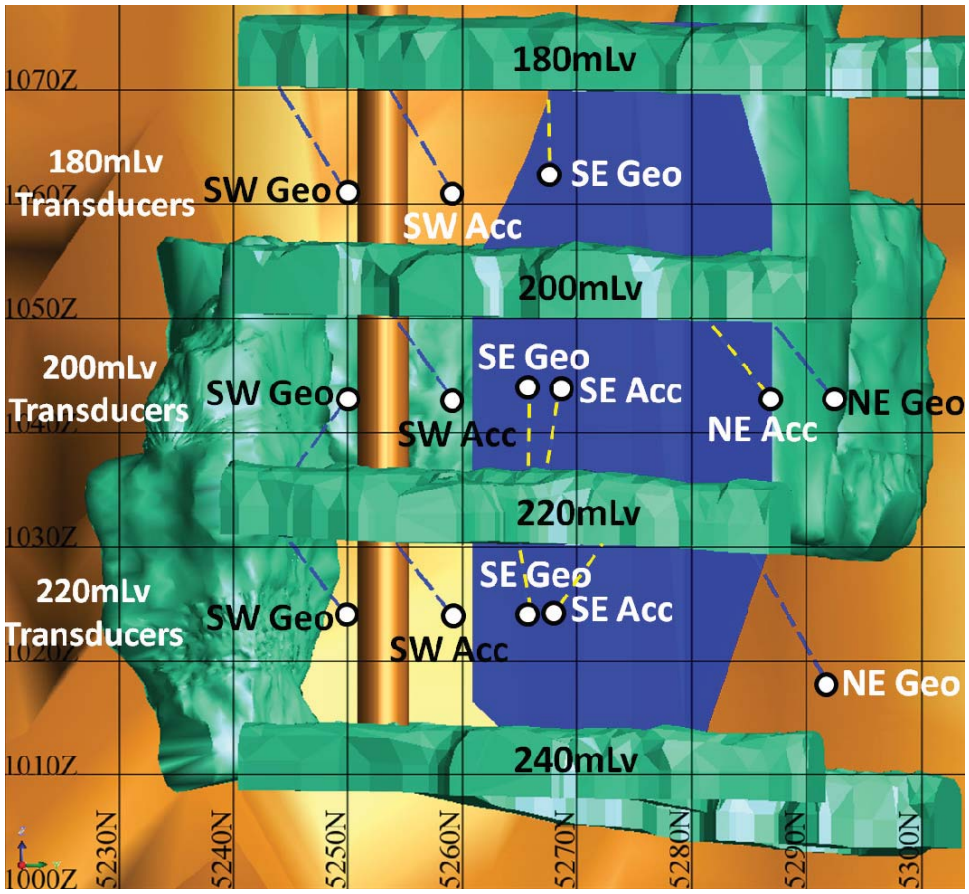

Figure 8.25. Isometric view of blast vibration monitoring instrumentation installed for the 220mLv, 200mLv and 180mLv firings in stope 24jC6HL (looking west).

A total of 14 tri-axial transducers were installed in stope 24jC6HL to monitor 12 stope firings. Only 6 tri-axial transducers could be monitored in a single firing in stope 24jC6HL as a function of the number of recording channels available on the three data acquisition units. In a number of stope firings, transducers located on different stope levels were monitored together to gain additional information on the behaviour of the blasting vibrations either above or below the firing level. This capability was most important for the final cleaner ring stope firing, where transducer arrays on the 180mLv, 200mLv and 220mLv were all monitored simultaneously. Table 8.9 lists the transducer types, locations and offsets from the 24jC6HL designed stope perimeter.

Table 8.9. Summary of North Zone stope 24jC6HL blast vibration monitoring instrumentation.

Level (mLv)	Wall of Stope	Tri-axial Transducer Type	Distance from Stope (m)
220	Northeast Wall (NE)	Geophone	9.6
220	Southeast Wall (SE)	500g Accelerometer Geophone	6.6 12.5
220	Southwest Wall (SW)	500g Accelerometer Geophone	5.0 15.0
200	Northeast Wall (NE)	1000g Accelerometer Geophone	5.0 10.9
200	Southeast Wall (SE)	1000g Accelerometer Geophone	4.9 12.8
200	Southwest Wall (SW)	1000g Accelerometer Geophone	5.0 15.0
180	Southeast Wall (SE)	Geophone	9.8
180	Southwest Wall (SW)	1000g Accelerometer Geophone	5.1 15.1

8.7.1 24jC6HL Stress Wave Velocities and Specific Attenuation Analyses

The stress wave velocities for each monitored wall of stope 24jC6HL were determined using the results of the blast vibration monitoring program. Table 8.10 lists the stress wave velocity values applied to the calculations of energy and strain for use in the nonlinear estimations discussed in later sections.

Table 8.10. Measured (M) and assumed (A) stress wave velocities for the monitoring orientations of stope 24jC6HL.

Stope Wall	Wave Velocity (m/s)
220mLv Northeast	5300 (M)
220mLv Southeast	5600 (M)
220mLv Southwest	5300 (A)
200mLv Northeast	5150 (M)
200mLv Southeast	6600 (M)
200mLv Southwest	5050 (M)
180mLv Southeast	5500 (A)
180mLv Southwest	5050 (A)

The clear outlier of all measured stress wave velocities for stope 24jC6HL was the Southeast wall of the 200mLv. The value of 6600m/s was 20-30% higher than the other measured values. The significant differences between the measured wave velocities required further investigation, as the indication of increased stiffness and the discontinuity orientations for the Southeast wave-path did not appear to fully account for the substantial increase. The expected difference in stress wave velocities as a function of the wave travel path relative to the discontinuity orientation was observed in the 220mLv sublevel. The stress wave velocity for the 220mLv Southeast orientation was approximately 6% higher than the Northeast orientation. To further investigate the velocity anomaly, the lithological and mineralisation models for the North Zone were reviewed as previously mentioned in Section 8.5.1.4.

8.7.1.1 Proposed Effects of Mineralisation Type on Stress Wave Velocity

The North Zone geological models were reviewed in the vicinity of stope 24jC6HL to aid in determining the likely contributions of the rock and mineralisation types to the velocity anomaly observed for the 200mLv Southeast monitoring orientation. Upon review of the geological models, a significant mineralisation contact was identified in the Southeast wall of stope 24jC6HL. Within this contact zone, three

types of mineralisation were discovered from the geological interpretations. The three types were Broadlands (BL), Burnham (BM) and Glenholme (GH) mineralisation. The BL, BM and GH mineralisation represent three of the nine types of mineralisation in the Cannington orebody, which are classified by the ratio of metals, ore grade, and gangue minerals (Walters and Bailey, 1998). The mineralisation contacts observed in the Southeast wall of stope 24jC6HL are shown in Figure 8.26.

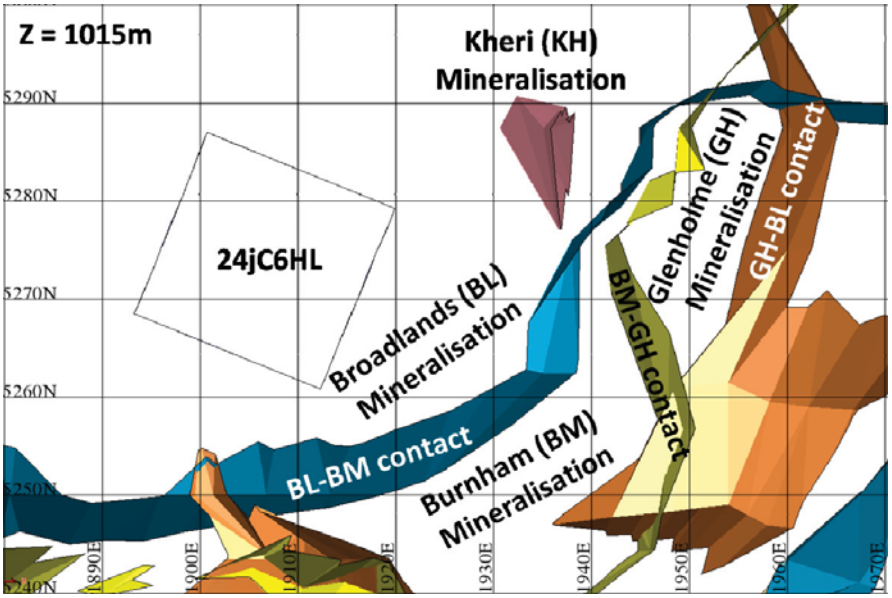

Figure 8.26. Plan view of stope 24jC6HL and mineralisation contacts in the Southeast wall of the stope at the 1015m elevation.

According to Walters and Bailey (1998), the BL mineralisation is associated with low to medium grades, whereas the BM and GH mineralisation is typically of high grade. The specific effect of the mineralisation type on the wave propagation characteristics at Cannington are not known, but the presence of the mineralised contacts would be expected to contribute to variations in stress wave velocities. Past researchers have observed the influence of mineralisation on the seismic properties of rocks (e.g. Rafat et al., 2001; Luo et al., 1998). Other factors that may have also influenced the stress wave velocities were the discontinuity orientation, density or condition (e.g. Maxwell and Young, 1996; Cosma et al., 2001) and the state of static stress (e.g. McGaughey et al., 1994; Friedel et al., 1996; Scott et al., 2004). Future

investigations would be required to specifically determine the influence of mineralisation type on stress wave propagation characteristics at Cannington.

8.7.1.2 Specific Amplitude Attenuation Analysis

The stress wave velocities and peak amplitude-frequency analyses for the North Zone block-scale assessment provided two methods of indicating the conditions of the rock mass around 24jC6HL. An additional geophysical method of rock mass assessment was proposed in Chapter 6, which involves comparison of the specific energy or amplitude attenuations measured along different monitoring orientations.

Specific attenuation analysis differs from traditional blast vibration attenuation regression analysis by studying the loss of amplitude or energy of a blast wave between two monitoring points in a monitoring array. The loss of energy or peak amplitude per metre of propagation in the assumed elastic wave zone serves as an indication of the rock mass conditions independent of the explosive source parameters and blasting geometry. This analysis method has been applied to the data sets collected for the 24jC6HL 200mLv firings to investigate the differences in specific attenuations in different propagation orientations. Figure 8.27 displays the resulting plots of VSPPA loss per metre of travel versus the VSPPA measured at the first transducer on each array.

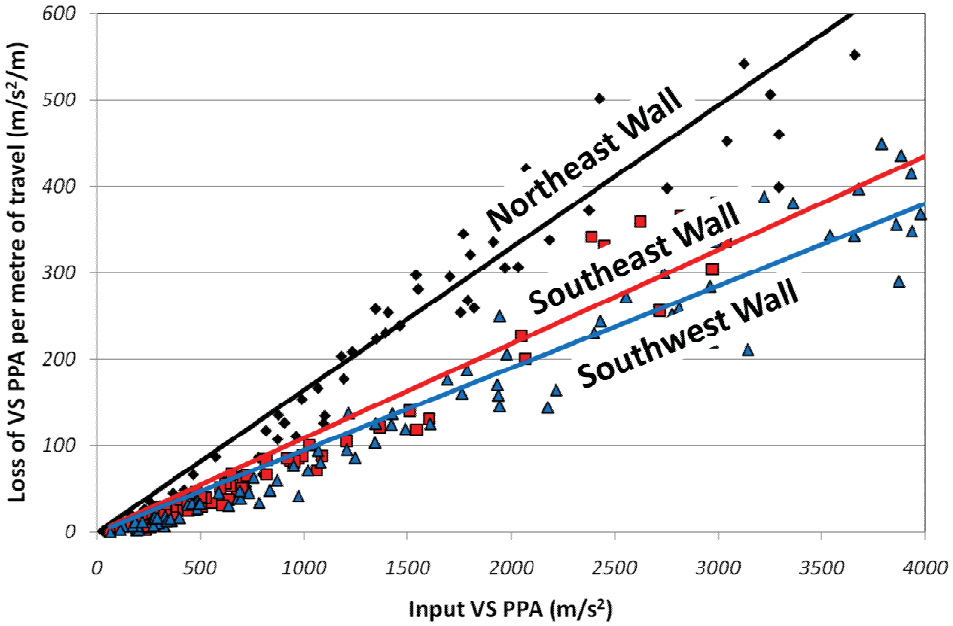

Figure 8.27. Plot of amplitude loss per metre of travel versus input amplitude for 200mLv firings in stope 24jC6HL.

Figure 8.27 suggests differences in the specific attenuations along different monitoring orientations as indicated by the differences in the slopes of the best-fit lines. The increased slope observed for the Northeast wall data would suggest that the loss of peak amplitude per metre of travel was higher for the same input amplitude when compared with the Southwest and Southeast walls. This finding was in agreement with the results of the peak amplitude-frequency analysis, where the Southwest wall was observed to have a slightly higher relative stiffness which would suggest a lower rate of attenuation.

The results of the specific attenuation assessment were viewed with caution, as the technique was largely sensitive to the separation distance between the transducers in each array. The rate of amplitude loss was observed to be dependent on the differential distance between the transducers because of the effects of nonlinear attenuation over distance. This attenuation sensitivity to distance would further account for the higher slope of the Northeast wall data best-fit line, as the transducer separation was only approximately 6m compared with 8m and 10m for the other two transducer pairs. For similar transducer separation distances, the comparisons of specific attenuation would be expected to be more reliable.

8.7.2 Dynamic Rock Mass Properties for Stope 24jC6HL

The dynamic rock mass properties were required to perform the calculations of $ED_{W\text{-}SS}$ and $\varepsilon_{W\text{-}MN}$ for use in the nonlinear estimations from vibration data collected for stope 24jC6HL. These values are listed in Table 8.11.

Table 8.11. In situ dynamic rock mass properties as indicated for stope 24jC6HL.

Wall	Rock Density (kg/m^3)	Calculated E_{dyn} (GPa)	v_{st}	Wave Velocity (m/s)	λ_L (GPa)
220mLv Northeast	3585	77	0.29	5300 (M)	41
220mLv Southeast	3585	86	0.29	5600 (M)	46
220mLv Southwest	3585	77	0.29	5300 (A)	41
200mLv Northeast	3585	73	0.29	5150 (M)	39
200mLv Southeast	3585	119	0.29	6600 (M)	64
200mLv Southwest	3585	70	0.29	5050 (M)	37
180mLv Southeast	3585	83	0.29	5500 (A)	44
180mLv Southwest	3585	70	0.29	5050 (A)	37

8.7.3 Blast Vibration Analysis Results for 24jC6HL Data Sets

Nonlinear estimations performed for combined 24jC6HL data were expected to be poorly correlated compared with those for individual data subsets due to the observed differences in stress wave velocities and indicated stiffness. The data was therefore segregated by two different criteria prior to nonlinear estimation of the regression constants. The first data division was segregation by individual stope wall orientations (Northeast, Southeast and Southwest). The second data division was by individual sublevels (220mLv, 200mLv and 180mLv). Either segregation approach would have been expected to increase correlation values over those for a combined data set based on observations from other stopes. Tables 8.12 and 8.13 list the nonlinear regression constants obtained for analyses of the data subsets segregated by the stope wall orientations and by stoping sublevel. Additional regression of alternate amplitudes, individual arrays and individual transducers are included in Appendix 9.

Table 8.12. 95% upper confidence nonlinear estimation results from 24jC6HL data as segregated by the individual stope wall orientations.

Model	Stope Wall	Data Points	*K*	*b*	*n*	Best-Fit R Value
95% $ED_{W\text{-}SS}$	Northeast	314	5.99×10^{9}	-0.834	-3.078	0.75
95% $\varepsilon_{W\text{-}MN}$			4.62×10^{4}	-0.046	-1.682	0.77
95% $ED_{W\text{-}SS}$	Southeast	487	9.80×10^{5}	0.395	-1.762	0.42
95% $\varepsilon_{W\text{-}MN}$			1682.92	0.296	-1.192	0.62
95% $ED_{W\text{-}SS}$	Southwest	557	2951.59	1.627	-1.000	0.41
95% $\varepsilon_{W\text{-}MN}$			227.92	0.793	-0.855	0.56

Table 8.13. 95% upper confidence nonlinear estimation results from 24jC6HL data as segregated by each production level.

Model	Sublevel	Data Points	*K*	*b*	*n*	Best-Fit R Value
95% $ED_{W\text{-}SS}$	220mLv	400	2.48×10^{14}	2.010	-11.350	0.74
95% $\varepsilon_{W\text{-}MN}$			5671.11	0.421	-1.625	0.65
95% $ED_{W\text{-}SS}$	200mLv	758	3.98×10^{4}	0.847	-1.410	0.45
95% $\varepsilon_{W\text{-}MN}$			361.89	0.620	-0.935	0.53
95% $ED_{W\text{-}SS}$	180mLv	155	2.56×10^{7}	2.143	-4.485	0.89
95% $\varepsilon_{W\text{-}MN}$			2407.89	1.463	-1.967	0.80

8.7.4 Response of an Unconfined Pillar to Late-Stage Blasting

The response of the pillar containing TbC5RAR to mining and blasting of stope 24jC6HL was one of the initial concerns during the North Zone monitoring period. An investigation into the pillar response attempted to assess any changes in the properties and wave propagation characteristics of the pillar rock mass prior to and after opening of the 24jC6HL stope void. The pillar confinement conditions prior to and after 24jC6HL production have been referred to as the closed wall condition (before the formation of the entire stope void) and the open wall condition (empty void prior to the final cleaner ring firing).

To perform the pillar response assessment, post-mining stress modelling and geophysical rock mass characterisations were used. The stope firing sequence allowed this type of assessment, as the final cleaner ring firing against the pillar was blasted after the stope was entirely emptied. The time required to empty the stope was adequate for stress redistribution around the stope void to occur.

8.7.4.1 Post-Mining Induced Static Stress Modelling

The MAP3D linear-elastic static stress modelling results were analysed for the 24jC6HL post-mining step to assess the effects of the stope void on the pillar containing TbC5RAR. The grid that was selected for the analysis was grid 4, which was vertical, oriented roughly NE-SW and passed through stope 24jC6HL and TbC5RAR. This modelling grid was selected due to the geotechnical concern of loss of confinement in the temporary pillar between the Southwest stope wall and TbC5RAR. Figure 8.28 illustrates the results of the MAP3D mining-induced static stress modelling of σ_2 and σ_3 for the 24jC6HL post-extraction step at grid 4.

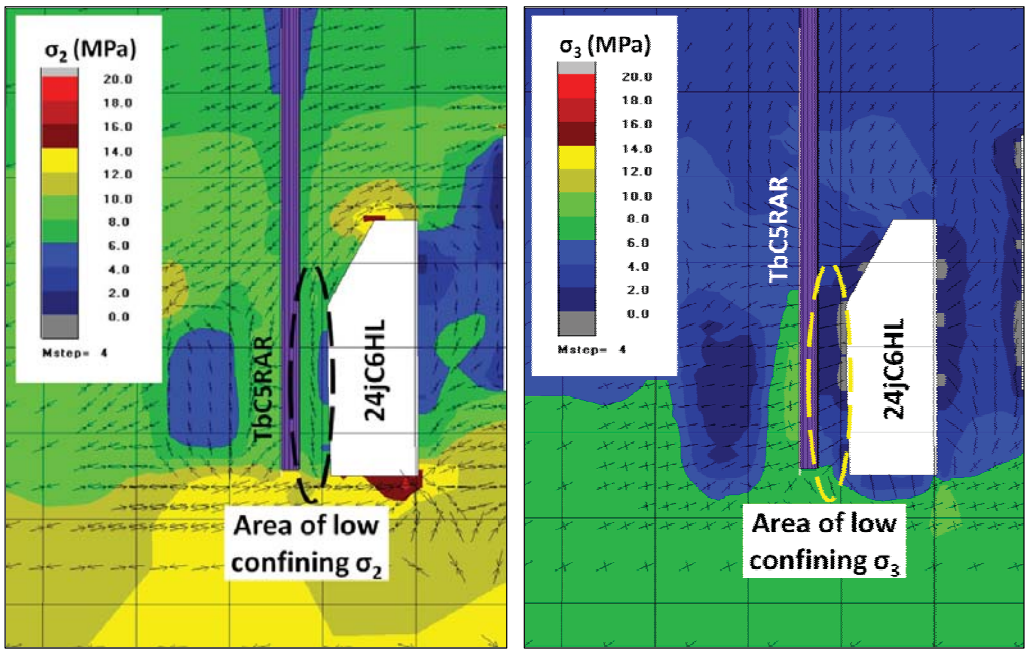

Figure 8.28. Results of σ_2 (left) and σ_3 (right) mining-induced static stress modelling of the 24jC6HL post-mining step at vertical grid 4 (looking northwest).

The potential loss of confinement in the pillar containing TbC5RAR was indicated in the stress modelling shown in Figure 8.28. Additional cable bolts were installed in the pillar between the Southwest wall of stope 24jC6HL and the TbC5RAR as a consequence of the concern for pillar unravelling from low confinement. The loss of confinement within the pillar once a large portion of the stope had been mined out would be expected to allow dilation of the existing discontinuities.

8.7.4.2 Comparison of the Confined and Unconfined Southwest Pillar

Changes in the stress wave transmission properties of the pillar rock mass were indicated from differences between the vibration data collected from the final stope firing (cleaner rings) and previous firings. It was proposed that these changes indicated possible blast damage or relaxation of the pillar after the majority of the stope 24jC6HL was mined. The methods used to compare the closed and open wall pillar conditions were the stress wave velocities, peak amplitude-frequency analyses and specific attenuation analyses.

A sharp reduction in the average stress wave velocity was observed for the cleaner ring firing (open wall) when compared with the closed wall measurements. The 200mLv transducers indicated an average stress wave velocity of 4200m/s for the open wall pillar condition versus approximately 5050m/s for the closed wall firings. The difference in average wave velocities of 850m/s represented a 17% decrease.

The second indication of pillar rock mass degradation was comparison of the closed wall and open wall peak amplitude-frequency analyses. These analyses were performed using the vibration data collected at each transducer pair in the pillar (220mLv, 200mLv and 180mLv). The closed wall analysis included the long-hole winze firings, cut-off slot firings and mass firings. The data set for the open wall analysis was a result of the cleaner rings, which were fired into the empty stope void. Figure 8.29 illustrates the plots of VSPPV versus VSPPA for the 200mLv open and closed wall analyses.

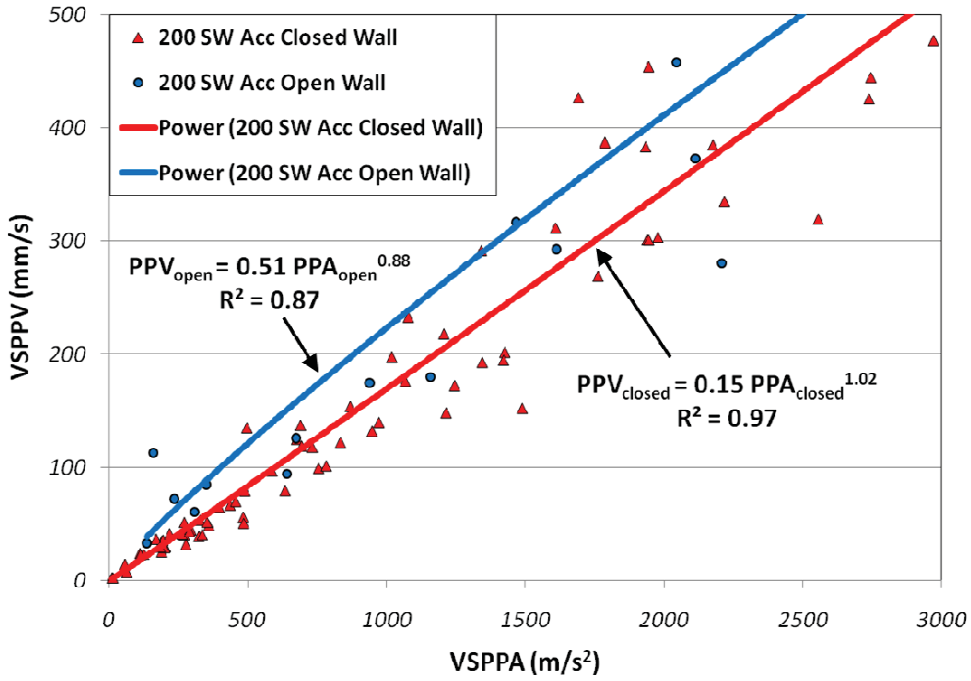

Figure 8.29. Comparison of the VSPPV versus VSPPA plots for the 200mLv accelerometer closed wall and open wall data.

Figure 8.29 suggests that the stiffness of Southwest pillar was reduced at the time of the open wall firing when compared with the closed wall condition. This condition was observed for both the 180mLv and 200mLv data. No change in stiffness was observed through comparison of the data sets for the 220mLv.

Although the difference between the indicated relative stiffness for the closed wall and open wall conditions was low, it was believed that the change in rock mass condition could indicate blasting damage or relaxation of the pillar. This relaxation due to low confining stresses would allow existing discontinuities or fresh fractures to open, thus reducing the wave velocity and frequency-supporting characteristics of the rock mass.

Specific amplitude attenuation analyses were applied to the data sets collected in the Southwest wall of the stope for the closed and open wall cases. The specific attenuation approach was expected to support the findings of the peak amplitude-frequency analyses. Figure 8.30 shows the results of the open and closed wall specific attenuation analyses.

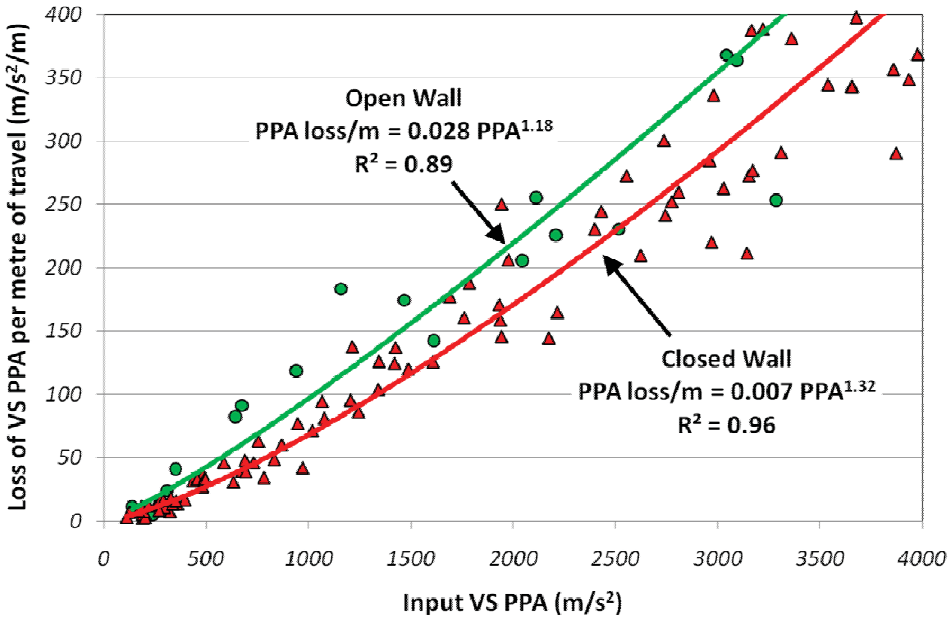

Figure 8.30. Specific amplitude attenuation (VSPPA) from 200mLv data for the closed and open wall pillar conditions.

The slightly higher rate of amplitude attenuation for the open wall data set as implied by the best-fit equation provided an additional indication of some change in pillar conditions. The increased rate of attenuation of VSPPA of approximately 25-30% for the open wall case was assumed to be a function of the dilation of existing discontinuities or fresh fracturing due to blast damage. The change in specific attenuation for the open and closed wall cases supported the previous assessment results of reduced stress wave velocity and reduction in indicated stiffness from the peak amplitude-frequency analysis.

8.7.5 Prediction of Strain-Related Blast Damage around Stope 24jC6HL

The large amount of blast vibration and geotechnical data collected for stope 24jC6HL allowed a full assessment of the stope performance during and after extraction. As part of the rigorous assessment of stope 24jC6HL, blast-induced damage prediction was performed using the author's proposed tensile strain criterion. The tensile strain-based blast damage prediction was performed for a horizontal grid plane at the 1038m elevation, between the 200mLv and 220mLv. This grid position has been previously defined as grid 5 in the MAP3D model (Figure 8.9).

8.7.5.1 Mining-Induced Static Strain Modelling for Stope 24jC6HL

The mining-induced mean normal static compressive strains were estimated within the rock mass near 24jC6HL using the results of the stress modelling at grid 5 for mining step 3. Mining step 3 was the step prior to extraction of 24jC6HL. Figure 8.31 shows the contour plot of the MAP3D modelled mining-induced mean normal static compressive strain (ε_{MN}) calculated for horizontal grid 5.

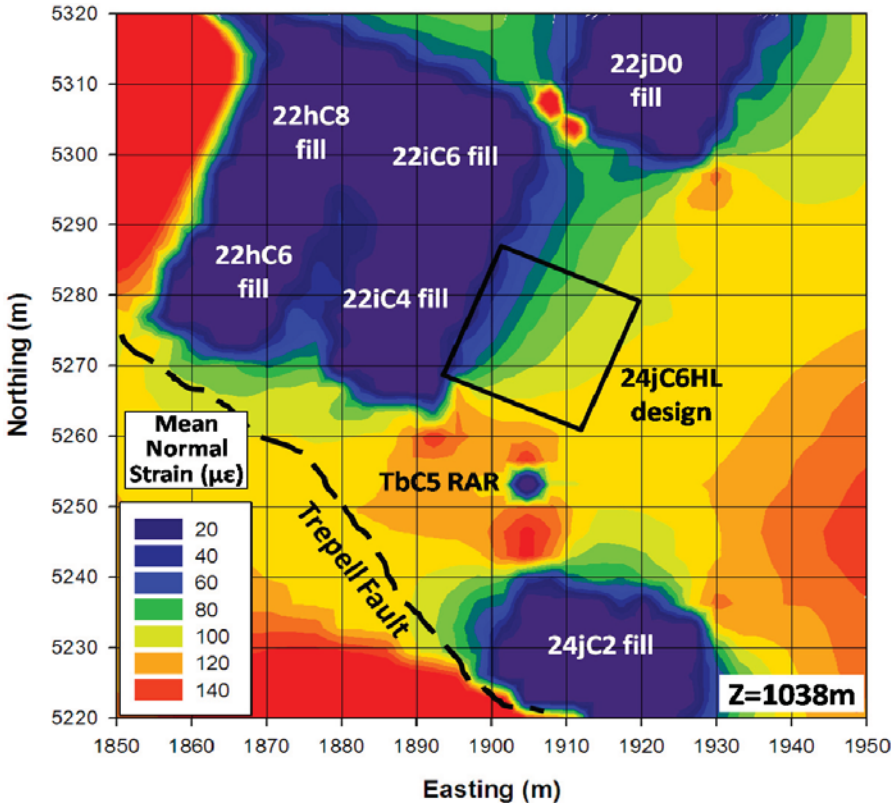

Figure 8.31. Plan view of modelled mining-induced mean normal static compressive strains (ε_{MN}) at Grid 5 at the 1038m elevation.

8.7.5.2 24jC6HL Rock Mass Required Tensile Failure Strains

The next step in the blast damage prediction process was to calculate the intact rock failure strains for the North Zone using the laboratory static rock testing results and the field measurements of the dynamic rock mass properties. The calculated dynamic compressive ($\varepsilon_{dyn(C)}$) and tensile ($\varepsilon_{dyn(T)}$) failure strains are in Table 8.14.

Table 8.14. Estimated rock mass compressive and tensile dynamic fracture strains for the rock mass around 24jC6HL.

Stope Wall	E_{dyn} (GPa)	Predicted $\varepsilon_{dyn(C)}$ (με)	σ_T (MPa)	Predicted $\varepsilon_{dyn(T)}$ (με)
200mLv Northeast	73	2872	13	183
200mLv Southeast	119	1749	13	112
200mLv Southwest	70	2987	13	191

Three different orientation-specific rock mass conditions have been implied from the dynamic rock properties in Figure 8.14. The different rock properties represented three regions of variable material response to blasting. This level of material complexity could not be considered in the current grid-based calculation approach for strain superposition, but a bi-material model was applied using a geometric filtering approach to determine tensile fracture strains at discrete points in the modelling grid. The two selected rock mass regions were the Northeast, defined by the $\varepsilon_{dyn(T)}$ of 183με and the Southwest with $\varepsilon_{dyn(T)}$ of 191με. Figure 8.32 shows the $\varepsilon_{dyn(T)}$ contours at grid 5.

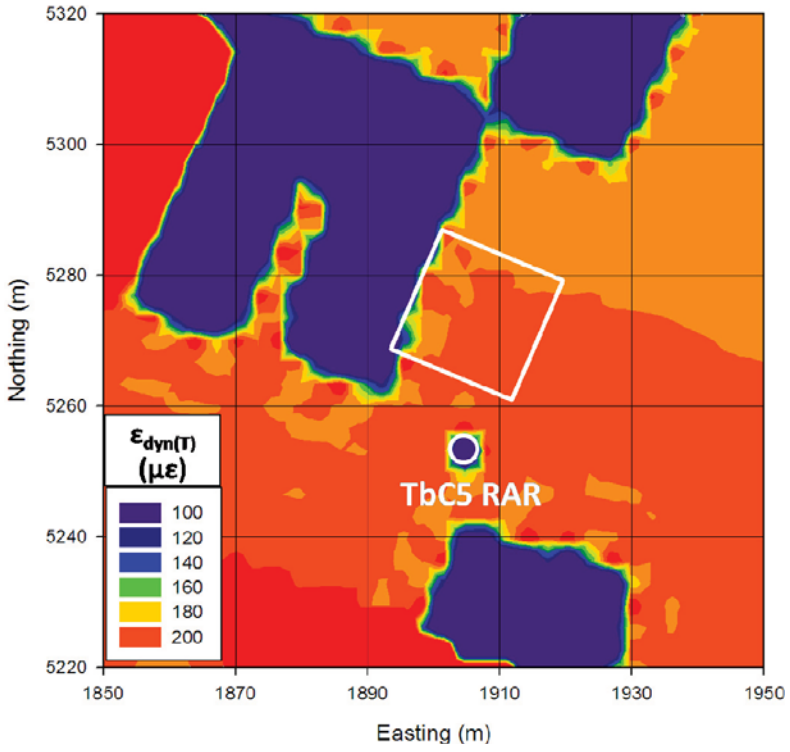

Figure 8.32. Plan view of $\varepsilon_{dyn(T)}$ contours at grid 5 around 24jC6HL.

The required additional blasting-induced mean normal tensile strains for tensile fracture were calculated using the values of ε_{MN} in Figure 8.31 and the $\varepsilon_{dyn(T)}$ in Figure 8.32. The additional mean normal tensile strain ($\varepsilon_{MN(T)}$) to induce tensile fracture was the sum of ε_{MN} and $\varepsilon_{dyn(T)}$. The contour plot of $\varepsilon_{MN(T)}$ at grid 5 is shown in Figure 8.33.

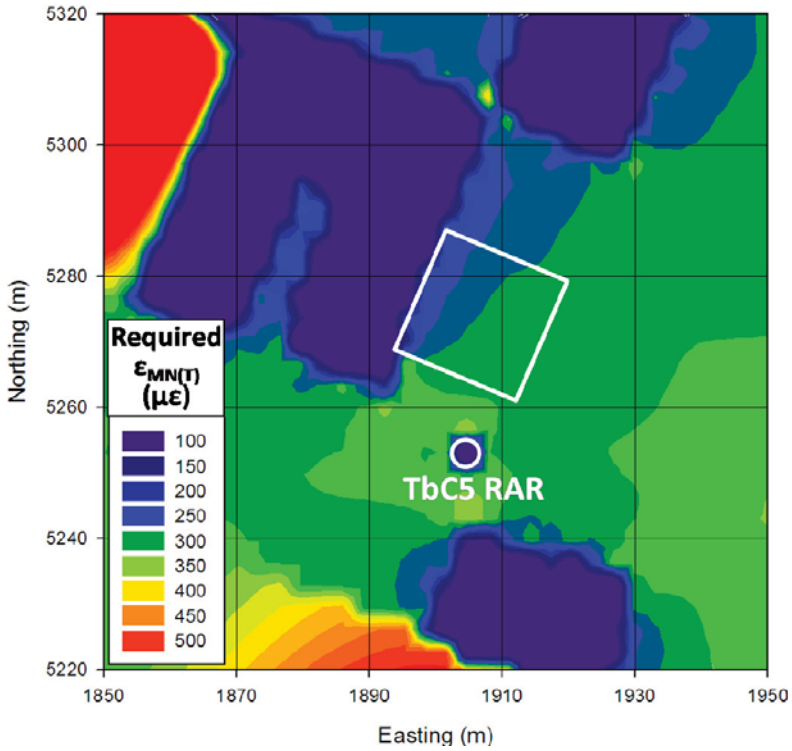

Figure 8.33. Contours of the required additional mean normal tensile strain to induce tensile damage ($\varepsilon_{MN(T)}$) at grid 5 around 24jC6HL.

Due to the low mining-induced static compressive strains in the North Zone, the additional blast-induced mean normal tensile strains required for tensile fracture around 24jC6HL were less than those for the high stress conditions at KBGM. Although the resistance to tensile damage may be expected to be less for low to moderate stress conditions, an increased resistance to blasting-induced compressive damage would be expected. The compressive damage case has not been pursued in the current prediction.

8.7.5.3 Modelling of Blasting-Induced Strain Fields for 24jC6HL

Three individual blastholes, located at three separate stope walls, were used to perform a concurrent analysis of tensile damage prediction. The concurrent prediction was an attempt to better represent the complex damage created by a multiple-hole blast. The blast damage prediction approach proposed in this thesis is based on single blasthole detonations, but multiple charges of adequate separation can be analysed concurrently. Concurrent analysis is performed by superimposing all single-hole strain fields on the modelling grid and selecting the maximum applied strain at points of overlap. The three explosive charges that were selected for the concurrent analysis of 24jC6HL were different charge weights, as characterised by the actual explosive loading within the blasthole rings of 24jC6HL (Table 8.15).

Table 8.15. Charge weights for blastholes against each wall of stope 24jC6HL as determined by average values from the charge plans of the 200mLv mass blast.

Hole Location	**Charge Weight (kg)**
Northwest Wall	75
Southeast Wall	50
Southwest Wall	75

As discussed in Chapter 7, the current model did not allow variable attenuations to be applied to each propagation orientation as determined from the individual vibration data analyses. Therefore, the $\varepsilon_{W\text{-}MN\text{-}95\%}$ prediction equation obtained for the 200mLv combined data set (Table 8.13) was applied to each of the three blastholes of variable charge weight to determine the blasting-induced strain fields (Equation 8.7).

$$\varepsilon_{W\text{-}MN\text{-}95\%} = 361.89\,(W)^{0.620}\,(D)^{-0.935} \qquad (8.\ 7)$$

The single strain prediction equation (Equation 8.7) would effectively over-predict the strain expected along different orientations, and therefore represents a significant limitation of the current model. Considerable differences in dynamic strains based on the orientations of wave propagation have been identified throughout the monitoring

program. Future development work on the model would allow for variable attenuation equations to be used such that the strain fields can be more accurately represented as a function of orientation.

Equation 8.7, the charge weights in Table 8.15 and the coordinates of the three specified blastholes were used to estimate the strain values at each grid point around the three charges. The maximum $\varepsilon_{W\text{-}MN}$ value at each overlapping grid point was then used to determine the maximum strain values throughout the entire grid from detonation of the three holes. No aggregation of strain was permitted due to assumed differences in firing times of the three blastholes. Figure 8.34 shows the contour plot of the maximum $\varepsilon_{W\text{-}MN}$ around the three charges at grid 5.

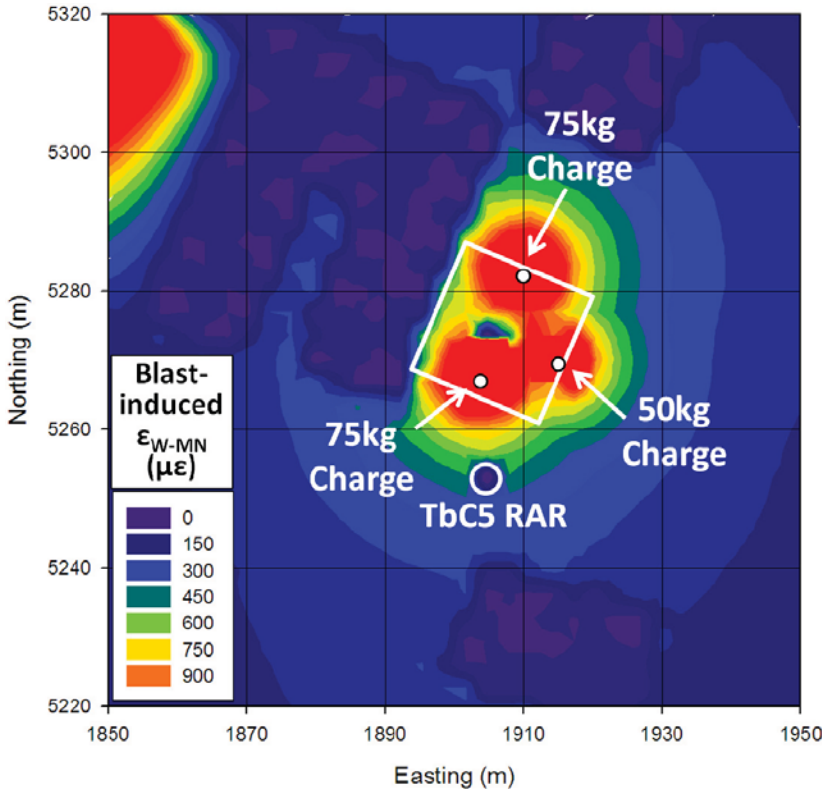

Figure 8.34. Contour plot of maximum $\varepsilon_{W\text{-}MN}$ around three modelled explosive charges at the perimeter of 24jC6HL at grid 5.

The final step in predicting the zone of possible tensile damage induced by the three blastholes was to superimpose the induced blasting strains, $\varepsilon_{W\text{-}MN}$ (Figure 8.34) onto the required additional tensile strains, $\varepsilon_{MN(T)}$ (Figure 8.33) to determine the excess

strain capacity at each grid point. The grid points where the excess strain capacity was zero or negative was assumed to be damaged by tensile mechanisms. Points where the excess strain capacity was greater than zero were assumed to remain undamaged. Contours of the excess strain capacity are shown in Figure 8.35.

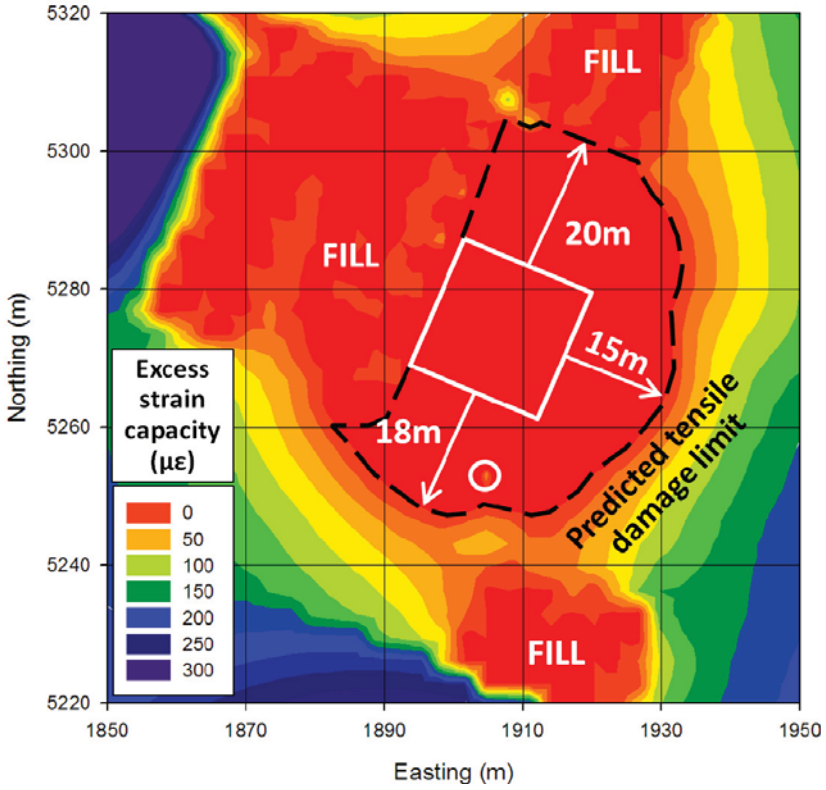

Figure 8.35. Contour plot of the excess strain capacity after superimposing the induced blasting strain onto the required additional tensile strain at grid 5.

The red area in Figure 8.35 represents the zones where the blast-induced mean normal tensile strain has exceeded the required mean normal tensile strain to cause tensile damage. The limit of tensile damage was therefore predicted by the leading edge of the zone of excessive blast-induced strain. The limit of predicted tensile damage in the Southwest wall was approximately 18m. The limit of predicted tensile damage for the Southeast wall was 15m, while the Northwest wall was approximately 20m and limited by the 22jD0HL fill mass.

The predicted tensile damage zone fully encompassed the Southwest pillar containing TbC5RAR, although no visual damage was observed within the RAR. It

is important to note that the tensile damage prediction model did not specify the scale (micro- to macro-) or severity of damage, and as such could not be used to predict rock mass failure potential. Some degree of strength reduction would be expected with the additional tensile fracturing.

The post-extraction CMS survey of the stope indicated an average depth of overbreak of approximately 1m for all stope walls. This depth of overbreak was common for the North Zone due to the competent nature of the rock mass. Further measurements, not available at the time of stope production, would have been required to validate the accuracy of model prediction based on the limit of subcritical rock mass damage.

8.7.5.4 Comparison of Proposed Blast Damage Prediction Results with Results of Critical Tensile Plane Strain Damage Predictions

The extent of blast-induced tensile strain damage predicted using the proposed model was compared with predictions using the critical tensile plane strain approach. The various forms of the equation for calculating PPV_{crit} were again utilised along with the different possible inputs. In total, 40 different versions of the critical tensile plane strain model were applied to predict the value of PPV_{crit} and the extent of predicted damage based on the different possible input variables, charge weights and the different orientations of propagation. Values of PPV_{crit} ranged from approximately 720mm/s to 1720mm/s with associated tensile fracture radii ranging from 3.2m to 14.1m. The extent of predicted damage using the proposed approach (average 17.5m) was significantly higher than those predicted using the multiple versions of the critical tensile plane strain model. Additional details of the damage predictions using the critical tensile plane strain approach are included in Appendix 10.

8.7.6 Stope Performance Assessment for Stope 24jC6HL

Visual inspections of the development and associated mine infrastructure after each stope firing were carried out for stope 24jC6HL in addition to post-extraction void analysis. Extensive excavation damage was observed within the LaDS main stope access drive on the 220mLv, 200mLv and 180mLv near 24jC6HL similar to the damage mapped for the 180mLv at the top level of 22gC6HL. The types of damage

observed on the three sublevels varied in type and areal coverage, as the surface support schemes on each sublevel were different.

Different surface support schemes were used within the development of the North Zone based on the service life of the drive and the opinion of the production supervisor at the time of ground support installation. The two surface support schemes generally observed were steel-weld mesh to the grade line or in-cycle shotcrete to the grade line. In some instances, surface support was only installed on the drive backs shoulders, such as the 220mLv near stope 24jC6HL. Portions of the 200mLv were meshed to the grade line and other portions were meshed only to the shoulders. In the 180mLv, a thin layer of shotcrete was sprayed from back to floor in place of mesh. As a result of the lack of mesh, heavy spall damage was observed for the 180mLv (Figure 8.36).

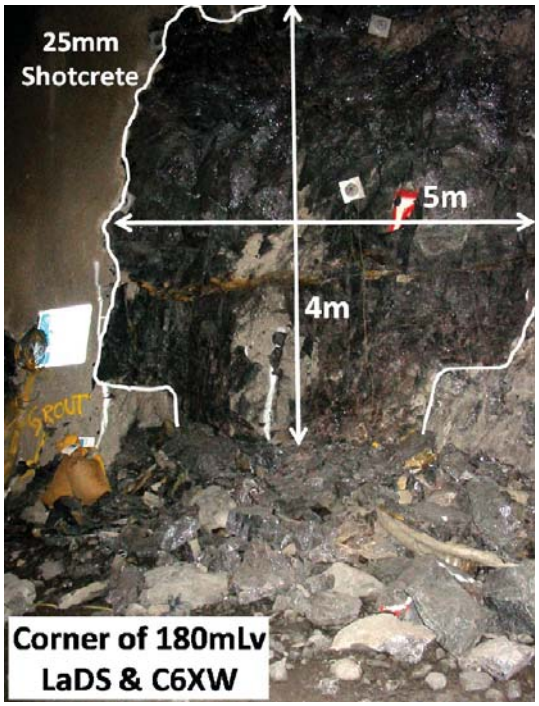

Figure 8.36. Photograph of 20m^2 of heavy spall damage of thinly shotcreted development on 180mLv drive LaDS after 180mLv mass firing.

The 200mLv experienced some spall and block failures where mesh cover did not exist. Most failures in the presence of mesh to the grade line occurred below the surface support line. Where surface support was only installed to the drive shoulder,

some falls of rock occurred from greater than 2.5m of height. These falls represented potential injury or fatality to mine personnel and were required to be reported by the mine geotechnical department as falls of ground.

In many cases of discrete block failure, one or more surfaces of the detached blocks were oxidised. This suggested likely release along existing discontinuities. Other block surfaces were freshly fractured with no alteration, signifying blast-induced or stress-related recent block formation. Two examples of blast-related block failures in the 220mLv LaDS drive adjacent to stope 24jC6HL are shown in Figure 8.37.

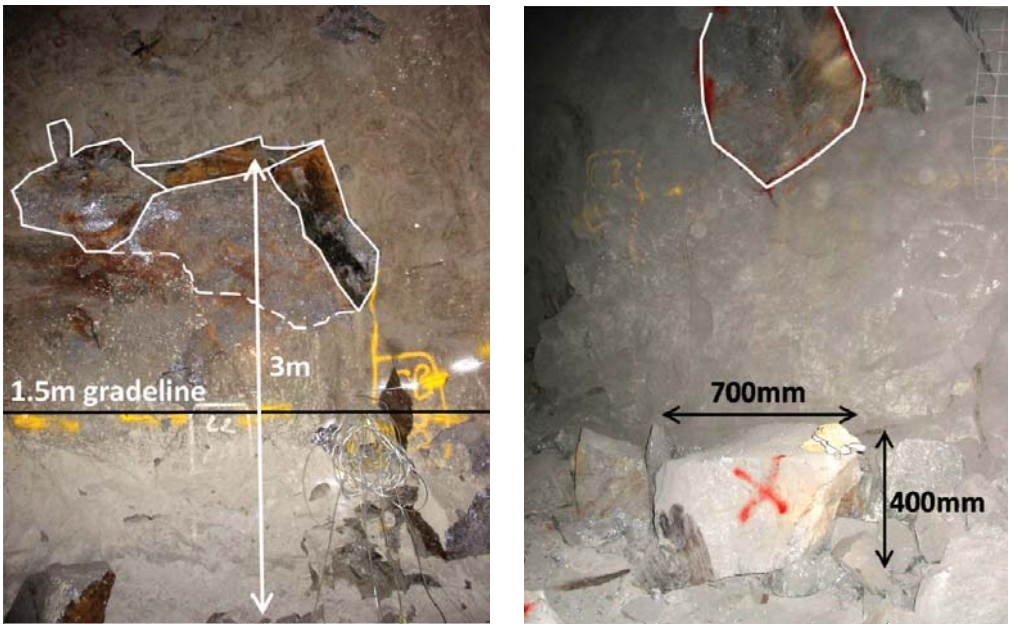

Figure 8.37. Block failure of 1 tonne from approximately 3.0m height after 220mLv firing #3 (left) and 500kg block fall after 180mLv mass blast (right) in drive 220mLv drive LaDS.

No damage to TbC5RAR was observed throughout the blasting program in stope 24jC6HL, although damage to the development near the RAR was recorded on several occasions. It was believed that the raise-bored excavation method and the cylindrical shape of the RAR reduced the influence of blasting vibrations. Previous blast damage during primary excavation, repeated vibrations from nearby stope firings and time-dependent degradation of the rock mass were believed to contribute to the occurrence of blast damage to the development near stope 24jC6HL.

8.7.6.1 24jC6HL Post-Extraction Stope Performance Assessment

The total stope overbreak and underbreak volumes for 24jC6HL were determined through comparison of the stope design and post-extraction CMS wireframes. These values are listed in Table 8.16.

Table 8.16. Stope overbreak and underbreak calculations resulting from comparison of the post-extraction CMS and design wireframes for North Zone stope 24jC6HL.

Stope Performance Criteria	Volume (m^3)	% of Design Volume
Total Overbreak	1376	7.4
Total Underbreak	1624	8.8

The multiple lifts of 24jC6HL were assessed separately for depth of overbreak, which offered a better understanding of the effect of drilling directions on the stope performance. The maximum depths of overbreak for each wall are in Table 8.17.

Table 8.17. Maximum depth of overbreak in each wall of stope 24jC6HL.

Stope Wall	Maximum Depth of Overbreak (m)
220mLv Northwest	1.8
220mLv Northeast	1.4
220mLv Southeast	0
220mLv Southwest	0.4
200mLv Northwest (paste)	0.6 (ore)
200mLv Northeast	1.4
200mLv Southeast	0.4
200mLv Southwest	0.8
180mLv Northwest (paste)	2.0 (ore)
180mLv Northeast	0
180mLv Southeast	0.4
180mLv Southwest	0.7

Stope 24jC6HL performed well, with a maximum overbreak of 2.0m in the Northwest wall between the 180mLv and 200mLv. This overbreak occurred along the upper, steeply-inclined portion of the stope wall, where blastholes were drilled parallel to the irregular stope surface. Stope overbreak was observed against the adjacent paste fill mass in the Northwest wall, but no dilution occurred as significant underbreak was experienced in the adjacent filled stope.

8.8 R4 Mining Area Rock Mass Characterisation and Blast Vibration Monitoring Results

The two study stopes of the R4 have been analysed similarly to the North Zone stopes as part of a mining block-scale assessment approach. The results of the geotechnical and geophysical rock mass characterisations, blast vibration analyses and stope performance assessments for the two monitored stopes of the R4 mining area are discussed in the following sections.

8.8.1 Intact Rock Properties for the R4 Mining Area

The low percentage of the mineable reserve in the R4 (approximately 3% of the Cannington reserve) restricted the amount of rock testing and rock mass characterisation performed prior to the initiation of mining in late 2007. As a result of the limited pre-mining characterisation, only a single test for rock tensile strength and two tests of UCS were discovered for the footwall area of the 520mLv (WASM, 2009b). No earlier testing results were found that could be associated directly with the R4 mining area. Table 8.18 lists the results of intact rock testing for the R4 mining area performed on core samples recovered from the 520mLv.

Table 8.18. Intact rock testing results for the R4 (WASM, 2009b and AMC, 1998).

Mine Area	Average UCS (MPa)	σ_T (MPa)	Average E_{st} (GPa)	Average v_{st}
R4	170[2]	10[1]	80[7]	0.29[7]

The values of E_{st} and v_{st} were assumed from the previously discussed values as specified by the reports on the main Southern Zone mineralisation (AMC, 1998). No elastic constants results were found in the most recent rock testing reports for the R4.

Cannington personnel provided rock density values for the two monitored R4 stopes derived from the ore grade block model (Li, 2009). Although the grades within the R4 were higher than those of the North Zone, the rock densities were lower for stopes 52h09HL and 52h04HL than those of 22gC6HL and 24jC6HL. Table 8.19 lists the rock densities as specified by the R4 block model.

Table 8.19. Rock density as supplied by the reserve block model (Li, 2009).

Stope	**Rock Density (kg/m^3)**
52h09HL	3450
52h04HL	3510

The reduction in density for the R4 rock mass along with the water content would have been expected to affect the blast vibration attenuation behaviours when compared with the higher density, largely dry North Zone rock mass.

8.8.2 R4 Discontinuity Mapping

Observation of the development drives of the R4 and the geological mapping results suggested that the rock mass of the R4 was generally highly fractured and contained several block-scale faults sub-parallel to the footwall shear and Hamilton Fault footwall and was largely saturated. The presence of large quantities of water was apparent from the water flowing from boreholes in the R4 development drives and severe ground support corrosion. Figure 8.38 shows one of the faults intersected by the development of the 500mLv.

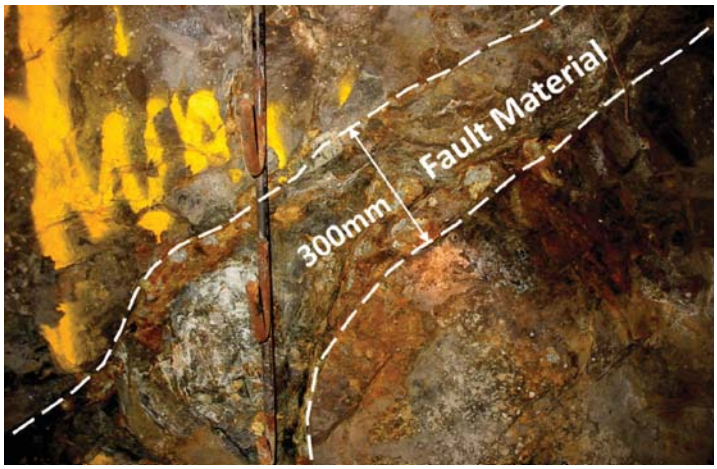

Figure 8.38. Picture of a gouge-type fault encountered on the 500mLv development.

No digital discontinuity mapping data was available for the R4 at the time of monitoring due to the lack of digitising of the mapping sheets. Hard copies of level mapping sheets of the 500mLv and 520mLv development were therefore collected from the geology department to determine the discontinuity orientation distribution. Figure 8.39 displays the physical mapping sheets for the 500mLv and 520mLv development drives around stopes 52h04HL and 52h09HL.

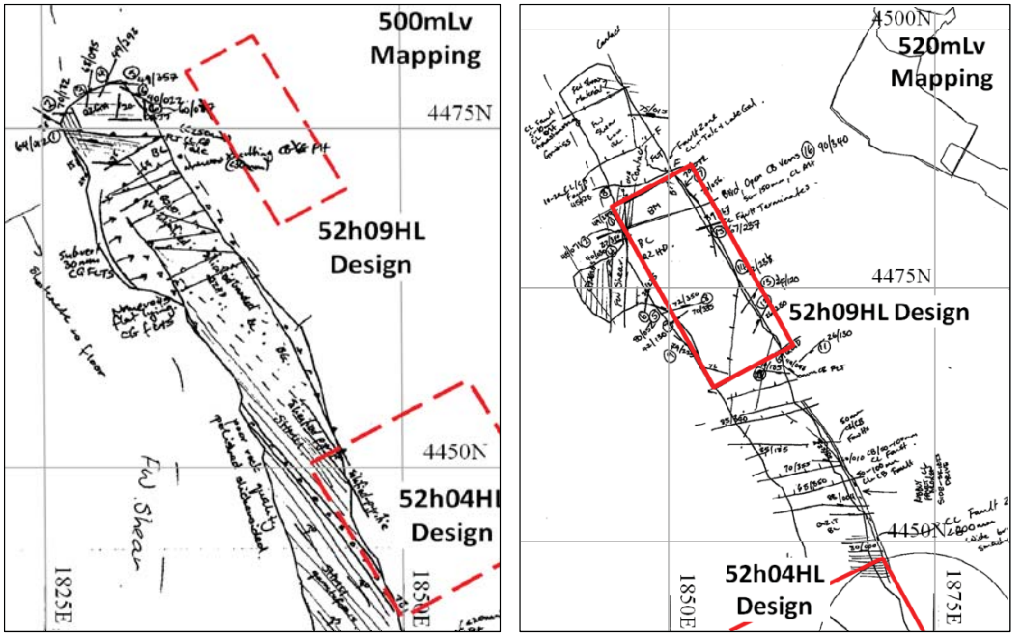

Figure 8.39. R4 development mapping of the 500mLv (left) and 520mLv (right) in the vicinity of stopes 52h09HL and 52h04HL.

As illustrated in Figure 8.39, a number of block-scale fault intersections and mineralised contacts were exposed in the 500mLv and 520mLv. These intersections were more prominent in the 500mLv, with some indication of the presence of the footwall shear zone. Figure 8.40 shows the resulting stereonet pole plot of the information from the backs mapping sheets.

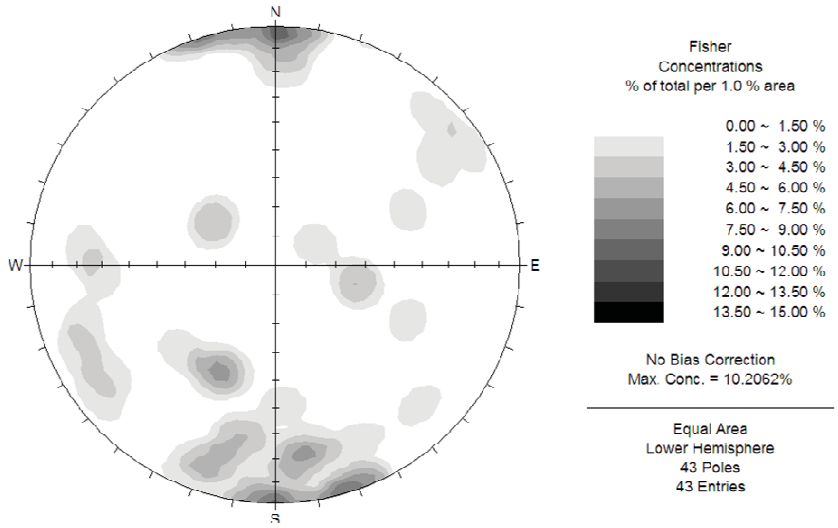

Figure 8.40. Discontinuity distribution from mapping of 500mLv and 520mLv in the vicinity of stopes 52h09HL and 52h04HL.

Figure 8.40 shows a number of prominent discontinuity sets. The most dominant set appeared to be near-vertical and striking East-West. The second set appeared to correspond with the orientation of the mineralisation contacts striking roughly NW-SE as observed in the 500mLv mapping (Figure 8.39, left). Additional random discontinuities were also represented.

8.8.3 R4 Blast Vibration Monitoring Instrumentation

Blast vibration monitoring in the R4 mining area began in November, 2007. Almost one year had passed since the final firing monitored in stope 24jC6HL in the North Zone. During the year break from monitoring, an additional data acquisition system was purchased by WASM which allowed for two additional tri-axial transducers to be monitored simultaneously. The total monitoring capability was then 8 tri-axial transducers sampled at 8192Hz simultaneously. This increase in channel capacity

was reflected in the number of transducers installed for monitoring the stopes of the R4. Figure 8.41 shows a plan view of the transducers installed for blast vibration monitoring of stopes 52h09HL and 52h04HL.

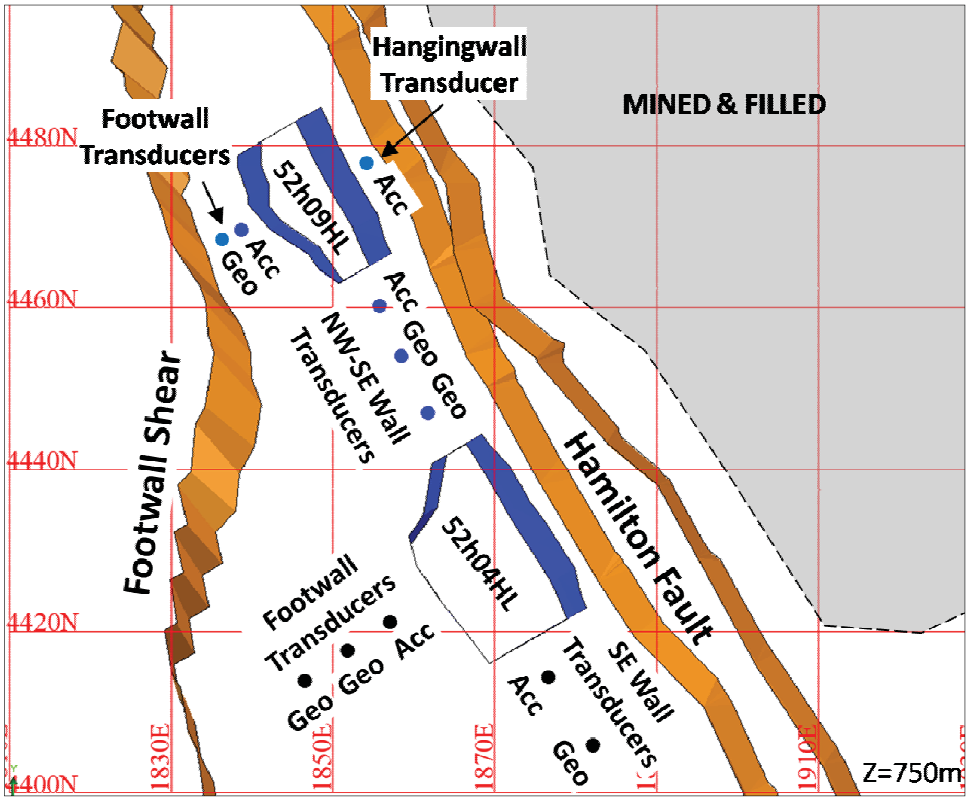

Figure 8.41. Plan view of transducers installed at the 750m elevation (between the 500mLv and 520mLv) in the R4 to monitor blasting vibrations from stopes 52h09HL and 52h04HL.

The monitoring configurations illustrated in Figure 8.41 resulted in reduced offset distances between the stope boundaries to the first accelerometer in several transducer arrays. This reduced offset would provide valuable information on the extreme near-field blast vibration behaviours within the R4. Table 8.20 lists the blast vibration monitoring instrumentation installed around stopes 52h09HL and 52h04HL at approximately the 750m elevation.

Table 8.20. Summary of 52h09HL and 52h04HL blast vibration monitoring instrumentation.

Stope Name	Wall of Stope	Transducer Type	Distance from Stope (m)
52h09HL	Hangingwall (HW)	1000g Accelerometer	4.0
	Footwall (FW)	1000g Accelerometer Geophone	3.9 7.8
	Southeast (SE)	1000g Accelerometer Geophone 1 Geophone 2	4.8 11.6 19.3
52h04HL	Northwest (NW)	1000g Accelerometer Geophone 1 Geophone 2	20.1 13.4 5.7
	Footwall (FW)	1000g Accelerometer Geophone 1 Geophone 2	6.6 12.9 19.4
	Southeast (SE)	1000g Accelerometer Geophone	5.0 15.0

The increased monitoring capacity allowed several triple-transducer arrays to be installed for 52h09HL and 52h04HL. The extra transducer on these arrays provided an increase in the amount of data collected in each monitoring orientation. Additionally, a better understanding of the distance-related blast vibration behaviours could be gained from the extra transducers.

The permanent pillar between stopes 52h09HL and 52h04HL allowed the triple-transducer array in the Southeast wall of 52h09HL to be re-used for the Northwest wall of 52h04HL. This was the only incidence of transducer re-use during the blast vibration monitoring program.

8.8.4 Stress Wave Velocities and Peak Amplitude-Frequency Analyses of the R4 Rock Mass

The stress wave velocities were determined for the monitoring orientations of the R4 based on the blast monitoring results. The velocities indicated no general condition of directional anisotropy in the R4, as observed in the North Zone. Table 8.21 lists the measured or assumed stress wave velocities for the 52h09HL and 52h04HL monitored directions.

Table 8.21. Measured (M) or assumed (A) stress wave velocities for the monitored orientations around 52h09HL and 52h04HL.

Stope	Orientation	Stress Wave Velocity (m/s)
52h09HL	Hangingwall	5175 (A)
	Footwall	5175 (M)
	Southeast Wall	5130 (M)
52h04HL	Footwall	5300 (M)
	Southeast Wall	5070 (M)
	Northwest Wall	5450 (M)

The stress wave velocity measurements were largely validated based on the values for the pillar between the Southeast wall of stope 52h09HL and Northwest wall of stope 52h04HL, determined from two different data sets. The difference between the two average wave velocity values was approximately 6%, which did not represent a significant change in relation to the scatter of the points around the average. All of the stress wave velocities in Table 8.21 were within an approximate 7% range, and therefore no anisotropies could be identified.

Peak amplitude-frequency analysis was applied to the blast vibration data subsets collected along each R4 monitoring orientation to investigate any differences in the directionally-variable indicated rock mass stiffness. Plots of VSPPV versus VSPPA for all individual R4 accelerometer data sets are illustrated in Figure 8.42.

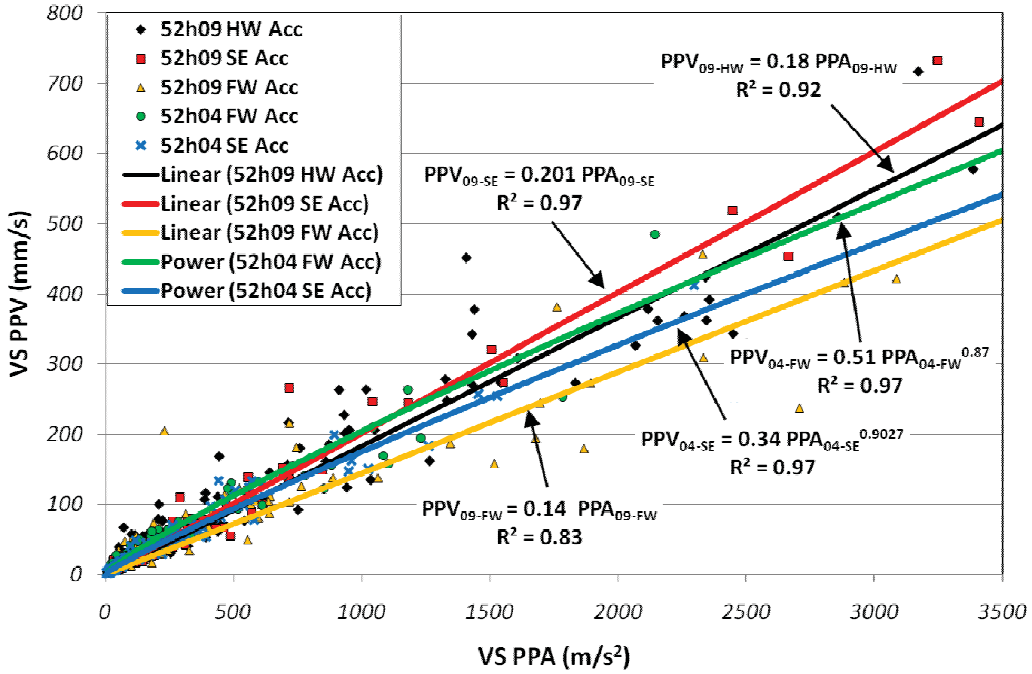

Figure 8.42. Plots of VSPPV versus VSPPA and best-fit relationships for the accelerometer data measured along each monitoring orientation around R4 stopes 52h09HL and 52h04HL.

The VSPPV-VSPPA relationships in Figure 8.42 indicated that the rock mass around stopes 52h09HL and 52h04HL was largely homogeneous with regards to the frequency-supporting characteristics along different orientations. This behaviour may have been attributed to the seemingly random fracturing of the rock mass as indicated by the discontinuity mapping of the 500mLv and 520mLv, the highly weathered ore zone or the degree of rock mass saturation.

8.8.5 Results of R4 Blast Vibration Data Analyses

The R4 blast monitoring data were analysed using the same approaches applied to the previous North Zone data sets to characterise the attenuations of energies and strains. The dynamic rock mass properties required for calculations of energies and strains are listed in Table 8.22.

Table 8.22. In situ dynamic rock mass properties for stopes 52h09HL and 52h04HL.

Stope	Wall	Rock density (kg/m^3)	E_{dyn} (GPa)	v_{st}	Wave Velocity (m/s)	λ_L (GPa)
52h09HL	Hangingwall	3450	71	0.29	5175	38
	Footwall	3450	71	0.29	5175	38
	Southeast	3450	69	0.29	5130	37
52h04HL	Footwall	3510	75	0.29	5300	40
	Southeast	3510	69	0.29	5070	37
	Northwest	3510	80	0.29	5450	43

The values of rock density, E_{dyn}, v_{st}, wave velocity and λ_L listed in Table 8.22 were used to calculate the $ED_{W\text{-}SS}$ and $\varepsilon_{W\text{-}MN}$ for all recorded data points and nonlinear estimations were performed to obtain the regression constants K, b and n. The first analysis of the R4 data was the combined data set from all transducers in 52h09HL and 52h04HL to characterise the block-scale blast vibration behaviour. Separate analyses were then performed for data subsets segregated by the instrumentation orientations within each individual stope. The nonlinear estimation results for the combined R4 data set are listed in Table 8.23.

Table 8.23. Best-fit and 95% upper confidence nonlinear estimation results for $ED_{W\text{-}SS}$ and $\varepsilon_{W\text{-}MN}$ for the R4 combined data set.

Model	Data points	K	b	n	Best-fit R
Best-fit $ED_{W\text{-}SS}$ (J/m^3)	1388	522.08	0.551	-1.006	0.31
95% $ED_{W\text{-}SS}$	1388	959.46	0.735	-0.819	
Best-fit $\varepsilon_{W\text{-}MN}$ ($\mu\varepsilon$)	1388	34.43	0.434	-0.685	0.51
95% $\varepsilon_{W\text{-}MN}$	1388	46.13	0.503	-0.607	

The surfaces represented by the 95% upper confidence regression constants listed in Table 8.23 are shown in Figures 8.43 and 8.44.

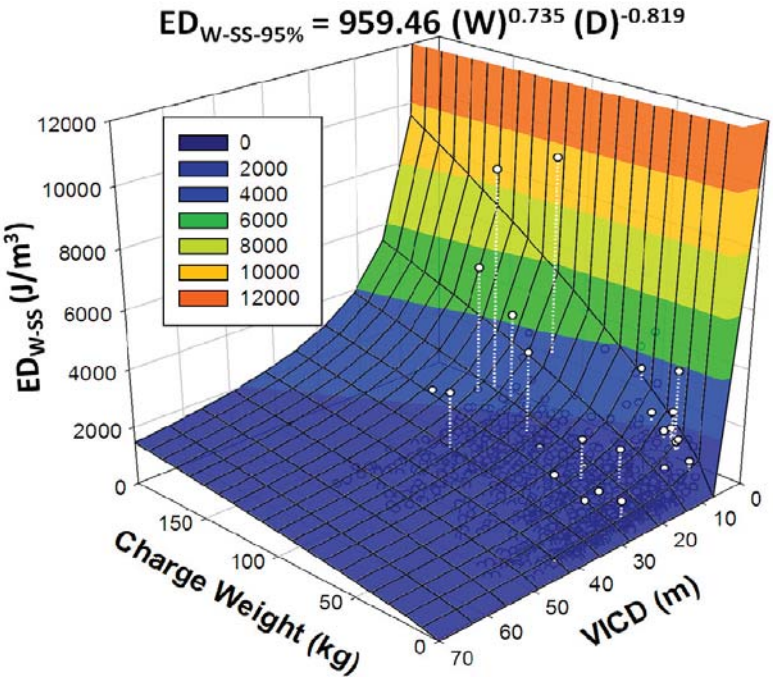

Figure 8.43. 95% upper confidence surface from nonlinear estimation of $ED_{W\text{-}SS}$ versus charge weight and VICD for Cannington R4 combined data.

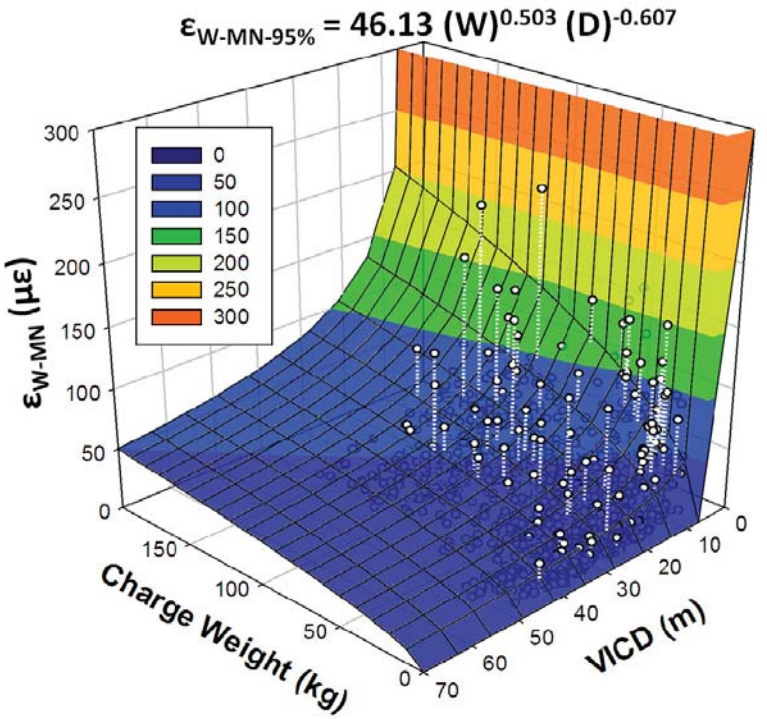

Figure 8.44. 95% upper confidence surface from nonlinear estimation of $\varepsilon_{W\text{-}MN}$ versus charge weight and VICD for Cannington R4 combined data.

The general trend of reduced correlation values observed in the KBGM D block and Cannington North Zone data sets were also present within the combined R4 nonlinear estimations. The data set was therefore segregated by the stope and the separate monitoring orientations within each stope. The resulting 95% confidence $ED_{W\text{-}SS}$ ($ED_{W\text{-}SS\text{-}95\%}$) and $\varepsilon_{W\text{-}MN}$ ($\varepsilon_{W\text{-}MN\text{-}95\%}$) nonlinear estimation results for the individual stope orientations are listed in Table 8.24. Additional regression results are included in Appendix 9.

Table 8.24. Stope 52h09HL and 52h04HL nonlinear estimation results for 95% upper confidence $ED_{W\text{-}SS}$ and $\varepsilon_{W\text{-}MN}$ as combined data sets for each stope wall.

Stope	Model	Stope Wall	Data Points	*K*	*b*	*n*	Best-Fit R
52h09HL	$ED_{W\text{-}SS\text{-}95\%}$	HW	101	562260	0.075	-1.308	0.52
	$\varepsilon_{W\text{-}MN\text{-}95\%}$			4949.14	0.072	-1.026	0.57
	$ED_{W\text{-}SS\text{-}95\%}$	FW	199	3274.81	0.626	-0.678	0.35
	$\varepsilon_{W\text{-}MN\text{-}95\%}$			145.98	0.357	-0.489	0.43
	$ED_{W\text{-}SS\text{-}95\%}$	SE	299	10365.57	0.968	-1.775	0.71
	$\varepsilon_{W\text{-}MN\text{-}95\%}$			196.34	0.603	-1.137	0.77
52h04HL	$ED_{W\text{-}SS\text{-}95\%}$	FW	283	2419.98	1.742	-0.491	0.32
	$\varepsilon_{W\text{-}MN\text{-}95\%}$			8.87	1.091	-0.207	0.60
	$ED_{W\text{-}SS\text{-}95\%}$	SE	245	19.14	1.872	-0.619	0.55
	$\varepsilon_{W\text{-}MN\text{-}95\%}$			14.25	0.797	-0.410	0.63
	$ED_{W\text{-}SS\text{-}95\%}$	NW	261	30118.16	1.305	-1.062	0.39
	$\varepsilon_{W\text{-}MN\text{-}95\%}$			477.59	0.662	-0.825	0.56

The nonlinear estimation results for each orientation delivered a range in *K*, *b* and *n* values and correlations, identifying some differences in orientation-specific blast vibration attenuation in the R4. These differences were not indicated in a significant way by other assessment approaches.

8.8.6 R4 Stope Performance Assessments

The stopes of the R4 were designed significantly smaller than the stopes of the other Cannington mining areas due to regional stability concerns for the Hamilton Fault and the lens-shaped geometry of the R4 lode. As a function of the reduced stope size, any stope overbreak or underbreak was expected to represent a larger percentage of the total stope volume. The results of the post-mining overbreak and underbreak assessments for stopes 52h09HL and 52h04HL are listed in Table 8.25.

Table 8.25. Stope overbreak and underbreak calculations resulting from comparison of the post-extraction CMS and design wireframes for 52h09HL and 52h04HL.

Stope	Performance Criteria	Volume (m^3)	% of Design Volume
52h09HL	Total Overbreak	548	18.5
	Total Underbreak	330	11.1
52h04HL	Total Overbreak	477	7.2
	Total Underbreak	752	11.4

The irregular shapes of stopes 52h09HL and 52h04HL required a combination of downholes drilled from the 500mLv and upholes drilled from the 520mLv to achieve the desired stope shapes. The large percentage of stope overbreak for stope 52h09HL was partially associated with the oblique drilling geometry and blasthole charging controls. The reduced overbreak percentage for stope 52h04HL when compared with 52h09HL reflected a more efficient drilling design based on the stope shape. Stope 52h04HL was mined using all upholes drilled to the stope perimeter from the 520mLv, whereas stope 52h09HL relied on downholes drilled at an oblique angle to the stope hangingwall and footwall. The maximum depth of overbreak experienced in each stope wall is listed in Table 8.26.

Table 8.26. Maximum depth of overbreak in each wall of stope 52h09HL.

Stope	Stope Wall	Maximum Depth of Overbreak (m)
52h09HL	Hangingwall	1.0
	Footwall	3.3
	Southeast	0.8
	Northwest	0.6
52h04HL	Hangingwall	2.3
	Footwall	0.7
	Southeast	1.0
	Northwest	1.0

The excessive overbreak in the footwall of stope 52h09HL occurred near the stope crown. Inspection of the charging logs indicated that the long-hole winze holes had been overcharged in firing #3, resulting in blasting of material beyond the designed stope crown. The oblique angle of the blastholes intersecting the design stope footwall and crown therefore contributed to the resulting over-charging and overbreak.

The overbreak profile in the hangingwall of stope 52h04HL was largely consistent and ranged in depth from 1m to 2.3m. The stope design in relation to the available drilling access on the 520mLv required toeing of blastholes into the hangingwall. This drilling configuration was expected to have contributed to the overbreak of the hangingwall, as any over-drilling of blastholes would directly influence the final shape. Inspections of the ore flow during stope production did not identify any fault material reporting to the drawpoint. Therefore, it was determined that the 5m pillar against the Hamilton Fault footwall remained largely intact during blasting and loading of 52h04HL.

8.9 Comparison of North Zone and R4 Blast Vibration Monitoring Results

The general responses of the North Zone and R4 rock masses to blasting have been compared using the results of the analyses of stopes 22gC6HL, 24jC6HL, 52h09HL and 52h04HL. The North Zone and R4 were believed by Cannington personnel to vary significantly in geological characteristics and geotechnical behaviours. The results of the analyses for the North Zone and R4 identified several differences between the geophysical characteristics and blast vibration attenuation behaviours for each mining area. Differences between the indicated stiffness as a result of peak amplitude-frequency analysis were also identified.

8.9.1 Comparison of Blast Vibration Attenuation Behaviours

The blasting conditions in the North Zone and the R4 stopes were significantly different due to the stope sizes. These variations in the blasting parameters were expected to account for some differences between the observed general blast vibration attenuation relationships. The influence of blasting geometry was expected to be minimal, as the blasthole diameter, explosive types, blasting patterns and associated powder factors were similar for both mining areas. The total charge weights and monitored distances in each mining area were also similar, such that the vibration attenuation relationships represented similar monitoring geometries. The similarities between the blasting programs in each mining area suggested that the observed differences between the large-scale attenuation behaviours were associated with the rock mass characteristics.

The block-scale attenuation relationships for the North Zone and R4 were compared at a charge weight of 50kg using the $\varepsilon_{W\text{-}MN\text{-}95\%}$ prediction equations from the analyses of the combined data sets. The resulting attenuation relationships of $\varepsilon_{W\text{-}MN\text{-}95\%}$ versus distance at a 50kg charge weight are shown on log-log axes in Figure 8.45.

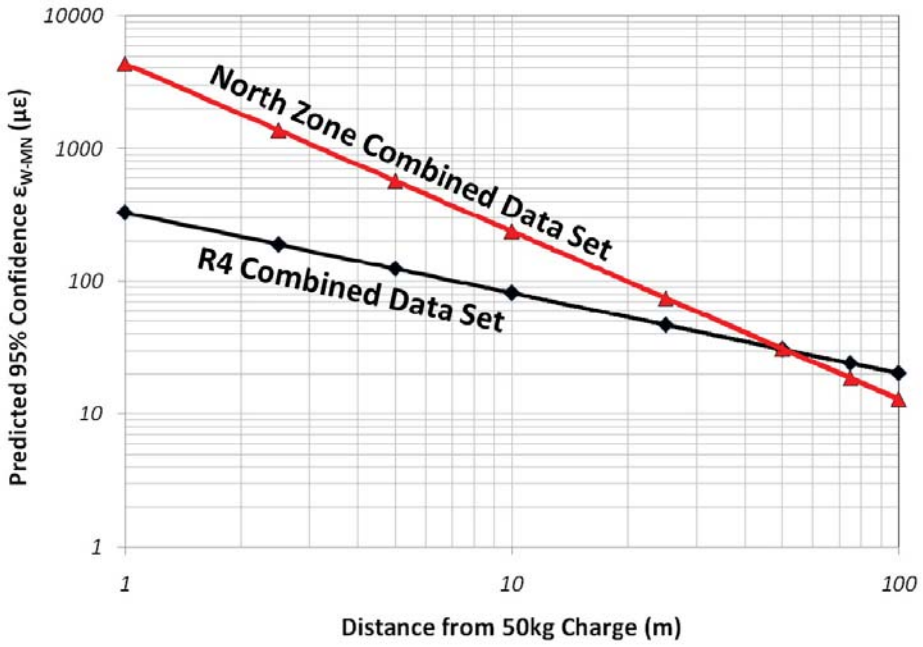

Figure 8.45. Predicted 95% upper confidence $\varepsilon_{W\text{-}MN}$ versus distance for the North Zone and R4 combined data sets for a 50kg charge weight.

The two attenuation relationships shown in Figure 8.45 clearly indicate significant differences between the rock masses of the North Zone and R4 mining areas. Some variation between the two rock masses would appear to be intuitive based on observations from mapping and visual inspection. The attenuation relationships presented in Figure 8.45 identify several characteristics of the rock mass response to blasting that would not be intuitive based on general rock mass observations.

According to the attenuation relationships in Figure 8.45, the consumption of explosive energy in the breakage zone for the North Zone was lower than that for the R4. This was indicated by comparing the intercept values of the two lines. A higher intercept value would suggest that a greater amount of the explosive energy was released as excess seismic energy or strain. Loosely interpreted, this result suggested that the fragmentation and associated rock damage in the immediate breakage zone would be reduced in the North Zone compared with the R4. The lower intercept value for the R4 zone suggested higher explosive energy consumption within the stope, resulting in better fragmentation and more intense damage to the rock mass near the blasthole prior to seismic propagation.

The differences between the two slopes revealed important information about the rock mass properties of the two mining areas. The steeper negative slope for the North Zone data set indicated a higher rate of strain attenuation over distance compared with the R4 mining area. This result was unexpected, as the more highly fractured and faulted R4 rock mass would have been expected to attenuate blasting vibrations at a higher rate than the highly competent North Zone. The strongly anisotropic behaviour of the North Zone rock mass likely contributed to the higher rate of attenuation for the combined data set.

Evaluation of the blast vibration attenuation relationships for each mining area could provide benefits to the drilling and blasting and geotechnical programs at Cannington. Understanding the consumption and attenuation of explosive and seismic energy within the rock masses of different mining areas can provide a useful design tool to maximise fragmentation and minimise blast-related rock mass damage. Further monitoring and analysis would be required to determine which blasting parameters at Cannington could contribute to an increase in the energy consumed near the blasthole to increase fragmentation.

8.9.2 Comparison of Specific Amplitude Attenuations

An additional comparison of the North Zone and R4 rock masses was performed using specific amplitude attenuation analysis results from the two mining areas. The specific attenuations provided characterisations of the inelastic attenuations of the blast vibrations outside of the breakage zones within the stopes.

One of the limitations of the specific amplitude attenuation approach is the sensitivity of the results to the separation distances between the transducers. Due to this sensitivity, only the measurements recorded on transducer arrays of identical separation distances could be used to compare the two mining areas. This geometry was only present within the data sets for the 24jC6HL 200mLv Southwest wall and the 52h04HL Southeast wall. These two data sets had the same differential transducer distances and could therefore be compared to evaluate the specific attenuations of the two rock masses. Additionally, both data sets were located in the same mineralisation type and absent of significant contributions from mineralised

contacts or large-scale geologic features such as the footwall shear zone in the R4. The results of the specific amplitude attenuations are shown in Figure 8.46.

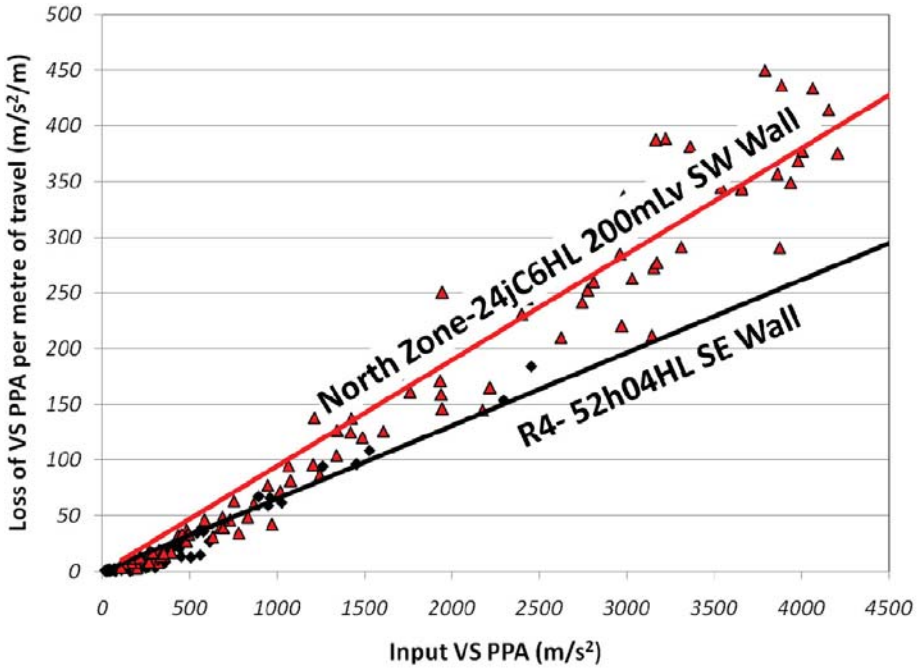

Figure 8.46. Comparison of specific amplitude attenuations for the North Zone and R4 Mining areas.

The higher rate of attenuation for the North Zone 24jC6HL Southwest wall orientation as reflected by the steeper slope of the best fit line further supported the blast vibration attenuation relationships observed in Figure 8.45. As a result of both analysis approaches, it became clear that the R4 mining area attenuated less energy per metre of wave propagation than the North Zone, which was largely unexpected based on the observable rock mass characteristics.

8.10 Discussion and Conclusions

The rock mass characterisations, blast vibration analyses and post-extraction stope performance assessments performed for the North Zone and R4 stopes at the Cannington Mine have provided substantial insight into the response of the two different rock masses to mining and blasting. In addition to identifying differences between the two rock masses with regards to explosive energy consumption and

attenuation, block-scale and localised rock mass differences were identified using the results of blast vibration monitoring and traditional geotechnical characterisation tools. The block-scale anisotropy within the North Zone, as indicated by several different assessment methods, was formerly not identified by the mine personnel. In addition, possible influences of mineralisation type or mineralised contacts on the stress wave propagation characteristics of the rock mass of the North Zone were identified.

The strain-related blast damage prediction performed for the 200mLv of stope 24jC6HL identified tensile strain-based damage zones of up to 20m from the stope boundary. This prediction was well in excess of the prediction using the critical tensile plane strain approach. As a result of the low to moderate mining-induced static stresses in the North Zone, the predicted damage extents around 24jC6HL were not largely influenced by the static stress distribution. Due to limitations on the availability of diamond core drilling equipment, no dedicated measurements of in situ rock mass damage were possible at the time of the Cannington monitoring period. For this reason, the results of visual assessment and post-extraction stope performance were the only available methods of damage assessment. Based on these results, the predicted damage zones could not be validated.

One of the original concerns of Cannington geotechnical personnel was the integrity of the two return air rises in the vicinity of stopes 22gC6HL and 24jC6HL. Although no damage was observed to the SdD0RAR or TbC5RAR, some indications of rock mass degradation or relaxation of the temporary pillar containing TbC5RAR were identified. These indications were based on comparing the stress wave velocities, peak amplitude-frequency analyses and specific attenuations for the confined and unconfined pillar conditions as a result of the blast vibration monitoring program. Reductions in the inferred stiffness and average stress wave velocity and an increase in specific attenuation were observed for the unconfined pillar condition. The combination of the three assessment methods indicated that the rock mass within the pillar had degraded due to possible contributions of existing discontinuity dilation, loss of confinement and blast-related rock mass alteration.

CHAPTER 9 : CONCLUSIONS

The prediction or assessment of blasting-related rock mass damage should consider many different factors to represent the mechanisms of damage and the interaction of near-field blasting vibrations with rock mass components. In general, existing analytical models for predicting rock mass damage from blasting do not adequately consider the following factors:

- The influence of rock mass properties on damage to intact rock or existing discontinuities
- The influence of mining-induced static stresses/strains on rock mass loading conditions resulting from dynamic blasting strains
- Accurate monitoring and representation of near-field blast vibrations
- Orientation-related and rock mass specific blast vibration attenuation behaviours

The methods of blast vibration monitoring, analysis and interpretation and blast damage prediction proposed in this thesis have attempted to address the factors listed above. These techniques were developed through analysis of over 5000 single-hole near-field and intermediate-field blast vibration waveforms recorded by the author over a three year blast vibration monitoring program at two Australian sublevel open stoping mines. The approaches proposed by the author for near-field blast vibration monitoring and analysis and blast damage prediction in the underground mining environment were necessary to address the shortcomings of existing empirical and semi-analytical models such as PPV damage criterion and the critical tensile plane strain model.

9.1 Original Contributions Provided by the Research Program

The techniques for measurement of near-field blasting vibrations used in the past have lacked standardised procedures for selection of transducer types, dynamic ranges, frequency responses, configurations and coupling mechanisms. The results

from highly variable methods of near-field vibration measurement have been published over the last 40 years. The lack of standardised near-field monitoring techniques has resulted in limitations in the ability to compare monitoring results from different blast monitoring programs. For example, a site-specific model that has been developed using surface-mounted uni-axial geophones to measure intermediate-field vibrations should not be compared with a model resulting from fully-encapsulated, tri-axial accelerometer measurements in the near-field. Underground near-field blast monitoring criteria and the processes for the design and implementation of a near-field blast monitoring program have been unambiguously proposed by the author in this thesis.

Recorded near-field blast vibration waveforms should be post-processed to accurately represent the measurement capabilities of the selected transducers based on the amplitude range and frequency responses. Discussions on post-processing procedures of blasting waveforms have largely been neglected in the published literature. As a result, published blast vibration monitoring results should be viewed with a degree of uncertainty. A series of vibration waveform processing techniques have been discussed in this thesis, as applied to the waveforms collected during the author's blast vibration monitoring program.

Traditional charge weight scaling blast vibration analysis and prediction approaches have been used for many years to characterise the attenuations of blasting vibrations in the near-field of blasting events. These models do not recommend any treatments for the selection of source to sensor distances under complex blasthole geometries such as those observed in ring drilling in sublevel open stoping. Comparisons of different distance models by the author has identified that for the data collected at the two sponsor sites, the geometric distance from the charge column midpoint to the monitoring location provided the highest correlations of regression for void-unaffected geometries. For those wave travel paths that were affected by an existing or forming stope voids, a standardised approach to determine void-affected wave travel distances was proposed, named the VICD method.

An alternative approach for analysis of near-field blast vibrations has been proposed by the author based on the total wave energy density ($ED_{W\text{-}tot}$) and the wave-induced

mean normal dynamic strain ($\varepsilon_{W\text{-}MN}$). These values have been proposed instead of instantaneous amplitudes such as PPV due to observations of variable distributions of energy and broad frequency spectra in recorded near-field waveforms. Additionally, the limitations linked with plane strain assumptions and the associated simplifications in the critical tensile plane strain model have been addressed based on the use of the mean normal dynamic strain invariant ($\varepsilon_{W\text{-}MN}$), related to the stored strain energy density ($ED_{W\text{-}SS}$).

Results of approximately 180 nonlinear regression analyses performed on combined and individual data sets using the general form of charge weight scaling have been presented in Appendix 9. These published regression results represented a small portion of thousands of individual analyses performed over the course of the three year data analysis period using different charge weight scaling models, wave characteristics, distance values and data combinations. The results in Appendix 9 have indicated a random distribution of correlation rankings based on regression of PPV, PPA, $ED_{W\text{-}tot}$ and $\varepsilon_{W\text{-}MN}$ data and large ranges in regression values based on the individual rock mass properties and monitoring orientations. Therefore, no single model or wave characteristic can accurately describe near-field blasting vibrations under complex geometries, geologies and blasting conditions.

The prediction of blast damage using past empirical and semi-analytical methods has largely relied on values of PPV or tensile plane strains as damage criteria. Three new blast damage criteria have been proposed by the author, based on both energy and strain-related fracture properties of rock. The proposed criteria consider blast-related rock mass damage as a two-component process, where both the fresh fracture of intact rock and activation and extension of discontinuities have been addressed.

Two criteria have been proposed for prediction of intact rock damage from blast wave loading based on either stored strain rupture energy (including the consideration of strain rate effects) or fracture strain. The strain rupture energy approach proposed by the author is unique due to the dependence on strain rate effects. No explicit consideration of strain rate effects is included in existing energy-based blast damage criteria. The proposed compressive and tensile fracture strain criteria are novel in that they include the influence of existing mining-induced or

virgin static strains on the predicted blast-induced damage. The existing static and blast-induced dynamic strain conditions are combined in the proposed approach using a mean normal strain superposition approach. No existing analytical model of blast damage prediction published in the past has included this important factor encountered in underground mining. The criterion that has been proposed by the author for predicting extension or dilation of discontinuities is based on the fracture mechanics principle of fracture strain energy of pre-cracked brittle solids.

The models and techniques of blast vibration collection, processing, analysis and interpretation presented in this thesis were developed as a result of near-field blast vibration monitoring at two Australian underground open stoping mines. The Kanowna Belle Gold Mine and the Cannington Mine represented a number of different rock mass characteristics, mining geometries and blasting conditions. Blast vibration data collected at each of the mine sites were used to perform stope assessments and rock mass characterisations to aid in understanding of the response of rock masses to blasting and the role of blast damage in stope performance. The results of the characterisations and assessments were unique to each individual mine site.

9.2 Limitations of the Research Program

Any research program that is based on the results of field measurements can introduce errors into the measurement process. A number of possible sources of error have been considered in the collection and processing of blast vibration data and the provided blast design and charging files from the mine sites. These possible sources of error included:

- Incorrect charge quantities based on inconsistencies in drillhole diameter, charge toe and collar location errors or explosive densities
- Errors in calculated charge to sensor distances based on drillhole deviation or misrepresentation of the VICD wave paths

- Errors in measured vibration values from under-sampling, inadequate transducer response ranges, masking of waveforms from resolution effects, loss of transducer coupling or human error
- Errors introduced during waveform processing such as frequency aliasing, selection of frequency filtering ranges and rounding errors in calculations
- Inaccuracies in the measured waveforms due to shielding or mounting effects of the installed transducers

In addition to the possible sources of error in the collection and processing of data, several assumptions were made to allow analysis of the data and development of the models. These assumptions included:

- Largely linear-elastic behaviour of the rock mass such that plastic deformation effects were not considered
- The general charge weight scaling prediction model adequately represented near-field vibration data to allow nonlinear estimation of blasting energies and strains
- Conditions of strain continuity within the rock masses such that the mining-induced mean normal static strains and blast-induced mean normal dynamic strains could be superimposed
- The average stress wave velocities for each monitored orientation adequately described the wave propagation characteristics
- Rock testing data and other data obtained from the case studies sites was accurate

The use of the mean normal dynamic blasting strains, the static and dynamic strain combination approach and the differential grid-based excess strain capacity calculations were simplistic in nature. These simplifications were required to enable generalisation of the complex wave behaviours observed in the near-field waveforms and to allow for accommodation of large and highly-variable data sets in the proposed analytical blast damage prediction approach. Consideration of more

complex interactions between the static and dynamic strains and individual strain components would likely necessitate the use of a numerical model instead of an analytical model. In addition, the true wave propagation behaviours identified through the blast monitoring program were not able to be represented in the current analytical-graphical approach. The use of a single 95% upper confidence energy density or strain prediction equation for all propagation directions would likely result in over-prediction at some locations within the rock mass. Therefore, the prediction of damage using the model would represent the worst-case scenario.

One of the most significant limitations of the blast damage predictions performed in the case studies was that measurement of actual damage within the confined rock mass around the stopes was not performed. This limitation was a result of the lack of available services and equipment at the mine sites, and represented a notable deficiency in the research program. Although some indirect methods of rock mass assessment were possible through analysis of blast waves and CMS surveys of post-extraction voids, dedicated borehole observation or cross-hole seismic assessments within the rock masses near the stopes were not performed. These methods would have allowed the actual extent of observable blast damage to be validated within the rock masses, away from the post-extraction void surfaces. Therefore, the blast damage predictions performed in Chapters 7 and 8 should be viewed as theoretical as the model has not been validated by dedicated damage measurements.

9.3 Future Work

The blast vibration monitoring program conducted for this thesis has created a significant database of near-field vibration data, but additional near-field vibration measurements are required to further investigate the influence of rock mass properties on blast vibrations. Analysis of additional waveforms along with re-analysis of existing data are expected to reveal additional factors contributing to peak amplitudes, frequency spectra and energy distributions. Additional field measurements using methods of indicating in situ rock mass damage would aid in validating and modifying the blast damage prediction approach. A detailed

parametric study on the influence of the input variables on the calculated energies and strains and the predicted damage extents would also aid in validating the model.

Computer programs have been being developed at WASM since the data analysis period, which are capable of performing vector rotations of recorded waveforms. These programs will allow the influence of monitoring orientations and wave type segregation to be assessed. These types of analyses will contribute to understanding of the distribution of energy between wave types in coupled near-field waves and allow better representation of the complex wave-induced strain fields from blasting. Improved understanding of wave components will also lead to development of approaches to more accurately determine dynamic rock mass loading conditions based on collected vibration data. These approaches may allow for the proposed blast damage prediction model to include more comprehensive rock failure criteria such as Hoek-Brown or Mohr-Coulomb criteria or to predict shear-based damage.

9.4 Industry Applications and Relevance

Blast vibration monitoring and analysis is generally under-utilised in the mining industry as a method of assessing the performance of underground blasting programs. Cheap and simple programs related to diagnostic monitoring can be very valuable to a mining operation from a safety and blast performance perspective. More expensive and intensive blast vibration monitoring programs such as those used to investigate near-field damage can provide valuable insights into the blasting process and the response of the rock mass to blasting practices at the mine. Careful design and implementation of a blast monitoring program can also provide additional information on the rock mass, as observed for the Kanowna Belle Gold Mine and Cannington Mine case studies. The rock mass characterisations and blast vibration analyses performed at the two sponsoring mine sites have identified otherwise undocumented rock mass behaviours and aided in refining blasting processes. As a result of the research program, a reduction in mining costs at the Cannington Mine was experienced through changes in blasting geometries.

Successful integration of blast damage-related effects into the stope and mine design process can aid in predicting stope performance and blast-induced damage to nearby excavations. As a result, a mine site may experience reductions in stope dilution, localised and large-scale rock mass instabilities and rock-fall related injuries or fatalities.

REFERENCES

Achenbach, JD (1973), Wave Propagation in Elastic Solids, Lauwerier and Koiter (eds), North-Holland Publishing Company, Netherlands.

Adamson, WR and Lund, AS (2001), 'On the Use of Mechanistic Blast-Outcome Measurement and Modelling for Optimisation of Explosive Selection in Underground Mining', Proceedings of EXPLO 2001, Hunter Valley, NSW, online resource, http://www.dynonobel.com/NR/rdonlyres/D6200378-495D-4FEA-84AB-734ACBC9C16D/0/MechanisticBlastOutcomeMeasurement.pdf

Adhikari, GR, Theresraj, AI and Gupta, RN (2005), 'Influence of Transducer-Ground Coupling on Vibration Measurements', Fragblast Journal, Vol. 9, No.2, Taylor and Francis Group, pp. 79-92.

Aimone-Martin, CT and Francke, JL (1997), 'Time Domain Reflectometry (TDR): A Comparison of Field Data to Laboratory Shear Tests', Int. J. Rock Mech. Min. Sci. Vol. 34, No. 3-4, Paper No. 84, Elsevier Science Ltd.

Ambraseys, NN and Hendron, AJ Jr (1968), 'Chapter 7: Dynamic Behaviour of Rock Masses', Rock Mechanics in Engineering Practice, Stagg and Zienkiewicz (eds), John Wiley and Sons Ltd, Great Britain, pp.203-236.

AMC (1998), 'Cannington Stress Measurement 68XC, 450mLv', Report from Australian Mining Consultants to BHP World Minerals- Cannington Project, Report #196066, May, 1998.

Andrieux, P (1996), Methods and Practice of Blast-Induced Vibration Monitoring, MEng Thesis, McGill University, Montreal, Quebec, Canada.

Andrieux, P and Heilig, J (1994), 'Near-Field Blast Vibration Monitoring-Practical Considerations and Issues', Seventeenth Study Sessions on Blasting Techniques, SEEQ, Quebec City, Canada.

Anon (2006), Geophones, Product line technical data sheets, Input/Output Inc, www.iongeo.com.

Armstrong, LW (2004), 'Blast Induced Vibration Monitoring and Waveform Analysis', Orica Mining Services internal document, Orica Technical Centre, Kurri Kurri, NSW.

Atchison, TC and Roth, J (1960), 'Comparative Studies of Explosives in Marble', USBM Report RI5797, United States Bureau of Mines.

Atchison, TC and Tournay, WE (1959), 'Comparative Studies of Explosives in Granite, USBM Report RI5509', United States Bureau of Mines.

Bažant, ZP, Bai, S-P and Gettu, R (1993), 'Fracture of Rock: Effect of Loading Rate', Eng. Fract. Mech., Vol. 45, No. 3, pp. 393-398.

Bergmann, OR, Riggle, JW and Wu, FC (1973), 'Model Rock Blasting-Effect of Explosives Properties and Other Variables on Blasting Results', Int. J. Rock Mech. Min. Sci. Geomech. Abstr., Vol. 10, Pergamon Press, Great Britain, pp.585-612.

Bhandari, S (1979), 'On the Role of Stress Waves and Quasi-static Gas Pressure in Rock Fragmentation by Blasting', Acta Astronautica, Vol. 6, Pergamon Press, Great Britain, pp. 365-383.

Bhandari, S (1996), 'Changes in Fragmentation Processes with Blasting Conditions', Proceeding of International Symposium on Rock Fragmentation by Blasting, Fragblast 5, Mohanty (ed), Montreal, Canada, A.A. Balkema, pp. 301-309.

Birkimer, DL (1970), 'A Possible Fracture Criterion for the Dynamic Tensile Strength of Rock', Dynamic Rock Mechanics: 12th Symposium on Rock Mechanics, Rolla Missouri, USA, 16-18 Nov, Clark (ed), Society of Mining Engineers, pp.573-590.

Blair, DP (2004), 'The Frequency Content of Ground Vibration', Fragblast Journal, Vol. 8, No.3, Taylor and Francis Group, pp. 151-176.

Blair, DP and Armstrong, LW (2001), 'The Influence of Burden on Blast Vibration', Fragblast Journal, Vol. 5, No 1-2, Swets and Zeitlinger, pp. 108-129.

Blair, BE and Duvall, WI (1954), 'Evaluation of Gages for Measuring Displacement, Velocity, and Acceleration of Seismic Pulses', USBM Report RI5073, United States Bureau of Mines.

Blair, D and Minchinton, A (1996), 'On the Damage Zone Surrounding a Single Blasthole', Rock Fragmentation by Blasting, Mohanty (ed), Balkema, Rotterdam, pp. 121-130.

Bloss, ML (2005), 'Mining Open Stopes at Cannington Mine Using a Vertical Retreat Open Stoping (VROS) Method', Ninth Underground Operators' Conference, Perth, WA, March 7-9, pp 323-327.

Bogdanoff, I (1996), 'Vibration Measurements in the Damage Zone in Tunnel Blasting', Rock Fragmentation by Blasting, Mohanty (ed), Balkema, Rotterdam, pp. 177-185.

Bradley, WB and Kobayashi, AS (1971), 'Fracture Dynamics-A Photoelastic Investigation', Eng. Fract. Mech., Vol. 3, Pergamon Press, Great Britain, pp. 317-332.

Brady, BHG and Brown, ET (2004), Rock Mechanics for Underground Mining: 3rd Edition, Kluwer Academic Publishers, Dordrecht, Netherlands.

Brent, GF and Smith, GE (1999), 'The Detection of Blast Damage by Borehole Pressure Measurement', Proceeding of International Symposium on Rock Fragmentation by Blasting, Fragblast 6, Johannesburg, South Africa, SAIMM, pp.9-13.

Brinkmann, JR (1990), 'An Experimental Study on the Effects of Shock and Gas Penetration in Blasting', Proceedings of the International Symposium on Rock Fragmentation by Blasting, Fragblast 3, Brisbane, Australia, AusIMM, pp.55-66.

Brochu, RR and Eltschlager, KK (1999), 'Proposed Draft of the I.S.E.E. Seismograph Performance Specifications and General Guidelines for Seismograph Field Use', Proceedings of the Conference on Explosives and Blasting Technique (CD-ROM), ISEE, Cleveland, OH, USA, Copyright 2000, pp.279-285.

Brüel and Kjaer (2006), Product Specification Sheet, B and K 4371 Accelerometer, www.bksv.com.

Butkovich, TR and Hearst, JR (1976), 'Prediction and Determination of Explosive-Induced Fracture', Proceedings of the Conference on Explosives and Blasting Technique (CD-ROM), ISEE, Cleveland, OH, USA, Copyright 2000, pp.301-328.

Butt, SD (2001), 'Experimental Measurement of P-wave Attenuation due to Fractures over the 100 to 300 kHz Bandwidth', Pure and Applied Geophysics, Vol. 158, Birkhäuser Verlag, Basel, pp. 1783-1796.

Cardarelli, E, Marrone, C and Orlando, L (2003), 'Evaluation of Tunnel Stability Using Integrated Geophysical Methods', J. App. Geoph., Vol. 52, Elsevier Science B.V., pp. 93-102.

Chitombo, G, Guest, A, Djordjevic, N and La Rosa, D (1999), 'In Search of the Fundamentals of Rock Breakage Under Controlled Dynamic Loading', Fragblast 1999, Johannesburg, SA, pp.73-79.

Cho, SH, Nakamura, Y and Kaneko, K (2004), 'Dynamic Fracture Process Analysis of Rock Subjected to Stress Wave and Gas Pressurization', Int. J. Rock Mech. Min. Sci. Vol. 41, No. 3, CD-ROM, Elsevier Science Ltd, pp.1-8.

Cho, SH, Ogata, Y and Kaneko, K (2003), 'Strain-rate Dependency of the Dynamic Tensile Strength of Rock', Int. J. Rock Mech. Min. Sci., Vol. 40, Elsevier Science Ltd, pp. 763-777.

Cosma, C, Olsson, O, Keskinen, J and Heikkinen, P (2001), 'Seismic Characterization of Fracturing at the Äspö Hard Rock Laboratory, Sweden, from the Kilometer Scale to the Meter Scale', Int. J. Rock Mech. Min. Sci., Vol. 38, Elsevier Science Ltd, pp. 859-865.

Crampin, S (1984), 'Effective Anisotropic Elastic Constants for Wave Propagation Through Cracked Solids', Geophysical Journal of the Royal Astrological Society, Vol. 76, pp. 135-145.

Crenwelge, OE (1991), 'Transient Data Analysis Procedure for Reducing Blast-Induced Ground and House Vibrations', Proceedings of the Conference on Explosives and Blasting Technique (CD-ROM), ISEE, Cleveland, OH, USA, Copyright 2000, pp. 29-47.

Cunningham, C (2006), 'Concepts of Blast Hole Pressure Applied to Blast Design', Fragblast Journal, Vol. 10, Nos 1-2, Taylor and Francis, pp. 33-45.

Daehnke, A, Rossmanith, H.P. and Knasmillner, R.E. (1996), 'Blast-Induced Dynamic Fracture Propagation', Rock Fragmentation by Blasting, Mohanty (ed), Balkema, Rotterdam, pp. 13-18.

Devine, JF, Beck, RH, Meyer, AVC and Duvall, WI (1965), 'Vibration Levels Transmitted Across a Presplit Fracture Plane', USBM Report RI6695, US Bureau of Mines.

Djordjevic, N (1999), 'Two-Component Model of Blast Fragmentation', Proceeding of the International Symposium on Rock Fragmentation by Blasting, Fragblast 6, Johannesburg, South Africa, SAIMM, pp. 213-219.

Donzé, FV, Bouchez, J and Magnier, SA (1997), 'Modeling Fractures in Rock Blasting', Int. J. Rock Mech. Min. Sci. Vol. 34, No. 8, Elsevier Science Ltd, Great Britain, pp.1153-1163.

Dowding, CH (1985), Blast Vibration Monitoring and Control, Prentice Hall Inc, Englewood Cliffs, NJ, USA.

Duvall, WI, Johnson, CF, Meyer, AVC and Devine, JF (1962), 'Vibrations from Instantaneous and Millisecond-Delayed Quarry Blasts', USBM Report RI6151, United States Bureau of Mines.

Duvall, WI and Petkof, B (1958), 'Spherical Propagation of Explosion-Generated Strain Pulses in Rock', USBM Report RI5483, United States Bureau of Mines.

Eissa, EA and Kazi, A (1988), 'Technical Note: Relation Between Static and Dynamic Young's Moduli of Rocks', Int. J. Rock Mech. Min. Sci. Geomech. Abstr., Volume 25, No. 6, pp.479-482.

Esen, S, Onederra, I and Bilgin, HA (2003), 'Modelling the Crushed Zone Around a Blasthole', Int. J. Rock Mech. Min. Sci. Vol. 40, Elsevier Science Ltd, Great Britain, pp.485-495.

Favreau, RF (1969), 'Generation of Strain Waves in Rock by an Explosion in a Spherical Cavity', Journal of Geophysical Research, Vol. 74, No. 17, American Geophysical Union, pp. 4267-4280.

Field, JE and Ladegaard-Pedersen, A (1971), 'The Importance of the Reflected Stress Wave in Rock Blasting', Int. J. Rock Mech. Min. Sci. Vol. 8, Pergamon Press, Great Britain, pp.213-226.

Fleetwood, K (2006), 'Borehole Deviation Survey: Stope C93-80 Upholes', Report to Kanowna Belle Gold Mine from the Western Australian School of Mines, May, 2006.

Fleetwood, K (2010), 'Investigation into Rock Mass Damage Associated with Drilling and Blasting in D-block at the Kanowna Belle Gold Mine', Confidential report submitted to Barrick Gold Corp-Kanowna Belle Gold Mine from the Western Australian School of Mines Rock Mechanics Research Group, July, 2010.

Fletcher, LR, Plis, MN and Stachura, VJ (1989), 'Overbreak Control in the White Pine Underground Mine', Proceedings of the Conference on Explosives and Blasting Technique (CD-ROM), ISEE, Cleveland, OH, USA, Copyright 2000, pp. 25-33.

Forsyth, WW (1993), 'A Discussion of Blast-Induced Overbreak Around Underground Excavations', Rock Fragmentation by Blasting, Rossmanith (ed), Balkema, Rotterdam, pp. 161-166.

Fourney, WL, Dick, RD and Weaver, TA (1996), 'Dynamic Response by Signal Integration', Proceeding of International Symposium on Rock Fragmentation by Blasting, Fragblast 5, Mohanty (ed), Montreal, Canada, A.A. Balkema, pp. 87-94.

Friedel, MJ, Jackson, MJ, Scott, DF, Williams, TJ and Olson, MS (1995), '3-D Tomographic Imaging of Anomalous Conditions in a Deep Silver Mine', J. App. Geoph., Vol. 34, Elsevier Science B.V., pp. 1-21.

Friedel, MJ, Scott, DF, Jackson, MJ, Williams, TJ and Killen, SM (1996), '3-D Tomographic Imaging of Anomalous Stress Conditions in a Deep US Gold Mine', J. App. Geoph., Vol. 36, Elsevier Science Ltd, pp. 1-17.

Furtney, JK, Cundall, PA and Chitombo, GP (2009), 'Developments in Numerical Modeling of Blast Induced Rock Fragmentation: Updates from the HSBM Project, Proceedings of the International Symposium on Rock Fragmentation by Blasting, Fragblast 9, Sanchidrián (ed), Granada, Spain, CRC Press, pp. 335-342.

Germain, P and Hadjigeorgiou, J (1997), 'Influence of Stope Geometry and Blasting Patterns on Recorded Overbreak', Int. J. Rock Mech. Min. Sci. Vol. 34, No. 3-4, paper no. 115, Elsevier Science Ltd.

Geyer, RL and Martner, ST (1969), 'SH Waves from Explosives Sources', Geophysics, Vol. 34, No. 6, Society of Exploration Geophysicists, pp. 893-905.

Grady, DE and Kipp, ME (1979), 'The Micromechanics of Impact Fracture of Rock', Int. J. Rock Mech. Min. Sci. Geomech. Abstr., Vol. 16, Pergamon Press Ltd, Great Britain, pp.293-302.

Grady, DE and Kipp, ME (1980), 'Continuum Modelling of Explosive Fracture in Oil Shale', Int. J. Rock Mech. Min. Sci. Geomech. Abstr., Vol. 17, Pergamon Press Ltd, Great Britain, pp.147-157.

Grady, DE and Lipkin, J (1980), 'Criteria for Impulsive Rock Fracture', Geophysical Research Letters, Vol. 7, No. 4, American Geophysical Union, pp. 255-258.

Graff, KF (1975), Wave Motion in Elastic Solids, Oxford University Press, Belfast.

Grandjean, G and Gourry, JC (1996), 'GPR Data Processing for 3D Fracture Mapping in a Marble Quarry (Thassos, Greece)', J. App. Geoph., Vol. 36, Elsevier Science B.V., pp. 19-30.

Grogan, A (1998), 'A Review of Suggested Geophone Attachment Methodologies from Commonly Referred to Monitoring Standards', Proceedings of the Conference on Explosives and Blasting Technique (CD-ROM), ISEE, Cleveland, OH, USA, Copyright 2000, pp.105-113.

Grote, DL, Park, SW and Zhou, M (2001), 'Dynamic Behaviour of Concrete at High Strain Rates and Pressures: I. Experimental Characterization', Intl. Journal of Impact Engineering, Vol. 25, Elsevier Science Ltd., pp. 869-886.

Hadjigeorgiou, J, Lessard, JF, Villaescusa, E and Germain, P (1995), 'An Appraisal of Structural Mapping Techniques', Proceedings of the 2nd International Conference on the Mechanics of Jointed and Faulted Rock-MJFR-2, Rossmanith (ed), Vienna, Austria, 10-14 April, 1995, AA. Balkema, pp. 193-199.

Hamdi, E, du Mouza, J and Fleurisson, JA (2001), 'Evaluation of the Part of Blasting Energy Used for Rock Mass Fragmentation', Fragblast Journal, Vol. 5, No. 3, Swets and Zeitlinger, pp. 180-193.

Hayles, JG, Everitt, RA and Woodcock, DR (1999), 'A 15kHz Cross-hole Seismic Survey Across a Fracture at the AECL Underground Research Laboratory', Canadian Journal of Earth Sciences, Vol. 36, NRC Canada, pp. 1517-1532.

Heelan, PA (1953), 'Radiation from a Cylindrical Source of Finite Length', Geophysics, Vol. 18, No. 3, Society of Exploration Geophysicists, pp. 685-696.

Heilig, J (2002), 'Analysis of Vibration Results from Blasting of the CP96-68 Stope', Internal report to the Western Australian School of Mines, Heilig and Partners Consulting Engineers, Dec 2002.

Heilig, J (2005), 'Comparison Between the Vibration Levels Recorded with Geophones and Accelerometers', Internal report to the Western Australian School of Mines, Heilig and Partners Consulting Engineers, Oct 2005.

Hendricks, C, Scoble, M, Peck, J and Szymans, J (1991), 'Blasthole Deviation: Measurement, Mechanisms and Impact on Dilution', Proceedings of the Conference on Explosives and Blasting Technique (CD-ROM), ISEE, Cleveland, OH, USA, Copyright 2000, pp. 11-20.

Hendron, AJ Jr (1968), 'Chapter 2: Mechanical Properties of Rock', Rock Mechanics in Engineering Practice, Stagg and Zienkiewicz (eds), John Wiley and Sons Ltd, Great Britain, pp.21-53.

Holmberg, R (1977), 'Results from Single Shot Ground Vibration Measurements', Report from the Swedish Detonic Research Foundation, DS 1977:9 (in Swedish).

Holmberg, R, Larsson, B and Sjoberg, C (1984), 'Improved Stability Through Optimized Rock Blasting', Proceedings of the Conference on Explosives and Blasting Technique (CD-ROM), ISEE, Cleveland, OH, USA, Copyright 2000, pp. 166-179.

Holmberg, R and Persson, PA (1978), 'The Swedish Approach to Contour Blasting', Proceedings of the Conference on Explosives and Blasting Technique (CD-ROM), ISEE, Cleveland, OH, USA, Copyright 2000, pp. 113-126.

Holmberg, R and Persson, PA (1979), 'Design of Tunnel Perimeter Blasthole Patterns to Prevent Rock Damage', Tunnelling '79: Proceedings of the Second International Symposium, London, England, 12-16 March, London: Institute of Mining and Metallurgy, pp. 280-283.

Howell, BF Jr and Budenstein, D (1955), 'Energy Distribution in Explosion-Generated Seismic Pulses', Geophysics, Vol. 20, No. 1, January, 1955, pp. 33-52.

Hudson, JA (1981), 'Wave Speeds and Attenuation of Elastic Waves in Material Containing Cracks', Geophysical Journal of the Royal Astrological Society, Vol. 64, pp. 133-150.

Hutchinson, DJ and Diederichs, MS (1996), Cablebolting in Underground Mines, BiTech Publishers, British Columbia, Canada.

Iverson, SR, Hustrulid, WA, Johnson, JC, Tesarik, D and Akbarzadeh, Y (2009), 'The Extent of Blast Damage from a Fully Coupled Explosive Charge', Proceedings of the International Symposium on Rock Fragmentation by Blasting, Fragblast 9, Sanchidrián (ed), Granada, Spain, CRC Press, pp. 459-468.

JKMRC, (1984), 'Effect of Blasting Practice on the Stability of the Hangingwall in an Open Stoping Application: 14 Orebody N663 and N658 Trial Stopes, Mt Isa Mines Limited', Technical Report to Mount Isa Mines, University of Queensland-JKMRC.

Jaeger, JC and Cook, NGW (1969), Fundamental of Rock Mechanics, Methuen and Co Ltd, Great Britain.

Jaeger, JC and Cook, NGW (1979), Fundamental of Rock Mechanics, Third Edition, Chapman and Hall, London, Great Britain.

Jimeno, CL, Jimeno, EL and Carcedo, FJA (1987), Drilling and Blasting of Rocks (Manual de Perforacion y Voladura de Rocas), Taylor and Francis, New York.

Jordan, DW (1962), 'The Stress Wave from a Finite, Cylindrical Explosive Source', Journal of Mathematics and Mechanics, Vol. 11, No. 4, Indiana University Dept of Mathematics, pp. 503-551.

Kanowna Belle Gold Mine (KBGM), (2008), 'GCMP (Ground Control Management Plan) Overview Document', Internal library database-Kanowna Belle Gold Mine, P:\GCMP\03_Library\Kanowna Belle\Background\Geology.

Katsabanis, PD (2001), 'Application of Numerical Modelling to Examine Damage in Wall Control Operations', Proceedings of the Conference on Explosives and Blasting Technique (CD-ROM), ISEE, Cleveland, OH, USA, Copyright 2001, pp. 25-37.

Keller, R and Kramer, N (2000), 'Considerations for Drill and Blast Excavation of a Geologic Repository for the Disposal of High-Level Radioactive Nuclear Waste at Yucca Mountain', Proceedings of the Conference on Explosives and Blasting Technique (CD-ROM), ISEE, Cleveland, OH, USA, Copyright 2000, pp. 31-48.

Kelsall, PC, Case, JB and Chabannes, CR (1984), 'Evaluation of Excavation-Induced Changes in Rock Permeability', Int. J. Rock Mech. Min. Sci. Geomech. Abstr., Vol. 21, No. 3, Pergamon Press Ltd, Great Britain, pp.123-135.

Kilebrant, M, Norrgård, T and Jern, M (2009), 'The Size of the Damage Zone in Relation to the Linear Charge Concentration', Proceedings of the International Symposium on Rock Fragmentation by Blasting, Fragblast 9, Sanchidrián (ed), Granada, Spain, CRC Press, pp. 449-457.

King, MS, Myer, LR and Renzowalli, JJ (1986), 'Experimental Studies of Elastic-wave Propagation in a Columnar-Jointed Rock Mass', Geophysical Prospecting, Vol. 34, pp. 1185-1199.

Kjartansson, E (1979), 'Constant Q-Wave Propagation and Attenuation', Journal of Geophysical Research, Vol. 84, No. B9, American Geophysical Union, pp.4737-4748

Kleine, TH, Cocker, A and Kavetsky, A (1990), 'The Development and Implementation of a Three Dimensional Model of Blast Fragmentation and Damage', Proceedings of the International Symposium on Rock Fragmentation by Blasting, Fragblast 3, Brisbane, Australia, AusIMM, pp.181-187.

Klepaczko, JR and Brara, A (2001), 'An Experimental Method for Dynamic Tensile Testing of Concrete by Spalling', Intl. Journal of Impact Engineering, Vol. 25, Elsevier Science Ltd, pp. 387-409.

Kolsky, H (1953), Stress Waves in Solids, Oxford: Clarendon Press, Great Britain.

Krech, WW (1974), 'The Energy Balance Theory and Rock Fracture Energy Measurements for Uniaxial Tension', Proceedings of the 3rd Congress of the Society for Rock Mechanics: Advances in Rock Mechanics, Vol. II, Part A, Denver, CO, USA, pp.167-173.

Kumar, A (1968), 'The Effect of Stress Rate and Temperature on the Strength of Basalt and Granite', Geophysics, Vol. 33, No. 3, June, Society of Exploration Geophysicists, pp. 501-510.

Kutter, HK and Fairhurst, C (1971),' On the Fracture Process in Blasting', Int. J. Rock Mech. Min. Sci. Vol. 8, Pergamon Press, Great Britain, pp.181-202.

Lambert, DE and Ross, CA (2000), 'Strain Rate Effects on Dynamic Fracture and Strength', Intl. Journal of Impact Engineering, Vol. 24, Elsevier Science Ltd, pp. 985-998.

Langefors, U and Kihlström, B (1978), The Modern Technique of Rock Blasting (3rd Edition), Almqvist and Wiksell Förlag, AB Stockholm, Sweden.

LeBlanc, TM, Heilig, J and Ryan, JM (1995), 'Predicting the Envelope of Damage from the Detonation of a Confined Charge', Sixth High Tech Seminar on Blasting Technology, Instrumentation and Explosives Applications (CD-ROM), July 8-13, 1995, ISEE, Cleveland, OH, USA, Copyright 2001, pp. 223-291.

Li, J (2002), 'Report on Rock Properties Testing for Kanowna Belle Gold Mine-AurionGold Limited', report submitted to the Kanowna Belle Gold Mine from the Western Australian School of Mines, Nov 2002.

Li, J (2007), 'Life of Mine (LOM) Geotechnical Assessment for Southern Zone and R4 Blocks at Cannington', internal report, BHP Billiton Cannington Mine, May, 2007.

Li, J (2009), Personal communications.

Li, T (1993), Modelling of Blast-Induced Rock Mass Damage, PhD Thesis, University of Queensland, JKMRC.

Li, HB, Zhao, J and Li, TJ (1999), 'Triaxial Compression Tests on a Granite at Different Strain Rates and Confining Pressures', Int. J. Rock Mech. Min. Sci. Vol. 36, Elsevier Science Ltd, pp. 1057-1063.

Li, XB, Lok, TS and Zhao, J (2005), 'Dynamic Characteristics of Granite Subjected to Intermediate Loading Rate', Rock Mech. Rock Eng., Vol. 38, No.1, Austria, pp. 21-39.

Lin, W and Heuze, FE (1987), 'Comparison of In Situ Dynamic Moduli and Laboratory Moduli of Mesaverde Rocks', Int. J. Rock Mech. Min. Sci. Geomech. Abstr., Volume 24, No. 4, pp.257-263.

Lindholm, US, Yeakley, LM and Nagy, A (1974), 'The Dynamic Strength and Fracture Properties of Dresser Basalt', Int. J. Rock Mech. Min. Sci. Geomech. Abstr., Vol. 11, Pergamon Press, Great Britain, pp.181-191.

Liu, L and Katsabanis, PD (1997), 'Development of a Continuum Damage Model for Blasting Analysis', Int. J. Rock Mech. Min. Sci. Vol. 34, No. 2, Elsevier Science Ltd, Great Britain, pp. 217-231.

Liu, Q and Proulx, R (1995), 'The Mechanisms of Rock Damage in Blasthole Open Stope Mining: Blast Induced Versus Stress Induced', Sixth High Tech Seminar on Blasting Technology, Instrumentation, and Explosives Applications (CD-ROM), July 8-13, 1995, ISEE, Cleveland, OH, USA, Copyright 2001, pp. 503-525.

Liu, Q, Tran, H, Fleury, D and Lessard, J-F (2000), 'Evaluations of Blast Damage to Pastefill at Louvicourt Mine', Proceedings of the Conference on Explosives and Blasting Technique (CD-ROM), ISEE, Cleveland, OH, USA, Copyright 2000, pp. 333-341.

Lownds, CM (1991), 'Energy Partition in Blasting', 3rd High-Tech Seminar on Blasting Technology, Instrumentation and Explosives Applications, 2-7 June, San Diego, CA, USA, ISEE.

Lu, W and Hustrulid, W (2003), 'The Lu-Hustrulid Approach for Calculating the Peak Particle Velocity Caused by Blasting', Proceedings of EFEE 2nd World Conference on Explosives and Blasting Technique, Holmberg (ed), Prague, Czech Republic, Swets and Zeitlinger, Lisse, Netherlands, pp. 291-300.

Lundborg, N, Holmberg, R and Persson, PA (1978), 'Relation Between Vibration, Distance and Charge Weight', Report of Swedish Council for Building Research, Report R11:1978 (in Swedish).

Luo X, Hatherly P and Fallon, G (1998), 'Seismic Tomographic Determination of Ore Boundaries at Scuddles Mine in Australia', Preview, Issue No. 4, June/July, http://www.cat.csiro.au/dem/msg/scirev/seistom1.pdf.

Ma, GW, Zhao, J and Hao, H (2004), 'Chamber Wall Damage Induced by a Contained Explosion', Int. J. Rock Mech. Min. Sci. Vol. 41, CD ROM, Elsevier Science Ltd.

Malatesta, L (2006), Performance of Sub-level Open Stopes at Kanowna Belle Gold Mine, BEng Thesis, Western Australian School of Mines.

Malmgren, L, Saiang, D, Töyrä, J and Bodare, A (2007), 'The Excavation Disturbed Zone (EDZ) at Kiirunavaara Mine, Sweden-by Seismic Measurements', J. App. Geoph., Vol. 61, Elsevier Science B.V., pp. 1-15.

Mandal, SK, Singh, MM, Bhagat, NK and Dasgupta, S (2007), 'Model for Energy-Based Evaluation of Blast Waves to Assess Safety of Structures', International Journal of Mining, Reclamation and Environment, Vol. 21, No. 2, June 2007, Taylor and Francis Group, pp. 111-125.

Martino, JB and Chandler, NA (2004), 'Excavation-Induced Damage Studies at the Underground Research Laboratory', Int. J. Rock Mech. Min. Sci. Vol. 41, Elsevier Science Ltd, pp.1413-1426.

Maxwell, SC and Young, RP (1996), 'Seismic Imaging of Rock Mass Responses to Excavation', Int. J. Rock Mech. Min. Sci. Geomech. Abstr., Vol. 33, Elsevier Science Ltd, Great Britain, pp.713-724.

McGaughey, WJ, McCreary, RG, Young, RP and Maxwell, SC (1994), 'Mining Applications of Seismic Tomography', CIM Bulletin, Vol. 87, No. 977, Canadian Institute of Mining and Metallurgy, pp. 49-56.

McHugh, S (1983), 'Crack Extension Caused by Internal Gas Pressure Compared with Extension Caused by Tensile Stress', Int. J. Fract., Vol. 21, Martinus Nijhoff Publishers, pp. 163-176.

McNally, GH (1998), Soil and Rock Construction Materials, Rutledge, New York.

Meyers, MA (1994), Dynamic Behaviour of Materials, John Wiley and Sons, Inc., New York.

Miller, GF and Pursey, H (1955), 'On the Partition of Energy between Elastic Waves in a Semi-Infinite Solid', Proceedings of the Royal Society on London, Series A, Mathematical and Physical Sciences, Vol. 233, No. 1192 (Dec. 6, 1955), pp. 55-69.

Minchinton, A and Lynch, PM (1996), 'Fragmentation and Heave Modelling Using a Coupled Discrete Element Gas Flow Code', Proceeding of International Symposium on Rock Fragmentation by Blasting, Fragblast 5, Mohanty (ed), Montreal, Canada, A.A. Balkema, pp. 71-80.

Mohanty, B and Prasad, U (2001), 'Degree of Rock Fragmentation Under High Strain Rates', Proceedings of the Conference on Explosives and Blasting Technique (CD-ROM), ISEE, Cleveland, OH, USA, Copyright 2001, pp. 89-95.

Morland, LW (1974), Elastic Response of Regularly Jointed Media, Geophysical Journal of the Royal Astrological Society, Vol. 37, pp. 435-446.

Nicholls, HR (1962), 'Coupling Explosive Energy to Rock,' Geophysics, Vol. 27, No. 3, June, 1962, Society of Exploration Geologists, pp. 305-316.

Nicholls, HR and Hooker, VE (1961), 'Comparative Study of Explosives in Salt', USBM Report RI 6041, United States Bureau of Mines.

Nicholls, HR and Hooker, VE (1964), 'Comparative Study of Explosives in Granite', USBM Report RI 6693, United States Bureau of Mines.

Northrop, RB (2005), Introduction to Instrumentation and Measurements, Second Edition, CRC Press, Taylor and Francis Group LLC, Boca Raton, FL, USA.

Oh, BH and Chung, CH (1989), 'Fracture Energy of Concrete Under Static and Dynamic Loading, Fracture Toughness and Fracture Energy: Test Methods for Concrete and Rock', International Workshop on Fracture Toughness and Fracture Energy, 12-14 October, 1988, Sendai, Mihashi, Takahashi and Wittmann (eds), AA Balkema, Rotterdam, Netherlands, pp. 477-488.

Ohlsson, U, Daerga, PA and Elfgren, L (1990), 'Fracture Energy and Fatigue Strength of Unreinforced Concrete Beams at Normal and Low Temperatures', Eng. Fract. Mech., Vol. 35, No. 1/2/3, Pergamon Press, Great Britain, pp. 195-203.

Okubo, S and Fukui, K (1996), 'Complete Stress-Strain Curves for Various Rock Types in Uniaxial Tension', Int. J. Rock Mech. Min. Sci. Geomech. Abstr., Vol. 33, No. 6, Elsevier Science Ltd, Great Britain, pp.549-556.

Olson, JJ, Fogelson, DE, Dick, RA and Hendrickson, AD (1972), 'Ground Vibrations from Tunnel Blasting in Granite: Cheyenne Mountain (NORAD),CO', USBM Report 7653, United States Bureau of Mines.

Olsson, WA (1991),' The Compressive Strength of Tuff as a Function of Strain Rate from 10-6 to 103/sec', Int. J. Rock Mech. Min. Sci. Geomech. Abstr., Vol. 28, No. 1, Pergamon Press plc, Great Britain, pp.115-118.

Olsson, M, Nie, S, Bergqvist, I and Ouchterlony, F (2002), 'What Causes Cracks in Rock Blasting?', Fragblast Journal, Vol. 6, No. 2, Swets and Zeitlinger, pp. 221-233.

Onederra, I, Chitombo, GP, Cundall, PA and Furtney, JK (2009), 'Towards a Complete Validation of the Lattice Scheme in the Hybrid Stress Blasting Model (HSBM)', Proceedings of the International Symposium on Rock Fragmentation by Blasting, Fragblast 9, Sanchidrián (ed), Granada, Spain, CRC Press, pp. 343-351.

Orica (2008), 'Subtek™ Charge System', Technical data sheet, Orica Mining Services.

Ouchterlony, F, Olsson, M and Bergqvist, I (2002), 'Towards New Swedish Recommendations for Cautious Perimeter Blasting', Fragblast Journal, Vol. 2, pp.235-261.

Ouchterlony, F, Olsson, M and Svärd, J (2009), 'Crack Lengths or Blast Damage from String Emulsion and Electronic Detonators', Proceedings of the International Symposium on Rock Fragmentation by Blasting, Fragblast 9, Sanchidrián (ed), Granada, Spain, CRC Press, pp. 469-480.

Ouchterlony, F, Sjoberg, C and Jonsson, BA (1993), 'Blast Damage Predictions from Vibration Measurements at the SKB Underground Laboratories at Äspö in Sweden', Proceedings of the Conference on Explosives and Blasting Technique (CD-ROM), ISEE, Cleveland, OH, USA, Copyright 2000, pp. 189-197.

OYO Geospace (1997), Product/Customer Specifications: 101LT 14Hz 900Ω Omni, Geospace Corporation, Houston, Texas.

Page, CH (1987), 'Controlled Blasting for Underground Mining', Proceedings of the Conference on Explosives and Blasting Technique (CD-ROM), ISEE, Cleveland, OH, USA, Copyright 2000, pp.33-46.

Paventi, M, Lizotte, Y, Scoble, M and Mohanty, B (1996), 'Measuring Rock Mass Damage in Drifting', Proceeding of International Symposium on Rock Fragmentation by Blasting, Fragblast 5, Mohanty (ed), Montreal, Canada, A.A. Balkema, pp.131-138.

PCB Group Inc (1999-2008), Accelerometer Technical Specifications, online information, http://www.pcb.com/techsupport/tech_accel.php, Copyright PCB Group Inc 1999-2008.

PCB Piezotronics Inc Vibration Division (PCB) (2004), Product Catalog, Vib-300E, Sensors for Acceleration, Shock, Vibration, and Acoustic Measurements, www.pcb.com.

Peacock, S and Hudson, JA (1990), 'Seismic Properties of Rocks with Distributions of Small Cracks', Geophysical Journal International, Vol. 102, pp. 471-484.

Perkins, R.D, Green, SJ and Friedman, M (1970), 'Uniaxial Stress Behaviour of Porphyritic Tonalite at Strain Rates to 10^3/second', Int. J. Rock Mech. Min. Sci. Vol. 7, Pergamon Press, Great Britain, pp.527-535.

Persson, P-A (1996), 'The Relationship Between Strain Energy, Rock Damage, Fragmentation, and Throw in Rock Blasting', Proceeding of International Symposium on Rock Fragmentation by Blasting, Fragblast 5, Mohanty (ed), Montreal, Canada, A.A. Balkema, p.113-120.

Peška, P and Zoback, MD (1998), 'Drilling-Induced Tensile Fractures: Formation and Constraints on the Full Stress Tensor', Proceedings of the 3rd International Conference on Mechanics of Jointed and Faulted Rock, 6-9 April, 1998, Vienna, Austria, Rossmanith (ed), AA. Balkema, Rotterdam, pp.331-337.

Peterson, JA (2001), Blast Damage at Ekati Mine, MSc Thesis, University of Alberta, Edmonton, Canada.

Plewman, RP and Starfield, AM (1965), 'The Effects of Finite Velocities of Detonation and Propagation on the Strain Pulses Induced in Rock by Linear Charges', Journal of the South African Institute of Mining and Metallurgy, Vol. 66, SAIMM, pp. 77-96.

Porter, DD and Fairhurst, C (1971), 'A Study of Crack Propagation Produced by the Sustained Borehole Pressure in Blasting', Ch. 25: Dynamic Rock Mechanics, 12th Symposium on Rock Mechanics, AIME, pp. 497-515.

Potyondy, DO, Cundall, PA and Sarracino, RS (1996), 'Modeling of Shock-and Gas-Driven Fractures Induced by a Blast Using Bonded Assemblies of Spherical Particles', Proceeding of International Symposium on Rock Fragmentation by Blasting, Fragblast 5, Mohanty (ed), Montreal, Canada, A.A. Balkema, p.55-62.

Pratt, RG and Chapman, CH (1992), 'Traveltime Tomography in Anisotropic Media-II. Application', Geophys. J. Int., Vol. 109, pp. 20-37.

Preece, DS and Thorne, BJ (1996), 'A Study of Detonation Timing and Fragmentation using 3-D Finite Element Techniques and a Damage Constitutive Model', Proceeding of International Symposium on Rock Fragmentation by Blasting, Fragblast 5, Mohanty (ed), Montreal, Canada, A.A. Balkema, pp. 147-155.

Priest, SD and Hudson, JA (1976), 'Discontinuity Spacings in Rock', Int. J. Rock Mech. Min. Sci. Geomech. Abstr., Vol. 13, Pergamon Press, Great Britain, pp.135-148.

Pusch, R (1989), 'Alteration of the Hydraulic Conductivity of Rock by Tunnel Excavation', Int. J. Rock Mech. Min. Sci. Geomech. Abstr., Vol. 26, No. 1, Pergamon Press plc, Great Britain, pp.79-83.

Pusch, R and Stanfors, R (1992), 'The Zone of Disturbance Around Blasted Tunnels at Depth', Int. J. Rock Mech. Min. Sci. Geomech. Abstr., Vol. 29, No. 5, Pergamon Press Ltd, Great Britain, pp. 447-456.

Pyrak-Nolte, LJ, Myer, LR and Cook, NG (1990), 'Transmission of Seismic Waves Across Single Natural Fractures', J. of Geoph. Res., Vol. 95, No. B6, American Geophysical Union, pp. 8617-8638.

Rafat, G, Lehmann, B, Toumani, A and Rueter, H (2001), 'Characterisation of Rock Ahead and Around Tunnels and Boreholes by Use of Geophysical and Geological Methods', Int. J. Rock Mech. Min. Sci., Vol. 38, Elsevier Science Ltd, pp. 903-908.

Ray, S.K, Sarkar, M and Singh, TN, (1999), 'Effect of Cyclic Loading and Strain Rate on the Mechanical Behaviour of Sandstone', Int. J. Rock Mech. Min. Sci., Vol. 36, Elsevier Science Ltd, pp. 543-549.

Redpath, BB and Ricketts, TE (1987), 'An Improved Scaling Procedure for Close-in Blast Motions', Proceedings of the Conference on Explosives and Blasting Technique (CD-ROM), ISEE, Cleveland, OH, USA, Copyright 2000, pp. 118-128.

Rholl, SA (1996), 'Frequency Analysis of Blasting Data', Proceedings of the Conference on Explosives and Blasting Technique (CD-ROM), ISEE, Cleveland, OH, USA, Copyright 2000, pp. 21-28.

Rinehart, JS (1975), Stress Transients in Solids, Hyperdynamics, Santa Fe, New Mexico.

Rorke, AJ and Milev, AM (1999), 'Near Field Vibration Monitoring and Associated Rock Damage', Proceeding of International Symposium on Rock Fragmentation by Blasting, Fragblast 6, Johannesburg, South Africa, SAIMM, pp.19-22.

Rossmanith, HP (2006), 'Advanced Blasting Technology Using Precise Initiation Systems to Minimize Rock Mass Damage to Underground Excavations', Workshop presented to CRC Mining-Curtin University, 11-13 February, Kalgoorlie, WA, Australia.

Rossmanith, HP, Daehnke, A, Knasmillner, RE, Kouzniak, N, Ohtsu, M and Uenishi, K (1997), 'Fracture Mechanics Applications to Drilling and Blasting', Fatigue and Fracture of Engineering Materials and Structures, Vol. 20, No. 11, Fatigue and Fracture of Engineering Materials and Structures Ltd, Great Britain, pp. 1617-1636.

Rossmanith, HP, Hochholdinger-Arsic, V and Uenishi, K (2005), 'Understanding Size and Boundary Effects in Scaled Model Blasts-Plane Problems', Fragblast Journal, Vol. 9, No. 2, June 2005, Taylor and Francis, pp. 93-125.

Rossmanith, HP and Uenishi, K (2005), 'On Size and Boundary Effects in Scaled Model Blasts-Spatial Problems', Fragblast Journal, Vol. 9, No. 3, September 2005, Taylor and Francis, pp.139-174.

Sambuelli, L (2009), 'Theoretical Derivation of a Peak Particle Velocity-Distance Law for the Prediction of Vibrations from Blasting', Rock Mech. Rock Eng., Vol. 42, Springer, pp. 547-556.

Sanchidrián, JA, Segarra, P and López, LM (2007), 'Energy Components in Rock Blasting', Int. J. Rock Mech. Min. Sci., Vol. 44, Elsevier Ltd, pp. 130-147.

Schoenberg, M and Douma, J (1988), 'Elastic Wave Propagation in Media With Parallel Fractures and Aligned Cracks', Geophysical Prospecting, Vol. 36, pp. 571-590.

Scott, CG (1998), The Effect of Blasting on the Stability of Underground Excavations in Bedded Strata, MEng. Science Thesis, University of Queensland.

Scott, DF, Williams, TJ, Tesarik, D, Denton, DK, Knoll, SJ and Jordan, J (2004), 'Geophysical Methods to Detect Stress in Underground Mines', Report of Investigations 9661, NIOSH.

Sellers, EJ, Kotze, M, Dipenaar, L and Ruest, M (2009), 'Large Scale Concrete Cube Blasts for the HSBM Model', Proceedings of the International Symposium on Rock Fragmentation by Blasting, Fragblast 9, Sanchidrián (ed), Granada, Spain, CRC Press, pp. 389-398.

Serzu, MH, Kozak, ET, Lodha, GS, Everitt, RA and Woodcock, DR (2004), 'Use of Borehole Radar Techniques to Characterize Fractured Granitic Bedrock at AECL's Underground Research Laboratory', J. App. Geoph., Vol. 55, Elsevier Science B.V., pp. 137-150.

Shah, SP, Swartz, SE and Ouyang, C (1995), Fracture Mechanics of Concrete: Applications of Fracture Mechanics to Concrete, Rock, and Other Quasi-Brittle Materials, John Wiley and Sons, New York.

Shan, R, Jiang, Y and Li, B (2000), 'Obtaining Dynamic Complete Stress-Strain Curves for Rock Using the Split Hopkinson Pressure Bar Technique', Int. J. Rock Mech. Min. Sci., Vol. 37, Elsevier Science Ltd, pp. 983-992.

Sharpe, JA (1942), 'The Production of Elastic Waves by Explosion Pressures. I. Theory and Empirical Field Observations', Geophysics, Vol. 7, No. 2, Society of Exploration Geophysicists, pp. 144-154.

Shockey, DA, Curran, DR, Seaman, L, Rosenberg, JT and Petersen, CF (1974), 'Fragmentation of Rock Under Dynamic Loads', Int. J. Rock Mech. Min. Sci. Geomech. Abstr., Vol. 11, Pergamon Press, Great Britain, pp. 307-317.

Singh, SP (1996), 'The Influence of Geology on Blasthole Deviation', Proceedings of the Conference on Explosives and Blasting Technique (CD-ROM), ISEE, Cleveland, OH, USA, Copyright 2000, pp. 320-330.

Singh, SP (1999), 'The Effect of Shock and Gas Energies on Rock Fracture Process', Proceedings of the Conference on Explosives and Blasting Technique (CD-ROM), ISEE, Cleveland, OH, USA, Copyright 2000, pp. 397-406.

Singh, SP (2001), 'The Influence of Geology on Blast Damage', CIM Bulletin, Vol. 94, No. 1048, Canadian Institute of Mining, Metallurgy, and Petroleum, pp. 121-127.

Singh, SP and Narendrula, R (2004), 'Assessment and Prediction of Rock Mass Damage by Blast Vibrations', Mine Planning and Equipment Selection, Hardygóra, Paszkowska and Sikora (eds), Taylor and Francis Group, London, pp. 317-322.

Siskind, DE (1996), 'Frequency Analysis and the Use of Response Spectra for Blast Vibration Assessment in Mining', Proceedings of the Conference on Explosives and Blasting Technique (CD-ROM), ISEE, Cleveland, OH, USA, Copyright 2000, pp.1-11.

Siskind, DE and Fumanti, RR (1974), 'Blast-Produced Fractures in Lithonia Granite', USBM Report RI 7901, United States Bureau of Mines.

Siskind, DE, Steckley, RC and Olson, JJ (1973), 'Fracturing in the Zone Around a Blasthole, White Pine, Mich', USBM Report RI 7753, United States Bureau of Mines.

Souley, M, Homand, F, Pepa, S and Hoxha, D (2001), 'Damage-Induced Permeability Changes in Granite: A Case Example at the URL in Canada', Int. J. Rock Mech. Min. Sci. Vol. 38, Elsevier Science Ltd, pp.297-310.

Spathis, AT (2006), 'A Scaled Charge Weight Superposition Model for Rapid Vibration Estimation', Fragblast Journal, Vol. 10, No. 1-2, Taylor and Francis, pp. 9-31.

Spathis, AT, Blair, DP and Grant, JR (1985), 'Seismic Pulse Assessment of the Changing Rock Mass Conditions Induced by Mining', Int. J. Rock Mech. Min. Sci. Geomech. Abstr., Vol. 22, No. 5, Pergamon Press, Great Britain, pp. 302-312.

Spathis, AT, Smith, GE, Yacob, I and Labriola, A (2001), 'Wall Control at the Freeport Grasberg Opencut Mine: Vibration and Gas Penetration Measurements as a Precursor to Improvements', Proceedings of the Conference on Explosives and Blasting Technique (CD-ROM), ISEE, Cleveland, OH, USA, Copyright 2001, pp. 319-332.

Sprott, D and Kitzinger, F (1988), 'Blast Vibration Monitoring Instrumentation at Noranda Minerals', Proceedings of the Conference on Explosives and Blasting Technique (CD-ROM), ISEE, Cleveland, OH, USA, Copyright 2000, pp. 30-41.

Stacey, TR (1981), 'A Simple Extensional Strain Criterion for Fracture of Brittle Rock', Int. J. Rock Mech. Min. Sci. Geomech. Abstr., Vol. 18, Pergamon Press, Great Britain, pp. 469-474.

Stagg, KG and Zienkiewicz, OC (1968), Rock Mechanics in Engineering Practice, John Wiley and Sons, London.

Stevens, KM, Lodha, GS, Holloway, AL and Soonawala, NM (1995), 'The Application of Ground Penetrating Radar for Mapping Fractures in Plutonic Rocks within the Whiteshell Research Area, Pinawa, Manitoba, Canada', J. App. Geoph., Vol. 33, Elsevier Science, pp. 125-141.

Streeton, GC (2000), 'Geotechnical Aspects of Open Stope Design at BHP Cannington', Proceedings of MassMin 2000, 29 Oct -2 Nov, 2000, Brisbane, QLD, Australia, pp. 747-753.

Summerfield, PN (1955), 'A Study of the Air and Rock Vibrations Produced by Impact Testing of Mine Roof', USBM Report RI5251, United States Bureau of Mines.

Szuladzinski, G (1993), 'Response of Rock Medium to Explosive Borehole Pressure', Proceedings of the 4th International Symposium on Rock Fragmentation by Blasting, Fragblast 4, Rossmanith (ed), Vienna, Austria, A.A. Balkema, Rotterdam, pp. 17-23.

Tannant, DD and Peterson, J (2001), 'Evolution of Blasting Practices at the Ekati Diamond Mine', 17th International Mining Congress and Exhibition of Turkey, IMCET2001, pp. 297-304.

Tariq, SM and Worsey, PN, (1996), 'An Investigation into the Effects of Some Aspects of Jointing and Single Decoupled Blast Holes on Pre-splitting and Boulder Blasting', Proceeding of International Symposium on Rock Fragmentation by Blasting, Fragblast 5, Mohanty (ed), Montreal, Canada, A.A. Balkema, p.438 (poster session).

Tawadrous, AS and Katsabanis, PD (2007), 'Numerical Modeling of the Effect of High Stresses on Blast Induced Damage', Proceedings of the Conference on Explosives and Blasting Technique (CD-ROM), ISEE, Cleveland, OH, USA, Copyright 2007, pp.1-15.

Terzaghi, RD (1965), 'Sources of Error in Joint Surveys', Geotechnique, Vol. 15, pp. 287-303.

Ulysal, Ö, Arpaz, E and Berber, M (2007), 'Studies on the Effect of Burden Width on Blast-induced Vibration in Open Pit Mines', Environmental Geology, Vol. 53, Springer-Verlag, pp. 643-650.

Van Heerden, WL (1987), 'Technical Note: General Relations Between Static and Dynamic Moduli of Rocks', Int. J. Rock Mech. Min. Sci. Geomech. Abstr., Volume 24, No. 6, pp.381-385.

Vásárhelyi, B, Deli, Á and Gálos, M (2000), 'Relationship between the Critical Dissipated Energy per Unit Volume and the Mechanical Properties of Different Rocks', Proceedings of the 4th North American Rock Mechanics Symposium: Pacific Rocks, 31 July-3 August, 2000, Girard, Liebman, Breeds and Doe (eds), A.A. Balkema, Rotterdam, Netherlands, pp. 1289-1293.

Vasconcelos, G, Lourenço, PB, Alves, CAS and Pamplona, J (2008), 'Experimental Characterization of the Tensile Behaviour of Granites', Int. J. Rock Mech. Min. Sci., Vol. 45, Elsevier Ltd, pp. 268-277.

Villaescusa, E (2004), 'Geotechnical Audit of the BHP Billiton Cannington Mine', Report submitted to the BHP Billiton Cannington Mine, Western Australian School of Mines, Curtin University of Technology.

Villaescusa, E (1991), A Three Dimensional Model of Rock Jointing, PhD Thesis, University of Queensland-JKMRC.

Villaescusa, E and Brown, ET (1992), 'Maximum Likelihood Estimation of Joint Size from Trace Length Measurements', Rock Mechanics and Engineering, Vol. 25, Springer-Verlag, Austria, pp. 67-87.

Villaescusa, E, Cepuritis, P, Li, J, Heilig, J, Wiles, T and Lund, T, (2003), 'Open Stope Design and Sequences at Great Depth at Kanowna Belle', WASM Research report generated for Placer Dome Kanowna Belle Gold Mine, May 2003.

Villaescusa, E, Scott, C and Onederra, I (1997), 'Near Field Blast Monitoring at Hilton', Internal Technical Report RES MIN 78, Mount Isa Mines Limited.

Walters, S and Bailey, A (1998), 'Geology and Mineralization of the Cannington Ag-Pb-Zn Deposit: An Example of Broken Hill-Type Mineralization in the Eastern Succession', Mount Isa Inlier, Australia, Economic Geology, Vol. 93, No. 8, pp.1307-1329.

Western Australian School of Mines (WASM), (2009a), 'Report on Intact Rock Properties for BHPB Cannington', Rock testing report submitted to BHP Billiton Cannington Mine, February, 2009.

Western Australian School of Mines (WASM), (2009b), 'Report on Intact Rock Properties for BHP Billiton Cannington', Rock testing report submitted to BHP Billiton Cannington Mine, March, 2009.

White, JE and Sengbush, RL (1963), 'Shear Waves from Explosive Sources', Geophysics, Vol. 28, No. 6, Society of Exploration Geophysicists, pp. 1001-1019.

Wilson, WH and Holloway, DC (1987), 'Fragmentation Studies in Instrumented Concrete Models', Proceedings of the International Congress on Rock Mechanics, Herget and Vongpaisal (eds), Montreal, Canada, International Society for Rock Mechanics, pp.735-741.

Windsor, CR (1987), 'Rock Deformation-Fundamental Considerations for Field Measurement', Geotechnical Field Instrumentation Course, Australian Geomechanics Group: Victoria Group, Institute of Engineers, Australia, Parkville, VIC, Australia, pp. 2.1-2.16.

Windsor, CR (2009), Personal communication.

Wittmann, FH (2002), 'Crack Formation and Fracture Energy of Normal and High Strength Concrete', Sādhanā, Vol. 27, Part 4, August, 2002, printed in India, pp.413-423.

Woods, RD (1968), 'Screening of Surface Waves in Soils', J. Soil Mech., Foundations Division, American Society of Civil Engineers, Vol. 94, July, pp.951-979.

Wu, K. and Zhang, B (1989), 'Fracture Energy of Lightweight Concrete, Fracture Toughness and Fracture Energy: Test Methods for Concrete and Rock', International Workshop on Fracture Toughness and Fracture Energy, 12-14 October, 1988, Sendai, Mihashi, Takahashi and Wittmann (eds), AA Balkema, Rotterdam, Netherlands, pp. 117-124.

Wu, H, Zhang, Q, Huang, F and Jin, Q (2005), 'Experimental and Numerical Investigation on the Dynamic Tensile Strength of Concrete', Intl. Journal of Impact Engineering, Vol. 32, Elsevier Ltd, pp. 605-617.

Xia, K, Nasseri, MHB, Mohanty, B, Lu, F, Chen, R and Luo, SN, (2008), 'Effects of Microstructures on Dynamic Compression of Barre Granite', Int. J. Rock Mech. Min. Sci., Vol. 45, Elsevier Ltd, pp. 879-887.

Yang, R (2006), 'Application of 3-D Plots and Regressions to Blast Vibration Analysis – Defining a Site-Specific Form of the Charge Weight Scaled Distance', Proceedings of the Conference on Explosives and Blasting Technique (CD-ROM), ISEE, Cleveland, OH, USA, Copyright 2006.

Yang, R, Bawden, WF and Katsabanis, PD (1996), 'A New Constitutive Model for Blast Damage', Int. J. Rock Mech. Min. Sci. Geomech. Abstr., Vol. 33, No. 3, Elsevier Science Ltd, Great Britain, pp. 245-254.

Yang, R, Bawden, WF, Talebi, S and Rocque, P (1993), 'An Integrated Technique for Vibration Monitoring Adjacent to a Blast Hole', CIM Bulletin, Vol. 86, No. 972, July-August 1993, Canadian Institute of Mining and Metallurgy, pp. 45-52.

Yang, RL, Rocque, P, Katsabanis, P and Bawden, WF (1994), 'Measurement and Analysis of Near-Field Blast Vibration and Damage', Geotech. Geol. Eng., Vol. 12, Chapman and Hall, pp.169-182.

Yang, R and Scovira, DS (2007), 'Using Blast Vibration Measurements to Estimate Rock Triaxial Strains/Stresses and Dynamic Rock Strength for Blast Damage Evaluation', Rock Mechanics: Meeting Society's Challenges and Demands, Eberhardt, Stead and Morrison (eds), Taylor and Francis Group, London, pp. 1547-1552.

Yoon, J and Jeon, S (2009), 'Use of a Modified Particle-Based Method in Simulating Blast-Induced Rock Fracture', Proceedings of the International Symposium on Rock Fragmentation by Blasting, Fragblast 9, Sanchidrián (ed), Granada, Spain, CRC Press, pp. 371-380.

Yu, TR (1980), 'Ground Control at Kidd Creek, Underground Rock Engineering', 13th Canadian Rock Mechanics Symposium, May 28-29, Toronto, Canada. Toronto: CIM, pp. 73-79.

Yu, TR and Vongpaisal, S (1996), 'New Blast Damage Criteria for Underground Blasting', CIM Bulletin, Vol. 89, No. 998, Canadian Institute of Mining, Metallurgy, and Petroleum, pp. 139-144.

Yuill, G and Farnfield, R (2001), 'Variations in Vibration Signals from Single Hole Quarry Blasts', Proceedings of the Conference on Explosives and Blasting Technique (CD-ROM), ISEE, Cleveland, OH, USA, Copyright 2001, pp.309-317.

Zhang, JC and Chang, C (1999), 'On Damage Mechanism of Microcrack Zone in Rock Blasting and Its Measurement', Proceeding of International Symposium on Rock Fragmentation by Blasting, Fragblast 6, Johannesburg, South Africa, SAIMM, pp.359-363.

Zhang, ZX, Kou, SQ, Jiang, LG and Lindqvist, P-A (2000), 'Effects of Loading Rate on Rock Fracture: Fracture Characteristics and Energy Partitioning', Int. J. Rock Mech. Min. Sci., Vol. 37, Elsevier Science Ltd, pp.745-762.

Zhao, J, Li, HB, Wu, M.B and Li, TJ (1999), 'Dynamic Uniaxial Compression Tests on a Granite', Int. J. Rock Mech. Min. Sci., Vol. 36, Elsevier Science Ltd, pp. 273-277.

Zhu, WC (2007), 'Numerical Modelling of the Effect of Rock Heterogeneity on Dynamic Tensile Strength', Rock Mech. Rock Eng., Vol. 41, No. 5, pp. 771-779.

Zou, DH and Wu, YK (2001), 'Investigation of Blast-Induced Fracture in Rock Mass Using Reversed Vertical Seismic Profiling', J. App. Geoph., Vol. 48, Elsevier Science B.V., pp. 153-162.

APPENDIX 1 : EXAMPLE WAVEFORMS AND CANNINGTON STOPE 52H04HL FOOTWALL DATA

A1.1 Example Waveforms Collected During the Blast Vibration Monitoring Program 340
A1.2 Example Data Set from Cannington Stope 52h04HL Footwall Transducers 347

A1.1 Example Waveforms Collected During the Blast Vibration Monitoring Program

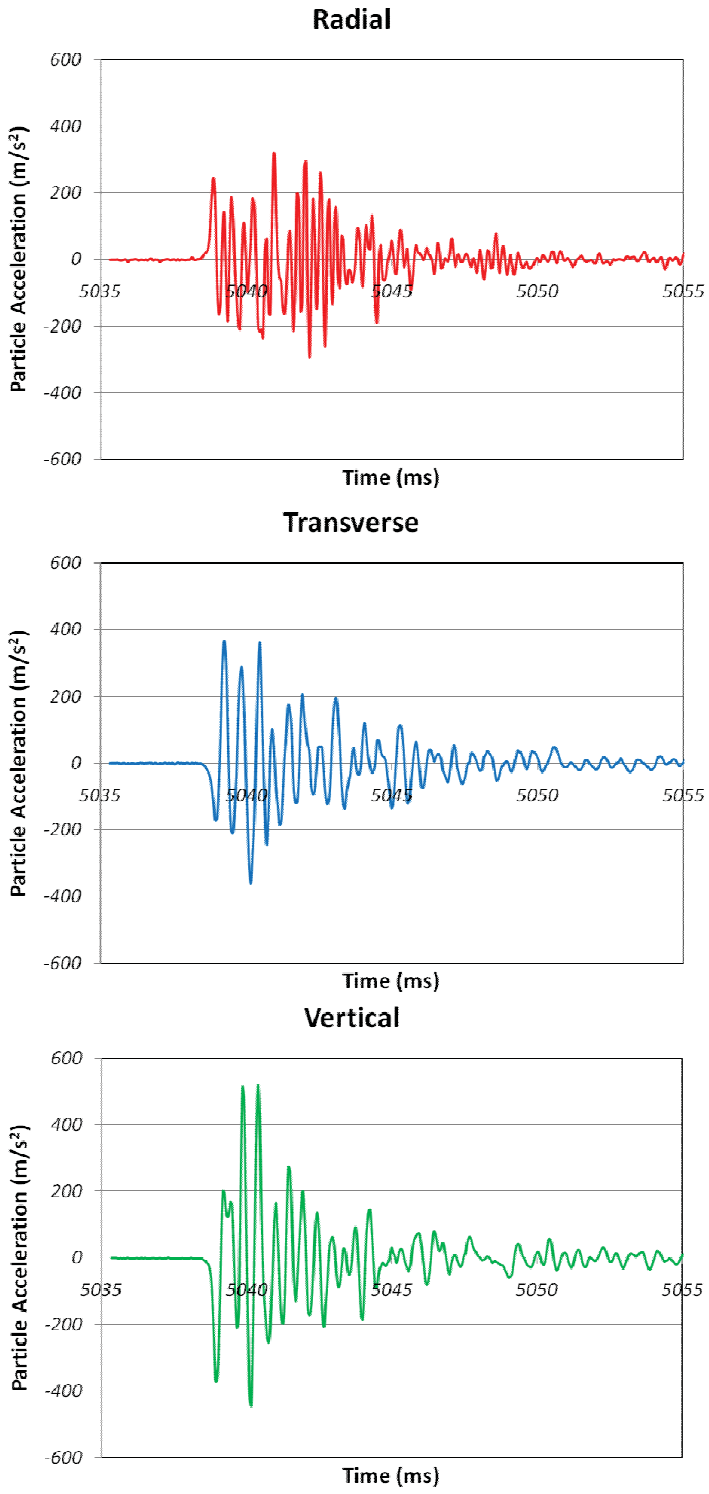

Figure A1.1. Example waveform components from KBGM dB10-38B East wall accelerometer: 10.8kg SANFOLD 50 charge at 18.6m distance.

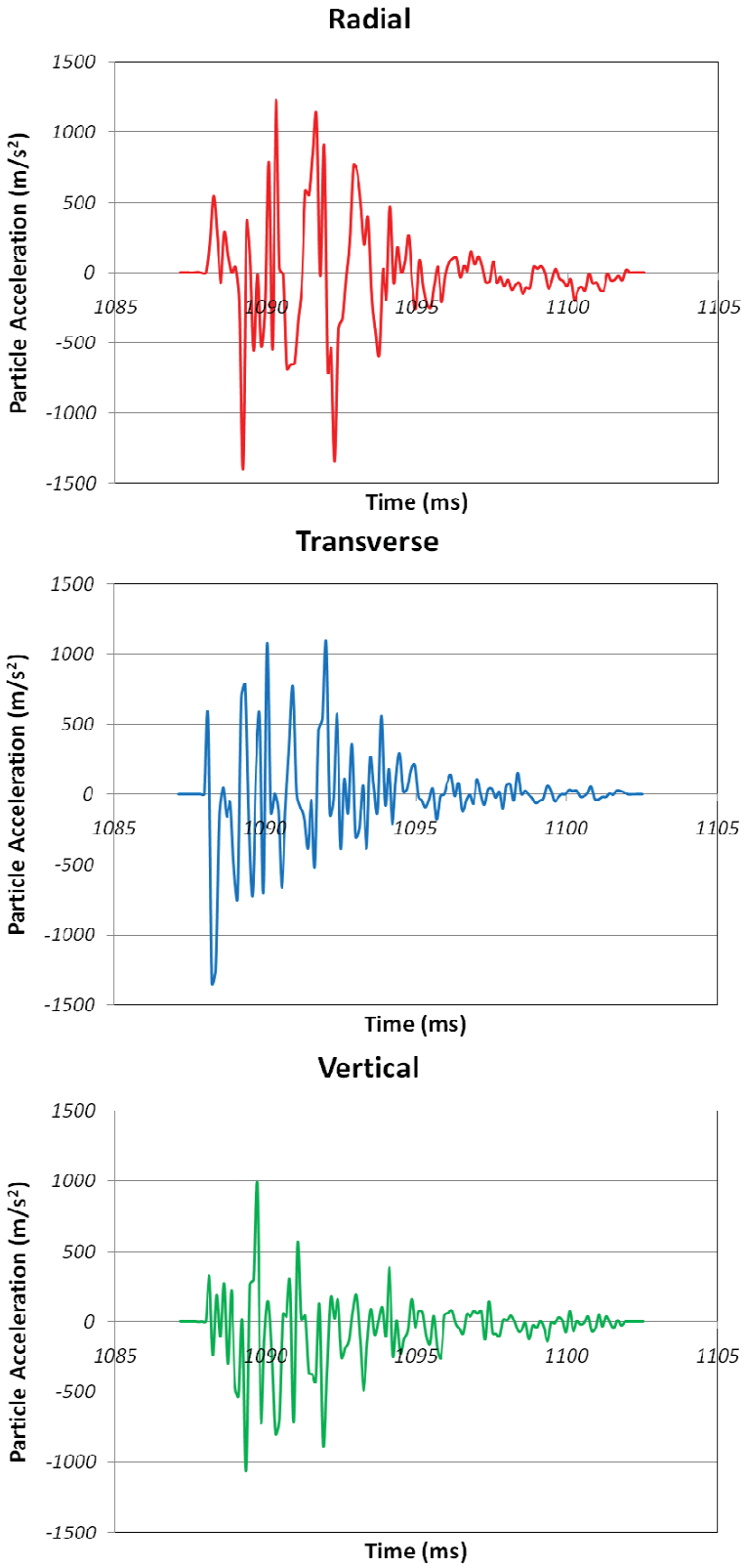

Figure A1.2. Example waveform components from KBGM dB10-38T East wall accelerometer: 38.1kg SANFOLD 50 charge at 10.1m distance.

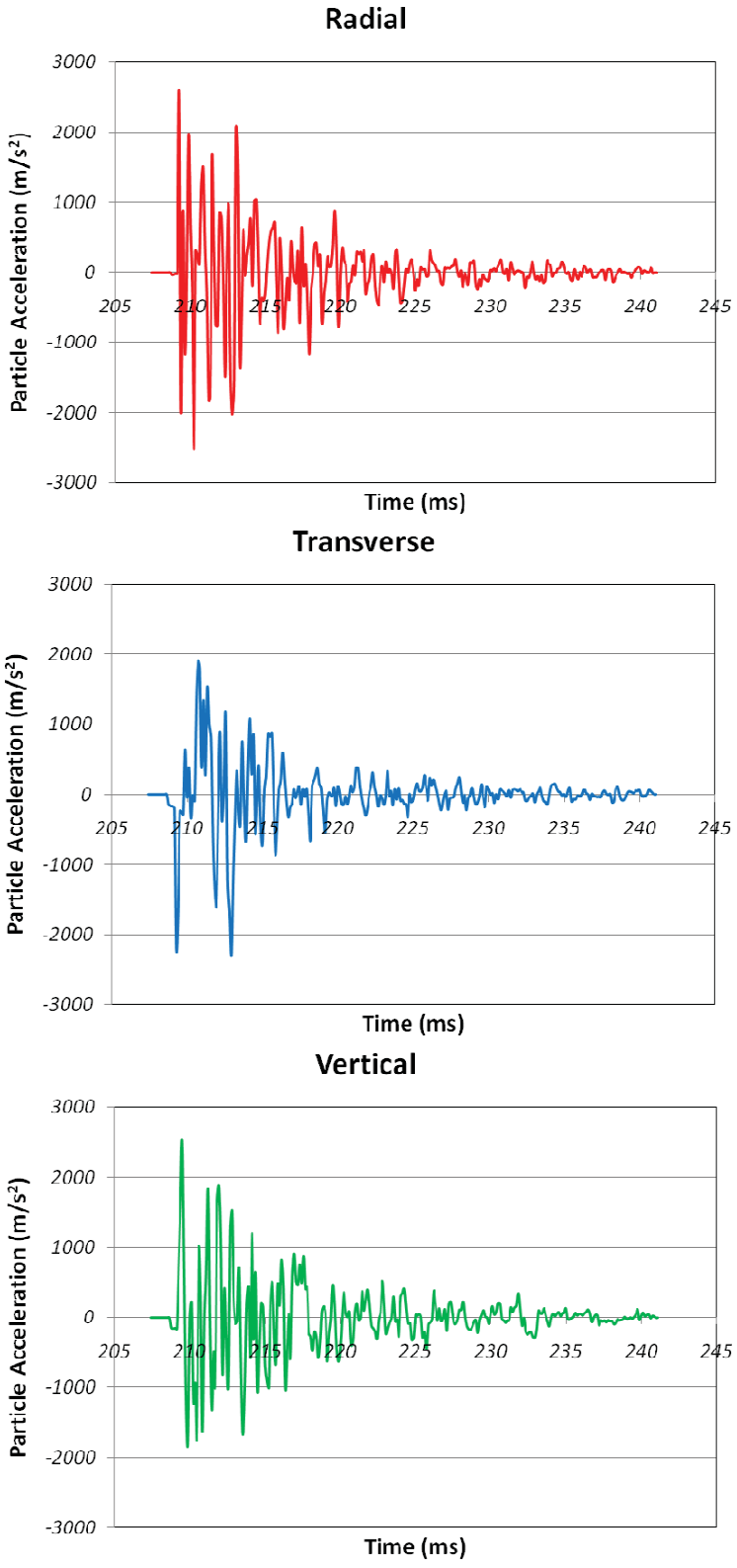

Figure A1.3. Example waveform components from Cannington stope 24jC6HL 200mLv Northeast wall accelerometer: 34.7kg 1.0g/cc emulsion charge at 10.7m distance.

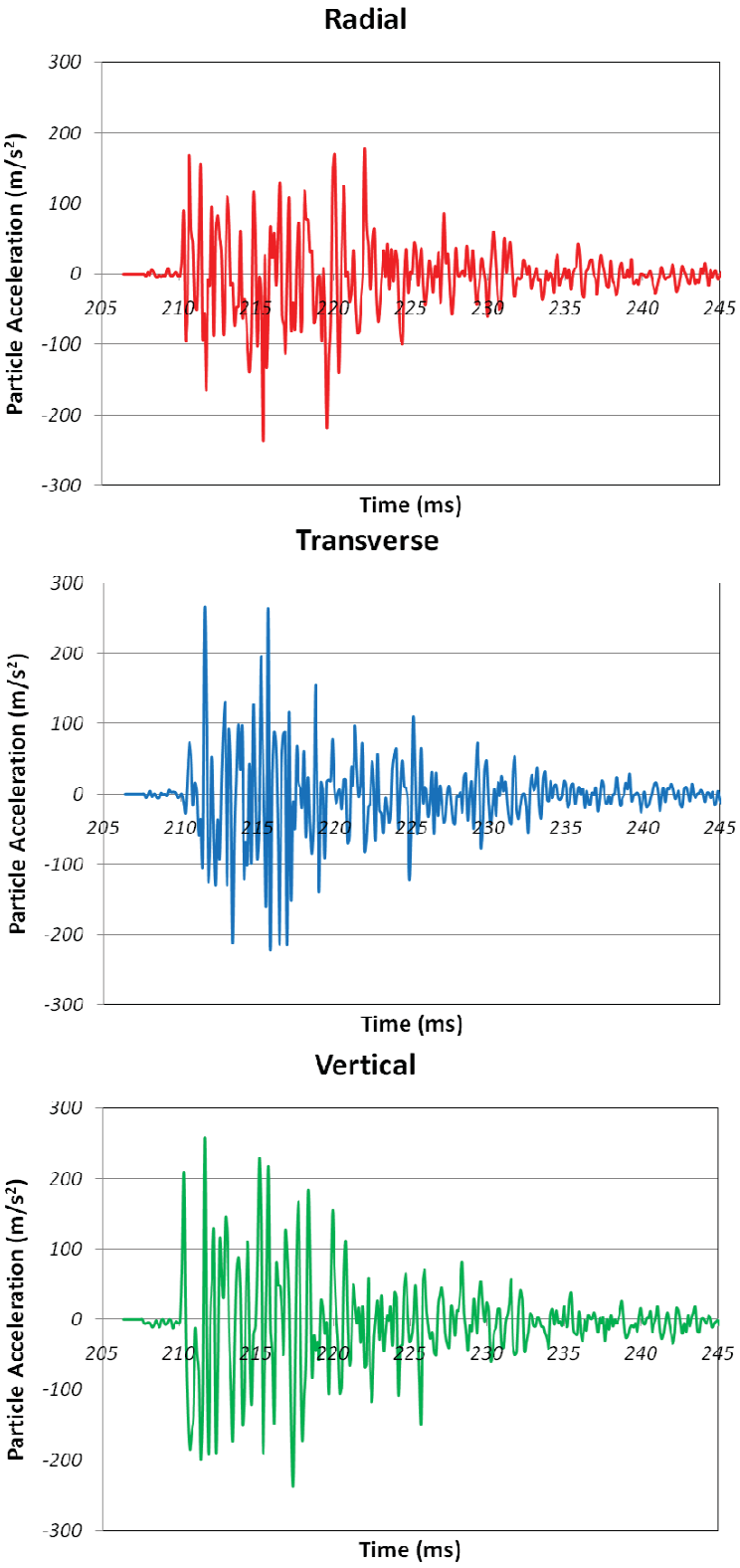

Figure A1.4. Example waveform components from Cannington stope 24jC6HL 200mLv Southeast wall accelerometer: 34.7kg 1.0g/cc emulsion charge at 23.5m distance.

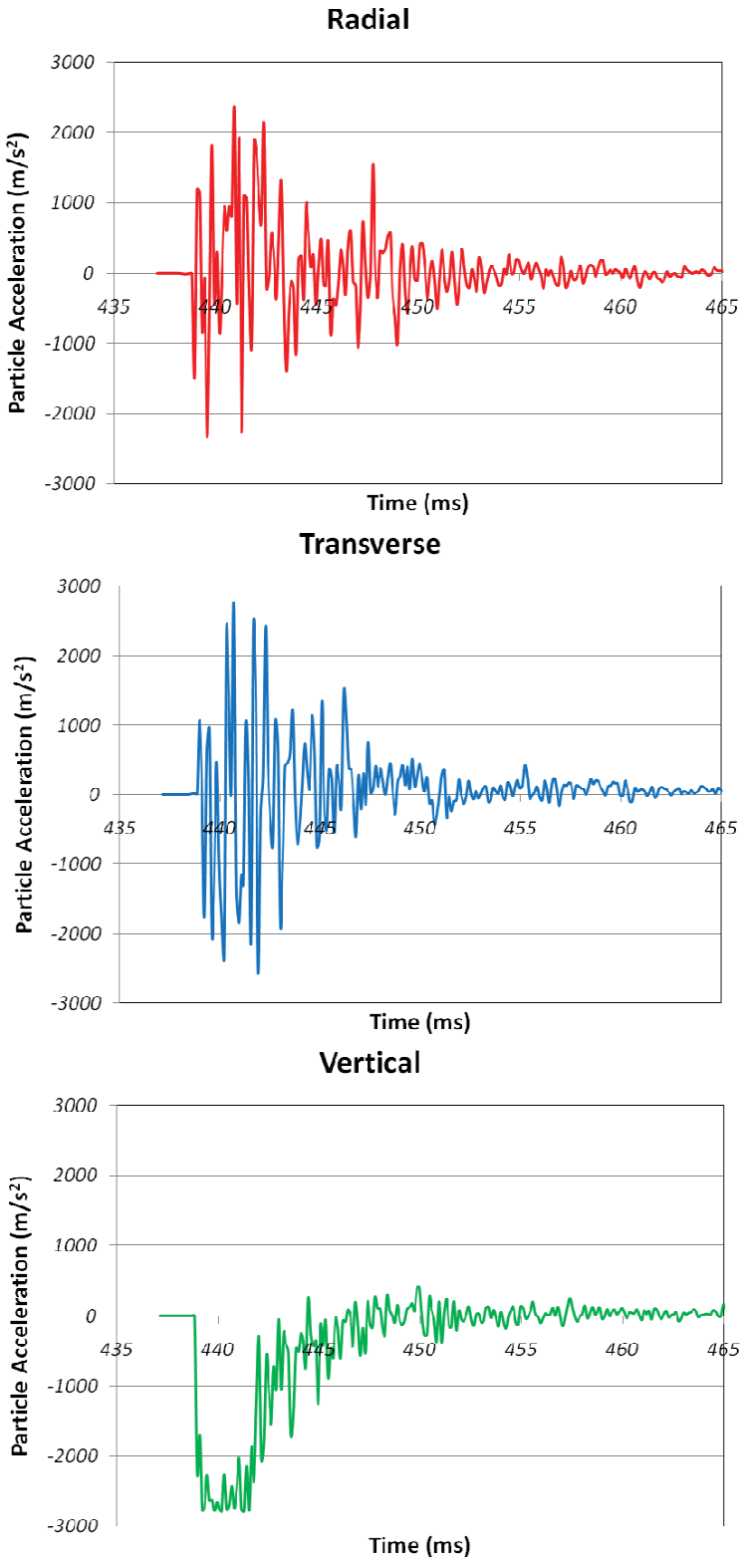

Figure A1.5. Example waveform components from Cannington stope 24jC6HL 200mLv Southwest wall accelerometer: 107.5kg 0.8g/cc emulsion charge at 5.9m distance.

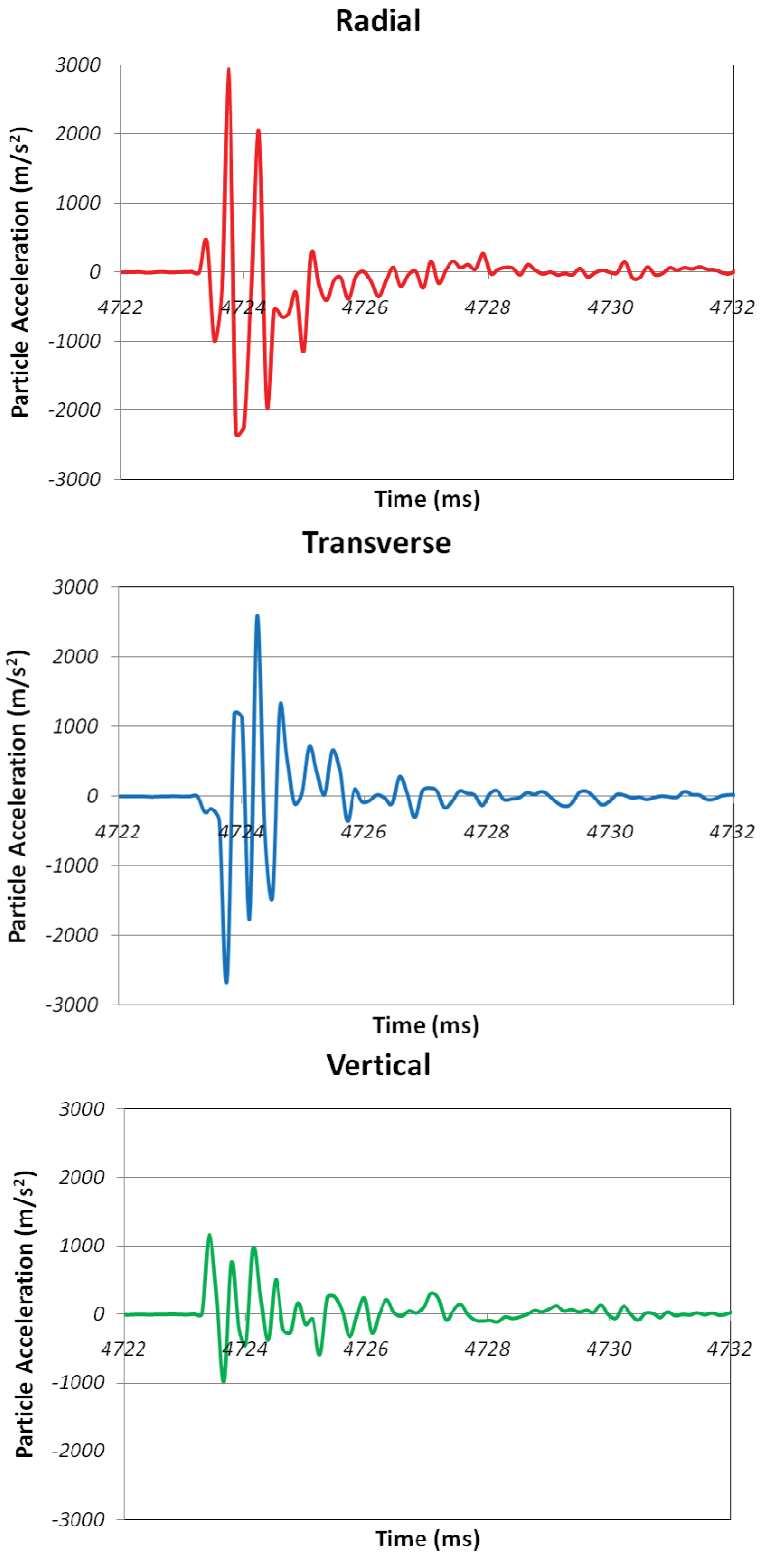

Figure A1.6. Example waveform components from Cannington stope 52h09HL hangingwall accelerometer: 50.2kg ANFO charge at 5.8m distance.

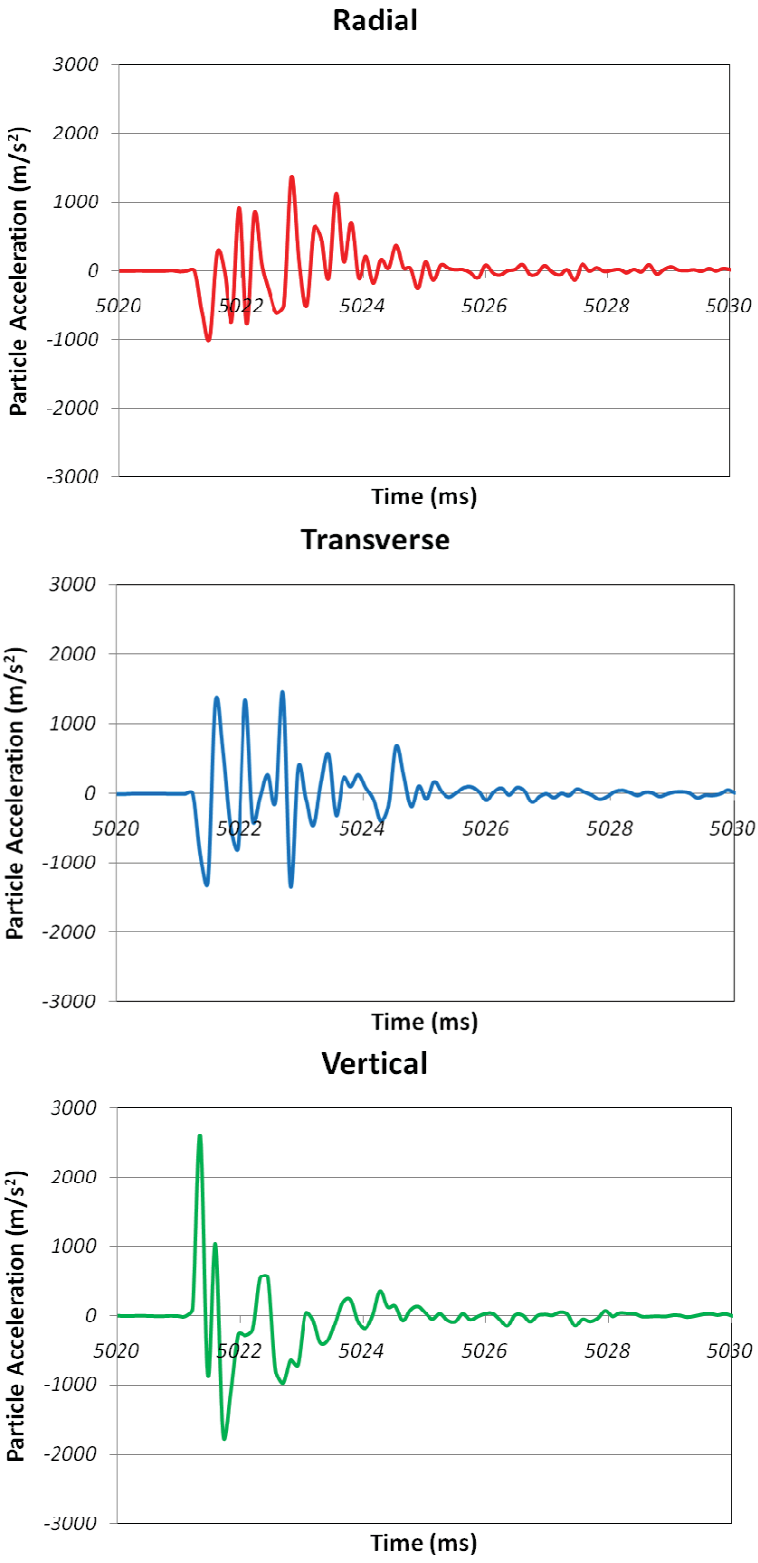

Figure A1.7. Example waveform components from Cannington stope 52h09HL hangingwall accelerometer: 43.4kg SANFOLD 50 charge at 3.9m distance.

52h04HL FOOTWALL ACCELEROMETER

Sensor Coordinates		
X (m)	Y (m)	Z (m)
1856.9	4421.2	750.6

Rock Mass Properties								
ρ_R	3510	kg/m3	E_{st}	80	GPa	λ_L	40.3	GPa
V_p	5300	m/s	E_{dyn}	75.2	GPa	ν	0.29	

Blasthole Info		Explosive Charge Information								Distance		Peak Amplitudes/Energy/Strain				
			Collar Coordinates			Toe Coordinates										
Firing	Hole #	Firing time (ms)	X (m)	Y (m)	Z (m)	X (m)	Y (m)	Z (m)	Explosive Load (kg)	Geom Dist (m)	VICD Dist (m)	PPA (m/s^2)	PPV (mm/s)	$ED_{W\text{-}tot}$ (J/m^3)	$ED_{W\text{-}SS}$ (J/m^3)	$\varepsilon_{W\text{-}MN}$ (με)
LHW #1	LHW01	5850	1862.2	4427.9	745.9	1862.2	4427.8	764.4	115.1	9.6	9.6	1231.1	194.5	1572.13	786.06	65.86
LHW #1	LHW02	4350	1862.7	4427.1	745.9	1862.6	4427.1	763.9	112.0	9.3	9.3	574.2	114.4	131.32	65.66	19.03
LHW #1	LHW03	1850	1863.0	4426.6	745.9	1863	4426.6	763.9	112.0	9.2	9.2	2143.8	484.6	7009.76	3504.88	139.07
LHW #1	LHW04	4100	1863.3	4426	745.9	1863.3	4426.0	763.9	112.0	9.1	9.1	1084.7	169.2	777.34	388.67	46.31
LHW #1	LHW05	5350	1863.7	4425.3	747.9	1863.7	4425.3	763.4	96.4	9.4	9.4	1785	252.9	1683.47	841.74	68.15
LHW #1	LHW06	3100	1863.1	4428.4	745.9	1863.1	4428.3	763.4	108.9	10.3	10.3	612.9	98.6	231.22	115.61	25.26
LHW #1	LHW07	150	1863.5	4427.6	745.9	1863.5	4427.6	764.4	115.1	10.3	10.3	882.7	155.5	646.24	323.12	42.23
LHW #1	LHW08	1100	1863.9	4427.1	745.9	1863.9	4427.1	763.4	108.9	10.0	10.0	332.6	55.4	36.69	18.34	10.06
LHW #1	LHW09	100	1864.2	4426.5	745.9	1864.2	4426.5	763.4	108.9	9.9	9.9	1043.4	209.6	1332.31	666.15	60.63
LHW #1	LHW10	3600	1864.6	4425.8	747.9	1864.6	4425.8	763.4	96.4	10.3	10.3	487.3	119.7	479.99	240.00	36.39
LHW #1	LHW11	5600	1864.0	4428.9	747.9	1863.9	4428.9	763.4	96.4	11.6	11.6	244.4	64.1	159.82	79.91	21.00
LHW #1	LHW13	2600	1864.7	4427.6	747.9	1864.7	4427.6	763.4	96.4	11.3	11.3	188.8	59.9	136.07	68.04	19.38
LHW #1	LHW14	4850	1865.0	4427	747.9	1865	4427.0	763.4	96.4	11.2	11.2	129.3	32.8	16.23	8.12	6.69
LHW #1	LHW15	6100	1865.5	4426.3	747.9	1865.4	4426.3	763.4	96.4	11.2	11.2	518	93	234.89	117.44	25.46
LHW #1	COS2-01	6600	1865.8	4428.2	748.4	1865.8	4428.2	762.8	89.6	12.4	12.4	146.3	28.9	34.06	17.03	9.69
COS #2	COS1-01	100	1867.7	4427.5	746.4	1867.7	4427.5	761.4	93.0	12.9	12.9	189.9	58	229.88	114.94	25.18
COS #2	COS1-02	400	1869.8	4428.8	748.0	1869.8	4428.8	758.6	65.9	15.2	15.2	97.4	40.4	79.97	39.99	14.85
COS #2	COS2-02	250	1868.0	4429.4	748.5	1868	4429.4	760.0	71.9	14.3	14.3	59.1	25.9	25.24	12.62	8.35
COS-Rng #3	C1-03	250	1872.0	4430	747.9	1872	4430.0	755.9	49.9	17.5	17.5	61.9	25.8	40.89	20.44	10.62
COS-Rng #3	C1-04	550	1874.1	4431.3	748.3	1874.1	4431.3	753.1	29.9	20.0	20.0	36.3	14.5	5.06	2.53	3.74
COS-Rng #3	C1-05	850	1876.0	4432.4	748.1	1876.2	4432.5	750.3	14.0	22.3	22.3	18.9	5.7	0.33	0.16	0.95
COS-Rng #3	C1-06	1150	1876.9	4432.9	745.6	1877.9	4433.4	747.8	15.4	24.0	24.0	23.3	5.2	0.50	0.25	1.18

COS-Rng #3	C1-08	1750	1877.9	4433.4	742.8	1879.7	4434.5	743.2	12.8	26.4	26.4	14.6	4.6	0.02	0.01	0.26
COS-Rng #3	C1-09	2050	1877.9	4433.4	741.4	1879.7	4434.5	740.6	13.8	27.1	27.1	21	7.2	1.70	0.85	2.17
COS-Rng #3	C2-04	400	1872.3	4431.9	746.0	1872.3	4431.9	754.4	52.4	18.8	18.8	24.8	8.4	3.11	1.56	2.93
COS-Rng #3	C2-05	700	1874.5	4433.2	746.3	1874.5	4433.2	751.6	32.8	21.3	21.3	27.8	8.9	1.85	0.93	2.26
COS-Rng #3	C2-06	1000	1875.5	4433.8	746.0	1876.3	4434.3	749.0	19.3	23.2	23.2	24.3	5.1	0.32	0.16	0.94
COS-Rng #3	C2-08	1600	1876.9	4434.6	743.3	1878.6	4435.6	744.1	13.1	26.0	26.0	18.7	4.3	0.06	0.03	0.41
COS-Rng #3	C2-10	2200	1876.9	4434.6	740.2	1878.2	4435.3	739.2	11.8	27.1	27.1	14.7	5.3	0.32	0.16	0.94
COS-Rng #3	R01-02	2910	1867.6	4433.5	743.9	1859.9	4429.0	747.9	61.0	13.0	13.0	1180.3	263.5	3672.96	1836.48	100.67
COS-Rng #3	R01-04	2880	1868.3	4433.9	745.5	1859.8	4429.0	755.7	88.3	12.5	12.5	2399.7	687.2	20155.29	10077.65	235.82
COS-Rng #3	R01-05	2865	1865.6	4432.4	751.1	1859.6	4428.9	761.0	75.4	12.3	12.3	695.1	139.8	469.07	234.54	35.97
COS-Rng #3	R01-06	2850	1869.5	4434.6	745.7	1861.4	4429.9	763.3	123.7	14.5	14.5	135.1	49.8	210.90	105.45	24.12
COS-Rng #3	R01-09	2930	1873.0	4436.6	746.3	1873.2	4436.7	750.3	25.1	22.5	24.1	43.4	27.9	50.44	25.22	11.80
COS-Rng #3	R01-11	2990	1875.1	4437.8	743.4	1876	4438.4	743.9	7.4	26.1	26.1	21.3	14.3	7.93	3.97	4.68
COS-Rng #3	R02-03	3260	1867.9	4436.2	743.3	1862	4432.8	745.7	45.2	16.7	17.0	594.9	132.3	193.17	96.58	23.09
COS-Rng #3	R02-04	3245	1865.4	4434.7	746.2	1859.8	4431.5	750.6	48.8	13.4	13.6	490.6	130.8	583.71	291.85	40.13
COS-Rng #3	R02-05	3230	1867.7	4436.1	745.3	1859.2	4431.2	755.2	86.1	14.1	14.4	190.7	45.5	86.71	43.36	15.47
COS-Rng #3	R02-06	3215	1865.0	4434.5	750.8	1858.8	4431.0	760.8	76.7	13.6	13.6	285.3	74.9	236.14	118.07	25.52
COS-Rng #3	R02-07	3200	1868.8	4436.7	745.5	1860.5	4431.9	763.2	125.4	15.7	16.1	211.8	53.6	62.98	31.49	13.18
COS-Rng #3	R03-02	3490	1867.6	4438.6	744.5	1862	4435.3	750.9	56.5	17.8	18.1	152.5	34.2	43.80	21.90	10.99
COS-Rng #3	R03-03	3475	1864.2	4436.6	751.1	1858.2	4433.1	761.2	76.3	15.4	15.5	177.7	55.2	160.66	80.33	21.05
COS-Rng #3	R03-04	3460	1867.9	4438.7	745.5	1865.4	4437.3	750.8	37.3	19.6	20.3	87.4	25.4	43.11	21.55	10.91
COS-Rng #3	R03-06	3510	1869.8	4439.9	746.4	1866.8	4438.1	755.9	63.2	21.2	22.4	29.6	17.5	12.14	6.07	5.79
COS-Rng #3	R04-02	4085	1866.9	4440.7	745.4	1858.3	4435.7	759.5	107.5	18.0	18.1	80.5	29.6	59.79	29.90	12.84
COS-Rng #3	R04-03	4070	1864.4	4439.3	751.4	1859.4	4436.4	761.8	73.9	18.4	18.4	106.9	30.4	50.48	25.24	11.80
COS-Rng #3	R04-05	4120	1868.9	4441.9	747.8	1867	4440.8	754.1	41.6	23.0	23.6	26.1	9.9	3.36	1.68	3.05
COS-Rng #3	R05-01	4300	1865.8	4442.6	745.8	1858.8	4438.6	760.3	103.4	20.3	20.3	111.2	30.9	59.34	29.67	12.80
COS-Rng #3	R05-02	4330	1867.3	4443.5	746.6	1861.4	4440.0	759.9	93.3	22.0	22.7	28.7	10.5	4.13	2.07	3.38
COS-Rng #3	R05-03	4360	1867.5	4443.6	749.1	1866.6	4443.1	753.0	25.5	24.4	25.6	19.5	5.3	0.18	0.09	0.71
Rings #4	R06-02	380	1874.3	4427.8	745.1	1865.4	4423.7	763.2	128.2	14.2	14.4	207.6	64.2	145.26	72.63	20.02
Rings #4	R06-03	410	1873.5	4427.7	750.3	1867.1	4424.8	763.2	91.7	15.6	15.8	78.4	26	32.22	16.11	9.43
Rings #4	R06-04	440	1876.3	4429	746.0	1872.7	4427.6	756.6	70.1	19.0	19.2	47.7	17	17.51	8.76	6.95
Rings #4	R06-05	470	1877.0	4429.5	747.7	1876.5	4429.5	752.0	26.9	21.5	21.8	27.7	9.6	3.85	1.93	3.26
Rings #4	R06-06	500	1878.1	4430.1	745.6	1878.6	4430.6	749.3	23.3	23.5	23.8	16.3	5.8	1.89	0.95	2.29
Rings #4	R06-07	530	1879.2	4430.6	744.6	1880.3	4431.4	746.5	14.1	25.4	25.7	9	3.2	0.27	0.14	0.87

Rings #4	R06-10	620	1880.0	4430.9	740.8	1881.6	4431.8	740.0	12.5	27.9	31.1	6.9	2.4	0.11	0.06	0.56
Rings #4	R07-01	100	1865.5	4422.8	746.1	1864.1	4422.8	761.4	95.8	8.7	8.7	1103.4	157.8	869.38	434.69	48.98
Rings #4	R07-02	115	1867.8	4424.2	746.3	1867.2	4424.2	754.5	51.6	11.0	11.2	126.8	47	80.36	40.18	14.89
Rings #4	R07-04	145	1870.2	4425.4	744.3	1871.6	4426.3	745.8	13.7	15.7	15.9	15.1	7.2	2.98	1.49	2.87
Rings #4	R07-05	175	1870.6	4425.5	742.9	1874	4427.6	743.8	25.3	17.8	18.0	30.6	8.4	2.44	1.22	2.59
Rings #4	R07-06	275	1870.6	4425.5	741.8	1874.2	4427.5	741.1	26.1	18.8	19.2	20.5	7.3	2.58	1.29	2.67
Rings #4	R08-05	1110	1875.1	4426.8	745.2	1866.5	4421.9	763.2	127.8	14.7	15.1	180.5	61.2	115.28	57.64	17.83
Rings #4	R08-06	1140	1875.0	4426.8	749.0	1868.3	4422.9	763.2	101.1	16.2	16.6	67.6	20.3	24.24	12.12	8.18
Rings #4	R08-07	1170	1877.1	4428	746.0	1874.1	4426.3	756.0	65.6	19.7	20.3	39.8	13.9	13.52	6.76	6.11
Rings #4	R08-08	1200	1878.2	4428.6	746.3	1878.1	4428.6	751.0	29.5	22.6	23.2	10.3	5.1	1.35	0.68	1.93
Rings #4	R08-09	1230	1879.6	4429.4	745.2	1880.5	4429.9	747.6	16.4	25.0	25.8	8.8	4.1	0.62	0.31	1.31
Rings #4	R08-12	1390	1880.6	4430	740.1	1882.2	4431.0	738.7	14.7	28.5	31.0	7.5	2.8	0.31	0.16	0.93
Rings #4	R09-01	830	1866.5	4421.8	746.2	1865.1	4421.1	761.9	97.7	9.5	9.5	776.9	140.6	880.06	440.03	49.28
Rings #4	R09-04	1005	1871.0	4424.5	740.0	1872.2	4425.1	739.0	10.4	18.8	19.8	21.5	6.6	3.08	1.54	2.92
Rings #4	R10-02	1575	1875.1	4424.3	741.6	1871.4	4422.2	741.2	26.3	18.9	21.0	31.9	9.1	3.81	1.90	3.24
Rings #4	R10-03	1560	1875.5	4424.6	742.6	1871.4	4422.2	743.8	30.4	18.3	19.8	13.2	3.6	0.80	0.40	1.49
Rings #4	R10-05	1780	1876.3	4425.1	745.3	1867.8	4420.1	763.1	126.7	15.6	16.4	95.9	29.4	38.30	19.15	10.28
Rings #4	R10-06	1810	1876.0	4424.9	749.4	1869.4	4421.0	763.3	98.5	16.9	17.7	40.4	13.3	7.14	3.57	4.44
Rings #4	R10-07	1840	1878.3	4426.2	746.1	1875.3	4424.4	756.1	66.1	20.3	21.6	29.2	12.7	6.98	3.49	4.39
Rings #4	R10-08	1870	1879.3	4426.8	746.5	1879	4426.6	751.3	30.0	23.0	24.2	11.7	3.1	0.40	0.20	1.05
Rings #4	R11-01	1500	1867.7	4420.1	746.0	1866.6	4419.4	761.6	97.0	10.8	10.8	730.2	155.2	600.97	300.49	40.72
Rings #4	R11-03	1530	1870.7	4421.8	746.0	1871.5	4422.3	749.9	24.9	14.5	15.5	23.4	10.1	4.44	2.22	3.50
Rings #4	R11-04	1675	1872.1	4422.6	740.0	1873.3	4423.3	738.9	11.2	19.4	20.9	70.6	19.8	13.38	6.69	6.08
Rings #4	R12-02	2245	1876.4	4422.6	741.6	1872.8	4420.5	741.2	25.7	19.9	19.9	22	7.2	3.60	1.80	3.15
Rings #4	R12-03	2230	1876.8	4422.9	742.7	1872.8	4420.5	744.1	30.3	19.3	21.1	29.4	7.6	3.59	1.80	3.15
Rings #4	R12-04	2215	1876.5	4422.6	744.5	1874.6	4421.6	746.4	17.6	19.3	21.2	20.1	5	1.00	0.50	1.66
Rings #4	R12-05	2450	1877.6	4423.3	745.1	1868.7	4418.2	763.2	129.9	16.7	17.8	90.9	27.9	35.02	17.51	9.83
Rings #4	R12-06	2480	1877.9	4423.5	748.4	1870.5	4419.2	763.3	106.6	18.1	19.4	52.3	15.5	12.57	6.29	5.89
Rings #4	R12-07	2510	1879.7	4424.5	746.4	1876.8	4422.8	755.3	58.9	21.5	23.3	28.9	8.8	3.10	1.55	2.92
Rings #4	R12-08	2540	1880.9	4425.2	746.2	1880.7	4425.1	749.9	22.8	24.3	26.4	11.8	4.1	0.40	0.20	1.04
Rings #4	R13-01	2170	1869.0	4418.3	746.1	1867.9	4417.7	760.3	89.0	12.2	12.2	852.7	122	605.12	302.56	40.86
Rings #4	R13-04	2200	1872.1	4420.1	745.9	1873	4420.6	749.7	24.9	15.9	17.6	25.2	7.4	1.91	0.96	2.30
Rings #4	R13-05	2345	1873.4	4420.9	739.8	1874.4	4421.4	739.0	8.5	20.4	22.1	111.3	20.3	32.72	16.36	9.50
Rings #4	R14-01	2830	1878.5	4421.3	740.1	1877.3	4420.7	739.1	10.1	23.7	26.0	79.9	19	11.18	5.59	5.55

Rings #4	R14-02	2725	1877.9	4421	741.5	1874.4	4419.0	740.9	25.4	21.4	23.8	30	6.9	3.28	1.64	3.01
Rings #4	R14-03	2710	1878.3	4421.2	742.5	1874.1	4418.8	743.6	31.0	20.8	22.7	19.6	6.2	1.95	0.98	2.32
Rings #4	R14-04	2695	1878.5	4421.3	743.9	1876	4419.9	746.1	22.5	21.1	23.2	15.8	5.2	1.17	0.59	1.80
Rings #4	R14-05	2930	1879.0	4421.6	745.4	1869.9	4416.4	763.2	128.9	18.1	19.6	93.7	28	27.33	13.67	8.68
Rings #4	R14-06	2960	1878.5	4421.3	749.6	1871.6	4417.4	763.3	98.4	19.1	20.9	35.9	10.9	6.30	3.15	4.17
Rings #4	R14-07	2990	1880.9	4422.7	746.3	1878.3	4421.2	754.4	53.4	22.7	25.1	16.9	4.6	1.31	0.65	1.90
Rings #4	R15-01	2650	1869.9	4416.4	746.0	1869.2	4416.0	760.7	91.6	13.9	13.9	477	122.6	711.33	355.66	44.30
Rings #4	R15-03	2680	1873.7	4418.6	745.4	1874.6	4419.1	748.6	20.5	17.8	19.4	20.1	7.1	3.57	1.78	3.14
Rings #4	R15-04	2825	1875.0	4419.3	739.9	1875.9	4419.8	739.1	8.0	21.6	23.2	11.2	3.2	0.11	0.05	0.55

Sensor	Sensor Coordinates		
	X (m)	Y (m)	Z (m)
	1851.7	4417.6	750.6

52h04HL FOOTWALL GEOPHONE 1

Blasthole Info		Explosive Charge Information								Distance		Peak Amplitudes/Energy/Strain				
Firing	Hole #	Firing time (ms)	Collar Coordinates X (m)	Collar Coordinates Y (m)	Collar Coordinates Z (m)	Toe Coordinates X (m)	Toe Coordinates Y (m)	Toe Coordinates Z (m)	Explosive Load (kg)	Geom Dist (m)	VICD Dist (m)	PPA (m/s^2)	PPV (mm/s)	$ED_{W\text{-}tot}$ (J/m^3)	$ED_{W\text{-}SS}$ (J/m^3)	$\varepsilon_{W\text{-}MN}$ (με)
LHW #1	LHW01	5850	1862.2	4427.9	745.9	1862.2	4427.8	764.4	115.1	15.4	15.4	507	111.3	628.37	314.19	41.64
LHW #1	LHW02	4350	1862.7	4427.1	745.9	1862.6	4427.1	763.9	112.0	15.1	15.1	666.2	183.8	691.28	345.64	43.67
LHW #1	LHW03	1850	1863.0	4426.6	745.9	1863	4426.6	763.9	112.0	15.1	15.1	792.5	289.7	2948.55	1474.27	90.20
LHW #1	LHW04	4100	1863.3	4426	745.9	1863.3	4426.0	763.9	112.0	15.0	15.0	571.8	182.6	856.44	428.22	48.61
LHW #1	LHW05	5350	1863.7	4425.3	747.9	1863.7	4425.3	763.4	96.4	15.1	15.1	478.2	191.2	1517.66	758.83	64.71
LHW #1	LHW06	3100	1863.1	4428.4	745.9	1863.1	4428.3	763.4	108.9	16.2	16.2	590.6	189.2	789.80	394.90	46.68
LHW #1	LHW07	150	1863.5	4427.6	745.9	1863.5	4427.6	764.4	115.1	16.1	16.1	579.8	162	1188.31	594.16	57.26
LHW #1	LHW08	1100	1863.9	4427.1	745.9	1863.9	4427.1	763.4	108.9	16.0	16.0	134	27.9	19.06	9.53	7.25
LHW #1	LHW09	100	1864.2	4426.5	745.9	1864.2	4426.5	763.4	108.9	15.9	15.9	655.3	251.4	2293.34	1146.67	79.55
LHW #1	LHW10	3600	1864.6	4425.8	747.9	1864.6	4425.8	763.4	96.4	16.1	16.1	440.9	160.7	683.01	341.51	43.41
LHW #1	LHW11	5600	1864.0	4428.9	747.9	1863.9	4428.9	763.4	96.4	17.4	17.4	126.7	35.6	63.06	31.53	13.19
LHW #1	LHW13	2600	1864.7	4427.6	747.9	1864.7	4427.6	763.4	96.4	17.2	17.2	388.4	168.5	940.10	470.05	50.93
LHW #1	LHW14	4850	1865.0	4427	747.9	1865	4427.0	763.4	96.4	17.1	17.1	123.1	22.1	21.79	10.89	7.75

LHW #1	LHW15	6100	1865.5	4426.3	747.9	1865.4	4426.3	763.4	96.4	17.0	17.0	409.3	184.7	1477.66	738.83	63.85
LHW #1	COS2-01	6600	1865.8	4428.2	748.4	1865.8	4428.2	762.8	89.6	18.3	18.3	225.2	88.7	329.08	164.54	30.13
COS #2	COS1-01	100	1867.7	4427.5	746.4	1867.7	4427.5	761.4	93.0	19.1	19.1	326.8	173.7	2142.89	1071.45	76.89
COS #2	COS1-02	400	1869.8	4428.8	748.0	1869.8	4428.8	758.6	65.9	21.5	21.5	165.5	96.5	620.59	310.30	41.38
COS #2	COS2-02	250	1868.0	4429.4	748.5	1868	4429.4	760.0	71.9	20.4	20.4	122	68.8	278.11	139.06	27.70
COS-Rng #3	C1-03	250	1872.0	4430	747.9	1872	4430.0	755.9	49.9	23.8	23.8	120.9	72.1	427.97	213.98	34.36
COS-Rng #3	C1-04	550	1874.1	4431.3	748.3	1874.1	4431.3	753.1	29.9	26.3	26.3	86.2	36.4	72.86	36.43	14.18
COS-Rng #3	C1-05	850	1876.0	4432.4	748.1	1876.2	4432.5	750.3	14.0	28.6	28.6	38.6	11.9	13.06	6.53	6.00
COS-Rng #3	C1-06	1150	1876.9	4432.9	745.6	1877.9	4433.4	747.8	15.4	30.3	30.3	45.2	13.8	9.40	4.70	5.09
COS-Rng #3	C1-07	1450	1877.6	4433.3	744.2	1879	4434.1	745.5	13.2	31.6	31.6	28	10.3	5.96	2.98	4.05
COS-Rng #3	C1-08	1750	1877.9	4433.4	742.8	1879.7	4434.5	743.2	12.8	32.5	32.5	30.6	9.7	4.57	2.28	3.55
COS-Rng #3	C1-09	2050	1877.9	4433.4	741.4	1879.7	4434.5	740.6	13.8	33.1	33.1	36.4	13	13.85	6.93	6.18
COS-Rng #3	C1-10	2350	1877.7	4433.3	740.2	1878.7	4433.9	739.2	9.3	32.8	32.8	29.8	9.2	4.20	2.10	3.40
COS-Rng #3	C2-04	400	1872.3	4431.9	746.0	1872.3	4431.9	754.4	52.4	25.1	25.1	51.2	34.3	100.17	50.09	16.62
COS-Rng #3	C2-05	700	1874.5	4433.2	746.3	1874.5	4433.2	751.6	32.8	27.6	27.6	40.3	28	50.24	25.12	11.77
COS-Rng #3	C2-06	1000	1875.5	4433.8	746.0	1876.3	4434.3	749.0	19.3	29.4	29.4	29.6	11.7	7.93	3.97	4.68
COS-Rng #3	C2-08	1600	1876.9	4434.6	743.3	1878.6	4435.6	744.1	13.1	32.2	32.2	38.7	12.5	5.57	2.78	3.92
COS-Rng #3	C2-09	1900	1877.0	4434.6	741.8	1878.7	4435.6	741.5	12.0	32.7	32.7	26.6	10.4	6.26	3.13	4.16
COS-Rng #3	C2-10	2200	1876.9	4434.6	740.2	1878.2	4435.3	739.2	11.8	33.0	33.0	43	9.5	4.20	2.10	3.40
COS-Rng #3	R01-02	2910	1867.6	4433.5	743.9	1859.9	4429.0	747.9	61.0	18.8	18.8	102	24.1	13.42	6.71	6.09
COS-Rng #3	R01-04	2880	1868.3	4433.9	745.5	1859.8	4429.0	755.7	88.3	18.6	18.6	1107.9	327.6	1220.72	610.36	58.03
COS-Rng #3	R01-05	2865	1865.6	4432.4	751.1	1859.6	4428.9	761.0	75.4	17.9	17.9	362.3	113.6	531.91	265.95	38.31
COS-Rng #3	R01-06	2850	1869.5	4434.6	745.7	1861.4	4429.9	763.3	123.7	20.5	20.5	232.4	115.9	774.71	387.36	46.23
COS-Rng #3	R01-09	2930	1873.0	4436.6	746.3	1873.2	4436.7	750.3	25.1	28.8	29.7	55.8	27.4	44.86	22.43	11.12
COS-Rng #3	R01-10	2960	1874.4	4437.4	745.4	1875.2	4437.8	746.9	10.5	30.9	32.2	29.6	7.2	0.68	0.34	1.37
COS-Rng #3	R01-11	2990	1875.1	4437.8	743.4	1876	4438.4	743.9	7.4	32.2	32.2	32.5	9.6	4.66	2.33	3.59
COS-Rng #3	R01-12	3020	1875.2	4437.9	741.5	1876.1	4438.4	741.3	7.1	32.9	32.9	24.6	6.7	1.30	0.65	1.89
COS-Rng #3	R01-13	3050	1875.0	4437.7	739.9	1875.8	4438.2	739.1	7.8	33.2	33.2	20.1	7.5	2.21	1.11	2.47
COS-Rng #3	R02-01	3290	1868.0	4436.2	741.1	1865.4	4434.7	739.7	20.5	25.4	27.0	57.6	12.5	9.60	4.80	5.15
COS-Rng #3	R02-02	3275	1867.2	4435.8	742.4	1863.6	4433.7	742.5	25.5	23.4	23.7	60.4	23.9	32.14	16.07	9.42
COS-Rng #3	R02-03	3260	1867.9	4436.2	743.3	1862	4432.8	745.7	45.2	22.4	22.6	257.1	65.5	153.53	76.76	20.58
COS-Rng #3	R02-04	3245	1865.4	4434.7	746.2	1859.8	4431.5	750.6	48.8	19.1	19.2	204.4	85	197.01	98.51	23.31
COS-Rng #3	R02-05	3230	1867.7	4436.1	745.3	1859.2	4431.2	755.2	86.1	19.9	19.9	177	93.6	314.71	157.36	29.47
COS-Rng #3	R02-06	3215	1865.0	4434.5	750.8	1858.8	4431.0	760.8	76.7	19.0	19.0	475	169.8	1516.13	758.07	64.68

COS-Rng #3	R02-07	3200	1868.8	4436.7	745.5	1860.5	4431.9	763.2	125.4	21.5	21.5	293.5	117.3	687.73	343.87	43.56
COS-Rng #3	R02-11	3310	1872.9	4439.1	746.3	1873.4	4439.4	748.3	12.8	30.7	31.9	26	6.5	1.53	0.77	2.06
COS-Rng #3	R03-02	3490	1867.6	4438.6	744.5	1862	4435.3	750.9	56.5	23.5	23.6	289	89.3	297.22	148.61	28.64
COS-Rng #3	R03-03	3475	1864.2	4436.6	751.1	1858.2	4433.1	761.2	76.3	20.5	20.6	284.5	173.7	1161.38	580.69	56.61
COS-Rng #3	R03-04	3460	1867.9	4438.7	745.5	1865.4	4437.3	750.8	37.3	25.4	25.7	162.8	95.6	659.64	329.82	42.66
COS-Rng #3	R03-06	3510	1869.8	4439.9	746.4	1866.8	4438.1	755.9	63.2	27.1	27.9	88.9	42	140.03	70.01	19.66
COS-Rng #3	R03-07	3540	1870.8	4440.4	746.6	1870.6	4440.3	750.7	25.9	29.7	30.9	47.1	24	28.78	14.39	8.91
COS-Rng #3	R04-02	4085	1866.9	4440.7	745.4	1858.3	4435.7	759.5	107.5	23.4	23.4	160.2	86.1	520.08	260.04	37.88
COS-Rng #3	R04-03	4070	1864.4	4439.3	751.4	1859.4	4436.4	761.8	73.9	23.4	23.5	186.9	86.8	652.30	326.15	42.42
COS-Rng #3	R04-05	4120	1868.9	4441.9	747.8	1867	4440.8	754.1	41.6	28.8	29.0	42.4	25.7	59.16	29.58	12.78
COS-Rng #3	R04-06	4150	1870.6	4442.8	746.6	1870.6	4442.9	748.2	10.1	31.7	32.1	31.4	7.2	1.04	0.52	1.69
COS-Rng #3	R05-01	4300	1865.8	4442.6	745.8	1858.8	4438.6	760.3	103.4	25.5	25.5	171.5	117.9	1131.59	565.79	55.88
COS-Rng #3	R05-02	4330	1867.3	4443.5	746.6	1861.4	4440.0	759.9	93.3	27.4	27.8	53.6	27.7	91.32	45.66	15.87
COS-Rng #3	R05-03	4360	1867.5	4443.6	749.1	1866.6	4443.1	753.0	25.5	30.0	30.8	36.7	16.8	14.29	7.15	6.28
COS-Rng #3	R05-04	4390	1868.8	4444.4	746.7	1868.7	4444.3	749.2	15.5	31.8	33.0	26.3	6.1	0.45	0.23	1.11
Rings #4	R06-02	380	1874.3	4427.8	745.1	1865.4	4423.7	763.2	128.2	20.2	20.3	334.6	143.6	1370.34	685.17	61.49
Rings #4	R06-03	410	1873.5	4427.7	750.3	1867.1	4424.8	763.2	91.7	21.4	21.6	203.3	82.3	361.41	180.70	31.58
Rings #4	R06-04	440	1876.3	4429	746.0	1872.7	4427.6	756.6	70.1	25.2	25.2	107.9	48.8	220.35	110.17	24.66
Rings #4	R06-05	470	1877.0	4429.5	747.7	1876.5	4429.5	752.0	26.9	27.7	27.8	70.8	25	54.07	27.03	12.21
Rings #4	R06-06	500	1878.1	4430.1	745.6	1878.6	4430.6	749.3	23.3	29.7	29.8	42.1	22.3	35.31	17.65	9.87
Rings #4	R06-07	530	1879.2	4430.6	744.6	1880.3	4431.4	746.5	14.1	31.5	31.6	27.3	11.7	7.50	3.75	4.55
Rings #4	R06-08	560	1879.8	4430.9	743.3	1881.5	4431.9	744.3	13.8	32.8	33.0	33.8	8.3	3.99	1.99	3.32
Rings #4	R06-09	590	1880.1	4431	741.9	1881.9	4432.0	741.9	12.9	33.5	36.9	12.5	7.5	3.00	1.50	2.88
Rings #4	R06-10	620	1880.0	4430.9	740.8	1881.6	4431.8	740.0	12.5	33.8	35.7	33.3	11.8	7.06	3.53	4.41
Rings #4	R07-01	100	1865.5	4422.8	746.1	1864.1	4422.8	761.4	95.8	14.4	14.5	768.5	380.6	4920.63	2460.31	116.52
Rings #4	R07-05	175	1870.6	4425.5	742.9	1874	4427.6	743.8	25.3	23.6	23.6	74.3	25.7	36.10	18.05	9.98
Rings #4	R07-06	275	1870.6	4425.5	741.8	1874.2	4427.5	741.1	26.1	24.3	24.9	56.8	17.9	21.08	10.54	7.63
Rings #4	R08-03	890	1874.3	4426.4	742.8	1869.9	4423.8	744.6	33.2	22.8	23.5	42.7	17	21.74	10.87	7.74
Rings #4	R08-04	875	1873.9	4426.1	744.6	1871.8	4424.9	746.7	19.7	23.1	23.3	51.7	27.6	25.40	12.70	8.37
Rings #4	R08-05	1110	1875.1	4426.8	745.2	1866.5	4421.9	763.2	127.8	20.6	20.7	384.9	136.8	1222.83	611.41	58.08
Rings #4	R08-06	1140	1875.0	4426.8	749.0	1868.3	4422.9	763.2	101.1	21.9	22.1	113.9	60.8	277.11	138.56	27.65
Rings #4	R08-07	1170	1877.1	4428	746.0	1874.1	4426.3	756.0	65.6	25.8	26.0	134.9	57.2	226.71	113.36	25.01
Rings #4	R08-08	1200	1878.2	4428.6	746.3	1878.1	4428.6	751.0	29.5	28.7	29.0	29.9	20	33.04	16.52	9.55
Rings #4	R08-09	1230	1879.6	4429.4	745.2	1880.5	4429.9	747.6	16.4	31.1	31.4	29.4	13.8	11.48	5.74	5.63

Rings #4	R08-10	1260	1880.5	4429.9	743.8	1881.9	4430.7	745.0	12.6	32.7	32.7	26.4	7.1	2.40	1.20	2.57
Rings #4	R08-11	1290	1880.8	4430.1	741.8	1882.2	4430.9	741.6	10.4	33.7	35.2	24.2	6.9	2.27	1.13	2.50
Rings #4	R08-12	1390	1880.6	4430	740.1	1882.2	4431.0	738.7	14.7	34.3	35.6	27.8	9.9	9.94	4.97	5.24
Rings #4	R09-01	830	1866.5	4421.8	746.2	1865.1	4421.1	761.9	97.7	15.0	15.0	805.7	319.3	3040.32	1520.16	91.59
Rings #4	R09-04	1005	1871.0	4424.5	740.0	1872.2	4425.1	739.0	10.4	23.9	24.5	37.3	10.9	9.81	4.91	5.20
Rings #4	R10-02	1575	1875.1	4424.3	741.6	1871.4	4422.2	741.2	26.3	24.1	25.8	43.7	15.4	20.69	10.35	7.56
Rings #4	R10-03	1560	1875.5	4424.6	742.6	1871.4	4422.2	743.8	30.4	23.7	24.5	39.3	12.2	6.85	3.43	4.35
Rings #4	R10-04	1545	1875.4	4424.5	744.3	1872.8	4423.0	746.7	24.0	23.8	24.4	26	8.3	3.57	1.78	3.14
Rings #4	R10-05	1780	1876.3	4425.1	745.3	1867.8	4420.1	763.1	126.7	21.3	21.6	239.8	106.2	688.90	344.45	43.60
Rings #4	R10-06	1810	1876.0	4424.9	749.4	1869.4	4421.0	763.3	98.5	22.4	22.8	86.4	54.6	148.95	74.48	20.27
Rings #4	R10-07	1840	1878.3	4426.2	746.1	1875.3	4424.4	756.1	66.1	26.3	26.7	87.7	33.4	131.31	65.65	19.03
Rings #4	R10-08	1870	1879.3	4426.8	746.5	1879	4426.6	751.3	30.0	28.9	29.5	40.5	15.7	14.36	7.18	6.30
Rings #4	R10-09	1900	1880.7	4427.6	745.5	1881.4	4428.0	747.6	14.0	31.3	31.9	31.4	7.4	2.54	1.27	2.65
Rings #4	R10-11	1960	1882.0	4428.3	741.6	1883.2	4429.0	741.4	8.3	34.0	36.3	24	6	0.98	0.49	1.65
Rings #4	R10-12	2060	1881.9	4428.3	740.2	1883.1	4428.9	739.3	10.4	34.4	36.0	20.6	5.3	0.65	0.33	1.34
Rings #4	R11-01	1500	1867.7	4420.1	746.0	1866.6	4419.4	761.6	97.0	15.9	15.9	602	228.6	2562.55	1281.28	84.08
Rings #4	R11-03	1530	1870.7	4421.8	746.0	1871.5	4422.3	749.9	24.9	20.1	20.8	81.6	25.8	32.00	16.00	9.40
Rings #4	R11-04	1675	1872.1	4422.6	740.0	1873.3	4423.3	738.9	11.2	24.4	25.3	39.1	12.7	9.76	4.88	5.19
Rings #4	R12-02	2245	1876.4	4422.6	741.6	1872.8	4420.5	741.2	25.7	25.0	25.0	56.9	25.7	31.73	15.86	9.36
Rings #4	R12-03	2230	1876.8	4422.9	742.7	1872.8	4420.5	744.1	30.3	24.5	25.3	57.7	22.3	31.70	15.85	9.35
Rings #4	R12-04	2215	1876.5	4422.6	744.5	1874.6	4421.6	746.4	17.6	24.8	25.5	46	16.5	19.79	9.90	7.39
Rings #4	R12-05	2450	1877.6	4423.3	745.1	1868.7	4418.2	763.2	129.9	22.0	22.5	309.2	86.1	434.89	217.44	34.64
Rings #4	R12-06	2480	1877.9	4423.5	748.4	1870.5	4419.2	763.3	106.6	23.4	24.1	166.6	68.4	211.20	105.60	24.14
Rings #4	R12-07	2510	1879.7	4424.5	746.4	1876.8	4422.8	755.3	58.9	27.2	28.0	120.4	26	64.75	32.38	13.37
Rings #4	R12-08	2540	1880.9	4425.2	746.2	1880.7	4425.1	749.9	22.8	30.1	31.1	48.7	12.6	9.43	4.71	5.10
Rings #4	R13-01	2170	1869.0	4418.3	746.1	1867.9	4417.7	760.3	89.0	16.9	16.9	553	182.9	1986.74	993.37	74.04
Rings #4	R13-04	2200	1872.1	4420.1	745.9	1873	4420.6	749.7	24.9	21.2	22.0	62.2	22.8	36.75	18.37	10.07
Rings #4	R13-05	2345	1873.4	4420.9	739.8	1874.4	4421.4	739.0	8.5	25.1	25.9	77.8	21.6	28.04	14.02	8.80
Rings #4	R14-02	2725	1877.9	4421	741.5	1874.4	4419.0	740.9	25.4	26.3	28.0	43.3	22	24.67	12.34	8.25
Rings #4	R14-03	2710	1878.3	4421.2	742.5	1874.1	4418.8	743.6	31.0	25.8	26.9	49.5	20.5	22.19	11.10	7.83
Rings #4	R14-04	2695	1878.5	4421.3	743.9	1876	4419.9	746.1	22.5	26.3	27.3	49.3	20.1	27.03	13.51	8.64
Rings #4	R14-05	2930	1879.0	4421.6	745.4	1869.9	4416.4	763.2	128.9	23.1	23.8	291	102.4	709.46	354.73	44.24
Rings #4	R14-06	2960	1878.5	4421.3	749.6	1871.6	4417.4	763.3	98.4	24.1	24.9	130.2	37.3	105.36	52.68	17.05
Rings #4	R14-07	2990	1880.9	4422.7	746.3	1878.3	4421.2	754.4	53.4	28.2	29.4	58.6	35.8	64.46	32.23	13.34

Rings #4	R14-08	3020	1882.3	4423.5	746.2	1882.3	4423.5	747.9	10.7	31.4	32.8	30.4	7.8	4.62	2.31	3.57
Rings #4	R15-01	2650	1869.9	4416.4	746.0	1869.2	4416.0	760.7	91.6	18.1	18.1	775.4	212.8	1791.70	895.85	70.31
Rings #4	R15-02	2665	1872.4	4417.8	745.7	1871.7	4417.4	755.2	59.1	20.4	20.8	85.6	58.9	240.67	120.33	25.77
Rings #4	R15-03	2680	1873.7	4418.6	745.4	1874.6	4419.1	748.6	20.5	22.8	23.5	49.3	31.2	53.44	26.72	12.14
Rings #4	R15-04	2825	1875.0	4419.3	739.9	1875.9	4419.8	739.1	8.0	26.3	27.0	39.7	14.5	13.21	6.60	6.04

Sensor Coordinates		
X (m)	Y (m)	Z (m)
1846.4	4413.9	750.3

52h04HL FOOTWALL GEOPHONE 2

Blasthole Info		Explosive Charge Information								Distance		Peak Amplitudes/Energy/Strain				
		Firing time	Collar Coordinates			Toe Coordinates			Explosive Load (kg)	Geom Dist (m)	VICD Dist (m)	PPA (m/s^2)	PPV (mm/s)	$ED_{W\text{-}tot}$ (J/m^3)	$ED_{W\text{-}SS}$ (J/m^3)	$\varepsilon_{W\text{-}MN}$ (με)
Firing	Hole #	(ms)	X (m)	Y (m)	Z (m)	X (m)	Y (m)	Z (m)								
LHW #1	LHW01	5850	1862.2	4427.9	745.9	1862.2	4427.8	764.4	115.1	21.6	21.6	183.1	59.9	259.84	129.92	26.78
LHW #1	LHW02	4350	1862.7	4427.1	745.9	1862.6	4427.1	763.9	112.0	21.4	21.4	247.4	66.8	215.11	107.56	24.36
LHW #1	LHW03	1850	1863.0	4426.6	745.9	1863	4426.6	763.9	112.0	21.4	21.4	421	140	1291.59	645.79	59.70
LHW #1	LHW04	4100	1863.3	4426	745.9	1863.3	4426.0	763.9	112.0	21.3	21.3	238.6	71.2	449.63	224.82	35.22
LHW #1	LHW05	5350	1863.7	4425.3	747.9	1863.7	4425.3	763.4	96.4	21.4	21.4	254.2	123.5	938.78	469.39	50.89
LHW #1	LHW06	3100	1863.1	4428.4	745.9	1863.1	4428.3	763.4	108.9	22.5	22.5	203.1	76.9	380.80	190.40	32.41
LHW #1	LHW07	150	1863.5	4427.6	745.9	1863.5	4427.6	764.4	115.1	22.4	22.4	211.3	115.9	814.93	407.46	47.42
LHW #1	LHW08	1100	1863.9	4427.1	745.9	1863.9	4427.1	763.4	108.9	22.3	22.3	64.6	13.8	4.87	2.43	3.66
LHW #1	LHW09	100	1864.2	4426.5	745.9	1864.2	4426.5	763.4	108.9	22.2	22.2	283.3	124.2	1399.06	699.53	62.13
LHW #1	LHW10	3600	1864.6	4425.8	747.9	1864.6	4425.8	763.4	96.4	22.4	22.4	306.8	100.7	410.89	205.45	33.67
LHW #1	LHW11	5600	1864.0	4428.9	747.9	1863.9	4428.9	763.4	96.4	23.7	23.7	54.9	30.2	36.31	18.15	10.01
LHW #1	LHW13	2600	1864.7	4427.6	747.9	1864.7	4427.6	763.4	96.4	23.5	23.5	211.2	101.1	362.01	181.00	31.60
LHW #1	LHW14	4850	1865.0	4427	747.9	1865	4427.0	763.4	96.4	23.4	23.4	50.1	13.5	15.77	7.88	6.60
LHW #1	LHW15	6100	1865.5	4426.3	747.9	1865.4	4426.3	763.4	96.4	23.4	23.4	186.5	126.2	694.88	347.44	43.79
LHW #1	COS2-01	6600	1865.8	4428.2	748.4	1865.8	4428.2	762.8	89.6	24.7	24.7	100.5	55.9	313.38	156.69	29.40
COS #2	COS1-01	100	1867.7	4427.5	746.4	1867.7	4427.5	761.4	93.0	25.5	25.5	196.6	147.5	1908.97	954.48	72.57
COS #2	COS1-02	400	1869.8	4428.8	748.0	1869.8	4428.8	758.6	65.9	27.9	27.9	106.4	91.1	818.97	409.48	47.53

COS #2	COS2-02	250	1868.0	4429.4	748.5	1868	4429.4	760.0	71.9	26.9	26.9	77.9	51	262.01	131.00	26.89
COS-Rng #3	C1-03	250	1872.0	4430	747.9	1872	4430.0	755.9	49.9	30.3	30.3	88.2	58	347.30	173.65	30.96
COS-Rng #3	C1-04	550	1874.1	4431.3	748.3	1874.1	4431.3	753.1	29.9	32.7	32.7	45.1	30.7	60.58	30.29	12.93
COS-Rng #3	C1-05	850	1876.0	4432.4	748.1	1876.2	4432.5	750.3	14.0	35.0	35.0	21.1	11.5	13.99	7.00	6.21
COS-Rng #3	C1-06	1150	1876.9	4432.9	745.6	1877.9	4433.4	747.8	15.4	36.6	36.6	40.1	11.3	9.39	4.69	5.09
COS-Rng #3	C1-07	1450	1877.6	4433.3	744.2	1879	4434.1	745.5	13.2	37.9	37.9	32	10.3	7.65	3.82	4.59
COS-Rng #3	C1-08	1750	1877.9	4433.4	742.8	1879.7	4434.5	743.2	12.8	38.8	38.8	28.6	8.7	5.26	2.63	3.81
COS-Rng #3	C1-09	2050	1877.9	4433.4	741.4	1879.7	4434.5	740.6	13.8	39.2	39.2	29.5	15.8	28.58	14.29	8.88
COS-Rng #3	C1-10	2350	1877.7	4433.3	740.2	1878.7	4433.9	739.2	9.3	38.9	38.9	18.6	7.6	2.61	1.30	2.68
COS-Rng #3	C2-04	400	1872.3	4431.9	746.0	1872.3	4431.9	754.4	52.4	31.5	31.5	34.4	27.9	98.37	49.19	16.47
COS-Rng #3	C2-05	700	1874.5	4433.2	746.3	1874.5	4433.2	751.6	32.8	34.1	34.1	42.3	19.9	54.10	27.05	12.22
COS-Rng #3	C2-06	1000	1875.5	4433.8	746.0	1876.3	4434.3	749.0	19.3	35.9	35.9	26.5	10.5	8.02	4.01	4.70
COS-Rng #3	C2-08	1600	1876.9	4434.6	743.3	1878.6	4435.6	744.1	13.1	38.4	38.4	27	10.9	5.78	2.89	3.99
COS-Rng #3	C2-09	1900	1877.0	4434.6	741.8	1878.7	4435.6	741.5	12.0	38.9	38.9	37	15.2	7.73	3.86	4.62
COS-Rng #3	C2-10	2200	1876.9	4434.6	740.2	1878.2	4435.3	739.2	11.8	39.0	39.0	24.3	10.5	5.88	2.94	4.03
COS-Rng #3	R01-02	2910	1867.6	4433.5	743.9	1859.9	4429.0	747.9	61.0	24.9	24.9	34.6	17.9	28.52	14.26	8.87
COS-Rng #3	R01-04	2880	1868.3	4433.9	745.5	1859.8	4429.0	755.7	88.3	24.9	24.9	416.1	139.5	574.59	287.29	39.82
COS-Rng #3	R01-05	2865	1865.6	4432.4	751.1	1859.6	4428.9	761.0	75.4	24.0	24.0	118.7	66.1	180.34	90.17	22.31
COS-Rng #3	R01-06	2850	1869.5	4434.6	745.7	1861.4	4429.9	763.3	123.7	26.8	26.8	169.4	110.3	861.45	430.72	48.75
COS-Rng #3	R01-09	2930	1873.0	4436.6	746.3	1873.2	4436.7	750.3	25.1	35.2	35.9	41.8	26.6	57.94	28.97	12.64
COS-Rng #3	R01-10	2960	1874.4	4437.4	745.4	1875.2	4437.8	746.9	10.5	37.2	38.4	27.8	11.3	12.40	6.20	5.85
COS-Rng #3	R01-11	2990	1875.1	4437.8	743.4	1876	4438.4	743.9	7.4	38.5	38.5	22	9.6	5.72	2.86	3.97
COS-Rng #3	R01-13	3050	1875.0	4437.7	739.9	1875.8	4438.2	739.1	7.8	39.2	39.2	31.3	8.6	3.31	1.65	3.02
COS-Rng #3	R02-01	3290	1868.0	4436.2	741.1	1865.4	4434.7	739.7	20.5	31.2	32.2	28.7	22.4	29.71	14.86	9.05
COS-Rng #3	R02-03	3260	1867.9	4436.2	743.3	1862	4432.8	745.7	45.2	28.3	28.4	148.5	46.5	138.11	69.05	19.52
COS-Rng #3	R02-04	3245	1865.4	4434.7	746.2	1859.8	4431.5	750.6	48.8	25.2	25.4	93	59.3	151.13	75.56	20.42
COS-Rng #3	R02-05	3230	1867.7	4436.1	745.3	1859.2	4431.2	755.2	86.1	26.1	26.2	130.5	64.9	227.24	113.62	25.04
COS-Rng #3	R02-06	3215	1865.0	4434.5	750.8	1858.8	4431.0	760.8	76.7	25.0	25.0	211.8	102.6	776.17	388.08	46.28
COS-Rng #3	R02-07	3200	1868.8	4436.7	745.5	1860.5	4431.9	763.2	125.4	27.7	27.7	152.5	98.5	601.76	300.88	40.75
COS-Rng #3	R02-11	3310	1872.9	4439.1	746.3	1873.4	4439.4	748.3	12.8	37.0	38.0	25.4	14.8	12.29	6.15	5.82
COS-Rng #3	R03-01	3505	1867.3	4438.4	743.2	1865.9	4437.6	743.7	10.4	32.2	32.4	70.7	45.8	117.17	58.58	17.98
COS-Rng #3	R03-02	3490	1867.6	4438.6	744.5	1862	4435.3	750.9	56.5	29.6	29.6	184.7	64.6	220.26	110.13	24.65
COS-Rng #3	R03-03	3475	1864.2	4436.6	751.1	1858.2	4433.1	761.2	76.3	26.3	26.4	207.9	95.2	740.72	370.36	45.21
COS-Rng #3	R03-04	3460	1867.9	4438.7	745.5	1865.4	4437.3	750.8	37.3	31.6	31.7	126.9	74.9	286.59	143.30	28.12

COS-Rng #3	R03-07	3540	1870.8	4440.4	746.6	1870.6	4440.3	750.7	25.9	36.0	36.9	34.8	24.7	60.47	30.23	12.92
COS-Rng #3	R03-08	3570	1872.2	4441.2	746.3	1872.4	4441.3	747.1	5.0	37.9	38.4	29.9	11.3	7.25	3.63	4.47
COS-Rng #3	R04-01	4100	1866.7	4440.6	744.2	1865.6	4439.9	745.0	9.6	33.4	33.6	34.3	23.5	31.90	15.95	9.38
COS-Rng #3	R04-02	4085	1866.9	4440.7	745.4	1858.3	4435.7	759.5	107.5	29.3	29.3	99.5	68.2	284.87	142.43	28.03
COS-Rng #3	R04-03	4070	1864.4	4439.3	751.4	1859.4	4436.4	761.8	73.9	29.2	29.2	74.4	60.4	325.98	162.99	29.99
COS-Rng #3	R04-05	4120	1868.9	4441.9	747.8	1867	4440.8	754.1	41.6	34.9	35.0	44.5	23.5	50.06	25.03	11.75
COS-Rng #3	R04-06	4150	1870.6	4442.8	746.6	1870.6	4442.9	748.2	10.1	37.8	38.1	22.8	14.5	13.36	6.68	6.07
COS-Rng #3	R05-01	4300	1865.8	4442.6	745.8	1858.8	4438.6	760.3	103.4	31.2	31.3	112	77.4	530.54	265.27	38.26
COS-Rng #3	R05-02	4330	1867.3	4443.5	746.6	1861.4	4440.0	759.9	93.3	33.3	33.6	33.9	29.3	73.44	36.72	14.23
COS-Rng #3	R05-03	4360	1867.5	4443.6	749.1	1866.6	4443.1	753.0	25.5	36.0	36.6	30.5	23.7	41.41	20.71	10.69
COS-Rng #3	R05-04	4390	1868.8	4444.4	746.7	1868.7	4444.3	749.2	15.5	37.8	38.8	18.5	8.3	3.14	1.57	2.94

APPENDIX 2 : MATHEMATICAL MODELS OF WAVE ATTENUATION

A2.1 Mathematical and Analytical Models of Wave Attenuation and Interaction with Discontinuities 358
A2.2 Transmission Characteristics of Discontinuities 361
A2.2.1 Attenuation of Blast Waves in Response to Interaction with Discontinuities 362

A2.1 Mathematical and Analytical Models of Wave Attenuation and Interaction with Discontinuities

To provide some theoretical background for the laboratory and field investigations of wave attenuation, a review has been completed of a number of mathematical models which predict wave attenuation based on interaction with existing discontinuities. These models include the work of Morland (1974), Hudson (1981), Crampin (1984), Schoenberg and Douma (1988), Pyrak-Nolte et al. (1990) and Rossmanith (2006).

Morland (1974) proposed a model for describing the elastic response to wave loading of a single joint set of known orientation, thickness, spacing and infill characteristics to investigate the change in the displacement field of a seismic wave interacting with a crack. Under the assumption of simple shear and uni-axial compression, the shear and normal stiffness ratios of tractions to displacements (transmission of displacement across the discontinuity) were defined by Equations A2.1 and A2.2.

$$\Lambda_s \approx \frac{d}{\delta}\mu' \qquad \text{(A2. 1)}$$

$$\Lambda_d \approx \frac{d}{\delta}\left(k' + \tfrac{4}{3}\mu'\right) \qquad \text{(A2. 2)}$$

Where Λ_s = shear stiffness ratio
Λ_d = normal stiffness ratio
d = joint separation
δ = joint thickness
μ' = shear modulus of joint infill material
k' = bulk modulus of joint infill material

From the combined anisotropic material compliance matrix, the effect of a single joint of normal orientation on the stress-strain transformation yielded Equation A2.3.

$$-2G\varepsilon_{11} = 2\left(\frac{K + \frac{1}{3}G}{3K} + \frac{G}{\Lambda_d}\right)\sigma_{11} - \frac{K - \frac{2}{3}G}{3K}\sigma_{\gamma\gamma} \quad (\gamma = 2,3) \qquad \text{(A2. 3)}$$

Where ε_{11} = normal strain in x direction
G = shear modulus of the intact rock
K = bulk modulus of intact rock
σ_{11} = normal stress in x direction
$\sigma_{\gamma\gamma}$ = normal stress in y and z directions

The effect of the reduced joint stiffness could be observed through reduction of the shear modulus (G/Λ_d) paired with the normal stress term. Further derivations proposed by Morland (1974) provided treatments for an equivalent elastic modulus for a material containing multiple joint sets of known orientations and conditions.

Hudson (1981) proposed attenuation factors for elastic waves propagating through jointed material by using the material modulus descriptions specified by Morland (1974). Coupling the modified material modulus with elastic wave equations, Hudson proposed Equation A2.4 to predict the attenuation factor (γ_P) of the P-wave due to a series of regularly spaced joints.

$$\gamma_P = \frac{\omega}{\beta}\left(va^3\right)\left(\frac{\omega a}{\alpha}\right)^3 \frac{1}{30\pi}\left[\left(\frac{3}{2}+\frac{\beta^5}{\alpha^5}\right)\left(\overline{u}_{11}\right)^2 \sin^2 2\theta\right.$$

$$\left.+\left(2+\frac{15\beta}{4\alpha}-\frac{10\beta^3}{\alpha^3}+\frac{8\beta^5}{\alpha^5}\right)\left(\overline{u}_{33}\right)^2\left(\frac{\alpha^2}{\beta^2}-2\sin^2\theta\right)^2\right. \quad \text{(A2. 4)}$$

And

$$\overline{u}_{11} = \frac{\mu}{va^3\left(\mu+\Lambda_s\right)} \quad \text{(A2. 5)}$$

$$\overline{u}_{33} = \frac{\mu}{va^3\left(\lambda+2\mu+\Lambda_d\right)} \quad \text{(A2. 6)}$$

Where
- ω = angular frequency
- β = shear wave velocity of intact material
- α = longitudinal wave velocity of intact material
- θ = angle of incidence to normal of joint set
- v = density number of joints of bulk material
- a = mean radius of joints
- λ, μ = Lame's constants of intact material
- Λ_s, Λ_d = as defined in Equations A2.1 and A2.2

Equation A2.4 suggests that an increase in the fracture density (reducing the fracture spacing) or fracture radius (scale) greatly influences the attenuation factor, reducing the amplitude of the wave by a higher rate over distance. The treatment by Hudson (1981) also took into account the angle of incidence and wave frequency, which helped to determine the percentage of the wave motion transmitted or reflected.

The formulations proposed by Hudson (1981) for treatment of materials containing multiple fracture sets were found to fit well with the model proposed by Crampin (1984). The results of mathematical modelling revealed that wave velocities and long

wavelengths (20-80Hz) were insensitive to the crack radius and crack filling, but that the attenuation factor was sensitive to many wave and crack properties. Figure A2.1 illustrates the calculated attenuation factors for long wavelength units passed through a material of constant crack density, but varying crack radii from 1 to 10m. These crack dimensions are considered to be representative of the discontinuities encountered in the mining environment.

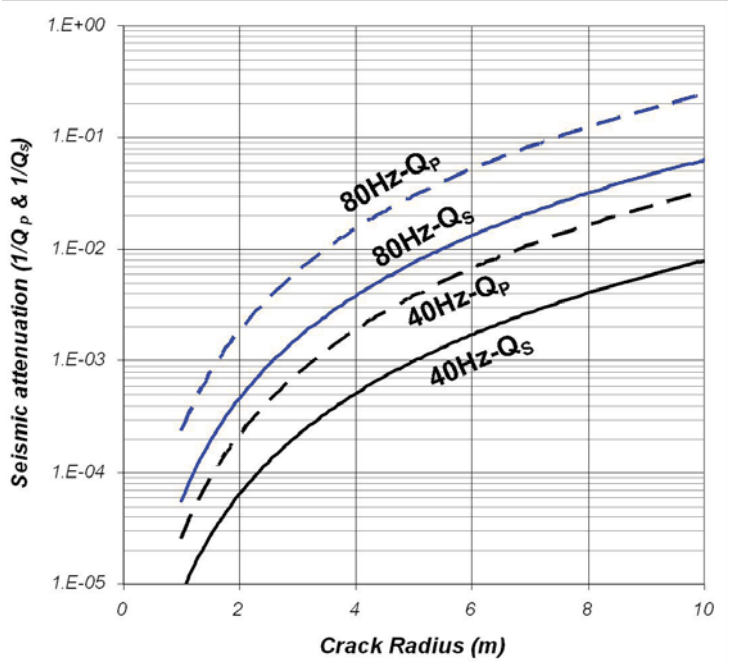

Figure A2.1. Maximum values of P-wave and S-wave attenuation factors for crack radii between 1m and 10m (dry cracks) with 40Hz and 80Hz input waves (after Crampin, 1984).

The ratio of wavelength to discontinuity dimension represented in Figure A2.1 (1-10m fracture radii) ranges from 1.56 to 62.5 times for a standard rock material with V_p = 5,000 m/s and V_s = 2,500 m/s as calculated for the 40 and 80Hz frequencies. This would simulate a condition where the wavelength is significantly larger than the discontinuity dimension, which may not be the conditions in the near-field of a blast where high frequency waves travel with significantly reduced wavelengths. For example, a 1kHz wave for the same fracture dimension range (2m-20m diameter) would exhibit ratios of 0.25 to 2.5 times. Therefore the assumption of a large wavelength would be incorrect and the attenuation factor for the high frequency, short wavelength elastic waves would be assumed to increase.

To investigate the behaviour of large discontinuities on the elastic compliance matrix, Schoenberg and Douma (1988) adopted the material anisotropic compliance matrices specified by Hudson (1981) to compare the elastic anisotropy models of various researchers. Using the assumption that fractured material behaves as a

system of transversely anisotropic background material containing discontinuity systems with a discrete modified compliance, Schoenberg and Douma suggested an inelastic compliance matrix. This matrix accounted for the change in isotropy (ΔN, ΔP, ΔM) based on the modified fracture compliances E_T (tangential) and E_N (normal). Equations A2.7 to A2.11 illustrate the change in isotropy for a series of dry joints of adequate thickness such that there is zero traction in a transversely anisotropic material.

$$\Delta N = -\begin{bmatrix} E_N(\lambda_b + 2\mu_b)/(1+E_N) & 0 & 0 \\ 0 & \mu_b E_T/(1+E_T) & 0 \\ 0 & 0 & \mu_b E_T/(1+E_T) \end{bmatrix} \quad \text{(A2. 7)}$$

$$\Delta P = -\lambda_b \frac{E_N}{(1+E_N)}\begin{bmatrix} 1 & 0 & 0 \\ 1 & 0 & 0 \\ 0 & 0 & 0 \end{bmatrix} \quad \text{(A2. 8)}$$

$$\Delta M = -\frac{\lambda_b^2}{(\lambda_b + 2\mu_b)}\frac{E_N}{(1+E_N)}\begin{bmatrix} 1 & 1 & 0 \\ 1 & 1 & 0 \\ 0 & 0 & 0 \end{bmatrix} \quad \text{(A2. 9)}$$

And

$$E_N = \frac{4}{3\gamma_b[1-\gamma_b]}e \quad \text{(A2. 10)}$$

$$E_T = \frac{16}{3[3-2\gamma_b]}e \quad \text{(A2. 11)}$$

Where λ_b, μ_b = Lame's constants for the background material
$\gamma_b = \mu_b/(\lambda_b + 2\mu_b)$
e = crack density

A2.2 Transmission Characteristics of Discontinuities

General elastic and plastic wave theories have been used in the literature to develop equations for predicting the behaviour of waves interacting with material interfaces having different material properties. The material interface models generally considered for use with stress waves in geomaterials are those related to either welded or cohesive or semi-cohesive contacts between similar or seismically dissimilar materials (illustrated by Rossmanith, 2006). As a function of wave propagation behaviour, calculation of reflection and transmission refraction angles

relative to the incident wave are quite straight forward. These angles are related to the geometry of the wave path relative to the interface and the material properties, without a general treatment for the condition of the interface (Graff, 1975). For the special condition of a stress-free boundary, the entire wave is reflected in two different modes (i.e. P-wave and S-wave).

In the case of a welded interface between two similar materials, the interface stiffness is assumed to be approximately equal to the virgin material and wave reflection is assumed to be minimal. This behaviour can be attributed to the infill material properties or confining stresses, as observed by Pyrak-Nolte et al. (1990). In this case, there is negligible attenuation. In mining rock masses, discontinuities displaying welded characteristics can occur due to high confining stresses or chemical processes leading to "healing". The North Zone rock mass studied at the BHP Cannington Mine consisted of mainly healed discontinuities and therefore the degree of attenuation resulting from wave-fracture interaction was expected to be minimal.

The types of fracture interfaces that are likely to exist in the perimeter of an excavation and alter the radiating stress waves from blasting are those of a cohesive or semi-cohesive nature. These discontinuities would generally have stiffness lower than that of the intact rock. The stiffness of an interface can be related to the viscosity of the infill material, saturation, level of contact between the two faces (roughness and asperity) and confining normal stresses (Pyrak-Nolte et al., 1990).

A2.2.1 Attenuation of Blast Waves in Response to Interaction with Discontinuities

Stress waves interacting with boundaries between similar materials (rock blocks or slabs) would be expected to result in anelastic attenuation over distance. In order to gain a better understanding of the effect of a single discontinuity on the attenuation of stress waves, Equations A2.12 to A2.15 are listed by Rossmanith (2006) describing the work of Rinehart (1975) for predicting the reflection and transmission of incident P-waves from a non-cohesive joint.

$$R_{PP} = \frac{\sigma_{P_1P_1}}{\sigma_{P_1}} = \kappa \sin 2\alpha \sin 2\beta \qquad \text{(A2. 12)}$$

$$R_{SP} = \frac{\tau_{S_1P_1}}{\sigma_{P_1}} = T_{SP} = \kappa \left(\frac{C_P}{C_S} \right) \sin 2\alpha \cos 2\beta \qquad \text{(A2. 13)}$$

$$T_{PP} = \frac{\sigma_{P_2P_1}}{\sigma_{P_1}} = \kappa \left(\frac{C_P}{C_S} \right)^2 \cos^2 2\beta \qquad \text{(A2. 14)}$$

And

$$\kappa^{-1} = \left(\frac{C_P}{C_S}\right)^2 \cos^2 2\alpha \sin 2\beta \qquad \text{(A2. 15)}$$

Where R_{PP} = ratio of stress amplitude of the reflected P_1P_1 wave
σ_{P1P1} = normal stress of reflected P-wave (Pa)
σ_{P1} = normal stress of incident P-wave (Pa)
R_{SP} = ratio of stress amplitude of reflected S_1P_1 wave
T_{SP} = ratio of stress amplitude transmitted in S_2P_1 wave
τ_{S1P1} = shear stress of reflected S-wave (Pa)
T_{PP} = ratio of stress amplitude transmitted in P_2P_1 wave
σ_{P2P1} = normal stress in transmitted P-wave (Pa)
κ = interface stiffness (dimensionless)
β = angle between interface normal and reflected S_1P_1 wave (º)
α = angle between interface normal and incident P_1 wave (º)
C_P = P-wave velocity (m/s)
C_S= shear wave velocity (m/s)

The wave types resulting from the reflection and refraction described in Equations A2.12 to A2.14 are shown in Figure A2.2.

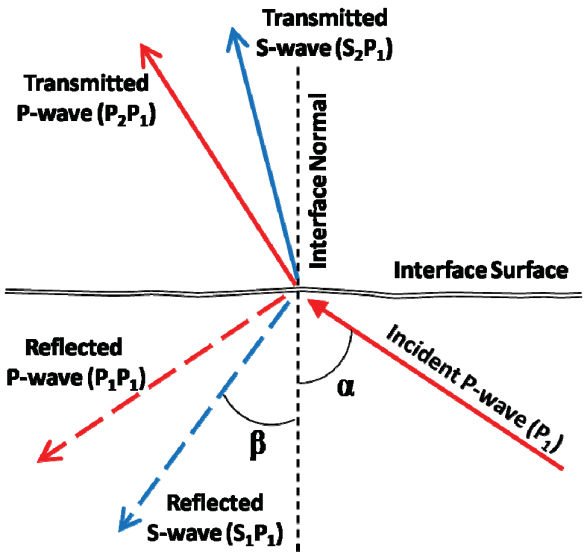

Figure A2.2. Transmitted and reflected wave types resulting from an incident wave interacting with a material interface.

To investigate the attenuation characteristics along a given wave path, the wave transmission ratios for a given material can be calculated for a range of incident angles using Equations A2.12 to A2.14. Although these equations only consider the incident P-wave and are independent of factors that influence wave transmission such as the wave frequency or wavelength (Graff, 1975), a basic understanding of the

transmission behaviour can be gained. Due to an assumption that the interface stiffness κ represents both normal and shear stiffness, incident shear wave transmission characteristics are assumed to be similar to incident P waves. The relative amplitudes of the transmitted and reflected waves based on the angle of incidence are illustrated in Figure A2.3. The material wave propagation assumptions were C_P = 5km/s, C_S = 2.9km/s, $\beta = \arcsin[(C_S \sin \alpha)/C_P]$ (Kolsky, 1953).

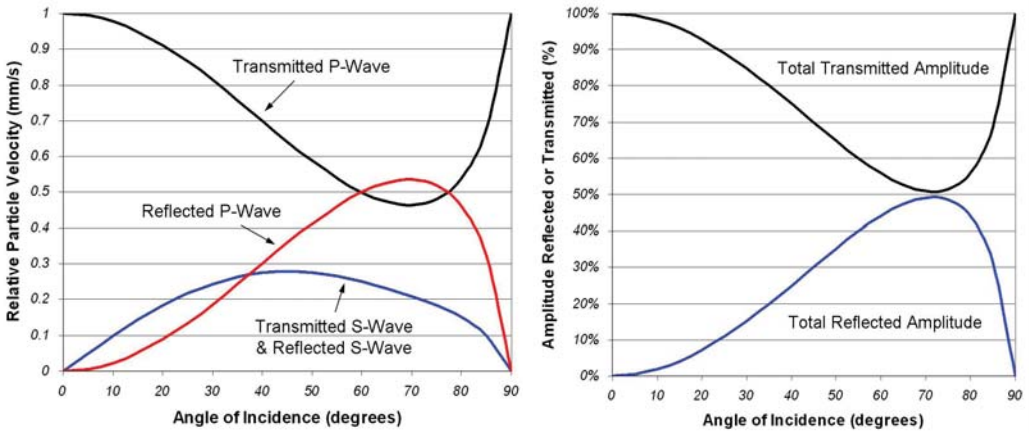

Figure A2.3. Relative amplitude of transmitted and reflected waves from an incident P-wave acting at a non-cohesive interface between similar materials (left)(after Rossmanith, 2006) and percentage of wave amplitude transmitted and reflected from the non-cohesive interface for a range in incident angles (right).

APPENDIX 3 : SMALL-SCALE TO FIELD-SCALE EXPLOSIVE BREAKAGE STUDIES

A3.1 Dynamic Damage on the Micro-scale 366

A3.1.1 Continuum Damage Based on Micro-fracture 367

A3.2 Small-scale Blast Simulation Models 368

A3.2.1 Small-scale Tests in PMMA 368

A3.2.2 Other Materials Used in Scaled Blasting Models 370

A3.2.2.1 Cement and Concrete Blasting Models 370

A3.2.2.2 Rock Blocks and Field-Scale Blasting Tests 371

A3.2.3 Limitations of Scaled Blasting Tests 372

A3.2.3.1 Model Geometry and Material Properties 373

A3.2.3.2 Specific Limitations of Scaled Models 373

A3.2.3.3 Effect of Borehole Liners on Wave Propagation 374

A3.3 Field Scale Damage Investigations 374

A3.1 Dynamic Damage on the Micro-scale

The first signs of material damage in response to static and dynamic loading are the formation of micro-cracks or extension of pre-existing flaws in the lattice of the rock material. As micro-flaws extend and coalesce, macro-fractures can form. These macro-fractures can further coalesce and subsequently lead to failure of the material. The process of micro-crack extension and coalescence is highly influenced by the intensity and duration of dynamic loading. A number of small-scale dynamic impact tests have been conducted on rock materials by various researchers to investigate this phenomenon.

Of the published literature investigating the dynamic fracture of small rock samples, the work published by Shockey et al. (1974) was one of the earliest and most regularly referenced in subsequent research due to the thorough treatment of the experimental procedures. During the study, dynamic impact testing was performed on 53 Arkansas Novaculite samples under different loading and boundary conditions. The study was conducted to evaluate sample damage and post-fracture fragment sizes based on the intensity of dynamic impact produced by a gas gun and projectile striking mechanism.

After the impact experiments, micro-damage evaluation was performed using fractographic methods. A computer wave simulation model was also developed to better understand the role of the strain waves contributing to sample rupture. Figure A3.1 illustrates the dynamic loading mechanism used in the investigations.

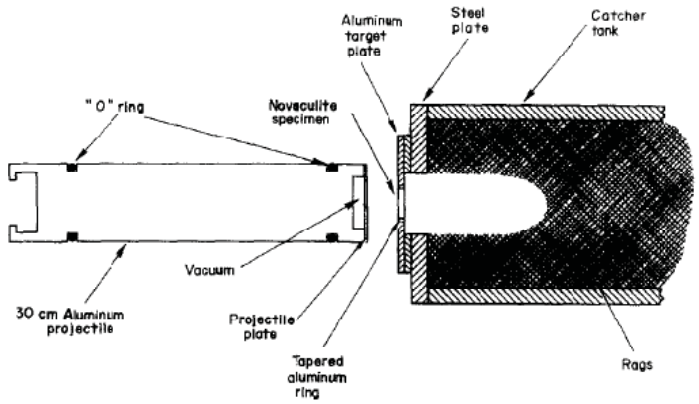

Figure A3.1. High strain-rate impact testing equipment for testing of Arkansas Novaculite rock samples (Shockey et al., 1974).

One of the main findings of the experiments conducted by Shockey et al. (1974) supported Griffith-Irwin fracture mechanics criterion through validation of a critical flaw activation dimension (c^*). Any existing flaw less than the c^* dimension would fail to activate under a given dynamic stress loading condition. This was an early example of the scale and time effects of flaw activation. The study also identified the

dependence of the fragment size and number of activated flaws on the applied strain rate, and suggested a value for the dynamic fracture toughness of Novaculite based on the largest existing flaw dimension and dynamic tensile strength.

A3.1.1 Continuum Damage Based on Micro-fracture

The observations of Shockey et al. (1974) were investigated further and confirmed by Grady and Kipp (1979) during experimental studies. The findings were integrated into mathematical and numerical continuum damage modelling based on classical fracture mechanics to evaluate the evolution of micro-damage. Grady and Kipp (1979) also suggested a link between fracture stress and strain rate following a cube-root relationship. Further extension of the work by Grady and Kipp (1980) presented one of the first continuum damage mechanics models applied to the problem of blast-related rock mass damage. The study was involved with investigating the explosive fracture of oil shale.

The basic tenets of the continuum damage approach are to represent a rock mass as a homogeneous medium containing a specified distribution of penny-shaped "Griffith" fractures of random sizes and orientations. The activation, growth and coalescence of these fractures leading to material damage have been assumed to follow certain material behaviour properties based on fracture strength and energy-absorbing fracture extension parameters.

Using a Weibull distribution of fractures, Grady and Kipp (1980) suggested the dependence of isotropic dynamic tensile damage on both the amplitude and duration of the input strain pulse (rate effects). Under dynamic behaviour, short, high-amplitude loading pulses would be expected to lead to a larger number of small flaw activations leading to finer fragmentation. Longer, lower amplitude pulses would be expected to activate only large flaws and thus lead to a distribution of larger fragments.

The application of continuum damage approaches was extended further by Yang et al. (1996) by specifying a different material failure mode for compressive and tensile mechanisms. The measure of damage was based on the reduction in elastic material modulus through the introduction of additional void volume (additional fractures). At a reduction of 22% of the original material modulus, the material was considered to be damaged such that the peak stress could no longer be supported in successive loadings.

Lui and Katsabanis (1997) suggested a continuum damage model that proposed a value of critical strain under which no fracture activation would occur. This approach bounded the model to a static stress equilibrium case and therefore fracture would be based on a critical value of volumetric strain as the fracture criterion instead of fracture strength. In addition, the damaged material would respond to consequent

external load based on damaged-induced degraded values of Young's Modulus (E) and shear modulus (G).

A3.2 Small-scale Blast Simulation Models

A large amount of information on the dynamic behaviour of rock and rock-like materials has been gained through laboratory impact testing of materials using gas guns, high displacement-rate hydraulic jacks and the Split Hopkinson Pressure Bar. These methods of material loading are typically repeatable and well controlled, but do not generate the highly variable and time-dependent dynamic stresses observed in rock breakage using explosives. Therefore, previous researchers have performed scaled blasting tests on various rock-like materials to more accurately examine the effect of explosive loading on the dynamic fracture process.

The first important consideration for a scaled blasting test is the selection of an appropriate material for testing. Several material characteristics should be considered when attempting to model rock response to blasting. Some of these properties are:

- Compressive and tensile strength (static and dynamic)
- Elastic constants
- Wave transmission characteristics
- Material homogeneity
- Other physical properties (e.g. fracture toughness or fracture energy)

In general, past scaled blasting studies have utilised homogeneous materials such as glass, Plexiglas or Homalite, semi-homogeneous materials such as cement or concrete or rock blocks extracted from exposed excavation surfaces. Each type of material faces testing constraints based on the available size, mechanical behaviour and scale-dependent effects.

A3.2.1 Small-scale Tests in PMMA

One attribute that was highly sought after in early explosive-fracture tests was the ability to observe the fracture patterns during and after the tests. Transparent materials such as glass and Plexiglas (otherwise known as PMMA, Polymethyl-methacrylate and Perspex) were therefore used. Comparisons by Kutter and Fairhurst (1971) of the behaviour of PMMA plates and rock samples illustrated comparable fracture patterns formed in the two materials. The similarities justified the use of acrylics in subsequent blast fracture studies. An additional attribute of the transparent acrylics was the ability to visualise stress bands in the material through polarisation of light. This property led to early observation of stress wave interaction with fractures and material boundaries.

In the early 1970s, scaled blasting tests using PMMA formed the basis of the understanding of the explosive fracture process and the contribution of dynamic stress waves and gas penetration on explosive fracture. In 1971, Kutter and Fairhurst conducted a series of experiments to investigate the role of shock energy and fluid penetration on the dynamic and quasi-static fracture process of Plexiglas plates and rock. Many important research outcomes were presented in the work, including the influence of in situ stress on the dynamic fracture process. The work of Kutter and Fairhurst was discussed in Chapter 2.

Field and Ladegaard-Pederson (1971) investigated the role of the reflected stress wave on the fracture process in small-scale PMMA blocks under various burdens and surface conditions. The basic experimental setup used in the scaled blasting tests is illustrated in Figure A3.2.

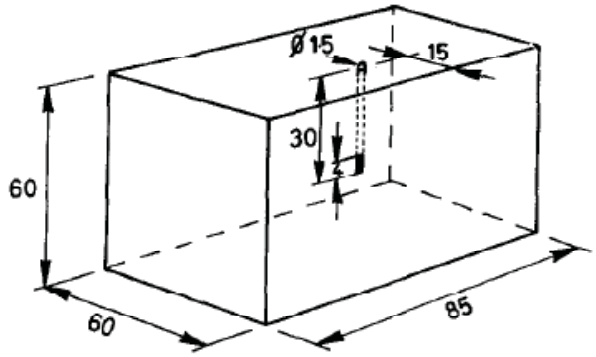

Figure A3.2. Scaled blasting test setup for Perspex blocks (60mm x 60mm x 85mm) to investigate spallation and reflected tensile wave damage from a 1.5mm charge of lead azide/lead stypnate (Field and Ladegaard-Pederson, 1971).

The results of the scaled blasting tests identified the influence of the reflected stress wave on the formation of radial fractures parallel to the free face. In addition, preferential extensions of single fractures were observed in directions towards the free face due to stress unloading at the crack tip. A series of experiments on the influence of the free face on the reflected wave identified diffraction and focusing of the reflected stress wave as a function of face shape. Tests conducted under infinite material matching conditions (immersion of the model in an acoustically-matched fluid) demonstrated a regularly-distributed fracture pattern commonly observed in larger models unaffected by wave reflections.

Daehnke et al. (1996) conducted investigations into the discrete role of shock and gas penetration on fracture formation in PMMA blocks to calibrate a numerical model characterising explosive-driven gas flow. Two cases were examined in the block-scale study. The first case allowed the explosively-generated gases to vent to the atmosphere prior to the development of the quasi-static cavity pressurisation to

simulate weak stemming in the blasthole. The second case sealed the explosive charge into the block to allow full containment of the developed gas pressure and facilitate gas-driven fracture extension.

In the stemmed test, a regularly-spaced radial fracture pattern of 3 planar cracks was formed. The crack surfaces were smooth, suggesting stable fracture growth and rapid arrest. The confined test exhibited a very complex fracture pattern, with conical fractures formed at the endpoints of the explosive charge. Results of numerical modelling of the process revealed that at a fracture velocity of 100m/s, the fractures were rapidly outpaced by the stress wave. As a result, only 8% of the fracture length could be attributed to the direct stress wave. Therefore, the contained gas pressure extended the fractures an additional 92% of the final length (Daehnke et al., 1996).

Rossmanith et al. (1997) extended the work conducted by Daehnke et al. (1996) by presenting an approach to predict fracturing and explosive-induced damage through the combined effect of wave propagation modelling and gas flow numerical modelling. The initial physical model consisted of PMMA blocks of 250mm x 250mm x 240mm size, blasted with 3mm diameter cylindrical charges of PETN, 66mm in length. The results of the modelling work identified the complex relationship required for representation of explosively-driven gas flow simulation. Incorporation of several disciplines such as fluid mechanics, elasticity, fracture mechanics and heat transfer were deemed necessary to reach a numerical solution. No analytical solution was found to exist for the complex loading conditions.

A3.2.2 Other Materials Used in Scaled Blasting Models

Scaled blast-induced fracture modelling in acrylic materials is generally bound by model size limitations due to the manufacturing process of the material and differences in the scale-dependent material properties when compared with rock. Therefore, test blasts have also been performed in cement and concrete samples to increase the size of the scaled model and explosive charges. The use of a larger model simulates the material properties and loading conditions more closely to the realistic blasting case. Cement and concrete generally have repeatable and adjustable physical properties based on the percentages of the constituents and aggregates added to the mixture. Therefore, a degree of material homogeneity can be gained, but with properties more closely related to those of rock.

A3.2.2.1 Cement and Concrete Blasting Models

Researchers in the past have conducted scaled-model explosive breakage experiments using concrete blocks of various engineered properties to simulate desired rock characteristics. Due to the great difficulty in obtaining large, intact samples of rock, cast concrete slabs and blocks have been used to more closely

replicate rock properties. Some of the advantages of using cast geoengineered material blocks include:

- High degree of homogeneity
- Reproducible strength properties
- Ability to cast transducers into the block to assure good coupling
- Sample size and shape flexibility

The results of blasting tests on cast cement and concrete samples have provided great insight into the fracture patterns resulting from single or multiple-hole blasts (e.g. Wilson and Hollaway, 1987), the role of shock and gas in explosive fracturing and fragment size distribution (e.g. Singh, 1999), the effect of discontinuities on fracture and vibration propagation (e.g. Bhandari, 1979; Tariq and Worsey, 1996; Singh and Narendrula, 2004) and calibration or validation of numerical models (e.g. Iverson et al., 2009; Sellers et al., 2009). Figure A3.3 illustrates the use of a cement model to investigate blast-induced fracture patterns under the influence of horizontal jointing.

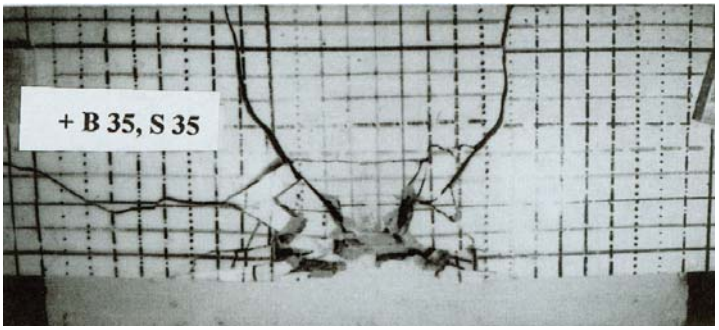

Figure A3.3. Top view of fracture pattern in cement model with simulated horizontal bedding (Bhandari, 1996).

Scaled blasting tests on concrete and cement blocks with controlled material properties have contributed significantly to the understanding of blast-induced fracture. Concrete models are a useful tool for understanding material behaviours under dynamic loading and are still utilised for calibrating high-level numerical models such as the HSBM code developed at the JKMRC in Queensland, Australia (Iverson et al., 2009; Onederra et al., 2009; Sellers et al., 2009).

A3.2.2.2 Rock Blocks and Field-Scale Blasting Tests

The next step in accurately investigating blasting-induced fracturing is scaled testing on rock blocks and slabs. Rock samples suitable for medium and large-scale blast testing should be free of dominant discontinuities and orientation-biased anisotropies. The rock types suitable for extraction of large, intact blocks are typically limited to highly homogeneous igneous or metamorphic rocks such as

granite or marble. Sedimentary rocks such as limestone and sandstone with thick bedding can also be utilised.

Of the published research on scaled rock block tests, some of the notable works include Bergmann et al. (1973), Singh (1999) and Olsson et al. (2002). These investigations generally supported the observations of the behaviour of explosively-driven fracture formation and propagation in PMMA and concrete models. The extent of damage and the breakage mechanisms were specific to different rock types blasted with more realistic charge diameters and geometries. Due to the use of rock blocks, investigation into anisotropy-associated breakage effects became important to more accurately translate the results into realistic blasting conditions.

From review of the published literature, the work conducted by Bergmann et al. (1973) presented one of the most complete data sets that investigated the effects of rock type, explosive properties, burden dimension and decoupling on the transmitted pressure pulse and fragmentation. The research conditions were such that blasting of small diameter charges took place under realistic charge to burden ratios. The tests of Bergmann et al. (1973) revealed a significant difference in pressure attenuation and fragment size distribution for a series of tests on granite, limestone and sandstone. A series of empirical pressure and fragment prediction equations were presented for each rock type, contributing a great deal of information to the effect of explosive properties, geometry and rock type on blasting performance. The general experimental setup is illustrated in Figure A3.4.

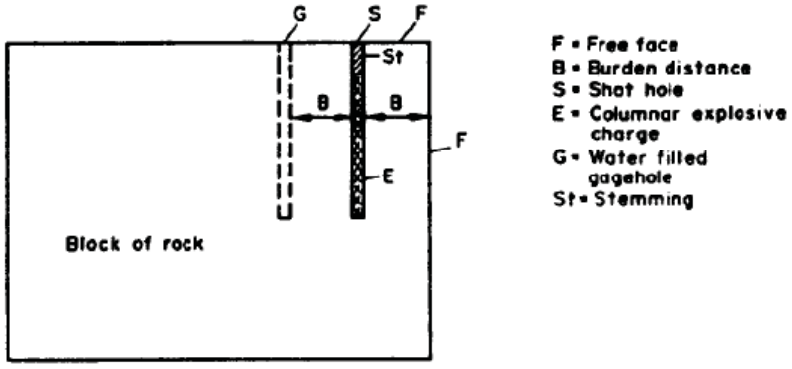

Figure A3.4. Block-scale experimental setup used by Bergmann et al. (1973) to investigate the effect of explosive properties and rock type on fragment size.

A3.2.3 Limitations of Scaled Blasting Tests

Care must be taken to consider the effects of experimental geometry and size when attempting to translate the results of scaled blasting tests into field-scale conditions. The influence of free faces on wave reflection and fracture propagation within model plates or blocks also becomes important. These factors can significantly influence

fracture propagation, especially when the mode of breakage is being investigated (stress wave versus gas penetration mechanisms).

A3.2.3.1 Model Geometry and Material Properties

To study field blasting conditions on a reduced scale, blocks of representative burden dimension of approximately 10-35 times the borehole diameter are recommended to avoid complete disintegration of the sample upon testing. If commercially representative explosive types are used, the issue of critical diameter adds greater restriction on the model size. For high explosives, borehole diameters as small as 3mm to 6mm may be used, requiring blocks of 30mm to 210mm burden dimension and 60mm to 420mm length and width. For commercial blasting agents such as emulsions, watergels or ANFO, critical diameter values are much larger than for high explosives; of the order of 15-35mm. Commercial explosives would therefore require much larger intact blocks in order to contain the explosion.

Typically, blocks of rock suitable for scaled block tests are monolithic and nearly homogeneous in nature such as those rock types used in dimension stone or large decorative construction applications. These rock types are generally free from persistent jointing or bedding, and contain a distribution of only fine micro-cracking. In full-field applications, in situ discontinuities greatly influence fragmentation and stress wave transmission. Under certain conditions, the pre-formed block size from existing discontinuities will dominate the blast-induce fragmentation. Explosive energy is therefore used only to dislocate the pre-existing fracture pattern.

A3.2.3.2 Specific Limitations of Scaled Models

Although small-scale blasting investigations in quasi-brittle material blocks provide significant insight into the breakage process, dynamic loading and geometric constraints should be investigated prior to prediction of full-scale behaviours. Some of the specific considerations of mine-scale blasting when compared with scaled blasting tests on isolated samples include:

- Ideal loading mechanisms will not reflect non-ideal energy release
- Bulk rock mass properties vary largely over two orders of scale magnitude
- Boundary conditions in mining are more complex than in scaled testing
- Bedding, jointing or faulting greatly influence the behaviour of rock-masses
- In situ and induced stresses influence rock mass fracture behaviour
- Borehole wall conditions are rarely regular shaped and smooth

In a series of papers published by Rossmanith et al. (2005), the effects of explosive properties and sample shape on the explosive-generated wave field were

investigated. The wave modelling identified a very complex interaction between sample boundaries and the wave fields contributing to fracture propagation and arrest (Figure A3.5). Based on this work, only model conditions simulating an infinite boundary using momentum traps or other methods of matching acoustic impedance can be deemed as directly translatable to the semi-infinite field conditions.

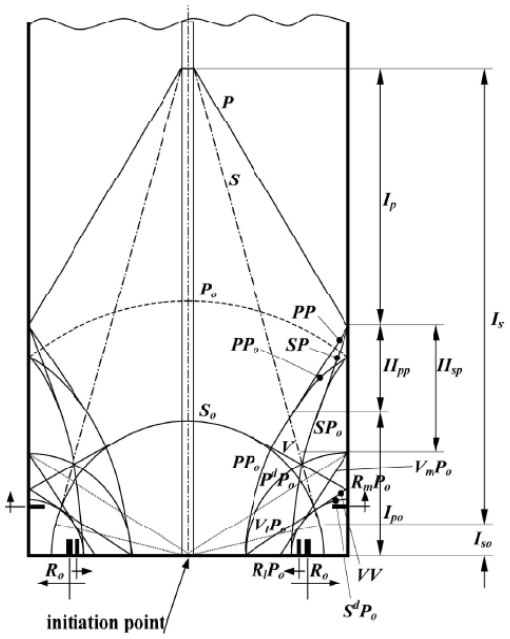

Figure A3.5. Section view of the complex wave-field generated at the sample boundaries for a continuous column charge under supersonic detonation conditions in a cylindrical sample (Rossmanith et al., 2005).

A3.2.3.3 Effect of Borehole Liners on Wave Propagation

Variations in the generated wave fields are of increasing importance in scaled blasting studies investigating the contribution of stress waves and gas penetration on fracturing using steel borehole liners (e.g. Brinkmann, 1990 and Singh, 1999). Changes in acoustic impedance at the borehole wall due to the presence of the steel liner modify the wave fields in the block material during and after detonation. No mention has been made in such studies to account for the alteration of the stress wave due to the lined borehole conditions.

A3.3 Field Scale Damage Investigations

Of the available published studies on blast-induced fracturing, studies conducted under actual field blasting conditions yield the best indication of fracture formation under mining geometries. Field investigations have been conducted for over 5 decades to study the effect of explosives and rock mass properties on the extent of blast-induced fracture near remaining excavation surfaces (e.g. pit faces, stope walls

and tunnel or drive boundaries). The importance of characterising and minimising blast-induced damage and its impact on rock mass stability in both the underground and open pit environment have led to a number of valuable insights into the interaction between explosive charges and rock masses.

Over the last 50 years, numerous blast damage studies have been conducted in both the open pit and underground mining geometries. Some of the available studies investigating damage caused by dynamic loading from blasting include Siskind et al. (1973), Holmberg and Persson (1978), Forsyth (1993), Li (1993), Liu and Proulx (1995), Villaescusa et al. (1997), Scott (1998), Keller and Kramer (2000), Olsson et al. (2002), Singh and Narendrula (2004) and Kilebrant et al. (2009).

The geometries and blasting conditions represented in the body of work cover a broad range, from open pit investigations in granite quarrying (e.g. Siskind et al., 1973 and Holmberg and Persson, 1978) to underground development rounds and tunnelling (e.g. Brinkmann, 1990; Forsyth, 1993; Singh and Narendrula, 2004) and finally underground mass mining (e.g. Scott, 1993 and Liu and Proulx, 1995). In all of the published works, an overall degradation of rock mass condition has been observed in the remaining excavation surface (and for some depth within). The extent of damage can range from tens of centimetres using small diameter charges typical of tunnelling up to tens of metres, typical of large-scale open pit mining. Some of the field-scale experimental setups are illustrated in Figures A3.6 to A3.8.

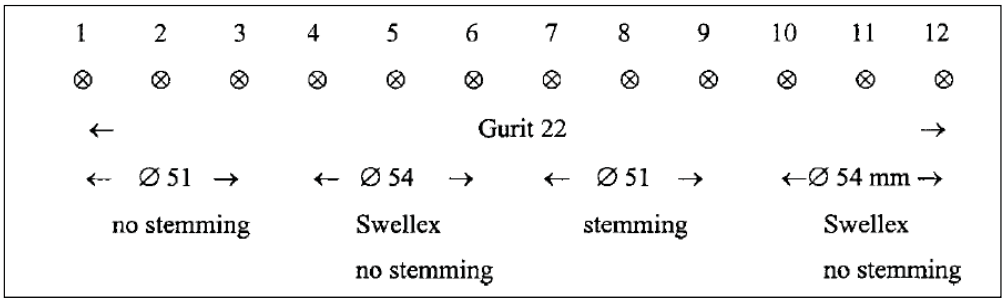

Figure A3.6. Field setup for blast damage testing in a granite quarry for various charge diameters under stemmed and unstemmed conditions (Olsson et al., 2002).

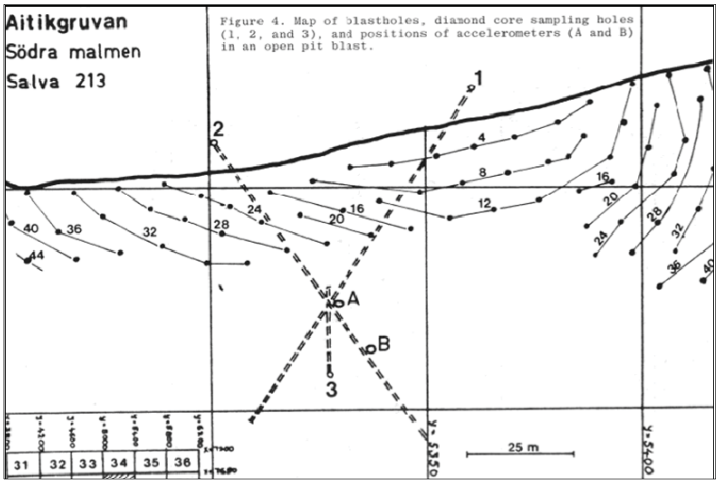

Figure A3.7. Experimental setup used by Holmberg and Persson (1978) to investigate blast damage in relation to measured vibration.

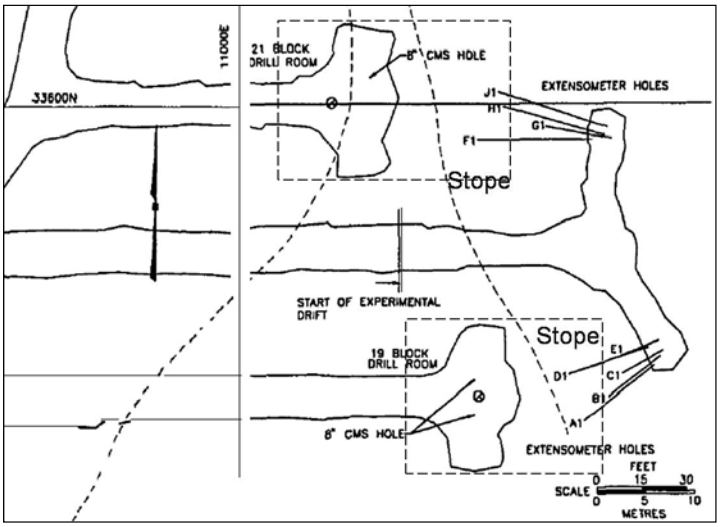

Figure A3.8. Underground open stoping blast damage study as illustrated by Liu and Proulx (1995).

The cases involving investigation of damage in sublevel open stoping have been reviewed extensively, as these were most relevant to the author's blast damage investigation. In general, the studies of production blasting in sublevel open stoping have revealed blasting and stress-induced damage occurring several metres beyond the stope perimeter (such as that found by Li, 1993 and Villaescusa et al., 1997).

The blast-affected damage zones in most underground experimental studies cannot be separated from the stress-affected zones. Observations and measurements of fracturing and damage typically occur under combined loading conditions. This highlights the complexity of the loading conditions under which rock masses are damaged in the presence of in situ stresses.

APPENDIX 4 : ADDITIONAL DETAILS OF NEAR-FIELD BLAST MONITORING PROGRAMS

A4.1 Transducer Types: Accelerometers 378

A4.1.1 Operational Considerations for the Use of Accelerometers in Near-Field Blast Monitoring 379

A4.1.2 Accelerometers used in Published Vibration Monitoring Studies 380

A4.2 Transducer Types: Geophones 381

A4.3 Integration of Multiple Transducer Types 383

A4.4 Selection of the Number of Components for Blast Monitoring 384

A4.4.1 Uni-axial Transducer Blast Vibration Monitoring 385

A4.4.2 Bi-axial and Tri-axial Blast Monitoring 386

A4.5 Consideration on Coupling of Transducers 386

A4.5.1 Matching of Coupling Acoustic Impedance 387

A4.6 Data Acquisition System Requirements 387

A4.6.1 Gain, Sensitivity, Resolution and Sampling Rate 388

A4.6.1.1 Impacts of Under-Sampling 391

A4.6.2 Data Storage Characteristics 392

A4.6.3 Data Acquisition System Triggering Mechanisms 392

A4.7 Manufacturing of Tri-axial Blast Vibration Monitoring Transducers for the Thesis Blast Monitoring Program 394

A4.8 Thesis Blast Vibration Monitoring Data Acquisition System Specifications 396

A4.8.1 Instantel Minimate Plus 397

A4.8.2 Custom-Built Junction Box 397

A4.8.3 Protection of Data Acquisition Systems Underground 398

A4.9 Installation of Near-Field Vibration Transducers in the Underground Environment 399

A4.9.1 Installation Challenges Related to Water 400

A4.1 Transducer Types: Accelerometers

Accelerometers are transducers that contain a piezoelectric element (typically quartz or ceramic crystal) which deforms under load, resulting in alignment of charged ions. As the piezo element is deformed through acceleration of an attached reference mass, an electrical output is produced that is proportional to the deformation. Several mechanical configurations can be utilised which allow the acceleration to be measured from the piezoelectric effect. Three of these configurations include compression, shear and flexural deformation of the piezo element. Figure A4.1 illustrates different piezo element configurations used in accelerometers.

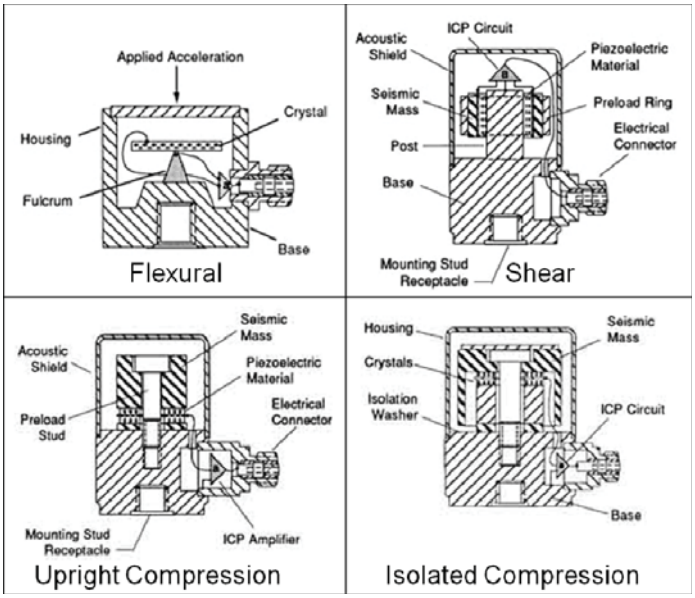

Figure A4.1. Piezo element configurations in a number of different accelerometer functionalities (PCB Group 1999-2008).

Because large mechanical motions are not required to produce the output voltage from the piezo elements, wide frequency and amplitude response ranges are measurable. Also, the lack of moving internal parts allows accelerometers to withstand large shock loads without sustaining physical damage. The general advantages and disadvantages of accelerometers used in vibration monitoring applications are well documented (e.g. Andrieux and Heilig, 1994).

One of the main advantages of accelerometers in measurement of blasting vibrations is the superior linear frequency response range when compared with other transducer types. To accurately measure high frequency vibration events in the near-field of blasting where wave frequencies can reach tens of thousands of Hertz, the frequency response is critical. Figure A4.2 illustrates the frequency response curve for the Brüel and Kjaer model 4371 uni-axial accelerometer component with a dynamic range of 6,000g (Brüel and Kjaer, 2005).

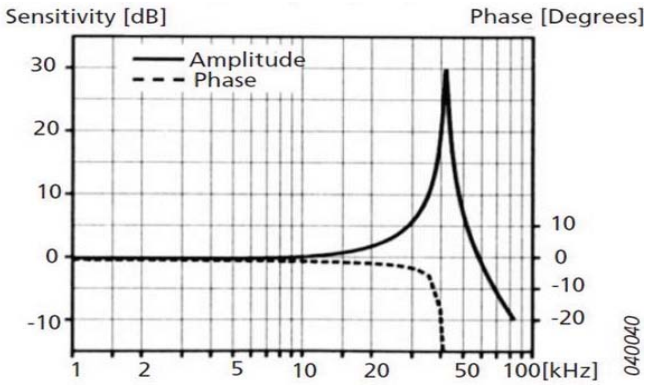

Figure A4.2. Frequency response curve for Brüel and Kjaer model 4371 uni-axial accelerometer (Brüel and Kjaer, 2005).

A4.1.1 Operational Considerations for the Use of Accelerometers in Near-Field Blast Monitoring

Due to the electronic circuitry required to amplify and condition the voltage output of an accelerometer, the expected dynamic amplitude range is a critical selection factor to reduce the likelihood of transducer saturation. When an accelerometer is exposed to a vibration level in excess of the dynamic range, the conditioning circuits are exposed to excess voltage and must discharge to the baseline carrier voltage to resume normal function. As observed in the author's blast monitoring program, this discharge time can lead to lost vibration signals or excessive DC offset in the vibration trace resulting in successive saturations or unrealistic low frequency content. The time required to return to the carrier voltage baseline can vary from several milliseconds to tens of milliseconds based on the discharge circuitry. A waveform collected as part of the author's blast vibration monitoring program that experienced significant accelerometer saturation is shown in Figure A4.3.

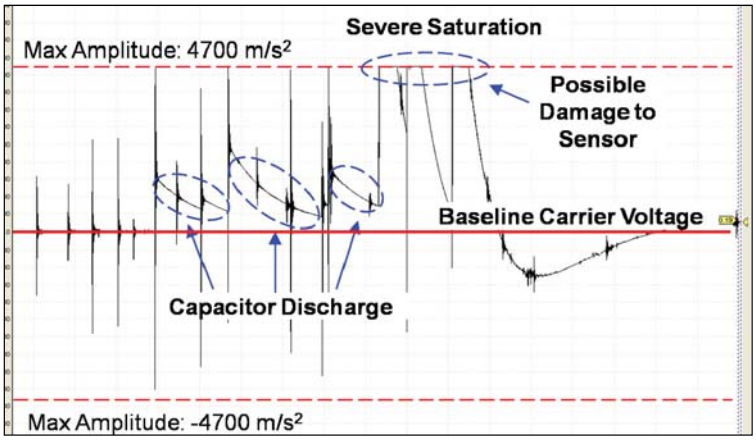

Figure A4.3. Saturation of a 500g accelerometer in the BHP Cannington Mine stope 24jC6HL, causing distortion of the acceleration signal.

Some waveform post-processing approaches do exist for treatment of saturated accelerometer signals. Saturation of an accelerometer waveform can be marginally amended through use of frequency filters or amplitude offsetting to return the signal to the baseline axis as illustrated in Figure A4.4. This type of treatment will inevitably lead to an erroneous loss in frequency content or misrepresentation of the amplitude in the saturated portions of the waveform. Consequent mathematical calculation of velocity or displacement could therefore suffer due to compromised frequency content.

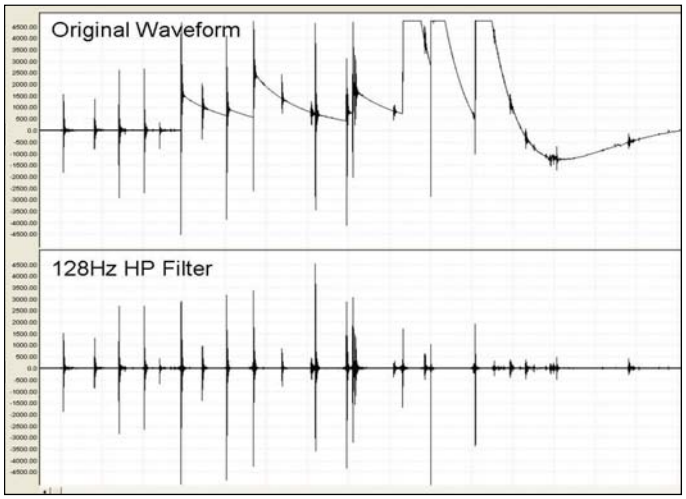

Figure A4.4. High-pass (HP) frequency filtering of saturated accelerometer signal to remove saturation-related voltage offsets for a winze blast at the Cannington Mine.

An additional operational constraint of accelerometers is the sensitivity to electrical noise from cable disturbance and physical abuse of monitoring components. In the event that cables are struck by rocks falling from drive surfaces, false voltage spikes can be generated and recorded during blasting. In some cases, these peaks can be identified based on the design firing times within the blast or due to the non-oscillatory shape (sharp single spike). Where cable disturbance occurs during the blasting event, no effective method exists to isolate the false peak outside of manual deletion from the waveform.

A4.1.2 Accelerometers used in Published Vibration Monitoring Studies

In past vibration monitoring studies using accelerometers, no standard unit or design has been applied. Due to the specialty application of accelerometers and near-field blast monitoring, a number of uni-axial, bi-axial and tri-axial configurations have been employed. In general, all of the systems outlined in the research include a method of transducer encasement, coupling and cabling within boreholes for installation close to blasting events. Figure A4.5 shows a number of accelerometer configurations used in near-field blast monitoring published in the literature.

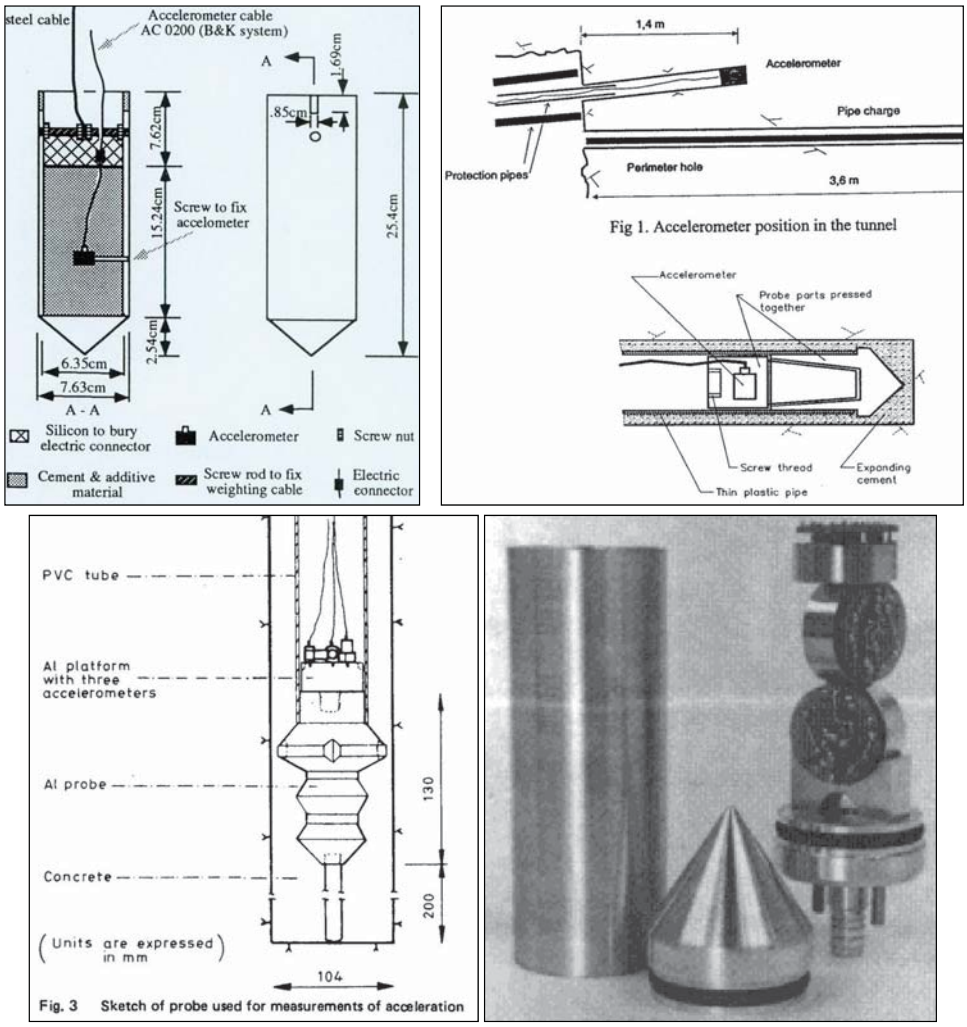

Figure A4.5. Uni-axial accelerometer sondes used by Yang et al., 1993 (top left) and Bogdanoff, 1996 (top right) and tri-axial accelerometer sondes used by Holmberg and Persson, 1979 (bottom left) and Sprott and Kitzinger, 1988 (bottom right).

A4.2 Transducer Types: Geophones

Geophones have been used successfully for measurement of blast-induced vibration for almost 6 decades. Several characteristics of geophone transducers make them attractive for use in blast vibration monitoring, especially in the underground environment. These characteristics include robust construction, low sensitivity to exterior sources of electrical excitation and isolation from signal distortion from cable disturbance.

The general, mechanical operation of a geophone consists of a magnet of given mass attached to a stiffened spring, moving relative to a wire-wound coil. As the magnet moves through the coil, a voltage is induced that is proportional to the velocity of motion. Figure A4.6 illustrates the interior components of a geophone transducer.

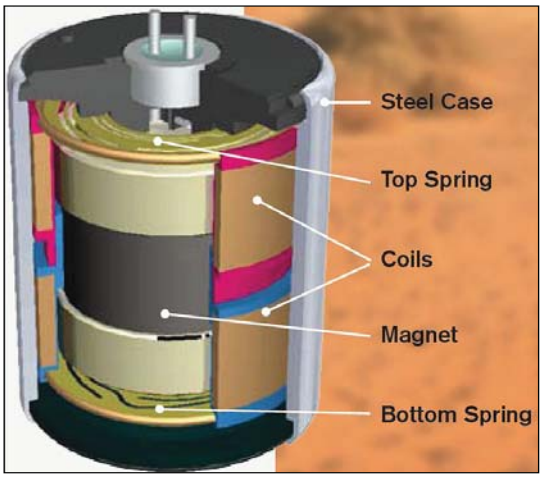

Figure A4.6. Internal design of I-O SENSOR SM-24 Geophone (Anon, 2006).

In contrast to the complicated circuitry required for signal amplification and conditioning of accelerometer signals, geophones require only simple data acquisition circuits. The robust construction of the geophone element and the relatively large voltage output over the useful dynamic range enables the transducer to experience minimal sensitivity to extraneous voltages or cable-induced noise. For these reasons, geophones have been the preferred choice of transducer for blast vibration monitoring over many distances in open pit and underground applications.

The internal structure that allows a geophone to be marginally insensitive to mining-induced disturbances also limits its use in the near-field of blasting operations. In general, geophones provide limited dynamic amplitude and frequency response when compared with accelerometers. Typically, the limited frequency response constrains geophone use to intermediate-field and far-field vibration monitoring.

The linear frequency response range of a majority of geophone elements is limited to moderate frequencies between 50 and 500 Hz in contrast to accelerometers of linear response from 0.5 Hz to 100 kHz. In the case of small charge weights or blasting in competent rock masses, near-field vibration frequencies can reach tens of thousands of Hertz. In large hole diameters using large charge weights, the frequency of vibration can approach or fall below the resonant frequency of the geophone, which is generally between 4 and 28Hz in most commercial models. Therefore, only a limited frequency range can be reliably represented by a geophone, as illustrated in the voltage-frequency response curve shown in Figure A4.7.

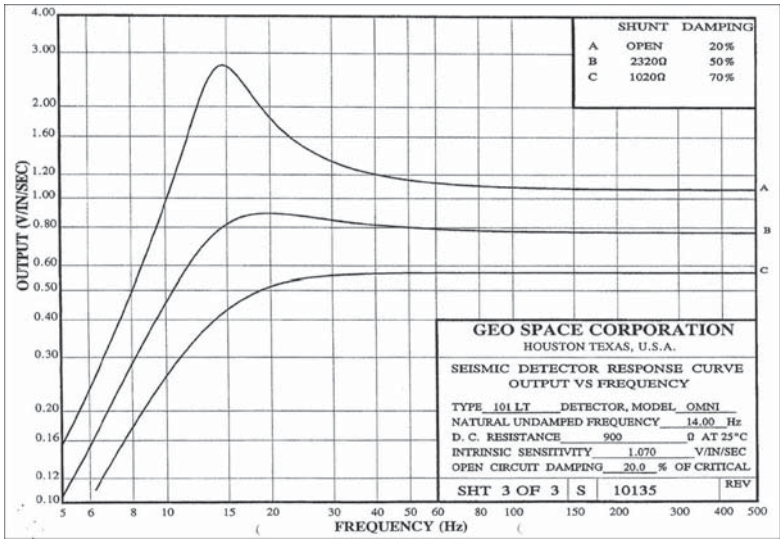

Figure A4.7. OYO Geospace 101LT 14Hz geophone standard voltage-frequency response curves (OYO Geospace, 1997).

An individual geophone unit is typically uni-axial in operation. Two or three separate units are therefore required to construct a multi-axial sonde. In most cases, geophone sondes are larger than accelerometer sondes based on the mechanical motion required to generate the output voltage. Depending upon the dynamic range and the resonant frequency, geophone units can vary greatly in size. Figure A4.8 illustrates several tri-axial geophone sondes owned by WASM for use in underground blast monitoring designed for mounting to the surfaces of excavations.

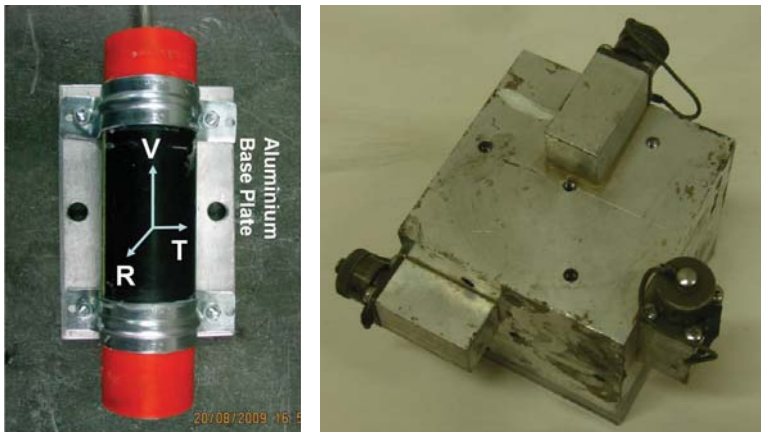

Figure A4.8. WASM-owned tri-axial geophone sondes on aluminium bases for underground monitoring on excavation surfaces.

A4.3 Integration of Multiple Transducer Types

Amongst the published blast vibration monitoring studies, an overwhelming majority of projects have employed geophones in near-field, intermediate-field and far-field

applications. Accelerometers have been utilised in a number of studies to more accurately measure the vibrations in the extreme near-field or near-field regions of tunnel blasting, quarry blasting, underground open stoping or test blasting (e.g. Holmberg and Persson, 1978; Sprott and Kitzinger, 1988; Yang et al., 1993; Bogdanoff, 1996), but monitoring systems utilising both accelerometers and geophones concurrently over a range of distances are rare in the published literature. In most applications where transducer types are combined, the main objective is to compare the individual transducer outputs to assess their suitability over a range of monitoring distances (Heilig, 2005) or to compare measured waves to predicted wave properties such as acceleration, velocity and strain (Nicholls and Hooker, 1964).

Mixture of transducer types in field applications can be complicated due to the differing electronic and powering requirements between geophones and accelerometers and the variations in signal output and response. Comparisons performed by Heilig (2005) showed large variations between the amplitude, frequency and number of recorded peak vibration traces recorded by an accelerometer and geophone in side-by-side monitoring. The variation between the two transducer output signals could be associated with the differences in amplitude and frequency ranges and responses.

Due to the complications introduced in field application and post-processing of two different input types, mixing of transducers is generally avoided. Intelligent design of the data acquisition system and strict post-processing controls can allow a blast monitoring system to be produced that is capable of measuring large ranges in amplitudes and frequencies, but at a reduced cost due to the use of geophones in place of accelerometers at larger distances.

A4.4 Selection of the Number of Components for Blast Monitoring

The initial selection of transducer type and required response characteristics depend on the expected amplitudes and frequency spectra generated by the blast at the point of monitoring. The distance range over which monitoring will be implemented is therefore influenced by the data requirements and the use of the data once it is collected. The data collected during a blast monitoring program can be used for a number of different purposes including regulatory compliance, blast diagnostics, blast vibration attenuation investigation and blast damage investigations.

The desired application of the collected data strongly influences the selection of the number of components used to measure the vibrations at a single monitoring point. The most common configurations of blast vibration monitoring transducers are uni-axial, bi-axial and tri-axial. To fully characterise blasting vibrations as a vector

quantity, tri-axial measurements are required. Any monitoring program that measures blasting vibrations using uni-axial or bi-axial configurations would therefore fail to fully characterise the wave field.

A4.4.1 Uni-axial Transducer Blast Vibration Monitoring

The most basic use for vibration monitoring is investigation of blasting performance through blast diagnostics. This type of analysis uses the arrival of seismic waves generated by explosive charges to indicate the time of firing of each charge or to compare the relative amplitude contributions between multiple charges. This approach is useful to diagnose issues related to misfires, sympathetic detonation, blasthole timing and blast geometry. Over a series of firings, chronic misfires indicated within a common region within multiple blasts can reveal issues with hole interaction or insufficient burden or spacing. Identification of misfires can also aid in understanding blast performance issues and help to indicate the presence of undetonated explosive products in the muckpile or within the remaining drillholes. Figure A4.9 illustrates the presence of misfired holes within a multi-hole blast.

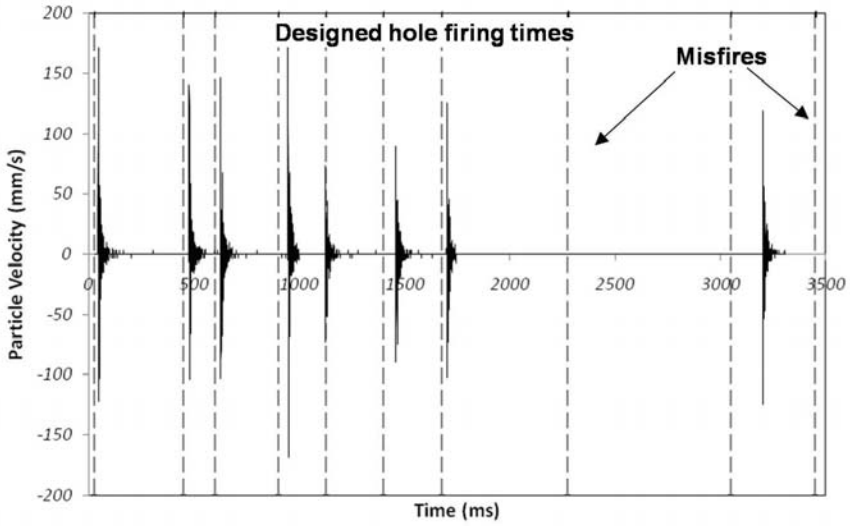

Figure A4.9. Blast vibration monitoring indication of blasthole misfires, BHP Cannington stope 22gC6HL long-hole winze firing.

A number of published studies investigating blast damage or wave attenuation in the near-field of blasting events have utilised uni-axial transducer configurations either coupled within a borehole (e.g. Yang et al., 1993; Rorke and Milev, 1999) or mounted to the surface of an excavation (Yu and Vongpaisal, 1996). In general, this configuration has been employed to measure the radial component of vibration when fully encapsulated in a borehole or the surface-normal component when mounted to the surface of an excavation. Uni-axial monitoring results should not be compared with full-field tri-axial vibration measurements.

There is typically no direct relationship between a uni-axial measurement and the full-field wave behaviour characterised by tri-axial measurements, but full-field correction factors have been suggested when uni-axial measurements have been performed (Yu and Vongpaisal, 1996). Andrieux and Heilig (1994) performed analysis of uni-axial versus tri-axial blast monitoring on the surface of an excavation, and identified a situation where uni-axial monitoring failed to accurately represent the blast. In analysis of the full-field vibration (tri-axial monitoring), the single component monitoring orientation failed to measure the event due to a lack of adequate particle motion along that axis of motion.

A4.4.2 Bi-axial and Tri-axial Blast Monitoring

The next step in blast monitoring complexity is the application of bi-axial monitoring. This configuration consists of two uni-axial elements mounted perpendicularly to one another. Bi-axial monitoring can be useful when only radial and either transverse or vertical components are of interest. Fully-encapsulated installations of bi-axial transducers are generally oriented such that the radial and vertical components are recorded. Through analysis of waveforms collected during the author's blast vibration monitoring program, no correlation has been observed between the separate vibration components in complex near-field blast waves. For this reason, tri-axial monitoring is essential to fully represent the vibration waveform and investigate the true wave motion (Andrieux, 1996).

A4.5 Consideration on Coupling of Transducers

Transducer-to-ground coupling mechanisms are well researched in surface blast monitoring. Guidelines for mechanical or chemical coupling as well as response spectra for different coupling mechanisms in open pit monitoring have been established (e.g. Grogan, 1998; Brochu and Eltschlager, 1999; Adhikari et al., 2005). In underground blast monitoring, such studies and guidelines do not exist. This lack of information is evident in the large variety of coupling mechanisms used in published underground vibration measurement studies, leading to a large variation in data quality.

Of the available transducer coupling mechanisms available for underground blast monitoring, the most commonly used are mechanical, chemical or a combination of mechanical/chemical coupling. Full encapsulation of transducers within a rock mass delivers the most accurate vibration monitoring results (Andrieux and Heilig, 1994) by removing coupling resonance effects. Only fully-encapsulated coupling has been reviewed and recommended for use in the blast monitoring program conducted as part of this thesis at the Kanowna Belle Gold Mine and the Cannington Mine.

A4.5.1 Matching of Coupling Acoustic Impedance

One characteristic that should be considered for underground blast vibration monitoring is the difference in acoustic impedance between the rock mass and the coupled transducer. Acoustic impedance concerns can be addressed in many systems by the use of aluminium coupling components, due to the close acoustic properties of aluminium when compared with many competent rock types. Severe mismatches in impedance between the rock mass and the transducer mount can result in a loss of transmission through the coupling from wave reflection, refraction or diffraction at the material interface.

For fully-encapsulated transducers, densification of the chemical or cement grout with tungsten (Brinkmann, 1990), aluminium (Yang et al., 1993), steel, slag or other materials can aid in matching the acoustic impedance with the rock mass and ensure more accurate monitoring results. Due to the expense and logistical problems associated with thickened or densified cement grout mixtures, most full-encapsulation applications use either standard Portland cement or various quick-setting, non-shrink cement formulations.

In the blast vibration monitoring program conducted in this thesis, application of densified cement grout mixtures was not considered feasible due to the large amount of cement grout required (tonnes) and the methods of mixing and delivery of the cement grout to the instrumentation holes. Two different types of standard cement grout have been used in the blast monitoring program depending on the supplier at each sponsor site. The two types of cement grout used for transducer encapsulation were standard low-heat Portland cement with batch-mixed accelerant at Kanowna Belle Gold Mine and special low-heat non-shrink cement with added fly-ash at the Cannington Mine. These cement grouts were typically mixed at water to cement ratios of 0.4:1 to 0.45:1 to allow adequate flowability and full hydration and strength development.

A4.6 Data Acquisition System Requirements

Following the selection of the type and configuration of transducers that fulfil the amplitude and frequency response requirements for the desired monitoring applications, data acquisition equipment must be selected. The acquisition system must be capable of adequately recording the transducer output. The main parameters of a data acquisition system that influence the quality of the measured vibrations include gain and sensitivity control, signal resolution and sampling rate, data buffering, writing and storage capabilities (memory) and triggering mechanisms.

A4.6.1 Gain, Sensitivity, Resolution and Sampling Rate

The voltage output of a transducer is captured by an acquisition system through periodic sampling of the electrical signal and digitising of the data using an analog-digital converter (ADC). The sampling and resolution characteristics of the ADC define the number of data points captured per unit time and the assigned vibration level based on a specified input sensitivity. Gain settings and transducer response sensitivities control the maximum amplitude range over which values will be digitised and the associated output value based on the input voltage. Therefore, accuracy of the recorded vibration waveform is defined along the time axis by the sampling rate and the amplitude axis by the gain, sensitivity, and resolution.

Gain settings amplify or attenuate the incoming signal voltage prior to digitisation (Andrieux and Heilig, 1994). The relationship between gain and resolution is discussed below. Modern blast collection systems typically include several gain settings, which amplify or attenuate the signal by factors of 2, 4 or 8. Specialty electronics can be designed to allow a greater range in gain controls with associated voltage-output sensitivities such that electronically-damped transducers can be utilised.

Properly specifying the gain settings requires some prediction of the maximum expected amplitude from a blasting event. If the gain setting is many times greater than the actual input amplitude, the quality of the signal will be poor due to a wide interval resolution. Conversely, if gain settings are too low (expected maximum amplitude lower than that encountered), the waveform will be clipped at the defined maximum amplitude and the true peak amplitudes will be lost as illustrated in Figure A4.10.

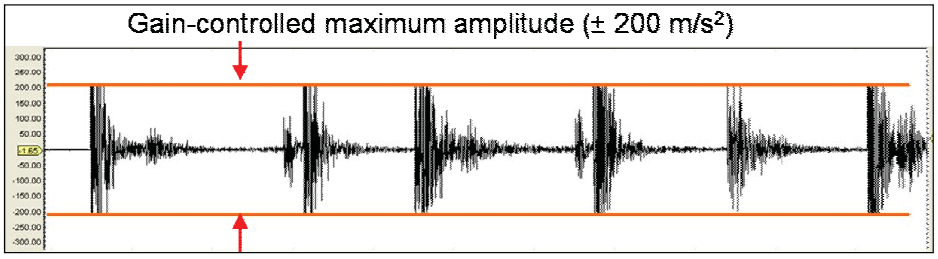

Figure A4.10. Waveform clipped at ±200m/s^2 from inadequate system gain setting.

Correct representation of amplitude is controlled by the system digitising resolution, which in general terms is related to the precision of the measurement and defined as the smallest unit which can be reliably detected (Northrop, 2005). Resolution is linked to the maximum amplitude gain setting, and is quantified by the number of encoding units over the specified maximum acquisition range. The number of encoding units (N) is defined by the relationship:

$$N = 2^{bit} \quad \text{(A4. 1)}$$

Where N = number of peak amplitude divisions over the maximum gain
bit = number of digitising bits of the ADC

Once the number of discrete intervals has been defined, the resolution of the system, R, can be calculated based on N and the specified range in desired maximum amplitude by Equation A4.2.

$$R = \frac{2A}{N} \quad \text{(A4. 2)}$$

Where A = maximum positive or negative peak amplitude
N = number of encoding intervals from Equation 4.2

Modern blast vibration monitoring equipment typically incorporates 8 to 12-bit encoding, although a number of 14, 16 or 24-bit systems have become available for specialty applications. Higher bit processors have not been widely used in mining outside of geophysical applications due to the large amount of required data storage.

Under conditions of highly variable or low amplitude vibrations, some waveforms may be poorly represented through a combination of a large gain setting and low bit resolution. Amplitudes between available resolution steps are typically rounded to either a lower or higher amplitude level, resulting in an amplitude error. Background sampling noise also becomes more problematic for lower amplitude pulses at high gain settings and low bit resolution as the expected background noise can be on the order of 1-2 resolution intervals. Sources of background noise in the monitoring system include that from passive resistors, active circuit elements, or induced transmission line noise (Northrop, 2005). Heavy waveform masking can result when low amplitude oscillations are digitised to levels equal to the background noise as illustrated in Figure A4.11.

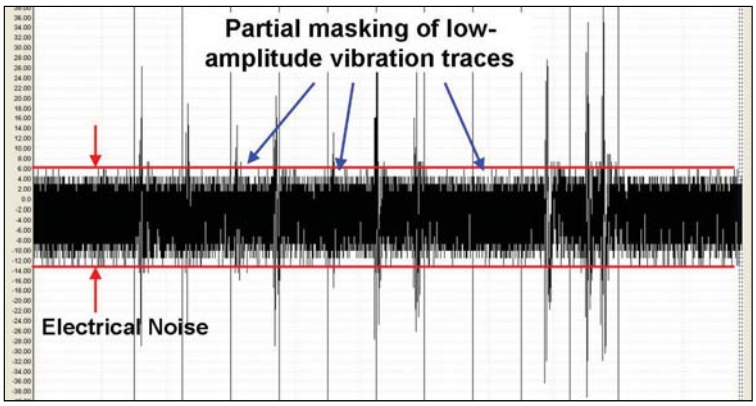

Figure A4.11. Masking of waveform due to high gain settings and coarse resolution.

The sampling rate of a data acquisition system refers to the number of discrete data points captured from the continuous analog voltage stream per unit time. For near-field blast monitoring using high-frequency response transducers, the acquisition sampling rate may be considered one of the most critical system characteristics. Systemic under-sampling of the transducer output can lead to errors in both frequency content and vibration amplitude, which will influence the accuracy of the recorded waveform. The effects of sampling rate on the peak vibration amplitude, polarity of the peak vibration and the dominant vibration frequency of a moderately high-frequency waveform are illustrated in Figure A4.12. The original single-hole radial-component waveform was measured with an accelerometer, sampled at a rate of 16 kHz. The number of sampling points was then reduced at set periods in order to represent 8 kHz, 4 kHz, and 2 kHz sampling rates.

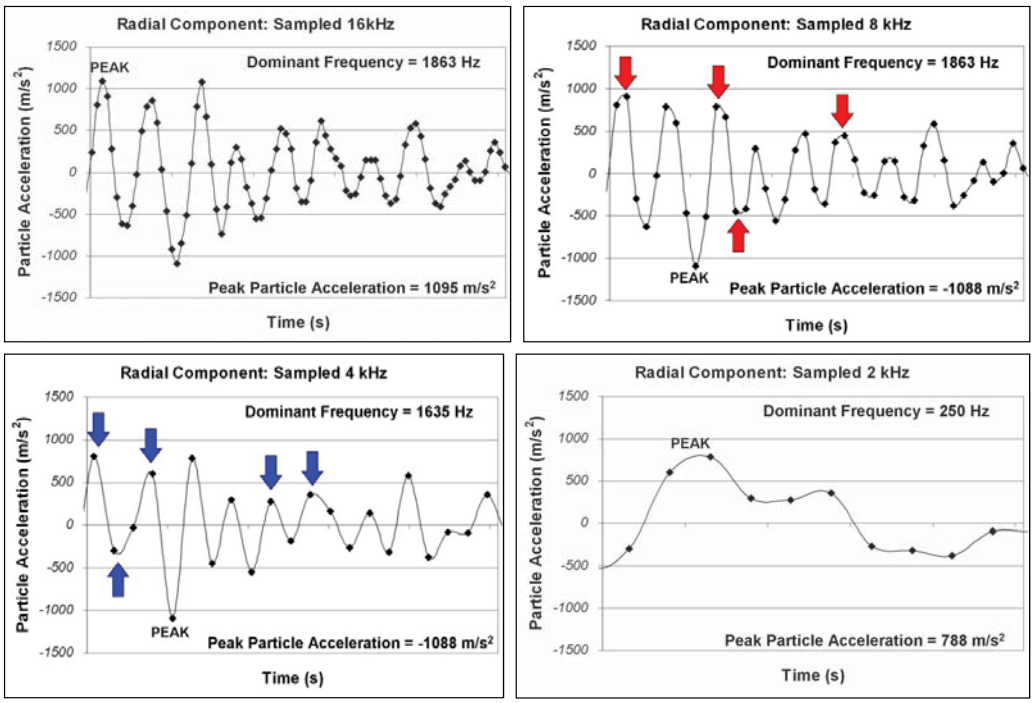

Figure A4.12. Effect of sampling rate on representation of amplitude and dominant frequency of a high-frequency near-field acceleration waveform for sampling rates of 16kHz (top left), 8kHz (top right), 4kHz (bottom left) and 2kHz (bottom right) for a common recording time of 10ms.

Figure A4.12 clearly illustrates the influence of sampling rate on the recorded amplitude and frequency. Over-sampling conditions at 16 kHz allowed the dominant waveform frequency and amplitude to be well represented, based on the number of data points defining the waveform. Once the sampling rate was dropped by half to 8 kHz, the absolute peak magnitude and frequency did not change significantly, but several effects of under-sampling were apparent. The observed effects of the reduced sampling rate on the waveform were:

- Minor peaks were underestimated (red arrows)
- Peak occurrence changed polarity from the positive to negative
- The time of the peak occurrence was shifted by approximately 1ms

As the sampling rate was further reduced from 8 kHz to 4 kHz, more minor peaks were misrepresented (blue arrows) as well as a downshift in dominant frequency of 12%. The peak amplitude and peak time remained the same as that for 8 kHz sampling. Once the sampling rate was reduced to 2 kHz, the resulting waveform was completely distorted in both frequency and amplitude. The peak amplitude changed back to positive polarity and the absolute value was reduced by 28% (down to 788m/s^2 against 1088m/s^2). The peak frequency was also reduced by 85%.

A4.6.1.1 Impacts of Under-Sampling

In vibration analysis approaches that only account for the absolute value or vector sum of a single peak particle motion (acceleration, velocity or displacement), the effects of inadequate sampling rate may not be as dramatic for moderate amplitude and frequency waveforms. In contrast, blast analysis approaches that depend on accurate reproductions of wave frequency content or polarity of peak values can be significantly influenced by under-sampling effects. One example of this effect is that for a radial component vibration signal, where a change in polarity of the recorded peak can represent a change in rock mass loading mechanism from compression to tension. Therefore, the polarity of the peak becomes increasingly important due to the marked difference in compressive and tensile rock strengths.

An often overlooked value when determining the required sampling rate is the Nyquist frequency. The Nyquist frequency is defined as one-half of the sampling rate, beyond which a system can no longer adequately represent the waveform frequency content (Northrop, 2005). Where waveform frequency components lie above the Nyquist value, the distribution of energy in the higher frequency spectra can no longer be determined and peak amplitudes may be dramatically under-estimated. Figure A4.13 illustrates the effect of signal under-sampling of a high-frequency vibration event captured from an accelerometer sampled at 8192Hz. The distribution of wave energy above the Nyquist frequency of 4096Hz was completely unknown and could have decayed rapidly or continued to increase with a rising energy-frequency trend.

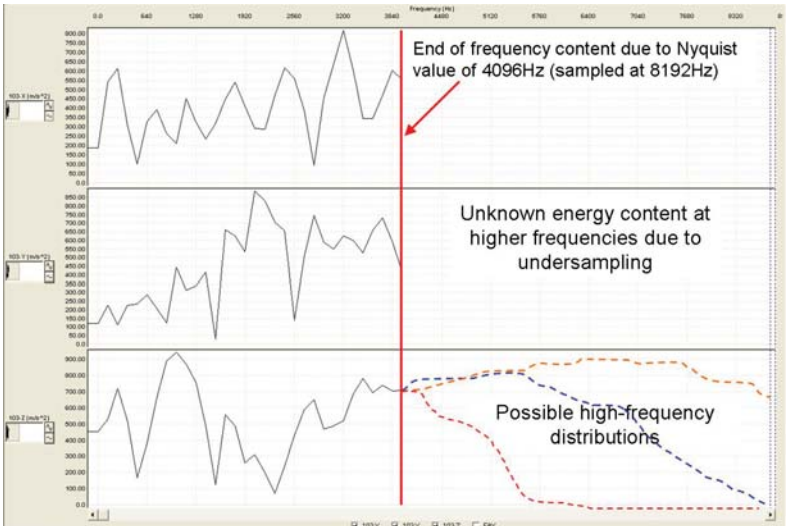

Figure A4.13. Fast Fourier transform (FFT) frequency-power analysis of under-sampled single-hole waveform with unknown energy distribution in frequencies higher than the Nyquist frequency.

Under some circumstances, a significant amount of energy does not reside in frequencies over the response frequency limit of the transducer or the sampling capacity of the system. The higher frequency representation is therefore not critical for further numerical derivation or integration to obtain alternate particle motion waveforms (Andrieux and Heilig, 1994). Where high-frequency components are not adequately represented due to inadequate sampling rate or transducer response, further mathematical derivation of the other forms of particle motion (e.g. velocity from acceleration through integration) can introduce further errors.

A4.6.2 Data Storage Characteristics

Adequate data storage is needed to maximise the sampling rate, event duration and number of events capable of being recorded prior to downloading of the memory. Digital data files of long-duration blasts using multiple channels and high sampling rates can be of significant storage size. Standard compliance monitors are typically not capable of adequate sampling rates or data storage capacity for use in near-field blast monitoring applications. Data storage capacity is an additional consideration when the size and transportability of a blast monitoring unit is a controlling design consideration. In the underground environment, data acquisition systems for blast monitoring should be compact, robust, easily transportable and capable of monitoring multiple blasts prior to memory download.

A4.6.3 Data Acquisition System Triggering Mechanisms

During blast vibration monitoring, the mechanism of triggering of the data acquisition system can aid in limiting data storage requirements and interpretation of

the collected waveforms. Correlation of a single blasthole vibration trace to a specific firing time is of considerable concern in complex blasts to investigate peak amplitudes in relation to blasting parameters. Therefore, proper time-based triggering control with respect to the recorded waveform zero-reference time can be important in interpreting blasting waveforms. Three main triggering mechanisms are available in modern vibration monitoring systems; namely, electric triggering, physical wire-break triggering or transducer threshold triggering.

Of the three types of triggering mechanisms, electric or wire-break triggering requires a physical connection between the data acquisition system and the blast initiation system. In the case of electric triggering, the electric firing signal from the blast initiating point can be used as a trigger identification voltage. This voltage triggers the acquisition system. Electrical triggering requires a blast initiation system that uses a firing line or other electrical impulse.

The other triggering system that requires physical connection between the acquisition system and the blast is a wire-break system. In such a system, an electric loop circuit attached to the acquisition system is physically connected to the blast initiation point. At the moment the wire is either severed or short-circuited by an initiation detonation, the acquisition system is triggered. For systems utilising detonating cord tie-ins and either electric or shock-tube blast initiation, the wire-break cable can be connected to the detonating cord near the point of initiation. For electronic blasting systems, the wire-break is connected to an extra initiator programmed to fire at zero delay or a specified delay prior to the first firing detonator in the blast.

The third type of triggering is a first-arrival transducer threshold trigger. Threshold triggering activates the acquisition system at a specified transducer output voltage. Threshold triggering does not require physical connection to the firing line or the blast, but selection of an appropriate triggering threshold can be complicated. The triggering amplitude should be selected such that the background environmental or electrical noise is not sufficient to trigger the system. False triggers prior to a blasting event can result in expenditure of the available memory or early triggering during a blasting event. In operations where wireless communication blast initiation systems are employed, firing of blasts in the vicinity of the monitored blast can cause early triggering. Threshold triggering also suffers from any effect of first blasthole misfire or under-performance of the explosive charge. In the case that the first firing blasthole fails to initiate or produces vibration insufficient to trigger the system, the relative timeline for the subsequent waveform becomes shifted in time to the first arrival above the threshold (generally the second firing blasthole). Interpretation of the waveform therefore becomes complicated. Based on the influence that the wave travel time has on the event trigger, multiple data acquisition systems in various locations using event triggers can generally not be synchronised.

A4.7 Manufacturing of Tri-axial Blast Vibration Monitoring Transducers for the Thesis Blast Monitoring Program

To maximise the accuracy of the data collected in the blast vibration monitoring program, tri-axial transducers were deemed necessary to characterise the near-field wave characteristics. Tri-axial transducer sondes contain three, orthogonal uni-axial elements. The basic uni-axial accelerometer and geophone elements used in construction of the tri-axial sondes employed in the thesis blast vibration monitoring program are illustrated in Figures A4.14.

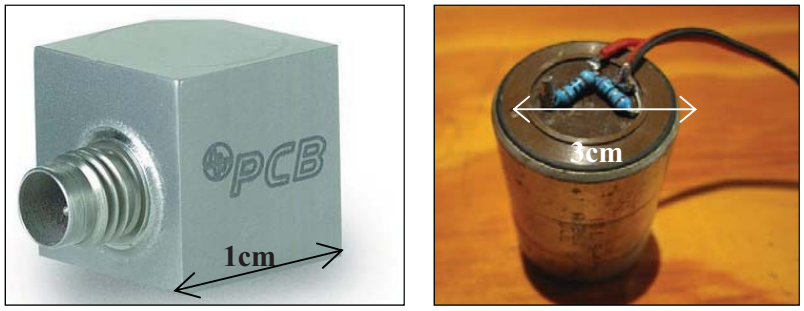

Figure A4.14. Uni-axial PCB 356A02 500g accelerometer component (left) (PCB, 2004) and OYO 101LT 14 Hz uni-axial geophone component (right).

To construct a tri-axial geophone sonde, three uni-axial elements were attached to an aluminium spine to orient each component in a right-handed orthogonal system (Figure A4.15). The elements were positioned such that the polarity of the direction of first motion would reflect the expected wave displacement direction. Damping resistors were added to the geophone elements and 50m of three-pair, shielded cable was connected to each component.

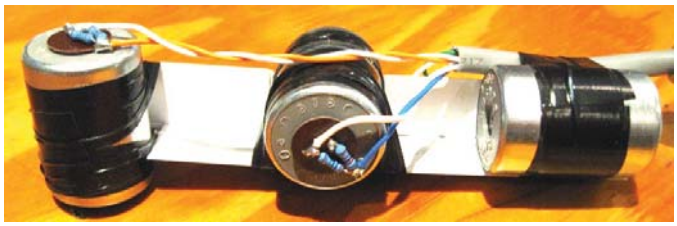

Figure A4.15. Three uni-axial geophone elements on backing spine for tri-axial orthogonal sonde construction.

Once the geophones or accelerometers were attached to the orientation spine and cabled, the spine was inserted into a piece of electrical conduit of desired diameter. Due to the dimension of a single geophone unit, the minimum conduit inner diameter was 46mm. Two different casing diameters were utilised in the manufacture of transducer sondes; 50mm outer diameter and 63mm outer diameter. The sondes were sealed within the conduit with a mixture of 2-component epoxy resin (Araldite). This

encasement method was designed to seal the units from moisture and to ensure coupling of the transducers with the outer conduit shell (Figure A4.16).

Figure A4.16. Epoxy resin encapsulation "potting" of geophone sondes in 50mm electrical conduit for installation into boreholes.

Prior to encapsulation of the spine in the conduit with resin, the transducer orientation within the conduit was referenced on the outer shell using a series of marks. These marks would serve for control of the installed transducer component orientations. Completed accelerometer and geophone sondes are illustrated in Figure A4.17.

Figure A4.17. PCB 500g tri-axial accelerometer sonde (left) and OYO101LT 14Hz tri-axial geophone sonde (right) in 63mm conduit for installation into boreholes.

A4.8 Thesis Blast Vibration Monitoring Data Acquisition System Specifications

The strict sampling, memory and flexibility requirements for the blast monitoring project effectively removed commercially-available blast vibration monitoring systems from consideration. The systems available on the market at the time were deemed inadequate to deliver the desired data quality and system flexibility. The use of multiple transducer types and input sensitivities required a custom-designed system that would be capable of receiving non-standard input signals from both geophones and accelerometers concurrently in a compact and robust construction. The specifications of the desired blast monitoring system for use in the program were as follows:

- Multi-transducer input capability
- Wire-break capability
- Adjustable voltage gain for resolution control
- Independent control of channel input sensitivities
- Internal powering to accelerometers
- Amplification of accelerometer channels
- Bypass set-up for accelerometer/geophone ports
- Minimal cross-channel interference
- Easy to use transducer connections
- Clear labelling of inputs to reduce operator error in connection
- Water-tight, corrosion resistant robust construction
- Tamper-proof enclosures

As a result of the required characteristics, the data acquisition system selected for the near-field blast monitoring program consisted of a commercially-available data collection unit along with a custom-designed junction box. The data recording unit selected was the Instantel Minimate Plus 8-channel unit with upgraded 5MB memory. From the author's past experience, the Instantel Minimate has been found to provide ease of use along with superior quality and resistance to damage.

To fulfil the acquisition flexibility requirements, a specialised junction box was designed and purpose-built for each blast monitoring unit. The large number of channels required for adequate monitoring coverage required purchase of four data collection units. A single combined unit of a Minimate Plus 8-Channel unit and custom junction box is illustrated in Figure A4.18.

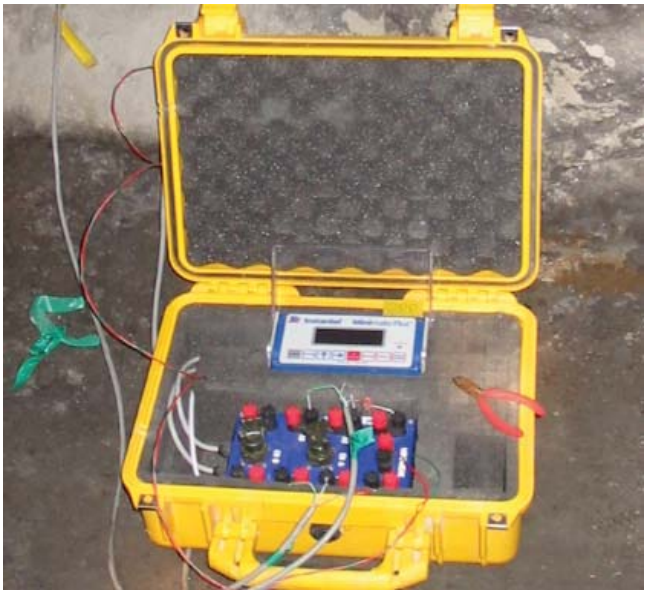

Figure A4.18. Blast Monitoring unit of Instantel Minimate Plus 8-Channel collection unit and custom-built junction box.

A4.8.1 Instantel Minimate Plus

The Instantel Minimate Plus 8-Channel vibration monitoring unit is a commercially-available 12-bit stand-alone compliance monitor. Upgrade of the system memory and advanced user package allowed sampling rates up to 16,384Hz for 4 channels or 8,192Hz simultaneously on all 8 channels. The small size, robust construction and supporting software were viewed as complementary for use in the blast monitoring program. There was a significant trade-off between unit size, resolution and sampling rate. Further technological advances in data processing and ADC construction since acquisition of the original systems have allowed sampling rates of up to 64 kHz on a similarly-sized unit.

A4.8.2 Custom-Built Junction Box

To achieve multiple transducer-type inputs and powering requirements, custom circuitry was designed within a junction box to be placed between the transducers and the Minimates. Within the junction box, attenuation circuits were added to allow the entire dynamic range of the accelerometers to be utilised based on the maximum acceptable voltage received by the Minimate units. Figure A4.19 shows the junction box exterior and the multiple available transducer inputs.

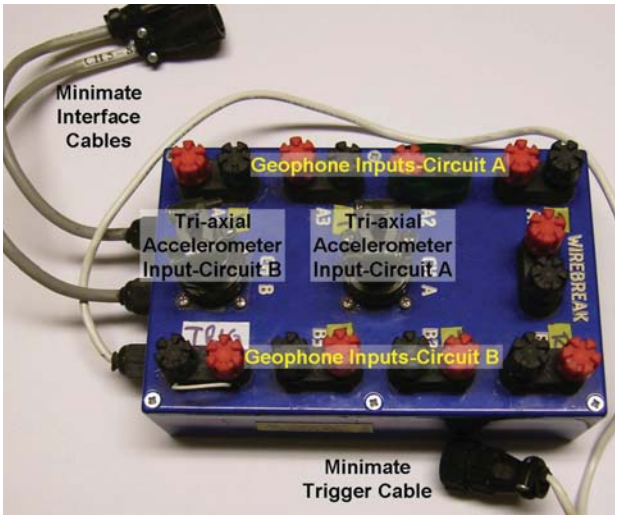

Figure A4.19. Custom-built junction box exterior, showing the flexible transducer inputs and Minimate interface.

To ensure the data acquisition system was highly visible, sealed against the mining environment and adequately protected from rock fall or impact, each system of a combined Minimate and junction box was fitted into a padded case.

A4.8.3 Protection of Data Acquisition Systems Underground

As a basic design specification, the relatively lightweight units could be easily secured to weld-mesh, eye-bolts, or any fastener installed in the wall using wire, zip ties, utility hooks or any type of strap or cable (Figure A4.20). To secure against airblast-related damage risks, the cases could also be strapped to mesh using rope or bungee cord lacing across the body or weighted down on the floor of the drive. The water and mud resistant nature of the case allowed placement on the drive floors where no wall fixture was available for hanging. Under these conditions, visibility of the box was limited, and the boxes became more susceptible to rock fall damage, burying by spalling pillars or interaction with underground equipment.

Figure A4.20. Blast monitoring equipment attached to weld-mesh using utility hooks at the BHP Cannington Mine.

During field applications where hanging was not possible, acquisition systems were placed on the drive floor near the monitored stope. After initial equipment damage was experienced due to rock fall, any unit on the drive floor was covered by bags of crushed-stone stemming. Prior to this, several blasting events caused damage to the boxes and cabling by spalling of pillars near the blast (Figure A4.21).

Figure A4.21. Data acquisition system buried by pillar spall on the 220mLv level at BHP Cannington Mine.

A4.9 Installation of Near-Field Vibration Transducers in the Underground Environment

Installation of fully-encapsulated vibration transducers in the underground environment requires a high degree of operational support. The transducer hole must be added to drill designs by an engineer, mark-out by mine surveyors and drilled at the expense of production drilling. In addition, transducer installation requires underground utility crews and materials to grout the holes. Figure A4.22 shows two types of cement grout delivery systems used at the sponsors' sites. Both systems required additional mine personnel for operation of equipment and assistance with cement grout delivery, mixing and pumping.

Figure A4.22. I.T. mounted grouting basket used at the Kanowna Belle Gold Mine (left) and portable piston pump and mixing bowl used in sensor installation at the Cannington Mine (right).

A4.9.1 Installation Challenges Related to Water

In instrumentation holes that are sub-vertical (downholes), water conditions in the rock mass can complicate transducer installation. Wet holes should be dewatered prior to sensor installation to ensure the cement grout curing process is not compromised. In sensor holes intersecting water-bearing structures or where the collar of the hole is located in a saturated area of the mine, installation is further complicated. Dewatering of drillholes in underground mines is usually accomplished using high-pressure air and a long pipe or hose. This practice is effective to a moderate depth (10-20m) in medium diameter drillholes (76-102mm), but presents many safety concerns from rapid ejection of water and drill chips. Complete dewatering of a borehole is typically not possible using compressed air in wet conditions. Therefore, at the pre-drilling design stage, residual water should be accounted for by overdesigning the hole length such that the transducer location is not located in standing water.

In the toe area of an instrumentation hole, incomplete grout setting can occur due to excessive water or drill cuttings. This issue can also be present at the top of a grout column in a downhole or at the toe of an uphole, where up to 10% of the column length can be affected by in-grout water migration (Hutchinson and Diederichs, 1996). In the thesis blast monitoring program, a minimum cement grout encapsulation length of 5m was adopted to ensure proper coupling and to reduce the effects of water migration or grout variability.

APPENDIX 5 : ADDITIONAL INFORMATION ON CHARGE WEIGHT SCALING APPROACHES

A5.1 Additional Information on the Holmberg-Persson Model 402
A5.1.1 Corrections for Explosive Type 403
A5.2 Additional Information on Comparisons between PPV Prediction Models 406
A5.2.1 Comparison of Predicted PPV Values with Measured Values 407
A5.3 Additional Analyses of Peak Amplitude Data versus Charge Confinement 409

A5.1 Additional Information on the Holmberg-Persson Model

The maximum vibration amplitude in the Holmberg-Persson model is assumed to be highly dependent on the distance from the closest elemental charge in the column to the transducer (R_0) and the elemental explosive weight ($dx \times l$). The original geometry identified by Holmberg and Persson (1979) is illustrated in Figure A5.1.

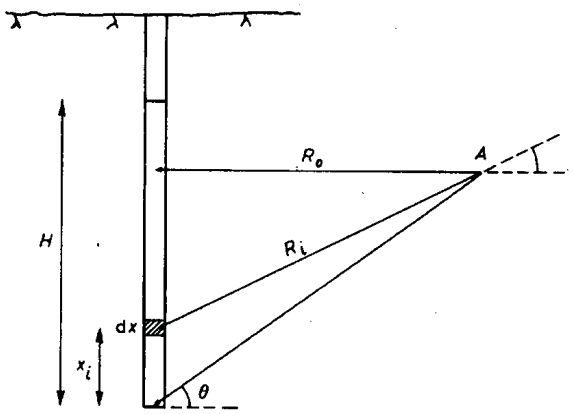

Figure A5.1. Geometry in the original Holmberg-Persson model, showing the unit element *dx*, the minimum and elemental distances R_0 and R_i and the monitoring point "A" (Holmberg and Persson, 1979).

Based on the geometry presented in Figure A5.1, the distance (R_i) from an elemental charge to a point of interest (A) could be calculated through simple geometry using Equation A5.1 (Holmberg and Persson, 1979).

$$R_i = \sqrt{R_0^{\,2} + \left(R_0 \tan\theta - x_i\right)^2} \qquad \text{(A5.1)}$$

Where R_0 = normal distance between a charge element and point A (m)
θ = elevation angle from charge toe to point A (º)
x_i = distance from charge toe to elemental charge (m)

The integration of the elemental charge *dx* over the entire charge length therefore yielded the general integral form of the Holmberg-Persson equation to predict PPV (v) in Equation A5.2.

$$v = k \cdot l^{\alpha} \left[\int_0^H \frac{dx}{\left[R_0^{\,2} + \left(R_0 \tan\theta - x\right)^2\right]^{\beta/2\alpha}} \right]^{\alpha} \qquad \text{(A5. 2)}$$

Where l = linear charge concentration (kg/m)
H = charge length (m)
k, α, β = regression constants (k = 700, α = 0.7, β = 1.5 suggested)

The regression constants k and α in Equation A5.2 can be defined by performing a linear regression of PPV versus the Holmberg Term (a), where a is defined by Equation A5.3.

$$a = l\left[\int_0^H \frac{dx}{\left[R_0^{\,2} + (R_0 \tan\theta - x)^2\right]^{\beta/2\alpha}}\right] \qquad \text{(A5.3)}$$

And $\beta = 2\alpha$

Such that

$$PPV = k(a)^{\alpha} \qquad \text{(A5.4)}$$

Using the recommended values for k, α and β, Holmberg and Persson (1979) calculated the expected maximum particle velocities for various charge concentrations typical of open pits and tunnel blasting. The proposed PPV-based damage criteria observed in Swedish tunnel blasting were also included in the graph to estimate damage envelopes around the proposed explosive charges (Figure A5.2).

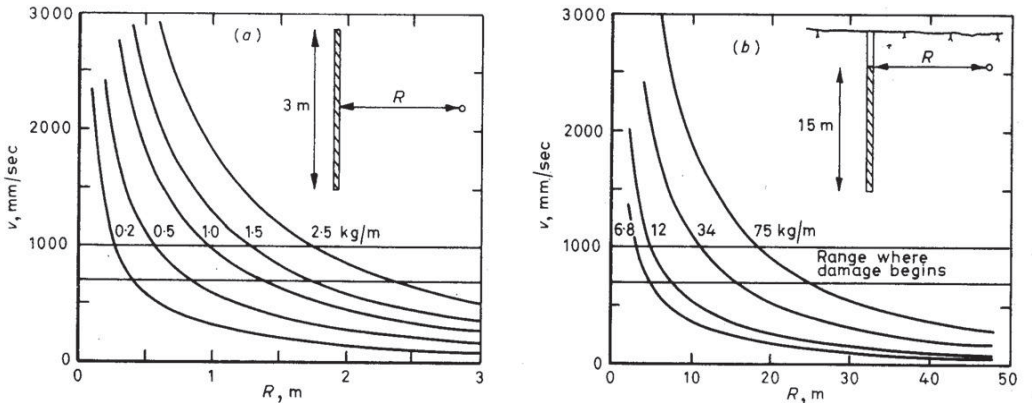

Figure A5.2. Predicted PPV at different distances from the charge axis for small (left) and large linear charge concentrations (right) as a result of Holmberg-Persson near-field vibration modelling (Holmberg and Persson, 1979).

A5.1.1 Corrections for Explosive Type

Observed variations in measured vibrations based on different explosive types were addressed in the Holmberg-Persson model through the suggestion of normalising the strength of each explosive to the strength of standard ANFO. The equivalent charge of explosives such as water gels and emulsions relative to ANFO (s_{ANFO}) can be calculated by Equation A5.5 (Holmberg and Persson, 1979).

$$s_{ANFO} = \frac{\left(Q + \frac{V_g}{0.85}\right)}{5.04} \qquad \text{(A5. 5)}$$

Where V_g = released gas volume of the explosive at STP (m^3/kg)
Q = heat of explosion of the blasting agent product (MJ/kg)

For modern explosive products, ideal detonation modeling or physical testing generally provides either an energy output value or ANFO-relative weight strength (RWS_{ANFO}). Where RWS_{ANFO} is not provided for a given explosive product, an alternate calculation can be used that compares the weight-energy release of the explosive in question with that of ANFO. The RWS_{ANFO} can then be calculated using Equation A5.6.

$$RWS_{ANFO} = \frac{Energy_{\exp}}{Energy_{ANFO}} \times 100 \qquad \text{(A5.6)}$$

Where $Energy_{exp}$ = Ideal output of energy from explosive (MJ/kg)
$Energy_{ANFO}$ = Ideal output of energy from ANFO (MJ/kg)

The equivalent weight of ANFO (EW_{ANFO}) for a different explosive formulation can be calculated based on the relationship between the linear charge concentration and a charge of equal diameter of ANFO (Equation A5.7)

$$EW_{ANFO} = \frac{100 \times W_{\exp}}{RWS_{ANFO}} \qquad \text{(A5. 7)}$$

Where W_{exp} = weight of new explosive (kg)

For the range of explosive types and blasthole diameters experienced in the blast vibration monitoring program conducted as part of this thesis, the ANFO-relative weight strengths and equivalent linear charge concentrations are listed in Table A5.1.

Table A5.1. ANFO-equivalent properties of various explosive products used at KBGM and the Cannington Mine.

Explosive Type	Density (g/cc)	Linear Charge Weight (kg/m)		RWS_{ANFO}	EW_{ANFO} (kg/m)	
Hole diameter(mm)		102	89		102	89
ANFO	0.85	6.95	5.29	100	6.95	5.29
SANFOLD 70	0.75	6.13	4.67	98	6.25	4.76
SANFOLD 50	0.55	4.49	3.42	95	4.73	3.60
General EP Emulsion	1.0	8.17	6.22	88	9.28	7.07
Low-density Emulsion	0.8	6.54	4.98	75	8.72	6.64
High-density Emulsion	1.2	9.81	7.47	101	9.71	7.40

To investigate the effect of normalizing the charge weights of different explosive types to an equivalent charge of ANFO on vibration prediction equations, a series of firings were studied. The monitored blasts were charged with a combination of general purpose and low density emulsions with densities of 1.0 g/cc and 0.8 g/cc in 89mm holes. The recorded PPV data was plotted against the Holmberg term (a) on log-log scale and then linear regression was performed. The results of the linear regression obtained for comparison were constants k and α and the linear regression coefficient of determination (R^2). To assess the effect of charge normalization in relation to model accuracy for vibration prediction, comparison was performed for the regression results of non-normalized and normalized models. The results of the comparison are listed in Table A5.2.

Table A5.2. Comparative linear regression statistics for ANFO normalized and non-normalized linear charge concentrations.

Data Set	k	α	R^2	Std Error	F-value
Non-normalized	38.32	0.57	0.41	0.38	156.4
Normalized (EW_{ANFO})	35.66	0.56	0.40	0.39	148.1

The results in Table A5.2 do not show a significant change in model accuracy (R^2 correlation), but a decrease in k of approximately 7% is observed compared with the non-normalized linear charge concentration. The slope of the regression line also changes slightly along with the standard error and distribution (F-value) of the data set. Due to the reduced k, normalization of the linear charge concentration to an equivalent ANFO weight strength would result in a slightly lower value of PPV being predicted for a given charge geometry. The differences between the PPV

prediction models for ANFO equivalent and actual charge concentrations in the examined data sets have not been viewed as significant based on the comparative statistics. For this reason, all Holmberg-Persson predictive models applied to the sponsors' site data have used the actual linear charge concentration without normalization to ANFO equivalent charges.

A5.2 Additional Information on Comparisons between PPV Prediction Models

Chapter 5 included a comparison between different charge weight scaling models for prediction of PPV and briefly discussed two additional models based on fundamental wave properties. A number of explosive and rock mass input parameters were required for the Lu-Hustrulid (2003) and Sambuelli (2009) models, which were not required for other charge weight scaling relationships. The input variables as applied in the analyses are listed in Table A5.3.

Table A5.3. Input parameters for the Lu-Hustrulid (2003) and Sambuelli (2009) models used to compare with other charge weight scaling approaches.

Model	Input	Value
Lu-Hustrulid	a	0.0445 m
	R	variable
	ρ_e	1000 kg/m^3 (EP Emulsion 1.0g/cc)
	D	5300 m/s (Adamson and Lund, 2001)
	ρ_c	3510 kg/m^3 (Li, 2009)
	C_p	5070 m/s (measured)
	γ	2.981 (Cunningham, 2006)
Sambuelli	Q	Variable
	r	Variable
	Φ	2,024,000 J/kg (Orica, 2008)
	r_h	0.089 m
	f	Variable
	δ	3510 kg/m^3 (Li, 2009)
	c	2757 (calculated from C_p)

A5.2.1 Comparison of Predicted PPV Values with Measured Values

The measured PPV values for the analysed data set have been plotted against the predicted values of PPV for the five prediction models with the highest correlation values (Table 5.3). The results are shown in Figures A5.3 to A5.7.

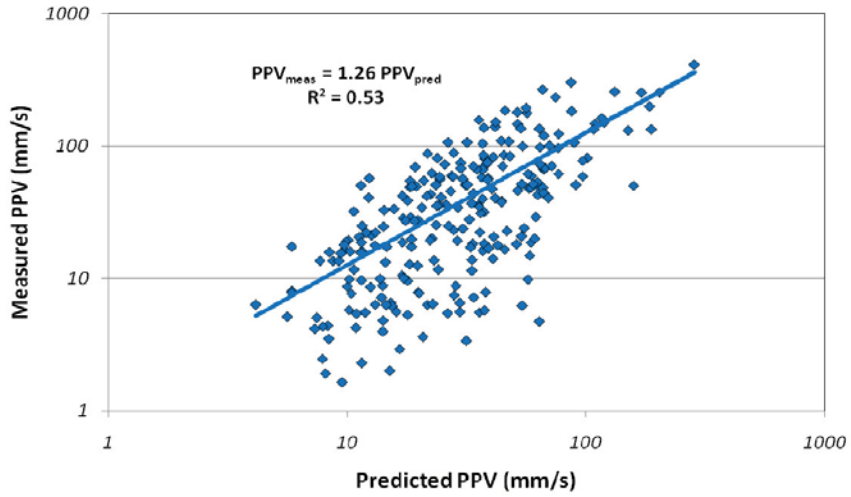

Figure A5.3. Measured PPV vs. predicted PPV using the square root Scaled Distance charge weight scaling model.

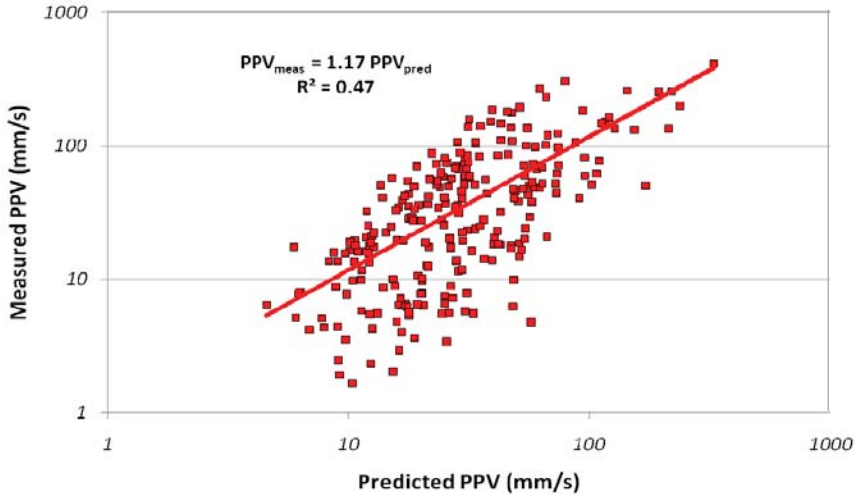

Figure A5.4. Measured PPV vs. predicted PPV using the cube root Scaled Distance charge weight scaling model.

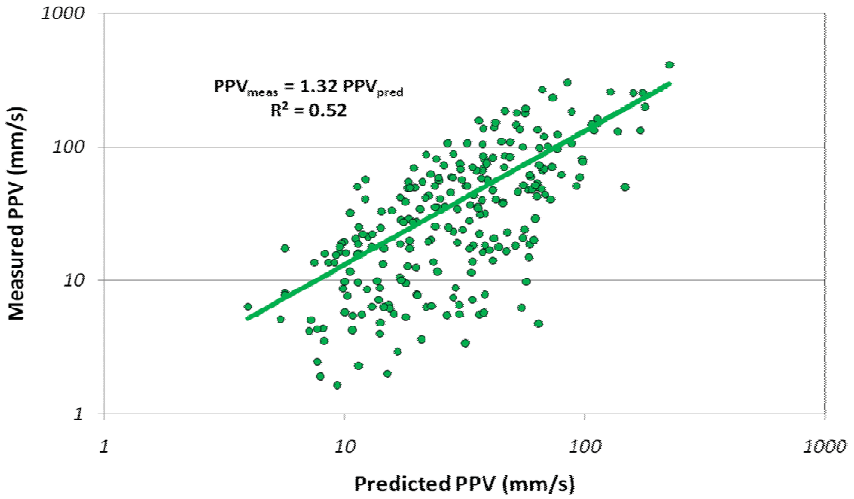

Figure A5.5. Measured PPV vs. predicted PPV using $SD_{Ouchterlony}$ scaling model.

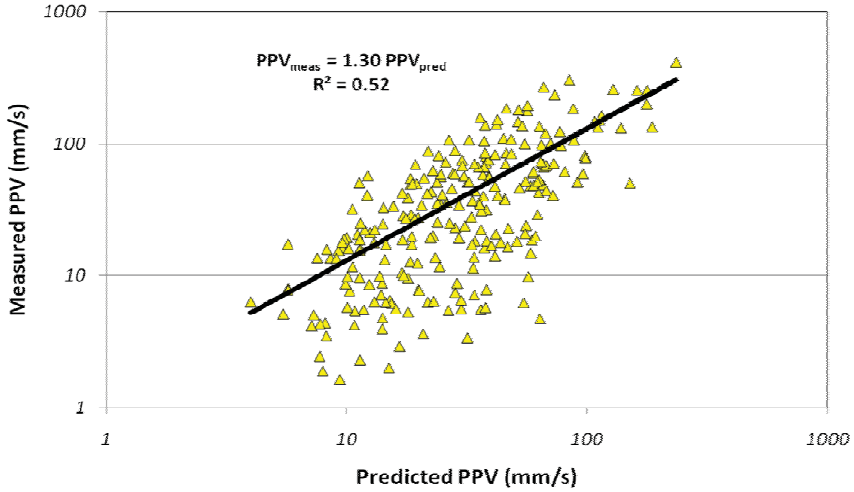

Figure A5.6. Measured PPV vs. predicted PPV using the H-P scaling model.

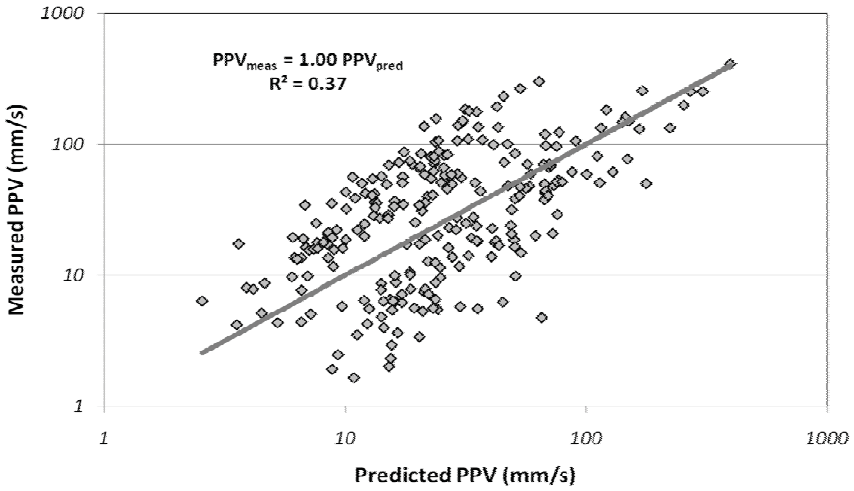

Figure A5.7. Measured PPV vs. predicted PPV using the Sambuelli model.

A5.3 Additional Analyses of Peak Amplitude Data versus Charge Confinement

The analyses performed in Chapter 5 for the influence of confinement on the measured peak amplitudes of blasting vibrations have been expanded. The additional information investigates the influence of simulated breakout angle, broken volume and broken powder factor on the measured peak amplitudes for the rise firing in stope 24jC6HL at the Cannington Mine. To isolate the data from shadowing effects introduced by the forming rise void at the two monitoring locations (North and South), only the intact travel path data have been plotted. Figures A5.8 to A5.10 show the plots of measured VSPPA versus the simulated breakout angle, broken volume per charge and charge powder factor (calculated from each broken volume).

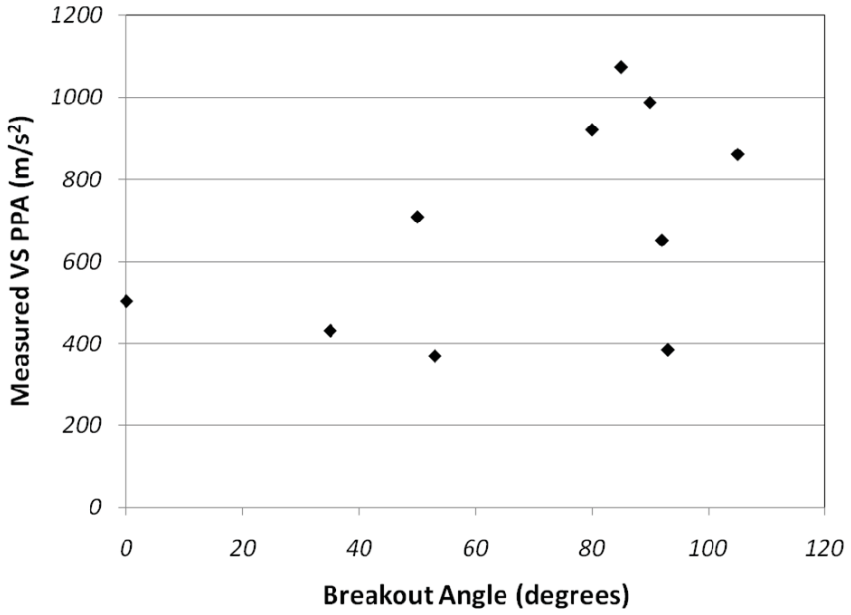

Figure A5.8. Measured VSPPA versus simulated breakout angle (Figure 5.8) for confined rise charges in Cannington stope 24jC6HL.

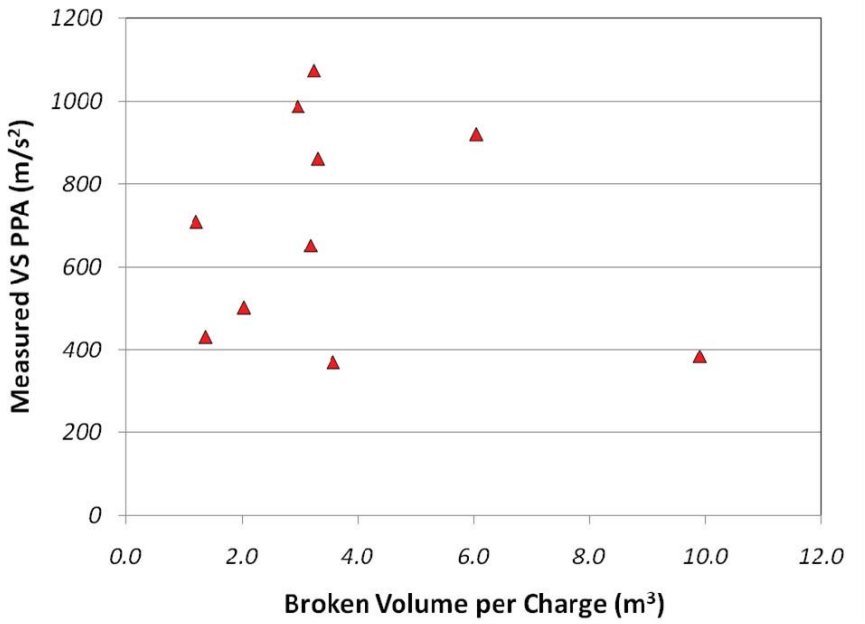

Figure A5.9. Measured VSPPA versus simulated broken volume for confined rise charges in Cannington stope 24jC6HL.

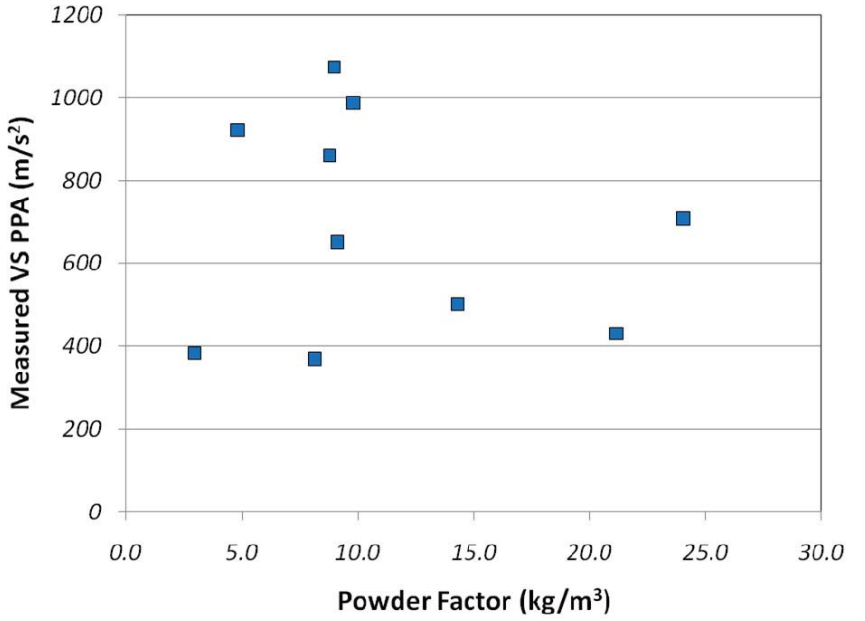

Figure A5.10. Measured VSPPA versus simulated broken powder factor for confined rise charges in Cannington stope 24jC6HL.

Figures A5.8 to A5.10 do not identify any particular relationship between the measured peak amplitude and the breakout angle, broken volume or broken powder factor. This further supports the author's proposal that the peak amplitude is more significantly influenced by factors other than the confinement under realistic blasting conditions.

APPENDIX 6 : NUMERICAL SIMULATION OF WAVE PROPAGATION AROUND A STOPE VOID

A6.1 Numerical Simulation of Wave Propagation and Attenuation around a Stope Void 412
A6.1.1 Wave Propagation Modelling Results 413
A6.1.2 Comparison of Simulated Amplitudes 415
A6.1.3 Validation of the Model with Field Results 416
A6.1.4 General Observations from Comparison of Field Data with Modelling Results 418

A6.1 Numerical Simulation of Wave Propagation and Attenuation around a Stope Void

To aid in understanding the physical effect of stope voids on the wave-field generated by a detonating explosive, two-dimensional numerical wave propagation simulation has been performed using *Wave2000 Plus*®. The characteristics and required inputs of the program have been described previously in Chapter 3. To confine the simulation to a two-dimensional geometry such that the results could be interpreted and compared with a field-monitored three-dimensional geometry, a number of model assumptions were made. These assumptions included:

- The simulation geometry represented a horizontal plane through a vertically-oriented columnar stope
- The source and receivers were located on the same elevation (in the horizontal plane) near the mid-span of the stope void
- The explosive source at a single point along the charge axis could be represented by a short, linear source
- The explosive source was seismic only, without an associated gas expansion phase

The main aim of the void-related series of propagation models was to simulate the effect of wave diffraction on the recorded waveforms at equal distances around a stope void. The model represented blast monitoring locations (receivers) along the Intact, Parallel Void and Normal Void geometries (Figure A6.1).

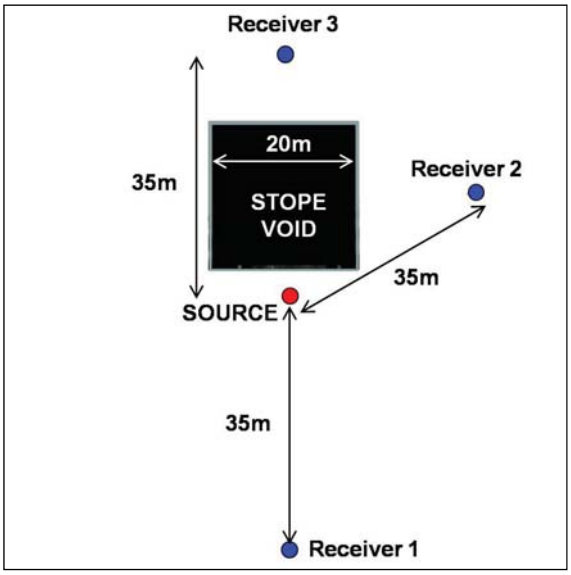

Figure A6.1. Plan view of the two-dimensional simulation plane containing the stope void footprint, source and transducer locations used in the void-affected wave propagation simulation.

The first in a series of simulations investigating wave propagation around an existing stope void was dedicated to modelling the effect of a 20m x 20m void footprint (Figure A6.1) on the wave-field generated by a single blasthole near the void boundary. These stope footprint dimensions were selected for the simulation based on the average size of the stopes monitored at the Kanowna Belle Gold Mine and Cannington Mine. The intact rock properties used in the simulation are listed in Table A6.1. These material properties are typical of a competent, unjointed massive rock type such as a granite or quartzite experienced in some underground mining environments.

Table A6.1. Mechanical properties of the rock mass simulated in Figure A6.1.

Material Property	**Value**
Rock Density	2700kg/m^3
Material Stiffness (λ)	61GPa
Material Shear Stiffness (μ)	25GPa

In the material model, the extracted stope was simulated by an air-filled void. The boundary between the void and the intact material was a fully-reflecting interface. To simulate the infinite model case, a fully absorbing boundary was applied to the outside of the model such that significant wave reflections were not experienced. The source parameters chosen for the model were exponentially-decaying sine waves of single period, applied along both the normal and shear directions.

A6.1.1 Wave Propagation Modelling Results

As observed in Figure A6.1, a series of receivers were placed at equal-distance locations away from the source along three orientations around the void. This configuration was used to remove the distance-related attenuation variability from the model such that only the effects of the stope void on amplitude and wave shape could be assessed. The receiver configuration within the model was similar to that utilised in the blast vibration monitoring program conducted by the author. Views of the model at various run times are displayed in Figure A6.2.

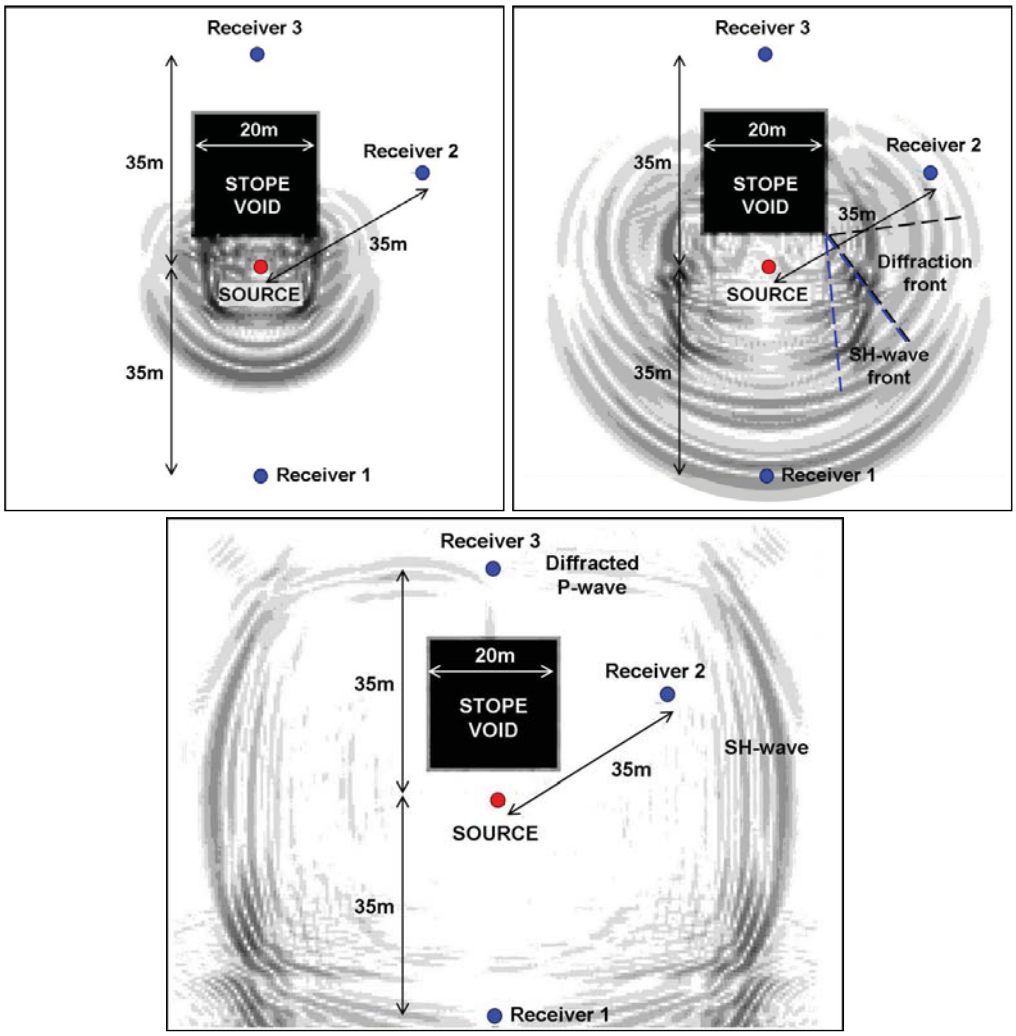

Figure A6.2. Plan view of seismic receivers located equidistant from a source near a simulated stope void and the generated wave-field early in the simulation (top left), mid-simulation (top right) and near the end of the simulation (bottom).

The simulated velocity waveforms recorded at each receiver location consisted of both in-plane longitudinal and in-plane shear components. These resulting vector sum particle velocity waveforms were analysed to determine the distance-related amplitudes and energy losses due to interaction with the stope void. Within the simulated waveforms, there were large variations in magnitude, shape and arrival time when compared between each receiver location. Figure A6.3 shows the simulated vector sum particle velocity waveforms for the Intact (Receiver 1), Parallel Void (Receiver 2) and Normal Void (Receiver 3) cases.

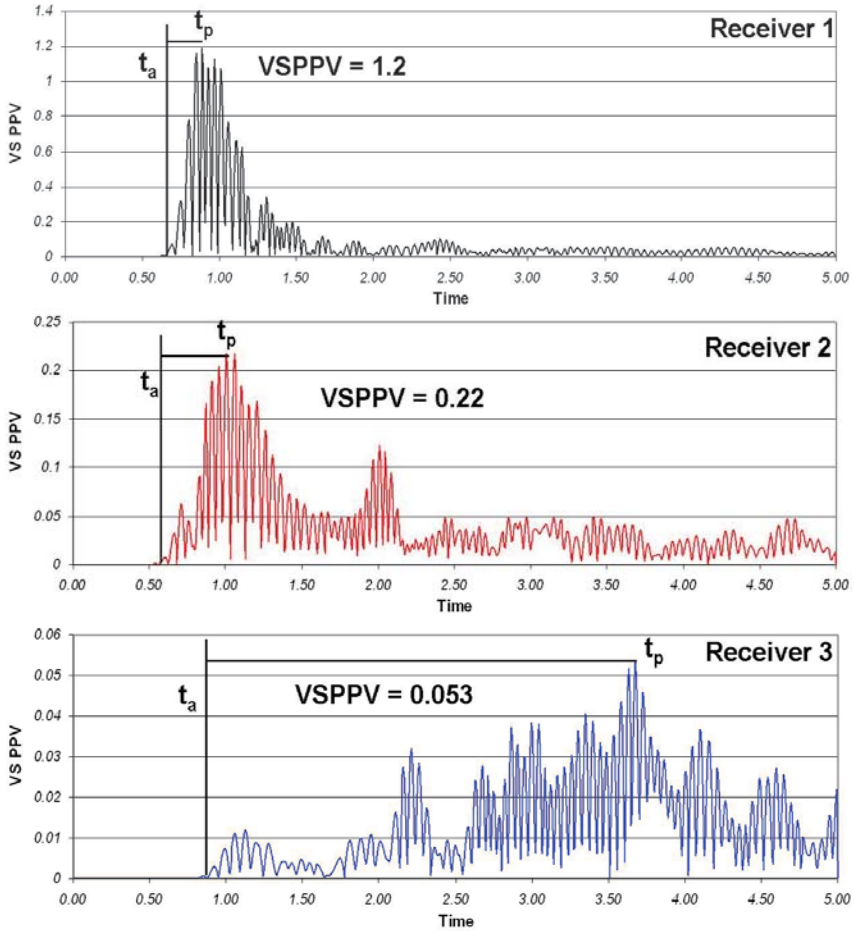

Figure A6.3. VSPPV waveforms for Receiver 1 (top), Receiver 2 (middle) and Receiver 3 (bottom) for equivalent distances around the stope void.

The VSPPVs contained within the void-affected waveforms (Receivers 2 and 3) appeared later in the waveform at a higher value of t_p (peak time). This delay in peak time signified the influence of either void-induced shear wave separation or time-delayed arrival of diffracted P- or S-waves. The VSPPV values for the parallel void (Receiver 2) and normal void (Receiver 3) were reduced by factors of 5.5 and 22 times respectively, compared with the non-void wave-path (Receiver 1).

A6.1.2 Comparison of Simulated Amplitudes

To more accurately compare the simulated amplitude results for the three receiver locations, source and distance-related attenuation equations for each monitoring orientation were determined. To establish the attenuation equations, both the slope and an intercept value were required following the general form:

$$Amplitude = K(D)^{\alpha} \qquad \text{(A6. 1)}$$

Due to the single transducer configuration used in each geometry in the void-affected simulation, K or α values could not be determined from the analysis of the simulated waveforms. Therefore, a baseline attenuation model was required to aid in determining K and α for each orientation. An undisturbed distance-related attenuation relationship was previously established from a control model performed without the presence of a void. This baseline attenuation relationship was observed in Chapter 3 in the unjointed model from the analyses of the effects of discontinuities on the attenuation rates of P-waves. The baseline material attenuation slope from the undisturbed elastic propagation model was -0.66. This slope and the simulated peak amplitudes recorded at each receiver location were then used to back-calculate the K values for each individual attenuation equation.

The process of determining the individual attenuation equations required the assumption that the rate of attenuation with respect to distance would not change from the presence of the void as the simulated material did not change. The effect of the void on the amplitude would be reflected by the K intercept due to the initial loss of amplitude under interaction with the void. The K value of each attenuation curve was calculated such that the basic material attenuation curve of slope -0.66 would pass through each peak amplitude point at the appropriate VICD as specified in the model. The resulting receiver-specific attenuation curves are pictured in Figure A6.4.

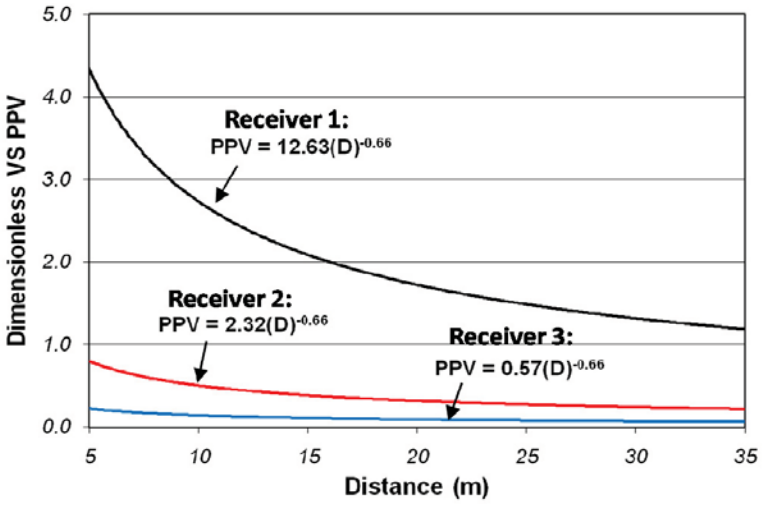

Figure A6.4. Proposed attenuation curves for the void-affected geometries with constant attenuation rates and variable intercepts as specified by modelling results.

A6.1.3 Validation of the Model with Field Results

To investigate the validity of the wave propagation simulation and the attenuation results shown in Figure A6.4, a sample field-collected data set was analysed having a receiver configuration similar to the model. The analysis was intended to compare actual measured wave attenuation behaviours for each orientation classification (Intact, Parallel Void and Normal Void) around an existing stope void. To represent

the intended geometry, the data analysed represented two blasts monitored in BHP Cannington stope 22gC6HL. The two blasts were fired on either side of the existing stope void. Figure A6.5 illustrates the monitoring geometry and the locations of the blasts with respect to the existing stope void.

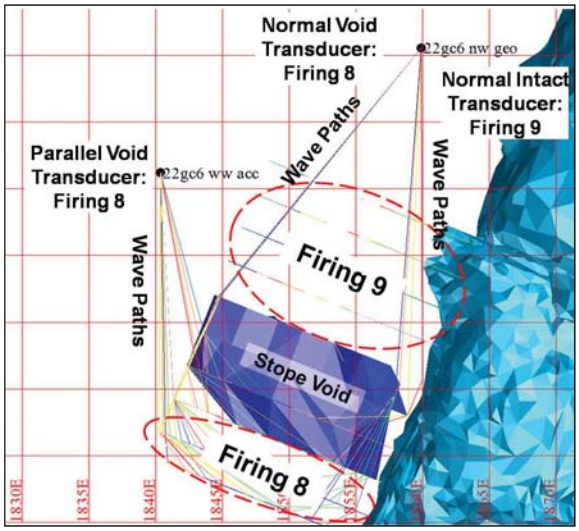

Figure A6.5. Plan view of transducer locations and blast locations in Stope 22gC6HL at BHP Cannington Mine used to compare the void-affected attenuation behaviours.

Due to the complex wave shapes experienced in diffraction-affected wave propagation, peak particle amplitude was deemed as inadequate to characterise the wave attenuation accurately. Cube root Scaled Distance scaling of $ED_{W\text{-}tot}$ was used in place of PPV. The best-fit attenuation curves for the three different monitoring geometries over similar Scaled Distance ranges are illustrated in Figure A6.6 and the regression constants are listed in Table A6.2. The actual data points have not been displayed due to excessive data scatter within the measured results.

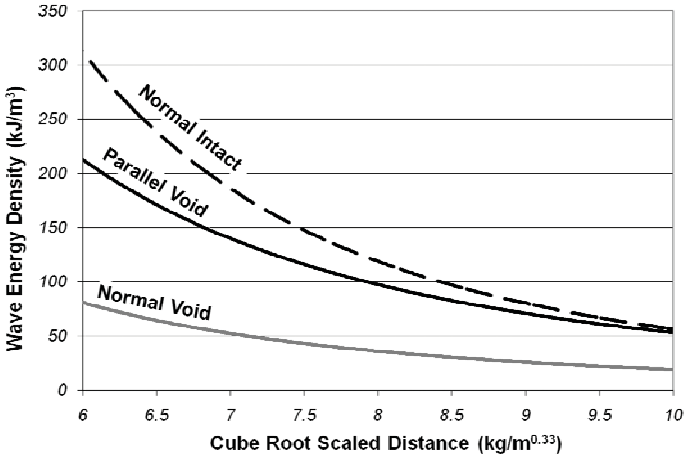

Figure A6.6. Comparison of best-fit regression curves of SD_{CubRT} versus $ED_{W\text{-}tot}$ for data collected for different geometric classifications with respect to the stope void.

Table A6.2. Regression results for the three best-fit curves in Figure A6.6.

Classification	K	α	R^2
Intact	1.26×10^5	-3.35	0.27
Parallel Void	2.75×10^4	-2.71	0.17
Normal Void	1.25×10^4	-2.81	0.14

Extremely poor Scaled Distance model correlations were obtained for the parallel void and normal void data sets regardless of the scaling factor and wave quantity. The R^2 correlation value for the Intact geometry was higher than that for the void-affected geometries, although it was still poor. As illustrated in Table A6.2, further decreases in model correlations were observed as the number of diffraction points increased. Further investigation would be required to substantiate the models in Figure A6.6 due to the differences in attenuation slopes (α) between the data sets collected for the two separate firings. The similar attenuation slopes for the Parallel Void and Normal Void data sets for firing #8 partially validate the results of the simulations.

A6.1.4 General Observations from Comparison of Field Data with Modelling Results

Although poor correlation values were observed within the data sets, some characteristic relationships have been noted through the analysis. Comparison of the field-data attenuation relationships with the wave propagation modelling results over a normalised range of distances and charge weights ($6.0 < SD_{CubRT} < 10.0$) produced similar results. In the case of the field-collected vibration data, the reduction in vibration energy for the parallel void direction as represented by the K value was approximately 30% compared with the Intact direction for a similar Scaled Distance range. The measurements taken in the Normal Void direction were 70% lower due to interaction with the stope void at similar distances. Therefore, the field-observed behaviour was not as severe as the modelled results, where the $ED_{W\text{-}tot}$ calculated from the simulated waveforms was 94% lower for the Parallel Void case and 99% lower for the Normal Void case through comparison of intercept values. The differences in the results may be attributed to the loss of three-dimensional effects in the two-dimensional simulation due to:

- Lack of a vertically-oriented shear wave
- Differences in attenuation rates based on the linear source configuration
- Loss of realistic large explosive energies and frequency ranges in the real blasting cases which are more resistant to attenuation
- Inability to capture wide variability within near-field blast wave results

APPENDIX 7 : USE OF WAVE FREQUENCY FOR ROCK MASS CHARACTERISATION

A7.1 Wave Frequency Content 420
A7.1.1 Methods of Determining Wave Frequency Content 420
A7.2 Additional Frequency-Related Data Analyses: Peak Amplitude-Frequency Analysis 424

A7.1 Wave Frequency Content

Chapters 2 and 3 stressed the importance of frequency content on the transmission characteristics of waves and the likelihood of damage to rock and existing discontinuities. At the current time, no rock mass blast damage criterion explicitly includes the effect of wave frequency on suspected damage. As previously discussed, large ranges in frequency spectra exist within a blast-generated wave-field. This complicates the determination of a discrete frequency value to characterise a complex blast-induced wave.

A7.1.1 Methods of Determining Wave Frequency Content

In blast vibration analyses, several methods are used to define the dominant frequencies present within a recorded waveform. One highly-utilised method of frequency calculation assumes simple sine wave behaviour of blasting vibrations. Using the sine wave approximation, the relationship between oscillation period and frequency can be used to calculate the frequency within the entire waveform or around the peak. This approach is commonly referred to as a "zero-crossing" method of frequency estimation. Other methods of determining the peak and dominant frequencies within a blast wave are through Fast Fourier Transform or amplitude-frequency analysis.

Calculation of zero-crossing frequencies of a blasting wave only requires identification of points in time where the signal crosses the zero amplitude axis (change in polarity). This type of analysis can be applied quickly through simple matching and amplitude analysis functions. The zero-crossing points for an example wave are shown in Figure A7.1.

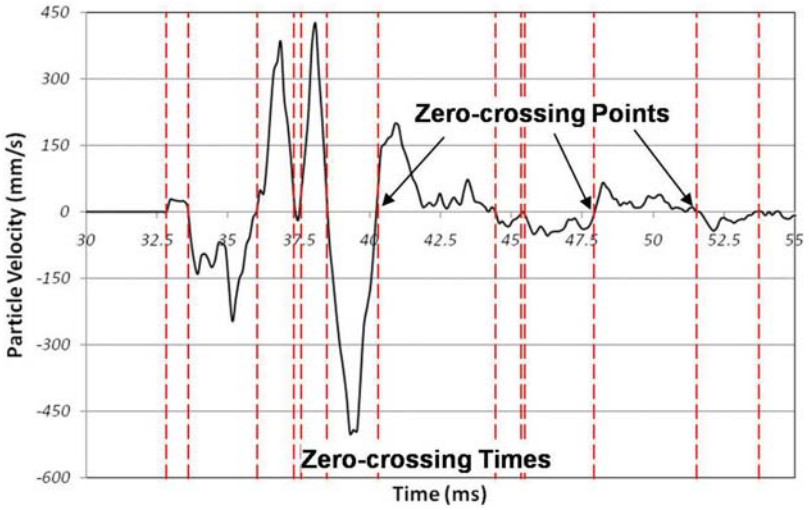

Figure A7.1. Illustration of zero-crossing points for a single hole radial waveform.

Once the zero-crossing times have been determined, the time lapse between zero-crossing points can be calculated and the difference between two adjacent points can be used to calculate the frequency based on the half period-frequency relationship. In practice, the zero-crossing frequency calculation is generally applied to a time window containing the peak amplitude and therefore the "peak" frequency is estimated. This frequency at the peak amplitude should not be confused with the dominant frequency of the entire waveform, which can either be higher or lower than the peak frequency. A histogram of the frequencies calculated from the waveform in Figure A7.1 is illustrated in Figure A7.2.

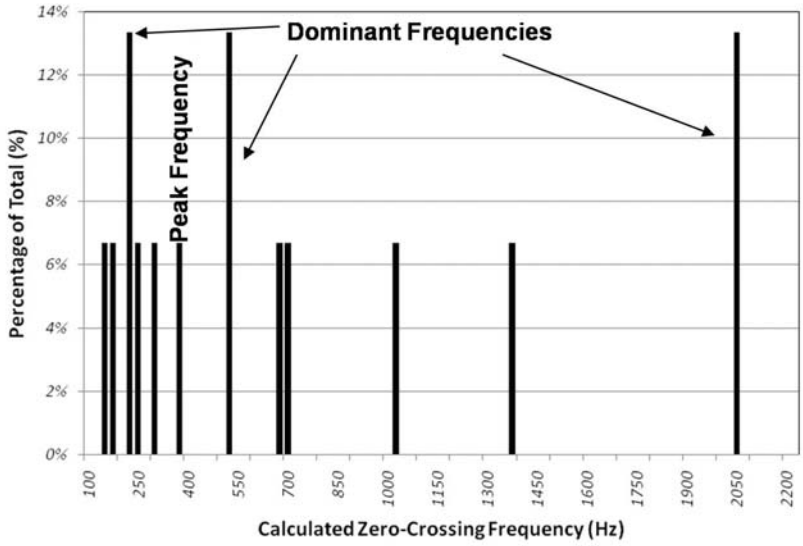

Figure A7.2. Histogram of frequency distribution showing the peak frequency and dominant frequencies as calculated with the zero-crossing method.

Although zero-crossing frequency calculations generally fail to treat a waveform as a complex arrangement of various frequencies, it has been used for many years as a standard calculation method for peak and dominant frequencies. Disadvantages of the zero-crossing calculation method have been discussed by past researchers (e.g. Blair, 2004).

Three different zero-crossing techniques for calculating either the peak or average wave frequencies are illustrated in Figures A7.3 to A7.5 for an example recorded waveform. The average frequency is the simple sine wave frequency over the entire duration. Each method utilises the zero crossing times and sine wave relationships between period and frequency. The approaches are referred to as the total duration average frequency (Figure A7.3), the single period peak frequency (Figure A7.4) and the half period peak frequency (Figure A7.5).

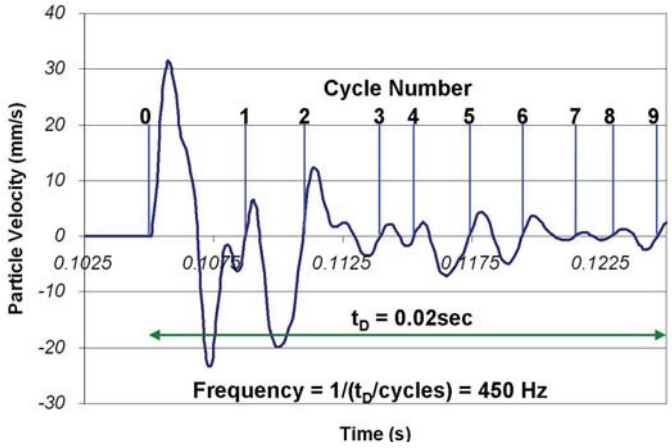

Figure A7.3. Calculation of average frequency from the total wave duration and number of oscillation periods for an example waveform.

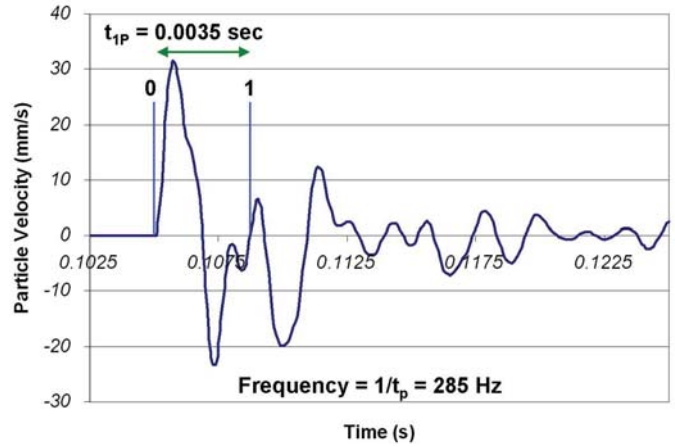

Figure A7.4. Calculation of the peak frequency using the single peak period zero crossing method.

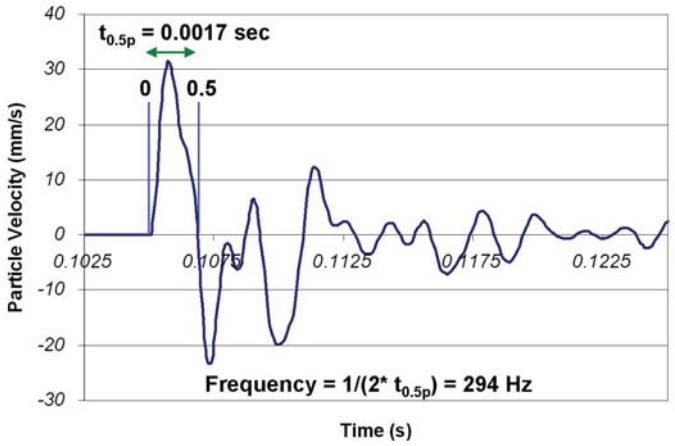

Figure A7.5. Calculation of peak frequency using the half peak period zero crossing method.

The three different zero-crossing frequency approximation methods reported frequency values ranging from 285 Hz peak frequency (Figure A7.4) up to 450 Hz average frequency (Figure A7.3) for the same waveform, highlighting some of the variability with the zero-crossing methods.

To fully represent the frequency spectrum contained within a blasting waveform, Fast Fourier Transform (FFT) analysis can be utilised to display the power-frequency relationship. This method indicates the frequency spectral distribution by applying a Discrete Fourier Transform (DFT) over a waveform of finite time (Northrop, 2005). Descriptions of the mathematical processes used in FFT analysis are well-documented elsewhere and therefore will not be discussed here. Many published research works recommend the use of FFT analysis for determination of blasting frequency spectra (e.g. Crenwelge, 1991; Fourney, et al., 1996; Rholl, 1996; Siskind, 1996). Comparisons of the FFT frequency-power spectra for the waveform depicted in Figures A7.3 to A7.5 with the peak and average frequencies calculated using zero-crossing methods are illustrated in Figure A7.6.

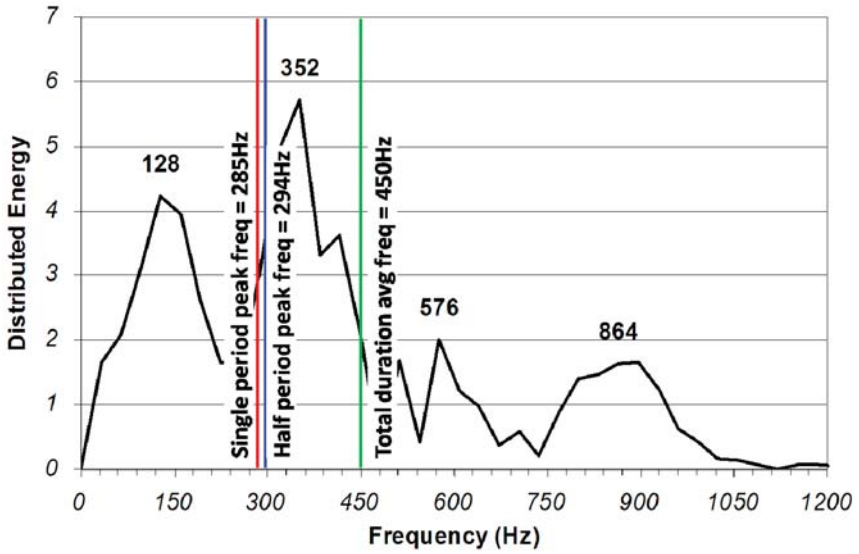

Figure A7.6. FFT analysis of a blast wave compared with the results of zero-crossing frequency calculation techniques for the same waveform.

By comparing the frequency spectrum in the FFT analysis to the peak and average frequencies calculated using zero-crossing methods (red, blue and green lines) the disadvantages of the zero-crossing approaches can be observed. In all three zero-crossing approaches, a single frequency has been identified under assumption of sine wave behaviour. The FFT analysis performed over the entire 20ms duration has identified four frequency bands over which appreciable energy content was contained. The zero-crossing and average period methods failed to identify the frequency components at 128Hz, 576Hz and 864Hz. All three zero-crossing

techniques estimated within ±30% the dominant frequency band displayed in the FFT analysis at 352Hz.

A7.2 Additional Frequency-Related Data Analyses: Peak Amplitude-Frequency Analysis

The relationship between peak particle velocity and peak particle acceleration is strongly influenced by the frequency content of the blast wave measured at a point within the rock mass. Highly competent, confined rock masses with a high effective stiffness will typically support higher frequencies than a rock mass of lower stiffness due to fracturing, weak discontinuity infill or poorly cemented particles. The frequency content of a seismic wave, and more importantly a blast wave, can therefore be used to indicate the relative stiffness of the rock mass in which the waves are monitored (as observed by Summerfield, 1955 and Blair, 2004).

The direct comparison of PPV with PPA as an indicator of blast wave frequency can be a valuable tool to indicate states of increased fracturing, rock mass anisotropy or general rock quality. The slope and intercept of the relationship between measured PPA and mathematically-derived PPV become important characteristics when describing a rock mass through which blasting vibrations are travelling. Blair (2004) illustrated the differences between rock mass properties and blast configurations based on inferred frequency content for a series of measurements under a number of various rock mass conditions (Figure A7.7).

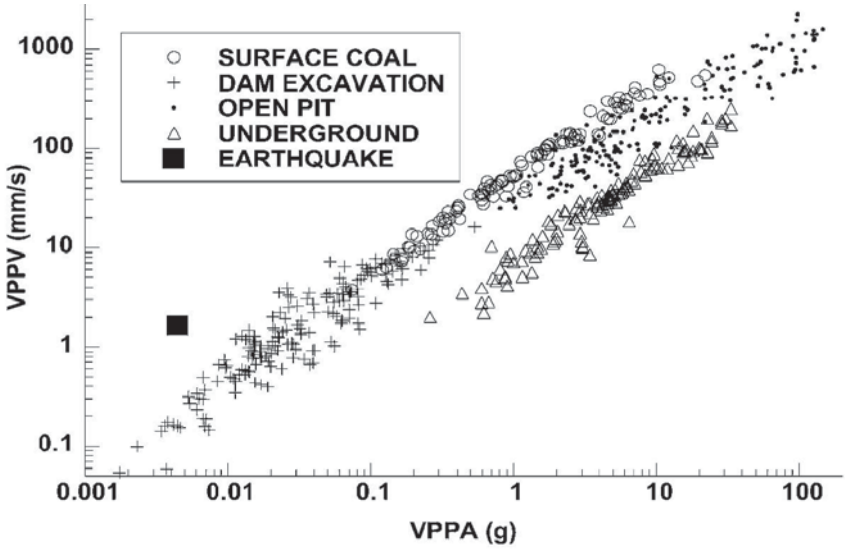

Figure A7.7. Comparison of vector sum PPV and vector sum PPA for a range of blasting applications to indicate the frequency-supporting characteristics of the rock mass or source frequency properties (Blair, 2004).

The peak amplitude-frequency approach illustrated in Figure A7.7 has been implemented in the KBGM and Cannington Mine case studies (Chapters 7 and 8) to investigate the influence of orientation effects and rock mass conditions on the inferred blast vibration frequencies at the measured peak amplitude. The relationships between the measured peak vector sum accelerations (VSPPA) and the peak vector sum particle velocities derived through integration (IntVSPPV) for multiple blastholes is shown in Figure A7.8 for Cannington Mine Stope 52h04HL footwall data.

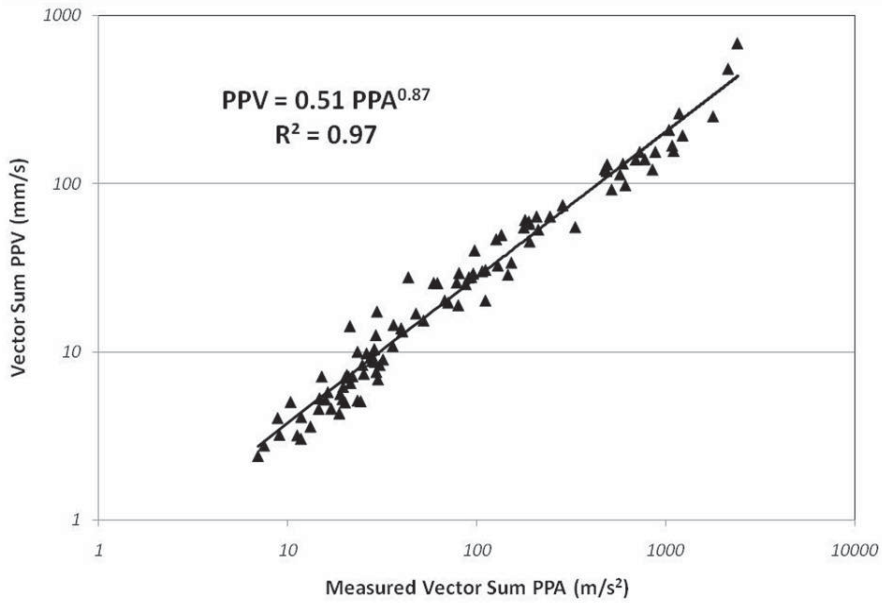

Figure A7.8. Log-Log scale plot of derived VSPPV versus measured VSPPA data collected for BHP Cannington Stope 52h04HL along the footwall orientation.

The relationship between VSPPA and VSPPV derived through integration in Figure A7.8 indicates that the frequency-supporting characteristics of the rock mass are consistent over a range in charge weights and distances. The high coefficient of determination for the linear regression (R^2=0.97) signifies a strong statistical relationship between the two variables over the monitored range.

To investigate directional anisotropies related to varying geologies or rock mass conditions, or changes in the rock mass quality over time, multiple transducer data can be plotted together on a PPV-PPA graph. Through comparison of multiple data sets, the slopes and intercepts of the regression lines can be used to indicate changes in, or variations of, the frequency-supporting rock mass characteristics (bulk indicated stiffness). Figure A7.9 shows the comparison of data obtained from two transducers oriented at 90 degree angles to one another installed in two adjacent stope walls in Cannington stope 52h04HL.

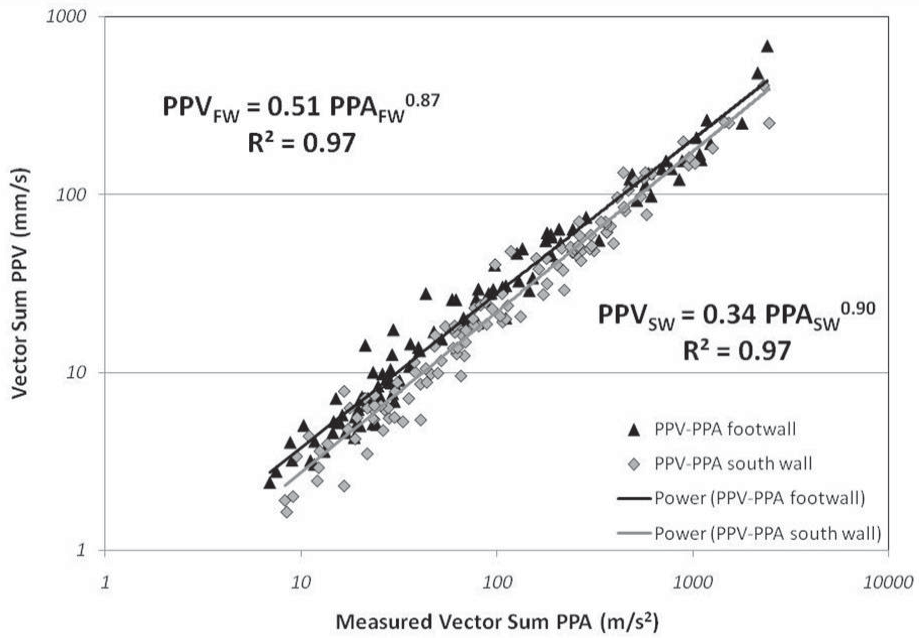

Figure A7.9. Comparison of best-fit linear regressions of VSPPV versus VSPPA for BHP Cannington Stope 52h04HL footwall (black line) and southeast wall (grey line) for the same blasts.

Figure A7.9 clearly indicates a difference between the best-fit curves for the two data sets collected in adjacent stope walls. The changes in both the intercept value and the slope indicate a possible difference in the frequency-supporting rock mass characteristics or inferred rock mass stiffness (bulk modulus). The regression line for the Southeast wall data (grey line) would predict a higher PPA for an assumed PPV, thus indicating a higher effective rock mass stiffness along the Southeast wall orientation. The curve for the footwall data (black line) indicates a lower stiffness due to a lower implied frequency-supporting condition (lower PPA for the same PPV). Comparison of 95% confidence regression results for the two data sets confirms that the footwall and southeast wall represented different populations in this case. The 95% confidence intercept value for the footwall data set was 0.65 and the southeast wall was 0.43 with nearly identical slopes as indicated by the best-fit equations.

Peak amplitude-frequency analysis is yet another tool that can be applied to rock mass assessment, and provides valuable insight into the degree of fracturing or implied rock mass competence. This tool can easily be incorporated with other geotechnical assessment tools such as discontinuity mapping, wave travel-time tomography or stress modelling to characterise a rock mass containing an excavation. Peak amplitude-frequency analysis will be utilised extensively in Chapters 7 and 8 to characterise the rock masses containing the study stopes at the project sponsor sites.

APPENDIX 8 : METHODS OF INDICATING ROCK MASS DAMAGE

A8.1 Methods of Indicating Rock Mass Damage from Blasting 428

A8.1.1 Direct Observation Techniques 429

A8.1.2 Indirect Observation Techniques 430

A8.1.2.1 Borehole Television Viewing (BHTV) 431

A8.1.2.2 Post-Mining Void Analysis 437

A8.1.3 In Situ Geophysical and Geomechanical Methods 440

A8.1.3.1 Seismic Tomography 440

A8.1.3.2 Ground Penetrating Radar (GPR) 441

A8.1.3.3 In Situ measurement of Permeability and Conductivity 441

A8.1.4 Rock Mass Deformation Measurement: Extensometers and TDR Cables 443

A8.1.5 Rock Properties Testing of Extracted Rock Samples 445

A8.1.6 Other Methods of Damage Indication: Gas Penetration Monitoring 446

A8.1 Methods of Indicating Rock Mass Damage from Blasting

A number of factors influence the impact of blast-induced damage on rock mass performance. These include:

- The scale and severity of damage
- Expected or possible damage mechanism
- Mechanical properties of the rock mass
- Dimensions of the excavation
- Existing damage from induced stress effects or prior mining activities

Drilling and blasting processes in mining are expected to fragment rock and dislocate the fragments to enhance digability. As a result of the propagation of strain waves and gas penetration, some degree of fracturing would be expected occur in all directions around the blasthole. The fracture network is desired within a designed excavation volume boundary, however once the fracture network extends outside the excavation perimeter, it is considered undesirable blast damage. This damage can manifest as complete rock mass failure, micro- or macro-fracture leading to reduction in load-bearing capabilities or mobilisation of large-scale faults.

One of the most significant challenges facing rock mechanics and blast damage investigations is the lack of a systematic method to directly measure the strength and condition of a rock mass in situ. At best, indirect assessment of rock mass conditions and induced damage are available where changes in rock mass properties are observed or measured. The degree of rock mass degradation or strength is then inferred from the results. Current tools do not allow for accurate indication of the scale of damage or damage mechanisms in practical field-scale applications and some methods of indicating rock mass damage require extraneous amounts of non-production drilling that can be disruptive to the production cycle. This is especially so in the underground environment, where limited access to the rock mass around excavations inhibit the ability to gain a complete picture of micro-, macro- and meso-scale damage within a confined rock mass.

Some properties of an in situ rock mass can be measured and then related to strength or fracture characteristics using empirical or analytical relationships. These physical properties include sonic velocity, density, elastic properties or degree of fracturing. Damage to a rock mass does not necessarily indicate failure, especially under conditions of confinement. Therefore, some calibration must take place between the indicated degree of rock mass degradation through indirect measurements and the potential for failure for any method of assessment to become a tool of any value.

Many methods specific to static rock mass monitoring and geophysical investigation have been used to characterise or locate dynamically-induced rock mass damage from blasting. These techniques have been used in conjunction with direct and indirect observation techniques and material testing of core or rock blocks extracted from the damaged zone. The results are then used to characterise the change of in situ and intact rock properties due to blast-induced damage. These methods have included:

- Void surveys
- Geophysical assessment
- Fracture density and continuity assessment
- Measurement of physical deformation around excavations
- Inferred damage envelope from measured blast vibration
- Numerical modelling

In most cases, a combination of the above mentioned methods have been used along with direct observation to investigate the relationship between the physical properties of the damaged rock and the blasting or vibration parameters. The following sections attempt to discuss the processes used in assessment of blast damage and to indicate some of the limitations of each approach.

A8.1.1 Direct Observation Techniques

One method of indicating blast damage is direct observation. Observed post-blasting rock mass responses can include rock fall, spalling, fracture formation, excavation condition or profile or large discontinuity displacement at existing excavation boundaries. Although observation is a purely qualitative method of characterising the effects of blasting on the surrounding rock mass, it can be useful to gain a perspective of the time-related rock mass response (Fletcher et al., 1989), extent of effects (Ouchterlony et al., 1993) or frequency-of-events. Early work in defining the extents of overbreak from tunnel blasting in Sweden utilised this method for assessment of the immediate extent of heavy blast damage (after Ouchterlony et al., 2002).

Past studies, largely conducted in development or tunnel blasting, have linked measured or predicted peak particle velocity amplitudes to degrees of observed blast-induced damage. From these studies, excavation surface effects such as fall of rock or loosening of rock blocks have commonly been included as the lowest observable damage threshold. The average vibration limit for excavation surface damage effects has ranged from approximately 200mm/s to 500mm/s as reported by past researchers. Table A8.1 outlines some of the lower vibration limits for assessment of visible secondary blast damage.

Table A8.1. Observed vibration-related damage limits as specified by past research.

Researcher	Type of Observed Damage	Vibration Limit (mm/s)
Langefors and Kihlström (1978)	Fall of rock	300
Yu (1980)	Minor scabbing	500
Holmberg et al. (1984)	Tensile damage	400
Page (1987)	Fall of unstable blocks	100 – 600
Tunstall (1997) (as listed by Singh and Narendrula, 2004)	Loosening of joints	500
Singh (2001)	Loosening of joints	50-400

Another direct visual inspection method for indicating blast damage during development blasting or tunnelling is assessment of the condition of the post-excavation profile. The percentage of visible half-casts or half-barrels at the perimeter of the drive is a measure of the severity or extent of damage. This method can be used to assess various rating factors such as a half cast factor (HCF) or other indices to be compared with blast vibration values or rock mass properties to gain a quantitative comparison technique for different blasting conditions (e.g. Yu and Vongpaisal, 1996; Paventi et al., 1996; Singh, 2001; Martino and Chandler, 2004).

Although direct observation methods are easy to implement, they provide only a superficial qualitative assessment of damage. The extent or severity of damage therefore cannot be determined outside the areas of direct rock mass exposure and cannot be applied within large open voids. To apply observation methods to areas of limited exposure, remote methods such as borehole camera televiewing in drilled boreholes or void surveying can be used to assess evolving rock mass damage. These methods are referred to as indirect observation techniques in this thesis.

A8.1.2 Indirect Observation Techniques

Under conditions of limited exposure or where direct observation would present hazards for mine personnel, indirect observation techniques can be employed to assess rock mass conditions. These indirect methods utilise equipment such as cameras, lasers or radar that are capable of viewing the rock mass through boreholes or can be placed within open voids. The accuracy of indirect observation techniques depends heavily on the equipment operator. Interpretation of the results is generally subjective and may fall upon unqualified mine personnel. The indirect observation techniques most widely utilised to assess rock mass responses to mining include borehole television viewing and post-mining void measurement.

A8.1.2.1 Borehole Television Viewing (BHTV)

Past research in field-scale blast damage studies have regularly utilised borehole inspection techniques to indicate damage limits or occurrence of fracturing from blasting operations (e.g. LeBlanc et al., 1995; Villaescusa et al., 1997; Liu et al., 2000; Keller and Kramer, 2000). The main goal of borehole inspection is to measure or observe changes in fracture frequency, fracture aperture or fracture shear displacement resulting from the interaction of cracks with the wall of an observation borehole.

Borehole inspection is typically carried out using a small diameter front or side-viewing television camera passed the length of a diamond-drilled hole. Use of a diamond-drilled hole is preferable as percussion-drilled boreholes can limit the accuracy of BHTV observations. This limitation is related to drilling-induced rock fracturing (Peška and Zoback, 1998) or loss of visibility of fractures due to irregular drillhole boundaries from percussion-induced rock damage. Figure A8.1 illustrates percussion drilling-induced rock mass damage as observed in percussion-drilled instrumentation hole televiewing at the BHP Cannington Mine.

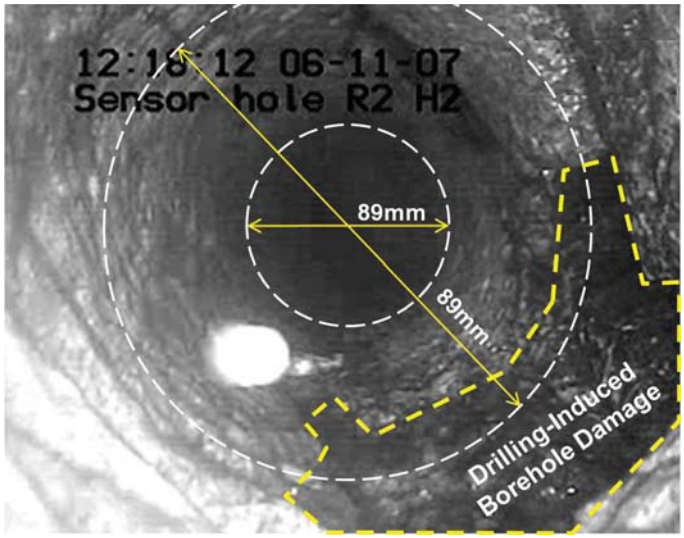

Figure A8.1. Borehole televiewing image of a percussion-drilled instrumentation hole in the R4 mining area at the BHP Cannington Mine damaged during drilling.

Borehole televiewing can be constrained by the availability or capability of diamond drilling equipment at the mine site. A typical borehole television camera configuration is illustrated in Figure A8.2, showing the camera head, flexible cable, and televiewer.

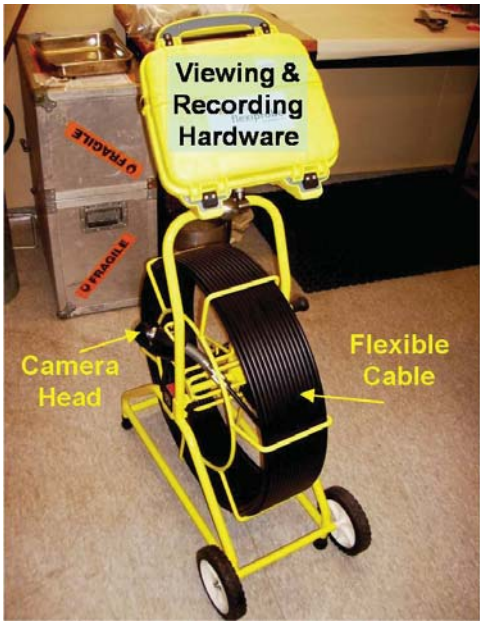

Figure A8.2. WASM-owned Pearpoint P330 Flexiprobe BHTV camera.

The basic stages of a borehole televiewing fracture assessment program includes design and drilling of observation boreholes, initial assessment of pre-mining fracturing and borehole surveys at various mining steps to indicate changes in borehole fracture conditions. Each step in the process can significantly influence the quality of the indicated fracture assessment and significant errors may be introduced.

As the first step in the borehole assessment process, design of observation holes around an excavation requires a good understanding of the type and extent of damage that may be expected during mining. Knowledge of the mining activities in and around the observed stope is also important. Issues that must be taken into consideration when designing observation hole locations, lengths and orientations closely follow those discussed in Chapter 4 in relation to the design of instrumentation holes. Some of these considerations include:

- Design shape and size of stope
- Likely performance of the stope and rock mass response to mining
- Available development from which to drill
- Availability of diamond-drilling equipment
- Interaction of mining activities with observation hole locations
- Water conditions within the rock mass
- Production and stope preparation scheduling
- In situ discontinuity orientation
- Capabilities of televiewing equipment (lighting, cable length, cable stiffness)

In addition to the issues mentioned above, the location and orientation of observation holes can influence the quality of the data obtained during televiewing. This influence is a function of the expected fracturing in relation to the drillhole orientation and physical interaction between the observation hole and the propagating seismic waves.

Observation holes can be drilled in several orientations with respect to the designed excavation boundary depending on the available drilling accesses. To ensure the state of pre-mining rock mass fracturing can be established, observation holes should be drilled prior to the start of stope extraction. This requires that a finalised stope perimeter design and production blasthole design have been approved and issued. As the intent of borehole televiewing is to track the changes in fracture intensity near the stope boundary, observation holes should be drilled to either intersect or closely follow the designed excavation perimeter. For scheduling purposes, observation holes that intersect the stope boundary should be drilled after production holes, as intersection of a production hole with an existing observation hole can complicate the drilling process. The likely results of hole intersection include drillhole deviation, loss of drilling pressure or hang-up of bits or drilling rods.

The types of fracturing expected from blasting or stress-related damage mechanisms suggest that the extent of blast-induced radial fracture may be best represented in observation holes drilled parallel to blastholes. For investigation of fracturing from sagging or dilation of parallel structures such as a stope hangingwall, holes perpendicular to the direction of bedding or unstable discontinuities would be expected to provide the best results. In some cases, access for drilling can be limited. As a result, observation holes must be drilled parallel, oblique or perpendicular to excavation boundaries. The results of fracture observation and interpretation will vary greatly based on the drillhole orientation.

To investigate mining and blasting-induced damage to the hangingwall of a steeply-inclined stope, a study at the Mount Isa Mines Hilton Mine utilised observation holes drilled perpendicular to the excavation surface (Figure A8.3). This type of observation hole orientation allowed close assessment of hangingwall dislocation and dilation of bedded structures under the influence of both blast-induced and stress-affected damage.

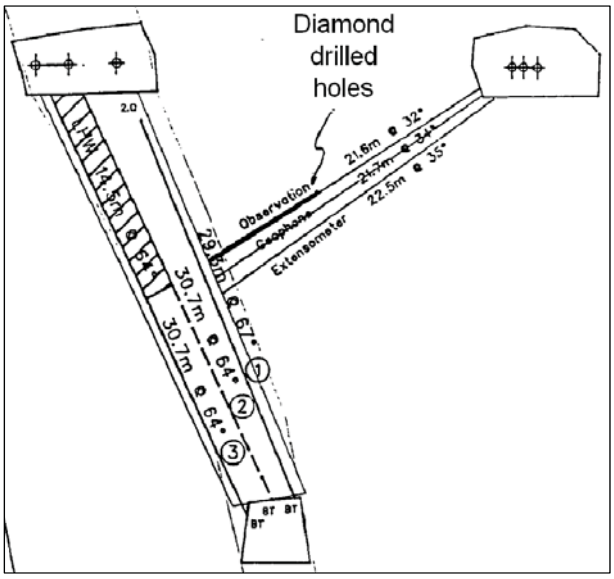

Figure A8.3. Cross section view of perpendicular orientation of instrumentation and observation holes at Mount Isa Mines Hilton Mine stope 5S52 (Villaescusa et al., 1997).

To capture radial fracture and shear dilation effects from the detonation of a single blasthole, Yang et al. (1994) utilised observation holes parallel to the explosive charge axis (Figure A8.4). This type of observation hole drilling required large areal exposure, and therefore may be used more frequently in open-pit investigation geometries.

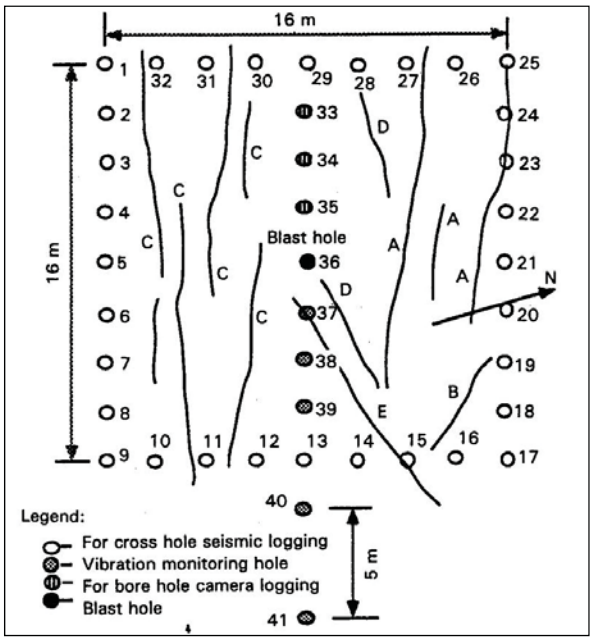

Figure A8.4. Observation hole collar locations (33-35) drilled parallel to the charge hole (hole 36) as utilised in an open pit or tunnelling geometries (Yang et al., 1994).

The orientation of observation holes can adversely affect the likelihood of intersection of fracturing. It is generally accepted that fracture patterns extending from a blasthole propagate in a radial direction. In homogeneous materials and instantaneous detonation characteristics, these cracks can be planar and oriented along the axis of the charge (Rossmanith et al., 1997). Similar fracturing patterns have been observed for non-ideal explosives in homogeneous rock types. Therefore, the probability of fracture intersection between an observation hole either perpendicular to or parallel to the charge column and a forming radial fracture could be limited (Figure A8.5).

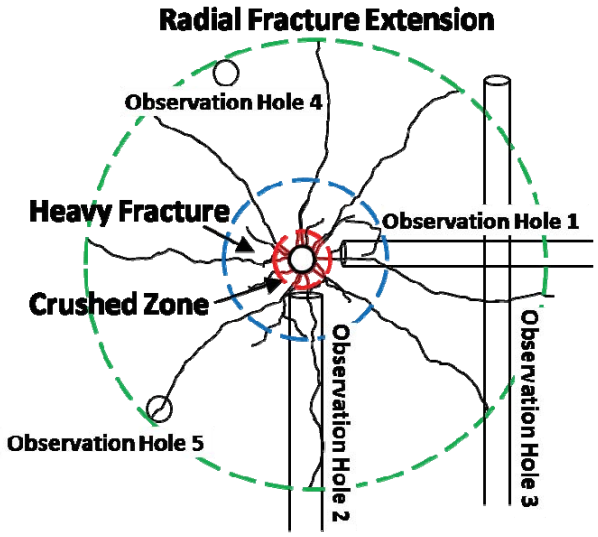

Figure A8.5. Fracture pattern in a plane normal to the charge axis and observation holes drilled perpendicular to the charge axis (holes 1, 2 and 3) and parallel to the charge axis (holes 4 and 5).

From the simulated fracture pattern in Figure A8.5, the maximum extent of fracturing would only be recorded in observation holes 2, 3 and 5. Due to the inability to predict the extent and orientations of fracture propagation and extension, the probability would be low that the limited locations and orientations of observation holes would intersect the longest radiating fractures.

An initial assessment of fracturing conditions should be performed prior to the start of blasting of an excavation. This assessment can be carried out through two different approaches; logging of the extracted core from the diamond-drilling of the observation hole or performing an initial televiewing survey. Either method can indicate the state of pre-mining fracture distribution and condition and can be compared to one another for calibration.

At different steps in the excavation process, borehole television surveys can be performed and analysed to assess the presence of new fractures or evaluate the

change to existing fractures. These results can then be compared with the baseline fracture characteristics to assess the rock mass response to the mining process. Figure A8.6 illustrates the results of pre and post-blast BHTV surveys conducted in the stope 4/7 crown at the Pasminco Elura Mine (Li, 1993), indicating the change in fracture count over different borehole intervals.

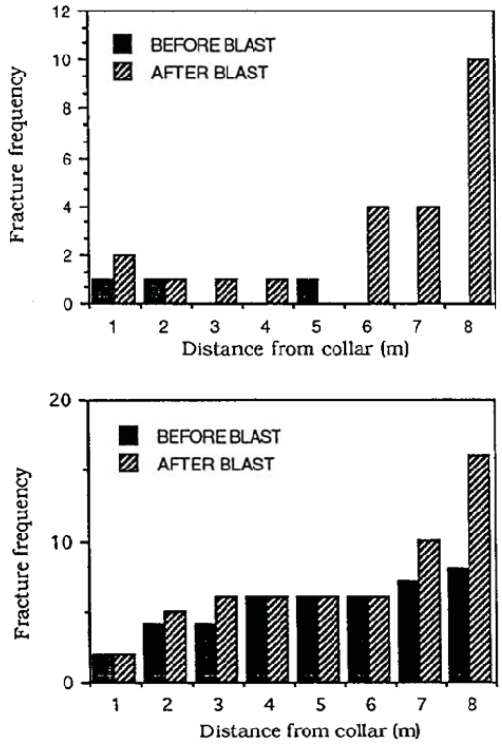

Figure A8.6. Pre- and post-blasting BHTV fracture observation for two different instrumentation locations in the crown of stope 4/7 at the Pasminco Elura Mine (Li, 1993).

The geometry represented in Figure A8.6 was such that the collars of the observation holes were located in a drive above the stope crown. Therefore, increasing length along the hole corresponded with the rock mass closer to the excavation. A general increase in fracture frequency along the blasthole was observed, along with a geometric increase closer to the stope crown.

Due to the complexity of wave interaction with free surfaces in the vicinity of blasting events, the use of observation holes can lead to false indication of in situ fracturing. Through introduction of a zero-stress boundary, fresh fracturing can occur at the borehole wall due to body wave reflection or Rayleigh Waves travelling along the open borehole. Strong compressive or tensile stress waves can interact with the borehole boundary and create cracks that may not be present in the confined rock mass between the explosive charge and the observation hole. In addition, drilling of the observation hole can introduce failure-source flaws, thus leading to the existence

of fractures not otherwise present without the hole. Propagating fractures in the rock mass can also be arrested by the open observation hole boundary, thus limiting the observable fracture extent.

Under states of stable or unstable crack propagation, fractures can be terminated by existing fractures or zero stress boundaries. In this sense, the inclusion of a synthetic large-aperture discontinuity (borehole) can lead to an underestimation of the extent of confined rock mass fracture due to the effects of fracture arrest. Very near a blasthole, intersection of an internally-pressurised propagating fracture with the observation hole can lead to pressure venting, again leading to artificial fracture arrest.

Several limitations of BHTV damage assessment methods exist which are related to the borehole viewing equipment and the observation holes. To ensure accuracy of the results, several factors related to the BHTV method should be considered prior to interpretation of the results. These factors include:

- In-hole lighting, which affects the camera resolution and visibility
- Wet borehole conditions limiting visibility
- Interpretation of fracturing
- Limited visibility of tightly-healed fractures and mineralisation banding
- Irregular borehole shape from damaged ground, faults or stress notching
- Orientation of the borehole with respect to the fracturing orientations
- Excessive shearing of discontinuities resulting in a loss of hole length

In addition to the above items, fracturing mechanisms cannot be determined from observation holes due to the inability to distinguish stress-related effects from dynamic-failure effects. In most cases, borehole TV inspection occurs at some significant time after blasting in underground applications. The delay can be attributed to post-blast no-entry conditions due to ventilation or seismic decay clearance times. During the delay between blasting and observation, rapid stress redistribution around the newly-formed excavation can lead to static rock mass damage or dislocation of new or existing fractures.

A8.1.2.2 Post-Mining Void Analysis

Another indirect observation method used for the assessment of rock mass behaviour is measurement and back analysis of the post-excavation void. This approach in the past has utilised methods of observation ranging from visual inspection and manual laser distance measurement to complex generation of three-dimensional void models from automated rotating laser or radar surveying methods. The use of post-extraction

void shape and size assessment is an important tool for back analysis of stope behaviour, but can also contribute a great deal of information with regards to blasting performance.

The blasting and rock mass parameters contributing to the formation of the final stope void are numerous and interact in very complicated ways. Factors related to drilling and blasting that can affect rock mass response include drillhole deviation, explosive load, design offset from stope perimeters and firing sequences. Some rock mass characteristics that influence the excavation response to blasting include in situ stress redistribution, discontinuity location, size, orientation and properties and time-dependent stope void behaviour. Therefore, results of a stope void survey can be affected by many factors including the time at which the survey is conducted. Germain and Hadjigeorgiou (1997) discovered no significant link between single parameters such as rock mass quality, stope hydraulic radius or charge size and the degree of stope overbreak in two Canadian underground mines.

In the blast damage study conducted as part of this thesis, laser-based Cavity Monitoring System (CMS) surveys were performed during and after study stope extraction to assess stope performance. The post-extraction CMS results were used to indicate stope performance by transforming the final surveyed point cloud into a stope void wireframe. This wireframe was then compared with the initial stope design wireframe to assess the areas and extents of stope overbreak and underbreak. Figure A8.7 illustrates the results of a post-extraction CMS survey of Stope 24jC6HL at the BHP Cannington Mine compared with the design wireframe.

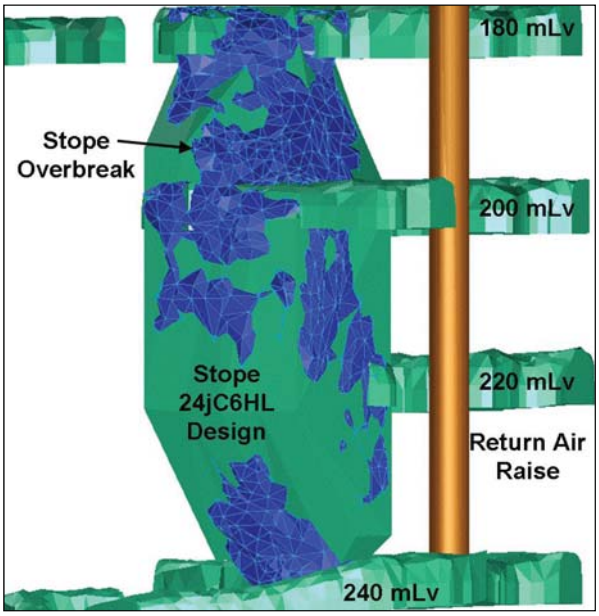

Figure A8.7. Isometric view of stope design (grey) and post-void CMS survey (blue) of stope 24jC6HL at the BHP Billiton Cannington Mine.

Analysis of the surfaces created from the design stope and the post-extraction CMS can provide a great deal of information on the extent, location and shape of underbreak and overbreak to assess the likely factors contributing to the final stope profile. By superimposing the drill and blast design on the final CMS results, factors such as drillhole length or deviation can be assessed as specified in charging reports or through drillhole deviation measurements. Figure A8.8 illustrates a cross-section taken from the designed stope and final CMS surface of KBGM stope dB10-38T along a ring of blastholes. The blasthole charging plan was generated as a result of measured blasthole collars and toes recorded during charging of the patterns.

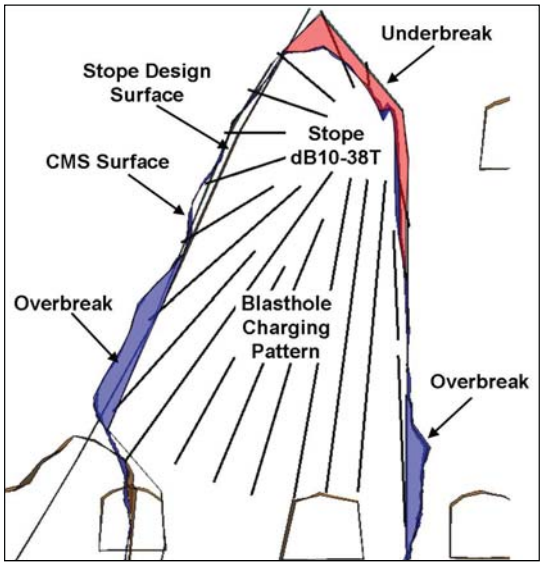

Figure A8.8. Cross section of the planned (brown) and post-extraction (blue) stope surfaces along a drilled blasthole ring for KBGM stope dB10-38T.

Characteristic failure shapes generated in the analysis of the CMS survey can aid in differentiating between blast-related breakage and failure along existing geologic features. From observation of Figure A8.8, several areas of stope overbreak appear to follow well-defined shapes such as existing blocks or discontinuities. Blasting effects are likely to have contributed to block failure and release through shock and gas loading, but overbreak in these circumstances cannot be contributed solely to blasting-induced rock fracture.

It is important to note that some sources of stope overbreak or underbreak cannot be avoided due to the presence of the discontinuities and the pre-formed blocks. Loss of confinement due to stress redistribution can be a contributing failure mechanism at the excavation boundary and therefore resulting overbreak is not restricted to the case of wall failure through blasting alone.

Due to limitations of laser surveying systems related to shadowing, dust, moisture and errors in referencing of the camera head, the results of CMS surveys contain a

degree of imprecision. Interpretation, translation, filtering and processing of the point cloud generated during the survey are generally performed after the survey to reduce the file size and the processing time for wire-framing of the model. Therefore, the results indicated in the final wireframe should be viewed with some degree of uncertainty based on the physical limitations of the laser surveying technology and the human interpretation of the results. In spite of the possible sources of error, the small degree of uncertainty is far outweighed by the value of the information that is provided by the results of CMS.

A8.1.3 In Situ Geophysical and Geomechanical Methods

In the underground mining environment, access to exposures in the rock mass is typically limited due to economic factors and rock mass stability concerns. The information collected at the limited number of exposures within an underground mine may not adequately describe the bulk properties of the rock mass on different scales due to variability related to discontinuities and mineralisation. Remote methods of assessing bulk in situ rock mass properties are therefore required to better understand the mechanical behaviour in response to mining. Tools commonly utilised in geophysical exploration and investigation can become useful to interpret rock mass characteristics through evaluating the wave transmission qualities. These tools include stress wave geotomography, penetrating radar and other remote sensing technologies.

A8.1.3.1 Seismic Tomography

One widely accepted geophysical method for characterising rock and rock mass conditions is analysis of seismic wave transmission characteristics. This approach is commonly referred to as seismic tomography, geotomography or seismic imaging. Seismic surveys are based on the behaviour of transmitted or reflected P- or S-waves travelling through a material. The seismic wave properties that have been most useful for rock mass characterisation are wave travel velocity (P-, S-, and Rayleigh Waves) and amplitude or frequency attenuation or wave rise time (as utilised by JKMRC, 1984; Spathis et al., 1985; Fletcher et al., 1989; Friedel et al., 1995, Zou and Wu, 2001; Cardarelli et al., 2003; Malmgren et al., 2007 and others). These wave properties form the basis of rock mass and engineering material characterisation as utilised in geophysical modelling for mineral exploration, earthquake science, location of changes of in situ stresses, hydrogeological surveys, foundation compaction and assessment of damage.

Several critical factors should be considered when performing or interpreting the results of a seismic survey. The scale or characteristics of an interpreted structure or velocity anomaly can be adversely influenced during the survey or during post-survey analysis and interpretation. During the physical survey, the density of seismic coverage (number of sources and sensors in a given volume), number of recorded

waves (number of sources generated per location) and the seismic source properties can affect the outcome. During analysis and interpretation, the size of the tomographic interpretation grid and assumed degrees of anisotropy can influence the results (Pratt and Chapman, 1992).

Selection of a seismic source should include a consideration of the scale of geologic structures of interest. The observable alteration of a seismic wave interacting with an existing fracture is related to the ratio of the source wavelength to the surface area or critical dimension of the discontinuity. Long wavelength, low relative frequency seismic sources (such as commercial explosives or impact sources) are typically unable to accurately depict small fractures. This is due to a lack of interaction between the source wave and the fracture based on the difference in wavelength versus dimension. For micro-fracture detection in materials, extremely high frequency (kHz or MHz), low amplitude seismic sources are typically required. For detection of large-scale discontinuities such as ore bodies or faults, longer wavelength, low frequency (10-1000 Hz) high energy sources such as explosives or heavy mass impactors may be required to ensure transmission across the highly attenuating structures.

Despite the complications involved in accurately performing a seismic survey and the degree of uncertainty introduced in the interpretation of results, changes in a rock mass can be measured and interpreted with great benefit. Changes in rock type or mineralisation (e.g. Rafat et al., 2001; Luo et al., 1998), indication of increased or persistent fracturing (e.g. Maxwell and Young, 1996; Cosma et al., 2001) or stress accumulation or relaxation (e.g. McGaughey et al., 1994; Friedel et al., 1996; Scott et al., 2004) have successfully been represented through the use of seismic tools as illustrated in many rock mass seismic assessments.

A8.1.3.2 Ground Penetrating Radar (GPR)

Another geophysical investigation method that can be used to characterise pre-mining or mining-affected rock masses is ground penetrating radar (GPR). The GPR method utilises high frequency radar waves (MHz range) to form high-resolution images of geologic anomalies. Direct transmission or reflection surveys can be performed from the surface or from boreholes using GPR similar to traditional seismic approaches. Although many past researchers have favoured seismic methods over GPR for use in rock mass observation in mining applications, GPR has been used successfully for rock mass characterisation (e.g. Grandjean and Gourry, 1996; Stevens et al., 1995; Serzu et al., 2004).

A8.1.3.3 In Situ measurement of Permeability and Conductivity

Hydraulic conductivity can serve as an indicator of the degree of interconnectivity of fractures in a rock mass or the aperture of discontinuities in the periphery of

excavations. It is arguable that in areas where the flow of pressurised fluids is increased through rock mass damage, attenuation characteristics and stress-bearing properties of the rock mass will also be altered. Where hydraulic conductivity increases, the rock mass has sustained an increased degree of damage. Also in these areas, the rock mass strength may be further reduced through introduction of additional fracture surface area and penetration of high pressure blast-driven detonation products.

A number of researchers have utilised hydraulic conductivity and permeability studies to characterise rock mass conditions around blasted or stress-damaged excavations. A majority of such studies have been performed with permeability especially in mind for the storage of nuclear waste and other materials in underground caverns (e.g. Pusch, 1989; Pusch and Stanfors, 1992). General investigations into permeability conducted at the Underground Research Laboratory (URL) in Canada have discovered significant changes (increase of up to 10,000 times) from both stress-induced effects and blast-induced damage (e.g. Souley et al., 2001; Martino and Chandler, 2004). Souley et al. (2001) identified that the rock mass permeability or transmissivity typically decreased by exponential decay-type behaviour with depth away from an excavation into the rock mass, and approached the virgin permeability (Figure A8.9).

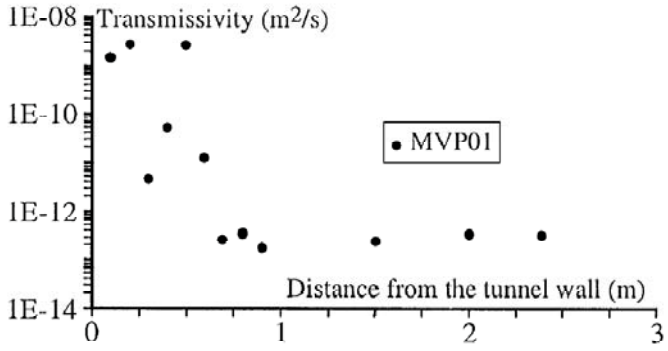

Figure A8.9. Reduction in hydraulic transmissivity with depth from the excavation (Souley et al., 2001).

Other investigations into changes in hydraulic conductivity were conduced to investigate gas flow through broken coal (Butkovich and Hearst, 1976) or the contribution of induced stresses and blasting on tunnel rock permeability (Kelsall et al., 1984). Figure A8.10 illustrates the measured and predicted changes in hydraulic conductivity at given distances from a tunnel wall due to static and dynamic stress loading conditions.

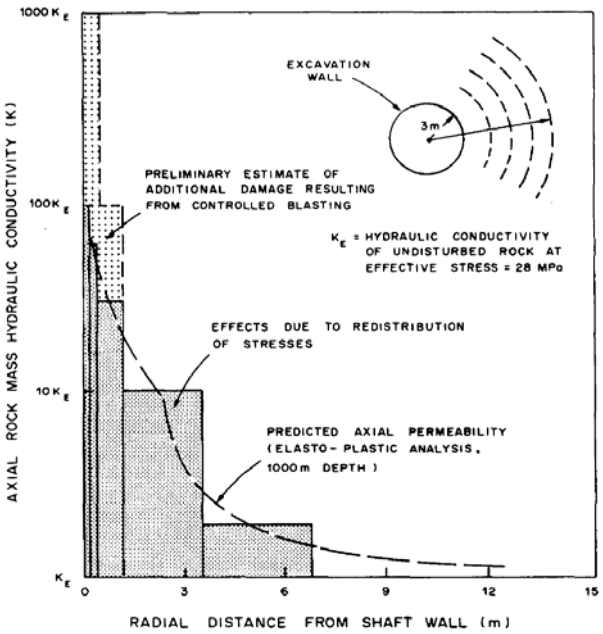

Figure A8.10. Changes in hydraulic conductivity in the wall of an excavation at a depth of 1km due to combined stress loading conditions (Kelsall et al., 1984).

A8.1.4 Rock Mass Deformation Measurement: Extensometers and TDR Cables

One of the basic rock mechanics tools for measurements of rock mass deformation is dilation or convergence monitoring. Early methods to measure the response of a rock mass to the excavation process include rod convergence monitors, tensioned and un-tensioned measuring bolts, differential surveying and anchored longitudinal displacement wires (Jaegar and Cook, 1969). Measurement of rock mass deformation within and around excavations provides a good indication of the response of a rock mass to the mining sequence and rate of extraction, and is the most commonly performed underground measurement (Brady and Brown, 2004).

The use of multiple-point borehole extensometers (MPBX) allows incremental deformations to be measured at various anchoring distances within a rock mass from a remote location. This type of extensometer can be used near rock mass exposures with limited access, such as the hangingwall of an open stope, to characterise the axial displacement of each anchor point with respect to the borehole collar. The changes in displacement magnitude or rate of movement for each anchor point can indicate gradual unravelling or sagging and may be precursors to large-scale failure.

Borehole extensometers have been used in conjunction with BHTV observation and blast vibration monitoring in open stope blast damage investigations. By measuring the deformation experienced within a crucial wall of the stope (for example an inclined hangingwall), the effects of stress redistribution and rock mass relaxation

can be characterised along with the effects of blasting. The combined assessment approach assumes that fresh fractures or existing discontinuities altered during blasting events will experience dilation that will then be indicated by measurements taken from MPBXs. The challenge is interpretation of the results in order to separate stress-related effects from blasting-related effects.

MPBXs have been utilised successfully to investigate blasting and stress-related damage to the walls of open stopes or field-scale blast damage studies as noted by Li (1993), Liu and Proulx (1995), Villaescusa et al. (1997) and Scott (1998). Linking the recorded deformations with blasting events and stress modelling can be a useful tool to determine the rock mass response to static and dynamic loading. Figure A8.11 illustrates the readings from an MPBX monitoring hangingwall response to mining as published by Villaescusa et al. (1997).

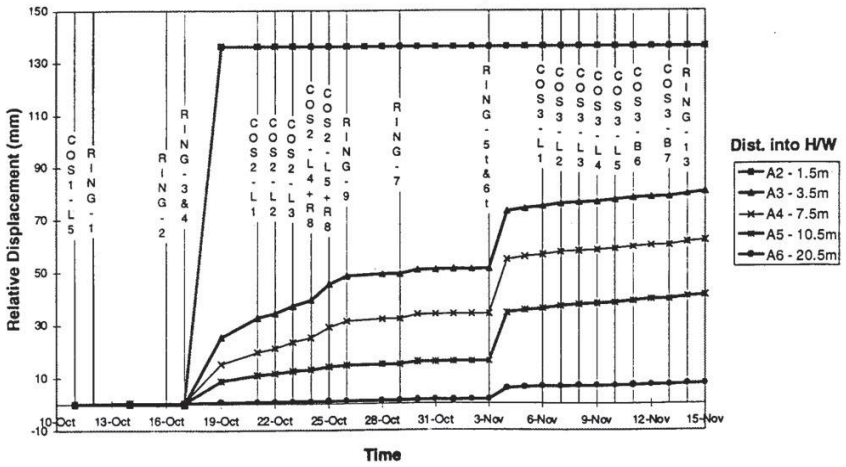

Figure A8.11. Hangingwall MPBX measurements over the life a stope at MIM Hilton Mine showing times of stope blasting events (Villaescusa et al., 1997).

Time Domain Reflectometry (TDR) is a technology employed in the telecommunications industry to determine the integrity of buried service lines through changes in an electric pulse travelling through standard coaxial cable. This technology has been adopted in rock mechanics in recent years to indicate rock mass failure or shear by determining the location of pulse alteration or distance to cable termination. TDR cables have been employed with mixed results in blast damage measurement, as demonstrated by LeBlanc et al. (1995).

Investigation into the efficacy of TDR cables for indication of rock mass shear displacements was conducted by Aimone-Martin and Francke (1997) at the WIPP site in New Mexico, USA. After laboratory calibration to investigate the change in the observed pulse with applied shear displacements, deformations were measured in the backs, walls and floor of a gallery in rock salt. Testing of TDR cables in the field tests and laboratory tests concluded that the minimum response limit of shear

detection varied with the rate of deformation and generally averaged approximately 0.5mm to 1.5mm. At large values of shear deformation, grout sliding and borehole crushing effects were indicated.

A8.1.5 Rock Properties Testing of Extracted Rock Samples

Testing of rock samples extracted after blasting events can provide valuable information on the degree of explosive-induced fracturing or rock mass alteration (e.g. Holmberg and Persson, 1978; Brinkmann, 1990; Ouchterlony et al., 1993; Kilebrant et al., 2009, Ouchterlony et al., 2009). The properties which can be measured from the extracted rock to assess the state of rock mass alteration at micro- and macro- scales include total fracture length, fracture frequency, rock density, seismic velocity, micro-crack density, rock strength and porosity. The traditional table of observed fracture lengths for different small-diameter charge concentrations is illustrated in Figure A8.12 based on cracks observed in extracted rock blocks.

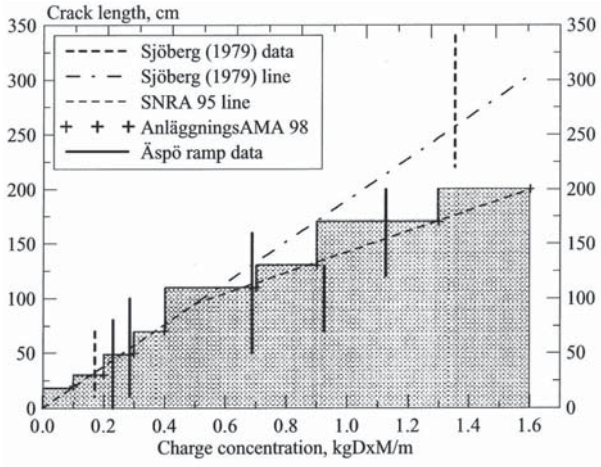

Figure A8.12. Swedish table of total fracture length from blasting with small diameter charge concentrations (Ouchterlony et al., 2009).

In general, testing of extracted cores or blocks yields valuable information on the changes in the physical properties of the rock mass. These changes are valuable indicators of the physical behaviour of the remaining rock mass and the ability to sustain further static and dynamic loads. Using a combination of physical testing methods such as fracture mapping, seismic properties and density and porosity measurements, Kilebrant et al. (2009) investigated the influence of charge concentration in combination with decoupling on the damaged zone around 64mm diameter blastholes in granite (Figure A8.13). The diamond-drilled cores were extracted from the remaining face behind the line of blastholes in a surface quarry.

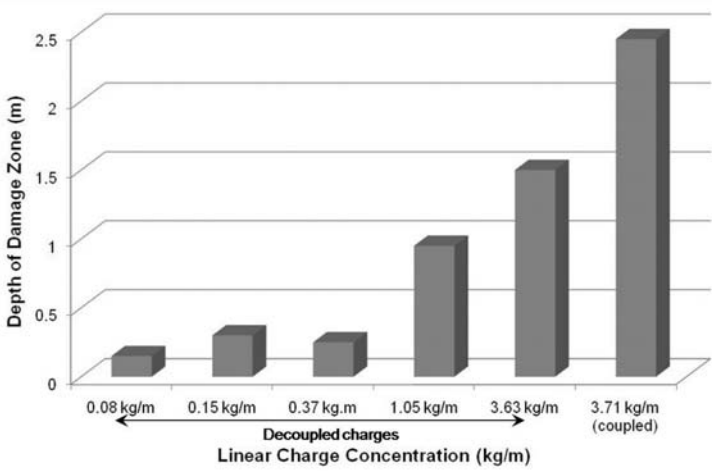

Figure A8.13. Depth of damage vs. charge concentration (after Kilebrant et al., 2009).

The results of the study by Kilebrant et al. (2009) were compared with the Swedish standards and work performed by other Swedish researchers with good agreement. Using the relationship established at the upper end of the results table (>3.7 kg/m) can aid in estimating the damaged zone around larger diameter blastholes and explosives types typical of sublevel open stoping.

A8.1.6 Other Methods of Damage Indication: Gas Penetration Monitoring

Researchers in the past have attempted to use gas penetration measurements to indicate the extent of blasting damage in open pit operations. This approach relies on an assumption that radiating planes of fracturing of a high degree of persistence and continuity are able to transmit internal fracture pressures over moderate distances. In order to indicate the presence of damage behind a blast, measurements of gas pressure in sealed observation holes in the proximity of blasting have been performed. In open pit operations, the works of Brent and Smith (1999), Spathis et al. (2001) and Tannant and Peterson (2001) discuss the mixed results of gas penetration measurement behind open pit blasts.

From the published references, the success of pressure measurements appears highly dependent on the distance between the monitoring holes and the nearest blastholes. Under conditions of excess distance, negative pressures have been measured; this has been interpreted as movement of the burden material without penetration of gas into the sealed instrumentation hole (Brent and Smith, 1999). Within several metres of the final row of blastholes or pre-split, positive gas pressures have been recorded by Tannant and Peterson (2001). In the underground environment, gas penetration measurement has not been widely accepted as a means of indicating blast damage. Confined fracture propagation conditions due to in situ stresses could be expected to reduce or eliminate the measurable internal crack pressure and lead to an underestimation of fracture extent.

APPENDIX 9 : NONLINEAR MULTI-VARIABLE DATA REGRESSION RESULTS

A9.1 Explanation of Regression Summary Tables 448
A9.2 KBGM Individual Regression Results: dA12-35 449
A9.3 KBGM Individual Regression Results: dB10-38B 450
A9.4 KBGM Individual Regression Results: dB10-38T 452
A9.5 Cannington Mine Individual Regression Results: 22gC6HL 457
A9.6 Cannington Mine Individual Regression Results: 24jC6HL 459
A9.7 Cannington Mine Individual Regression Results: 52h09HL 471
A9.8 Cannington Mine Individual Regression Results: 52h04HL 474

A9.1 Explanation of Regression Summary Tables

The nonlinear, multivariable regression results obtained for each analysed data set using the general form of the charge weight scaling equation (Equation 5.2) were output from Statistica 8.0 in the form of a summary table. The items listed in the summary table were the regression constants for the best fit ("Estimate" values *K*, alpha and epsilon), the R value (coefficient of correlation), the standard error for all regression constants, t- and p-values and the upper and lower 95% confidence regression constants ("Up. Conf Limit" and "Lo. Conf Limit", respectively). The number of data points in the data set is also listed as the "df" value under the t-value. The "alpha" value in the tables refers to the "*b*" value (the power associated with the charge weight) and the "epsilon" value is the "*n*" regression constant corresponding with the power term associated with the distance. The general charge weight scaling equation according to the regression results would therefore be:

$$VSPPV,\ VSPPA,\ ED_{W\text{-}tot},\ \varepsilon_{W\text{-}MN} = K \cdot (W)^{alpha} \cdot (D)^{epsilon}$$

During the data analysis period, in excess of 1000 individual regressions were performed using various combinations of data subsets, charge weight scaling models, regression techniques and source-to-sensor distances. The results included in this appendix are the nonlinear regressions of VSPPV, VSPPA, $ED_{W\text{-}tot}$ and $\varepsilon_{W\text{-}MN}$ (referred to as "MNS" {mean normal strain} in the tables) for 60 individual and combined data sets. Due to the excessive number of individual analyses, only the instantaneous amplitude (VSPPV and VSPPA) having the highest correlation value (R) regression result is included along with the results for $ED_{W\text{-}tot}$ and $\varepsilon_{W\text{-}MN}$. In some cases, the highest correlation value is represented by instantaneous amplitude such as VSPPV or VSPPA. In other data sets, $ED_{W\text{-}tot}$ or $\varepsilon_{W\text{-}MN}$ represented the highest correlation values. No regression results have been listed for the stored strain energy density ($ED_{W\text{-}SS}$) used in the blast damage criteria discussed in Chapter 6 and used in Chapters 7 and 8. The regression constants can be determined from the regressions of $ED_{W\text{-}tot}$. The *K* value for $ED_{W\text{-}SS}$ is one-half of the *K* value for the $ED_{W\text{-}tot}$ regressions with the same *b* (alpha) and *n* (epsilon) values, as the $ED_{W\text{-}SS}$ has been calculated as ½ of the $ED_{W\text{-}tot}$.

Details of the transducer data represented in the regression are expressed in the top line of each data table. The mine name is followed by the stope name, the wall in which the transducer(s) is installed and the transducer type/name. The term "Acc" refers to a tri-axial accelerometer, "Geo" refers to a tri-axial geophone sonde, and "Acc-Geo" or "Geo1-Geo2" refers to the combined data set generated by multiple transducers on a directional transducer array.

A9.2 KBGM Individual Regression Results: dA12-35

dA12-35 Footwall Accelerometer and Geophone

	KBGM dA12-35 Acc-Geo Dep. Var. : PPA -- R = 0.335 Level of confidence: 95.0% (alpha=0.050)					
	Estimate	Standard error	t-value df = 217	p-value	Lo. Conf Limit	Up. Conf Limit
K	48240.83	41472.78	1.16319	0.246029	-33500.2	129981.9
alpha	-0.341	0.173	-1.97028	0.050078	-0.681	0.000
epsilon	-1.072	0.315	-3.40292	0.000794	-1.694	-0.451

	KBGM dA12-35 Acc-Geo Dep. Var. : EDW-tot -- R = 0.252 Level of confidence: 95.0% (alpha=0.050)					
	Estimate	Standard error	t-value df = 217	p-value	Lo. Conf Limit	Up. Conf Limit
K	858612.2	1467984	0.58489	0.559228	-2034720	3751945
alpha	-0.574	0.341	-1.68447	0.093529	-1.246	0.098
epsilon	-1.543	0.623	-2.47817	0.013968	-2.770	-0.316

	KBGM dA12-35 Acc-Geo Dep. Var. : MNS -- R = 0.260 Level of confidence: 95.0% (alpha=0.050)					
	Estimate	Standard error	t-value df = 217	p-value	Lo. Conf Limit	Up. Conf Limit
K	1023.415	826.5100	1.23824	0.216966	-605.600	2652.430
alpha	-0.140	0.1522	-0.92021	0.358482	-0.440	0.160
epsilon	-0.942	0.2953	-3.18917	0.001638	-1.524	-0.360

dA12-35 Footwall Accelerometer

	KBGM dA12-35 Acc Dep. Var. : PPA -- R = 0.289 Level of confidence: 95.0% (alpha=0.050)					
	Estimate	Standard error	t-value df = 106	p-value	Lo. Conf Limit	Up. Conf Limit
K	6926.670	8326.287	0.83190	0.407333	-9581.00	23434.34
alpha	-0.585	0.230	-2.54642	0.012320	-1.040	-0.130
epsilon	0.074	0.474	0.15633	0.876070	-0.866	1.014

	KBGM dA12-35 Acc Dep. Var. : EDW-tot -- R = 0.209 Level of confidence: 95.0% (alpha=0.050)					
	Estimate	Standard error	t-value df = 106	p-value	Lo. Conf Limit	Up. Conf Limit
K	55605.21	123253.8	0.45114	0.652807	-188757	299967.9
alpha	-0.6691	0.417	-1.60593	0.111264	-1.495	0.1569
epsilon	-0.2387	0.903	-0.26438	0.792004	-2.029	1.5512

	KBGM dA12-35 Acc Dep. Var. : MNS -- R = 0.217 Level of confidence: 95.0% (alpha=0.050)					
	Estimate	Standard error	t-value df = 106	p-value	Lo. Conf Limit	Up. Conf Limit
K	262.7669	319.6824	0.82196	0.412943	-371.035	896.5682
alpha	-0.4375	0.2348	-1.86311	0.065216	-0.903	0.0281
epsilon	0.0183	0.4976	0.03675	0.970751	-0.968	1.0048

dA12-35 Footwall Geophone

	KBGM dA12-35 Geo Dep. Var. : PPA -- R = 0.417 Level of confidence: 95.0% (alpha=0.050)					
	Estimate	Standard error	t-value df = 108	p-value	Lo. Conf Limit	Up. Conf Limit
K	320140.5	638813.9	0.50115	0.617287	-946099	1586380
alpha	0.119	0.104	1.13642	0.258296	-0.088	0.326
epsilon	-2.412	0.670	-3.59815	0.000485	-3.740	-1.083

	KBGM dA12-35 Geo Dep. Var. : EDW-tot -- R = 0.489 Level of confidence: 95.0% (alpha=0.050)					
	Estimate	Standard error	t-value df = 108	p-value	Lo. Conf Limit	Up. Conf Limit
K	114028.4	382603.4	0.29803	0.766251	-644358	872414.7
alpha	1.300	0.319	4.07202	0.000089	0.67	1.932
epsilon	-3.510	1.106	-3.17235	0.001969	-5.70	-1.317

	KBGM dA12-35 Geo Dep. Var. : MNS -- R = 0.602 Level of confidence: 95.0% (alpha=0.050)					
	Estimate	Standard error	t-value df = 108	p-value	Lo. Conf Limit	Up. Conf Limit
K	2143.075	2755.118	0.77785	0.438357	-3318.05	7604.198
alpha	0.593	0.088	6.76301	0.000000	0.419	0.767
epsilon	-2.113	0.426	-4.95461	0.000003	-2.958	-1.267

A9.3 KBGM Individual Regression Results: dB10-38B

dB10-38B East Wall Accelerometer and Geophone

	KBGM dB10-38B EW Acc-Geo Dep. Var. : PPV -- R = 0.733 Level of confidence: 95.0% (alpha=0.050)					
	Estimate	Standard error	t-value df = 172	p-value	Lo. Conf Limit	Up. Conf Limit
K	11400.53	4980.836	2.2889	0.023302	1569.097	21231.96
alpha	0.117	0.072	1.6225	0.106534	-0.025	0.259
epsilon	-1.977	0.110	-17.9119	0.000000	-2.195	-1.759

	KBGM dB10-38B EW Acc-Geo Dep. Var. : EDW-tot -- R = 0.901 Level of confidence: 95.0% (alpha=0.050)					
	Estimate	Standard error	t-value df = 172	p-value	Lo. Conf Limit	Up. Conf Limit
K	681350.0	318147.6	2.1416	0.033632	53373.67	1309326
alpha	0.820	0.155	5.2921	0.000000	0.51401	1.126
epsilon	-4.034	0.162	-24.9423	0.000000	-4.35370	-3.715

	KBGM dB10-38B EW Acc-Geo Dep. Var. : MNS -- R = 0.797 Level of confidence: 95.0% (alpha=0.050)					
	Estimate	Standard error	t-value df = 172	p-value	Lo. Conf Limit	Up. Conf Limit
K	1380.161	523.9961	2.6339	0.009210	345.8699	2414.45
alpha	0.377	0.0691	5.4594	0.000000	0.2410	0.51
epsilon	-1.880	0.0960	-19.5922	0.000000	-2.0694	-1.69

dB10-38B Footwall Accelerometer and Geophone

	KBGM dB10-38B FW Acc-Geo Dep. Var. : PPV -- R = 0.808 Level of confidence: 95.0% (alpha=0.050)					
	Estimate	Standard error	t-value df = 177	p-value	Lo. Conf Limit	Up. Conf Limit
K	10322756	8656628	1.1925	0.234674	-6760730	27406241
alpha	-0.665	0.099	-6.7214	0.000000	-0.860	-0.469
epsilon	-3.406	0.283	-12.0152	0.000000	-3.965	-2.846

	(KBGM dB10-38B FW Acc-Geo) Dep. Var. : EDW-tot -- R = 0.686 Level of confidence: 95.0% (alpha=0.050)					
	Estimate	Standard error	t-value df = 177	p-value	Lo. Conf Limit	Up. Conf Limit
K	3.889E+09	6.478E+09	0.60029	0.5491	-8.895E+09	1.667E+10
alpha	-0.640	0.173	-3.69390	0.0003	-0.983	-0.298
epsilon	-4.877	0.577	-8.45091	0.0000	-6.016	-3.738

	(KBGM dB10-38B FW Acc-Geo) Dep. Var. : MNS -- R = 0.795 Level of confidence: 95.0% (alpha=0.050)					
	Estimate	Standard error	t-value df = 177	p-value	Lo. Conf Limit	Up. Conf Limit
K	1118302	820695.8	1.3626	0.174731	-501306	2737910
alpha	-0.522	0.0847	-6.1621	0.000000	-0.689	-0.355
epsilon	-3.110	0.2546	-12.2127	0.000000	-3.612	-2.607

dB10-38B Footwall Accelerometer

	(KBGM dB10-38B FW Acc) Dep. Var. : PPV -- R = 0.786 Level of confidence: 95.0% (alpha=0.050)					
	Estimate	Standard error	t-value df = 93	p-value	Lo. Conf Limit	Up. Conf Limit
K	3676862	4748027	0.77440	0.440660	-5751779	13105502
alpha	-0.683	0.130	-5.23711	0.000001	-0.942	-0.424
epsilon	-2.987	0.448	-6.66605	0.000000	-3.877	-2.097

	(KBGM dB10-38B FW Acc) Dep. Var. : EDW-tot -- R = 0.646 Level of confidence: 95.0% (alpha=0.050)					
	Estimate	Standard error	t-value df = 93	p-value	Lo. Conf Limit	Up. Conf Limit
K	2.163E+09	5.239E+09	0.41299	0.6806	-8.239E+09	1.257E+10
alpha	-0.639	0.235	-2.72248	0.0077	-1.104	-0.173
epsilon	-4.649	0.843	-5.51603	0.0000	-6.322	-2.975

	(KBGM dB10-38B FW Acc) Dep. Var. : MNS -- R = 0.795 Level of confidence: 95.0% (alpha=0.050)					
	Estimate	Standard error	t-value df = 93	p-value	Lo. Conf Limit	Up. Conf Limit
K	691068.9	787963.2	0.87703	0.382729	-873670	2255808
alpha	-0.583	0.111	-5.24381	0.000001	-0.804	-0.362
epsilon	-2.858	0.402	-7.10377	0.000000	-3.657	-2.059

dB10-38B Footwall Geophone

	(KBGM dB10-38B FW Geo) Dep. Var. : PPV -- R = 0.607 Level of confidence: 95.0% (alpha=0.050)					
	Estimate	Standard error	t-value df = 81	p-value	Lo. Conf Limit	Up. Conf Limit
K	1190.655	1309.898	0.90897	0.366064	-1415.63	3796.942
alpha	0.504	0.084	6.02233	0.000000	0.34	0.670
epsilon	-1.764	0.349	-5.05637	0.000003	-2.46	-1.070

	(KBGM dB10-38B FW Geo) Dep. Var. : EDW-tot -- R = 0.827 Level of confidence: 95.0% (alpha=0.050)					
	Estimate	Standard error	t-value df = 81	p-value	Lo. Conf Limit	Up. Conf Limit
K	841103.7	2404774	0.34976	0.727423	-3943642	5625850
alpha	2.605	0.30	8.71263	0.000000	2.010	3.200
epsilon	-6.202	0.94	-6.58205	0.000000	-8.077	-4.327

	(KBGM dB10-38B FW Geo) Dep. Var. : MNS -- R = 0.747 Level of confidence: 95.0% (alpha=0.050)					
	Estimate	Standard error	t-value df = 81	p-value	Lo. Conf Limit	Up. Conf Limit
K	2147.466	2798.313	0.76741	0.445066	-3420.30	7715.231
alpha	0.866	0.102	8.45584	0.000000	0.662	1.069
epsilon	-2.585	0.409	-6.31455	0.000000	-3.400	-1.771

A9.4 KBGM Individual Regression Results: dB10-38T

dB10-38T East Wall Accelerometer and Geophone

	(KBGM-dB10-38T EW Acc-Geo) Dep. Var. : PPA -- R = 0.769 Level of confidence: 95.0% (alpha=0.050)					
	Estimate	Standard error	t-value df = 217	p-value	Lo. Conf Limit	Up. Conf Limit
K	0.91774	0.715046	1.28347	0.200695	-0.49158	2.32707
alpha	2.79	0.121	22.97377	0.000000	2.551	3.030
epsilon	-2.08	0.244	-8.49532	0.000000	-2.558	-1.595

	(KBGM-dB10-38T EW Acc-Geo) Dep. Var. : EDW-tot -- R = 0.788 Level of confidence: 95.0% (alpha=0.050)					
	Estimate	Standard error	t-value df = 217	p-value	Lo. Conf Limit	Up. Conf Limit
K	0.11999	0.128645	0.93274	0.351990	-0.13356	0.37355
alpha	3.13	0.146	21.36842	0.000000	2.838	3.414
epsilon	-1.89	0.301	-6.27363	0.000000	-2.482	-1.295

	(KBGM-dB10-38T EW Acc-Geo) Dep. Var. : MNS -- R = 0.593 Level of confidence: 95.0% (alpha=0.050)					
	Estimate	Standard error	t-value df = 217	p-value	Lo. Conf Limit	Up. Conf Limit
K	8.73479	5.247645	1.66452	0.097452	-1.60809	19.07767
alpha	1.089	0.1145	9.50428	0.000000	0.863	1.314
epsilon	-1.149	0.1478	-7.77139	0.000000	-1.440	-0.858

dB10-38T East Wall Accelerometer

(KBGM-dB10-38T EW Acc)
Dep. Var. : PPV -- R = 0.577
Level of confidence: 95.0% (alpha=0.050)

	Estimate	Standard error	t-value df = 42	p-value	Lo. Conf Limit	Up. Conf Limit
K	61.63801	113.1690	0.54465	0.588871	-166.746	290.0223
alpha	1.2491	0.464	2.68987	0.010211	0.312	2.1862
epsilon	-1.6961	0.500	-3.39302	0.001518	-2.705	-0.6873

(KBGM-dB10-38T EW Acc)
Dep. Var. : EDW-tot -- R = 0.361
Level of confidence: 95.0% (alpha=0.050)

	Estimate	Standard error	t-value df = 42	p-value	Lo. Conf Limit	Up. Conf Limit
K	6695.241	18676.34	0.35849	0.721774	-30995.1	44385.63
alpha	0.219	0.663	0.32982	0.743178	-1.119	1.5561
epsilon	-1.322	0.700	-1.88837	0.065896	-2.734	0.0908

(KBGM-dB10-38T EW Acc)
Dep. Var. : MNS -- R = 0.470
Level of confidence: 95.0% (alpha=0.050)

	Estimate	Standard error	t-value df = 42	p-value	Lo. Conf Limit	Up. Conf Limit
K	90.74952	166.3106	0.54566	0.588184	-244.879	426.3779
alpha	0.48756	0.4331	1.12574	0.266669	-0.386	1.3616
epsilon	-1.21126	0.4467	-2.71139	0.009665	-2.113	-0.3097

dB10-38T East Wall Geophone

(KBGM-dB10-38T EW Geo)
Dep. Var. : PPA -- R = 0.875
Level of confidence: 95.0% (alpha=0.050)

	Estimate	Standard error	t-value df = 172	p-value	Lo. Conf Limit	Up. Conf Limit
K	32301.29	56590.06	0.57079	0.568884	-79399.1	144001.7
alpha	2.108	0.096	22.02432	0.000000	1.919	2.297
epsilon	-4.399	0.526	-8.35688	0.000000	-5.438	-3.360

(KBGM-dB10-38T EW Geo)
Dep. Var. : EDWtot -- R = 0.897
Level of confidence: 95.0% (alpha=0.050)

	Estimate	Standard error	t-value df = 172	p-value	Lo. Conf Limit	Up. Conf Limit
K	28811.00	48090.16	0.59910	0.549892	-66111.9	123733.9
alpha	2.136	0.093	23.05311	0.000000	1.953	2.319
epsilon	-4.305	0.497	-8.65827	0.000000	-5.286	-3.323

(KBGM-dB10-38T EW Geo)
Dep. Var. : MNS -- R = 0.829
Level of confidence: 95.0% (alpha=0.050)

	Estimate	Standard error	t-value df = 172	p-value	Lo. Conf Limit	Up. Conf Limit
K	3660.867	2672.321	1.3699	0.172497	-1613.90	8935.633
alpha	0.897	0.060	15.0141	0.000000	0.779	1.015
epsilon	-2.756	0.221	-12.4533	0.000000	-3.193	-2.319

dB10-38T Footwall Accelerometer and Geophone

(KBGM-dB10-38T FW Acc-Geo)
Dep. Var. : PPA -- R = 0.581
Level of confidence: 95.0% (alpha=0.050)

	Estimate	Standard error	t-value df = 316	p-value	Lo. Conf Limit	Up. Conf Limit
K	2028.367	856.6829	2.3677	0.018501	342.8438	3713.890
alpha	0.609	0.0786	7.7485	0.000000	0.4545	0.764
epsilon	-1.558	0.1255	-12.4115	0.000000	-1.8049	-1.311

(KBGM-dB10-38T FW Acc-Geo)
Dep. Var. : EDW-tot -- R = 0.384
Level of confidence: 95.0% (alpha=0.050)

	Estimate	Standard error	t-value df = 316	p-value	Lo. Conf Limit	Up. Conf Limit
K	377.7617	549.2684	0.68775	0.492112	-702.924	1458.447
alpha	1.827	0.382	4.78971	0.000003	1.077	2.578
epsilon	-2.076	0.332	-6.24380	0.000000	-2.730	-1.422

(KBGM-dB10-38T FW Acc-Geo)
Dep. Var. : MNS -- R = 0.514
Level of confidence: 95.0% (alpha=0.050)

	Estimate	Standard error	t-value df = 316	p-value	Lo. Conf Limit	Up. Conf Limit
K	15.99994	10.65218	1.50203	0.134087	-4.95822	36.95810
alpha	1.189	0.155	7.69166	0.000000	0.885	1.493
epsilon	-1.300	0.166	-7.82497	0.000000	-1.627	-0.974

dB10-38T Footwall Accelerometer

(KBGM-dB10-38T FW Acc)
Dep. Var. : PPA -- R = 0.549
Level of confidence: 95.0% (alpha=0.050)

	Estimate	Standard error	t-value df = 164	p-value	Lo. Conf Limit	Up. Conf Limit
K	716.7407	447.5084	1.60163	0.111163	-166.880	1600.362
alpha	0.700	0.117	5.96549	0.000000	0.468	0.932
epsilon	-1.285	0.197	-6.54097	0.000000	-1.673	-0.897

(KBGM-dB10-38T FW Acc)
Dep. Var. : EDW-tot -- R = 0.376
Level of confidence: 95.0% (alpha=0.050)

	Estimate	Standard error	t-value df = 164	p-value	Lo. Conf Limit	Up. Conf Limit
K	109.9562	170.4444	0.64511	0.519754	-226.592	446.5046
alpha	1.381	0.375	3.68605	0.000309	0.641	2.120
epsilon	-0.792	0.454	-1.74346	0.083128	-1.689	0.105

(KBGM-dB10-38T FW Acc)
Dep. Var. : MNS -- R = 0.512
Level of confidence: 95.0% (alpha=0.050)

	Estimate	Standard error	t-value df = 164	p-value	Lo. Conf Limit	Up. Conf Limit
K	4.036989	3.587627	1.12525	0.262126	-3.04690	11.12088
alpha	1.130	0.197	5.74272	0.000000	0.741	1.518
epsilon	-0.652	0.257	-2.53909	0.012045	-1.159	-0.145

dB10-38T Footwall Geophone

	(KBGM-dB10-38T FW Geo) Dep. Var. : PPV -- R = 0.589 Level of confidence: 95.0% (alpha=0.050)					
	Estimate	Standard error	t-value df = 149	p-value	Lo. Conf Limit	Up. Conf Limit
K	325.7481	229.6404	1.41851	0.158129	-128.024	779.5205
alpha	0.615	0.083	7.39557	0.000000	0.451	0.780
epsilon	-1.265	0.236	-5.36880	0.000000	-1.730	-0.799

	(KBGM-dB10-38T FW Geo) Dep. Var. : EDWtot -- R = 0.599 Level of confidence: 95.0% (alpha=0.050)					
	Estimate	Standard error	t-value df = 149	p-value	Lo. Conf Limit	Up. Conf Limit
K	264.9772	278.5053	0.95143	0.342929	-285.353	815.3074
alpha	1.654	0.253	6.52507	0.000000	1.153	2.154
epsilon	-2.150	0.436	-4.92637	0.000002	-3.012	-1.287

	(KBGM-dB10-38T FW Geo) Dep. Var. : MNS -- R = 0.626 Level of confidence: 95.0% (alpha=0.050)					
	Estimate	Standard error	t-value df = 149	p-value	Lo. Conf Limit	Up. Conf Limit
K	172.4608	111.5108	1.54658	0.124085	-47.8860	392.8075
alpha	0.576	0.073	7.90025	0.000000	0.432	0.721
epsilon	-1.315	0.216	-6.09364	0.000000	-1.741	-0.889

dB10-38T Hangingwall Accelerometer and Geophone

	(KBGM-dB10-38T HW Acc-Geo) Dep. Var. : PPA - R = 0.486 Level of confidence: 95.0% (alpha=0.050)					
	Estimate	Standard error	t-value df = 216	p-value	Lo. Conf Limit	Up. Conf Limit
K	3208.022	2989.378	1.07314	0.284406	-2684.06	9100.108
alpha	0.440	0.084	5.24405	0.000000	0.275	0.605
epsilon	-1.618	0.279	-5.81019	0.000000	-2.167	-1.069

	(KBGM-dB10-38T HW Acc-Geo) Dep. Var. : EDW-tot -- R = 0.591 Level of confidence: 95.0% (alpha=0.050)					
	Estimate	Standard error	t-value df = 216	p-value	Lo. Conf Limit	Up. Conf Limit
K	0.094020	0.115309	0.815381	0.415753	-0.133254	0.321294
alpha	1.220	0.170	7.157385	0.000000	0.884	1.556
epsilon	0.329	0.319	1.033797	0.302387	-0.299	0.957

	(KBGM-dB10-38T HW Acc-Geo) Dep. Var. : MNS -- R = 0.614 Level of confidence: 95.0% (alpha=0.050)					
	Estimate	Standard error	t-value df = 216	p-value	Lo. Conf Limit	Up. Conf Limit
K	0.356423	0.241264	1.477316	0.141047	-0.119110	0.831955
alpha	0.633	0.065	9.745984	0.000000	0.505	0.761
epsilon	0.255	0.193	1.320201	0.188165	-0.126	0.635

dB10-38T Hangingwall Accelerometer

	(KBGM-dB10-38T HW Acc) Dep. Var. : PPV -- R = 0.569 Level of confidence: 95.0% (alpha=0.050)					
	Estimate	Standard error	t-value df = 109	p-value	Lo. Conf Limit	Up. Conf Limit
K	228.9140	284.4334	0.80481	0.422683	-334.824	792.6517
alpha	0.530	0.098	5.42997	0.000000	0.337	0.724
epsilon	-1.479	0.391	-3.78371	0.000253	-2.253	-0.704

	(KBGM-dB10-38T HW Acc) Dep. Var. : EDW-tot -- R = 0.588 Level of confidence: 95.0% (alpha=0.050)					
	Estimate	Standard error	t-value df = 109	p-value	Lo. Conf Limit	Up. Conf Limit
K	0.76734	1.488664	0.51545	0.607281	-2.18315	3.717820
alpha	1.88	0.359	5.24266	0.000001	1.171	2.595
epsilon	-1.41	0.653	-2.16734	0.032385	-2.708	-0.121

	(KBGM-dB10-38T HW Acc) Dep. Var. : MNS -- R = 0.581 Level of confidence: 95.0% (alpha=0.050)					
	Estimate	Standard error	t-value df = 109	p-value	Lo. Conf Limit	Up. Conf Limit
K	25.37605	27.79999	0.91281	0.363358	-29.7226	80.47473
alpha	0.536	0.087	6.16841	0.000000	0.364	0.708
epsilon	-1.071	0.343	-3.12246	0.002297	-1.751	-0.391

dB10-38T Hangingwall Geophone

	(KBGM-dB10-38T HW Geo) Dep. Var. : PPV -- R = 0.669 Level of confidence: 95.0% (alpha=0.050)					
	Estimate	Standard error	t-value df = 104	p-value	Lo. Conf Limit	Up. Conf Limit
K	5339.351	8053.177	0.66301	0.508790	-10630.4	21309.10
alpha	0.487	0.075	6.52829	0.000000	0.339	0.635
epsilon	-2.059	0.436	-4.72080	0.000007	-2.924	-1.194

	(KBGM-dB10-38T HW Geo) Dep. Var. : EDWtot -- R = 0.760 Level of confidence: 95.0% (alpha=0.050)					
	Estimate	Standard error	t-value df = 104	p-value	Lo. Conf Limit	Up. Conf Limit
K	1966.394	3715.991	0.52917	0.597815	-5402.56	9335.344
alpha	1.291	0.188	6.85877	0.000000	0.918	1.664
epsilon	-2.588	0.586	-4.41545	0.000025	-3.750	-1.425

	(KBGM-dB10-38T HW Geo) Dep. Var. : MNS -- R = 0.811 Level of confidence: 95.0% (alpha=0.050)					
	Estimate	Standard error	t-value df = 104	p-value	Lo. Conf Limit	Up. Conf Limit
K	225.6413	245.1053	0.92059	0.359395	-260.412	711.6943
alpha	0.684	0.066	10.33664	0.000000	0.553	0.815
epsilon	-1.633	0.315	-5.18182	0.000001	-2.258	-1.008

A9.5 Cannington Mine Individual Regression Results: 22gC6HL

22gC6HL Northeast Wall-240mLv Geophones

	(Cann 22gC6 NE-240 Geo) Dep. Var. : PPV -- R = 0.736 Level of confidence: 95.0% (alpha=0.050)					
	Estimate	Standard error	t-value df = 560	p-value	Lo. Conf Limit	Up. Conf Limit
K	2544.179	878.8927	2.8948	0.003942	817.8495	4270.508
alpha	0.397	0.0487	8.1388	0.000000	0.301	0.492
epsilon	-1.575	0.0739	-21.3069	0.000000	-1.721	-1.430

	(Cann 22gC6 NE-240 Geo) Dep. Var. : EDWtot -- R = 0.679 Level of confidence: 95.0% (alpha=0.050)					
	Estimate	Standard error	t-value df = 560	p-value	Lo. Conf Limit	Up. Conf Limit
K	862.0171	612.8098	1.4067	0.160082	-341.669	2065.704
alpha	1.393	0.118	11.7945	0.000000	1.161	1.625
epsilon	-2.106	0.131	-16.0915	0.000000	-2.363	-1.849

	(Cann 22gC6 NE-240 Geos) Dep. Var. : MNS -- R = 0.760 Level of confidence: 95.0% (alpha=0.050)					
	Estimate	Standard error	t-value df = 560	p-value	Lo. Conf Limit	Up. Conf Limit
K	519.8647	151.4868	3.4317	0.000644	222.3129	817.4165
alpha	0.396	0.042	9.5446	0.000000	0.315	0.478
epsilon	-1.433	0.062	-23.0362	0.000000	-1.555	-1.311

22gC6HL Northwest Wall Accelerometer and Geophone

	(Cann 22gC6 NW Acc-Geo) Dep. Var. : PPA -- R = 0.760 Level of confidence: 95.0% (alpha=0.050)					
	Estimate	Standard error	t-value df = 437	p-value	Lo. Conf Limit	Up. Conf Limit
K	905225.2	379009.9	2.3884	0.017346	160316.3	1650134
alpha	0.204	0.060	3.3870	0.000771	0.086	0.32
epsilon	-2.814	0.106	-26.6459	0.000000	-3.022	-2.61

	(Cann 22gC6 NW Acc-Geo) Dep. Var. : EDW-tot -- R = 0.503 Level of confidence: 95.0% (alpha=0.050)					
	Estimate	Standard error	t-value df = 437	p-value	Lo. Conf Limit	Up. Conf Limit
K	1386.467	1233.828	1.12371	0.261752	-1038.51	3811.440
alpha	1.169	0.141	8.27951	0.000000	0.892	1.447
epsilon	-1.878	0.199	-9.45871	0.000000	-2.268	-1.487

	(Cann 22gC6 NW Acc-Geo) Dep. Var. : MNS -- R = 0.563 Level of confidence: 95.0% (alpha=0.050)					
	Estimate	Standard error	t-value df = 437	p-value	Lo. Conf Limit	Up. Conf Limit
K	62.95069	27.30386	2.3056	0.021603	9.28747	116.6139
alpha	0.687	0.064	10.7256	0.000000	0.561	0.812
epsilon	-1.190	0.109	-10.9255	0.000000	-1.404	-0.976

22gC6HL Northwest Wall Accelerometer

Cann 22gC6 NW Acc
Dep. Var. : PPV -- R = 0.767
Level of confidence: 95.0% (alpha=0.050)

	Estimate	Standard error	t-value df = 165	p-value	Lo. Conf Limit	Up. Conf Limit
K	54744.48	40632.27	1.3473	0.179726	-25481.7	134970.7
alpha	0.439	0.095	4.5976	0.000008	0.250	0.627
epsilon	-2.925	0.200	-14.5910	0.000000	-3.321	-2.529

(Cann 22gC6 NW Acc)
Dep. Var. : EDW-tot -- R = 0.767
Level of confidence: 95.0% (alpha=0.050)

	Estimate	Standard error	t-value df = 165	p-value	Lo. Conf Limit	Up. Conf Limit
K	3707549	3994990	0.9280	0.354737	-4180342	11595440
alpha	0.756	0.125	6.0637	0.000000	0.510	1.002
epsilon	-4.298	0.348	-12.3543	0.000000	-4.985	-3.611

(Cann 22gC6 NW Acc)
Dep. Var. : MNS -- R = 0.775
Level of confidence: 95.0% (alpha=0.050)

	Estimate	Standard error	t-value df = 165	p-value	Lo. Conf Limit	Up. Conf Limit
K	9027.719	6022.807	1.4989	0.135805	-2863.99	20919.42
alpha	0.418	0.086	4.8383	0.000003	0.248	0.589
epsilon	-2.691	0.178	-15.1226	0.000000	-3.042	-2.340

22gC6HL Northwest Wall Geophone

(Cann 22gC6 NW Geo)
Dep. Var. : PPV -- R = 0.783
Level of confidence: 95.0% (alpha=0.050)

	Estimate	Standard error	t-value df = 269	p-value	Lo. Conf Limit	Up. Conf Limit
K	18763.95	9456.630	1.9842	0.048248	145.5331	37382.38
alpha	0.334	0.050	6.6992	0.000000	0.236	0.432
epsilon	-2.101	0.127	-16.5935	0.000000	-2.350	-1.851

(Cann 22gC6 NW Geo)
Dep. Var. : EDWtot -- R = 0.536
Level of confidence: 95.0% (alpha=0.050)

	Estimate	Standard error	t-value df = 269	p-value	Lo. Conf Limit	Up. Conf Limit
K	3376.385	5127.045	0.65854	0.510752	-6717.85	13470.62
alpha	1.213	0.210	5.77792	0.000000	0.800	1.627
epsilon	-2.102	0.337	-6.24340	0.000000	-2.765	-1.439

(Cann 22gC6 NW Geo)
Dep. Var. : MNS -- R = 0.690
Level of confidence: 95.0% (alpha=0.050)

	Estimate	Standard error	t-value df = 269	p-value	Lo. Conf Limit	Up. Conf Limit
K	376.1976	225.2813	1.6699	0.096102	-67.3412	819.7363
alpha	0.611	0.067	9.1110	0.000000	0.479	0.743
epsilon	-1.563	0.148	-10.5683	0.000000	-1.854	-1.272

A9.6 Cannington Mine Individual Regression Results: 24jC6HL

24jC6HL 220mLv Northeast Wall Geophone

(Cann 24jC6 220 NE Geo)
Dep. Var. : PPA -- R = 0.721
Level of confidence: 95.0% (alpha=0.050)

	Estimate	Standard error	t-value df = 88	p-value	Lo. Conf Limit	Up. Conf Limit
K	4290.125	2630.350	1.63101	0.106462	-937.143	9517.393
alpha	0.553	0.148	3.74744	0.000319	0.260	0.846
epsilon	-1.537	0.164	-9.35502	0.000000	-1.864	-1.210

(Cann 24jC6 220 NE Geo)
Dep. Var. : EDW-tot -- R = 0.480
Level of confidence: 95.0% (alpha=0.050)

	Estimate	Standard error	t-value df = 88	p-value	Lo. Conf Limit	Up. Conf Limit
K	555.2835	799.2412	0.69476	0.489034	-1033.04	2143.607
alpha	1.433	0.424	3.38118	0.001078	0.591	2.275
epsilon	-1.737	0.441	-3.93414	0.000166	-2.614	-0.859

(Cann 24jC6 220 NE Geo)
Dep. Var. : MNS -- R = 0.616
Level of confidence: 95.0% (alpha=0.050)

	Estimate	Standard error	t-value df = 88	p-value	Lo. Conf Limit	Up. Conf Limit
K	97.25710	61.06208	1.59276	0.114800	-24.0909	218.6051
alpha	0.660	0.151	4.37267	0.000034	0.360	0.960
epsilon	-1.144	0.175	-6.52871	0.000000	-1.493	-0.796

24jC6HL 220mLv Southeast Wall Accelerometer and Geophone

(Cann 24jC6 220 SE Acc-Geo)
Dep. Var. : PPA -- R = 0.780
Level of confidence: 95.0% (alpha=0.050)

	Estimate	Standard error	t-value df = 144	p-value	Lo. Conf Limit	Up. Conf Limit
K	245290.8	146155.8	1.6783	0.095461	-43597.1	534178.8
alpha	-0.017	0.116	-0.1488	0.881953	-0.247	0.212
epsilon	-2.248	0.175	-12.8738	0.000000	-2.593	-1.903

(Cann 24jC6 220 SE Acc-Geo)
Dep. Var. : EDWtot -- R = 0.816
Level of confidence: 95.0% (alpha=0.050)

	Estimate	Standard error	t-value df = 144	p-value	Lo. Conf Limit	Up. Conf Limit
K	838.7918	6768371	0.000124	0.999901	-13377355	13379033
alpha	33.4548	4059	0.008242	0.993435	-7989	8056
epsilon	-61.4081	3791	-0.016200	0.987097	-7554	7431

(Cann 24jC6 220 SE Acc-Geo)
Dep. Var. : MNS -- R = 0.719
Level of confidence: 95.0% (alpha=0.050)

	Estimate	Standard error	t-value df = 144	p-value	Lo. Conf Limit	Up. Conf Limit
K	6406.943	4368.974	1.4665	0.144702	-2228.66	15042.55
alpha	0.462	0.133	3.4648	0.000699	0.199	0.726
epsilon	-2.428	0.202	-12.0476	0.000000	-2.826	-2.029

24jC6HL 220mLv Southeast Wall Accelerometer

(Cann 24jC6 220 SE Acc)
Dep. Var. : PPA -- R = 0.726
Level of confidence: 95.0% (alpha=0.050)

	Estimate	Standard error	t-value df = 62	p-value	Lo. Conf Limit	Up. Conf Limit
K	127488.9	135252.1	0.94260	0.349543	-142876	397854.0
alpha	-0.027	0.183	-0.14977	0.881433	-0.393	0.338
epsilon	-1.939	0.332	-5.83990	0.000000	-2.603	-1.275

(Cann 24jC6 220 SE Acc)
Dep. Var. : EDWtot -- R = 0.813
Level of confidence: 95.0% (alpha=0.050)

	Estimate	Standard error	t-value df = 62	p-value	Lo. Conf Limit	Up. Conf Limit
K	1702.316	24008799	0.000071	0.999944	-47991203	47994607
alpha	33.801	7255	0.004659	0.996298	-14469	14536
epsilon	-62.412	6776	-0.009211	0.992680	-13607	13482

(Cann 24jC6 220 SE Acc)
Dep. Var. : MNS -- R = 0.715
Level of confidence: 95.0% (alpha=0.050)

	Estimate	Standard error	t-value df = 62	p-value	Lo. Conf Limit	Up. Conf Limit
K	35719.58	55567.41	0.64282	0.522714	-75358.1	146797.2
alpha	0.399	0.229	1.74082	0.086675	-0.059	0.856
epsilon	-3.091	0.505	-6.11868	0.000000	-4.101	-2.081

24jC6HL 220mLv Southeast Wall Geophone

(Cann 24jC6 220 SE Geo)
Dep. Var. : PPA -- R = 0.664
Level of confidence: 95.0% (alpha=0.050)

	Estimate	Standard error	t-value df = 79	p-value	Lo. Conf Limit	Up. Conf Limit
K	110081.0	124960.3	0.88093	0.381029	-138646	358808.4
alpha	0.086	0.123	0.70386	0.483592	-0.158	0.331
epsilon	-2.150	0.385	-5.58207	0.000000	-2.917	-1.383

(Cann 24jC6 220 SE Geo)
Dep. Var. : EDWtot -- R = 0.620
Level of confidence: 95.0% (alpha=0.050)

	Estimate	Standard error	t-value df = 79	p-value	Lo. Conf Limit	Up. Conf Limit
K	176918.1	459934.1	0.38466	0.701523	-738558	1092394
alpha	1.167	0.232	5.03745	0.000003	0.706	1.628
epsilon	-3.391	0.897	-3.78031	0.000303	-5.176	-1.605

(Cann 24jC6 220 SE Geo)
Dep. Var. : MNS -- R = 0.658
Level of confidence: 95.0% (alpha=0.050)

	Estimate	Standard error	t-value df = 79	p-value	Lo. Conf Limit	Up. Conf Limit
K	701.7333	586.2467	1.19699	0.234889	-465.162	1868.628
alpha	0.545	0.108	5.04030	0.000003	0.330	0.761
epsilon	-1.695	0.272	-6.22630	0.000000	-2.237	-1.153

24jC6HL 220mLv Southwest Wall Accelerometer and Geophone

(Cann 24jC6 220 SW Acc-Geo)
Dep. Var. : PPA -- R = 0.752
Level of confidence: 95.0% (alpha=0.050)

	Estimate	Standard error	t-value df = 159	p-value	Lo. Conf Limit	Up. Conf Limit
K	1368057	1065586	1.2839	0.201061	-736470	3472585
alpha	-0.165	0.101	-1.6399	0.103004	-0.364	0.034
epsilon	-2.468	0.204	-12.0714	0.000000	-2.871	-2.064

(Cann 24jC6 220 SW Acc-Geo)
Dep. Var. : EDWtot -- R = 0.553
Level of confidence: 95.0% (alpha=0.050)

	Estimate	Standard error	t-value df = 159	p-value	Lo. Conf Limit	Up. Conf Limit
K	20917733	38030600	0.55002	0.583075	-54192558	96028024
alpha	-0.216	0.213	-1.01409	0.312081	-0.637	0.205
epsilon	-2.968	0.483	-6.14837	0.000000	-3.922	-2.015

(Cann 24jC6 220 SW Acc-Geo)
Dep. Var. : MNS -- R = 0.654
Level of confidence: 95.0% (alpha=0.050)

	Estimate	Standard error	t-value df = 159	p-value	Lo. Conf Limit	Up. Conf Limit
K	24199.90	18480.63	1.3095	0.192263	-12299.3	60699.08
alpha	-0.115	0.108	-1.0624	0.289668	-0.329	0.099
epsilon	-1.976	0.197	-10.0470	0.000000	-2.364	-1.588

24jC6HL 220mLv Southwest Wall Accelerometer

(Cann 24jC6 220 SW Acc)
Dep. Var. : PPA -- R = 0.662
Level of confidence: 95.0% (alpha=0.050)

	Estimate	Standard error	t-value df = 76	p-value	Lo. Conf Limit	Up. Conf Limit
K	588001.1	746723.6	0.78744	0.433472	-899228	2075230
alpha	-0.136	0.142	-0.95848	0.340858	-0.420	0.147
epsilon	-2.174	0.352	-6.16728	0.000000	-2.876	-1.472

(Cann 24jC6 220 SW Acc)
Dep. Var. : EDWtot -- R = 0.453
Level of confidence: 95.0% (alpha=0.050)

	Estimate	Standard error	t-value df = 76	p-value	Lo. Conf Limit	Up. Conf Limit
K	4150207	11628791	0.35689	0.722163	-19010538	27310952
alpha	-0.112	0.303	-0.36829	0.713679	-0.716	0.492
epsilon	-2.478	0.773	-3.20445	0.001979	-4.019	-0.938

(Cann 24jC6 220 SW Acc)
Dep. Var. : MNS -- R = 0.585
Level of confidence: 95.0% (alpha=0.050)

	Estimate	Standard error	t-value df = 76	p-value	Lo. Conf Limit	Up. Conf Limit
K	37972.66	54023.97	0.70289	0.484275	-69625.4	145570.7
alpha	-0.216	0.163	-1.32410	0.189438	-0.540	0.109
epsilon	-2.003	0.400	-5.01110	0.000003	-2.798	-1.207

24jC6HL 220mLv Southwest Wall Geophone

	(Cann 24jC6 220 SW Geo) Dep. Var. : PPV -- R = 0.480 Level of confidence: 95.0% (alpha=0.050)					
	Estimate	Standard error	t-value df = 80	p-value	Lo. Conf Limit	Up. Conf Limit
K	475.0084	659.9982	0.71971	0.473800	-838.430	1788.447
alpha	0.477	0.127	3.74689	0.000337	0.223	0.730
epsilon	-1.166	0.379	-3.07995	0.002837	-1.919	-0.413

	(Cann 24jC6 220 SW Geo) Dep. Var. : EDWtot -- R = 0.341 Level of confidence: 95.0% (alpha=0.050)					
	Estimate	Standard error	t-value df = 80	p-value	Lo. Conf Limit	Up. Conf Limit
K	380.8502	1625.559	0.23429	0.815359	-2854.12	3615.816
alpha	1.151	0.476	2.41885	0.017840	0.204	2.098
epsilon	-1.327	1.066	-1.24546	0.216597	-3.448	0.794

	(Cann 24jC6 220 SW Geo) Dep. Var. : MNS -- R = 0.454 Level of confidence: 95.0% (alpha=0.050)					
	Estimate	Standard error	t-value df = 80	p-value	Lo. Conf Limit	Up. Conf Limit
K	33.27337	51.29889	0.64862	0.518443	-68.8147	135.3614
alpha	0.606	0.151	4.01919	0.000131	0.306	0.906
epsilon	-0.759	0.416	-1.82551	0.071655	-1.586	0.068

24jC6HL 200mLv Northeast Wall Accelerometer and Geophone

	(Cann 24jC6 200 NE Acc-Geo) Dep. Var. : PPA -- R = 0.828 Level of confidence: 95.0% (alpha=0.050)					
	Estimate	Standard error	t-value df = 178	p-value	Lo. Conf Limit	Up. Conf Limit
K	3052905	2246952	1.3587	0.175965	-1381187	7486996
alpha	-0.579	0.122	-4.7392	0.000004	-0.821	-0.338
epsilon	-2.266	0.132	-17.1242	0.000000	-2.527	-2.005

	(Cann 24jC6 200 NE Acc-Geo) Dep. Var. : EDWtot -- R = 0.783 Level of confidence: 95.0% (alpha=0.050)					
	Estimate	Standard error	t-value df = 178	p-value	Lo. Conf Limit	Up. Conf Limit
K	3.440731E+10	5.369672E+10	0.6408	0.5225	-7.1557E+10	1.4037E+11
alpha	-1.672	0.239	-7.0035	0.0000	-2.143	-1.201
epsilon	-3.720	0.304	-12.2401	0.0000	-4.319	-3.120

	(Cann 24jC6 200 NE Acc-Geo) Dep. Var. : MNS -- R = 0.797 Level of confidence: 95.0% (alpha=0.050)					
	Estimate	Standard error	t-value df = 178	p-value	Lo. Conf Limit	Up. Conf Limit
K	222917.4	155512.7	1.4334	0.153488	-83968.3	529803.1
alpha	-0.644	0.116	-5.5395	0.000000	-0.873	-0.415
epsilon	-2.092	0.128	-16.3464	0.000000	-2.344	-1.839

24jC6HL 200mLv Northeast Wall Accelerometer

(Cann 24jC6 200 NE Acc)
Dep. Var. : PPA -- R = 0.800
Level of confidence: 95.0% (alpha=0.050)

	Estimate	Standard error	t-value df = 86	p-value	Lo. Conf Limit	Up. Conf Limit
K	818596.6	808262.6	1.0128	0.314004	-788176	2425369
alpha	-0.441	0.160	-2.7566	0.007132	-0.760	-0.123
epsilon	-1.895	0.187	-10.1590	0.000000	-2.266	-1.525

(Cann 24jC6 200 NE Acc)
Dep. Var. : EDW-tot -- R = 0.757
Level of confidence: 95.0% (alpha=0.050)

	Estimate	Standard error	t-value df = 86	p-value	Lo. Conf Limit	Up. Conf Limit
K	4.390336E+09	9.1523E+09	0.4797	0.6327	-1.3804E+10	2.2584E+10
alpha	-1.411	0.314	-4.4883	0.0000	-2.036	-0.786
epsilon	-3.230	0.417	-7.7399	0.0000	-4.059	-2.400

(Cann 24jC6 200 NE Acc)
Dep. Var. : MNS -- R = 0.778
Level of confidence: 95.0% (alpha=0.050)

	Estimate	Standard error	t-value df = 86	p-value	Lo. Conf Limit	Up. Conf Limit
K	209574.9	210283.2	0.99663	0.321739	-208454	627604.0
alpha	-0.714	0.159	-4.47556	0.000023	-1.030	-0.397
epsilon	-1.914	0.198	-9.68337	0.000000	-2.307	-1.521

24jC6HL 200mLv Northeast Wall Geophone

(Cann 24jC6 200 NE Geo)
Dep. Var. : PPA -- R = 0.816
Level of confidence: 95.0% (alpha=0.050)

	Estimate	Standard error	t-value df = 89	p-value	Lo. Conf Limit	Up. Conf Limit
K	119915.0	87699.37	1.3673	0.174962	-54341.8	294171.8
alpha	-0.013	0.094	-0.1350	0.892949	-0.199	0.174
epsilon	-2.097	0.179	-11.7138	0.000000	-2.452	-1.741

(Cann 24jC6 200 NE Geo)
Dep. Var. : EDWtot -- R = 0.890
Level of confidence: 95.0% (alpha=0.050)

	Estimate	Standard error	t-value df = 89	p-value	Lo. Conf Limit	Up. Conf Limit
K	2499.844	2325.881	1.0748	0.285372	-2121.63	7121.320
alpha	1.264	0.156	8.1223	0.000000	0.955	1.574
epsilon	-2.391	0.183	-13.0720	0.000000	-2.754	-2.028

(Cann 24jC6 200 NE Geo)
Dep. Var. : MNS -- R = 0.835
Level of confidence: 95.0% (alpha=0.050)

	Estimate	Standard error	t-value df = 89	p-value	Lo. Conf Limit	Up. Conf Limit
K	131.7065	72.12172	1.8262	0.071178	-11.5978	275.0108
alpha	0.619	0.084	7.3875	0.000000	0.453	0.786
epsilon	-1.348	0.122	-11.0569	0.000000	-1.590	-1.106

24jC6HL 200mLv Southeast Wall Accelerometer and Geophone

(Cann 24jC6 200 SE Acc-Geo)
Dep. Var. : PPA -- R = 0.832
Level of confidence: 95.0% (alpha=0.050)

	Estimate	Standard error	t-value df = 196	p-value	Lo. Conf Limit	Up. Conf Limit
K	5913.674	3203.802	1.8458	0.066425	-404.676	12232.02
alpha	0.479	0.112	4.2554	0.000032	0.257	0.700
epsilon	-1.489	0.071	-21.0009	0.000000	-1.629	-1.349

(Cann 24jC6 200 SE Acc-Geo)
Dep. Var. : EDWtot -- R = 0.745
Level of confidence: 95.0% (alpha=0.050)

	Estimate	Standard error	t-value df = 196	p-value	Lo. Conf Limit	Up. Conf Limit
K	728.0696	606.2843	1.2009	0.231250	-467.609	1923.748
alpha	1.117	0.175	6.3934	0.000000	0.772	1.461
epsilon	-1.403	0.101	-13.8545	0.000000	-1.602	-1.203

(Cann 24jC6 200 SE Acc-Geo)
Dep. Var. : MNS -- R = 0.773
Level of confidence: 95.0% (alpha=0.050)

	Estimate	Standard error	t-value df = 196	p-value	Lo. Conf Limit	Up. Conf Limit
K	20.25011	9.354335	2.1648	0.031613	1.802043	38.69818
alpha	0.739	0.092	8.0492	0.000000	0.558	0.920
epsilon	-0.813	0.061	-13.2256	0.000000	-0.934	-0.692

24jC6HL 200mLv Southeast Wall Accelerometer

(Cann 24jC6 200 SE Acc)
Dep. Var. : PPA -- R = 0.818
Level of confidence: 95.0% (alpha=0.050)

	Estimate	Standard error	t-value df = 96	p-value	Lo. Conf Limit	Up. Conf Limit
K	3613.837	2733.473	1.3221	0.189287	-1812.06	9039.739
alpha	0.516	0.154	3.3374	0.001204	0.209	0.822
epsilon	-1.315	0.108	-12.1890	0.000000	-1.530	-1.101

(Cann 24jC6 200 SE Acc)
Dep. Var. : EDWtot -- R = 0.749
Level of confidence: 95.0% (alpha=0.050)

	Estimate	Standard error	t-value df = 96	p-value	Lo. Conf Limit	Up. Conf Limit
K	1332.929	1689.199	0.78909	0.432004	-2020.11	4685.963
alpha	1.051	0.263	3.99278	0.000128	0.528	1.573
epsilon	-1.572	0.175	-8.96841	0.000000	-1.920	-1.224

(Cann 24jC6 200 SE Acc)
Dep. Var. : MNS -- R = 0.810
Level of confidence: 95.0% (alpha=0.050)

	Estimate	Standard error	t-value df = 96	p-value	Lo. Conf Limit	Up. Conf Limit
K	41.25986	28.40950	1.4523	0.149672	-15.1326	97.65228
alpha	0.678	0.138	4.9049	0.000004	0.404	0.953
epsilon	-1.036	0.096	-10.8072	0.000000	-1.226	-0.846

24jC6HL 200mLv Southeast Wall Geophone

(Cann 24jC6 200 SE Geo)
Dep. Var. : PPV -- R = 0.846
Level of confidence: 95.0% (alpha=0.050)

	Estimate	Standard error	t-value df = 97	p-value	Lo. Conf Limit	Up. Conf Limit
K	262.6313	151.6477	1.7319	0.086479	-38.3473	563.6100
alpha	0.709	0.096	7.3832	0.000000	0.519	0.900
epsilon	-1.213	0.110	-11.0564	0.000000	-1.431	-0.996

(Cann 24jC6 200 SE Geo)
Dep. Var. : EDWtot -- R = 0.798
Level of confidence: 95.0% (alpha=0.050)

	Estimate	Standard error	t-value df = 97	p-value	Lo. Conf Limit	Up. Conf Limit
K	2363.629	2414.727	0.97884	0.330094	-2428.93	7156.193
alpha	1.206	0.183	6.58731	0.000000	0.843	1.569
epsilon	-1.855	0.213	-8.72145	0.000000	-2.277	-1.433

(Cann 24jC6 200 SE Geo)
Dep. Var. : MNS -- R = 0.828
Level of confidence: 95.0% (alpha=0.050)

	Estimate	Standard error	t-value df = 97	p-value	Lo. Conf Limit	Up. Conf Limit
K	57.80581	33.38355	1.73157	0.086530	-8.45129	124.0629
alpha	0.687	0.094	7.30001	0.000000	0.500	0.873
epsilon	-1.026	0.108	-9.48623	0.000000	-1.241	-0.812

24jC6HL 200mLv Southwest Wall Accelerometer and Geophone

(Cann 24jC6 200 SW Acc-Geo)
Dep. Var. : PPA -- R = 0.517
Level of confidence: 95.0% (alpha=0.050)

	Estimate	Standard error	t-value df = 199	p-value	Lo. Conf Limit	Up. Conf Limit
K	8267.647	8728.591	0.94719	0.344690	-8944.76	25480.05
alpha	0.634	0.188	3.37107	0.000899	0.263	1.006
epsilon	-1.510	0.229	-6.60400	0.000000	-1.961	-1.059

(Cann 24jC6 200 SW Acc-Geo)
Dep. Var. : EDWtot -- R = 0.366
Level of confidence: 95.0% (alpha=0.050)

	Estimate	Standard error	t-value df = 199	p-value	Lo. Conf Limit	Up. Conf Limit
K	2160.352	3813.697	0.56647	0.571711	-5360.09	9680.797
alpha	1.019	0.312	3.26303	0.001297	0.403	1.635
epsilon	-1.147	0.373	-3.07743	0.002382	-1.882	-0.412

(Cann 24jC6 200 SW Acc-Geo)
Dep. Var. : MNS -- R = 0.503
Level of confidence: 95.0% (alpha=0.050)

	Estimate	Standard error	t-value df = 199	p-value	Lo. Conf Limit	Up. Conf Limit
K	48.02281	44.76834	1.07270	0.284707	-40.2584	136.3040
alpha	0.830	0.162	5.12375	0.000001	0.511	1.150
epsilon	-0.934	0.194	-4.80898	0.000003	-1.317	-0.551

24jC6HL 200mLv Southeast Wall Accelerometer

(Cann 24jC6 200 SW Acc)
Dep. Var. : PPV -- R = 0.519
Level of confidence: 95.0% (alpha=0.050)

	Estimate	Standard error	t-value df = 98	p-value	Lo. Conf Limit	Up. Conf Limit
K	0.206165	0.328916	0.626801	0.532247	-0.446558	0.858888
alpha	1.229	0.225	5.461824	0.000000	0.783	1.676
epsilon	0.769	0.362	2.123458	0.036234	0.050	1.488

(Cann 24jC6 200 SW Acc)
Dep. Var. : EDWtot -- R = 0.467
Level of confidence: 95.0% (alpha=0.050)

	Estimate	Standard error	t-value df = 98	p-value	Lo. Conf Limit	Up. Conf Limit
K	0.145899	0.355090	0.410879	0.682058	-0.558765	0.850563
alpha	1.542	0.349	4.422998	0.000025	0.850	2.234
epsilon	1.482	0.537	2.759441	0.006910	0.416	2.547

(Cann 24jC6 200 SW Acc)
Dep. Var. : MNS -- R = 0.529
Level of confidence: 95.0% (alpha=0.050)

	Estimate	Standard error	t-value df = 98	p-value	Lo. Conf Limit	Up. Conf Limit
K	0.156333	0.230995	0.676780	0.500140	-0.302070	0.614735
alpha	1.172	0.208	5.620161	0.000000	0.758	1.585
epsilon	0.594	0.337	1.762833	0.081046	-0.075	1.262

24jC6HL 200mLv Southeast Wall Geophone

(Cann 24jC6 200 SW Geo)
Dep. Var. : PPV -- R = 0.470
Level of confidence: 95.0% (alpha=0.050)

	Estimate	Standard error	t-value df = 98	p-value	Lo. Conf Limit	Up. Conf Limit
K	94.48607	128.4055	0.73584	0.463585	-160.330	349.3026
alpha	0.683	0.160	4.27693	0.000044	0.366	0.999
epsilon	-0.797	0.348	-2.28971	0.024183	-1.488	-0.106

(Cann 24jC6 200 SW Geo)
Dep. Var. : EDWtot -- R = 0.477
Level of confidence: 95.0% (alpha=0.050)

	Estimate	Standard error	t-value df = 98	p-value	Lo. Conf Limit	Up. Conf Limit
K	44.65285	107.8464	0.41404	0.679749	-169.365	258.6706
alpha	1.467	0.287	5.11670	0.000002	0.898	2.036
epsilon	-0.932	0.629	-1.48079	0.141872	-2.180	0.317

(Cann 24jC6 200 SW Geo)
Dep. Var. : MNS -- R = 0.513
Level of confidence: 95.0% (alpha=0.050)

	Estimate	Standard error	t-value df = 98	p-value	Lo. Conf Limit	Up. Conf Limit
K	20.82148	24.60043	0.84639	0.399399	-27.9973	69.64024
alpha	0.707	0.137	5.14424	0.000001	0.434	0.980
epsilon	-0.638	0.302	-2.11641	0.036844	-1.237	-0.040

24jC6HL 180mLv Southeast Wall Geophone

	(Cann 24jC6 180 SE Geo) Dep. Var. : PPV -- R = 0.745 Level of confidence: 95.0% (alpha=0.050)					
	Estimate	Standard error	t-value df = 38	p-value	Lo. Conf Limit	Up. Conf Limit
K	836.5110	1821.968	0.45912	0.648760	-2851.87	4524.893
alpha	0.764	0.289	2.64568	0.011792	0.179	1.348
epsilon	-1.688	0.453	-3.72304	0.000636	-2.606	-0.770

	(Cann 24jC6 180 SE Geo) Dep. Var. : EDWtot - R = 0.747 Level of confidence: 95.0% (alpha=0.050)					
	Estimate	Standard error	t-value df = 38	p-value	Lo. Conf Limit	Up. Conf Limit
K	0.19573	0.951382	0.20574	0.838096	-1.73024	2.121705
alpha	3.954	1.118	3.53792	0.001082	1.692	6.217
epsilon	-2.837	1.014	-2.79892	0.008011	-4.889	-0.785

	(Cann 24jC6 180 SE Geo) Dep. Var. : MNS -- R = 0.810 Level of confidence: 95.0% (alpha=0.050)					
	Estimate	Standard error	t-value df = 38	p-value	Lo. Conf Limit	Up. Conf Limit
K	7.74315	13.84883	0.55912	0.579361	-20.2923	35.77863
alpha	1.263	0.269	4.68983	0.000035	0.718	1.808
epsilon	-1.134	0.342	-3.31681	0.002012	-1.826	-0.442

24jC6HL 180mLv Southwest Wall Accelerometer and Geophone

	(Cann 24jC6 180 SW Acc-Geo) Dep. Var. : PPV -- R = 0.892 Level of confidence: 95.0% (alpha=0.050)					
	Estimate	Standard error	t-value df = 79	p-value	Lo. Conf Limit	Up. Conf Limit
K	6444.327	6275.746	1.0269	0.307619	-6047.23	18935.89
alpha	0.510	0.164	3.1106	0.002597	0.183	0.836
epsilon	-1.836	0.130	-14.1350	0.000000	-2.095	-1.578

	(Cann 24jC6 180 SW Acc-Geo) Dep. Var. : EDWtot -- R = 0.977 Level of confidence: 95.0% (alpha=0.050)					
	Estimate	Standard error	t-value df = 79	p-value	Lo. Conf Limit	Up. Conf Limit
K	8419694	7603127	1.1074	0.271482	-6713952	23553340
alpha	0.731	0.152	4.8030	0.000007	0.428	1.034
epsilon	-3.301	0.143	-23.0421	0.000000	-3.586	-3.016

	(Cann 24jC6 180 SW Acc-Geo) Dep. Var. : MNS -- R = 0.932 Level of confidence: 95.0% (alpha=0.050)					
	Estimate	Standard error	t-value df = 79	p-value	Lo. Conf Limit	Up. Conf Limit
K	2463.026	2275.408	1.0825	0.282344	-2066.06	6992.113
alpha	0.702	0.159	4.4140	0.000032	0.39	1.019
epsilon	-1.999	0.117	-17.1128	0.000000	-2.23	-1.766

24jC6HL 180mLv Southwest Wall Accelerometer

(Cann 24jC6 180 SW Acc)
Dep. Var. : PPV - R = 0.905
Level of confidence: 95.0% (alpha=0.050)

	Estimate	Standard error	t-value df = 38	p-value	Lo. Conf Limit	Up. Conf Limit
K	519.4789	624.9695	0.83121	0.411049	-745.706	1784.664
alpha	0.808	0.199	4.05763	0.000238	0.405	1.210
epsilon	-1.350	0.164	-8.24763	0.000000	-1.681	-1.018

(Cann 24jC6 180 SW Acc)
Dep. Var. : EDWtot -- R = 0.983
Level of confidence: 95.0% (alpha=0.050)

	Estimate	Standard error	t-value df = 38	p-value	Lo. Conf Limit	Up. Conf Limit
K	1336665	1478768	0.9039	0.371741	-1656943	4330274
alpha	0.929	0.184	5.0527	0.000011	0.557	1.301
epsilon	-2.899	0.171	-16.9293	0.000000	-3.245	-2.552

(Cann 24jC6 180 SW Acc)
Dep. Var. : MNS -- R = 0.945
Level of confidence: 95.0% (alpha=0.050)

	Estimate	Standard error	t-value df = 38	p-value	Lo. Conf Limit	Up. Conf Limit
K	260.5938	299.5277	0.8700	0.389755	-345.768	866.9560
alpha	0.971	0.195	4.9865	0.000014	0.577	1.365
epsilon	-1.567	0.148	-10.5876	0.000000	-1.867	-1.268

24jC6HL 180mLv Southwest Wall Geophone

(Cann 24jC6 180 SW Geo)
Dep. Var. : PPV -- R = 0.890
Level of confidence: 95.0% (alpha=0.050)

	Estimate	Standard error	t-value df = 38	p-value	Lo. Conf Limit	Up. Conf Limit
K	1251.994	1220.136	1.02611	0.311328	-1218.04	3722.030
alpha	0.487	0.112	4.34855	0.000099	0.260	0.714
epsilon	-1.494	0.185	-8.07429	0.000000	-1.869	-1.120

(Cann 24jC6 180 SW Geo)
Dep. Var. : EDWtot -- R = 0.858
Level of confidence: 95.0% (alpha=0.050)

	Estimate	Standard error	t-value df = 38	p-value	Lo. Conf Limit	Up. Conf Limit
K	419.7394	1513.672	0.27730	0.783054	-2644.53	3484.008
alpha	1.831	0.540	3.39048	0.001640	0.738	2.924
epsilon	-2.267	0.496	-4.56614	0.000051	-3.272	-1.262

(Cann 24jC6 180 SW Geo)
Dep. Var. : MNS -- R = 0.901
Level of confidence: 95.0% (alpha=0.050)

	Estimate	Standard error	t-value df = 38	p-value	Lo. Conf Limit	Up. Conf Limit
K	79.61594	113.8885	0.69907	0.488766	-150.939	310.1712
alpha	1.032	0.188	5.47473	0.000003	0.650	1.413
epsilon	-1.568	0.239	-6.56142	0.000000	-2.051	-1.084

24jC6HL Cleaner 220-200-180 Southwest Wall Acc's and Geo's

(Cann 24jC6 CR 220-200-180 SW Acc-Geo)
Dep. Var. : PPA -- R = 0.682
Level of confidence: 95.0% (alpha=0.050)

	Estimate	Standard error	t-value df = 78	p-value	Lo. Conf Limit	Up. Conf Limit
K	1806.419	2077.959	0.86932	0.387337	-2330.48	5943.316
alpha	0.537	0.228	2.35613	0.020978	0.083	0.991
epsilon	-1.181	0.156	-7.58942	0.000000	-1.491	-0.871

Cann 24jC6 CR 220-200-180 SW Acc-Geo
Dep. Var. : EDWtot -- R = 0.633
Level of confidence: 95.0% (alpha=0.050)

	Estimate	Standard error	t-value df = 78	p-value	Lo. Conf Limit	Up. Conf Limit
K	1972.509	5448.168	0.36205	0.718294	-8873.96	12818.98
alpha	1.230	0.538	2.28733	0.024887	0.159	2.301
epsilon	-1.931	0.359	-5.37204	0.000001	-2.646	-1.215

(Cann 24jC6 CR 220-200-180 SW Acc-Geo)
Dep. Var. : MNS -- R = 0.645
Level of confidence: 95.0% (alpha=0.050)

	Estimate	Standard error	t-value df = 78	p-value	Lo. Conf Limit	Up. Conf Limit
K	102.8963	119.4772	0.86122	0.391756	-134.965	340.7572
alpha	0.595	0.232	2.57084	0.012048	0.134	1.056
epsilon	-1.049	0.149	-7.03815	0.000000	-1.346	-0.752

24jC6HL Cleaner 220mLv Southwest Wall Acc and Geo

(Cann 24jC6 CR 220 SW Acc-Geo)
Dep. Var. : PPA -- R = 0.959
Level of confidence: 95.0% (alpha=0.050)

	Estimate	Standard error	t-value df = 12	p-value	Lo. Conf Limit	Up. Conf Limit
K	88005.95	79820.33	1.10255	0.291844	-85907.6	261919.5
alpha	0.936	0.190	4.93184	0.000347	0.523	1.350
epsilon	-3.197	0.418	-7.63973	0.000006	-4.109	-2.285

(Cann 24jC6 CR 220 SW Acc-Geo)
Dep. Var. : EDWtot -- R = 0.915
Level of confidence: 95.0% (alpha=0.050)

	Estimate	Standard error	t-value df = 12	p-value	Lo. Conf Limit	Up. Conf Limit
K	1.565309E+09	5.7580E+09	0.2719	0.7904	-1.0980E+10	1.411085E+10
alpha	0.864	0.473	1.8280	0.0925	-0.166	1.893
epsilon	-6.364	1.553	-4.0986	0.0015	-9.747	-2.981

(Cann 24jC6 CR 220 SW Acc-Geo)
Dep. Var. : MNS -- R = 0.929
Level of confidence: 95.0% (alpha=0.050)

	Estimate	Standard error	t-value df = 12	p-value	Lo. Conf Limit	Up. Conf Limit
K	11050.39	10897.17	1.01406	0.330564	-12692.5	34793.28
alpha	0.421	0.171	2.45756	0.030173	0.048	0.7934
epsilon	-2.445	0.374	-6.53556	0.000028	-3.260	-1.6300

24jC6HL Cleaner 200mLv Southwest Wall Acc and Geo

(Cann 24jC6 CR 200 SW Acc-Geo)
Dep. Var. : PPA -- R = 0.677
Level of confidence: 95.0% (alpha=0.050)

	Estimate	Standard error	t-value df = 32	p-value	Lo. Conf Limit	Up. Conf Limit
K	1763.906	3046.997	0.57890	0.566710	-4442.62	7970.435
alpha	0.519	0.331	1.56712	0.126923	-0.155	1.193
epsilon	-1.141	0.281	-4.05959	0.000296	-1.713	-0.568

(Cann 24jC6 CR 200 SW Acc-Geo)
Dep. Var. : EDWtot -- R = 0.624
Level of confidence: 95.0% (alpha=0.050)

	Estimate	Standard error	t-value df = 32	p-value	Lo. Conf Limit	Up. Conf Limit
K	1503.966	7302.525	0.20595	0.838133	-13370.8	16378.72
alpha	1.375	0.931	1.47726	0.149380	-0.521	3.270
epsilon	-2.158	0.801	-2.69407	0.011147	-3.789	-0.526

(Cann 24jC6 CR 200 SW Acc-Geo)
Dep. Var. : MNS -- R = 0.639
Level of confidence: 95.0% (alpha=0.050)

	Estimate	Standard error	t-value df = 32	p-value	Lo. Conf Limit	Up. Conf Limit
K	42.19436	85.78748	0.49185	0.626184	-132.549	216.9377
alpha	0.766	0.392	1.95211	0.059722	-0.033	1.565
epsilon	-1.011	0.284	-3.55979	0.001184	-1.589	-0.432

24jC6HL Cleaner 180mLv Southwest Wall Acc and Geo

Cann 24jC6 CR 180 SW Acc-Geo)
Dep. Var. : PPA -- R = 0.729
Level of confidence: 95.0% (alpha=0.050)

	Estimate	Standard error	t-value df = 28	p-value	Lo. Conf Limit	Up. Conf Limit
K	38.40883	112.6602	0.34093	0.735704	-192.365	269.1827
alpha	2.844	0.871	3.26506	0.002887	1.060	4.628
epsilon	-3.468	0.713	-4.86632	0.000040	-4.928	-2.008

(Cann 24jC6 CR 180 SW Acc-Geo)
Dep. Var. : EDWtot -- R = 0.861
Level of confidence: 95.0% (alpha=0.050)

	Estimate	Standard error	t-value df = 28	p-value	Lo. Conf Limit	Up. Conf Limit
K	2546.277	5802.253	0.43884	0.664143	-9339.10	14431.65
alpha	3.268	0.860	3.79898	0.000718	1.506	5.031
epsilon	-5.202	0.973	-5.34817	0.000011	-7.195	-3.210

(Cann 24jC6 CR 180 SW Acc-Geo)
Dep. Var. : MNS -- R = 0.713
Level of confidence: 95.0% (alpha=0.050)

	Estimate	Standard error	t-value df = 28	p-value	Lo. Conf Limit	Up. Conf Limit
K	28.18264	71.55053	0.39388	0.696650	-118.382	174.7472
alpha	2.230	0.749	2.97740	0.005940	0.696	3.764
epsilon	-3.150	0.625	-5.03776	0.000025	-4.431	-1.869

A9.7 Cannington Mine Individual Regression Results: 52h09HL

52h09HL Footwall Accelerometer and Geophone

	(Cann 52h09 FW Acc-Geo) Dep. Var. : PPA -- R = 0.699 Level of confidence: 95.0% (alpha=0.050)					
	Estimate	Standard error	t-value df = 196	p-value	Lo. Conf Limit	Up. Conf Limit
K	127758.0	67105.28	1.9038	0.058395	-4583.11	260099.1
alpha	-0.495	0.113	-4.3674	0.000020	-0.719	-0.272
epsilon	-1.746	0.113	-15.4795	0.000000	-1.968	-1.524

	(Cann 52h09 FW Acc-Geo) Dep. Var. : EDWtot -- R = 0.357 Level of confidence: 95.0% (alpha=0.050)					
	Estimate	Standard error	t-value df = 196	p-value	Lo. Conf Limit	Up. Conf Limit
K	2446.858	2075.150	1.17912	0.239779	-1645.63	6539.347
alpha	0.253	0.190	1.33083	0.184791	-0.122	0.627
epsilon	-1.072	0.200	-5.35761	0.000000	-1.466	-0.677

	(Cann 52h09 FW Acc-Geo) Dep. Var. : MNS -- R = 0.433 Level of confidence: 95.0% (alpha=0.050)					
	Estimate	Standard error	t-value df = 196	p-value	Lo. Conf Limit	Up. Conf Limit
K	80.20311	33.35209	2.40474	0.017114	14.42809	145.9781
alpha	0.183	0.088	2.07440	0.039349	0.009	0.357
epsilon	-0.701	0.108	-6.52050	0.000000	-0.914	-0.489

52h09HL Footwall Accelerometer

	(Cann 52h09 FW Acc) Dep. Var. : PPA -- R = 0.791 Level of confidence: 95.0% (alpha=0.050)					
	Estimate	Standard error	t-value df = 96	p-value	Lo. Conf Limit	Up. Conf Limit
K	912890.1	674138.5	1.3542	0.178865	-425264	2251044
alpha	-0.882	0.156	-5.6663	0.000000	-1.192	-0.573
epsilon	-2.167	0.171	-12.6962	0.000000	-2.505	-1.828

	(Cann 52h09 FW Acc) Dep. Var. : EDWtot -- R = 0.621 Level of confidence: 95.0% (alpha=0.050)					
	Estimate	Standard error	t-value df = 96	p-value	Lo. Conf Limit	Up. Conf Limit
K	260641.9	320247.9	0.81388	0.417730	-375045	896329.1
alpha	-0.636	0.264	-2.40999	0.017858	-1.159	-0.1121
epsilon	-2.120	0.276	-7.68591	0.000000	-2.667	-1.5723

	(Cann 52h09 FW Acc) Dep. Var. : MNS -- R = 0.712 Level of confidence: 95.0% (alpha=0.050)					
	Estimate	Standard error	t-value df = 96	p-value	Lo. Conf Limit	Up. Conf Limit
K	754.0316	444.5387	1.6962	0.093086	-128.371	1636.434
alpha	-0.156	0.126	-1.2447	0.216262	-0.406	0.093
epsilon	-1.386	0.137	-10.1147	0.000000	-1.658	-1.114

52h09HL Footwall Geophone

(Cann 52h09 FW Geo)
Dep. Var. : PPV -- R = 0.621
Level of confidence: 95.0% (alpha=0.050)

	Estimate	Standard error	t-value df = 97	p-value	Lo. Conf Limit	Up. Conf Limit
K	3394.900	2104.377	1.61326	0.109937	-781.705	7571.506
alpha	0.171	0.116	1.46705	0.145598	-0.060	0.402
epsilon	-1.538	0.218	-7.07264	0.000000	-1.970	-1.107

(Cann 52h09 FW Geo)
Dep. Var. : EDWtot -- R = 0.599
Level of confidence: 95.0% (alpha=0.050)

	Estimate	Standard error	t-value df = 97	p-value	Lo. Conf Limit	Up. Conf Limit
K	26460.64	26579.03	0.99555	0.321948	-26291.4	79212.65
alpha	1.089	0.254	4.28971	0.000042	0.585	1.592
epsilon	-3.157	0.498	-6.33407	0.000000	-4.146	-2.168

(Cann 52h09 FW Geo)
Dep. Var. : MNS -- R = 0.626
Level of confidence: 95.0% (alpha=0.050)

	Estimate	Standard error	t-value df = 97	p-value	Lo. Conf Limit	Up. Conf Limit
K	214.8625	105.1678	2.04304	0.043760	6.13345	423.5916
alpha	0.376	0.095	3.94952	0.000149	0.187	0.565
epsilon	-1.228	0.179	-6.84209	0.000000	-1.584	-0.872

52h09HL Hangingwall Accelerometer

(Cann 52h09 HW Acc)
Dep. Var. : PPV -- R = 0.561
Level of confidence: 95.0% (alpha=0.050)

	Estimate	Standard error	t-value df = 98	p-value	Lo. Conf Limit	Up. Conf Limit
K	9591.248	7634.883	1.25624	0.212015	-5559.93	24742.42
alpha	-0.199	0.142	-1.40633	0.162790	-0.480	0.082
epsilon	-1.489	0.209	-7.11152	0.000000	-1.904	-1.073

(Cann 52h09 HW Acc)
Dep. Var. : EDW-tot -- R = 0.518
Level of confidence: 95.0% (alpha=0.050)

	Estimate	Standard error	t-value df = 98	p-value	Lo. Conf Limit	Up. Conf Limit
K	330750.7	401902.0	0.82296	0.412527	-466811	1128312
alpha	-0.373	0.226	-1.64686	0.102791	-0.822	0.076
epsilon	-1.897	0.298	-6.37353	0.000000	-2.488	-1.307

(Cann 52h09 HW Acc)
Dep. Var. : MNS -- R = 0.576
Level of confidence: 95.0% (alpha=0.050)

	Estimate	Standard error	t-value df = 98	p-value	Lo. Conf Limit	Up. Conf Limit
K	2032.211	1469.882	1.38257	0.169940	-884.722	4949.144
alpha	-0.179	0.127	-1.41652	0.159794	-0.431	0.072
epsilon	-1.407	0.192	-7.32191	0.000000	-1.788	-1.026

52h09HL Southeast Wall Accelerometer and Geophones 1 and 2

	(Cann 52h09 SE Acc-Geo1-Geo2) Dep. Var. : PPA -- R = 0.811 Level of confidence: 95.0% (alpha=0.050)					
	Estimate	Standard error	t-value df = 296	p-value	Lo. Conf Limit	Up. Conf Limit
K	6078.672	1974.152	3.0791	0.002271	2193.520	9963.824
alpha	0.479	0.071	6.7319	0.000000	0.339	0.619
epsilon	-1.675	0.062	-27.2277	0.000000	-1.796	-1.554

	(Cann 52h09 SE Acc-Geo1-Geo2) Dep. Var. : EDWtot -- R = 0.709 Level of confidence: 95.0% (alpha=0.050)					
	Estimate	Standard error	t-value df = 296	p-value	Lo. Conf Limit	Up. Conf Limit
K	9090.362	5938.215	1.5308	0.126881	-2596.11	20776.83
alpha	0.669	0.152	4.4087	0.000015	0.371	0.968
epsilon	-2.000	0.114	-17.5014	0.000000	-2.225	-1.775

	(Cann 52h09 SE Acc-Geo1-Geo2) Dep. Var. : MNS -- R = 0.771 Level of confidence: 95.0% (alpha=0.050)					
	Estimate	Standard error	t-value df = 296	p-value	Lo. Conf Limit	Up. Conf Limit
K	129.3199	34.05718	3.7971	0.000178	62.29499	196.3448
alpha	0.493	0.056	8.7765	0.000000	0.382	0.603
epsilon	-1.237	0.051	-24.1953	0.000000	-1.338	-1.137

52h09HL Southeast Wall Accelerometer

	(Cann 52h09 SE Acc) Dep. Var. : PPV -- R = 0.803 Level of confidence: 95.0% (alpha=0.050)					
	Estimate	Standard error	t-value df = 100	p-value	Lo. Conf Limit	Up. Conf Limit
K	1111.703	656.0362	1.6946	0.093268	-189.855	2413.260
alpha	0.487	0.127	3.8443	0.000213	0.236	0.739
epsilon	-1.632	0.126	-12.9384	0.000000	-1.882	-1.381

	(Cann 52h09 SE Acc) Dep. Var. : EDWtot -- R = 0.693 Level of confidence: 95.0% (alpha=0.050)					
	Estimate	Standard error	t-value df = 100	p-value	Lo. Conf Limit	Up. Conf Limit
K	12230.39	14681.54	0.83305	0.406804	-16897.4	41358.14
alpha	0.604	0.272	2.21913	0.028738	0.064	1.143
epsilon	-2.024	0.252	-8.03182	0.000000	-2.524	-1.524

	(Cann 52h09 SE Acc) Dep. Var. : MNS -- R = 0.797 Level of confidence: 95.0% (alpha=0.050)					
	Estimate	Standard error	t-value df = 100	p-value	Lo. Conf Limit	Up. Conf Limit
K	221.5965	113.5210	1.9520	0.053731	-3.62587	446.8189
alpha	0.451	0.108	4.1652	0.000066	0.236	0.666
epsilon	-1.453	0.111	-13.1176	0.000000	-1.673	-1.233

52h09HL Southeast Wall Geophones 1 and 2

	(Cann 52h09 SE Geo1-Geo2) Dep. Var. : PPA -- R = 0.797 Level of confidence: 95.0% (alpha=0.050)					
	Estimate	Standard error	t-value df = 193	p-value	Lo. Conf Limit	Up. Conf Limit
K	10165.49	3830.021	2.6542	0.008614	2611.419	17719.56
alpha	0.507	0.058	8.7088	0.000000	0.392	0.622
epsilon	-1.898	0.099	-19.1543	0.000000	-2.094	-1.703

	(Cann 52h09 SE Geo1-Geo2) Dep. Var. : EDWtot -- R = 0.829 Level of confidence: 95.0% (alpha=0.050)					
	Estimate	Standard error	t-value df = 193	p-value	Lo. Conf Limit	Up. Conf Limit
K	12005.72	6433.167	1.8662	0.063527	-682.621	24694.06
alpha	1.074	0.119	9.0123	0.000000	0.839	1.310
epsilon	-2.633	0.142	-18.5369	0.000000	-2.914	-2.353

	(Cann 52h09 SE Geo1-Geo2) Dep. Var. : MNS -- R = 0.802 Level of confidence: 95.0% (alpha=0.050)					
	Estimate	Standard error	t-value df = 193	p-value	Lo. Conf Limit	Up. Conf Limit
K	325.4837	108.3185	3.0049	0.003010	111.8438	539.1236
alpha	0.541	0.051	10.6970	0.000000	0.441	0.641
epsilon	-1.534	0.086	-17.7368	0.000000	-1.704	-1.363

A9.8 Cannington Mine Individual Regression Results: 52h04HL

52h04HL Northwest Wall Accelerometer and Geophones 1 and 2

	(Cann 52h04 NW Acc-Geo1-Geo2) Dep. Var. : PPV -- R = 0.560 Level of confidence: 95.0% (alpha=0.050)					
	Estimate	Standard error	t-value df = 258	p-value	Lo. Conf Limit	Up. Conf Limit
K	2178.947	1610.996	1.35255	0.177385	-993.428	5351.322
alpha	0.454	0.095	4.76446	0.000003	0.266	0.642
epsilon	-1.501	0.183	-8.21378	0.000000	-1.861	-1.141

	(Cann 52h04 NW Acc-Geo1-Geo2) Dep. Var. : EDWtot -- R = 0.386 Level of confidence: 95.0% (alpha=0.050)					
	Estimate	Standard error	t-value df = 258	p-value	Lo. Conf Limit	Up. Conf Limit
K	13868.76	24040.28	0.57690	0.564512	-33471.4	61208.92
alpha	0.766	0.274	2.79783	0.005533	0.227	1.305
epsilon	-1.799	0.375	-4.79444	0.000003	-2.538	-1.060

	(Cann 52h04 NW Acc-Geo1-Geo2) Dep. Var. : MNS -- R = 0.386 Level of confidence: 95.0% (alpha=0.050)					
	Estimate	Standard error	t-value df = 258	p-value	Lo. Conf Limit	Up. Conf Limit
K	203.5748	139.1509	1.46298	0.144690	-70.4413	477.5908
alpha	0.488	0.088	5.52442	0.000000	0.314	0.662
epsilon	-1.148	0.164	-6.98968	0.000000	-1.472	-0.825

52h04HL Northwest Wall Accelerometer

(Cann 52h04 NW Acc)
Dep. Var. : PPA -- R = 0.915
Level of confidence: 95.0% (alpha=0.050)

	Estimate	Standard error	t-value df = 120	p-value	Lo. Conf Limit	Up. Conf Limit
K	19651713	12186979	1.6125	0.109476	-4477657	43781084
alpha	0.613	0.061	10.0574	0.000000	0.492	0.734
epsilon	-3.793	0.176	-21.5344	0.000000	-4.142	-3.444

(Cann 52h04 NW Acc)
Dep. Var. : EDWtot -- R = 0.909
Level of confidence: 95.0% (alpha=0.050)

	Estimate	Standard error	t-value df = 120	p-value	Lo. Conf Limit	Up. Conf Limit
K	250522567	277519340	0.9027	0.368482	-298946413	799991547
alpha	1.296	0.146	8.8908	0.000000	1.007	1.584
epsilon	-5.148	0.281	-18.3114	0.000000	-5.705	-4.592

(Cann 52h04 NW Acc)
Dep. Var. : MNS -- R = 0.890
Level of confidence: 95.0% (alpha=0.050)

	Estimate	Standard error	t-value df = 120	p-value	Lo. Conf Limit	Up. Conf Limit
K	54359.68	29188.82	1.8623	0.065000	-3432.15	112151.5
alpha	0.599	0.059	10.0798	0.000000	0.481	0.72
epsilon	-2.755	0.146	-18.8371	0.000000	-3.044	-2.47

52h04HL Northwest Wall Geophones 1 and 2

(Cann 52h04 NW Geo1-Geo2)
Dep. Var. : PPA -- R = 0.835
Level of confidence: 95.0% (alpha=0.050)

	Estimate	Standard error	t-value df = 135	p-value	Lo. Conf Limit	Up. Conf Limit
K	80910.04	49433.93	1.6367	0.104016	-16855.1	178675.1
alpha	0.493	0.081	6.0856	0.000000	0.333	0.654
epsilon	-2.529	0.177	-14.3157	0.000000	-2.879	-2.180

(Cann 52h04 NW Geo1-Geo2)
Dep. Var. : EDWtot -- R = 0.795
Level of confidence: 95.0% (alpha=0.050)

	Estimate	Standard error	t-value df = 135	p-value	Lo. Conf Limit	Up. Conf Limit
K	857010.7	1209897	0.7083	0.479959	-1535793	3249815
alpha	1.273	0.26	4.8304	0.000004	0.752	1.795
epsilon	-4.245	0.32	-13.3208	0.000000	-4.875	-3.615

(Cann 52h04 NW Geo1-Geo2)
Dep. Var. : MNS -- R = 0.814
Level of confidence: 95.0% (alpha=0.050)

	Estimate	Standard error	t-value df = 135	p-value	Lo. Conf Limit	Up. Conf Limit
K	1698.926	1068.081	1.5906	0.114031	-413.409	3811.262
alpha	0.588	0.090	6.5452	0.000000	0.411	0.766
epsilon	-2.120	0.168	-12.6535	0.000000	-2.452	-1.789

52h04HL Footwall Accelerometer and Geophones 1 and 2

	(Cann 52h04 FW Acc-Geo1-Geo2) Dep. Var. : PPA -- R = 0.739 Level of confidence: 95.0% (alpha=0.050)					
	Estimate	Standard error	t-value df = 278	p-value	Lo. Conf Limit	Up. Conf Limit
K	5284.066	5300.817	0.9968	0.319709	-5150.77	15718.90
alpha	0.602	0.175	3.4322	0.000690	0.257	0.947
epsilon	-1.977	0.153	-12.9359	0.000000	-2.278	-1.676

	(Cann 52h04 FW Acc-Geo1-Geo2) Dep. Var. : EDW-tot -- R = 0.323 Level of confidence: 95.0% (alpha=0.050)					
	Estimate	Standard error	t-value df = 278	p-value	Lo. Conf Limit	Up. Conf Limit
K	776.2358	2089.948	0.37141	0.710612	-3337.90	4890.370
alpha	0.794	0.483	1.64485	0.101130	-0.156	1.745
epsilon	-1.289	0.407	-3.17063	0.001691	-2.090	-0.489

	(Cann 52h04 FW Acc-Geo1-Geo2) Dep. Var. : MNS -- R = 0.598 Level of confidence: 95.0% (alpha=0.050)					
	Estimate	Standard error	t-value df = 278	p-value	Lo. Conf Limit	Up. Conf Limit
K	3.387096	2.851967	1.18763	0.235991	-2.22710	9.001290
alpha	0.824	0.136	6.08046	0.000000	0.557	1.091
epsilon	-0.492	0.145	-3.38200	0.000823	-0.778	-0.206

52h04HL Footwall Accelerometer

	(Cann 52h04 FW Acc) Dep. Var. : PPA -- R = 0.747 Level of confidence: 95.0% (alpha=0.050)					
	Estimate	Standard error	t-value df = 96	p-value	Lo. Conf Limit	Up. Conf Limit
K	632945.5	1744442	0.36284	0.717525	-2829744	4095635
alpha	0.186	0.396	0.46941	0.639843	-0.601	0.973
epsilon	-3.230	0.545	-5.92182	0.000000	-4.312	-2.147

	(Cann 52h04 FW Acc) Dep. Var. : EDW-tot -- R = 0.254 Level of confidence: 95.0% (alpha=0.050)					
	Estimate	Standard error	t-value df = 96	p-value	Lo. Conf Limit	Up. Conf Limit
K	66615.39	527503.3	0.12628	0.899771	-980470	1113701
alpha	0.299	1.258	0.23738	0.812868	-2.199	2.797
epsilon	-2.263	1.712	-1.32151	0.189473	-5.661	1.136

	(Cann 52h04 FW Acc) Dep. Var. : MNS -- R = 0.566 Level of confidence: 95.0% (alpha=0.050)					
	Estimate	Standard error	t-value df = 96	p-value	Lo. Conf Limit	Up. Conf Limit
K	2066.195	6068.266	0.34049	0.734230	-9979.22	14111.61
alpha	0.260	0.408	0.63825	0.524831	-0.549	1.069
epsilon	-2.140	0.584	-3.66241	0.000409	-3.300	-0.980

52h04HL Footwall Geophones 1 and 2

(Cann 52h04 FW Geo1-Geo2)
Dep. Var. : PPA -- R = 0.850
Level of confidence: 95.0% (alpha=0.050)

	Estimate	Standard error	t-value df = 179	p-value	Lo. Conf Limit	Up. Conf Limit
K	65564.76	65303.54	1.0040	0.316734	-63299.1	194428.6
alpha	0.531	0.129	4.1043	0.000062	0.276	0.786
epsilon	-2.623	0.203	-12.8906	0.000000	-3.025	-2.222

(Cann 52h04 FW Geo1-Geo2)
Dep. Var. : EDWtot -- R = 0.723
Level of confidence: 95.0% (alpha=0.050)

	Estimate	Standard error	t-value df = 179	p-value	Lo. Conf Limit	Up. Conf Limit
K	732807.5	1402273	0.52259	0.601909	-2034306	3499921
alpha	0.588	0.27	2.17593	0.030871	0.055	1.122
epsilon	-3.205	0.38	-8.42697	0.000000	-3.956	-2.455

(Cann 52h04 FW Geo1-Geo2)
Dep. Var. : MNS -- R = 0.806
Level of confidence: 95.0% (alpha=0.050)

	Estimate	Standard error	t-value df = 179	p-value	Lo. Conf Limit	Up. Conf Limit
K	72.86444	60.47297	1.20491	0.229829	-46.4672	192.1961
alpha	0.683	0.101	6.77033	0.000000	0.484	0.882
epsilon	-1.223	0.176	-6.96491	0.000000	-1.570	-0.877

52h04HL Southeast Wall Accelerometer and Geophone

(Cann 52h04 SE Acc-Geo)
Dep. Var. : PPA -- R = 0.829
Level of confidence: 95.0% (alpha=0.050)

	Estimate	Standard error	t-value df = 242	p-value	Lo. Conf Limit	Up. Conf Limit
K	692.9389	291.8515	2.3743	0.018364	118.0455	1267.832
alpha	0.789	0.078	10.0967	0.000000	0.635	0.943
epsilon	-1.523	0.076	-20.1721	0.000000	-1.672	-1.375

(Cann 52h04 SE Acc-Geo)
Dep. Var. : EDWtot -- R = 0.547
Level of confidence: 95.0% (alpha=0.050)

	Estimate	Standard error	t-value df = 242	p-value	Lo. Conf Limit	Up. Conf Limit
K	10.56865	14.07681	0.75078	0.453512	-17.1601	38.29736
alpha	1.354	0.263	5.13961	0.000001	0.835	1.873
epsilon	-0.906	0.145	-6.22509	0.000000	-1.192	-0.619

(Cann 52h04 SE Acc-Geo)
Dep. Var. : MNS -- R = 0.627
Level of confidence: 95.0% (alpha=0.050)

	Estimate	Standard error	t-value df = 242	p-value	Lo. Conf Limit	Up. Conf Limit
K	7.682693	3.332693	2.30525	0.021999	1.117903	14.24748
alpha	0.645	0.077	8.38890	0.000000	0.494	0.797
epsilon	-0.580	0.087	-6.70536	0.000000	-0.750	-0.410

52h04HL Southeast Wall Accelerometer

	(Cann 52h04 SE Acc) Dep. Var. : PPV -- R = 0.897 Level of confidence: 95.0% (alpha=0.050)					
	Estimate	Standard error	t-value df = 120	p-value	Lo. Conf Limit	Up. Conf Limit
K	187.7344	83.96244	2.2359	0.027205	21.49460	353.9742
alpha	0.733	0.079	9.3248	0.000000	0.577	0.889
epsilon	-1.621	0.095	-17.0305	0.000000	-1.809	-1.432

	(Cann 52h04 SE Acc) Dep. Var. : EDWtot -- R = 0.823 Level of confidence: 95.0% (alpha=0.050)					
	Estimate	Standard error	t-value df = 120	p-value	Lo. Conf Limit	Up. Conf Limit
K	567.4199	573.6346	0.9892	0.324572	-568.337	1703.176
alpha	1.104	0.182	6.0527	0.000000	0.743	1.466
epsilon	-2.363	0.212	-11.1392	0.000000	-2.783	-1.943

	(Cann 52h04 SE Acc) Dep. Var. : MNS -- R = 0.873 Level of confidence: 95.0% (alpha=0.050)					
	Estimate	Standard error	t-value df = 120	p-value	Lo. Conf Limit	Up. Conf Limit
K	55.50591	22.65631	2.4499	0.015733	10.64799	100.3638
alpha	0.578	0.070	8.2700	0.000000	0.439	0.716
epsilon	-1.407	0.093	-15.1800	0.000000	-1.591	-1.224

52h04HL Southeast Wall Geophone

	(Cann 52h04 SE Geo) Dep. Var. : PPV -- R = 0.860 Level of confidence: 95.0% (alpha=0.050)					
	Estimate	Standard error	t-value df = 119	p-value	Lo. Conf Limit	Up. Conf Limit
K	2209.932	1238.421	1.7845	0.076895	-242.265	4662.129
alpha	0.659	0.062	10.6014	0.000000	0.536	0.782
epsilon	-1.946	0.156	-12.4380	0.000000	-2.256	-1.637

	(Cann 52h04 SE Geo) Dep. Var. : EDWtot -- R = 0.847 Level of confidence: 95.0% (alpha=0.050)					
	Estimate	Standard error	t-value df = 119	p-value	Lo. Conf Limit	Up. Conf Limit
K	12368.52	14564.64	0.8492	0.397467	-16470.9	41207.96
alpha	1.406	0.167	8.4151	0.000000	1.075	1.737
epsilon	-3.061	0.276	-11.1033	0.000000	-3.607	-2.515

	(Cann 52h04 SE Geo) Dep. Var. : MNS -- R = 0.868 Level of confidence: 95.0% (alpha=0.050)					
	Estimate	Standard error	t-value df = 119	p-value	Lo. Conf Limit	Up. Conf Limit
K	302.7290	146.7139	2.0634	0.041250	12.22074	593.2373
alpha	0.655	0.055	11.8651	0.000000	0.545	0.764
epsilon	-1.624	0.134	-12.1508	0.000000	-1.889	-1.360

APPENDIX 10 : CRITICAL TENSILE PLANE STRAIN DAMAGE PREDICTIONS FOR STUDY STOPES

A10.1 KBGM Stope dB10-38T 480
A10.2 Cannington Mine 24jC6HL..... 483

A10.1 KBGM Stope dB10-38T

A comparison was performed for KBGM stope dB10-38T between the damage predicted using the author's proposed strain and energy-based approaches and the critical tensile plane strain model. A number of possible rock tensile strengths were used in the critical tensile plane strain damage predictions, as identified by various proposed forms of the equation in the published literature. These tensile strengths were defined by ratios of the UCS to σ_T; the values specified in the various forms of the critical tensile plane strain model are 10 and 15. Additionally, the value of 12 was selected based on the Griffith fracture criteria. To compare the static and dynamic conditions, both the static and dynamic Young's Modulus were used.

Two different approaches were applied for predicting the distances at which the values of PPV_{crit} were exceeded. These approaches included traditional log-log linear regression using cube root Scaled Distance and nonlinear multi-variable regression using the general charge weight scaling relationship discussed in Chapter 5. The data set used in both regressions was the combined data set for all monitoring orientations in stope dB10-38T. Figure A10.1 and A10.2 show the two different vibration prediction model results and the 95% upper confidence limits for both data sets.

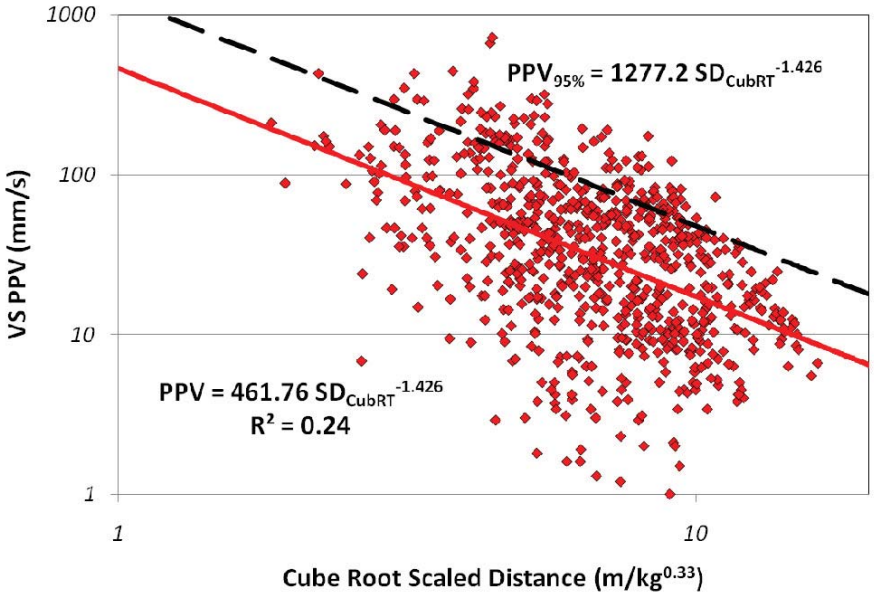

Figure A10.1. Log-log linear regression of KBGM dB10-38T combined data set.

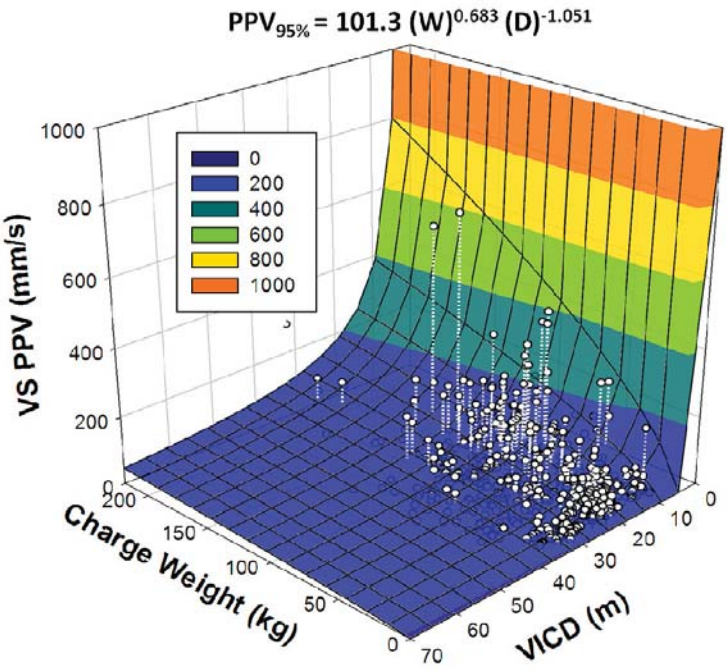

Figure A10.2. Nonlinear regression surface of KBGM dB10-38T combined data set.

The calculated vales of PPV_{crit} and the predicted radius of tensile fracture (PPV_{crit} radius) and fracture extension (PPV_{Ext} radius) for the dB10-38T rock mass are shown in Tables A10.1 to A10.4. Tables A10.1 and A10.2 show the results for a 50kg charge weight. Tables A10.3 and A10.4 show the results for a 100kg charge weight. The differences between the tables with the same charge weight are the PPV prediction models (log-log linear regression of SD_{CubRT} versus nonlinear regression of the charge weight scaling equation).

Table A10.1. Comparisons of PPV_{crit} and predicted tensile fracture radii for the critical tensile plane strain model and nonlinear regression of PPV for a 50kg charge.

UCS (MPa)	UCS/σ_T	σ_T (MPa)	V_p (m/s)	E_{st} (GPa)	E_{dyn} (GPa)	PPV_{crit} (mm/s)	PPV_{crit} Radius (m)	PPV_{Ext} Radius (m)
113*	10	11	5940**	62*		1083	4.7	23.2
113*	12	9	5940**	62*		862	6.1	30.1
113*	15	7.5	5940**	62*		719	7.5	37.1
113*	10	11	5940**		76**	883	5.9	29.3
113*	12	9	5940**		76**	703	7.7	38.0
113*	15	7.5	5940**		76**	586	9.5	46.9

* data determined from rock testing
** values from field measurement/calculations by the author

Table A10.2. Comparisons of PPV_{crit} and associated predicted tensile fracture radii using various forms of the critical tensile plane strain approach and log-log linear regression prediction of PPV for a 50kg charge.

UCS (MPa)	UCS/σ_T	σ_T (MPa)	V_p (m/s)	E_{st} (GPa)	E_{dyn} (GPa)	PPV_{crit} (mm/s)	PPV_{crit} Radius (m)	PPV_{Ext} Radius (m)
113*	10	11	5940**	62*		1083	4.1	10.9
113*	12	9	5940**	62*		862	4.8	12.8
113*	15	7.5	5940**	62*		719	5.5	14.6
113*	10	11	5940**		76**	883	4.8	12.6
113*	12	9	5940**		76**	703	5.6	14.8
113*	15	7.5	5940**		76**	586	6.4	16.8

* data determined from rock testing
** values from field measurement/calculations by the author

Table A10.3. Comparisons of PPV_{crit} and associated predicted tensile fracture radii using various forms of the critical tensile plane strain approach and nonlinear regression prediction of PPV for a 100kg charge.

UCS (MPa)	UCS/σ_T	σ_T (MPa)	V_p (m/s)	E_{st} (GPa)	E_{dyn} (GPa)	PPV_{crit} (mm/s)	PPV_{crit} Radius (m)	PPV_{Ext} Radius (m)
113*	10	11	5940**	62*		1083	9.0	44.3
113*	12	9	5940**	62*		862	11.7	57.6
113*	15	7.5	5940**	62*		719	14.4	71.0
113*	10	11	5940**		76**	883	11.4	56.0
113*	12	9	5940**		76**	703	14.7	72.8
113*	15	7.5	5940**		76**	586	18.2	89.8

* data determined from rock testing
** values from field measurement/calculations by the author

Table A10.4. Comparisons of PPV_{crit} and associated predicted tensile fracture radii using various forms of the critical tensile plane strain approach and log-log linear regression prediction of PPV for a 100kg charge.

UCS (MPa)	UCS/σ_T	σ_T (MPa)	V_p (m/s)	E_{st} (GPa)	E_{dyn} (GPa)	PPV_{crit} (mm/s)	PPV_{crit} Radius (m)	PPV_{Ext} Radius (m)
113*	10	11	5940**	62*		1083	5.2	13.8
113*	12	9	5940**	62*		862	6.1	16.1
113*	15	7.5	5940**	62*		719	6.9	18.3
113*	10	11	5940**		76**	883	6.0	15.9
113*	12	9	5940**		76**	703	7.0	18.6
113*	15	7.5	5940**		76**	586	8.0	21.2

* data determined from rock testing
** values from field measurement/calculations by the author

A10.2 Cannington Mine 24jC6HL

The blast damage predictions for Cannington stope 24jC6HL 200mLv using the critical tensile plane strain model were performed for both the combined data set measured in all three monitored walls and for each independent wall. The only PPV prediction model that was applied to the data was the cube root Scaled Distance model. In addition to the recommended UCS/σ_T ratios of 10, 12, and 15, the tensile strength from rock testing results (13MPa) was used in the prediction of PPV_{crit}. The values of V_p used in the PPV_{crit} calculations reflected values measured in the author's blast vibration monitoring program.

Figures A10.3 to A10.6 show the log-log linear regressions of VSPPV versus SD_{CubRT} for the combined data set collected on the 200mLv and the individual data sets collected in each wall. Significant differences between the attenuation behaviours can be observed for the individual wall data sets.

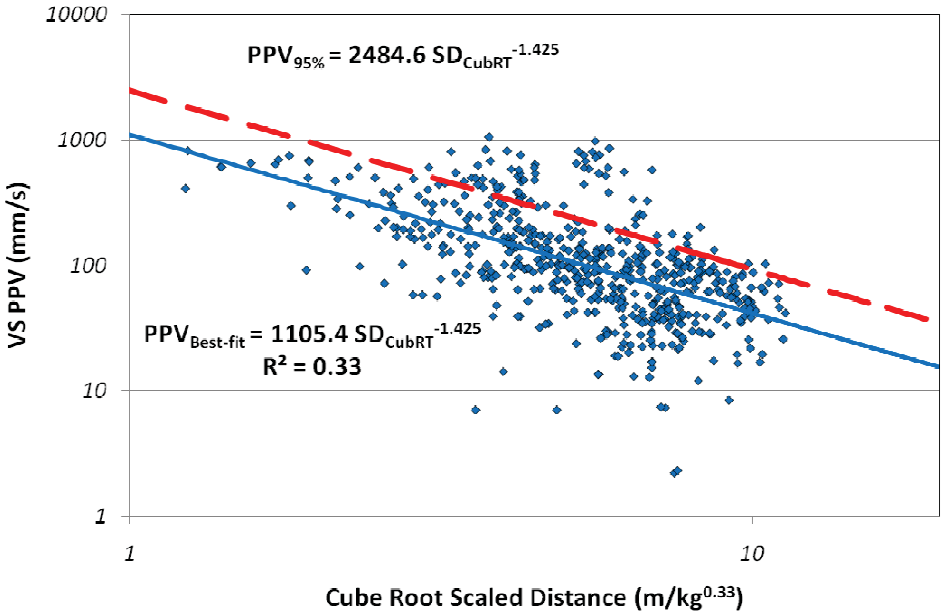

Figure A10.3. Plot of VSPPV versus cube root Scaled Distance for the 24jC6HL 200mLv combined data set.

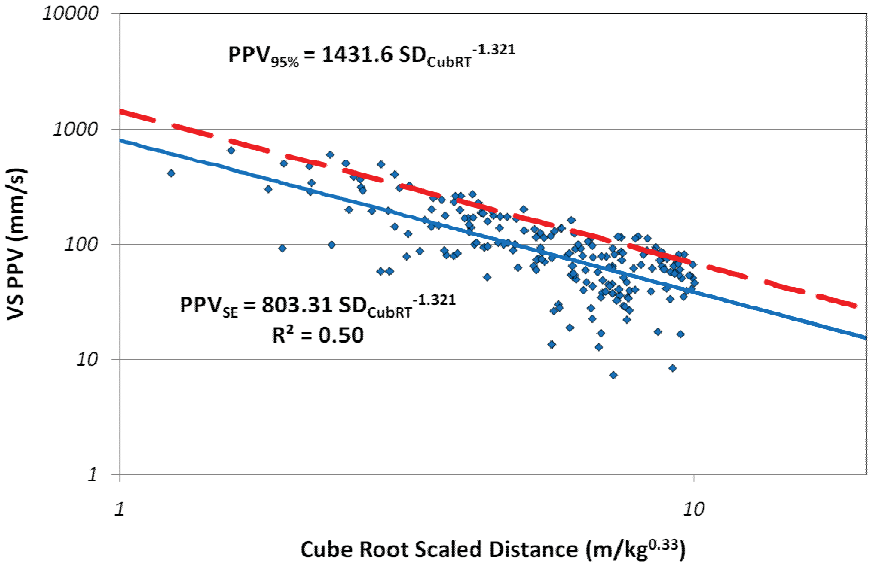

Figure A10.4. Plot of VSPPV versus cube root Scaled Distance for the 24jC6HL 200mLv Southeast wall data set.

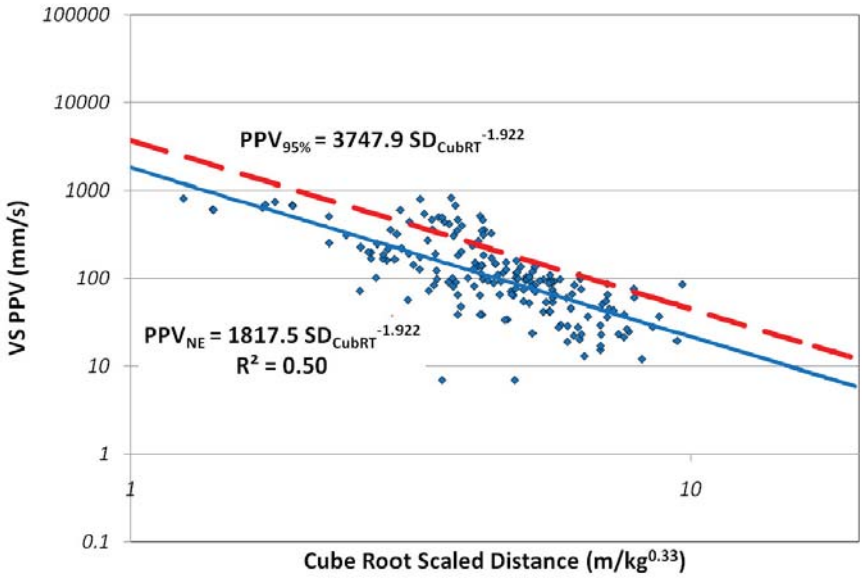

Figure A10.5. Plot of VSPPV versus cube root Scaled Distance for the 24jC6HL 200mLv Northeast wall data set.

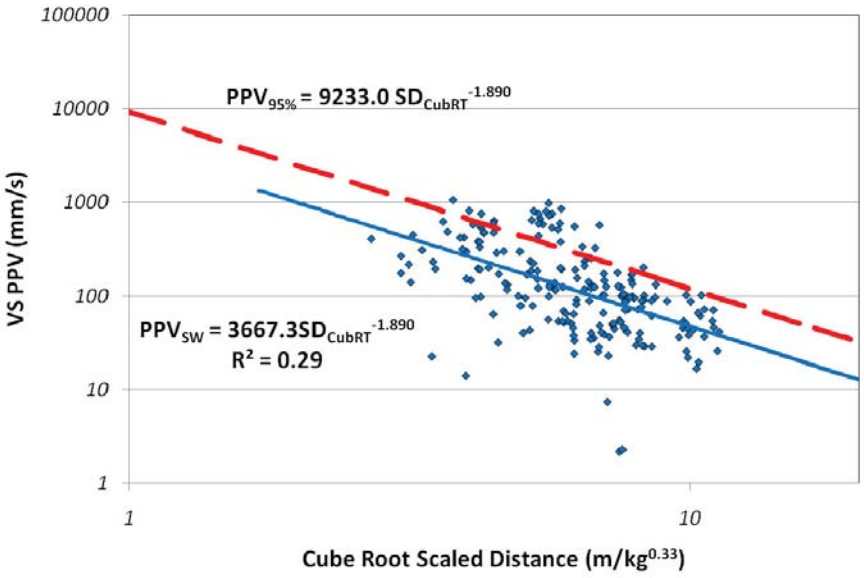

Figure A10.6. Plot of VSPPV versus cube root Scaled Distance for the 24jC6HL 200mLv Southwest wall data set.

Using the 95% upper confidence predictions equations for the combined or individual data sets and the calculated values of PPV_{crit} and PPV_{Ext} (0.25 PPV_{crit}), the extents of fresh tensile fracture and existing discontinuity extension were predicted. The material input values, PPV_{crit} values and the predicted damage extents are shown in Tables A10.5 to A10.9. The charge weights used for each set of calculations reflected those chosen for the damage predictions in Chapter 8.

Table A10.5. Comparisons of predicted PPV_{crit} and associated tensile fracture radii using various forms of the critical tensile plane strain approach and cube root Scaled Distance log-log linear regression prediction of all PPV data for a 50kg charge.

UCS (MPa)	UCS/σ_T	σ_T (MPa)	V_p (m/s)	E_{st} (GPa)	E_{dyn} (GPa)	PPV_{crit} (mm/s)	PPV_{crit} Radius (m)	PPV_{Ext} Radius (m)
209*	10	21	5600**	80*		1463	5.3	14.1
209*	12	17	5600**	80*		1219	6.1	16.1
209*	15	14	5600**	80*		975	7.1	18.8
		13*	5600**	80*		910	7.5	19.7
209	10	21	5600**		87**	1345	5.7	15.0
209	12	17	5600**		87**	1121	6.4	17.0
209	15	14	5600**		87**	897	7.5	19.9
		13*	5600**		87**	837	7.9	20.9

* data determined from rock testing
** values from field measurement/calculations by the author

Table A10.6. Comparisons of predicted PPV_{crit} and associated tensile fracture radii using various forms of the critical tensile plane strain approach and cube root Scaled Distance log-log linear regression prediction of all PPV data for a 75kg charge.

UCS (MPa)	UCS/σ_T	σ_T (MPa)	V_p (m/s)	E_{st} (GPa)	E_{dyn} (GPa)	PPV_{crit} (mm/s)	PPV_{crit} Radius (m)	PPV_{Ext} Radius (m)
209*	10	21	5600**	80*		1463	6.1	16.2
209*	12	17	5600**	80*		1219	7.0	18.4
209*	15	14	5600**	80*		975	8.1	21.5
		13*	5600**	80*		910	8.5	22.6
209	10	21	5600**		87**	1345	6.5	17.1
209	12	17	5600**		87**	1121	7.4	19.5
209	15	14	5600**		87**	897	8.6	22.8
		13*	5600**		87**	837	9.1	23.9

* data determined from rock testing
** values from field measurement/calculations by the author

Table A10.7. Predicted PPV_{crit} and associated tensile fracture radii for the Southeast stope wall using various forms of the critical tensile plane strain approach and cube root Scaled Distance log-log linear regression prediction of PPV for a 50kg charge.

UCS (MPa)	UCS/σ_T	σ_T (MPa)	V_p (m/s)	E_{st} (GPa)	E_{dyn} (GPa)	PPV_{crit} (mm/s)	PPV_{crit} Radius (m)	PPV_{Ext} Radius (m)
209*	10	21	6600**	80*		1724	3.2	9.1
209*	12	17	6600**	80*		1437	3.7	10.5
209*	15	14	6600**	80*		1150	4.3	12.4
		13*	6600**	80*		1073	4.6	13.0
209	10	21	6600**		119**	1159	4.3	12.3
209	12	17	6600**		119**	966	5.0	14.1
209	15	14	6600**		119**	773	5.9	16.8
		13*	6600**		119**	721	6.2	17.7

* data determined from rock testing
** values from field measurement/calculations by the author

Table A10.8. Predicted PPV_{crit} and associated tensile fracture radii for the Northeast stope wall using various forms of the critical tensile plane strain approach and cube root Scaled Distance log-log linear regression prediction of PPV for a 75kg charge.

UCS (MPa)	UCS/σ_T	σ_T (MPa)	V_p (m/s)	E_{st} (GPa)	E_{dyn} (GPa)	PPV_{crit} (mm/s)	PPV_{crit} Radius (m)	PPV_{Ext} Radius (m)
209*	10	21	5150**	80*		1345	7.2	14.8
209*	12	17	5150**	80*		1121	7.9	16.2
209*	15	14	5150**	80*		897	8.9	18.2
		13*	5150**	80*		837	9.2	18.9
209	10	21	5150**		73**	1474	6.8	14.0
209	12	17	5150**		73**	1228	7.5	15.5
209	15	14	5150**		73**	983	8.5	17.4
		13*	5150**		73**	917	8.8	18.0

* data determined from rock testing
** values from field measurement/calculations by the author

Table A10.9. Predicted PPV_{crit} and associated tensile fracture radii for the Southwest stope wall using various forms of the critical tensile plane strain approach and cube root Scaled Distance log-log linear regression prediction of PPV for a 75kg charge.

UCS (MPa)	**UCS/σ_T**	**σ_T (MPa)**	**V_p (m/s)**	**E_{st} (GPa)**	**E_{dyn} (GPa)**	**PPV_{crit} (mm/s)**	**PPV_{crit} Radius (m)**	**PPV_{Ext} Radius (m)**
209*	10	21	5050**	80*		1319	11.8	24.5
209*	12	17	5050**	80*		1099	13.0	27.0
209*	15	14	5050**	80*		880	14.6	30.4
		13*	5050**	80*		821	15.1	31.6
209	10	21	5050**		70**	1508	11.0	22.9
209	12	17	5050**		70**	1256	12.1	25.2
209	15	14	5050**		70**	1005	13.6	28.3
		13*	5050**		70**	938	14.1	29.4

* data determined from rock testing
** values from field measurement/calculations by the author